NATIONAL TECHNICAL UNIVERSITY OF ATHENS
SCHOOL OF MECHANICAL ENGINEERING
MECHANICAL DESIGN & CONTROL SYSTEMS DIVISION
DYNAMICS & ACOUSTICS LABORATORY (DAL)

INNOVATIVE VIBRATION ABSORBERS AND METAMATERIALS FOR LOW-FREQUENCY WAVE MITIGATION

By

Moris Kalderon

Athens, February 2023

Supervising Professor: Dr. Antoniadis A. Ioannis.

DOCTORAL DISSERTATION
A dissertation submitted in partial fulfillment of the requirements
for the degree of Doctorate of Philosophy in Engineering

Εθνικο Μετσοβιο Πολυτεχνειο
Σχολη Μηχανολογων Μηχανικων
Τομεας Μηχανολογικων Κατασκευων & Αυτοματου Ελεγχου
Εργαστηριο Δυναμικης & ακουστικης

Καινοτομες Διαταξεις Απορροφησης Κραδασμων και Μεταυλικων για Ελεγχο Χαμηλοσυχνων Κυματων

Μωρίς Καλδερών

Αθήνα, Φεβρουάριος 2023

Επιβλέπων καθηγητής: Δρ. Αντωνιάδης Α. Ιωάννης

ΔΙΔΑΚΤΟΡΙΚΗ ΔΙΑΤΡΙΒΗ
για τον Επιστημονικό Τίτλο του Διδάκτορα Μηχανικού υποβληθείσα στη Σχολή Μηχανολόγων Μηχανικών του Εθνικού Μετσόβιου Πολυτεχνείου

NATIONAL TECHNICAL UNIVERSITY OF ATHENS
SCHOOL OF MECHANICAL ENGINEERING
MECHANICAL DESIGN AND CONTROL SYSTEMS DIVISION
DYNAMICS AND ACOUSTICS LABORATORY

INNOVATIVE VIBRATION ABSORBERS AND METAMATERIALS FOR LOW-FREQUENCY WAVE MITIGATION

DOCTORAL DISSERTATION

for the title of Doctor of Philosophy submitted in the School of Mechanical Engineering, National Technical University of Athens

MORIS KALDERON

M.Sc. Imperial College London, Diploma in Civil Engineering N.T.U.A.

ADVISORY COMMITTEE:

1. Dr. Antoniadis A. Ioannis,
   Professor N.T.U.A. (Supervisor)
2. Dr. Sapountzakis J. Evangelos,
   Professor N.T.U.A.
3. Dr. Provatidis Christophoros,
   Professor N.T.U.A.

EXAMINATION COMMITTEE:

1. Dr. Antoniadis A. Ioannis,
   Professor N.T.U.A. (Supervisor)
2. Dr. Sapountzakis J. Evangelos,
   Professor N.T.U.A.
3. Dr. Provatidis Christophoros,
   Professor N.T.U.A.
4. Dr. Spitas Vasilis,
   Associate Professor N.T.U.A.
5. Dr. Dimitris Koulocheris,
   Associate Professor NTUA
6. Dr. Savvas Triantafyllou
   Assistant Professor N.T.U.A.
7. Dr. Paradeisiotis Andreas,
   Special Scientist/Researcher CMMI & UCY

ATHENS 2023

The research for this dissertation has received funding from the European Union's Horizon 2020 research and innovation programme under the Marie Skłodowska-Curie grant agreement No 813424 (INSPIRE—Innovative Ground Interface Concepts for Structure Protection).

ABSTRACT

The scope of this dissertation is to provide theoretical and experimental insight towards the mitigation of low-frequency vibrations and noise, by exploiting novel absorbing and metamaterial concepts. Specifically, this research work introduces innovative negative stiffness absorbers as an upgrade to conventional sound absorbing panels and metamaterials. In addition, the potency of amplification mechanisms is harnessed to enhance the vibration control, and sound attenuation properties of locally resonant and phononic metamaterials.

Initially, the KDamper oscillator is implemented in various applications to address many of the inadequacies of conventional passive noise control mechanisms, especially in the low-frequency regime. The concept comprises an optimal combination of appropriate stiffness, damping, and mass elements, including a negative stiffness element. In this work, the KDamper is coupled with a developed inertial amplification mechanism (IAM) and a series of novel mounts are presented based on the synergetic KDamper – IAM concept. This coupled absorber is applied in a novel mounting system for flexible acoustic panels, resulting in a wide and deep frequency band of improved vibration and noise attenuation. The system is subsequently adopted to enhance the unit-cell properties of metamaterial mechanisms. Specifically, the proposed designs aim towards the development of metamaterial-based noise insulation panels that target the low-frequency range. Herein, conceptual implementations are proposed, and the presented mechanisms are evaluated using both analytical and numerical analyses.

Next, a novel dynamic directional amplifier, namely the DDA mechanism, is introduced as a means to artificially increase the resonating mass of an oscillator, with no requirement of complex geometries and heavy parasitic masses. The mechanism comprises a simple rigid link that increases inertia towards the desired direction of motion by coupling the kinematic DoFs of the resonating mass and

forcing the oscillator to move through a prescribed circumferential path. An analytical and experimental framework is developed, and analysis is undertaken to identify the beneficial effects of the DDA to the dynamic response of the system. The DDA is subsequently applied to phononic and locally resonant metamaterials as a means to enhance their dynamic properties. Analytical, numerical and experimental results showcase significant improvements and advantages over the conventional phononic and acoustic structures, such as broader bandgaps and increased damping ratio. Finally, a conceptual design of a seismic metamaterial in the form of a metabarrier is proposed and an investigation of its response under seismic excitation is analyzed. Results indicate the beneficial role of the device and DDA mechanism, hence placing the concept as a compelling alternative to existing seismic protection technologies.

ACKNOWLEDGEMENTS

First and foremost, I would like to express my sincere gratitude to my teacher and supervisor Professor Ioannis Antoniadis, for the exemplary guidance and constant encouragement throughout this incredible journey. His continuous support, motivation, and dedicated involvement in every step of the way extend beyond his academic role. Thank you for supporting my research and for giving me the trust and freedom to implement my ideas.

I would also like to express my deep gratitude and thanks to Professor Evangelos Sapountzakis and Professor Christoforos Provatidis for serving at my Doctoral Advisory Committee. I feel grateful for sharing their expertise and experience with me and helping me grow both as an engineer and a person. Moreover, I would like to express my most sincere gratitude to the other members of my examination committee. Associate Professor Dimitris Koulocheris, Associate Professor Vasileios Spitas, and Assistant Professor Savvas Triantafyllou for serving on my Doctoral Examination Committee and for their constructive comments which enriched this dissertation. Moreover, I would like to extend my most sincere gratitude to Assistant Scientist CMMI Dr. Andreas Paradeisiotis. Thank you for being a member of my Doctoral Examination Committee and especially for all the inspiring discussions we had, the many interesting ideas you gave me, but also the constructive feedback you provided me. I greatly appreciated all this.

Next, I would like to express my warm thanks to my coworkers and friends from the Dynamics & Acoustics Lab, Kostas Fouskas, Christos Yiakopoulos, Dimitris Mylonas and Alberto Erspamer for the pleasant and productive environment we shared, their support and cooperation which helped immensely throughout all these years. I would also like to thank Kyriakos Chondrogiannis from ETH for the fruitful discussions we had and for helping me during the laboratory experiments.

Most of all, my sincere gratitude goes to Antonis Mantakas, more than just a colleague to me. I will always be grateful to you for always being by my side. Thank you for all the interesting discussions, help and proofreading! Without you, this Doctoral journey would not be the same. Looking forward to our next projects!

Finally, I thank my family for their unconditional love and support. My deepest appreciation is expressed to them for being a constant source of inspiration.

Last but not least, I would like to acknowledge "INSPIRE—Innovative Ground Interface Concepts for Structure Protection"). Without the financial support of the European Union's Horizon 2020 research and innovation programme - Marie Sklodowska-Curie this research would not be feasible.

ΣΥΝΟΨΗ

Αντικείμενο της παρούσας διδακτορικής διατριβής αποτελεί η θεωρητική και πειραματική διερεύνηση μέσων για τον μετριασμό δονήσεων και του χαμηλόσυχνου θορύβου, αξιοποιώντας καινοτόμα δυναμικά συστήματα απορρόφησης ταλαντώσεων, καθώς και τις δυναμικές ιδιότητες των μεταϋλικών. Συγκεκριμένα, προτείνονται νέα συστήματα παθητικής μόνωσης αρνητικής δυσκαμψίας και περιοδικές διατάξεις, με στόχο τον σχεδιασμό νέων, και την αναβάθμιση συμβατικών ηχοαπορροφητικών πετασμάτων. Επιπλέον, εξετάζονται οι δυνατότητες διαφόρων μηχανισμών δυναμικής ενίσχυσης με σκοπό τη βελτίωση των ιδιοτήτων ηχομείωσης ακουστικών μεταϋλικών και φωνονικών κρυστάλλων σε εφαρμογές ελέγχου θορύβου και χαμηλόσυχνων κραδασμών.

Με στόχο την αντιμετώπιση πολλών από τις ανεπάρκειες των συμβατικών παθητικών μέσων ελέγχου θορύβου και ταλαντώσεων, ιδίως στη περιοχή χαμηλών συχνοτήτων, εισάγεται ο βελτιωμένος ταλαντωτής KDamper. Ο KDamper είναι ένα καινοτόμο σύστημα παθητικής μόνωσης ταλαντώσεων και απόσβεσης, βασισμένο στον βέλτιστο συνδυασμό στοιχείων στιβαρότητας, συμπεριλαμβανομένου και ενός στοιχείου αρνητικής στιβαρότητας. Ο σχεδιασμός των συστημάτων με βάση τον KDamper βασίζεται σε πρόβλημα βελτιστοποίησης βασισμένο σε τεχνικά κριτήρια, ανάλογα με την εκάστοτε κατασκευή. Συγκεκριμένα, στην παρούσα έρευνα, συνδυάζεται με τον μηχανισμό αδρανειακής ενίσχυσης (IAM) με στόχο την ανάπτυξη βάσεων στήριξης ακουστικών πετασμάτων. Ο συζευγμένος μηχανισμός KDamper-IAM στη συνέχεια υιοθετείται σε περιοδικές διατάξεις οι οποίες παρουσιάζουν ζώνες μερικού η πλήρους εξασθένισης της διάδοσης του ήχου σε συγκεκριμένα εύρη συχνοτήτων (bandgaps). Στο πλαίσιο αυτό, προτείνονται υλοποιήσεις για την κατασκευή πετασμάτων τύπου σάντουιτς οι οποίες αξιολογούνται χρησιμοποιώντας τόσο αναλυτικές όσο και αριθμητικές αναλύσεις.

Στη συνέχεια, παρουσιάζεται ένας νέος δυναμικός ενισχυτής κατεύθυνσης, ο μηχανισμός DDA, ως μέσο για την τεχνητή αύξηση της μάζας συντονισμού ενός ταλαντωτή, χωρίς την απαίτηση πολύπλοκων γεωμετριών. Ο μηχανισμός αποτελείται από έναν απλό, άκαμπτο σύνδεσμο που αυξάνει την αδράνεια προς την επιθυμητή κατεύθυνση κίνησης, περιορίζοντας τους κινηματικούς βαθμούς ελευθερίας της μάζας συντονισμού. Με τον τρόπο αυτό ο ταλαντωτής αναγκάζεται να κινηθεί μέσω μιας προδιαγεγραμμένης διαδρομής. Εν προκειμένω, ο μηχανισμός DDA εφαρμόζεται στη βάση φωνονικών κρυστάλλων και σε τοπικά συντονισμένα μεταϋλικά ως μέσο ενίσχυσης της αδράνειας των στοιχείων τους. Τα αναλυτικά, αριθμητικά και πειραματικά αποτελέσματα αναδεικνύουν σημαντικές βελτιώσεις και πλεονεκτήματα σε σχέση με τις αντίστοιχες συμβατικές περιοδικές δομές, όπως ευρύτερες ζώνες περιορισμού της διάδοσης του κύματος και αυξημένο λόγο απόσβεσης. Τέλος, παρουσιάζεται ο σχεδιασμός ενός σεισμικού μεταϋλικού για την προστασία κατασκευών έναντι επιφανειακών κυμάτων και διερευνάται η απόκριση του υπό σεισμική διέγερση. Τα αποτελέσματα αναδεικνύουν τον ευεργετικό ρόλο της διάταξης και του μηχανισμού DDA, τοποθετώντας έτσι την ιδέα ως μια επιτακτική εναλλακτική λύση στις υπάρχουσες τεχνολογίες.

TABLE OF CONTENTS

LIST OF FIGURES

LIST OF TABLES

I. INTRODUCTION

1 INTRODUCTION

1.1 Introduction & Motivation

The founding pillar of this research work lies in the mitigation of vibrations and the enhancement of the dynamic properties of a variety of engineering structures. Specifically, the main goal of the studied vibration control mechanisms is the acoustic treatment and consequently, noise reduction through various proposed frameworks that target the low-frequency domain of an incoming acoustic wave. Inspired by the use of novel metamaterials and amplification mechanisms, a series of innovative systems are conceptualized, designed and presented herein, seeking for solutions to low-frequency vibration control and sound attenuation problems.

To begin with, environmental Noise Pollution is currently considered the second largest cause of pollution in the world, next only to air pollution. Exposure to severe environmental noise contributes to several health impacts and is currently a growing concern of both the general public and policymakers. It is undoubtedly a serious issue in modern urban areas that can significantly deteriorate the quality of life of people living in such conditions. According to WHO, excessive exposure to high levels of road traffic noise can increase the health risks of ischemic heart disease (IHD), stroke and diabetes. In addition, annoyance and sleep disturbances may occur to people exposed to high levels of ambient noise for long periods of time. Similar consequences to human health can be provoked by railway and aircraft noise, that are very common in modern European cities. For the aforementioned health reasons, the Environmental Noise Guidelines for the European region propose the reduction of the noise level produced by road traffic to 53 dB L_{day} (day - evening noise level) and to 45 dB L_{night} (night noise level). Similar noise level limitations are proposed for aircraft and railway noise. The actual situation in the EU countries, concerning noise pollution, is far from these limitations proposed by the

WHO. As a result, actions should be taken to align with the European Noise Directive (END) and the European Green Deal and thus, reduce noise pollution and its consequences.

Among the urban environments, where the reduction of noise level is critical, are residential and work buildings, schools, hospitals, and the public space around this infrastructure. Aiming to achieve the goal of significant noise mitigation at these spaces, various measures can be taken that refer to either the noise source, the propagation path or the receivers' end. Traditional approaches for noise attenuation focus on passive techniques that mainly include soundproofing panels and sound barriers made of conventional materials (e.g., polyester, steel, concrete). However, these structures are usually bulky (especially for the mitigation of low-frequency noise) and non-sustainable as they require the use of significant amount of material to achieve the required mass of the panel.

Current noise protection measures in the low-frequency range, below 500Hz and especially within the region between 20Hz and 100Hz, are neither effective nor applicable. On the contrary, many environmental noise sources have a significant frequency content in this range; A typical example are vehicles of all types (cars, trucks, trains, aircrafts, etc.), which produce impact or random broadband noise, with its most significant part being in this frequency range. Another example are construction activities (i.e., dynamic compaction, roadbed compaction, pile driving, blasting) with frequency spectrum well below 100Hz. To this end, designing lightweight structures with low-frequency vibration control properties and sound radiation has always been technically demanding and practically crucial. Towards this direction, the need for low-cost and low-mass vibration isolation within the modern aerospace, automotive, and construction industry has motivated research groups at a worldwide level to develop novel vibration isolation concepts and sound mitigation mechanisms.

Inspired by the need to achieve vibration control and mitigate low-frequency sound and noise, this research work focuses on the conceptualization, design, analysis and experimental verification of different vibration control systems. The overarching goal is to achieve applicable solutions in the low-frequency domain, by adopting the extraordinary dynamic properties of phononic and locally resonant metamaterials, as well as various mechanical amplifiers and elements that increase the phenomenal inertia of a structure and eliminate in this way the need to introduce large additional masses. In the following sections, a brief literature review of acoustic metamaterials as well as of existing mass amplification mechanisms is presented. In addition, an outline of this Doctoral thesis along with the main originalities and research novelties of the study are briefly demonstrated.

1.2 Brief Literature Review

1.2.1 Sound and Noise

The word noise refers to the unwanted sound, unexpected and/or unpleasant which interferes with thinking, concentrating, working, sleeping and any other potential human activity. The word originates from the Latin word 'Nausea' and although sound and noise have a similar meaning, noise refers to an undesired, unpleasant form of sound (Firdaus and Ahmad, 2010). Noise in urban areas is generated from highways, airplanes, industrial plants, construction sites, music spaces, ventilation systems etc. During the last decades, advancements in transportation, industry and construction technology has led in a dramatic increase of noise levels in urban areas and consequently, human beings living in such areas are more prone to hearing problems and other health issues such as anxiety, sleep disturbance, cardiovascular problems etc. (Goines and Hagler, 2007; Passchier-Vermeer and Passchier, 2000). These issues may develop both due to a sudden short-time high level noise, and due to prolonged exposure to certain noise levels and frequencies. To this end, the scientific community studies various methodologies and concepts to achieve mitigation of noise and protection of human health and wellbeing. Noise control usually refers to the following three major methodologies: (i) mitigation of noise at the source of sound; this may be achieved by technologies that produce less sound to operate or require less vibration to be effective, (ii) reduction of noise along its path; this is usually undertaken by considering absorption, isolation and other attenuation methods, and (iii) protection of the receiver by using sound-proof equipment at the receiver's end, e.g., ear protection (Crocker, 2008; Kishore et al., 2021).

By all means, the sound that is detected by human beings and other species is the reflected acoustic wave that travels back to our ears after hitting a surface. Longitudinal sound waves, travelling through air, are waves of alternating pressure deviations from the equilibrium pressure, causing local regions of compression and rarefaction. In terms of frequency, sound waves are divided to three categories: infrasound, audible sound, and ultrasound. The infrasound has frequencies less than 20 Hz, and it can be usually detected by animals such as whales, cats, and alligators. The ultrasound drops on a frequency spectrum higher than 20 kHz. It can be detected by bats, dolphins, moths, and lacewings. The audible sound has a frequency spectrum such that the human ear can detect, and generally ranges from 20 Hz to 20 kHz.

The loudness/strength of a sound wave is dependent on its amplitude. In acoustic applications and research, the sound pressure level (SPL) is usually employed as a measure of the acoustic wave's amplitude and is defined as $SPL = 20 \times log_{10} | p / p_0 |$. The units of the SPL are decibels (dB), p is the sound pressure and p_0 the reference sound pressure.

The strength of sound, which human ears perceive, is called loudness. Mathematically, the higher SPL, the louder sound. However, at different frequencies, human ears have different sensitivity. Generally, human is less sensitive to lower than higher frequency sound. Figure 1-1 depicts the equal loudness contours for which a listener perceives the same loudness. The unit of the loudness is phon, and the phon of each contour is the SPL at 1 kHz.

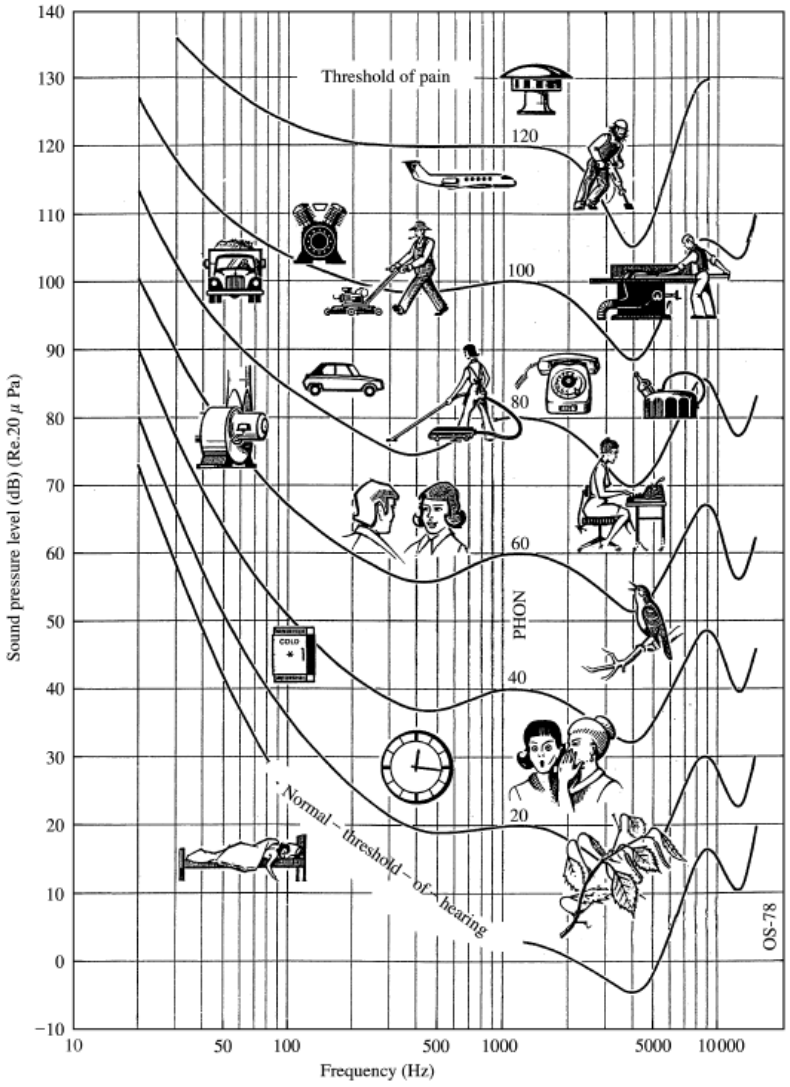

Figure 1-1: The equal loudness contours and the SPL spectrum of some popular noise sources as illustrated by the insets. (based on the figure of Nguyen 2021)

1.2.2 State-of-the-Art in Low-Frequency Noise Mitigation

In the last two decades, there is tremendous development in the acoustic field to absorb or suppress sound wave propagation. However, traditional acoustic materials have certain limitations for sound insulation and absorption at low-frequency. Investigation of the acoustic performance of common means of acoustic treatment, such as plasterboard panels, is most often focused on middle to high

frequency regions and, particularly, in the coincidence region of sound transmission. Meanwhile, the sound transmission in the critical frequency range of 0–200 Hz has only recently begun to be addressed frequently.

A metric of acoustic performance of a passive solution for acoustic treatment, especially referring to panel or layer type of solutions, is the sound transmission loss (STL). The STL of a conventional sandwich panel-type of solution, which can be modeled as an "m-k-m" system, is stiffness and resonance controlled at the low-frequency range, while frequencies above the fundamental, are dominated by the mass law. The stiffness-controlled region depends primarily on the elastic stiffness of the mounting and the bending stiffness of the panel, transforming the issue to a classic vibration isolation/absorption problem. However, since the STL curve of a finite panel has a first major reduction at the resonant frequency, conventional sandwich panels demonstrate a certain inefficiency in this range.

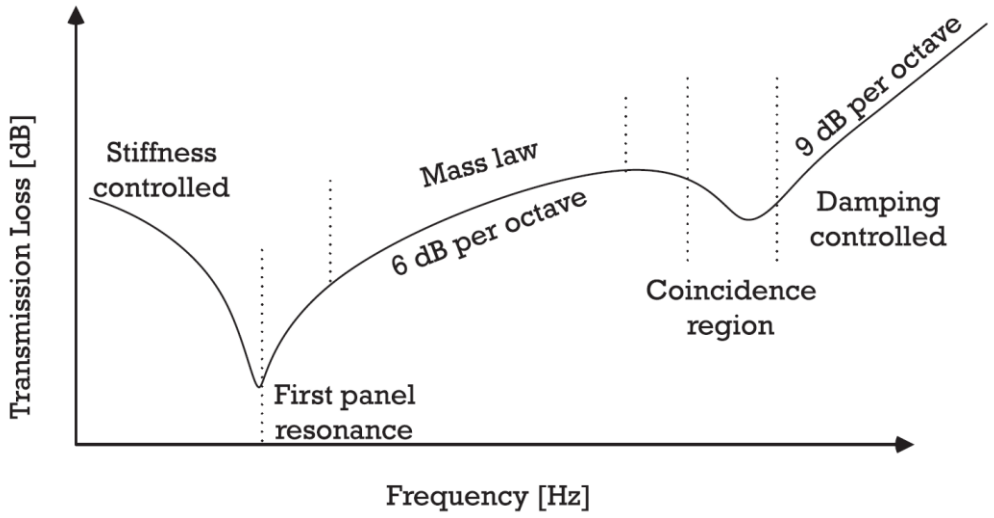

Figure 1-2: Typical STL profile of a panel.

Generally, since the “mass law” that governs the mid-frequency range above the fundamental frequency states that the level of sound transmission loss (STL) can be improved only by increasing the mass density of the panel, this leaves only the mitigation of the fundamental panel resonance region, as in Figure 1-2, especially when the addition of extra mass needs to be avoided.

Passive solutions such as foam layers, sound, natural fibers and recycled materials are alternatives to conventional materials due to their low cost and less environmental effect (Kishore et al., 2021). However, natural materials have certain limitations like high flammability and moisture absorption. Sandwich panels, diffusing panels and blocks, sandwich panels and many others (Makris et al., 1986)

constitute widespread means for acoustic treatment in a vast range of applications from room acoustics to loudspeaker enclosures, etc. In addition, although they are considered the most common solution (de Melo Filho et al., 2019), their effectiveness in low-frequency isolation has not been extensively documented, even in cases where novel composite honeycomb arrangements (Moore and Lyon, 1991) with negative stiffness element inclusions (Chronopoulos et al., 2017) are considered.

As a summary, state-of-the-art research includes various acoustic materials such as natural fibers and recycled materials, metamaterials, acoustic black holes, micro-perforated panels, and advanced foams aiming to achieve broadband noise mitigation. The capability of new technologies and research allows to build complex systems like perforated panels, gradient-index, space-coiling, and metamaterial-based periodic structures that seek a solution towards mitigation of low-frequency noise, without the need of huge masses. An overall schematic representation of acoustic materials for noise reduction is presented in Figure 1-3.

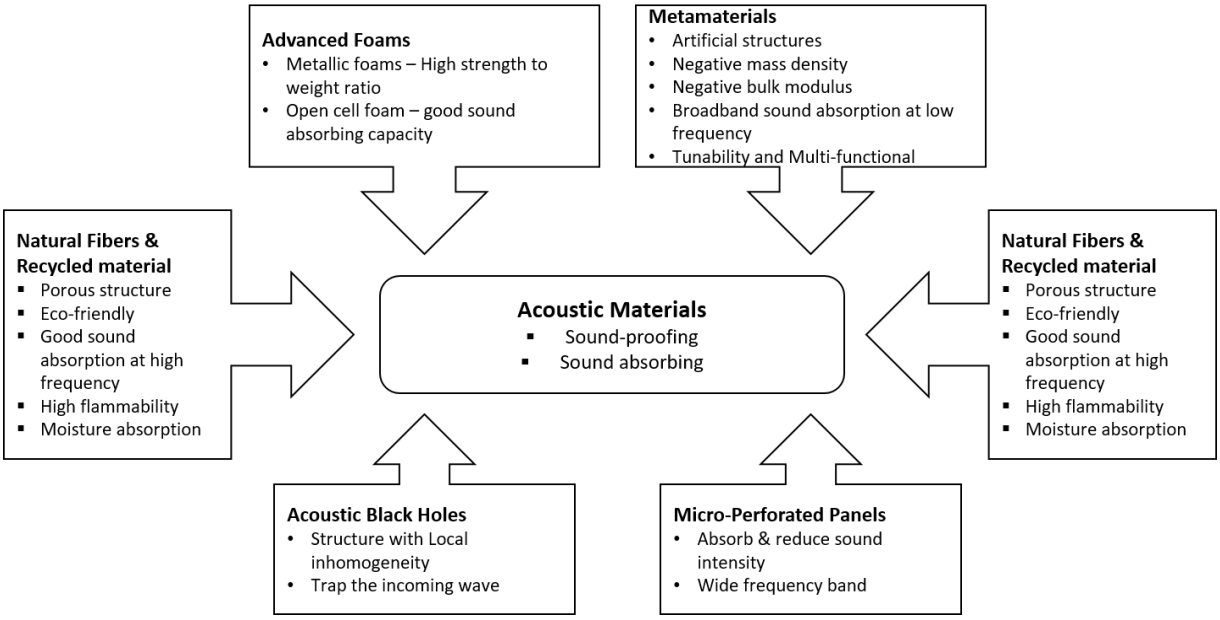

Figure 1-3: Overall schematic representation of acoustic materials (based on the figure of Kishore et al., 2021)

In the following sections a short explanation, history and literature review of metamaterial concepts are presented along with details on their extraordinary wave manipulation properties. Recent applications in vibration control and sound attenuation are also provided.

1.2.2.1 Metamaterials for noise mitigation & low-frequency vibration control

Aiming to achieve vibration control and noise mitigation in the low-frequency domain, researchers have turned their attention to the development of new technologies that overcome the main drawbacks of conventional acoustic materials. State-of-the-art includes the introduction of metamaterials as a means to control noise and attenuate low-frequency vibration. In the following paragraphs, a definition and short history of metamaterials is presented, along with a number of major metamaterial applications for wave manipulation and recent research on their applicability in noise attenuation.

1.2.2.2 What are metamaterials?

The word metamaterial comprises the words meta and materia. The word meta stems from the Greek prefix and has the meaning of beyond, and after. When combined with words in English, meta usually signifies “change” or “alteration”. The word material stems from the Latin word materia, carrying a meaning of matter or material (Wang et al., 2022). In this way, the term “metamaterials” is generally used to describe artificial composite materials that gain their properties primarily from their structural configuration, rather than their composition. These are manmade, usually periodic or random structures whose periodicity can be in the material phases, the internal geometry, or the boundary conditions and enable in this way, manipulation of the dispersive properties of vibrational waves. Initial studies on metamaterials, and specifically on phononic crystals were carried out in 1992, indicating that appropriate design of such microstructures can filter and significantly alter the propagation of elastic waves within elastic media (Gao et al., 2022; Sigalas and Economou, 1992).

1.2.2.3 Classification of metamaterials

Phononic crystals and acoustic metamaterials are considered as the two major classes of metamaterials and have generated significant scientific interest for their adoption in diverse technological applications. These range from sound attenuation to ultrasonic imaging, telecommunications, thermal management and thermoelectricity, and even to mitigation of seismic surface waves. The main interesting feature of such metamaterials is their ability to attenuate waves in specific frequency ranges, known as stopbands or bandgaps.

These bandgaps can be broadly classified in two physical mechanisms: (i) Bragg scattering, the property of phononic crystals (Brillouin, 1946), and (ii) local resonance, the property of acoustic metamaterials (Mahmoud I. Hussein et al., 2014; Liu et al., 2000; Mead, 1996). In general, the Bragg-

type bandgaps occur at wavelengths in the direction of sound wave propagation and require a periodic arrangement of scatterers with dimensions and periods comparable to the wavelength (Liu et al., 2020). On the other hand, acoustic metamaterials have the added feature of local resonance, and although often designed as periodic structures, their properties do not rely on periodicity. Their locally resonant bandgaps correspond to internal resonances due to their microstructure, and they can be generated using resonators (Li and Chan, 2004; Mei et al., 2006; Pennec et al., 2008; Wu et al., 2008). As a result, the structural features of acoustic metamaterials can be significantly smaller than the wavelength of the waves they are affecting. Locally resonant structures may exhibit negative effective dynamic mass density and bulk modulus and hence, lead to such unusual dispersion properties. Both types of wave filtering and attenuation can be achieved by customizing the structure of the unit-cell (Mead, 1996; Zhou et al., 2017). For example, researchers usually obtain low-frequency Bragg-type bandgaps by embedding high-density materials in low-density host materials, by constructing large unit-cells to retain low wave speed or by using large lattice constants (Sprik and Wegdam, 1998; Suzuki and Yu, 1998). On the contrary, locally resonant bandgaps may be easily obtained at low-frequencies, yet they require heavy resonators to obtain wide bandwidths, which may prohibit their practical implementation. Whether these materials impact wave dispersion (i.e., band structure) through Bragg's scattering or local resonant oscillators, they can achieve a wide range of unusual spectral (o-space), wave vector (k-space), and phase (ϕ'-space) properties.

While most studies have focused on actual, realistic models of locally resonant acoustic or elastic metamaterials, much can be learned by exploring the problem in the context of a simple "mass-in-mass" lumped parameter model as done by Huang et al. (2009). An overview of the typical unit-cell of a periodic phononic and acoustic metamaterial structure, using a simplified lumped parameter model is presented in Figure 1-4 below.

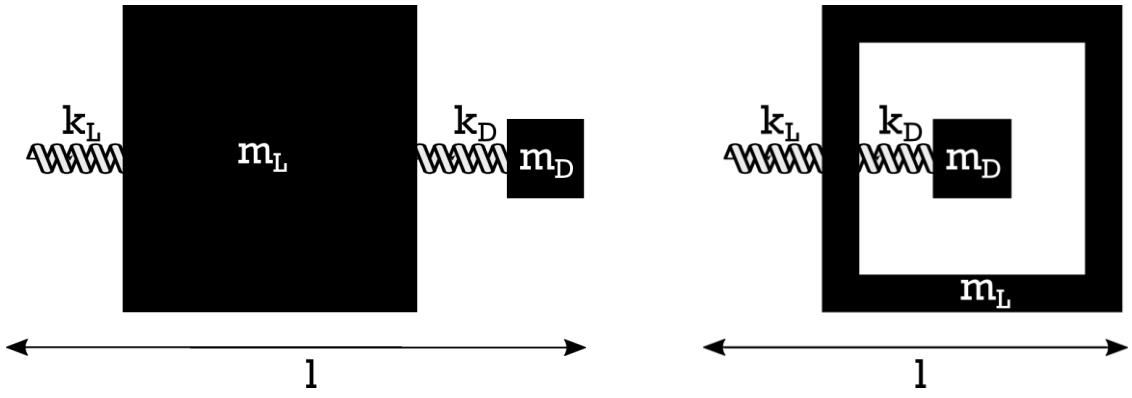

Figure 1-4: Lumped parameter unit-cell model of (a) phononic crystal (mass-and- mass) and (b) acoustic metamaterial (mass-in-mass)

1.2.2.4 Properties and history of phononic and acoustic metamaterials

The development of phononic crystals for the control of vibrational waves followed by a few years the analogous concept of photonic crystals (1987) for electromagnetic waves (Yablonovitch, 1987). Both concepts are based on the idea that a structure composed of a periodic arrangement of scatterers can affect quite strongly the propagation of classical waves, such as acoustic/elastic or electromagnetic waves. It is interesting to observe that the concept was first theoretically proposed in the field of electromagnetism by Veselago (1968). Since then, metamaterial configurations with negative equivalent permittivities and permeabilities have been implemented in experiments (Smith et al., 2000). Similar concepts have been used for heat transfer (Liu et al., 2011), mechanics (Zheng et al., 2014) and optics, (Hao et al., 2010) which have promoted both the emergence and rapid development of acoustic metamaterials, in parallel with research on phononic crystals.

Specifically, phononic and photonic crystals/metamaterials are associated with a collective excitation in a periodic elastic arrangement of molecules (phonons) and elementary particles of electromagnetic waves (photons), respectively. An initial study on a periodic structure aiming to manipulate wave propagation of phonons was presented by Narayanamurti et al. (1979). The proposed superlattice is nowadays considered as one of the first one-dimensional phononic crystals. During the early 1990s, Sigalas and Economou (1992) demonstrated the elastic wave propagation and bandgap formation in a two-dimensional phononic crystal, consisted of fictitious materials. In 1993, they repeated their study in two-dimensional fluid and solid systems constituted of periodic arrays of gold cylindrical inclusions in a beryllium host structure, incorporating out-of-plane shear waves (Sigalas and Economou, 1993). The above pioneering research work is considered as the birth of phononic metamaterials. In 1994, Kushwaha et al. (1994, 1993) calculated for the first time the full band structure of out-of-plane wave propagation in a periodic array in an aluminum alloy matrix.

Meanwhile, there has also been significant interest in the applications of sonic crystals consisting of multiple phases arrays of liquids or gases. Towards this direction, In 1995, Francisco Meseguer and colleagues determined experimentally the aural filtering properties of a perfectly real but fortuitous phononic crystal, a minimalist sculpture by Eusebio Sempere standing in a park in Madrid, Spain (Martínez-Sala et al., 1995) (Figure 1-5). This sculpture is a two-dimensional periodical square arrangement of steel tubes in air. They showed that attenuation of acoustic waves occurs at certain frequencies due not to absorption since steel is a very stiff material but due to multiple interferences of sound waves as the steel tubes behave as very efficient scatterers for soundwaves. The periodic arrangement of the tubes leads to constructive or destructive interferences depending on the frequency of the waves. The destructive interferences attenuate the amplitude of transmitted waves,

and the phononic structure is said to exhibit forbidden bands or band gaps at these frequencies. The acoustic band structure of these systems was also reported by the experimental investigations of Sanchez-Perez et al. (1998) (audible range) and Montero de Espinosa (1998) (ultrasonic range).

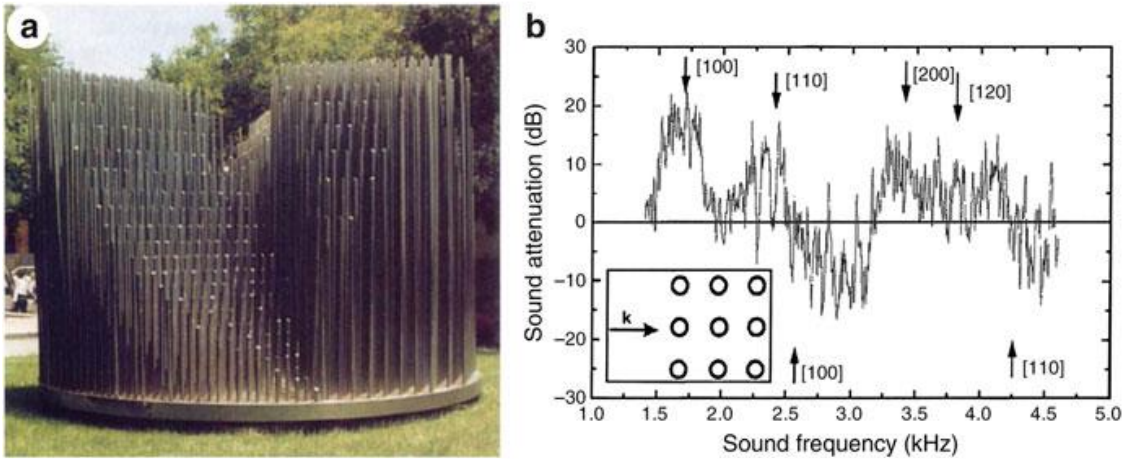

Figure 1-5: (a) Eusebio Sempere's sculpture in Madrid, Spain, (b) Measured sound attenuation as a function of frequency. The inset illustrates the direction of propagation of sound waves. The brackets [hkl] represent, in the vocabulary of X-ray diffraction, crystallographic planes for which Bragg interferences will occur (Martínez-Sala et al., 1995).

Acoustic metamaterials (AMs), on the other hand, exhibit extraordinary dynamic properties due to their local features and uniquely engineered configurations, namely their "microstructures". These microstructures are usually materialized in the form of locally resonant elements or other dissipation mechanisms incorporated within a host structure, and periodicity is not required for the formation of bandgaps. For the first time, in 2000, Liu et al. (2000) presented this new class of locally resonant sonic materials that exhibited spectral gaps with lattice constants two orders of magnitude smaller than the relevant sonic wavelength. Their work adopted a rubber material to coat a high-density core to obtain a local resonance unit that exhibits negative mass density at the frequencies where these sub-wavelength microstructures resonate and move out of phase with the excitation. Their proposed structure exhibited a good sound absorption effect resulting from local resonance in the low-frequency band. An overview of their work is depicted in Figure 1-6.

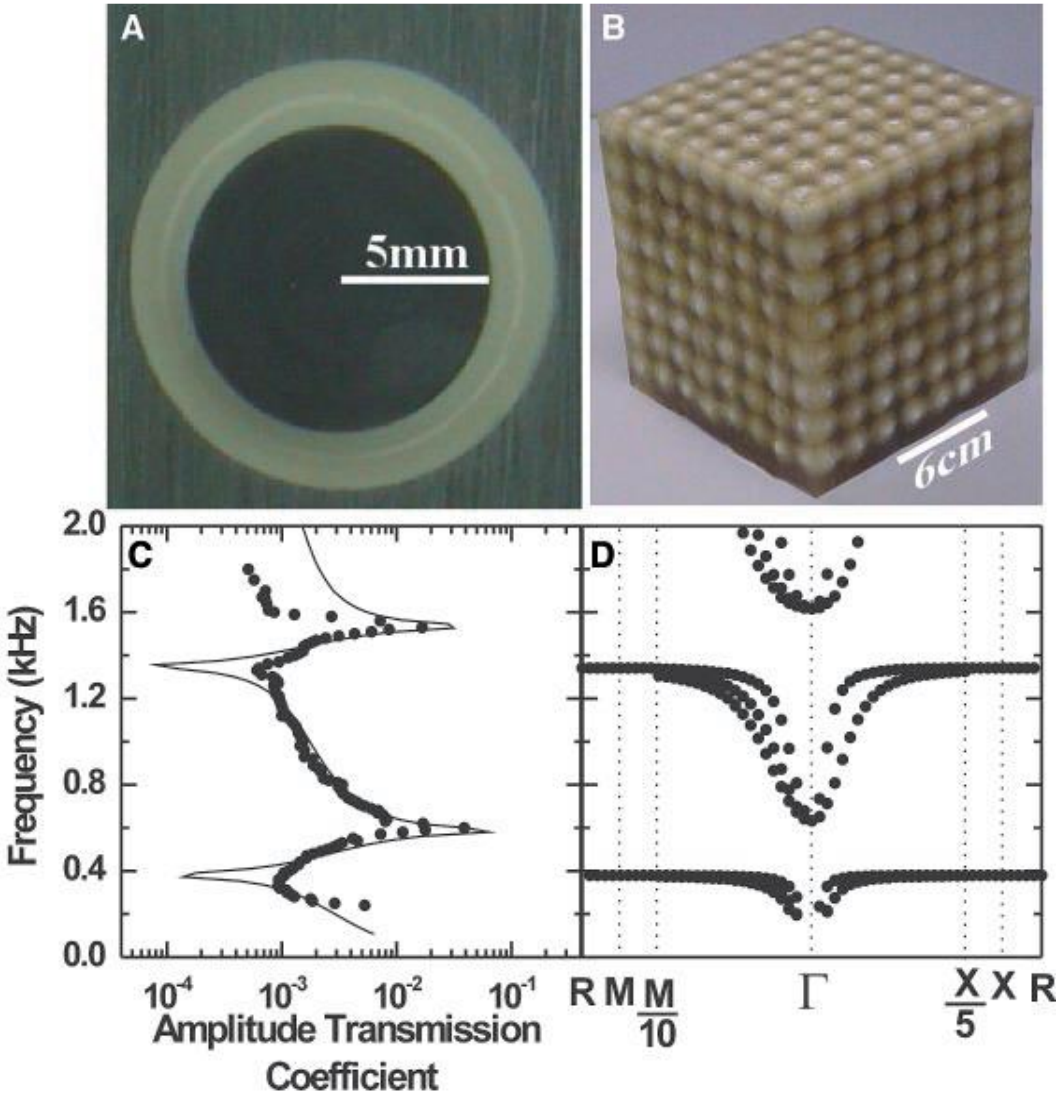

Figure 1-6: (a) Cross section of a coated lead sphere that forms the basic structure unit (b) for an 8 X 8 X 8 sonic crystal. (c) Calculated (solid line) and measured (circles) amplitude transmission coefficient along the [100] direction as a function of frequency, (d) calculated band structure of a simple cubic structure of coated spheres in very good agreement with measurements (the directions to the left and the right of the G point are the [110] and [100] directions of the Brillouin zone, respectively (Liu et al., 2000).

Subsequently, negative effective acoustic parameters were observed in many other structures, including periodically arranged Helmholtz resonators (Fang et al., 2006) (Figure 1-7), membrane-type structures (Yang et al., 2008), and coil-up space structures. The material parameters of such metamaterials can be tuned to any values in material space by adjusting their microstructures. In other words, their architecture can be designed to produce the desired response, including negative effective mass (Huang et al., 2009; Huang and Sun, 2009; Lu et al., 2009; Yao et al., 2008), negative Poisson's ratio (Lakes, 1993), and negative stiffness (Huang and Sun, 2012).

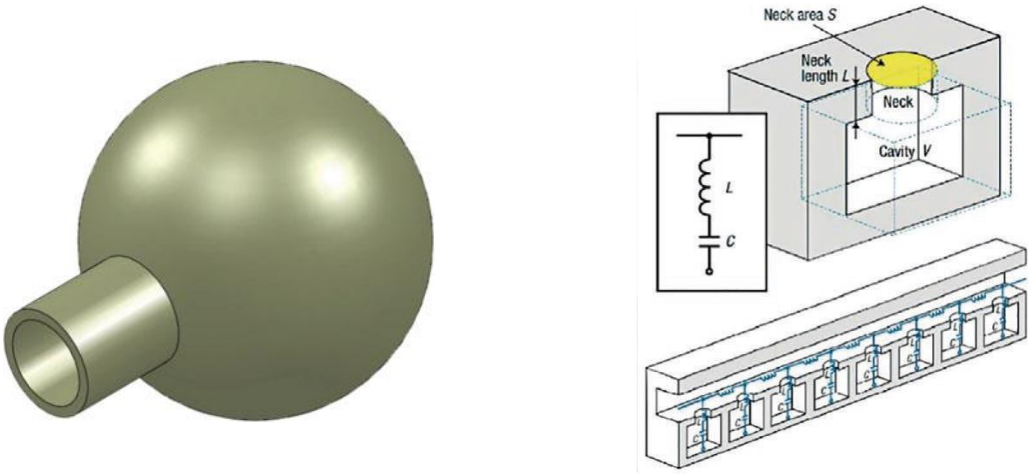

Figure 1-7: (a) A typical Helmholtz resonator (Mei et al., 2013) , (b) Schematic representation of the structure of a series of Helmholtz resonators coupled together (Liu et al., 2000).

Although acoustic meta-materials have long been considered to present the only available direction to create bandgaps at wavelengths much longer than the lattice size, and thus enable low-frequency vibration attenuation, the width of the resulting band gaps is generally very narrow –especially when referring to the conventional "mass-spring-mass" and tuned mass-damper (TMD) based periodic structures – since it depends on the ratio of the internal oscillating mass to the external mass of the unit lattice.

1.2.2.5 Acoustic Metamaterial applications & state-of-the-art in noise abatement

As discussed in the previous sections, acoustic and locally resonant metamaterials harness their potency from their low-frequency, subwavelength characteristics. There exists a vast number of acoustic metamaterial applications including implementations for vibration control, noise abatement, subwavelength focusing on fine-scale imaging applications, acoustic cloaking and recently, even for mitigation of seismic waves. A detailed review of the state-of-the-art acoustic metamaterial applications and theory can be find in Gao et al. (2022), Hussein et al. (2014) and Liao et al. (2021)

In general, acoustic metamaterials do not obey the mass law that governs the low to mid-frequency range and consequently, they may exhibit much higher noise insulation properties than any other typical acoustic material, especially in the low-frequency domain (Bilal and Hussein, 2013; Ding and Zhao, 2011; Ho et al., 2003). To this end, the concept finds application to sound proofing in buildings, mitigation of noise from highways and airports, vibration minimization in vehicle structures and machines, shock mitigation, etc. In addition to isolation, where reflection is desired, researchers also considered sound absorption as an objective, that on the contrary, requires the minimization of reflection (Mei et al., 2012; Romero-Garca et al., 2011).

In 2008, the first membrane-type acoustic metamaterial was proposed (Yang et al., 2008). The investigated material consisted of a tensioned elastic membrane with an additional mass on a support frame. Results showcased sound insulation properties much greater than the ones predicted by the mass law. Since then, membrane-type metamaterials have attracted the interest of researchers and the industry due to their simple structure that seems promising for future applications. Studies have developed a number of analytical and numerical models to estimate the acoustic characteristics of these novel concepts (Chen et al., 2014; Langfeldt et al., 2015; Zhang et al., 2012), and performed experimental validation tests (Gao et al., 2018) in acoustic impedance tubes.

However, membrane-type acoustic metamaterials may suffer damage due to the pre-stress tensor of the membrane and consequently their practical implementation is significantly reduced. Therefore, a more realistic alternative for noise reduction applications comprises thin-plate type acoustic metamaterials. Langfeldt et al. (2019) proposed an analytical method to estimate the eigenmode and sound transmission loss (STL) of thin-plate metamaterials while Varanasi et al. (2013), proposed to replace the concept of the elastic membrane with a lightweight thin plate acting together with a mass block, and a frame. More recently, the sound insulation performance of a large square-plate acoustic metamaterial panel composed of a periodic array of square elements which was evaluated under normal excitation (X. Wang et al., 2019). Characteristic examples of low-frequency membrane and thin plate type acoustic metamaterials are presented in Figure 1-8.

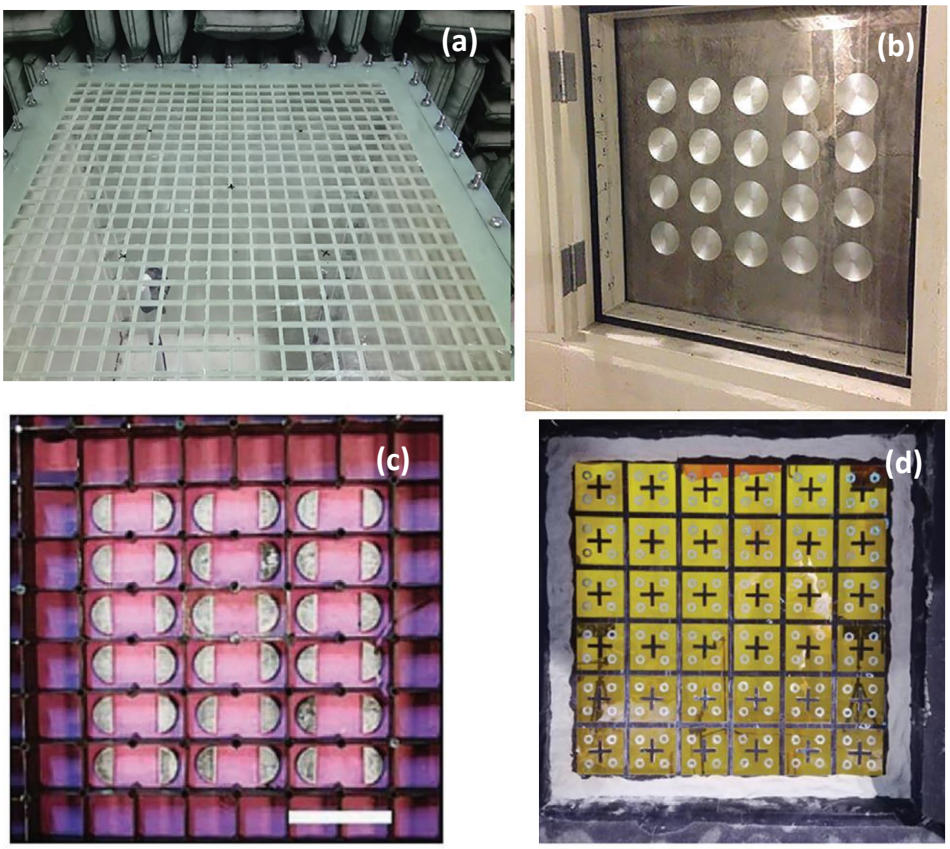

Figure 1-8:Examples of membrane-type and thin plate acoustic metamaterials for sound isolation: (a) large square-plate acoustic metamaterial panel composed of a periodic array of square elements (X. Wang et al., 2019)*, (b) 2D acoustic black hole thin-plate for sound insulation* (Conlon and Feurtado, 2018)*, (c) a semi-cylindrical mass attached to the surface of an elastic membrane* (Mei et al., 2012)*, and (d) low-frequency acoustic metamaterial membrane type* (Zhou et al., 2020).

Another intriguing application of acoustic/elastic metamaterials is cloaking, whereby an acoustic (or an elastic) wave is steered around an object rather than be scattered by it. A common approach for this problem is based on transformation acoustics (or elasticity) theory, whereby a target material distribution around the object of interest is mathematically synthesized from the point of view of heterogeneity and anisotropy (Chen and Chan, 2007; Cummer and Schurig, 2007; Milton et al., 2006; Norris, 2009). Acoustic/elastic metamaterials are viewed as promising candidates for practically realizing the unusually extreme material properties that emerge from this transformation process (Milton and Nicorovici, 2006; Spiousas et al., 2011). This is an open area of research that promises to continue to attract the attention and imagination not only of scientists, but also of the general public as a whole.

Elastic wave cloaking and locally resonant metamaterials in the form of metabarriers have also been studied recently as a mitigation measure for seismic surface waves. Brûlé et al. (2013), undertook a large scale experiment to test the properties of a seismic metamaterial consisting of a mesh of vertical

empty inclusions bored in the initial soil. Tests were carried out using seismic waves generated by a monochromatic vibrocompaction probe. Measurements of the velocities and accelerations indicated an alteration of the seismic energy distribution in the presence of the metamaterial, which was in agreement with previous numerical simulations, and showcased the applicability of the system as a realistic seismic protection measure. As another example, Colombi et al. (2016), have claimed that resonances in trees result in forests acting as locally resonant metamaterials for Rayleigh surface waves. A geophysical experiment indicated that surface waves were significantly attenuated over two separate large frequency bandgaps. Other engineered metabarriers have been proposed as a means to mitigate seismic surface waves, e.g., (Dertimanis et al., 2016; Palermo et al., 2016). Figure 1-9 illustrates indicative examples of seismic acoustic metamaterials proposed in the literature.

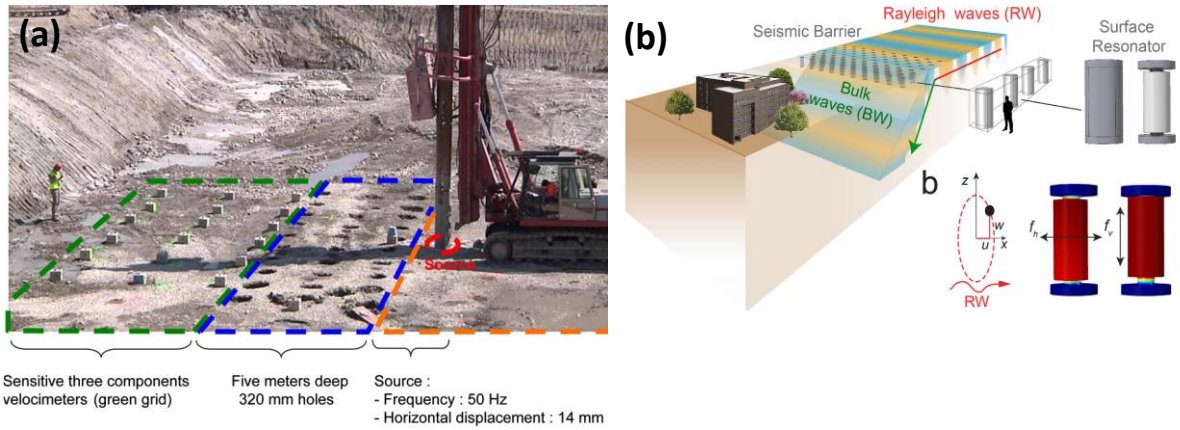

Figure 1-9: Examples of seismic acoustic metamaterials: (a) large-scale seismic surface wave cloak (Brûlé et al., 2013)*, and (b) engineered metabarrier for Rayleigh surface wave attenuation* (Palermo et al., 2016)*.*

1.2.2.6 Limitations of acoustic metamaterials

Although conventional locally resonant metamaterials appear promising in the field of vibration control and sound attenuation, there are still some critical limitations and constraints that require scientific attention and further study. One of the major issues is the requirement of bulky internal parasitic masses and large amplitudes of the internally oscillating structures which may complicate the implementation of these acoustic metamaterials (Kulkarni and Manimala, 2016). To this end, state-of-the-art research focuses on various mechanisms to artificially increase the inertia of the resonating mass and develop realistic mechanisms that may achieve broadband mitigation of acoustic waves. A brief review of the existing amplification methodologies is provided in the following sections.

1.2.3 The need for Inertial Amplification Mechanisms

Amplification of the vibrational response of mechanical and structural systems is of key significance to enhance their dynamic properties and upgrade their key performance attributes. To this end, various inertial and displacement amplification mechanisms have been developed and implemented in numerous engineering fields.

The performance of such mechanisms has been explored by researchers in various applications including sensors and electromechanical signal amplifiers (Aghamohammadi et al., 2020; Dolev and Bucher, 2016; Iqbal et al., 2021) energy harvesting mechanisms (Adhikari and Banerjee, 2022; Dai and Yang, 2021; Ha and Fang, 2014; Miranda et al., 2020; Shahosseini and Najafi, 2014; Wang et al., 2016; Yang et al., 2021), as well as vibration and sound mitigation technologies (Bergamini et al., 2019; Niels M.M. Frandsen et al., 2016). In addition, flexure-based displacement amplifiers, e.g., lever-principle based amplifiers, triangular-principle based amplifiers, and compliant mechanisms, have been proposed in the past decades showcasing their significance and cost-effectiveness in various fields such as bioengineering, optical instruments and other ultra-precision and nano-manipulation technologies (Chen et al., 2012, 2020; Guo et al., 2022; Hong et al., 2022; Sun et al., 2022; Zhu et al., 2016).

1.2.3.1 Mass amplification for vibration control

Specifically, vibration control has received considerable research interest in the past few decades, with special emphasis on developing effective, simple, affordable and applicable control systems to mitigate the vibration of mechanical systems, introduce sound attenuation and protect structures against natural or man-made hazards (Ma et al., 2021). Vibration control advancements focus lately on the development of passive, semi-active, and active vibration control approaches. Among others, these include the incorporation of additional oscillating masses, that introduce damping to the dynamic system (e.g., Tuned Mass Dampers - TMD), the application of negative stiffness elements (i.e., Negative Stiffness Devices – NS, and Quasi-Zero Stiffness Oscillators – QZS).

Aiming to overcome the hefty mass requirements of the existing systems, various methodologies have been proposed to artificially increase the inertial forces of the oscillating masses. Recently, Smith et al. (2002) introduced an innovative damping mechanism, namely the inerter, that takes advantage of amplified effective inertia in order to mitigate vibration of various structures. Amplification is realized by adopting a levered mass mechanism in parallel with a spring, generating an additional force that is proportional to the acceleration between the two, inerter connected, nodes. Although the system was

originally designed for machinery and specifically train and other vehicle suspension mechanisms, its application was extended lately as a solution to numerous vibration control problems.

In particular, such inertial amplification devices have been introduced and experimentally tested as a means to enhance the performance of conventional base isolation and TMD systems (Chowdhury et al., 2021; Moraes et al., 2018; Nakamura et al., 2014; Shi et al., 2022). As an example, Marian and Giaralis (2014) and Giaralis and Taflanidis (2018) proposed an inerter-enhanced TMD, namely the tuned-mass-damper inerter, as a seismic protection measure of structures. In a similar way, Cheng et al. (Cheng et al., 2020) presented a simple inertial amplification mechanism, the IAM, that improves the performance of the classic TMD using the amplification effect of a triangular shape mechanical system.

1.2.3.2 Applications in Metamaterials

As previously mentioned, conventional locally resonant metamaterials (LRMs) (Huang et al., 2009) may require hefty internal parasitic masses, as well as additional constraints at the amplitudes of the internally oscillating locally resonating structures, which may prohibit their practical implementation (Kulkarni and Manimala, 2016). Therefore, achieving wide and low-frequency bandgaps, based solely on traditional LRM structures is a challenge. Recently, attempts have been made towards artificially increasing the resonating mass's inertia via amplification mechanisms.

Inspired by the successful application of inertial amplifiers in engineering applications, several works proved their suitability in the context of periodic structures (Acar and Yilmaz, 2013; Mi and Yu, 2021; Taniker and Yilmaz, 2017; Yilmaz and Hulbert, 2010; Yuksel and Yilmaz, 2015). Researchers (Feifei and Lei, 2019; Kulkarni and Manimala, 2016; Wang, 2020) studied the longitudinal elastic wave propagation characteristics of inertant acoustic metamaterial configurations having inerters either in the local attachments or in the lattice, using effective models for their one-dimensional discrete element lattice chains. These analyses indicated that up or downshifting of the bandgap frequency range and its extent depends on the inerter configuration while retaining static mass addition to the host structure to a minimum level. Frandsen (2016) investigated wave motion propagation in a continuous elastic rod with periodically attached inertial amplification mechanisms, which he utilized in a manner that alters the intrinsic properties of the continuous structure. He concluded that the inertial amplification system is superior, as the simple local resonance system requires approximately twenty times heavier mass to obtain a comparable bandgap width. Li and Li (2018) extended Frandsen's model and included inertial amplification to infinite elastic beams.

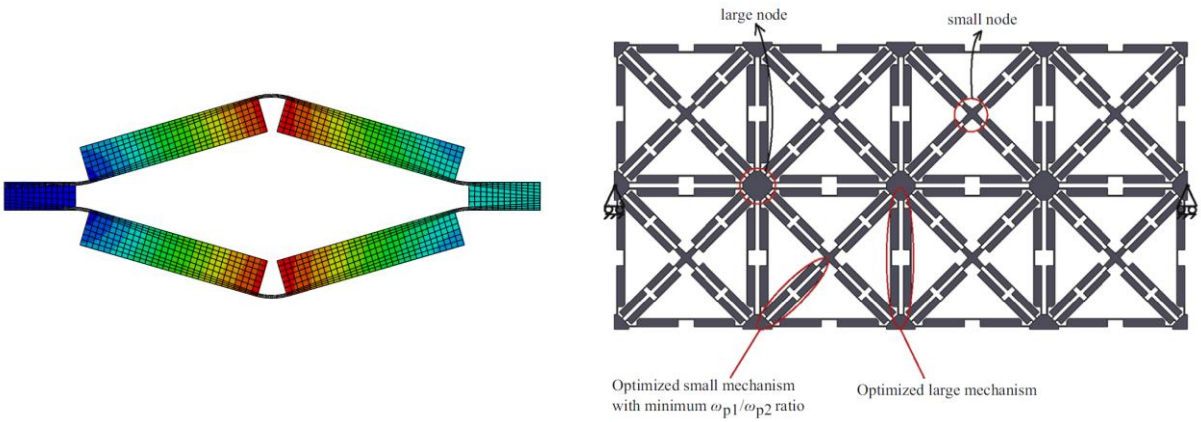

Figure 1-10: Example of inertial amplification in metamaterial concepts: (left) view of the numerical model of the inertial amplification mechanism, and (right) The two-dimensional acoustic metamaterial model with embedded inertial amplification mechanisms (Acar and Yilmaz, 2013).

1.2.3.3 Negative stiffness elements as inertial amplifiers

In addition, the introduction of negative stiffness (NS) elements has been proposed as an artificial way to increase the inertia of oscillators and to improve the dynamic response of various structures. A negative stiffness element is a stiffness element that generates force in the direction of movement instead of opposing it. The adoption of negative stiffness elements or "anti-springs" was initially introduced as a vibration isolation methodology by Molyneaux (1957) and was more recently further developed in the work of Platus (1992). The concept behind the vibration control properties of such systems is the reduction of the isolator's stiffness during vibration, consequently leading to a decrease of the natural frequency of the system. In this way, the eigenfrequency of the structure shifts away from the vibration frequency spectrum, hence acting as an isolation mechanism. In some cases, the frequency of the system reaches almost zero (Carrella et al., 2007) levels being, thus, called "Quasi-Zero Stiffness" (QZS) oscillators. A review of QZS oscillators was presented in the work of Ibrahim (2008). NS elements have been introduced by Nagarajaiah et al. (2007) and Pasala et al. (2013) as an approach for the seismic protection of structures. They proposed an adaptive stiffness device that introduced negative stiffness at the base of the structure and results in significant reduction of the input seismic forces.

Advances in mechanical engineering and expertise have facilitated the application of more complex mechanisms, such as newly fabricated hardware that incorporates negative stiffness. These are implemented for seismic isolation (Sarlis et al., 2016; Shen et al., 2017; Sun et al., 2017; M. Wang et al., 2019), in vehicle and automotive suspensions (Le and Ahn, 2013; Lee and Goverdovskiy, 2012) and torsional vibrations (Zhou et al., 2015). More recently, periodic structures that combine positive and

negative stiffness elements have been proposed as advanced mechanisms to enhance dynamic behaviour and provided additional damping (Antoniadis et al., 2015; Michelis and Spitas, 2010).

Another example of such an NS-based absorber is the KDamper (KD) concept that has been examined in various engineering applications such as seismic mitigation and protection of structures (Konstantinos A Kapasakalis et al., 2020; Konstantinos A. Kapasakalis et al., 2020; Mantakas et al., 2022) and low-frequency sound attenuation (Kalderon et al., 2021; Paradeisiotis et al., 2020). Additional information and details on the concept are provided in the following chapters of this thesis.

In the context of metamaterial structure, the inclusion of negative stiffness elements to the oscillating system shows promising results in addressing this issue, to a certain extent, revealing the potential of the use of negative stiffness (Antoniadis et al., 2015, 2016; Paradeisiotis et al., 2020) towards the design of low-frequency acoustic metamaterials (I Antoniadis and Paradeisiotis, 2018; Ioannis Antoniadis and Paradeisiotis, 2018; Chronopoulos et al., 2017, 2015).

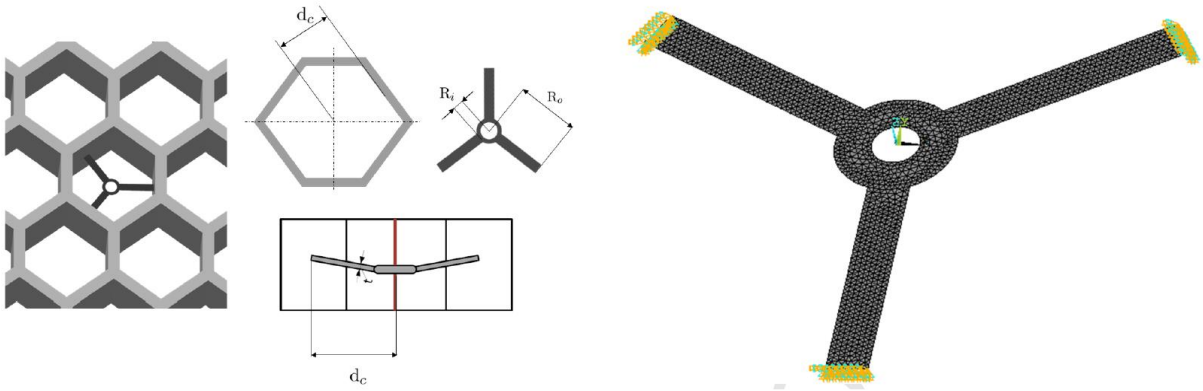

Figure 1-11: Examples of a negative stiffness enhanced acoustic metamaterial: (left) view of the proposed honeycomb architecture and the employed NS element, and (right) numerical model of the proposed tripod NS mechanism (Chronopoulos et al., 2017)

1.3 Scope & Originalities of the Thesis

The scope of this research work lies in the mitigation of vibrations and enhancement of the dynamic properties of noise attenuation and vibration control mechanisms. Specifically, the main goal of the study is the acoustic treatment and the proposition of noise reduction frameworks that specifically target the low-frequency regime of an incoming acoustic wave. The envisaged mechanisms are inspired by the use of phononic and acoustic metamaterials as well as the inclusion of amplification mechanisms and are designed and conceptualized to seek solutions to low-frequency vibration control and sound mitigation problems. A series of analytical and numerical frameworks as well as

experimental set-ups are developed in order to evaluate and subsequently validate the effectiveness of the proposed systems.

The applications introduced and studied herein include the introduction of negative stiffness elements and more specifically, the introduction of KDamper absorbers in the form of mounts that enhance the sound attenuation properties of acoustic panels. In addition, metamaterial designs with the inclusion of KDamper and mass amplifiers are presented; analytical and FE analysis indicates the beneficial role of the system towards low-frequency sound mitigation. Aiming to further explore the boundaries of low-frequency vibration control, a simple dynamic amplification mechanism, namely the DDA, is introduced and implemented for the first time in various applications; these include phononic and locally resonant metamaterials, as well as panels for acoustic treatment. Analysis includes analytical, numerical and experimental evaluation and showcases the beneficial effect of the DDA mechanism towards low-frequency vibration control. The overarching goal of the dissertation is to delve into the state-of-the-art research in acoustic and vibration control by exploring the extraordinary properties of metamaterial structures enhanced with negative stiffness elements as well as amplification mechanisms.

The research work presented herein is considered original and its essential features and novel aspects are summarized as follows:

i. The KDamper vibration control mechanism is designed and implemented in acoustic panels and metamaterial assemblies as a means to enhance the vibration control and noise attenuation properties of a system and achieve mitigation in the low-frequency range.

ii. The simple to realize inertial amplification mechanism (IAM) system is presented to enhance the vibration mitigation performance of the classic K-Damper. By coupling the IAM system with the classic KDamper a new inerter equivalent KDamper is introduced, namely the KD-IAM; the addition of the IAM allows to suppress the dynamic response of both the primary structure and the absorber. The theory of classic KDamper is extended to investigate the dynamic properties of the coupled mechanism.

iii. The KD-IAM is applied as a noise panel mounting mechanism; equations of motion are extended to include the deformable panel according to the in-series Lamped Parameter Model (LPM) approximation. An optimization procedure is presented for selecting the absorber's parameters to minimize the STL of the panel in the prescribed frequency range. An indicative realization of the KD-IAM-based mounting system is presented utilizing Belleville

springs for the negative stiffness element of the KDamper and other common elements, such as rubber pads and simple linkages.

iv. A novel Dynamic Directional Amplifier, namely the DDA mechanism, is introduced as a means to artificially increase the resonating mass of an oscillator, with no requirement of complex geometries and heavy parasitic masses. A simple experimental set-up is presented along with parametric shaking-table testing results for various DDA angles.

v. The DDA mechanism is implemented as an inertial amplifier of a phononic lattice. Analysis of the 2D lattice via Bloch's theory is performed, and the corresponding dispersion relations are derived.

vi. A locally resonant metamaterial consisting of resonating masses amplified by a DDA mechanism is presented. A feasible metabarrier design with enhanced properties is developed based on the proposed concept, showing that metamaterials can be implemented in real life applications.

vii. Experimental prototypes of DDA enhanced Phononic and locally resonant metamaterials are designed, built and tested providing a validation of the proposed vibration absorption and low-frequency noise mitigation concept.

1.4 Outline of the Dissertation & List of Publications

This doctoral dissertation is organized in 10 chapters that are subsequently divided in sub-sections and 4 appendices. The structure of each section comprises the background and respective literature review of the research field, the problem statement, the proposed configurations and mechanisms, the representative analytical, numerical examples and experimental testing, and finally the obtained concluding remarks. In the final chapter, the main conclusions drawn in this dissertation are summarized while directions for further research are proposed. The appendices include information necessary to understand the content of the main chapters of the dissertation. A short summary of the information provided in each chapter is presented below.

Chapter 2: In this chapter, the theoretical background of the acoustic theory and modelling methodologies are presented and subsequently implemented in the proposed advanced absorbers and metamaterial designs. Initially, the mathematical formulation of the *Impedance approach* introduced by Kim (2010) is described. This approach is adopted as a basis of the more accurate *"in series" LPM approximation,* introduced in this research work. The theory concludes to the inclusion of "soft mounts" to enhance the noise attenuation properties of panels. In this case, the total stiffness of

the mounts is lower than the generalized stiffness of the simply supported panel. When the panel is supported regionally on soft elastic mounts, the values of the eigenfrequencies of the structure are reduced. Consequently, the fundamental eigenfrequency can be explicitly defined and shifted outside the frequency range of interest. Analytical models are developed and indicate adequate agreement with the respective FE model, showcasing that they can be used as a quick design tool for acoustic panels.

Chapter 3: Herein, the KDamper vibration control mechanism is presented along with its analytical framework. The proposed mechanism is designed and implemented in acoustic panels and metamaterial assemblies as a means to enhance the vibration control and noise attenuation properties of a system and achieve mitigation in the low-frequency range. A simple to realize inertial amplification mechanism (IAM) system is subsequently presented to enhance the vibration mitigation performance of the classic KDamper. By coupling the IAM system with the classic KDamper, a new inerter equivalent absorber is introduced, namely the KD-IAM. The theory of KDamper is thus extended to investigate the dynamic properties of the coupled mechanism.

Chapter 4: A design of an acoustic isolation/absorption concept that targets the low-frequencies is proposed herein in the form of a panel mounted on bearings, based on the KD-IAM concept. The proposed idea leads to an improved dynamic behaviour of the panel that is predominant in the STL curve around the resonant frequency. This coupled absorber is applied in a novel mounting system for flexible acoustic panels, resulting in a wide and deep frequency band of improved vibration and noise attenuation. The methodology employed in this work is based on a lumped parameter model (LPM) utilizing a first mode approximation for the STL of a simply supported panel, and an optimization procedure is formulated for the selection of the KD parameters. The theoretical framework has been expanded for improved modelling of the fluid–structure interaction of the panel and subsequent representation in terms of a dynamic system with discrete degrees of freedom (DoFs). An indicative implementation for an initial case study of a stiffened panel is demonstrated along with a conceptual design and realization of the KD-IAM mounts. This case study of a simplified, more stripped-down application aims to demonstrate the capability of this advanced negative stiffness absorber in the area of low-frequency noise mitigation. Finally, the analytical framework is verified by employing a more detailed 3D numerical model to estimate the corresponding STL.

Chapter 5: In this chapter, metamaterial designs based on the KDamper-IAM concept are presented. The major limitations of conventional linear metamaterials, such as the limited frequency band of the attenuation zone can be overcome by adopting an advanced unit-cell design that includes inertial amplification mechanisms such as the proposed IAM and KDamper concept. Initially, the KDamper-

based metamaterial designs are presented along with their detailed analytical framework. The concept is subsequently enhanced by developing an inertial amplification system (IAM) supplementary to the initial mechanism; such addition allows for further improvement of the dynamic behavior of the structure. The proposed designs target the development of metamaterial-based noise barriers. Initial conceptual implementations are proposed herein, and the presented mechanisms are evaluated using both analytical and numerical analyses.

Chapter 6: In Chapter 6, a novel Dynamic Directional Amplifier, namely the DDA mechanism, is introduced as a means to artificially increase the resonating mass of an oscillator, with no requirement of complex geometries and heavy parasitic masses. The mechanism's rationale lies in the dynamics of a system that is subjected to a holonomic constrain; the vibrating mass is fixed to a simple rigid link that increases inertia towards the desired direction of motion by coupling the kinematic DoFs of the resonating mass and forcing the oscillator to move through a prescribed circumferential path. An analytical framework is developed, and analysis is undertaken to identify the beneficial effects of the DDA to the dynamic response of the system (transfer functions). Finally, a simple experimental set-up of a mass-stiffness-DDA model is presented along with parametric shaking-table testing for various DDA angles. The mechanism will be subsequently introduced to phononic and acoustic metamaterials in order to enhance their vibration attenuation properties (chapter 7 & 8).

Chapter 7: The DDA mechanism that was analytically and experimentally tested in Chapter 6 of the dissertation, is included within a two-dimensional (2D) phononic metamaterial. This amplifier is designed to present the same mass and use the same damping element as an initial reference phononic metamaterial. Hence, no increase in the structure mass or the viscous damping is needed. Analysis of the 2D lattice via Bloch's theory is performed, and the corresponding dispersion relations are derived. The numerical results of an indicative case study show significant improvements and advantages over the conventional phononic structure, such as broader bandgaps and increased damping ratio. Finally, a conceptual design is provided highlighting the applicability of the concept in potential mechanical systems, such as mechanical filters, sound and vibration isolators, and acoustic waveguides.

Chapter 8: In this chapter, the dynamic directional amplifier (DDA) is introduced as a means to increase the resonating mass of an LRM structure artificially, without the need of complex geometries and additional mass. The amplification is achieved with a rigid link that improves inertia and damping on the desired direction of motion, by simply coupling the kinematic DoFs of the internal resonating mass. The main aim of this study is to illustrate, via the use of a formal mathematical framework, that the performance of LR structures can be enhanced while retaining or even improving the practical

constraints such as having compact, lightweight, and buildable unit-cells. Towards this goal, a mass-in-mass model is adopted, and a preliminary parametric analysis is performed using both Bloch's theory on two-dimensional infinite lattices and conventional vibration theory on finite lattices. A numerical example is studied as a seismic mitigation application in order to highlight the advantages of the proposed arrangement over the initial study. To this end, a conceptual design of a seismic metamaterial in the form of a metabarrier is proposed and an investigation of its response under seismic excitation is analysed.

Chapter 9: In this chapter, the DDA enhanced Phononic and Locally Resonant metamaterial configurations introduced in chapters 7 and 8 are experimentally studied. In particular, the metamaterial models are constructed using LEGO® components and are tested under dynamic loading. The aim of this study is to validate the analytical and numerical models developed in the previous chapters, highlight the extraordinary properties of the proposed structures and to illustrate that realistic full-scale designs are feasible.

Chapter 10: The main conclusions drawn in this dissertation are summarized and the key advantages and novelties of the proposed vibration control and noise attenuation concepts are highlighted. In addition, directions for further research are suggested.

It is worth mentioning that the outcome of the conducted research activity presented in this Doctoral dissertation has been published in international journals, in national and international conferences, in workshops and exhibitions and fairs, as presented in the following section.

LIST OF PUBLICATIONS

International Scientific Journals

1. Kalderon, M., Paradeisiotis A., Antoniadis, I., "2D Dynamic Directional Amplification (DDA) in Phononic Metamaterials", *Materials* (2021), Volume 14, Issue 9, April 2021 (Editor's Choice). DOI: 10.3390/ma14092302.
2. Paradeisiotis A., Kalderon, M., Antoniadis, I., "Advanced Negative Stiffness Absorber for Low Frequency Noise Insulation of Panels", *AIP Advances,* Volume 11, Issue 6, June 2021, Pages 065003. DOI:10.1063/5.0045937.
3. Kalderon, M., Mantakas, A., Paradeisiotis A., Antoniadis, I., Sapountzakis, E.J., "Locally resonant metamaterials utilizing Dynamic Directional Amplification: an application for seismic mitigation", *Applied Mathematical Modelling*, Volume 110, October 2022, Pages 1-16. DOI: 10.1016/j.apm.2022.05.037.
4. Kalderon, M., Mantakas, A., Antoniadis I., "Dynamic modelling and experimental testing of a Dynamic Directional Amplification mechanism for vibration mitigation", *Journal of Vibration Engineering & Technologies*, 2022 (under review).

International Scientific Conferences

1. Paradeisiotis, A., Kalderon, M., Antoniadis, I., & Fouriki, L. (2020). "Acoustic Performance Evaluation of a panel utilizing negative stiffness mounting for low frequency noise control." *Proceedings of XI International Conference on Structural Dynamics (EURODYN 2020*), Athens, Greece, 23-26 November 2020, Pages 4093–4110. DOI: 10.47964/1120.9335.19276.

2. Kalderon, M., Paradeisiotis, A., Antoniadis, I., "A Phononic Metamaterial Incorporating Directional Amplification for Low Frequency Isolation", *ICONHIC 2021, Prep Virt. Workshop*, 22-23 June 2021.

3. Kalderon, M., Paradeisiotis A., Antoniadis, I., "Simulating Low Frequency Sound Transmission Loss of Mounted Panels.", *8th ECCOMAS Thematic Conference on Computational Methods in Structural Dynamics and Earthquake Engineering* (*COMPDYN 2021)*, Athens, Greece, 27—30 June 2021.

4. Kalderon, M., Paradeisiotis A., Antoniadis, I., "A Meta-structure for Low-frequency Acoustic Treatment Based on a KDamper-Inertial Amplification Concept.", *EURONOISE 2021*, Madeira, Portugal, 25—27 October 2021, Pages 1333-1343.

5. Paradeisiotis A., Kalderon, M., Antoniadis, I., "An Enhanced KDamper Absorber for Low Frequency Noise Control of Panels.", *International Congress on Computational Mechanics (10th GRACM),* virtual, July 5-7, 2021

6. Kalderon, M., Kalogerakou, M., Paradeisiotis A., Antoniadis, I., "Locally resonant metamaterials utilizing Dynamic Directional amplification., *16th International Conference – Dynamical Systems– Theory and Applications 2021,* 6—9 December 2021, Pages 216-217. DOI:10.34658/9788366741201

7. Kalderon, M., Paradeisiotis, A., Antoniadis, I., "A Phononic Metamaterial Incorporating Directional Amplification for Low Frequency Isolation", *3rd International Conference on Natural Hazards & Infrastructure (ICONHIC 2022)*, Athens, Greece, 5-7 July 2022.

8. Mantakas, A., Kalderon, M., Antoniadis, I.A., Sapountzakis, E.J., "Locally Resonant Metamaterials with Dynamic Directional Amplification for mitigation of seismic waves", *3rd International Conference on Natural Hazards & Infrastructure (ICONHIC 2022)*, Athens, Greece, 5-7 July 2022.

9. Kalderon M., Mantakas A., Chondrogiannis K., Antoniadis I.A., "A DDA-Enhanced Locally Resonant Metamaterial: Experimental Testing on a LEGO® Technic Assembly", *XII International Conference on Structural Dynamics (EURODYN 2023)*, Delft, The Netherlands, 02-05 July 2023. (Abstract submitted)

10. Kalderon M., Mantakas A., Chondrogiannis K., Antoniadis I.A., "Experimental Testing of a Dynamic Directional Amplifier (DDA) Enhanced Phononic Metamaterial on a LEGO® Technical Device", *29th International Congress on Sound and Vibration (ICSV29*), Prague, 9-13 July 2023. (Abstract accepted)

11. Kalderon, M., Mantakas, A., Chondrogiannis, K., Antoniadis, I.A., "Experimental Study in Phononic Structures with DDA Enhanced Unitcells", *9th International Conference on Computational Methods*

in Structural Dynamics and Earthquake Engineering (COMPDYN 2023), Athens, Greece, 12-14 June 2023. (Abstract submitted)

12. **Καλδερών, Μ**., Μάντακας, Α., Ι., Αντωνιάδης, Ι. (2022). "Εφαρμογή ενός καινοτόμου συστήματος δυναμικής ενίσχυσης (DDA) για την χαμηλόσυχνη ηχομόνωση κτιριακών στοιχείων", *11ο Πανελλήνιο Συνέδριο «ΑΚΟΥΣΤΙΚΗ 2022»*, Θεσσαλονίκη, Ελλάδα 14-16 Οκτωβρίου 2022.

Other publications

International Scientific Journals

1. Kapasakalis, K., Mantakas, A., **Kalderon, M.,** Antoniou, M., and Sapountzakis, E.J. "Performance Evaluation of Distributed Extended KDamper Devices for Seismic Protection of Mid-Rise Building Structures.", *Journal of Earthquake Engineering*, 2022 (under review).
2. **Kalderon, M.**, Smith, E. & O'Sullivan, C. "Comparative analysis of porosity coarse-graining techniques for discrete element simulations of dense particulate systems." *Comp. Part. Mech.,* Volume 9, Issue 1, February 2022, Pages 199-219. DOI:10.1007/s40571-021-00402-4.

International Scientific Conferences

1. Mantakas, A., **Kalderon, M.**, Antoniadis, I.A., Sapountzakis, E.J., "Locally Resonant Metamaterials with Dynamic Directional Amplification for mitigation of seismic waves", *3rd International Conference on Natural Hazards & Infrastructure (ICONHIC 2022)*, Athens, Greece, 5-7 July 2022.
2. **Kalderon, M.,** Smith, E., O'Sullivan, C., "From Micro to Large Scale Models: Porosity Homogenization Schemes for DEM Simulations", *3rd International Conference on Natural Hazards & Infrastructure (ICONHIC 2022)*, Athens, Greece, 5-7 July 2022.
3. Mantakas, A., Kapasakalis, K.A., Antoniou, M., **Kalderon, M.**, Antoniadis, I.A., Sapountzakis, E.J., "Design of a Negative Stiffness Vibration Absorber for Seismic Upgrade of Residential Buildings on Rocking Foundations", *13th HSTAM International Congress on Mechanics*, Patras, Greece, 24-27 August 2022.
4. Budd, O., **Kalderon, M.**, "Two New Integral Underbridges to Serve the Proposed 'Super Hub' at Old Oak Common", *International fib Symposium on Conceptual Design of Structures* Madrid, Spain, 26-28 September 2019.
5. Mantakas, A., Chondrogiannis, K., **Kalderon, M.**, Kapasakalis, K.A., Chatzi, E., Sapountzakis, E.J., Antoniadis, I.A., "Design and Experimental Verification of an Extended KDamper - Based Vibration

Absorber", *XII International Conference on Structural Dynamics (EURODYN 2023)*, Delft, The Netherlands, 02-05 July 2023. (Abstract submitted)

6. Mantakas A., Kapasakalis K.A., **Kalderon M.**, Antoniou. M, Antoniadis I.A., Sapountzakis, E.J., "3D Numerical Investigation of an Extended KDamper Absorber for Seismic Retrofitting of Low-Rise Buildings", *9th International Conference on Computational Methods in Structural Dynamics and Earthquake Engineering (COMPDYN 2023),* Athens, Greece, 12-14 June 2023. (Abstract submitted)
7. Kapasakalis, K.A., Mantakas, A., **Kalderon, M.**, Antoniou, M., Sapountzakis, E.J., "Performance Evaluation of Negative Stiffness-Based Vibration Control Devices for Seismic Protection of Building Structures", *9th International Conference on Computational Methods in Structural Dynamics and Earthquake Engineering (COMPDYN 2023)*, Athens, Greece, 12-14 June 2023. (Abstract submitted)

National Scientific Conferences, Exhibitions and Fairs

1. Καπασακάλης, Κ.Α., Μάντακας, Α., **Καλδερών, Μ.**, Σαπουντζάκης, Ε.Ι., Antoniadis, I.A., "Σεισμική Προστασία Υφιστάμενων Κτιρίων με Σεισμική Βάση Απορρόφησης Κραδασμών Αρνητικής Στιβαρότητας", *5ο Πανελλήνιο Συνέδριο Αντισεισμικής Μηχανικής και Τεχνικής Σεισμολογίας, 5ΠΣΑΜΤΣ*, Αθήνα, Ελλάδα, 20-22 Οκτωβρίου 2022.
3. "KDamper: An Advanced Negative Stiffness Vibration Absorber", National Technical University of Athens booth, 86th Thessaloniki International Fair, Thessaloniki, Greece 10-18 September 2022.
4. "Απορρόφηση ταλαντώσεων με συσκευές αρνητικής στιβαρότητας", περίπτερο INSPIRE, 2022 Βραδιά του Ερευνητή στο ΕΜΠ, Αθήνα, Ελλάδα, 30 Σεπτεμβρίου 2022.

Theses

5. **Καλδερών Μ.**, Σχεδιασμός Πειραματικής Διάταξης Υπογείου Μεταλλικού Αγωγού σε Διασταύρωση με Σεισμικό Ρήγμα., *Διπλωματική εργασία, ΕΜΠ,* 2015.
6. **Kalderon M.**, A fundamental assessment of computational porosity. *MSc thesis, Imp. Coll. London*. 2017.

Peer review activity

1. review activity for *Building Acoustics Journal* (Springer).
2. review activity for Journal of *Soil Dynamics and Earthquake Engineering* (Elsevier).
3. review activity for International Journal of *Mechanical Sciences* (Elsevier).

II. Modelling of Low-Frequency Sound Transmission Loss of Mounted Panels

2 MODELLING OF LOW-FREQUENCY SOUND TRANSMISSION LOSS OF MOUNTED PANELS

2.1 Background

Noise in the low-frequency range has been overlooked in the past when considering sound mitigation applications and currently, the research community lacks understanding of the processes and modelling methods governing the sound transfer in this frequency domain. Almost exclusively, the focus is on the region of the coincidence frequency of finite partitions. The lack of complete industrial standardization and guidance for such cases, especially below 100 Hz is also a factor. Yet, a large research program was conducted by NGI (the Norwegian Geotechnical Institute) between 2010-2016 on the low-frequency sound transmission in buildings, comprising of laboratory, full scale and numerical testing (Norén-Cosgriff et al., 2016). The disseminating research findings of the program were very insightful, although there are still uncharted areas in this field. When it comes to acoustic treatment in rooms there are a lot of misconceptions among the general public. Full scale tests reveal that when noise transmission occurs inside a building, the peaks of the low-frequency sound spectrum are of the same order as the fundamental acoustic room-modes (Løvholt et al., 2011), leading to a collection of resonances, which compromise the measurements. International standards provide procedures that extend the measurement range down to the 50 Hz one-third octave band (*ISO 10140*, n.d., *ISO 15186*, n.d., *ISO 717*, n.d.). Prescriptions include the use of specific source and receiver positions; however, the procedure is complex, with the worst-case scenario to propose the use of a sufficiently large number of source-receiver combinations as a means to smooth the large spatial variations in measured levels. Moreover, regarding the laboratory geometry, large rooms with volumes $V > 200m^3$ and specific room size ratios

are suggested when low frequency measurements are conducted. Recently, Ayr et al. (2017) presented a detailed low-frequency qualification procedure for a typical reverberant test room in order to perform sound power measurements, by taking advantage of a room finite element model. Similarly, Løvholt et al. (2017) developed a finite element methodology that incorporates a two-way coupled fluid-structure interaction and they compared their numerical results with experimental measurements including low-frequency sound transmission of plain walls, and walls with windows. Aretz M. and Vorlander M. (2010) also worked on room to room acoustic simulations, focusing on the room boundary conditions and the uncertainties of the computational models.

As far as analytical methods are concerned, acoustic radiation from plates has long been an important subject in structural dynamics and acoustics, thus, numerous mathematical models describing the structural response to noise, acoustic fatigue, and sound transmission of partitions have been developed. Aiming to develop a concrete theoretical framework assessing the effectiveness of these solutions, researchers developed mathematical models describing the structural response to noise, acoustic fatigue, and sound transmission of partitions. Even though sound transmission has been investigated since the early 20th century, there still remain open questions. Beranek L. and Ver I. (1992), Cremer et al. (2005), Ordubadi and Lyon (1979), and London (1950) derived equations for the unbounded/infinite partitions ("infinite-panel theory"), hence simplifying the problem. Later, ad hoc corrections were added to enhance the accuracy of the Sound Transmission Loss (STL) formulas. As far as high frequency noise mitigation is concerned, although the infinite panel theory can approximate pretty accurately the panel response, it is known that bounded plates vibrating at frequencies below the critical frequency are very much influenced by the presence of their boundaries (Callister et al., 1999; Pellicier and Trompette, 2007). Similarly, Kim (2010) approached the sound transmission through a flat wall from the standpoint of impedance mismatch, due to the different media via which the sound waves are propagated. He applied the same laws in the case of a partition assuming a limp wall (a wall that has only mass). In other words, the mass effect is dominant compared to the stiffness or internal damping. Despite the merits of the aforementioned approaches, the modal response of the structure in the low-frequency range, significantly affects its noise transmission properties. The inability of the infinite panel theory to predict accurately the panel's performance, led to the development of analytical theories for finite plates mounted in an infinite rigid baffle, using modal superposition (Lee and Ih, 2004; Takahashi, 1995; Wang, 2015). In the 1960s and 1970s, Maidanik (1966) first proposed a model for the radiation efficiency of a baffled plate assuming broadband excitation and multi-mode response. Similarly, Wallace (1972) used the Rayleigh integral to calculate the radiation efficiency of simply supported plates for individual vibration modes. Later, Leppington (1987) proposed an improvement of Maidanik's model, especially for the result near the critical frequency, and Roussos (1985) solved

analytically the radiation problem of a simply supported plate. Putra (2010) extended Wallace's (1972) asymptotic solution for simply supported boundary conditions to guided boundary conditions. However, despite all the efforts towards analytically expressing the acoustic performance of flexible structures, solutions exist only for simple plates with common boundary conditions, where mode shapes can be expressed in analytical form. Aiming to understand the importance of the mounting conditions on the panel's dynamic response, other techniques have been developed to solve the problem of general elastic supports (Ou, 2015). An example is the Rayleigh-Ritz method (Du et al., 2012; Li et al., 2009; Zhang and Li, 2010), where rotational and translational springs can be placed along the edges or nodes of the panel. Nowadays, numerical methods based on FEM and BEM can be employed to solve the vibro-acoustic problem, modelling in this way complex geometries and mounting conditions (Ang et al., 2017; den Wyngaert et al., 2018; Jung et al., 2017; Løvholt et al., 2017). However, building a 3D structural-acoustic interaction model can be an onerous, time-consuming task with increased computational cost.

The idea of utilizing "soft mounts" to reduce the fundamental frequency of the system delves into the investigation of what constitutes soft mounting. Intuitively, following the general concepts of vibration isolation for the reduction of the eigenfrequency through the reduction of stiffness, supporting an existing panel on elastic mounts, the "mass law" behaviour may be dragged into lower frequencies and the resonant region of the new system panel-mount will be moved below a critical frequency; for example, around 20 Hz, considering the threshold of human hearing.

The aim of this chapter is to present a simple, analytical, method, namely the "*In series LPM approximation*", for the STL estimation of mounted panels. The advantage of the proposed method compared to the Rayleigh-Ritz or any other exact solution is that any boundary conditions can be modelled without the use of complex mathematical formulations or sophisticated numerical models. Of course, the trade-off is the reduced accuracy of the model, as only the first mode of the panel is considered. Yet, as we will subsequently observe, the proposed method can capture the fundamental properties of the vibrating panel, especially when compared to the KIM's (2010) *Impedance approach*. Additionally, the effects of elastic mounts in the STL performance are investigated by considering a relevant case of single-leaf plasterboard partitions; investigation showcases that uncertainties due to practical factors can be diminished by adopting this approach. The analysis is conducted via both simple mathematical models and a coupled finite element vibro-acoustic model where the room-to-room sound transmission is described based on the laboratory set-up in SINTEF Building laboratory in Oslo, Norway (Løvholt et al., 2017)

2.2 Analytical formulation of Sound Transmission Loss of a Panel

In this section the theory of Sound Transmission Loss (STL) through a single panel is briefly presented. There are several methods to simulate the propagation of sound in the presence of obstacles and derive the consequent STL (Kim, 2010; Moore and Lyon, 1991; Zhang and Sheng, 2018). Herein, an impedance-based approach as well as a more sophisticated approach, namely the "*In series approximation*", are presented and adopted for analysis in order to capture the fundamental physics of the sound transmission problem.

2.2.1 Impedance approach

This approach considers the sound propagation through a single, infinite, rectangular thin plate, simply supported (hinged) in an infinite, rigid baffle. Transmission loss of sound occurs when there is an impedance mismatch between the propagation media of the traveling sound waves, thus sound is reflected and/or absorbed. Direct sound transmission through thin panels depends on the mass, stiffness and damping of the system plate-support. Figure 1-1 of the previous chapter shows a typical form of the STL curve for sound propagation through a thin plate (Cowan, 2013).

This curve presents five distinct regions in corresponding frequency ranges, depending on the properties of the system.

Stiffness Controlled Region: This region concerns the low-frequencies, namely frequencies lower than the fundamental natural frequency of the system. The STL curve in this region, is primarily dependent on the elastic stiffness of the panel mounting (panel bending stiffness). In general, STL presents approximately a 6 dB decrease per octave in this region.

Resonance Controlled Region: The transmission behaviour of the panel in this region is related to the natural frequency of the system which depends on the dimensions of the panel and the speed of sound in the panel's material. In this frequency region, the first major STL reduction of the finite panel is observed. In more detail, the resonant frequencies of an isotropic, rectangular plate may be calculated as follows:

$$f_0 = \frac{\lambda_{11}}{2\pi l_y^2}\sqrt{\frac{Eh^2}{12\rho(1-\nu^2)}} \tag{2-1}$$

where ρ is the volumetric density, E the Young's Modulus and ν the Poisson's Ratio of the plate. For a simply supported plate, the parameter λ_{11} is calculated as $\lambda_{11} = \pi^2(1+\beta^2)$, where $\beta = l_y / l_x$ is the

ratio of the width and height l_x and l_y. For a plate with clamped edges in a frame, then $\lambda_{11} = \beta^2(89.3\beta + 36.7\beta^2 - 5.27\beta^3)$.

Mass Controlled region – Mass Law: In a general case, as in Figure 2-1 (a), the STL is investigated via the assumption of a propagating plane wave between two different media. The impedance mismatch comes from the difference of impedance that the propagation medium of the incident waves $\tilde{Z}_0$, has to the propagation medium of the transmitted waves $\tilde{Z}_1$. In order to quantify the consequences of this mismatch, the transmission coefficient τ is introduced. This coefficient is defined as the ratio between the complex amplitude of the transmitted sound pressure to the complex amplitude of the incident sound pressure:

$$\frac{\tilde{p}_t}{\tilde{p}_i} = \tau = 2\frac{\tilde{Z}_1}{\tilde{Z}_1 + \tilde{Z}_0} \tag{2-2}$$

Figure 2-1 (b) illustrates a wall, a rigid flat surface that consists only of mass, oscillating in an infinite rigid baffle with air on both sides, subjected to normal incident plane waves $p_i = \tilde{p}e^{j(\omega t - \kappa_0 z)}$. This particular case is referred to as the "limp wall" assumption and the resulting frequency response of the STL is known as the "mass law".

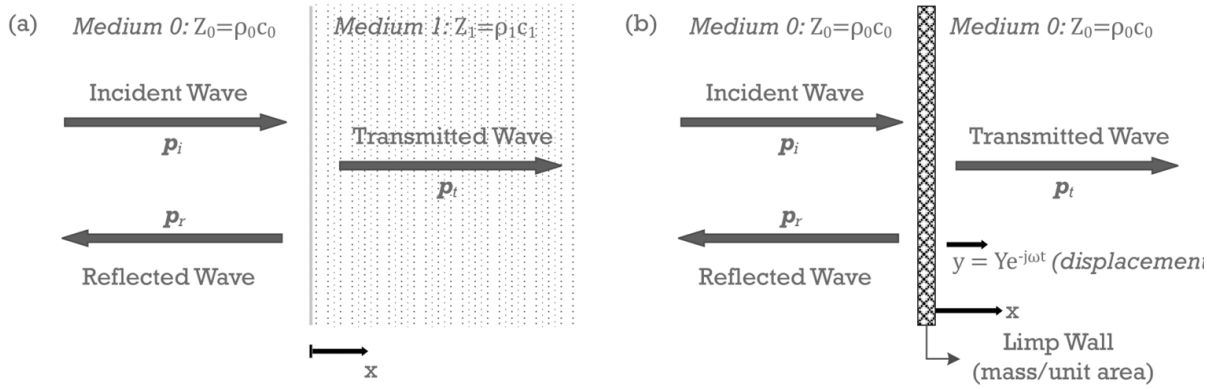

Figure 2-1: (a) Wave propagation in the presence of impedance mismatch (b) Limp wall assumption.

For frequencies higher than the natural frequency f_0, the STL is controlled by the mass per unit area of the panel. This corresponds to an increase of 6 dB per octave in STL. Specifically, for a thin panel, neglecting stiffness and damping (limp wall), the STL is calculated as:

$$STL = 10\log\left[\frac{\omega^2\bar{m}^2}{4(\rho_0 c_0)^2/\cos^2\theta}\right] \tag{2-3}$$

where θ is the angle of incidence of the propagated sound waves, c_0 is the speed of sound in air, ρ_0 the air density, and $\bar{m}$ (kg/m^2) is the mass per unit area of the panel. In the case of normal incident waves, then $\theta = 0$.

Coincidence Controlled region: A second major reduction of STL is observed in this region which comes from the coincidence of incident sound waves and bending waves in the panel. When the trace wavelength, namely the component of the incident wavelength parallel to the panel's surface, becomes equal to the free flexural wavelength of the panel, the incident wave speed is also equal to the bending wave speed in the panel. The coincidence frequency is calculated as:

$$f_c = \frac{c_0^2}{2\pi h}\sqrt{\frac{12\rho(1-\nu^2)}{E}} \tag{2-4}$$

Now, as illustrated in Figure 2-2, assuming that the same laws apply in case of a partition, then by applying pressure and velocity continuity conditions at the interface of air and plate, the transmission coefficient comes as:

$$\tau = \frac{2\tilde{Z}_0}{-j(\omega m - k/\omega) + (2\tilde{Z}_0 + c)} \tag{2-5}$$

The imaginary part in the denominator of Eq. (2-5) indicates that the mass contribution ωm and the spring contribution $-k/\omega$ have a phase difference of 180°, while the term $2\tilde{Z}_0$ indicates the radiation at both sides of the wall. The transmission coefficient can also be written as:

$$\tau = \frac{2\tilde{Z}_f}{\tilde{Z}_p + \tilde{Z}_f} \tag{2-6}$$

where $\tilde{Z}_p = -j(\omega m + jc - k/\omega)$ is the partition (mechanical) impedance, and $\tilde{Z}_f = 2\tilde{Z}_0$ is the fluid loading impedance in both directions (Kim, 2010).

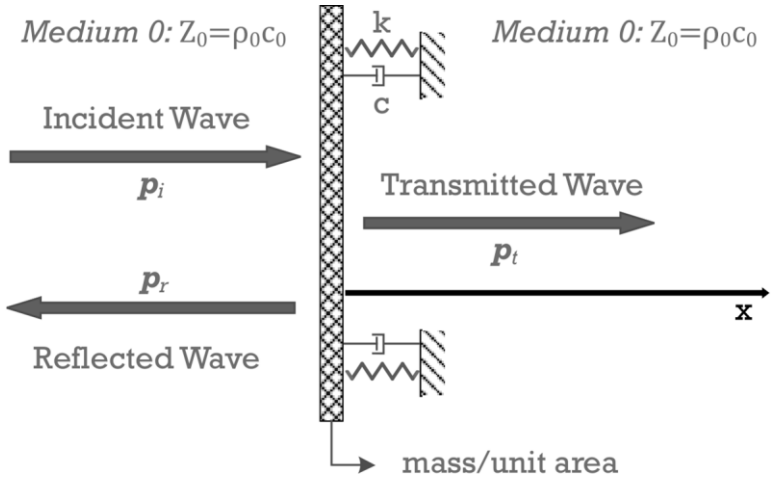

Figure 2-2: Wave propagation at a partition.

For the calculation of the Sound Transmission Loss (STL) in the case of a thin plate, using the single DoF model, the expression of the mechanical impedance $\tilde{Z}_p$ can be rearranged to include the transfer function of the displacement (Paradeisiotis, 2019), namely:

$$\tilde{Z}_p = \frac{-1}{j\omega}\frac{\left|\tilde{T}_{XF}\right|^{-1}}{A} \tag{2-7}$$

where A is the surface of the plate subjected to the excitation. Therefore, the STL is calculated as follows:

$$STL = 10\log_{10}\frac{1}{|\tau|^2}\ \text{(dB)} \tag{2-8}$$

2.2.2 Vibrating plate approximations

2.2.2.1 Sound radiation from a rectangular panel in an infinite rigid baffle

The fluid domain is assumed homogeneous and compressible. The mass density of air and sound speed are noted as ρ_0 and c_0, respectively. The infinitely large acoustic rigid baffle divides the space into two domains i.e., the excitation domain V^- and the receiver domain V^+. The panel is subjected to the incident pressure p_i, with incidence angle θ_i and azimuth angle φ_i. Therefore, the excitation domain consists of the incident pressure p_i, the reflected pressure p_r, and the re-radiated pressure p_{rad}^- due to the motion of the finite panel.

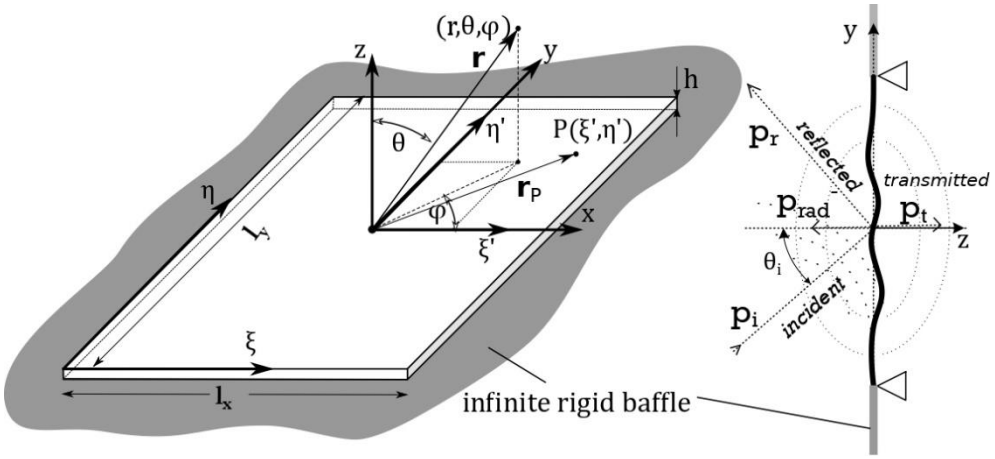

Figure 2-3: (a) Wave propagation in the presence of impedance mismatch (b) Limp wall assumption.

The receiver domain consists only of the transmitted pressure p_t, namely the radiated pressure due to the motion of the panel p_{rad}^{+}. Assuming that the incident sound pressure p_i is a harmonic function, we may derive the following expression:

$$p_i(x,\ y,\ z,\ t)\ = P_i e^{-j(\kappa_x x+\kappa_y y+\kappa_z z)} e^{j\omega t} = \tilde{p}_i(x,\ y,\ z) e^{j\omega t} \tag{2-9}$$

where $\tilde{p}_i(x,\ y,\ z)$ the time invariable complex amplitude and $\kappa = \omega / c_0$ is the wavenumber with:

$$\kappa_x = \kappa \sin\theta \cos\varphi,\ \kappa_y = \kappa \sin\theta \sin\varphi,\ \kappa_z = \kappa \cos\theta \tag{2-10}$$

The reflected pressure by the surface of the panel is then expressed as:

$$p_r(x,\ y,\ z,\ t)\ = P_r e^{-j(\kappa_x x+\kappa_y y+\kappa_z z)} e^{j\omega t} = \tilde{p}_r(x,\ y,\ z) e^{j\omega t} \tag{2-11}$$

having the opposite direction from the incident wave.

Lord Rayleigh (1896) determined a relationship expressing the radiated (transmitted) pressure in terms of the structural velocity based on Green's function:

$$p^{+}{}_{rad}(\mathbf{r},t)\ = p_t(\mathbf{r},t) = \frac{j\omega\rho_0}{2\pi} e^{j\omega t} \int_{-l_{x/2}}^{l_{x/2}} \int_{-l_{y/2}}^{l_{y/2}} \frac{e^{-j\kappa R}}{R} \frac{\partial w(\xi',\eta')}{\partial t} d\eta' d\xi' \tag{2-12}$$

where R ,referring to Figure 2-3, is defined as:

$$R = |\boldsymbol{r} - \boldsymbol{r}_P| = \sqrt{(x-\xi')^2 + (y-\eta')^2 + z^2} \tag{2-13}$$

and $r = (x,\ y,\ z)$ is the position vector of a point in the receiver domain while $\boldsymbol{r}_p = (\xi',\ \eta',0)$ is the position vector of the centre of an elemental radiator with surface ΔS on the panel, having a normal velocity amplitude $\dot{w} = (\xi',\ \eta')$. For the local coordinates, it holds that $\xi' = \xi - \frac{l_x}{2}$, $\eta' = \eta - \frac{l_y}{2}$.

Following the derivation of the transmitted pressure expression, there are two different ways used to determine the radiated (transmitted) power. The first method is to integrate the intensity on a hemisphere in the far-field by enclosing the plate which is followed in this work, while the second one is to integrate the acoustic intensity over the surface of the vibrating plate. Both approaches require the knowledge of the distribution of the velocity over the plate, and they assume a weak coupling between the vibrating structure and the radiated sound field.

Applying the far-field approximation, as described in Appendix A.1, the transmitted intensity I_t is calculated as $r_P = (\xi',\ \eta',\ 0)$ is the position vector of the centre of an elemental radiator with surface:

$$I_t(r,\theta,\varphi) = \frac{\left|p_t(r,\theta,\varphi)^2\right|}{2\rho_0 c_0} \tag{2-14}$$

Then, the transmitted power Π_t is derived by integrating the transmitted intensity on a hemisphere in the far field which is enclosing the plate as:

$$\Pi_t = \int_0^{2\pi}\int_0^{2\pi} \mathrm{I}_t r^2 \sin\theta d\theta d\varphi \tag{2-15}$$

while the incident power on the panel is defined as:

$$\Pi_i = \frac{\left|p_i\right|^2 l_x l_y \cos\theta}{2\rho_0 c_0} \tag{2-16}$$

2.2.2.2 Vibration of a panel subject to external pressure

With reference to Figure 2-3, the finite-sized flat panel partition is assumed to be rectangular and baffled, with lengths l_x and l_y along the x and y axes, respectively. The panel of thickness h, is considered homogeneous and isotropic and is modelled as a classical thin plate, implying that the effects

of both the rotary inertia and the transverse shear deformation can be neglected. Hereinafter, the equation of motion governing the bending vibration of the plate is given by:

$$D\left[\frac{\partial^4 w(\xi,\eta,t)}{\partial\xi^4}+2\frac{\partial^4 w(\xi,\eta,t)}{\partial\xi^2\partial\eta^2}+\frac{\partial^4 w(\xi,\eta,t)}{\partial\eta^4}\right]+\rho h\frac{\partial^2 w(\xi,\eta,t)}{\partial t^4}= \\ =p_i(\xi,\eta,t)+p_r(\xi,\eta,t)+p_{rad}^{-}-p_{rad}^{+} \tag{2-17}$$

where $D=\tilde{E}h^3/12\left(1-\nu^2\right)$ is the bending stiffness of the plate, E, h, ρ and ν are the Young's modulus, thickness, mass density and Poisson's ratio of the plate, respectively. $w(\xi,\ \eta,\ t)$ is the instantaneous transverse displacement. In order to account for energy dissipation due to structural damping, a complex modulus of elasticity is introduced, $\tilde{E}=E\left(1\ +\ jn\right)$, where n is the loss factor. The right-hand side of Eq. (2-17) must satisfy the velocity continuity at the surface of the panel $\left(z=0\right)$. In that case, it holds that $p_r=\ p_i$ and since $p_t=p_{rad}^{+}=-p_{rad}^{-}$, the right-hand side becomes as follows:

$$p_i(\xi,\eta,t)+p_r(\xi,\eta,t)+p_{rad}^{-}-p_{rad}^{+}=2p_i(\xi,\eta,t)+2p_t(\xi,\eta,t) \tag{2-18}$$

The so-called "blocked pressure" $p_b=2p_i$ (Kim, 2010), is the pressure when the incident wave meets a rigid wall.

2.2.2.3 Free Finite Rigid (FFR) panel approximation

Aiming to replace the infinite panel approximation (limp wall) with a more appropriate reference for finite panels, the free finite rigid (FFR) panel approximation is formulated. In this case, it is assumed that the panel is rigid consisting only of mass and oscillates freely in an infinite rigid baffle; however, it has finite dimensions, as demonstrated in Figure 2-4. Since the panel is considered rigid, the spatial derivatives of Eq. (2-17) are eliminated. Also, considering only the blocked pressure $p_b=2p_i$ as the forcing pressure, and that p_i are incident plane waves, the equation of motion becomes:

$$\rho h\ddot{w}\ =\ 2P_i e^{j\omega t} \tag{2-19}$$

The forcing pressure is a harmonic function; therefore, the steady-state transverse displacement of the panel can be expressed as:

$$w=W\left(\xi,\eta\right)q\left(t\right) \tag{2-20}$$

where:

$$q(t) = Ce^{j\omega t} \tag{2-21}$$

For the rigid panel assumption, the shape function is independent of the position (ξ,η) on the surface of the panel, namely $W(\xi,\eta)=1$.

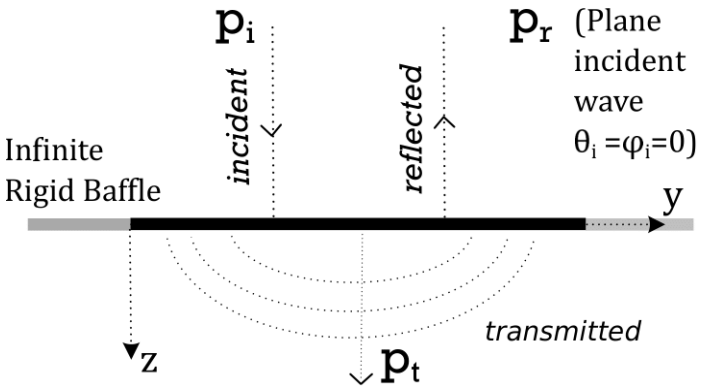

Figure 2-4: Coordinate systems of a rectangular plate in a rigid baffle.

Substituting the solution into Eq. (2-19), and solving the equation for C, gives the following:

$$C_{FFR} = \frac{2P_i}{\rho h \omega^2} \tag{2-22}$$

The transmission coefficient then is calculated as:

$$\tau_{FFR} = \frac{1}{l_x l_y}\left(\frac{\rho_0}{\pi}\right)^2 \frac{1}{\bar{m}^2} I_{\theta\varphi} \tag{2-23}$$

where $\bar{m} = \rho h$ is the mass density (mass per surface area) of the panel, and $I_{\theta\varphi}$ is the double integral over a hemisphere in the receiver domain, as presented in Appendix A.2.

2.2.2.4 Simply supported panel 1st mode approximation

Analytical solutions of the problem can be derived via modal superposition methods; for example such methods are formulated by Roussos (1985) and are briefly presented in Appendix A.3. However, in order to reduce complexity, in these analytical approaches past researchers usually avoid to include the re-radiated pressure $2p_t(\xi,\eta,t)$ (often referred to as "fluid loading") of Eq. (2-18) in their calculations . According to Roussos (1985), neglecting the effect of the re-radiated pressure allows an accurate

solution over a large frequency range, and gives invalid answers only for frequencies near the panel's fundamental resonant frequency.

In this section, since the low-frequency range of interest in the present case is within the range near the fundamental resonance of the panel, an attempt for a more accurate and practical approximation is formulated, including the effect of fluid loading. Considering only the 1st vibrational mode of the simply supported plate, the spatially dependent amplitude of the transverse displacement $w(\xi,\eta) = W_1(\xi,\eta,t)e^{-j\omega t}$ is assumed by the shape function:

$$W_1 = C_1 \sin\left(\frac{\pi\xi}{l_x}\right)\sin\left(\frac{\pi\eta}{l_y}\right) \tag{2-24}$$

The resulting expression for the transmitted (radiated) power Π_t is given by Eq. (A-37). The detailed analysis is presented in Appendix A.4. Assuming normal incident waves $(\theta_i = 0)$, the incident power is established as:

$$\Pi_i = \frac{P_i^2 l_x l_y}{2\rho_0 c_0} \tag{2-25}$$

leading to the transmission coefficient τ described as:

$$\tau_1 = \frac{1}{l_x l_y}\frac{\left(16\omega^2\rho_0\right)^2}{\left|\pi^3 rh(\omega_1^2-\omega^2) - 16\omega^2\rho_0\dfrac{e^{-jkr}}{r}\right|^2} I_{\theta\varphi} \tag{2-26}$$

where distance r needs to be large enough to satisfy the far-field approximation and frequency of the 1st mode, resulting from the homogeneous form of Eq. (2-17), as:

$$\omega_1^2 = \frac{D\pi^4}{\rho h}\left(\frac{1}{l_x^2}+\frac{1}{l_y^2}\right)^2 \tag{2-27}$$

By expressing the dynamic behaviour of the simply supported panel continuous system (approximated by the 1st mode), as a single degree of freedom (SDoF) lumped parameter model (LPM), the corresponding generalized mass and stiffness (YANG et al., 2012) are described as:

$$m_1^* = \frac{\rho h l_x l_y}{4} = \frac{\bar{m} l_x l_y}{4} = \frac{m}{4} \tag{2-28}$$

$$k_1^* = \frac{D\pi^4 l_x l_y}{4} = \left(\frac{1}{l_x^2} + \frac{1}{l_y^2} \right)^2 \tag{2-29}$$

The transmission coefficient is then calculated as:

$$\tau_{LPM} = l_x l_y \left(\frac{4\omega^2 \rho_0}{\pi^3} \right)^2 \frac{1}{\left[m_1^* \left| \omega_1^2 - \omega^2 \right| \right]^2} \mathrm{I}_{\theta\varphi} \tag{2-30}$$

In Figure 2-5, the "red dashed line" represents the FFR panel approximation as given by Eq. (2-23). Intuitively, this approximation should constitute the ideal case regarding the STL of a panel with finite dimensions and may act as a reference curve for various comparisons. This methodology may substitute the infinite panel approximation, which is invalid in the lower frequency range, examined herein. The "yellow line" corresponds to the 1st mode approximation of the simply supported panel, while the "blue line" is the lumped parameter model, as derived from the 1st mode approximation.

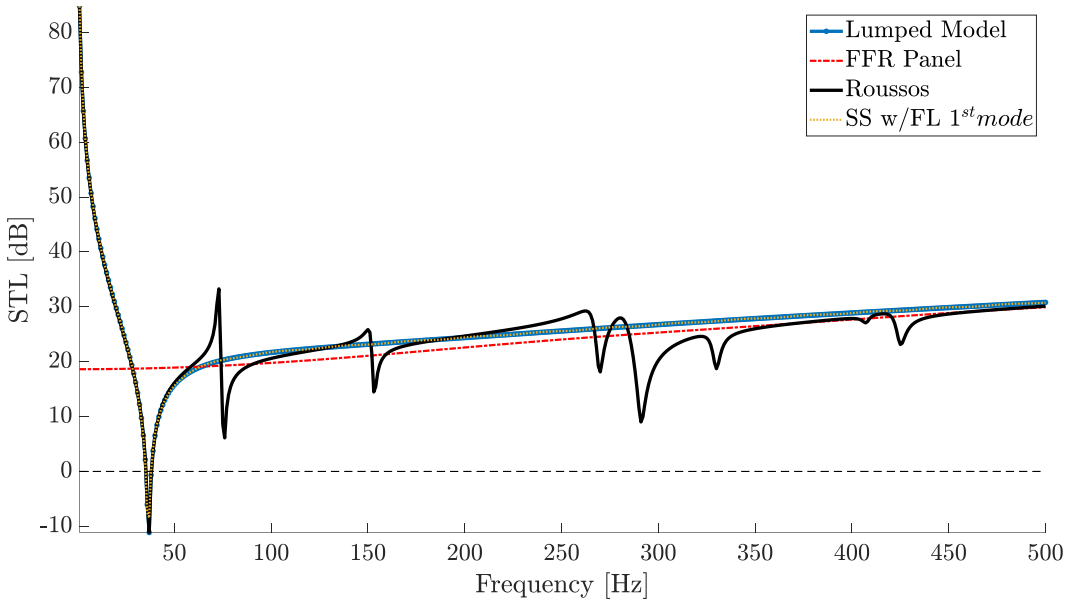

Figure 2-5: Comparison among Roussos, 1st mode, LPM and rigid approximations.

The difference between the two methods is essentially the effect of fluid loading (FL), whereas in the latter model, this is not included. It is observed that the fluid loading has very little effect on the damping of the first resonance. Thus, the elimination of its participation in the respective models is justified and

is considered as a safe approximation. Lastly, the "Black line" represents the modal superposition method, as formulated by Roussos (1985). The objective of the simplified models is to provide a more straightforward and fast prediction of the acoustic performance of the panel along with the ability to extract intuitive and revealing expressions of the main dynamic parameters that govern its frequency response. Since the higher modes have significantly lower modal participation factors in the frequency response than the fundamental mode, they are relatively easily damped. With that thinking, the approximation using only the 1st mode is considered appropriate in order to study this low-frequency region, and following, the effect of elastic mounting and damping.

The slight deviation of the STL between the FFR panel and the other three methods when $\omega \gg \omega_1$, can be explained by looking at the amplitude of the steady state solution. From the 1st mode approximation without the effect of fluid loading (LPM – Appendix A.5), the following expression is defined:

$$C_1 = \frac{8P_i l_x l_y}{\pi^2} \frac{1}{m_1^*(\omega_i^2 - \omega^2)} = \frac{32P_i}{\pi^2} \frac{1}{\bar{m}(\omega_1^2 - \omega^2)} \tag{2-31}$$

which for $\omega \gg \omega_1$ becomes:

$$C_1 = -\frac{32P_i}{\pi^2} \frac{1}{\bar{m}\omega^2} \tag{2-32}$$

This is an indication that for this condition the response depends only on the mass density of the panel, as stated by the "mass law". However, by comparing this expression with the equivalent for the FFR panel approximation, we have the following:

$$C_{FFR} = -\frac{-2P_i}{\bar{m}\omega^2} \tag{2-33}$$

The resulting ratio of Eqs. (2-32) and (2-33), in combination with Eq. (2-24) results in the following relationship for the velocity amplitudes in the two cases:

$$\frac{|\dot{w}_1|}{|\dot{w}_{FFR}|} = \frac{16}{\pi^2} \approx 1.6 \tag{2-34}$$

Namely, the maximum velocity amplitude of the 1st mode approximation is higher than the velocity amplitude of the FFR approximation by a factor ≈ 1.6. Then, by considering the mean velocity $\left|\overline{\dot{w}_1}\right|$ in the case of the 1st mode approximation we have the following expression:

$$\left|\overline{\dot{w}_1}\right| = \frac{64}{\pi^4}\left|\dot{w}_{FFR}\right| = 0.657\left|\dot{w}_{FFR}\right| \tag{2-35}$$

This means that the mean velocity amplitude of the simply supported panel is lower than the amplitude in the case of the FFR panel assumption. Therefore, the resulting STL is slightly higher.

2.2.3 In series Lumped Parameter Model approximation for elastic mounts

The exact theoretical calculation of how the bending stiffness of the panel is combined with the stiffness of the supporting elastic mounts is a cumbersome and complicated procedure (Du et al., 2012; Zhang and Li, 2010). The goal is to formulate a streamlined procedure for the investigation of how the bending stiffness of the panel couples with the mounting stiffness in the case where the panel is supported on elastic mounts and how the acoustic performance is affected. In order to do that, the main assumption is that the bending stiffness of the deformable plate is in a way in series with the stiffness of the mounting. Therefore, the resulting stiffness is:

$$\mathrm{k}_{\mathrm{tot}} = \frac{k_1^* k'_0}{k_1^* + k'_0} \tag{2-36}$$

When the mounting is very stiff ($k_0^{'} \gg k_1^*$), leads to $k_{tot} = k_1^*$, namely, the case of the simply supported plate is approached. When the mounting stiffness tends to zero, the plate is essentially free floating. In the case that the mounting stiffness k_0 is of comparative order of magnitude with k^*_1, there is some deviation between the resulting eigenfrequency of the model and the actual eigenfrequency. However, in cases when $k_0^{'} \gg k_1^*$ or $k_0^{'} \ll k_1^*$, the deviation is negligible.

Figure 2-6 illustrates the equivalent dynamic SDoF model of the deformable thin panel when it is supported on elastic mounts, according to the "in-series" assumption. This is achieved by utilizing the generalized values of the structure, namely generalized mass and the corresponding generalized stiffness for the appropriate modes, as calculated from Eqs. (2-28)-(2-29), for the 1st mode approximation of the simply supported panel.

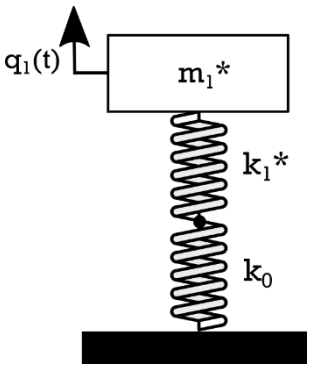

Figure 2-6: Modelling of a deformable plate on elastic mounts with stiffness $k_0^{'}$.

Since the loss factor (n) can represent more accurately the dynamic response of nonlinear systems compared to the damping ratio which is defined on the grounds of the linear single degree of freedom (SDOF) viscous model (Carfagni et al., 1998; Koblar and Boltežar, 2013), hysteretic damping is introduced indirectly considering complex stiffness elements as:

$$k'_0 = k_0(1+jn) \tag{2-37}$$

The STL is then calculated as $STL = 10\log_{10}\left(\frac{1}{\tau}\right)^2$, where the transmission coefficient τ comes as:

$$\tau = l_x l_y \left(\frac{4\omega^2\rho_0}{\pi^3}\right)^2 \frac{1}{\left|-\omega^2 m_1^* + k_1^*(1-TF_{21})\right|^2} I_{\theta\varphi} \tag{2-38}$$

And the transfer function TF for the case of simple elastic mounts is $TF = 0$

Thus:

$$\tau_{el} = l_x l_y \left(\frac{4\omega^2\rho_0}{\pi^3}\right)^2 \frac{1}{\left|-\omega^2 m_1^* + k_{tot}\right|^2} I_{\theta\varphi} \tag{2-39}$$

2.3 3D vibro-acoustic FE model

In addition to the aforementioned analytical methodologies, a 3D FE coupled vibro-acoustic model is developed on the commercial finite element software package ABAQUS® (Smith, 2009). In the present simulations, the geometry of the SINTEF laboratory (Løvholt et al., 2017) is utilized as the computational domain, as shown in Figure 2-7 (a) and (b).

It is noted that the laboratory geometry and the measurement procedure do not accurately follow the ISO standards guidance, however, the developed model can be used for room-to-room sound

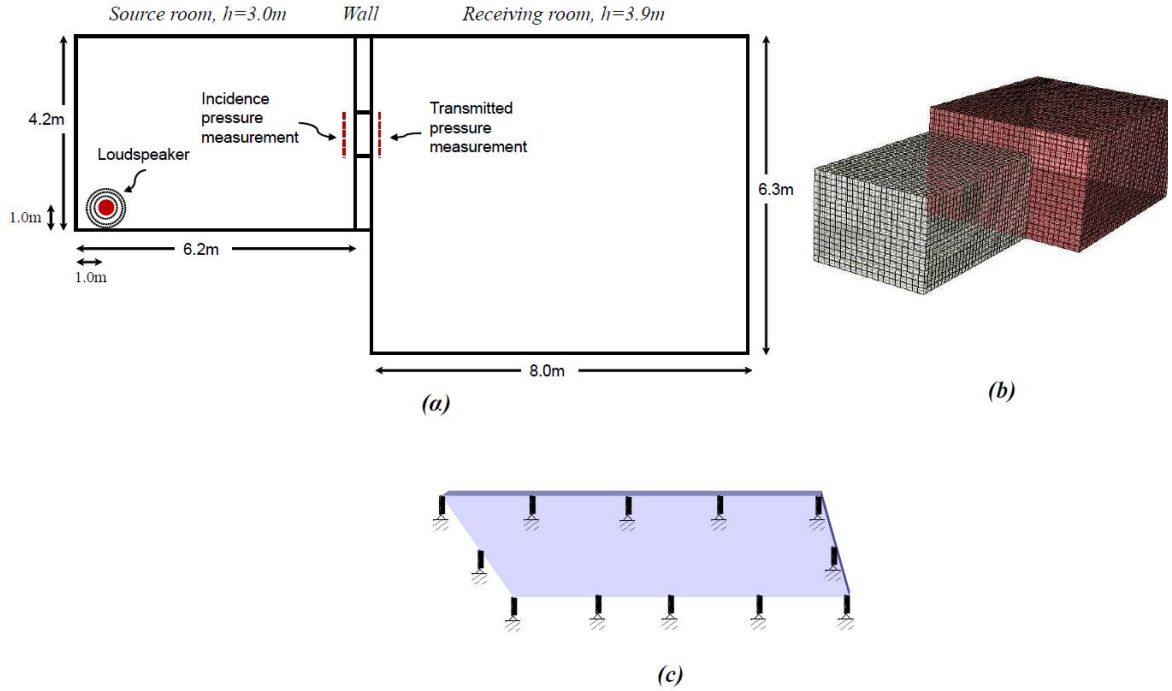

Figure 2-7: (a) Plan view of the sound laboratory setup used in ABAQUS model. (b) Depiction of the vibro-acoustic model. (c) Positioning of the twelve (12) mounts on the surface of the panel.

transmission predictions. The panel is excited by the source located in the left corner of the source room and the incidence and radiated acoustic pressure is extracted from the fluid-structure interface nodes. An arithmetic average is performed as follows:

$$\bar{P}_t = \frac{1}{n}\sum_{i=1}^{n} \left| p_{t,i} \right| \tag{2-40}$$

$$\bar{P}_i = \frac{1}{n}\sum_{i=1}^{n} \left| p_{i,i} \right| \tag{2-41}$$

where n denotes the total number of measuring nodes; i denotes the node number; p_i denotes the incidence pressure. and p_t denotes the transmitted pressure. Then the averaged pressure was used to compute the simulated STL by the following expression:

$$STL = 20\log_{10}\left(\frac{\left|\bar{P}_i\right|}{\bar{P}_t}\right) \tag{2-42}$$

The panel is discretized by 20-node quadratic solid hexahedral elements, while the fluid domain is discretized by 20-node quadratic acoustic hexahedral elements. Tie constraints are used to simulate the coupling at the fluid-structure interface, while reflecting boundary conditions are specified to simulate the room conditions. In cases that the plate is supported on elastic mounts, connectors are installed on the required locations with the appropriate properties. Lastly, the discretization of the fluid domain has more than three quadratic elements across the wavelength of interest, aiming to increase the accuracy of the computational results (Marburg, 2002).

2.4 Numerical Example - Parametric investigation of STL

In this section, the elements that affect the STL of a rectangular plate are investigated, especially in the case of a single leaf plasterboard partition. Initially, the analytical models proposed in the previous section are employed. A 0.625 x 1.6m rectangular plasterboard is considered, according to real-life masonry applications. The width corresponds to the horizontal distance between the upright supporting beams, hence providing the stable frame of the plasterboard. Typically, the height of such a plasterboard is around 3.2 m, meaning that it can be covered by two pieces of the considered dimensions. The selected dimensions correspond also to a frontal surface of 1 m^2. The relevant properties of the plasterboard are summarized in Table 2-1.

Table 2-1: Plasterboard properties.

ρ_p [kg/m^3]	l_x [m]	l_y [m]	h_p [mm]	E_p [MPa]	v_p [-]	η_p [-]
668	1.2	2.4	12.5	2900	0.31	0.01

2.4.1 Validation of FE model

Figure 2-8 is presented in conjunction with Figure 2-5. Herein the panel with the simply supports conditions is examined in terms of STL numerically and is compared with the established analytical methods. The yellow line corresponds to the 1st mode approximation of the simply supported panel and the black dashed line represents the modal superposition method, as formulated by Roussos and the grey line with markers shows the STL as calculated from the finite element model. In general, a good agreement is observed among the analytical methods and the full numerical model where the geometry of the SINTEF laboratory is adopted.

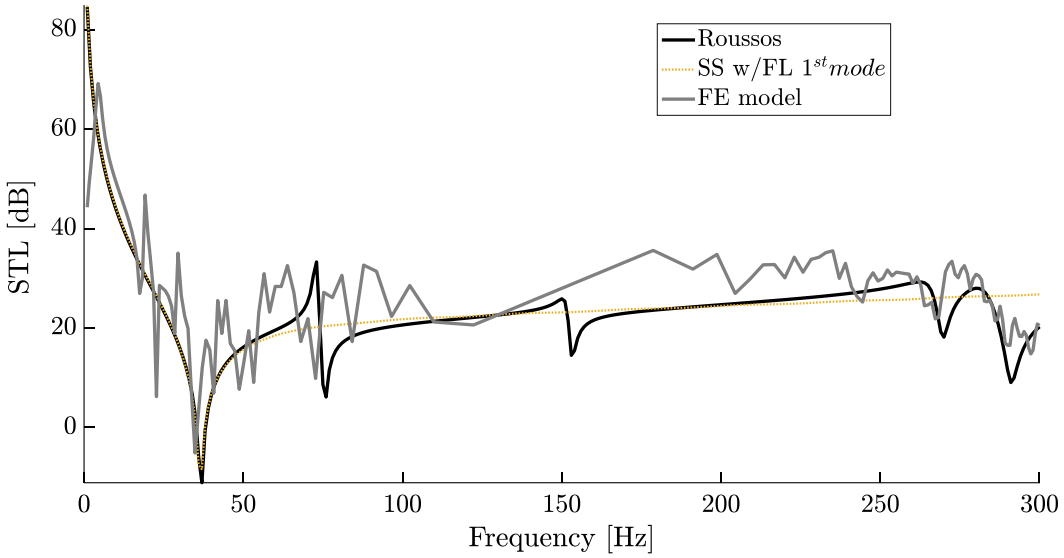

Figure 2-8: Comparison of 1st mode, rigid approximations and numerical model.

2.4.2 Effect of material properties in STL

As a following step, a parametric investigation for the effect of the rigidity of the panel itself was carried out for various assumed values of Young's Modulus E. Plasterboard panels present various compositions or even different homogeneity in the same product line; therefore a variation of their rigidity is expected. In addition, fluctuations in temperature or humidity in the environment can affect the value of the Young's Modulus. Figure 2-9, illustrates the shifting of the eigenfrequencies of the panel's first nine modes, assuming three different values of E. These deviations, of up to 123%, are representative of the effects of the aforementioned factors. This observation leads to the conclusion that such variation introduces significant uncertainty concerning the dynamic behaviour of the panel and consequently its acoustic performance in the low-frequency regime.

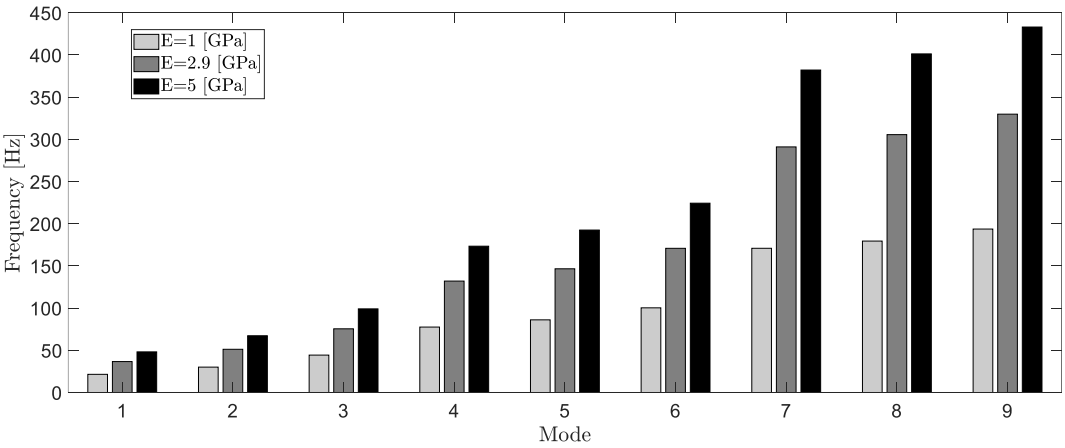

Figure 2-9: Dependence of modal frequencies with the variation of the panel's Young's Modulus, E.

2.4.3 Effect of support conditions in STL

In order to investigate the effects of elastic mounting in the following FE vibro-acoustic simulations, twelve (12) linear springs were attached to the panel, as presented in Figure 2-7 (c). The resulting STL frequency response compared to the simply supported and clamped configurations are presented in Figure 2-10. The total stiffness of the mounting is considered equal to the generalized stiffness of the simply supported panel ($k = k_1^* = 1.1 \times 10^5\ [N/m]$), while no damping is considered for the mounts.

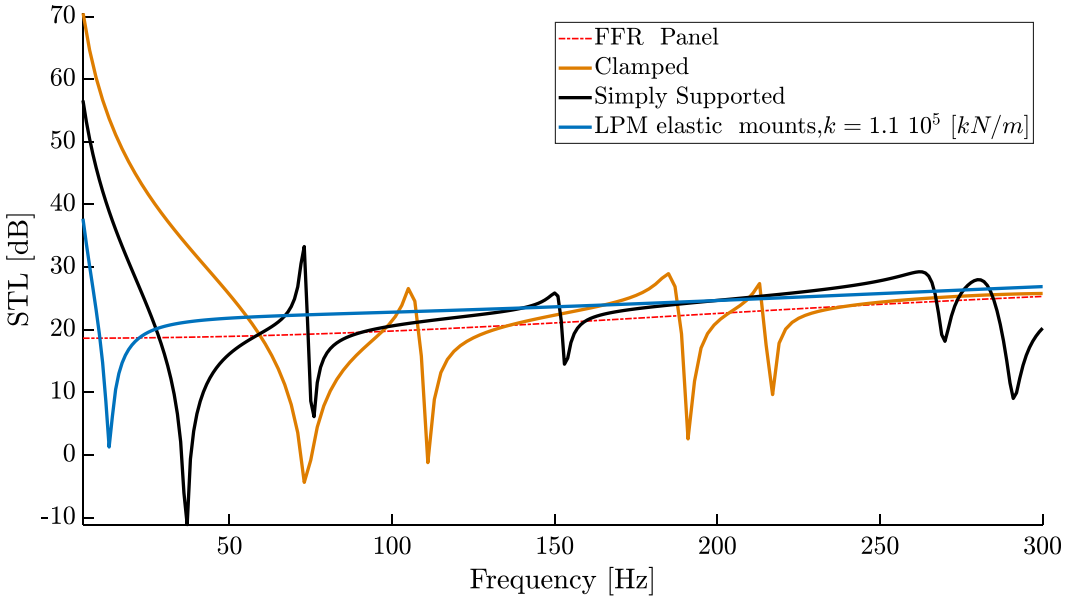

Figure 2-10: Effect of support conditions in Sound transmission loss (STL).

Following the logic of classic vibration isolation, the eigenfrequency of the panel can be lowered enough and moved outside the frequency range of interest, e.g., above 20 Hz. However, a significant decrease of this frequency can have certain implications. On the one hand, it leads to slightly reduced STL frequency response, while on the other hand, it may present practical problems including excessive vibration magnitude, possible resonances with other supportive structural elements such as bolts or the frame, or even inadequate rigidity to undertake impact loads. The optimal solution requires a combination that leads to a relatively low fundamental eigenfrequency that can be effectively dampened without the need of excessive damping. At the same time, the fundamental frequency is required to be high enough, so that the overall STL is not significantly reduced, and no vibrational implications come into play when the mounting is very soft.

Another purpose of the comparison in Figure 2-10 is to highlight the deviation of the eigenfrequencies between the simply supported and clamped panels that is derived from the uncertainty introduced by this fact in real world installations. Depending on the technique of the installation the exact support conditions may vary in these two cases. However, the inclusion of the soft elastic mounts, eliminates

this uncertainty as it produces an explicit, calculated frequency response by design. Additionally, the reduction of the eigenfrequencies alone almost eliminates the participation of the higher modes even without the consideration of any energy diffusive elements besides the structural damping of the panel itself which holds for all three cases compared here.

2.4.4 Effect of damping

Further examination considers the effect of damping introduced by the elastic mounts. Assuming the same stiffness for the mounts as in section 2.4.3 a comparison is presented in Figure 2-11.

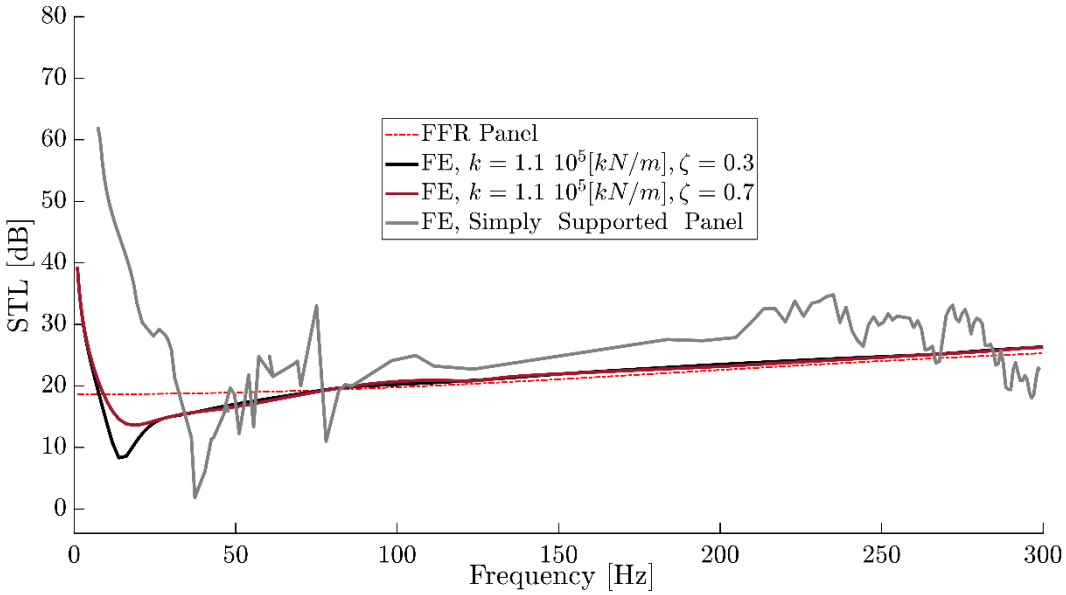

Figure 2-11: Effect of damping in Sound transmission loss (STL).

The results are meant to demonstrate the expected level of damping in order to effectively damp the fundamental frequency. As already mentioned, even in cases of low damping, the STL response is flattened as the higher eigenfrequencies are effectively damped while only the first eigenfrequency requires significant damping. Whether the actual values of the assumed viscous dampers for high damping ratios are realistic, is surely a matter of discussion and depends on practical factors such as the material used for the mounts and spatial considerations of the implementation.

Certainly, the positions of the mounts have a significant role on their damping effectiveness. Especially in this case of viscous damping, the velocity amplitude is maximum at the centre of the panel and minimum along the edges, therefore a mount positioned at the centre would most effectively dampen the fundamental resonance. However, this case would change the dynamic behaviour of the panel and would also require an additional supporting frame along the middle of the panel, which is something that is preferably avoided. For these reasons such a modification is not investigated in the current contribution.

2.5 Concluding Remarks

In this chapter, the theoretical background of the acoustic theory was presented which will be subsequently implemented in the proposed advanced absorbers and metamaterial designs. Initially, the mathematical formulation of the *Impedance approach* introduced by KIM (2010) was described. This approach was adopted as a basis of the more accurate *"in series" LPM approximation,* suggested in this research work.

The theory concludes to the inclusion of "soft mounts" to enhance the noise attenuation properties of panels. In this case, the total stiffness of the mounts is lower than the generalized stiffness of the simply supported panel. When the panel is supported regionally on soft elastic mounts, the values of the eigenfrequencies of the structure are reduced. This has two main consequences:

- The value of the fundamental eigenfrequency can be explicitly defined, depending on the stiffnesses of the mounts, and be moved outside the frequency range of interest, namely below 20 Hz.
- The contribution of the higher modes is almost nullified, without the need of any significant damping in the mounts.

Therefore, the utilization of soft mounts displaces the STL curve towards lower frequencies, providing a smooth performance in the entire low-frequency range. Additionally, this practice diminishes any uncertainties introduced in the acoustic performance either due to practical support conditions or variations in the rigidity of the panel.

Finally, the analytical models indicated adequate agreement with the developed FE model, showcasing that they can be used as a quick design tool for acoustic panels.

III. Advanced negative stiffness absorbers

3 KDAMPER

3.1 Background

The idea of the KDamper absorber is based on other popular vibration control devices that have been proposed by researchers many years before. The Tuned Mass Damper (TMD) is one of the most well-known and well-established approaches to achieve passive vibration control. The concept was initially applied more than 100 years ago by Frahm (1911) and later optimized by Den Hartog (1956). The idea consists of an oscillating mass, stiffness and damping elements that are attached to the original structure, and when tuned accordingly, provide significant vibration attenuation properties. Since its initial application, the TMD has been implemented in various applications and many forms of structures. A non-exhaustive list of recent applications includes vibration absorption due to ground motion and wind loading in bridges, skyscrapers (McNamara, 1977; Qin et al., 2009), and in the bases of structures (De Domenico and Ricciardi, 2018a; Palazzo et al., 1997; Tsai, 1995). Although the TMD is considered a reliable vibration control method and its applicability has been widely tested, it presents disadvantages that are not negligible: (a) the mass requirements are significant compared to the total mass of the structure, and (b) environmental factors and material behavior uncertainties may lead to gradual detuning of the system and consequently, to loss of its damping properties and effectiveness (Weber and Feltrin, 2010).

Aiming to overcome the large mass requirements of the above system, various methodologies have been proposed to artificially increase the inertial forces. In the early 2000s, Smith et al. (2002) introduced the inerter, a novel two-terminal element with the property of generating an additional force that is proportional to the relative acceleration of the two terminals. The proposed configuration was profitably adopted as a means to increase the damping properties of a Formula One racing car

suspension system. This innovative mechanism, namely the “J-damper”, was originally introduced by Chen et al. (2009). Since then, a significant number of applications have adopted the inerter as a means of vibration control, such as in applications for seismic protection of structures and in suspensions of railway vehicles (Takewaki et al., 2012; Wang et al., 2012).

In Giaralis & Taflanidis (2018) a modification of the original TMD has been proposed that includes the addition of an inerter. This device, namely the Tuned Mass Damper Inerter (TMDI), incorporates an inerter element that is connected to the TMD’s secondary mass; the concept is used to artificially increase the inertial forces of the damper, without the need to increase the actual mass of the system. The proposed configuration has been applied as a base absorber and vibration control mechanism in various research works, and results indicated a significant improvement of the dynamic behavior of the structure with the TMDI, compared to the systems with equivalent conventional TMD devices (De Domenico and Ricciardi, 2018b; Lazar et al., 2014; Saitoh, 2012). However, although the implementation of the inerter appears to substantially advance the attributes of the TMD, the considered TMDI device has to be precisely tuned to achieve reliable performance. Due to the complex and elaborate mechanical configurations required for the practical implementation of the TMDI, this required optimal tuning is hard to be accomplished.

Inspired by the potential of the vibration control systems presented previously, Antoniadis et al. (2018) have proposed the KDamper, a novel passive vibration absorption concept based on the optimal combination of appropriate stiffness, mass and damping elements, including a negative stiffness element. The idea of introducing negative stiffness (NS) elements is to assist movement instead of opposing it, as is the case of a positive stiffness element (Molyneaux, 1957). The system combines the beneficial characteristics of the NS and of the traditional TMD, leading to a device that introduces extraordinary damping properties to the structure. For structural systems, the required NS may be achieved using conventional pre-compressed springs arranged in appropriate geometry, post-buckled beams, plates and other pre-stressed mechanical elements (Virgin et al., 2008; Winterflood et al., 2002). Antoniadis & Paradeisiotis (2018), developed NS elements by adopting pre-stressed disc (Belleville) springs, arranged in appropriate geometrical configurations. By incorporating the additional NS element, the inertial forces of the damper are increased and the need for large mass is significantly reduced (K.A. Kapasakalis et al., 2020; Paradeisiotis et al., 2021, 2020). In addition, the proper allocation of the stiffness – mass elements of the device, leads to a system that is both statically and dynamically stable; the properties of the KDamper can be designed to maintain the initial/static stiffness of the structure and hence, avoid potential instabilities. Figure 3-1 presents a schematic

representation of the mechanisms of the conventional TMD, the TMDI as well as the innovative concept of the KDamper.

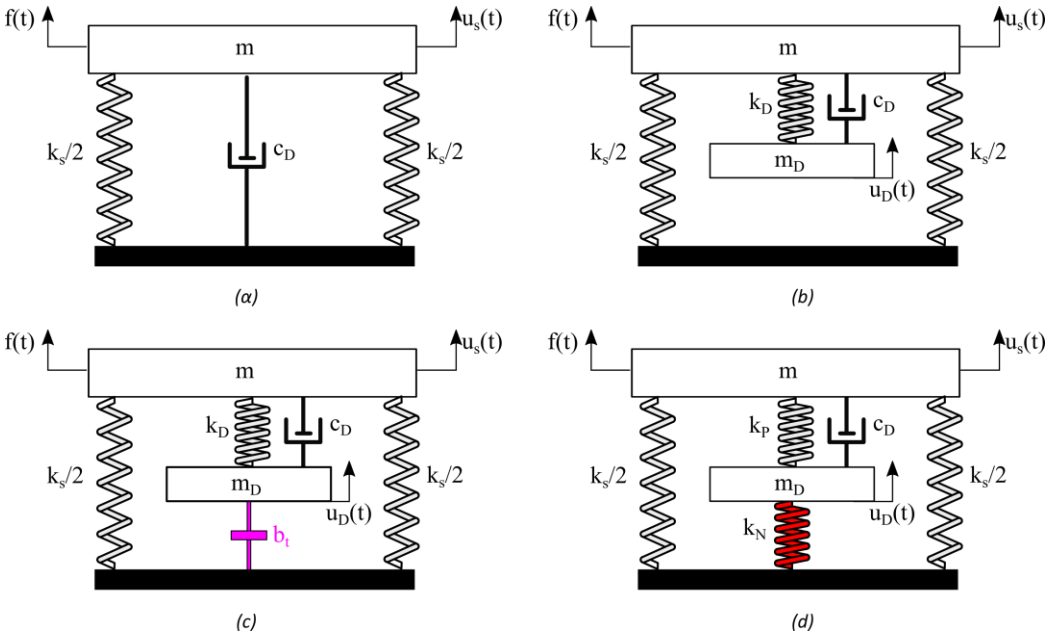

Figure 3-1: (a) SDoF oscillator (M-C-K), (b) conventional Tuned Mass Damper system (TMD), (c) enhanced TMD with grounded inerter (TMDI), (d) KDamper concept.

The KDamper vibration control system has been examined for the protection of bridges (Sapountzakis et al., 2017, 2016) wind turbines (Kampitsis et al., 2022; Konstantinos A. Kapasakalis et al., 2021b), as well as, structural systems (K.A. Kapasakalis et al., 2021; Konstantinos A. Kapasakalis et al., 2021a, 2020; Mantakas et al., 2022), achieving reduction of the displacement demand at the base level. Specifically, Kapasakalis et al. (2021), introduced the extended version of the KDamper concept as a vibration absorber for low-rise buildings; the system was applied supplementary to conventional base isolation for a typical RC structure. Optimization and subsequent analysis were performed by adopting a simplified structural model and by assuming linear structural behavior and linear KDamper components.

In this research work, the KDamper vibration control mechanism is designed and implemented in acoustic panels and metamaterial assemblies as a means to enhance the vibration control and noise attenuation properties of a system and achieve mitigation in the low-frequency range. More details of the proposed configurations are provided in the following sections of this thesis.

3.2 The KDamper Concept

As described in section 3.1, the KDamper (Figure 3-1 (d) is a novel passive vibration isolation and damping concept, based essentially on the optimal combination of appropriate stiffness elements. It incorporates a negative stiffness element, which generates extraordinary damping properties, avoiding the drawbacks of the traditional linear oscillator, or of the "zero stiffness" designs. This oscillator is designed to present the same overall (static) stiffness as a traditional reference original oscillator. However, it differs both from the original SDoF oscillator, as well as from the known negative stiffness oscillators, by appropriately redistributing the individual stiffness elements and by reallocating the damping. The KDamper supplements the inertial forces of the added TMD mass with the stiffness force of the negative stiffness element, while the presence of the additional mass acts as an energy dissipation mechanism (energy is transferred from the structure to the additional mass), reducing the adverse effects of the vibrating load.

Several KDamper-based vibration absorption concepts have been proposed, the most prominent of which are (i) the "classic" KDamper, (ii) "the base excited" KDamper, (iii) the extended version of KDamper, (iv) the extended KDamper equipped with inerter and (v) the KDamper equipped with an Inertial Amplification Mechanism. Herein, "the classic" mass and base excited KDamper and the Extended KDamper concepts are described and an Enhanced KDamper equipped with an Inertial Amplification Mechanism is introduced as a novel absorber.

3.2.1 "Classic" KDamper (mass excited)

Figure 3-2 presents the fundamental concept of the KDamper. The device overcomes the sensitivity problems of TMDs as the tuning is mainly controlled by the negative stiffness element's parameters.

The first basic requirement of the KDamper is that the overall static stiffness of the system is maintained:

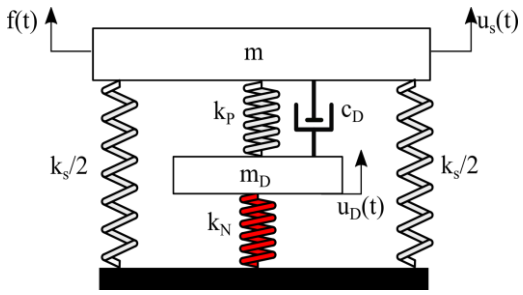

Figure 3-2: Schematic presentation of the "classic" KDamper absorber excited at the mass m.

$$k_0 = k_S + \frac{k_p k_N}{k_p + k_N} = (2\pi f_0)^2 (m + m_D) \tag{3-1}$$

Thus, the equations of motion of the KDamper excited by a harmonic motion in mass m are:

$$m\ddot{u}_S \; + \; c_D(\dot{u}_S - \dot{u}_D) \; + \; k_S u_S \; + \; k_P(u_S - u_D) \; = \; f(t) \tag{3-2}$$

$$m_D\ddot{u}_D - c_D(\dot{u}_S - \dot{u}_D) + \; k_N u_D - k_P(u_S - u_D) = 0 \tag{3-3}$$

Assuming a harmonic excitation in the form of:

$$f(t) \; = \; \tilde{F}e^{j\omega t} \; = \; k_0 U_{ST} e^{j\omega t} \tag{3-4}$$

and a steady state complex response of:

$$u_S(t) = \tilde{U}_S e^{j\omega t} \tag{3-5}$$

$$u_D(t) = \tilde{U}_D e^{j\omega t} \tag{3-6}$$

where $\tilde{U}_S, \tilde{U}_D$ denote the response complex amplitude, the equations of motion of the KDamper become:

$$-\omega^2 m\tilde{U}_S + j\omega c_D(\tilde{U}_S - \tilde{U}_D) + k_P(\tilde{U}_S - \tilde{U}_D) + k_S\tilde{U}_S = f(t) \tag{3-7.a}$$

$$-\omega^2 m\tilde{U}_D + j\omega c_D(\tilde{U}_S - \tilde{U}_D) - k_P \; (\tilde{U}_S - \tilde{U}_D) + k_N\tilde{U}_D = 0 \tag{3-7.b}$$

A careful examination of Eq. (3-7) reveals that the amplitude F_{MD} of the inertia force of the additional mass and the amplitude F_N of the negative stiffness force are exactly in phase, owing to the negative value of k_N. These forces are calculated as follows:

$$F_{MD} = -\omega^2 m_D \left|\tilde{U}_D\right| \tag{3-8.a}$$

$$F_N = k_N \left|\tilde{U}_D\right| \le 0 \tag{3-8.b}$$

Thus, similarly to the inerter (Smith, 2002), the KDamper essentially becomes an indirect approach to increase the inertia of the additional mass m_D, without however increasing the mass m_D itself. Moreover, it should be noticed that the value of F_{MD} depends on the frequency, whereas the value of F_N is constant in the entire frequency range. The latter is proved to be of great importance, specifically in the case of low-frequency vibration isolation applications.

The optimal design of the KDamper parameters follows exactly the corresponding steps as in Den Hartog (1956). First, the Transfer Function of the KDamper results from equations (3-7). The transfer

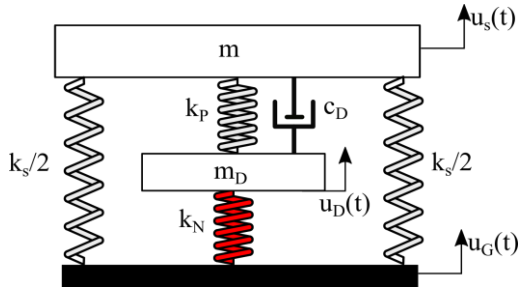

Figure 3-3: Schematic presentation of the "classic" KDamper absorber excited at its base.

function of the amplitude $\tilde{U}_S$ of the response $u_s(t)$ to the amplitude $\tilde{F}$ of an excitation $f(t)$ for the KDamper oscillator, is described as:

$$\tilde{T}_{UF} = \frac{-m_D\omega^2 + j\omega c_D + k_P + k_N}{mm_D\omega^4 - (m+m_D)c_D\omega^3 - (m(k_P+k_N) + m_Dk_S + m_Dk_P)\omega^2 + c_D(k_S+k_N)s + k_S(k_P+k_N) + k_Pk_N} \quad (3\text{-}9)$$

The transfer function of the dynamic magnification factor can be expressed as:

$$\tilde{H}_{US} = \frac{\tilde{U}_S}{U_{ST}} = k_0\tilde{T}_{UF} \quad (3\text{-}10)$$

while the transfer function of the of the amplitude $\tilde{U}_D$ of the response $u_D(t)$ to the amplitude U_{ST} is given by:

$$\tilde{H}_{UD} = \frac{\tilde{U}_D}{U_{ST}} = \frac{\tilde{U}_D}{\tilde{U}_S}\tilde{H}_{US} = \frac{(j\omega c_D + k_P)k_0}{-\omega^2 m_D + j\omega c_D + k_D}\tilde{H}_{US} \quad (3\text{-}11)$$

Subsequently, the basic parameters of the KDamper concept are defined as:

$$\mu = m_D / m \quad (3\text{-}12.a)$$

$$k_D = k_N + k_P \quad (3\text{-}12.b)$$

$$\omega_D = \sqrt{k_D / m_D} = \sqrt{(k_N + k_P)/m_D} \quad (3\text{-}12.c)$$

$$\zeta_D = c_D / 2\omega_D m_D = c_D / 2\sqrt{(k_N + k_P)m_D} \quad (3\text{-}12.d)$$

$$m_{tot} = m + m_D \quad (3\text{-}12.f)$$

$$f_0 = \sqrt{k / m_{tot}} / 2\pi = \sqrt{(k_S + k_Pk_N / k_P + k_N)/(m+m_D)} / 2\pi \quad (3\text{-}12.g)$$

3.2.2 "Classic" KDamper (Base excited)

Figure 3-3 presents the fundamental concept of the "classic" KDamper excited at its base.

The equations of motion are:

$$m\ddot{u}_S + c_D(\dot{u}_S - \dot{u}_D) + k_S u_S + k_P(u_S - u_D) = -m\ddot{u}_G \quad (3\text{-}13.a)$$

$$m_D\ddot{u}_D - c_D(\dot{u}_S - \dot{u}_D) + k_N u_D - k_P(u_S - u_D) = -m_D\ddot{u}_G \quad (3\text{-}13.b)$$

Assuming a harmonic excitation and steady-state response, the Eqs. of motion (3-13) of the KDamper become:

$$-\omega^2 m\tilde{U}_S + j\omega c_D(\tilde{U}_S - \tilde{U}_D) + k_S\tilde{U}_S + k_P(\tilde{U}_S - \tilde{U}_D) = -m\ddot{U}_G \quad (3\text{-}14.a)$$

$$-\omega^2 m_D\tilde{U}_D - j\omega c_D(\tilde{U}_S - \tilde{U}_D) + k_N\tilde{U}_D - k_P(\tilde{U}_S - \tilde{U}_D) = -m_D\ddot{U}_G \quad (3\text{-}14.b)$$

The Transfer Functions of the KDamper system finally result:

$$\begin{bmatrix}\tilde{H}_{US}\\ \tilde{H}_{UD}\end{bmatrix} = \begin{bmatrix}\tilde{U}_S/\ddot{U}_G\\ \tilde{U}_D/\ddot{U}_G\end{bmatrix} = -\tilde{H}^{-1}\begin{bmatrix}m\\ m_D\end{bmatrix} \quad (3\text{-}15.a)$$

$$\tilde{H}_{AS} = \ddot{U}_S/\ddot{U}_G = 1 - \omega^2\tilde{H}_{US} \quad (3\text{-}15.b)$$

$$\tilde{H}_{AD} = \ddot{U}_D/\ddot{U}_G = 1 - \omega^2\tilde{H}_{UD} \quad (3\text{-}15.c)$$

$$\tilde{H} = \begin{bmatrix}-\omega^2 m + j\omega c_D + k_P + k_S & -j\omega c_D - k_P\\ -j\omega c_D - k_P & \omega^2 m_D + j\omega c_D + k_P + k_N\end{bmatrix} \quad (3\text{-}15.d)$$

The following non-dimensional parameters that concern the KDamper are introduced:

$$\mu = m_D/m \quad (3\text{-}16.a)$$

$$k_D = k_N + k_P \quad (3\text{-}16.b)$$

$$\omega_D = \sqrt{k_D/m_D} = \sqrt{(k_N + k_P)/m_D} \quad (3\text{-}16.c)$$

$$\zeta_D = c_D/2\omega_D m_D = c_D/2\sqrt{(k_N + k_P)m_D} \quad (3\text{-}16.d)$$

$$m_{tot} = m + m_D \quad (3\text{-}16.f)$$

$$f_0 = \sqrt{k/m_{tot}}/2\pi = \sqrt{(k_S + k_P k_N/k_P + k_N)/(m + m_D)}/2\pi \quad (3\text{-}16.g)$$

3.2.3 Extended KDamper (Base excited)

The proposed vibration absorption concept is an extension of the KDamper referred to herein as the EKD system, illustrated in Figure 3-4. In a similar way to the KDamper, the EKD incorporates a system of masses, negative stiffness and positive stiffness elements as well as artificial dampers. The main

variation would be the change of the system configuration where the positive stiffness spring (k_P) connects the damper mass (m_D) to the base of the system while the negative stiffness element (k_N), is attached between the damper mass (m_D) and the mass of the oscillator (m). Also, an additional artificial damper is adopted and placed in parallel with the negative stiffness element so that we end up having two dampers, namely c_D and c_P .

The following equations of motion for the EKD are derived:

$$m\ddot{u}_S + c_{NS}(\dot{u}_S - \dot{u}_D) + k_{NS}(u_S - u_S) + k_S u_S = -m\ddot{u}_G \tag{3-17.a}$$

$$m_D\ddot{u}_D - c_N(\dot{u}_S - \dot{u}_D) - k_{NS}(u_S - u_D) + k_{PS}u_D + c_{PS}\dot{u}_D = -m_D\ddot{u}_G \tag{3-17.b}$$

Assuming a harmonic excitation and steady-state responses, the equations of motion (3-17) of the EKD become:

$$-\omega^2 m\tilde{U}_S + j\omega c_{NS}(\tilde{U}_S - \tilde{U}_D) + k_{NS}(\tilde{U}_S - \tilde{U}_D) + k_S\tilde{U}_S = -m\ddot{U}_G \tag{3-18.a}$$

$$-\omega^2 m_D\tilde{U}_D - j\omega c_{NS}(\tilde{U}_S - \tilde{U}_D) - k_{NS}(\tilde{U}_S - \tilde{U}_D) + k_{PS}\tilde{U}_D + j\omega c_{pS}U_D = -m_D\ddot{U}_G \tag{3-18.b}$$

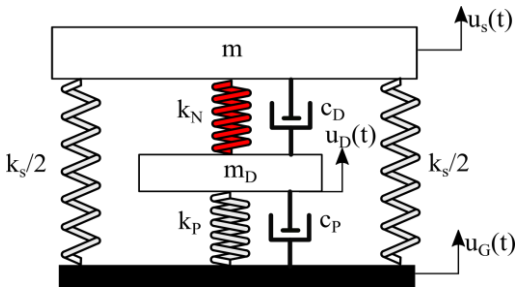

Figure 3-4: Schematic presentation of the Extended KDamper (EKD) absorber excited at its base.

And the Transfer Functions of the KDamper system finally result:

$$\begin{bmatrix}\tilde{H}_{US}\\ \tilde{H}_{UD}\end{bmatrix} = \begin{bmatrix}\tilde{U}_S/\ddot{U}_G\\ \tilde{U}_D/\ddot{U}_G\end{bmatrix} = -\tilde{H}^{-1}\begin{bmatrix}m\\ m_D\end{bmatrix} \tag{3-19}$$

$$\tilde{H}_{AS} = \ddot{U}_S/\ddot{U}_G = 1 - \omega^2\tilde{H}_{US} \tag{3-20}$$

$$\tilde{H}_{AD} = \ddot{U}_D/\ddot{U}_G = 1 - \omega^2\tilde{H}_{UD} \tag{3-21}$$

$$\tilde{H} = \begin{bmatrix}-\omega^2 m + j\omega c_{NS} + k_{NS} + k_S & -j\omega c_{NS} - k_{NS}\\ -j\omega c_{NS} - k_{NS} & -\omega^2 m_D + j\omega(c_{NS} + c_{PS}) + k_{PS} + k_{NS}\end{bmatrix} \tag{3-22}$$

This is an extended version of the classic KDamper concept. The purpose of this configuration is to retain the displacements and velocities within reasonable limits and display a realistic and efficient design.

The following non-dimensional parameters that concern the EKD are introduced:

$$\mu = m_D / m \tag{3-23.a}$$

$$k_D = k_{NS} + k_{PS} \tag{3-23.b}$$

$$\omega_D = \sqrt{k_D / m_D} = \sqrt{(k_{NS} + k_{PS}) / m_D} \tag{3-23.c}$$

$$\zeta_{NS} = c_{NS} / 2\omega_D m_D = c_{NS} / 2\sqrt{(k_{NS} + k_{PS}) m_D} \tag{3-23.d}$$

$$\zeta_{PS} = c_{PS} / 2\omega_D m_D = c_{PS} / 2\sqrt{(k_{NS} + k_{PS}) m_D} \tag{3-23.e}$$

$$m_{tot} = m + m_D \tag{3-23.f}$$

$$f_0 = \sqrt{k / m_{tot}} / 2\pi = \sqrt{(k_S + k_{PS} k_{NS} / k_{PS} + k_{NS}) / (m + m_D)} / 2\pi \tag{3-23.g}$$

where μ is the mass ratio of the additional mass of the EKD, ζ_{NS} and ζ_{PS} are the damping ratios of the artificial dampers c_{NS} and c_{PS}, respectively, and f_0 is the EKD nominal frequency.

3.2.4 Enhanced KDamper with Inertial amplifier (KD-IAM) Concept

In this work the simple to realize inertial amplification mechanism (IAM) system is presented to enhance the vibration mitigation performance of the classic K-Damper. Compared to the widely known flywheel-gear inerter (Smith, 2002), the mass amplification effect of the IAM system is a result of the geometrical amplification effect of a triangular shape mechanical system. This amplification mechanism is very common in nature (Feng et al., 2019; Feng and Jing, 2019; Wang and Jing, 2019) and has been exploited to enhance the performance of other mechanical systems, such as the TMD (Cheng et al., 2020). Here, by coupling the IAM system with the classic KDamper we introduce a new inerter equivalent KDamper, namely the KD-IAM, which is proposed to enhance the performance of traditional KDampers. In particular, the addition of the IAM allows to suppress the responses of both the primary structure and the absorber. The theory of classic KDamper is thus extended to investigate the dynamic properties of the coupled mechanism.

Figure 3-5 (a) shows the KDamper with the inclusion of the inertial amplifier (IAM), where m_j is the connecting mass, which is assumed to be negligible in order to act just as a connector, namely, an

additional DoF. Figure 3-5 (b) shows an equivalent model to Figure 3-5 (a); the effective mass of the IAM configuration is superimposed to the connecting mass m_j and is in total denoted as m_B.

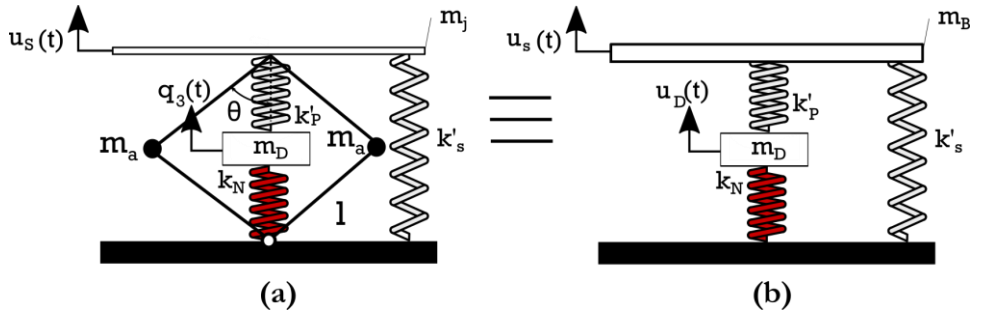

Figure 3-5: Schematic presentation of the KDamper-Inertial Amplification (KD-IAM) absorber. (a) KD-IAM model mount. (b) Equivalent KD-IAM model considering the IAM's effective mass.

The effective mass of the IAM is calculated according to Cheng et. al (2020) as

$$m_B = m_a\left(cot^2\theta + 1\right) \tag{3-24}$$

And the theoretical derivation can be found in Appendix B. The equations of motion resulting from the model illustrated in Figure 3-5 (b) are

$$m_a\left(cot^2\theta + 1\right)\ddot{u}_S \; + \; c_D(\dot{u}_S - \dot{u}_D) \; + \; k_S u_S \; + \; k_P(u_S - u_D) \; = \; f(t) \tag{3-25.a}$$

$$m_D\ddot{u}_D - c_D(\dot{u}_S - \dot{u}_D) + \; k_N u_D - k_P(u_S - u_D) = 0 \tag{3-25.b}$$

The transfer function of the amplitude $\tilde{U}_S$ of the response $u_s(t)$ to the amplitude $\tilde{F}$ of an excitation $f(t)$ for the KD-IAM, comes as

$$\tilde{T}_{UF} = \frac{-m_D\omega^2 \; + \; j\omega c_D \; + \; k_P + k_N}{m_B m_D\omega^4 - (m + m_D)c_D\omega^3 - (m(k_P + k_N) + m_D k_S + m_D k_P)\omega^2 + c_D(k_S + k_N)s + k_S(k_P + k_N) + k_P k_N} \tag{3-26}$$

The rest of the transfer functions can be estimated according to the "classic" KDamper formulas given in Eqs. (3-10) - (3-11).

3.3 Traditional Optimal design approach for the selection of the KDamper parameters

Regarding the optimal design of the KDamper, numerous approaches could be followed, as found in the literature for the optimal design of other passive vibration absorption concepts (TMDs, QZS, NS designs, TMDIs, etc.). In this chapter, the optimal design approach for the selection of the KDamper

parameters follows the steps of the classic minmax ($H\infty$) procedure, proposed by Den Hartog (1956). The KDamper initial adaptation to the minmax ($H\infty$) procedure was implemented by Antoniadis et al. (2016), while minor modifications have been applied afterwards to fit the application specific requirements. In this chapter, the initial design approach is briefly discussed, while any proposed alterations are outlined in the following chapters.

The minmax approach minimizes a specific Transfer Function for a harmonic excitation, which in this case, is a base acceleration excitation. The free design variables of the system are the additional mass ratio $\mu = m_D / m$ and the stiffness ratio $\kappa = -k_N / (k_P + k_N)$, Considering the selection of ζ_D, numerous approaches are possible, the detailed treatment of which is beyond the scope of the dissertation. A straightforward approach is to calculate ζ_D numerically, so that it minimizes the peak of the selected Transfer Function (q, ζ_D). The parameter $\rho = \omega_D / \omega$ is calculated with respect to the Transfer Function selected for optimization. Once the values of the four parameters μ, κ, ζ_D and ρ are determined and after some algebraic manipulations the values of the KDamper elements, can be finally obtained from the following relations:

$$\kappa_S = \frac{k_S}{k_0} = 1 + \kappa(1+\kappa)\mu\rho^2 \tag{3-27}$$

$$\kappa_P = \frac{k_P}{k_0} = (1+\kappa)\mu\rho^2 \tag{3-28}$$

$$\kappa_N = \frac{k_N}{k_0} = \kappa\mu\rho^2 \tag{3-29}$$

leading to the calculation of the stiffness elements (k_S, k_P, k_N) of the oscillator. Furthermore, k_D is defined as $k_D = k_P + k_N$, thus, for a specific damping ratio ζ_D , the damping constant is calculated as:

$$c_D = 2\zeta_D\sqrt{k_D m_D} \tag{3-30}$$

Inserting the non-dimensional parameters of the KDamper μ, ρ, κ and ζ_D along with the ratio $q = \omega / \omega_0$, the resulting transfer functions can be expressed as:

$$\tilde{H}_{US} = \frac{\tilde{U}_S}{U_{ST}} = \frac{A + j2\zeta_D B}{C + j2\zeta_D D} \tag{3-31}$$

$$\tilde{H}_{USD} = \frac{\tilde{U}_D}{\tilde{U}_S} = \frac{E + j2\zeta_D B}{A + j2\zeta_D B} \tag{3-32}$$

$$\tilde{H}_{UD} = \frac{\tilde{U}_D}{U_{ST}} = \frac{E + j2\zeta_D B}{C + j2\zeta_D D} \tag{3-33}$$

and their respective magnitudes:

$$\left|\tilde{H}_{US}\right| = \frac{\left|\tilde{U}_S\right|}{U_{ST}} = \sqrt{\frac{A^2 + (j2\zeta_D)^2 B^2}{C^2 + (j2\zeta_D)^2 D^2}} \tag{3-34}$$

$$\left|\tilde{H}_{USD}\right| = \left|\frac{\tilde{U}_D}{\tilde{U}_S}\right| = \sqrt{\frac{E^2 + (j2\zeta_D)^2 B^2}{A^2 + (j2\zeta_D)^2 B^2}} \tag{3-35}$$

$$\left|\tilde{H}_{UD}\right| = \frac{\left|\tilde{U}_D\right|}{U_{ST}} = \frac{\left|\tilde{U}_D\right|}{\left|\tilde{U}_S\right|}\frac{\left|\tilde{U}_S\right|}{U_{ST}} = \sqrt{\frac{E^2 + (j2\zeta_D)^2 B^2}{C^2 + (j2\zeta_D)^2 D^2}} \tag{3-36}$$

Where

$$A = \rho^2 - q^2 \tag{3-37.a}$$

$$B = \rho q \tag{3-57.b}$$

$$C = q^4 - q^2\left[1 + \rho^2 + (1+\kappa)^2 \mu\rho^2\right] + \rho^2 \tag{3-57.c}$$

$$D = \rho q\left[\left(1 + \kappa^2 \mu\rho^2\right) - q^2(1+\mu)\right] \tag{3-57.d}$$

$$\mathrm{E} = (1+\kappa)\rho^2 \tag{3-57.e}$$

By all means, these parameters correspond to the "classic" KDamper formulation, in the case that the selected transfer function for minimization is the magnification factor while equivalent formulations can be easily derived for the rest of the KDamper cases, described in section 3.2.

Examination of the factor $H(q,\zeta_D))$ for the limit cases of the damping ratio, reveals that:

$$H(\zeta_D \to 0) = \left|\frac{A}{C}\right|,\ H(\zeta_D \to \infty) = \left|\frac{B}{D}\right| \tag{3-38}$$

The optimal value of ρ where the transfer function of the amplitude of the displacement $u_s(t)$ with regard to the excitation amplitude is minimized at a selected frequency, is defined as:

$$\rho_{opt} = \sqrt{\frac{1}{(1+\mu+\kappa\mu)(1+\mu) - \kappa^2\mu}} \tag{3-39}$$

The equation is defined in terms of the parameters μ and κ. The optimization procedure for ρ is described in detail in Antoniadis et al. (2016). By setting the denominator of ρ_{opt} equal to zero, the maximum value of κ is determined as:

$$\kappa_{\max} = \frac{(1+\mu)(1+\sqrt{1+4/\mu})}{2} \tag{3-40}$$

In addition, in order to ensure the static stability of the system, variations of the k_N should be considered. These variations take place due to temperature fluctuations, manufacturing tolerances or nonlinear behavior, since almost all negative stiffness designs are derived from unstable nonlinear systems. Consequently, an increase of the absolute value of k_N by a factor ε may lead to a new value of k_{NL} where the structure becomes unstable. The static stability margin ε is estimated as:

$$\varepsilon = \frac{1}{\kappa\left[1+(1+\kappa)^2\,\mu\rho^2\right]} \tag{3-41}$$

Therefore, the value of κ is selected as a fraction of $\kappa_{\max}$, namely $\kappa = (0:1)\kappa_{\max}$. The oscillator presents better vibration absorption capabilities when $\kappa \to \kappa_{\max}$ but at the same time needs to be considered that for $\kappa \to \kappa_{\max}$, the static stability margin of the oscillator $\varepsilon \to 0$, because the overall static stiffness k_0 of the system becomes negative (Paradeisiotis, 2019).

3.4 Experimental Proof of Concept

This section briefly presents the design of the Extended KDamper (EKD) experimental prototype (Mantakas et al., 2023; Καπασακάλης et al., 2022), which serves as a proof of concept. The experimental setup is depicted in Figure 3-6 (a).

In order for the EKD to be effective, high values of NS are required. The only feasible option regarding the realization of the NS elements in such applications is with elastic forces. Among others, special mechanical designs involving conventional positive stiffness prestressed elastic mechanical elements, such as post-buckled beams, plates, shells, and pre-compressed springs, arranged in appropriate geometrical configurations can generate controlled NS with the desired magnitude. In this work, the mechanism proposed by Kapasakalis et al. (2021) is adopted; the schematic presentation of this configuration is presented in Figure 3-6 (b). Here, the negative stiffness element is realized by a prestressed prismatic spring and a rigid link (steel) that connects the internal mass (m_D) to the oscillating mass (m) of the EKD through hinged connections (ball bearings).

The following expressions can be derived for the potential energy U, the nonlinear force N, and the equivalent nonlinear stiffness k_N of this mechanism:

$$U(u_{NS}) = \frac{1}{2} k_c \left(l_H - l_{Hi}\right)^2 \tag{3-42}$$

$$N(u_{NS}) = \frac{\partial U}{\partial u_{NS}} = -k_c \left(1 + \frac{l_{Hi} - d}{\sqrt{a^2 - u_{NS}^2}}\right) u_{NS} \tag{3-43}$$

$$K_N(u_{NS}) = \frac{\partial N}{\partial u_{NS}} = -k_c \left(1 + \frac{(l_{Hi} - d)/a}{\sqrt[3]{\left(1 - u_{NS}^2/a^2\right)}}\right) \tag{3-44}$$

Where a is the undeformed height of the NS device, d the length of the lever arm, l_{HI} the length of the undeformed conventional spring, and k_c the spring stiffness. The negative stiffness configuration is schematically presented in Figure 3-6 (b) and the parameters of the NS mechanism are presented in detail in Table 3-1.

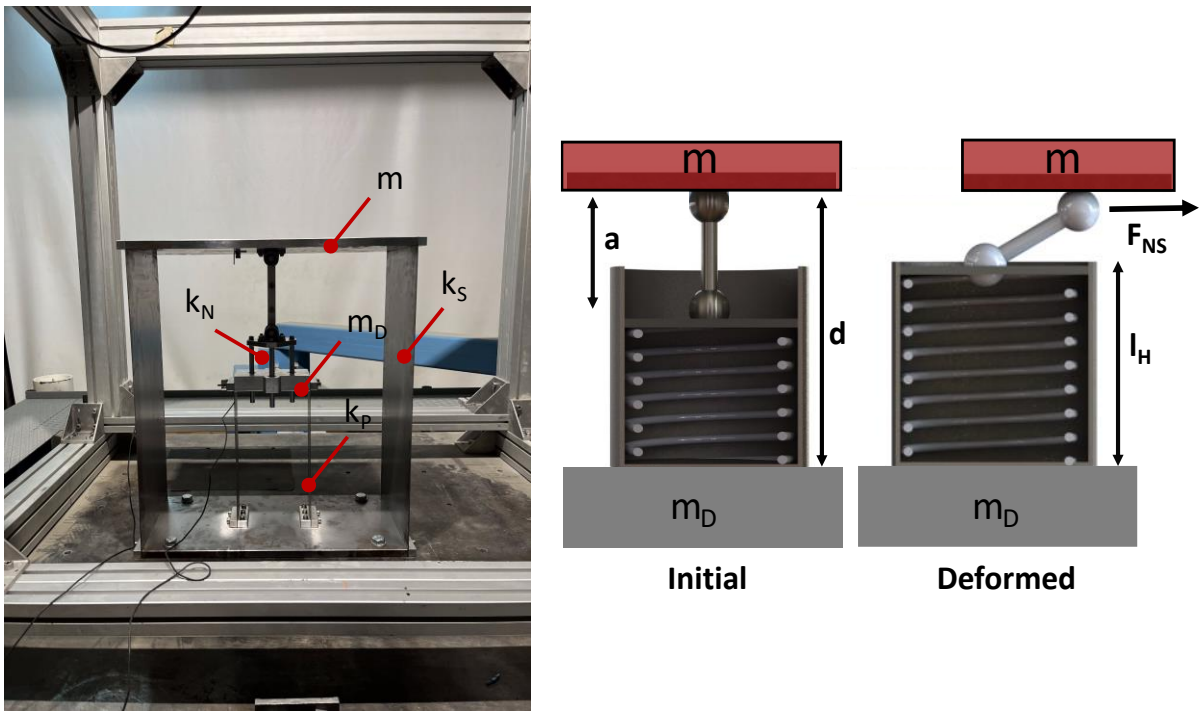

(a) *(b)*

Figure 3-6: (a) View of the EKD prototype. (b) Conceptual configuration of the NS element.

Table 3-1: Negative stiffness (NS) mechanism set up parameters.

k_c[kN/m]	a [m]	l_{HI} [m]	d [m]	F_{NS}
4100	0.146	0.1	0.203	73.8

The oscillating mass (m) is constructed by a steel plate with dimensions 0.25x0.15x0.01, the internal mass of the damper (m_D) by a steel plate with dimensions 0.1x0.5x0.015 and the positive stiffness elements k_P and k_S by steel sheets with dimensions 0.27x0.0.07x0.001 and 0.585x0.0.25x0.0015, respectively. The values of the optimized EKD components are presented in Table 3-2.

Table 3-2: Values of the optimized EKD components.

m [kg]	m_D [kg]	k_S [kN/m]	k_P [kN/m]	k_N (u_{NS}=0) [kN/m]
16.3	0.815	1770	1440	-500

A series of single frequency-harmonic input tests were carried out, at the horizontal movement shaking table of the Laboratory of soil mechanics, National Technical University of Athens. For the experimental measurements, accelerometers where installed at the base of the absorber, the oscillating mass (m) and the internal mass (m_D) while small amplitude excitations were applied to ensure the linear behaviour of the absorber. Two different configurations were tested; (a) the EKD and (b) a SDoF mechanism with the same mass and spring stiffness properties. No extra damping elements are added in neither configuration while the structural damping ratio of the EKD was calculated from a free vibration test $\xi = 8\%$ and the damping ratio of the SDoF $\xi = 2\%$.

Figure 3-7 illustrates the experimentally and the theoretically estimated frequency response of the EKD absorber and the SDoF oscillator. The results validate the theoretical expected behaviour of the KDamper, while the analytically derived equations of motion are confirmed. The comparison of the the corresponding magnification factor of the system when the seismic mass is mounted only on the k_S stiffness elements (black line) demonstrates the effectiveness of the device. Namely, the fundamental resonance peak is reduced approximately by 60% and by extension, this leads to an isolation frequency of ≈ 1.4 Hz which is in line with the intended goal of the device.

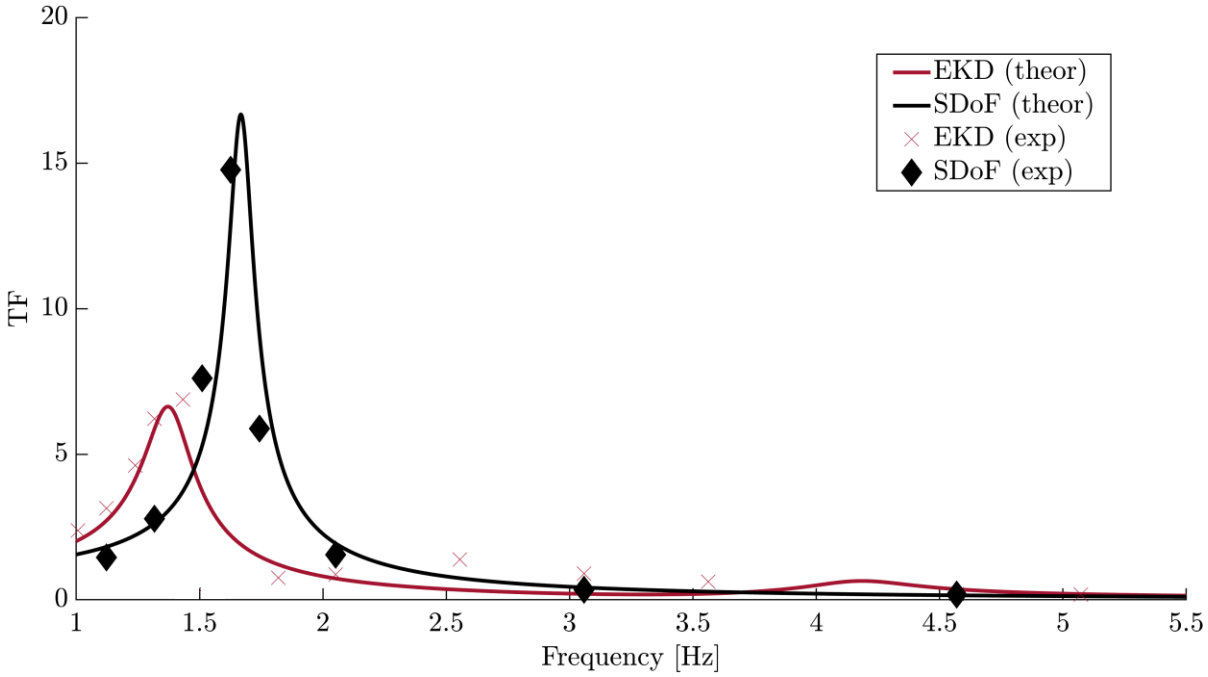

Figure 3-7: Theoretical and experimental Dynamic response of the EKD device vs the SDoF oscillator.

3.5 Concluding Remarks

In this chapter, the most prominent KDamper configurations are discussed and a novel KDamper absorber combined with an Inertia Amplifier is introduced as an inerter equivalent configuration. Additionally, the Traditional Optimal design approach (based on Den Hartog (1956)) is briefly presented as a baseline procedure which showcases the design limitations of the absorbers. Finally, based on the selected optimized parameters an experimental validation of the KD concept is illustrated.

4 ACOUSTIC MOUNTS BASED ON THE ENHANCED KDAMPER (KD-IAM) CONCEPT

4.1 Background

The KDamper, as described in chapter 3, can address many of the inadequacies of conventional passive noise control mechanisms, especially in the low-frequency range. Therefore, a design of an acoustic isolation/absorption concept that targets the low-frequencies is proposed herein in the form of a panel mounted on bearings, based on the KDamper concept. The proposed idea leads to an improved dynamic behavior of the panel that is predominant in the STL curve around the resonant frequency.

The idea of panels supported on KDamper mount designs was initially introduced by Paradeisiotis (2019; 2019). These initial investigations indicated the potential of the proposed system in efficiently mitigating sound transmission in the fundamental resonance region for target frequencies below 100 Hz. In these studies, the impedance approach (see chapter 2) was adopted to possess an initial estimation of the noise absorption properties of the KDamper-enhanced panel. As previously discussed, although this approach is only able to capture the acoustic behaviour of a rigid panel, it still serves as a rational simplification that provides a reliable initial approximation of the system's sound mitigation response. In addition, the effectiveness and characteristics of the inertial amplification mechanism - IAM concept can be also utilized in low-frequency noise insulation.

In this chapter, a combination of an IAM with the KDamper is proposed as a novel mounting system aiming to increase the width and depth of the generated low-frequency attenuation band. An

extended KDamper framework that incorporates an IAM is thus investigated. This coupled absorber is applied in a novel mounting system for flexible acoustic panels, resulting in a wide and deep frequency band of improved vibration and noise attenuation. The methodology employed in this research work is based on a lumped parameter model (LPM) utilizing a first mode approximation for the STL of a simply supported panel, as described in chapter 2, and an optimization procedure is formulated for the selection of the KD parameters. One of the developments presented in this work is the refinement of the initial optimization procedure of the KDamper, aiming to minimize the STL in the vicinity of the fundamental resonance. The theoretical framework has been expanded for improved modelling of the fluid–structure interaction of the panel and subsequent representation in terms of a dynamic system with discrete degrees of freedom (DoFs).

Investigation shows that increasing the rigidity of the panel improves the attenuation band. Based on this observation, an indicative implementation for an initial case study of a stiffened panel is demonstrated along with a conceptual design and realization of the KD-IAM mounts. This case study of a simplified, more stripped-down application aims to demonstrate the capability of this advanced negative stiffness absorber in the area of low-frequency noise mitigation. In addition, the analytical framework formulated herein serves as a basis for detailed investigations and designs verified by subsequent Finite Element Analysis (FEA).

4.2 KDamper mount designs

4.2.1 “In-series” LPM approximation for classical KDamper mounts

As already seen in chapter 2, the effective damping of the fundamental resonance requires significant damping capacity of the mounts positioned along the edges of the panel. For this reason, the KDamper vibration absorption and damping concept is proposed as an alternative realization of the elastic mounts. The KDamper has significantly higher modal damping than the TMD and achieves greater attenuation in a wider frequency band while utilizing significantly lower additional mass.

Figure 4-1 shows the equivalent model when the simple elastic mount is replaced with an elastic mount based on the KDamper design, where m_j is the connecting mass which is assumed as negligible in order to act just as a connector, namely an additional DoF. Since certain categories of rubbers also present damping properties, defined by the loss factor due to their hysteretic, viscoelastic behaviour, hysteretic damping is introduced indirectly considering a complex stiffness element as:

$$k'_S = k_S(1+jn) \tag{4-1}$$

$$k'_P = k_P(1+jn) \tag{4-2}$$

The mathematical model described in this section is an extension of the "*In-series LPM approximation*", presented in paragraph 2.2.2, and the aim is to formulate a straightforward method to approximate this coupling between the panel and the mount. At this point, it is reminded that the main assumption of the method is that the bending stiffness of the deformable plate is in a way in series with the stiffness of the mounting.

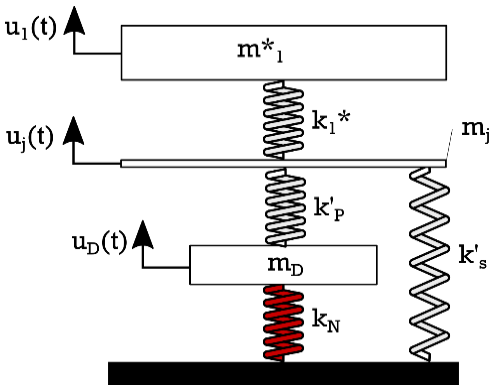

Figure 4-1: Mathematical model of a KDamper mounted deformable plate.

The inclusion of stiffeners for increasing the panel's rigidity, and hence its fundamental eigenfrequency, helps reinforce this "in-series" approximation. Namely, with the LPMs, it is essentially assumed that the panel is rigid; consequently, the dynamic response along the surface of the panel is uniform. Therefore, increasing the rigidity is an attempt to approximate the rigid assumption regarding the displacement/velocity amplitude distribution. Thus, the model can be used for estimation of the required stiffness level and as a guidance in designing the mounts.

The STL of the KDamper model is then calculated as:

$$STL_{KD} = 10\log_{10}\left(\frac{1}{\tau_{KD}}\right) \tag{4-3}$$

The transmission coefficient τ_{KD} is estimated according to Eq. (2-38), where the transfer function TF_{21} (Appendix-A.6) is described as follows:

$$TF_{21} = \frac{C_2}{C_1} = \frac{k_1^*}{k_1^* + k_S^{'} + k_P^{'}(1-TF_{32})} \tag{4-4}$$

$$TF_{32} = \frac{C_3}{C_2} = \frac{k_P^{'}}{-\omega^2 m_D + k_P^{'} + k_N} \tag{4-5}$$

4.2.2 "In-series" LPM approximation for KDamper-IAM mounts

Aiming to explore the combined KDamper-IAM framework introduced in chapter 3, the inclusion of inertial amplifiers as part of the mounting system is studied herein. Figure 4-2 shows the mathematical model of a KD-IAM mounted panel, considering that the effective mass of the IAM configuration is superimposed to the connecting mass m_j and, in total, denoted as $m_B = m_a\left(cot^2\theta + 1\right)$ (Eq. (3-21)).

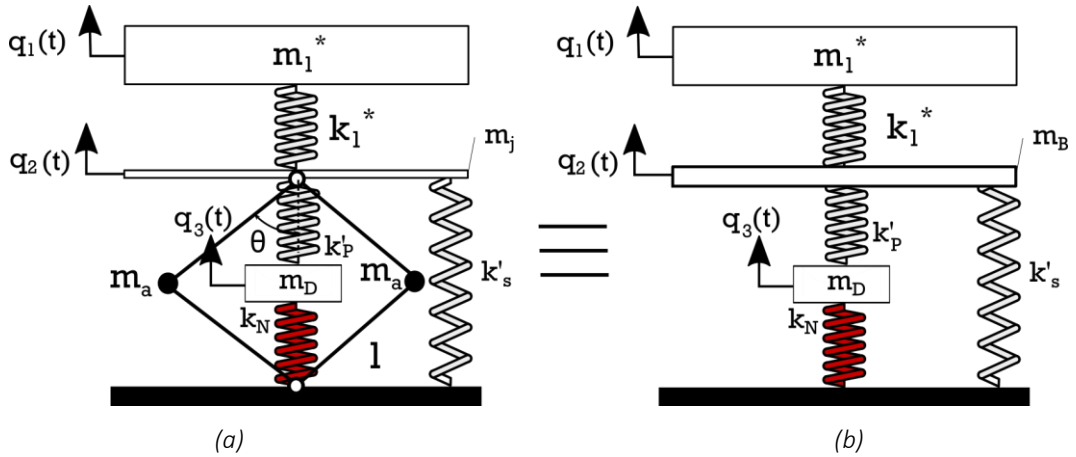

Figure 4-2: (a) Modeling of a deformable panel supported on KD-IAM elastic mount and (b) Equivalent KD-IAM model considering the IAM's effective mass.

Once again, hysteretic damping is assumed according to Eqs. (4-1)-(4-2).

The equations of motion resulting from the model illustrated in Figure 4-2, are an extension of the equations of motion shown in Eq. (3-22) and are given as:

$$m_1^*\ddot{q}_1 + k_1^*(q_1 - q_2) = \frac{8P_i l_x l_y}{\pi^2} e^{j\omega t} \tag{4-6}$$

$$m_a\left(cot^2\theta + 1\right)\ddot{q}_2 - k_1 q_1 + (k_1 + k^{'}_P + k^{'}_S)q_2 - k^{'}_P q_3 = 0 \tag{4-7}$$

$$m_D\ddot{q}_3 + (k^{'}_P + k^{'}_S)q_3 - k^{'}_P q_2 = 0 \tag{4-8}$$

where the generalized degrees of freedom are defined as:

$$q_i(t) = C_i e^{j\omega t} \tag{4-9}$$

where C_i is the corresponding amplitude of motion and the relevant transfer functions are:

$$TF_{21} = \frac{C_2}{C_1} = \frac{k^*}{-\omega^2 m_B + k_1 + k_S^{'} + k_P^{'}(1 - TF_{32})} \tag{4-10}$$

$$TF_{32} = \frac{C_3}{C_2} = \frac{k^{'}_P}{-\omega^2 m_D + k_P^{'} + k_N} \tag{4-11}$$

And the corresponding STL is estimated by Eq. (4-3).

4.3 Optimal Design Approach for the KDamper acoustic mounts

4.3.1 Specification of non-dimensional parameters

The static stiffness k_0 of the KDamper is defined according to Eq. (3-1), where f_0 can be seen as a central or design frequency of the KDamper. Normally, in previous vibration absorption applications of the KDamper, (Antoniadis et al., 2015, 2016; Paradeisiotis et al., 2020a, 2020b) f_0 corresponded to the operational excitation frequency of the system in question, around which the attenuation band would be centered (see section 3.3). However, in this investigation, f_0 is set as one of the optimization variables for maximization of the STL of the mounted panel.

The stiffness parameters of the KDamper are selected according to Eq. (3-1) in order to maintain the total stiffness of the system. However, an increase in the absolute value of k_N, or reduction in the absolute value of k_P or k_S, may endanger the static stability of the system. These parameters may present fluctuations due to material fatigue, manufacturing tolerances, non-linear behavior of structural elements, and among others, temperature variations.

In order to ensure that potential loss of the static stability is prevented, the possible variations of k_N, k_P and k_S are taken into account during the optimization procedure of the KDamper parameters, (Kapasakalis, 2020) contrary to the classic KDamper design, which foresees variation only in the negative stiffness element k_N. In this way, these static stability margins are imposed via the introduction of the tolerances ε_N, ε_P, and ε_S, respectively:

$$\varepsilon_N = \frac{k_{N_{\lim}} - k_N}{k_N} \tag{4-12}$$

$$\varepsilon_P = \frac{k_{P_{\lim}} - k_P}{k_P} \tag{4-13}$$

$$\varepsilon_S = \frac{k_{S_{\lim}} - k_S}{k_S} \tag{4-14}$$

so that the limiting values of the stiffness elements are expressed as:

$$k_{N_{\lim}} = (1+\varepsilon_N)k_N \tag{4-15}$$

$$k_{P_{\lim}} = (1+\varepsilon_P)k_P \tag{4-16}$$

$$k_{S_{\lim}} = (1+\varepsilon_S)k_S \tag{4-17}$$

Defining the parameters:

$$r_N = (1-\varepsilon_N) \tag{4-18}$$

$$r_P = (1-\varepsilon_P) \tag{4-19}$$

$$r_S = (1-\varepsilon_S) \tag{4-20}$$

the neutral point for static stability corresponds to:

$$\frac{(r_P k_P)(r_N k_N)}{(r_P k_P)+(r_N k_N)} + r_S = 0 \tag{4-21}$$

Consequently, for an assumed value of the non-dimensional parameter $\kappa_N = k_N / k_0$ —or the absolute value of the negative stiffness element k_N —and selected tolerances, the rest of the stiffness elements result as follows:

$$\kappa_S = \frac{-b-\Delta}{2\alpha} \tag{4-22}$$

where κ_S is the non-dimensional parameter of the k_S stiffness element and:

$$\Delta = \sqrt{b^2 - 4ac} \tag{4-23}$$

$$a = r_S(r_P - r_N) \tag{4-24}$$

$$b = \kappa_N r_N(r_P - r_S) + r_S(r_N - r_P) \tag{4-25}$$

$$c = -r_P r_N \kappa_N \tag{4-26}$$

while the non-dimensional κ_P is:

$$\kappa_P = \frac{\kappa_N(1-\kappa_S)}{\kappa_S + \kappa_N - 1} \tag{4-27}$$

Then, the stiffness elements are calculated as:

$$k_N = \kappa_N k_0 \tag{4-28}$$

$$k_P = \kappa_P k_0 \tag{4-29}$$

$$k_S = \kappa_S k_0 \tag{4-30}$$

The non-dimensional parameter ρ of the KDamper is also defined as:

$$\rho = \frac{\omega_D}{\omega_0} = \frac{\sqrt{(k_P + k_N)/m_D}}{\sqrt{k_0/m_1}} \tag{4-31}$$

Where $m_D = \mu m_1$. The parameter ρ essentially represents the "distance" between the two eigenfrequencies of the KDamper, acting as a marker of the absorption frequency band of the oscillator.

4.4 Optimization algorithm

The aim of the optimization process is the selection of the optimal values for the KDamper elements, in order to obtain the maximum possible STL performance, especially in the resonance region of the system. A comparison to the initial system, where the plate is simply supported on its edges, is undertaken in order to evaluate the effectiveness of the mechanism.

The "*fmincon*" function of the MATLAB code for local minimization of non-linear multivariable functions and constraints is utilized for the optimization process. The optimization algorithm is formulated as follows:

$$\min_x f(x) s.t. \begin{Vmatrix} c(x) \le 0 \\ c_{eq}(x) = 0 \\ Ax \le b \\ A_{eq}x = b_{eq} \\ \boldsymbol{lb} \le \boldsymbol{x} \le \boldsymbol{ub} \end{Vmatrix} \tag{4-32}$$

where b and b_{eq} are vectors, A and A_{eq} are matrices, $c(x)$ and $c_{eq}(x)$ are functions that return vectors, and $f(x)$ is a function that returns a scalar. $f(x)$, $c(x)$, and $c_{eq}(x)$ can be nonlinear functions $\boldsymbol{x}, \boldsymbol{lb}$, and $\boldsymbol{ub}$ can be vectors or matrices, x is the vector containing the optimization variables, and $f(x)$ is the objective function to be minimized. Thus, $\boldsymbol{x}$ starts at $\boldsymbol{x_0}$ and attempts to

find a minimizer $\boldsymbol{x}$ of the function described in $f(x)$ subjected to the linear inequalities $Ax \leq b$, aiming for a solution that is always in the range $\boldsymbol{lb} \leq \boldsymbol{x} \leq \boldsymbol{ub}$.

In this case the vector $\boldsymbol{x}$ is:

$$x = \{\kappa_N \quad f_0 \quad m_B\}^T \tag{4-33}$$

The minimum value of the STL of the model is considered as the objective function:

$$f(x) = -min(STL_{KD}) \tag{4-34}$$

Therefore, the optimization problem becomes:

$$\min_x f(x) s.t. \begin{Bmatrix} \varepsilon_N = 10\% \\ \varepsilon_P = 5\% \\ \varepsilon_S = 5\% \\ lb \leq x \leq ub \end{Bmatrix} \tag{4-35}$$

with the optimization variables between the lower bounds $\boldsymbol{lb} = \{-0.8\ 10\ 0\}^T$ and the upper bounds $\boldsymbol{ub} = \{0\ 120\ 10\}^T$.

Some of the choices regarding the constraints and the bounds of the optimization variables result from past investigations of the KDamper and relate closely to considerations regarding possible practical implementations, which can be found in Paradeisiotis (2019). The boundaries of the KDamper design frequency f_0, can be selected by the designer based on the project requirements.

4.5 Effects of the panel's rigidity

In this section, an examination of the KD-IAM concept is presented, considering the low-frequency acoustic performance of a stiffened panel. During this approach towards increasing low-frequency noise insulation, instead of lowering the fundamental resonance of the structure and taking advantage of the STL region governed by the mass law, the aim is to lift the panel's fundamental resonance and take advantage of the absorption properties of the mounts in the stiffness region. A common practice to enhance the rigidity of a panel involves incorporating a grid of stiffeners, where the density and shape of these ribs define the enhanced stiffness of the system. The panel under investigation is assumed to comprise a conventional plasterboard enhanced by stiffeners to improve the panel's rigidity and manipulate the value of its fundamental eigenfrequency.

The relevant properties of the plasterboard are summarized in Table 4-1. In order to investigate the effect of the panel's rigidity on the STL frequency response, the KD-IAM model is employed assuming four different arrangements. The first case corresponds to a non-enhanced plasterboard with a fundamental eigenfrequency of 10.8 Hz, while the next three cases correspond to stiffened panels with fundamental eigenfrequencies of 30, 50, and 100 Hz.

Table 4-1: Plasterboard properties.

ρ_p [kg/m^3]	l_x [m]	l_y [m]	h_p [mm]	E_p [MPa]	v_p [-]	η_p [-]
668	1.2	2.4	12.5	2900	0.31	0.01

In Figure 4-3, the red dashed line represents the FFR panel approximation as given by Eq. (2-23). Intuitively, this approximation should constitute the ideal case regarding the STL of a panel with finite dimensions and may act as a reference curve for various comparisons instead of the infinite panel approximation, which is invalid in the lower frequency range that is being examined. The analysis is conducted for both KDamper mounts without the inclusion of the IAM ($m_B = 0$), see Figure 4-1, and with KD-IAM mounts, see Figure 4-2, in order to highlight the effect of IAM to the dynamic response of the oscillator. The results obtained for each case after the optimization procedure are provided in Table 4-2 and Table 4-3. Results of Figure 4-3 indicate that the KD mounted panel is effectively dampened in the resonance region as the STL level is improved compared to the FFR panel. As expected, all curves coincide for higher frequencies, where the mass law prevails. The properties of the KD mounts are highlighted in the case of f_1 =100Hz, where the resonance effect on the STL is almost eliminated and, at the same time, an increased attenuation band is formed in the region. Resonances of higher modes that would appear while using a more extensive modeling approach are also mitigated without a significant amount of damping, especially compared to the fundamental resonance.

Considering the case where the mounts are positioned along the edges of the real panel, the displacement amplitude at the edges is lower than the mean amplitude of the panel due to the shape function of the first mode. Thus, damping will be less effective in reality. For this reason, the considered loss factor in the model is just η =0.1, to avoid presenting a misleading frequency response. However, in the cases of the stiffened panel, the displacement/velocity amplitudes are more uniformly distributed between the edges and the middle of the panel. As a result, the validity of the modeling assumptions is reinforced.

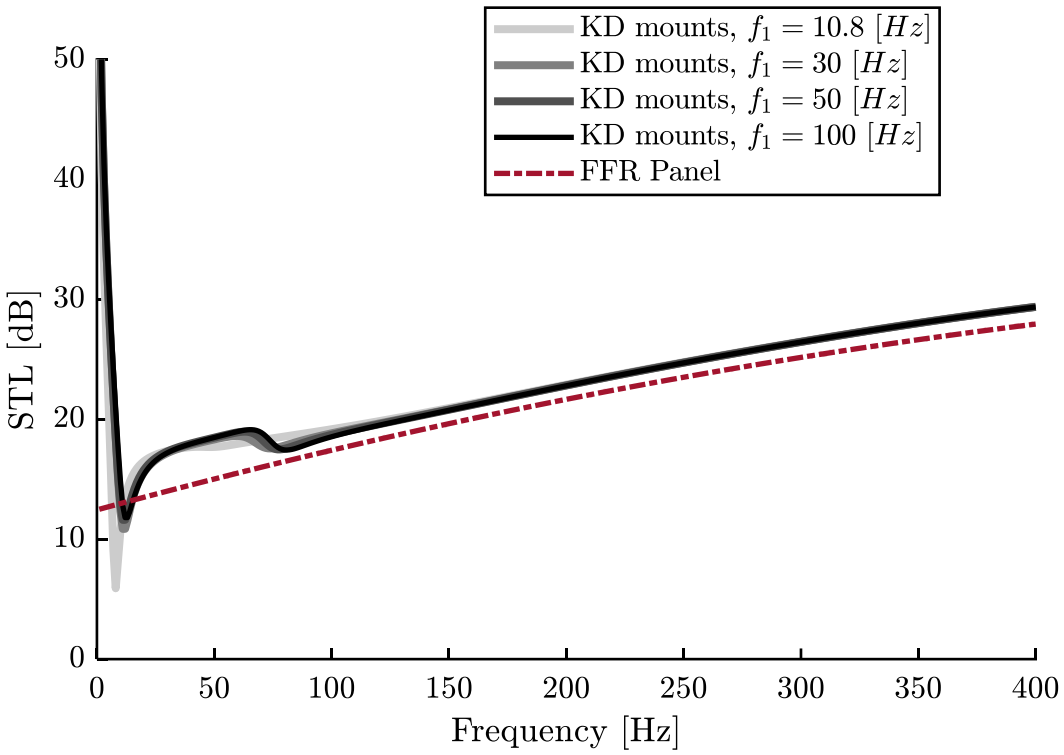

Figure 4-3: Correlation of the panel rigidity and STL of the mounted panel for increasing rigidity of the panel utilizing KDamper mounts.

The inclusion of the inertial amplifier on the KD mounting system substantially improves the acoustic performance of the system. Figure 4-4 showcases that the presence of the added mass further increases the damping capabilities of the panel and establishes a wider and deeper bandgap in the first resonance region. For the sake of comparison, the effect of the panel's rigidity is once again described for the four aforementioned cases. Similar to the previous comparison, the optimized KD parameters were utilized for each scenario. For this case, the IAM mass was included in the optimization process. It is observed that for the non-enhanced panel, the effect of the IAM is barely noticeable; however, even for a small panel stiffness increase, the amplification effect is evident. The STL curve is shifted towards lower frequencies, while the anti-resonance compensates the detrimental effect of the natural resonance of the simply supported panel.

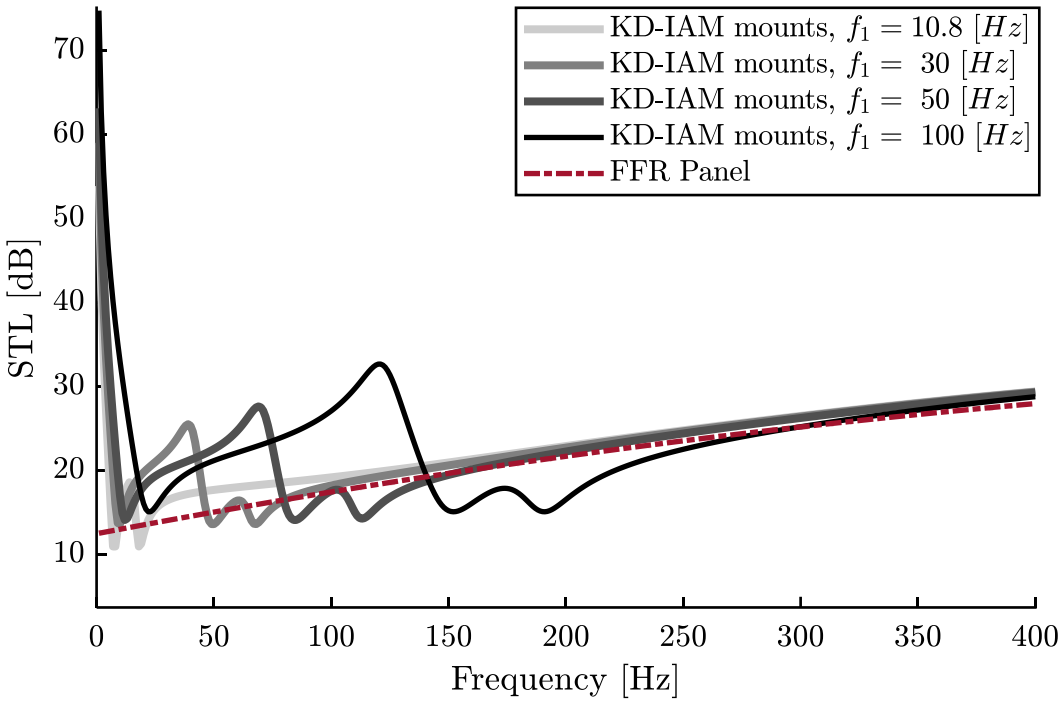

Figure 4-4: Correlation of the panel rigidity and STL of the mounted panel for increasing rigidity of the panel utilizing KD-IAM mounts.

However, as expected, a slight drawback of this extraordinary improvement in the resonance region is the following narrow band of reduced attenuation, which is mitigated slightly due to the resonance effect of the internal mass m_D. Another important observation is that the attenuation band increases as the panel's rigidity increases, while this increase is not proportional to the size of the IAM mass. Specifically, the optimized mass for the case of f_1=10.8Hz is m_B=7.6kg and, at the same time, the width of the attenuated band is almost invisible, while for f_1=100Hz and IAM mass equal to m_B=3.5kg, a significantly wide attenuated frequency band is observed. By comparing the STL curves of the panels with eigenfrequencies f_1=50Hz and 100Hz we observe that the latter has an outstanding performance below 140Hz; nonetheless, above 140Hz, the former prevails and has a more flattened/uniform response without a large deviation from the FFR panel.

Table 4-2: Values of the optimized KD parameters.

Case	f_1 [Hz]	f_0 [Hz]	κ_N [-]	STL_{max} [dB]
1	10.8	10.67	-0.800	17.7
2	30.0	11.30	-0.511	18.6
3	50	13.80	0.771	19.0
4	100	26.80	-0.679	19.1

Table 4-3: Values of the optimized KD-IAM parameters.

Case	f_1 [Hz]	f_0 [Hz]	κ_N [-]	m_B [kg]	b_W [Hz]	STL_{max} [dB]
1	10.8	10.8	-0.786	5.52	14.3	18.6
2	30.0	11.3	-0.511	2.70	41.9	25.5
3	50	13.8	-0.771	2.40	75.2	27.6
4	100	26.8	-0.679	3.49	119.7	32.6

4.6 Numerical Example

Following the investigation on the effect of the panel's rigidity on the STL, an indicative scenario is studied herein to showcase the advantages of the proposed system. One simple way to increase the panel's rigidity is by adopting a grid of box-type section stiffeners, as presented in Figure 4-5 (a). The width (w_x) corresponds to the horizontal distance between the upright supporting beams providing the stable frame of the plasterboard. The selected setup is presented as an example of a stiffened panel, while other configurations with stiffeners in a cross or "X" layout, or even tensegrity structures/mechanisms could comprise effective alternatives. In real-life masonry applications, it is common practice to support the drywall in stable frames, which can further increase the rigidity of the panel. However, this investigation falls out of the scope of the current contribution, the purpose of which is to demonstrate the capabilities of the KD-IAM concept in low-frequency acoustic problems. This is the reason that the added mass of the stiffeners is not taken into account in the STL performance; therefore, as a result of their geometric configuration, the stiffeners are seen as a means to increase the fundamental eigenfrequency of the panel.

The fundamental eigenfrequency of the panel is derived via modal analysis in ABAQUS® FE software, assuming simply supported boundary conditions. The panel is discretized by 20-node quadratic solid hexahedral elements, and the stiffeners are discretized by 8-node quadratic doubly curved thick shell elements. The fundamental mode of the panel is depicted in Figure 4-5 (b) and occurs at f_0 =90.1Hz. The properties of the stiffeners are summarized in Table 4-4.

Table 4-4: Properties of stiffeners.

ρ_S [kg/m^3]	a_s [mm]	b_S [mm]	h_S [mm]	w_x [m]	w_y [m]	E_S [GPa]	v_p [-]
7800	50	50	7	0.375	0.575	210	0.3

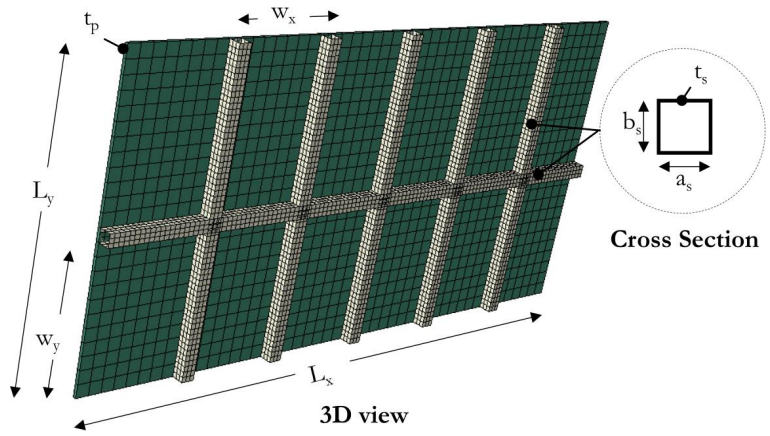

(a)

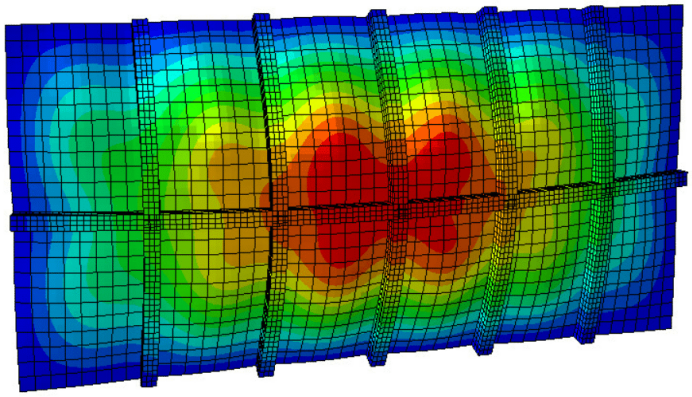

(b)

Figure 4-5: Illustration of the stiffened panel, simply supported on its peripheral edges. (a) Positioning and geometry of the stiffeners. (b) Fundamental mode of vibration of the stiffened panel at f_1 *= 90.1. Hz.*

It is noted that the FE model is used only as a means to define the natural frequency of the panel, while the generalized mass, and consequently stiffness in the analysis are accounted for via the assumptions of the LPM. The optimal properties of the KD-IAM are defined by utilizing the optimization algorithm and by assuming hysteretic damping. A conservative loss factor of η =0.1 was adopted; nonetheless, nowadays someone can easily find industrially produced rubber materials with loss factors up to 0.4 (Carfagni et al., 1998). The optimized parameters of the KD-IAM mounts are summarized in Table 4-5.

Table 4-5: Values of the optimized KD-IAM parameters.

f_1 [Hz]	f_0 [Hz]	k_0 [Nm^{-1}]	k_S [Nm^{-1}]	k_P [Nm^{-1}]	k_N [Nm^{-1}]	μ [-]	η [-]	κ_N [-]	m_B [kg]
90.1	25.1	1.405×10^5	3.613×10^5	1.386×10^5	-8.654×10^4	0.01	0.1	-0.660	3.35

Figure 4-6 presents the enhanced acoustic performance of the KD-IAM mounted panel, with the black dotted line corresponding to the lumped parameter model, as derived from the first mode approximation of the simply supported panel. By comparing the STL curves of the KD-IAM mounted panel with those of the simply supported panel, we observe that the mounted panel shows a 110Hz wide absorption band between 25 and 135Hz which corresponds to the resonance region of the simply supported case. Additionally, a maximum STL gain of 32dB occurs which, compared to the FFR panel, is a 13dB increase in STL.

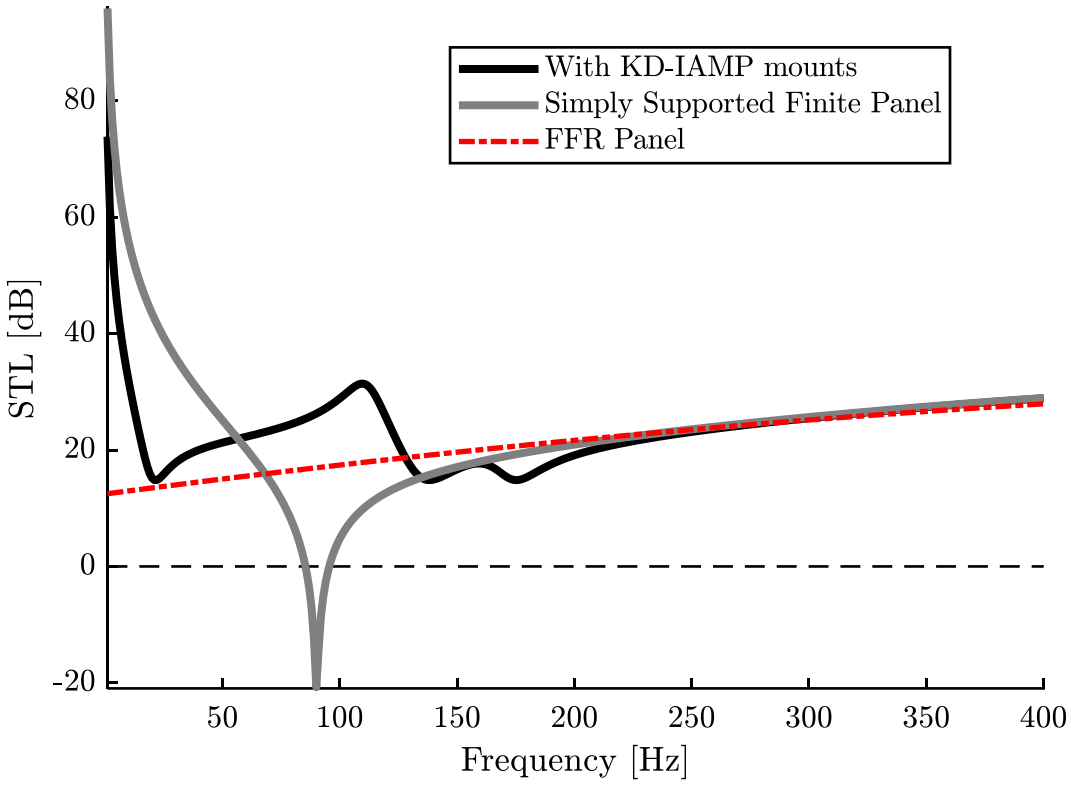

Figure 4-6: STL for the case study of the KD-IAM mounted panel in comparison to the simply supported panel.

4.7 Indicative KD-IAM mount designs

In this section, an implementation according to the parameters provided in Table 4-5 and for design frequency equal to f_0 [Hz] is presented. Generally, according to section 3.3, for $\kappa \geq 90\%\kappa_{\max}$, the negative stiffness elements are more difficult to be realized in practice. In structural mechanics, negative stiffness is generally obtainable through post-buckling processes (snap-through phenomenon). This means that high k_N results to more unstable and difficult to control

implementations (Paradeisiotis, 2019). A tolerable compromise is a value of κ somewhere between 85-90%, which is high enough to exploit the advantages of the KDamper while the slope of the curve is not as sharp as between 90-95%. In this way, the increase of k_N is within reasonable limits. Herein, the negative stiffness springs are envisaged as Bellville springs.

4.7.1 Inertia Amplification Mechanism (IAM)

As presented in Eq. (3-21), the mass m_a of the IAM has an amplification factor equal to ($cot^2\theta+1$), which is plotted in Figure 4-7 (a), as a function of angle θ. Therefore, for realization of the IAM considering four inertial amplification mechanisms positioned under the panel, a combination of (m_a, θ) needs to be selected in order to provide the desired m_B resulting from the optimization procedure of the KD-IAM model divided in four.

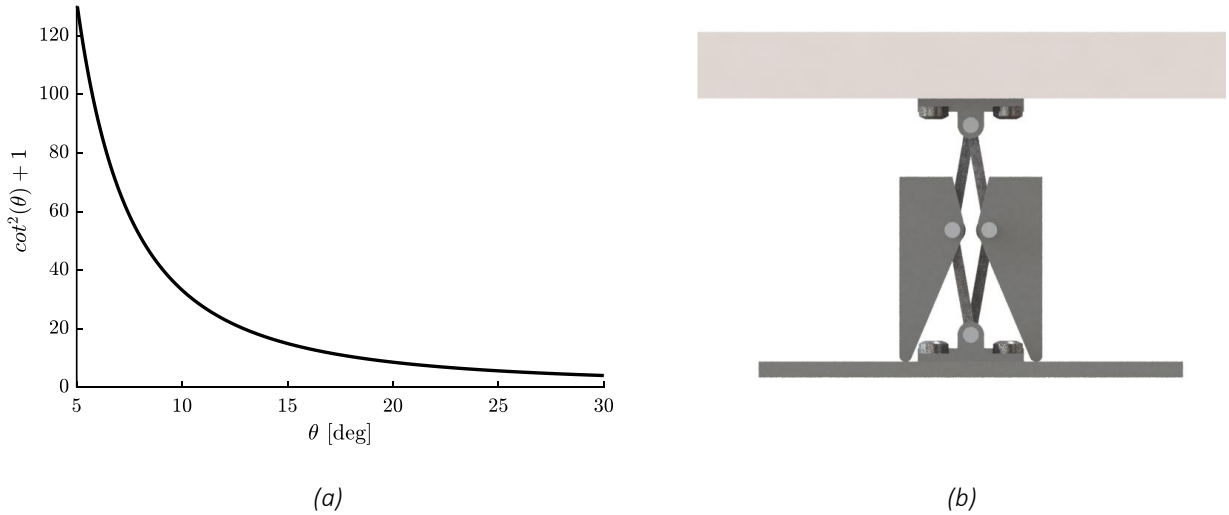

(a) *(b)*

Figure 4-7: (a) Amplification factor of the inertial amplifier as a function of angle ϑ. (b) Conceptual realization of the Inertial Amplification Mechanism (IAM).

For this particular design, assuming structural steel (ρ=7800 kg m^{-3}) for the material of the masses m_a with general dimensions 10×30×35 [mm^3], the relevant parameters for the IAM mechanism are summarized in Table 4-6. A conceptual realization of the proposed IAM is depicted in Figure 4-7 (b).

Table 4-6: IAM mechanism parameters.

$m_B/4$ [kg]	$cot^2\theta + 1$	θ [deg]	m_a [kg]	l [m]
0.838	33.163	10	0.051	0.020

4.7.2 KD mount with Belleville springs

Considering four KDamper mounts at each corner of the panel that act in parallel, the optimized parameters given in Table 4-5 are divided in four, corresponding to each mount.

4.7.2.1 Realization of Negative Stiffness Elements

In this implementation, the negative stiffness element of the oscillator is realized utilizing disk (Belleville) springs. The exerted force and the equivalent stiffness of this type of springs are nonlinear functions of the vertical displacement s of the inner diameter D_i. The height of the spring is denoted by l_0, D_e (the external diameter), and $h_0 \approx l_0 - t$, where t is the thickness. The relevant notation is demonstrated in Figure 4-8. More specific information about disk springs is provided by manufacturers (Bauer, 2008).

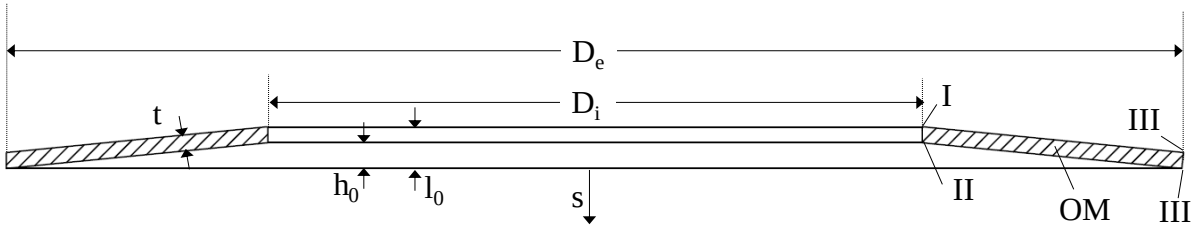

Figure 4-8: Notation and dimensions of disc (Belleville) spring (based on (Paradeisiotis, 2019)*).*

Specifically, the calculation of the exerted force of an individual spring as a function of the deformation s is the following:

$$F(s) = F_c\left[K_4^2\left(\frac{h_0}{t} - \frac{s}{t}\right)\left(\frac{h_0}{t} = \frac{s}{2t}\right) + 1\right]s \tag{4-36}$$

where $F_c = F\left(s = h_0\right)$ is the exerted force when the disc is at its flattened position and is estimated as:

$$F_c = \frac{4E}{1-\nu^2}\frac{t^3 h_0}{K_1 D_e^2}K_4^2 \tag{4-37}$$

By setting the ratio of the outer to the inner diameter of the disk ($\delta = D_e / D_i$) parameters K_i are defined as:

$$K_1 = \frac{1}{\pi}\frac{\left(\frac{\delta-1}{\delta}\right)^2}{\frac{\delta+1}{\delta-1}-\frac{2}{\ln(\delta)}} \tag{4-38}$$

$$K_2 = \frac{6}{\pi}\frac{\frac{\delta-1}{\ln(\delta)}-1}{\ln(\delta)} \tag{4-39}$$

$$K_3 = \frac{3}{\pi}\frac{\delta-1}{ln(\delta)} \tag{4-40}$$

The stresses developed are described by the following equations:

$$\sigma_{OM} = \sigma_0 \frac{3}{\pi} \tag{4-41}$$

$$\sigma_I = \sigma_0\left[K_2K_4\left(\frac{h_0}{t}-\frac{s}{2t}\right)+K_3\right] \tag{4-42}$$

$$\sigma_{III} = \sigma_0\left[\left(K_2-2K_3\right)K_4\left(\frac{h_0}{t}-\frac{s}{2t}\right)-K_3\right]\frac{1}{\delta} \tag{4-43}$$

$$\sigma_{IV} = \sigma_0\left[\left(K_2-2K_3\right)K_4\left(\frac{h_0}{t}-\frac{s}{2t}\right)+K_3\right]\frac{1}{\delta} \tag{4-44}$$

Where

$$\sigma_0 = \frac{4E}{1-\nu^2}\frac{t^2}{K_1D_e^2}K_4\frac{s}{t} \tag{4-45}$$

Standard disk springs dimensioned in accordance to DIN 2093 have ratios of h_0/t up to 1.3. However, in order for such a disk to demonstrate negative stiffness behaviour, this ratio needs to be $h_0/t>\sqrt{2}$, which is categorized as non-standard. Furthermore, for $h_0/t>\sqrt{8}$ the disc becomes a bistable element, meaning that in a certain range of deformation s (snap-through region), the exerted force becomes negative thus, these types of discs may act as switch elements. On the other hand, it has to be taken into account that as this ratio increases, considering all other parameters constant, the force F_c increases too and the developing stresses are getting higher. This fact is problematic, especially for cyclic operation as in this case, due to the low fatigue strength of the mechanism.

The range of the vertical displacement s where the disk exhibits the desired negative stiffness characteristics is centered around the flat position of the disk where the exerted force is F_c and the

stiffness attains its maximum negative value. By all means, this translates to the application of a certain pre-stress condition on the spring in order to remain to its flat position at the equilibrium state of the mount. The height h_0 of the disk spring has to be such that the displacement amplitude C_3 of the internal mass m_D is covered by the resulting range of s corresponding to the negative stiffness values near the maximum within an appropriate margin.

The Belleville spring geometrical parameters are presented in Table 4-7. The material properties of the specific disk spring made of ABS plastic are presented in Table 4-8. In order to achieve the required negative stiffness value, $k_N / 4$ = -2.193×10^4 [Nm^{-1}], with the geometrical properties presented In Table 4-7, a total number of six (6) disk springs have to be configured in parallel. The resulting stiffness of this case in comparison with the single spring curve is demonstrated in Figure 4-9 (a). The bold dashed line indicates the maximum negative stiffness value of k_N, which corresponds to the $k_N / 4$ value, derived from the optimized model.

Table 4-7: Belleville spring geometrical parameters.

T [mm]	δ [-]	D_e/t [-]	h_0/t [-]	F_c [N]	$k_{N,max}$ [Nm^{-1}]
1.3	2.5	32	1.64	31.797	-3.570×10^3

Table 4-8: Material properties of the disk spring.

ρ [kg m^{-3}]	σ_{yield}[MPa]	E [MPa]	v [-]
1020	48	2206.3	0.3

Figure 4-9 (b) shows the developed disc stresses as a function of deformation s at five characteristic points of the spring. Stresses σ_I , σ_{II}, σ_{III} ,and σ_{IV} correspond to the four corners of the cross section of the disk, while σ_{OM} is the equivalent Von Mises stress at the center of the cross section. The value of the resulting stress σ_{OM} must be within certain limits, that especially in dynamic applications, define a nominal number of maximum operation cycles for the disk spring. These values are derived using endurance and fatigue strength diagrams.

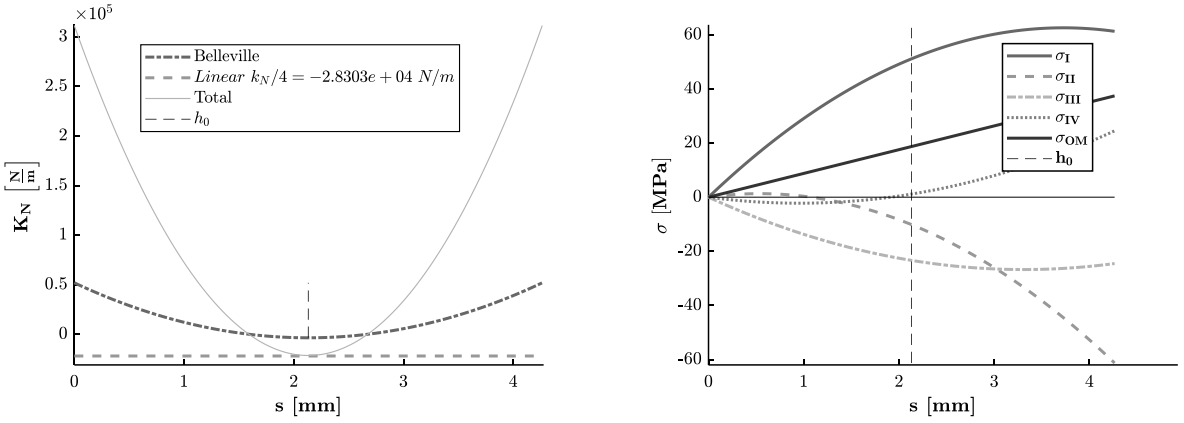

(a) *(b)*

Figure 4-9: Resulting stiffness and stress during deformation of disk springs. (a) Equivalent stiffness of a single spring and six disk springs in a parallel configuration. (b) Development of stress in each disk spring.

The realization of the negative stiffness element via six (6) parallel disks, is reconfigured into two stacks of three, positioned on a fixed base as demonstrated in Figure 4-11 (a) and (b). The discs are held together by a bolt and two washers at their flat position. This way, the two stacks still act as two parallel springs, resulting in the desired k_N value; however, the exerted forces of each stack have the same magnitude but opposite directions, meaning that they cancel each other out and the equilibrium position is neutrally stable.

4.7.2.2 Realization of Positive Stiffness Elements

For the positive stiffness elements of the mount, namely the k_S and k_P elements of the KDamper, the material of choice is rubber. Since certain categories of rubbers also present damping properties, defined by the loss factor due to their hysteretic, viscoelastic behaviour, they comprise an obvious option to combine along with the aforementioned stiffness elements in the form of rubber pads. Specifically, drawings of the circular pads with a hole in the middle are illustrated in Figure 4-10. The selected material for the realization of the positive stiffness elements of the mount $k_S / 4$ and $k_P / 4$ is CR07 (chloroprene rubber with 7% carbon black) in the form of rubber pads. Common rubber materials, such as chloroprene rubbers with black carbon additives, demonstrate the desired damping effects due to internal friction. Typical values range from $\eta = 0.05$ up to $\eta = 0.7$, depending on the composition and quality of the material.

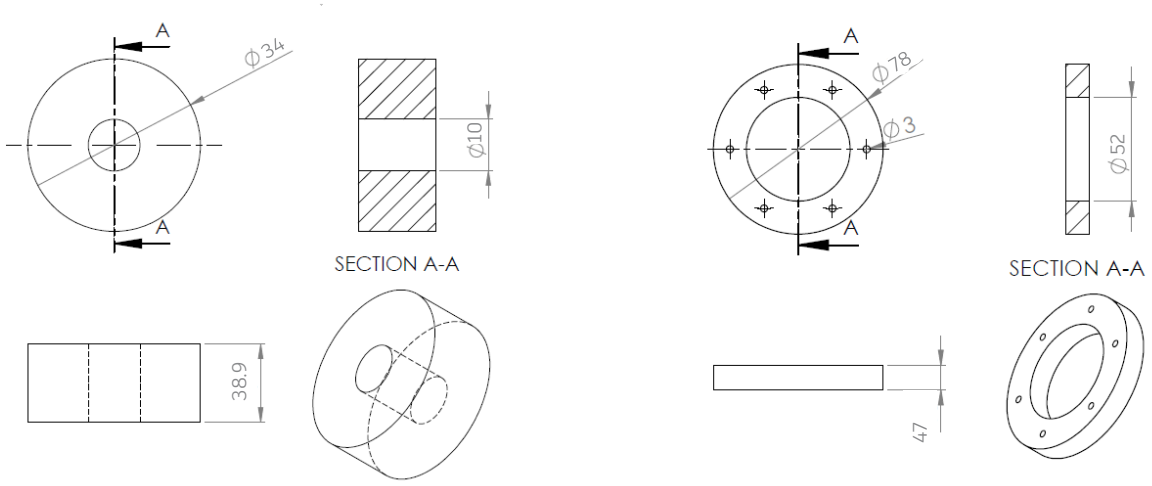

Figure 4-10: Designs of the rubber pads for the realization of the positive stiffness elements (based on (Paradeisiotis, 2019)*).*

The stiffness of the rubber pads depends on their dimensions. An indicator of the compressive stiffness of a rubber pad is the shape factor S, which is defined as the ratio of the one loaded surface area A to the area that is free to bulge. Specifically, for hollow cylindrical rubber pads, the shape factor is calculated as

$$S = \frac{\left(D^2 - d^2\right)}{4\left(D - d\right)h} \tag{4-46}$$

where D and d are the outer and inner diameters, respectively, and t is the thickness of the pad. The compressive stiffness of the rubber pad is calculated as:

$$k_{comp} = \frac{E_{corr} A}{h} \tag{4-47}$$

Where

$$E_{corr} = E_0(1 + S^2) \tag{4-48}$$

is the corrected Young's modulus of the material obtained using the calculated shape factor. Obviously, this requires the knowledge of the initial E_0, which can be provided by relevant stress-strain tests of the material in question. For the purpose of this indicative design, the hyperelastic properties of rubber are neglected; consequently, the calculated value from Eq. (4-47) is an approximation that can be used as a starting point for the detailed dimensioning of the rubber pads. The dimensions of the rubber pads are summarized in Table 4-9.

Table 4-9: Dimensions of rubber pads (chloroprene rubber, 7% carbon black, CR07).

	D [mm]	d [mm]	h [mm]
$k_P/4$	34	10	38.9
$k_S/4$	75	52	47

4.7.2.3 Design

In order to apply the appropriate pre-stress conditions required to provide the necessary negative stiffness of the disc springs, an M6 bolt holds all of the six-disc springs flattened, while at the top and bottom interface between the springs and the bolt, the two washers, as shown in Figure 4-11 (a) and (b), also act as the added mass m_D of the KDamper oscillator.

Figure 4-11 (c) and (d) shows an indicative configuration for incorporating the eight mounts to the gypsum board. In reality, the fixed base of each mount belongs to the unified aluminum part of the frame or the stiffeners on which the board is fixed.

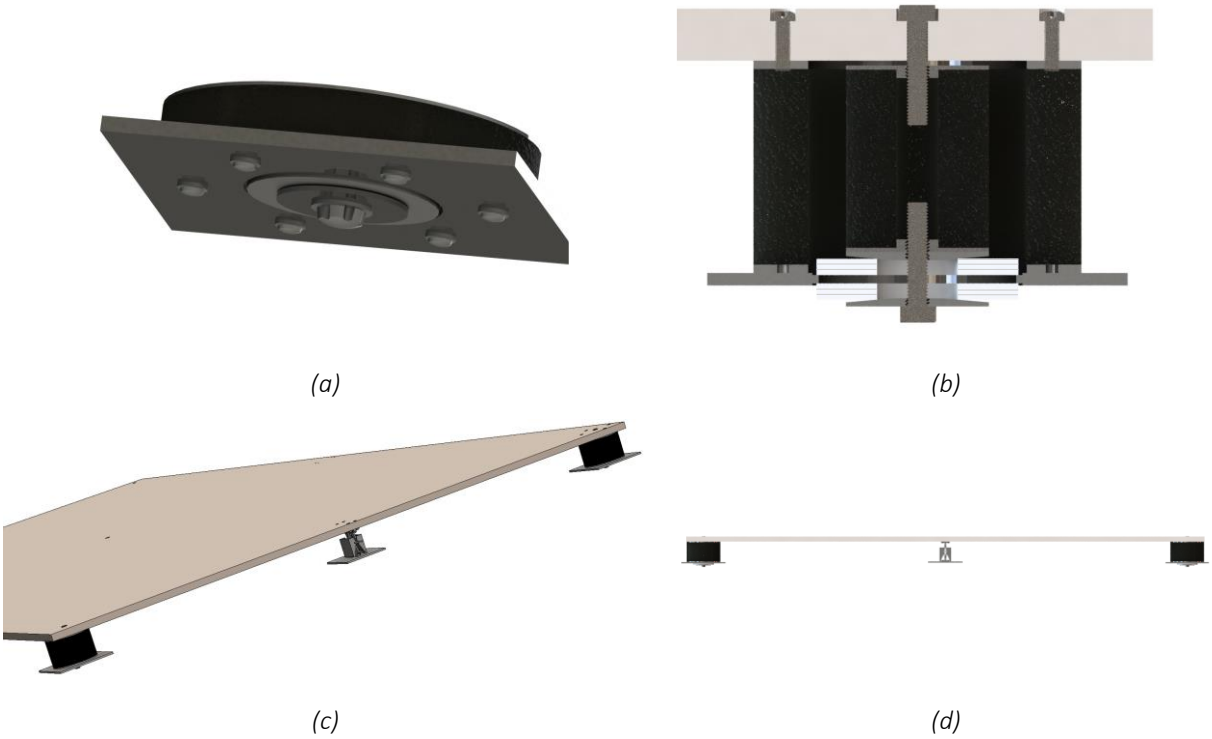

(a) *(b)*

(c) *(d)*

Figure 4-11: Indicative realization of the mounted panel. (a) KDamper mounts with Belleville springs. (b) section view. (c) Indicative configuration of the mounts. (d) Indicative mounting of the panel.

4.8 Numerical modeling of the KDamper-IAM mounted panel

To validate the aforementioned LPM, a 3-D FE coupled vibro-acoustic model was developed on the commercial finite element software ABAQUS®. As a simplification, only the transmission side of the air domain was modeled, and the panel was excited by directly applying a blocked pressure ($p_b = 2p_i$) on its surface (Figure 4-12).

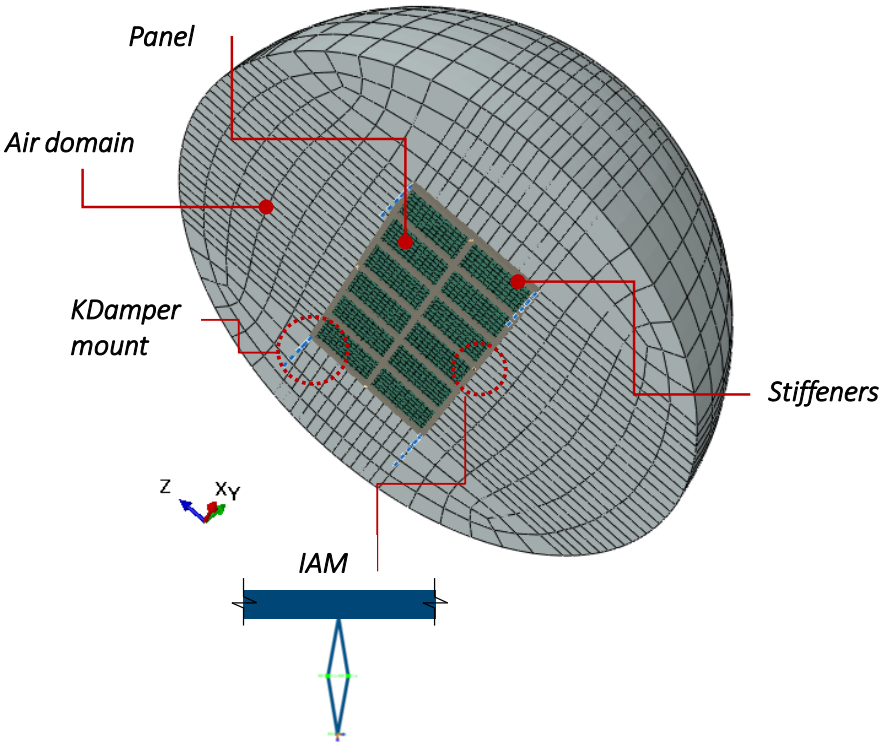

Figure 4-12: Depiction of the FE vibro-acoustic panel-KD-IAM mounts model.

The acoustic pressure was derived from the fluid-structure interface nodes, and an arithmetic average was performed by:

$$\overline{P}_t = \frac{1}{n}\sum_{t=1}^{n}\left|p_{t,i}\right| \tag{4-49}$$

where n denotes the total number of nodes; i denotes the node number; and p_t the transmitted pressure. Then the averaged pressure was used to compute the simulated STL by:

$$STL = 20\log_{10}\left(\frac{|P_i|}{\overline{P}_t}\right) \tag{4-50}$$

The panel was discretized by 20-node quadratic solid hexahedral elements, the stiffeners were discretized by 2-node linear elements while the fluid domain was discretized by 20-node quadratic acoustic hexahedral elements. Regarding the amplifiers, beam elements were used to simulate the links connected with MPC pin constraints. Tie constraints were used to simulate the coupling of the fluid-structure interface and the stiffeners-panel interface, while non-reflecting boundary conditions were specified to generate the infinite fluid domain. The KDamper mount elements were modeled by assigning connectors with the appropriate elastic properties. Lastly, the discretization of the fluid domain had more than three quadratic elements across the wavelength of interest to increase the accuracy of the computational results (Marburg, 2002).

In Figure 4-13, the acoustic performance of the KD-IAM mounted panel in terms of STL is evaluated. The direct comparison between the STL curves derived from the LMP approximation and the FE analysis shows that the analytical model accurately predicts the system's acoustic properties, considering the assumptions of the method. Specifically, the LMP indicated bandgap is approximately 20Hz shifted to higher frequencies compared to the FE model, while the bandwidth remains the same. Naturally, more peaks and valleys appear in the numerical predictions due to the panel-mount system's higher modes.

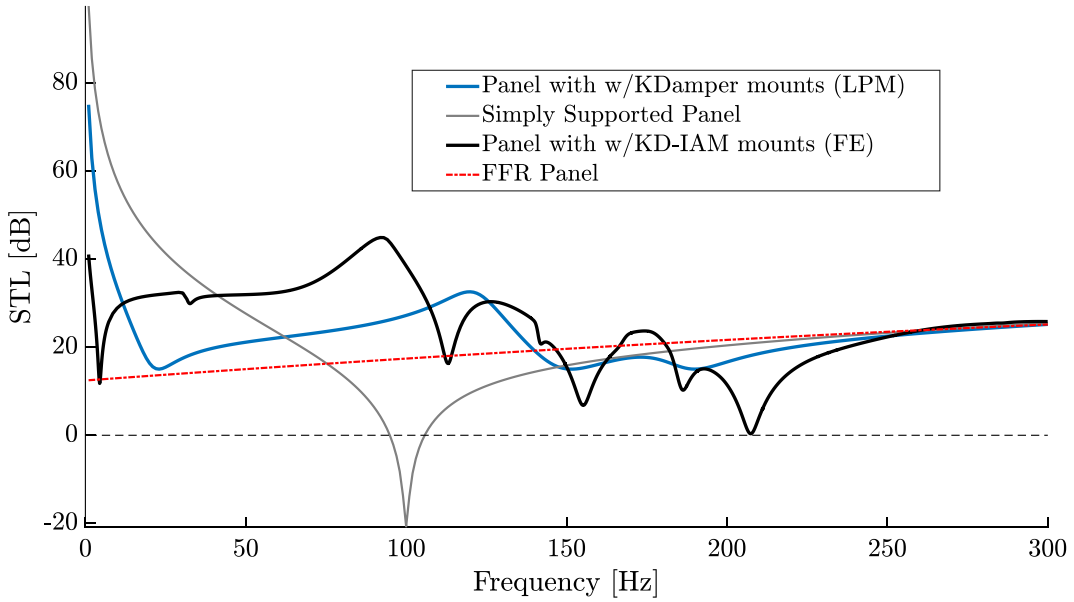

Figure 4-13: STL for the case study of the KD-IAM mounted panel; comparison between the FE and the LPM.

4.9 Concluding Remarks

In this chapter, the KDamper is implemented as an advanced absorber for acoustic panel mounts in combination with an inertia amplification system, namely the KD-IAM concept. The KD-IAM equations of motion are extended to include the deformable panel according to the in-series LPM approximation. An optimization procedure is presented for selecting the absorber's parameters to maximize the STL of the panel in the prescribed frequency range. The optimization procedure for the selection of the absorber's parameters based on the described modeling approximations demonstrated the relation between the rigidity and the STL performance of the mounted panel. Finally, an indicative realization of the KD-IAM-based mounting system is presented utilizing Belleville springs for the negative stiffness element of the KDamper and other common elements, such as rubber pads and simple linkages.

Based on the dynamic analysis and the results obtained from an indicative case study of a drywall, the following concluding remarks can be made:

- Utilizing stiffeners to increase the rigidity and, consequently, the fundamental frequency of the panel, the resulting optimized mounts based on the KD-IAM achieve a wider and deeper frequency band of improved STL in the resonance region of the system.
- The presented implementation utilizing the proposed KD-IAM advanced absorber for the panel's mounting shows a wide and deep frequency band of improved vibration and noise attenuation in terms of STL in the resonance region and at frequencies of ∼20–150 Hz.
- Including the inertial amplifier on the KD mounting system substantially improves the system's acoustic performance.
- The vibro-acoustic FE model results proved that the *KD-IAM in series approximation* is a useful and accurate design tool.

5 METAMATERIAL DESIGNS BASED ON THE KDAMPER – IAM CONCEPT

5.1 Background

As previously presented, conventional locally resonant (LR) metamaterials require relatively heavy, additional, internally moving masses, as well as high displacement amplitudes, which may prohibit their practical implementation. Indicatively, current applications of LR metamaterials in acoustics (Groby et al., 2014; Weisser et al., 2016) often address frequencies well above 500 Hz.

In this study, we claim that the major limitations of conventional linear metamaterials such as the limited frequency band of the attenuation zone can be overcome by adopting an advanced unit-cell design that includes inertial amplification mechanisms such as the proposed IAM and KDamper concept. Several studies in the recent literature integrate inertial amplifiers to metamaterial concepts (Taniker and Yilmaz, 2017; Wanjura et al., 2020; Yilmaz, 2018) studying their dynamic properties, while others investigate the effect of non-linear phenomena and negative stiffness elements, revealing the benefits in terms of larger attenuation bandwidths, that can be obtained by exploiting such mechanisms. To this end, negative stiffness phenomena are very promising for vibration isolation and can be generated by adopting prestressed conventional springs, buckled beams, disc springs or even gas springs, as shown in the literature and recent applications. Towards this direction, Al-Shudeifat (2014) and Chen et al. (2019) investigate the effects of nonlinear energy sinks with negative stiffness elements, showing promising results in terms of vibration attenuation. These concepts help towards focusing the attention on the potential advantages of negative stiffness for elastic metamaterials. Chen et al. (2020), Morris et al. (2019) and Salari-Sharif et al. (2019) propose unique

metamaterial designs incorporating negative stiffness unit-cells, revealing the potential of such systems towards energy dissipation and structural protection. In 2022, Chondrogiannis et al. (2022), investigated the introduction of non-linear negative stiffness geometrical inclusions as a means to artificially increase the unit-cell mass of a phononic structure. Experimental testing on a LEGO technic assembly indicated that enhanced low-frequency energy dissipation and improved bandgap properties can be generated by incorporating such mechanisms.

In a similar way, the KDamper concept aims at vibration isolation, utilizing negative stiffness elements that improve the dynamic behavior of a TMD-inspired oscillating mass and taking into consideration the stability of the system, therefore maintaining a positive overall stiffness. The application of the KDamper (KD) concept towards the design of highly dissipative low-frequency elastic/acoustic metamaterials Antoniadis and Paradeisiotis (I Antoniadis and Paradeisiotis, 2018; I. Antoniadis and Paradeisiotis, 2018) shows promise in addressing the issue of low-frequency noise mitigation up to a certain extent. The initial form of the KDamper was optimized to minimize the displacement of the seismic mass under harmonic excitation and was geared more toward applications for machine mounting. Recently, as presented in the previous chapter, the research team of the Dynamics and Acoustics laboratory, School of Mechanical Engineering of the NTUA have implemented the KDamper as a panel mounting mechanism, aiming to attenuate low-frequency noise (Paradeisiotis, 2019; 2020).

In this chapter, KDamper-based metamaterial designs are presented along with their detailed analytical framework. The concept is subsequently enhanced by developing an inertial amplification system (IAM) supplementary to the initial mechanism; such addition allows for further improvement of the dynamic behavior of the structure. The proposed designs target the development of metamaterial-based noise barriers. Initial conceptual implementations are proposed herein, and the presented mechanisms are evaluated using both analytical and numerical analyses

5.2 KDamper “traditional” metamaterial design

5.2.1 Bloch analysis and bandgap estimation

The KDamper based metamaterials essentially comprise a periodic repetition of unit-lattice cells of KDamper elements, as presented in Figure 5-1.

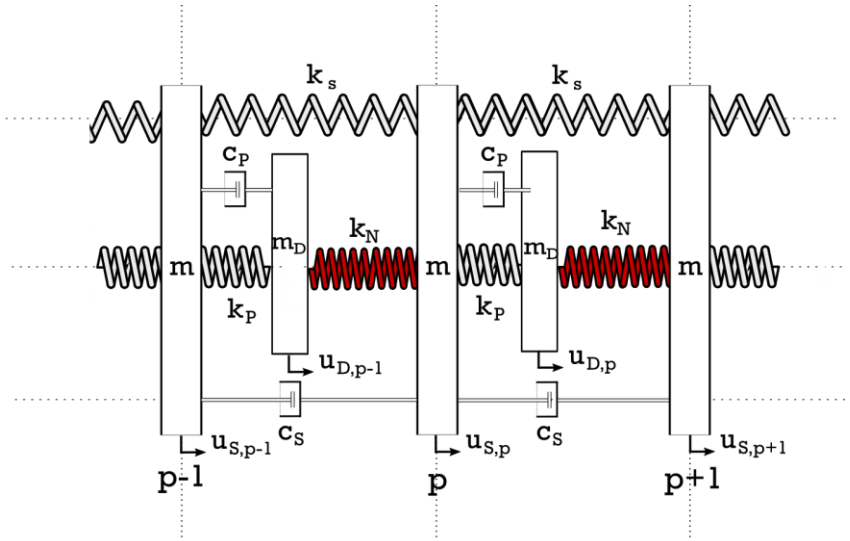

Figure 5-1: Unit-cell of KDamper metamaterial.

As evident from Figure 5-1, setting the value of the negative stiffness element of the KDamper unit-cell as $k_N = 0$, makes it equivalent to the TMD based, acoustic/elastic locally resonant metamaterial. Consequently, the equations of motion of a typical unit-cell are derived as:

$$\begin{aligned} &m\ddot{u}_{S,p} + c_S(\dot{u}_{S,p} - \dot{u}_{S,p-1}) + c_S(\dot{u}_{S,p} - \dot{u}_{S,p+1}) + k_S(u_{S,p} - u_{S,p-1}) \\ &+ k_S(u_{S,p} - u_{S,p+1}) + k_P(u_{S,p} - u_{D,p}) + k_N(u_{S,p} - u_{D,p-1}) = 0 \end{aligned} \tag{5-1}$$

$$m_D\ddot{u}_{D,p} + c_D(\dot{u}_{D,p} - \dot{u}_{S,p}) + k_P(u_{D,p} - u_{S,p}) + k_N u_{D,p} - u_{S,p+1}) = 0 \tag{5-2}$$

For each of the system of Eqs (5-1) and (5-2), the generalized form of Bloch's (1929) theorem is applied:

$$u_{S,p} = U_S e^{\lambda t} \tag{5-3}$$

$$u_{S,p+1} = U_S e^{j\kappa l + \lambda t} = U_{S,p+1} e^{\lambda t} \tag{5-4}$$

$$u_{S,p-1} = U_S e^{-j\kappa l + \lambda t} = U_{S,p-1} e^{\lambda t} \tag{5-5}$$

$$u_{D,p} = U_D e^{\lambda t} \tag{5-6}$$

$$u_{D,p+1} = U_D e^{j\kappa l + \lambda t} = U_{D,p+1} e^{\lambda t} \tag{5-7}$$

$$u_{D,p-1} = U_D e^{-j\kappa l + \lambda t} = U_{D,p-1} e^{\lambda t} \tag{5-8}$$

where u_s, u_D are the wave amplitudes at node p, l is the unit-cell length, κ is the wave number and λ is a complex frequency function that permits wave attenuation in time. In the limiting case of no damping ($\zeta = 0$), the time factor that indicates harmonic wave propagation $e^{-\zeta\omega \pm j\omega\sqrt{1-\zeta^2}}$ is taken as

$e^{j\omega t}$ and the usual form of Bloch's theorem is recovered. Substitution of Equations (5-3)-(5-8) into Equations (5-1)-(5-2), leads to:

$$[\lambda^2 m + \lambda(\gamma c_S + c_D) + (\gamma k_S + k_P + k_N)U_S - (\lambda c_D + k_P + e^{j\kappa l}k_N)U_D = 0 \quad (5\text{-}9)$$

$$[\lambda^2 m_D + \lambda c_D + (k_P + k_N)U_D - (\lambda c_D + k_P + e^{-j\kappa l}k_N)U_S = 0 \quad (5\text{-}10)$$

where

$$\gamma = 2 - (e^{j\kappa l} + e^{-j\kappa l}) = 2(1 - \cos\kappa l) \ = 2(1 - \cos \mathrm{q}) \quad (5\text{-}11)$$

$$\mathrm{q} = \kappa l \quad (5\text{-}12)$$

Substituting U_D from Eq. (5-10) into Eq. (5-9), leads to:

$$[\alpha_4\lambda^4 + \alpha_3\lambda^3 + \alpha_2\lambda^2 + \alpha_1\lambda + \alpha_0]U_S \quad (5\text{-}13)$$

where

$$a_4 = m_D m \quad (5\text{-}14)$$

$$a_3 = (m_D + m)c_D + \gamma c_D + \gamma c_S m_D \quad (5\text{-}15)$$

$$a_2 = (m_D + m)k_D\gamma(c_S c_D + k_S m_D) \quad (5\text{-}16)$$

$$a_1 = \gamma c_S k_D + \gamma c_D(k_S + k_N) \quad (5\text{-}17)$$

$$a_0 = \gamma k_S k_D + \gamma k_P k_N \quad (5\text{-}18)$$

where $k_D = k_P + k_N$

Eq. (5-13) yields a characteristic equation of the form:

$$\alpha_4\lambda^4 + \alpha_3\lambda^3 + \alpha_2\lambda^2 + \alpha_1\lambda + \alpha_0 = 0 \quad (5\text{-}19)$$

The roots may be expressed as:

$$\lambda_B = -\zeta_B\omega_B \pm j\omega_B\sqrt{1-\zeta_B{}^2}, B = 1,2 \quad (5\text{-}20)$$

where B=1 represents the lower branch number and B=2 represents the upper branch number of the two dispersion curves, while ω_B, ζ_B represent the corresponding natural frequency and damping ratio.

Assuming an undamped system, $a_3 = a_1 = 0$, $\lambda = \omega^2$, and referring to the total stiffness k_0 of the KDamper and the non-dimensional parameters of the KDamper μ, ρ, κ, it holds that $(k_S k_D + k_P k_N) = k_0 k_D$ the characteristic equation may be written as

$$A\lambda^2 + B\lambda + C = 0 \tag{5-21}$$

and the above coefficients are the following:

$$A = 1 \tag{5-22}$$

$$B = \frac{-[(m+m_D)k_D + \gamma k_S m_D]}{mm_D} = -[(1+\mu)\omega_D^2 + \gamma\omega_S^2] \tag{5-23}$$

$$C = \gamma[k_S k_D + k_P k_N] = \gamma\omega_0^2\omega_D^2 \tag{5-24}$$

where

$$\omega_D = \sqrt{k_D / m}_D \tag{5-25}$$

$$\omega_S = \sqrt{k_S / m} = \omega_0\sqrt{1+\kappa(1+\kappa)\mu\rho^2} \tag{5-26}$$

$$\omega_0 = \sqrt{k_0 / m} = \omega_D / \rho \tag{5-27}$$

$$\rho = \omega_D / \omega_0 \tag{5-28}$$

It should be noted that from now onwards, the Greek letter κ, refers to the non-dimensional parameter of the KDamper; the wavelength is included in the parameter q defined in Eq. (5-12). The roots of Eq. (5-21) are calculated as follows:

$$\lambda_{1,2} = \frac{-\mathrm{B} \pm \sqrt{\Delta - 4AC}}{2A} \tag{5-29}$$

Finally, the dispersion curves can be obtained from $\lambda_{1,2}$ as:

$$\omega_+(\mathrm{q}) = \sqrt{\lambda_1} \tag{5-30}$$

$$\omega_-(\mathrm{q}) = \sqrt{\lambda_2} \tag{5-31}$$

Consequently, ω_L, ω_H are the bandgap limits ($\omega_L \le \omega \le \omega_H$):

$$\omega_H = \omega_+(\mathrm{q}=0) = \omega_D\sqrt{1+\mu} = \omega_0\rho\sqrt{1+\mu} \tag{5-32}$$

$$\omega_L^2 = \frac{\omega_0^2}{\frac{1}{\rho^2} + \kappa(1+\kappa)\mu} = \frac{\omega_D^2}{1+(1+\kappa)\mu\rho^2} \tag{5-33}$$

And b_w the normalized bandwidth:

$$b_w = \frac{\omega_H - \omega_L}{\omega_L} = \sqrt{(1+\mu)[1+\kappa(1+\kappa)\mu\rho^2]} - 1 \tag{5-34}$$

By setting $\kappa = 0$, the corresponding band-gap limits of the TMD unit-cell can be obtained from Eq. (5-33)-(5-28) as follows:

$$\omega_L \xrightarrow{\kappa \to 0} \omega_D = \sqrt{k_P / m_D} \tag{5-35}$$

$$b_w \xrightarrow{\kappa \to 0} = \sqrt{(1+\mu)} - 1 \tag{5-36}$$

According to Eq. (5-33)-(5-34) the normalized bandgap width b_W can be increased not only by increasing the parameter μ (i.e., the value of the internally oscillating mass m_D), but also the value of the parameter κ (i.e., the magnitude of the negative stiffness element k_N). This can be considered among others as a consequence of Eq. (3-8), since the usage of a negative stiffness element can be considered as an indirect approach to artificially increase the inertia of the system.

Figure 5-2 presents the resulting normalized bandgap widths b_W for a variation of both the κ and μ parameters of the KDamper metamaterial. As it can be observed, a normalized bandgap width of $b_W = 3$ may already be achieved for values of κ close to $\kappa_{\max}$, even for negligible values of the internal oscillating mass ($\mu = 0$)(I. Antoniadis and Paradeisiotis, 2018). Thus, the extraordinary properties of the KDamper metamaterial chain showcase that large bandgaps can be accomplished compared to those generated by conventional acoustic metamaterials, even for chains with high values of internal oscillating masses ($\mu \geq 10$).

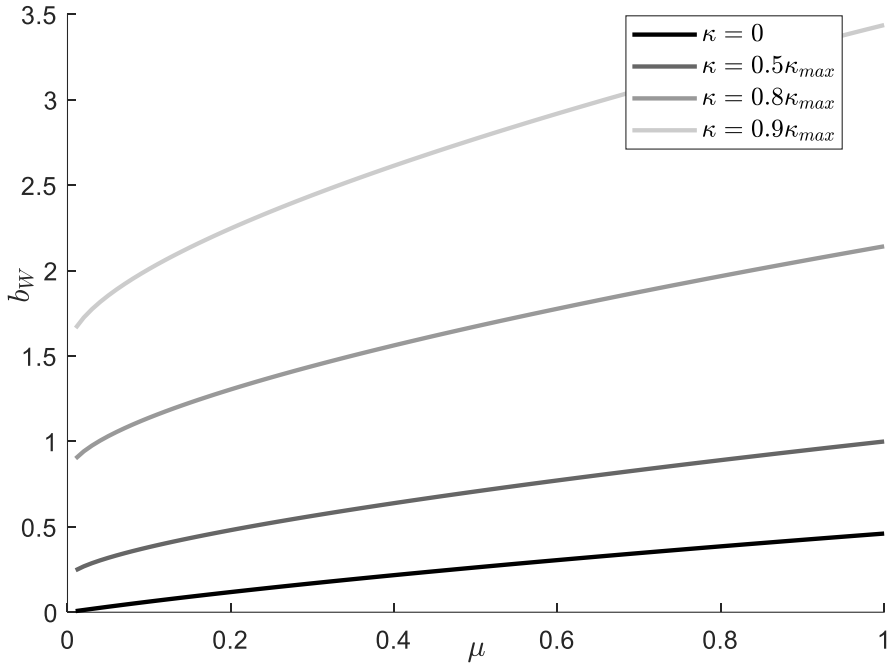

Figure 5-2: Normalized bandgap width as a function of the κ and μ KDamper parameters.

5.2.2 Transfer function of the KDamper metamaterial

The equation of motion of the metamaterial, for M number of unit-cells (Figure 5-3) is expressed in matrix formulation as:

$$\boldsymbol{M}^{metaKD}\ddot{u}(t)+\boldsymbol{C}^{metaKD}\dot{u}(t)+\boldsymbol{K}^{metaKD}u(t)=\boldsymbol{f}(t) \tag{5-37}$$

where $\boldsymbol{M}_{pxp}^{metaKD},\boldsymbol{K}_{pxp}^{metaKD},\boldsymbol{C}_{pxp}^{metaKD},\boldsymbol{u}_{px1},\dot{\boldsymbol{u}}_{px1},\ddot{\boldsymbol{u}}_{px1},\boldsymbol{F}_{px1}$ and $p=2M+1$ is the number of degrees of freedom of the metamaterial. For a single unit-cell, M=1, the mass (M^{metaKD}), damping (C^{metaKD}) and stiffness (K^{metaKD}) matrices are the following:

$$\boldsymbol{M}^{metaKD}=\begin{bmatrix} m & 0 & 0 \\ 0 & m_D & 0 \\ 0 & 0 & m \end{bmatrix} \tag{5-38.a}$$

$$\boldsymbol{K}^{metaKD}=\begin{bmatrix} k_S+k_P & -k_P & -k_S \\ -k_P & k_N+k_P & -k_N \\ -k_S & -k_N & k_S+k_N \end{bmatrix} \tag{5-38.b}$$

$$\boldsymbol{C}^{metaKD}=\begin{bmatrix} c_S+c_P & -c_P & -c_S \\ -c_P & c_N+c_P & -c_N \\ -c_S & -c_N & c_S+c_N \end{bmatrix} \tag{5-38.c}$$

$$\boldsymbol{F} = \begin{bmatrix} 1 \\ 0 \\ 0 \end{bmatrix} \tag{5-38.d}$$

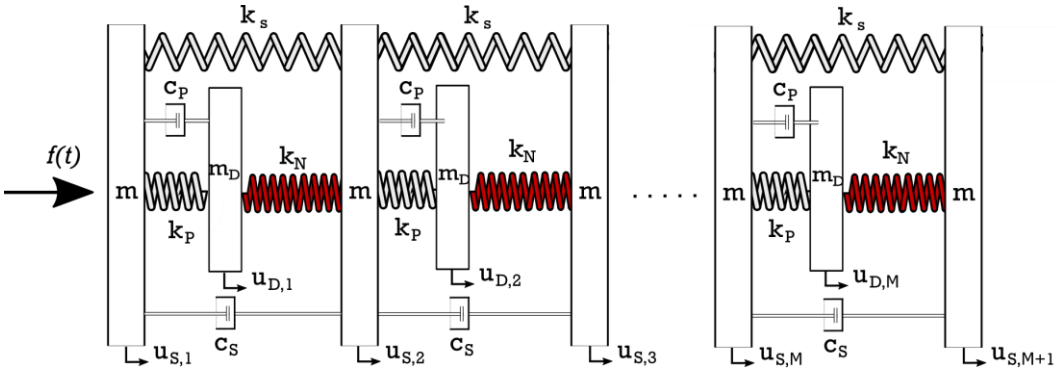

Figure 5-3: KDamper acoustic metamaterial finite lattice.

For $\boldsymbol{M} > 1$, the above matrices of the single unit-cell, are formulated appropriately. Therefore, the frequency response of the lattice may be calculated via the following expression:

$$TF^{metaKD} = (-\omega_2 M + jC + K)^{-1} F \tag{5-39}$$

where

$$\boldsymbol{TF}_{px1}^{metaKD} = \left\{ \frac{\tilde{U}_{S,1}}{\tilde{F}} \frac{\tilde{U}_{D,1}}{\tilde{F}} \frac{\tilde{U}_{S,2}}{\tilde{F}} \cdots \frac{\tilde{U}_{S,M+1}}{\tilde{F}} \right\}^T \tag{5-40}$$

5.3 Enhanced KDamper-IAM metamaterial for acoustic applications

Aiming to further improve the KDamper metamaterial dynamic characteristics, a new configuration is developed based on the KD-IAM concept, as initially presented in chapter 3. The enhanced meta-structure is realized by adopting the KDamper unit-cell rationale with the inclusion of an inertial amplifier (IAM). The KDamper mechanism can find multiple applications in low-frequency damping and absorption applications. An indicative concept for the implementation of KDamper based metamaterials towards the design of acoustic low-frequency attenuation panels is examined herein.

Figure 5-4 depicts the model of a KD-IAM unit-cell for the simplest case of a meta-structure that is based on the periodic repetition of such unit-cells. Specifically, m_j is the connecting mass, which is assumed to be negligible in order to act just as a connector, namely asan additional DoF. The effective

mass of the IAM configuration is superimposed to the connecting mass, which is calculated as $m_B = \frac{m_a}{2}(\cot^2\theta + 1)$.The periodicity is considered one dimensional, and the IAMs are fixed on one end.

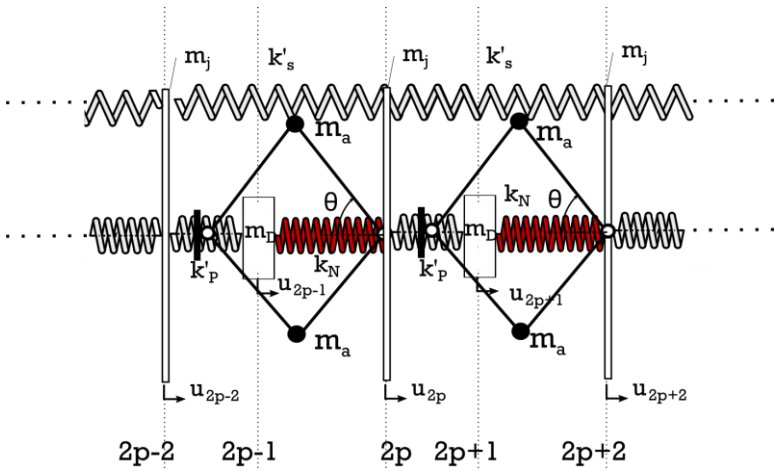

Figure 5-4: KD-IAM unit-cell.

5.3.1 Application of Bloch's theorem

The displacement of a DoF at a certain position $2p$ of the lattice depicted in Figure 5-4, can be expressed in a complex notation as:

$$u_{2p} = \tilde{u}_{2p} e^{\lambda t} = U(2p\kappa l) e^{j2p\kappa l} \tag{5-41}$$

with κ being the wavenumber and l the length of the unit-cell.

Utilizing Bloch's theory, the propagation of elastic waves between the unit-cells can be described by considering the interaction of displacements and forces, as detailed in the analysis of the previous section. By taking into consideration the spatial part of the solution, this is expressed as:

$$u_{2p} = U e^{j2p\kappa l} \tag{5-42}$$

$$u_{2p-2} = u_{2p} e^{-j2\kappa l} \tag{5-43}$$

$$u_{2p+2} = u_{2p} e^{j2\kappa l} \tag{5-44}$$

$$u_{2p\text{-}1} = U_D e^{j2p\kappa l} e^{-j2\kappa l} \tag{5-45}$$

$$u_{2p+1} = u_{2p-1}\, e^{j2\kappa l} \tag{5-46}$$

Assuming the case without damping, substitution into the equations of motion of the unit-cell leads to:

$$m_B m_D \omega^4 - [m_B k_D + (\gamma k_s + k_D) m_D]\omega^2 + \gamma(k_s k_D + k_P k_N) = 0 \tag{5-47}$$

where again $\gamma = 2(1 - cos\ \mathrm{q})$ for $q = 2\kappa L$ and $k_D = k_P + k_N$. Setting $\lambda = \omega^2$, Eq. (5-47) can be written in the form of Eq. (5-21), while the parameters A, B, C are defined as follows:

$$A = 1 \tag{5-48}$$

$$B = -[(1+\mu_B)\omega_D^2 + \gamma\omega_{S,B}^2] \tag{5-49}$$

$$C = \gamma\omega_B^2\omega_D^2 \tag{5-50}$$

while the following characteristic frequencies and parameters are:

$$\omega_B = \sqrt{\frac{k_0}{m_B}},\ \omega_{S,B} = \sqrt{\frac{k_S}{m_B}},\ \mu_B = \frac{m_D}{m_B} \tag{5-51}$$

As a following step, the dispersion relations are given by the two solutions λ_1, λ_2 of Eq. (5-21), resulting in the upper $\omega_+(\mathrm{q}) = \sqrt{\lambda_1}$ and lower $\omega_-(\mathrm{q}) = \sqrt{\lambda_2}$ branches, respectively.

The dispersion relations are $2\pi / l$ -periodic in the wavenumber space; therefore, $\omega(\mathrm{q}) = \omega(\mathrm{q} + 2\pi)$. Furthermore, considering the irreducible Brillouin zone, the two-characteristic high (ω_H) and low (ω_L) frequencies of the generated bandgap can be calculated as:

$$\omega_H = \omega_+(\mathrm{q}=0) = \omega_D\sqrt{1+\mu_B} = \omega_{\mathbf{B}}\rho_B\sqrt{1+\mu}_B \tag{5-52}$$

$$\omega_L = \omega_-(\mathrm{q}=\pi) = \frac{1}{\sqrt{2}}\sqrt{(4\omega_{S,B}^2 + \omega_H^2)^2 - (4\omega_B\omega_D)^2} \tag{5-53}$$

where $\rho_B = \omega_D\omega_B$. In addition, for the case where zero damping wave propagation is completely prohibited, the "central" frequency of the bandgap is calculated as:

$$\omega_\infty = \frac{\omega_B\rho_B}{\sqrt{1 - \frac{\kappa_N}{\kappa_D}\left(1 + \frac{\kappa_N}{\kappa_D}\right)m_B\rho_B^2}} \tag{5-54}$$

The above frequencies can be used to tune the meta-structure according to the requirements of a specific application and to define the normalized bandgap width bw.

5.3.2 Transmission loss of the KDamper-IAM metamaterial

For the case of M number of unit-cells, the equation of motion of the KD-IAM metamaterial is expressed in matrix formulation as follows:

unit-

$$\boldsymbol{M}^{metaKD-IAM}\ddot{\boldsymbol{u}}(t)+\boldsymbol{C}^{metaKD-IAM}\dot{\boldsymbol{u}}(t)+\boldsymbol{K}^{metaKD-IAM}\boldsymbol{u}(t)=\boldsymbol{f}(t) \tag{5-55}$$

where $M_{pxp}^{metaKD-IAM}, K_{pxp}^{metaKD-IAM}, C_{pxp}^{metaKD-IAM}, u_{px1}, \dot{u}_{px1}, \ddot{u}_{px1}, F_{px1}$ and $p=2M+3$ is the number of degrees of freedom of the metamaterial.

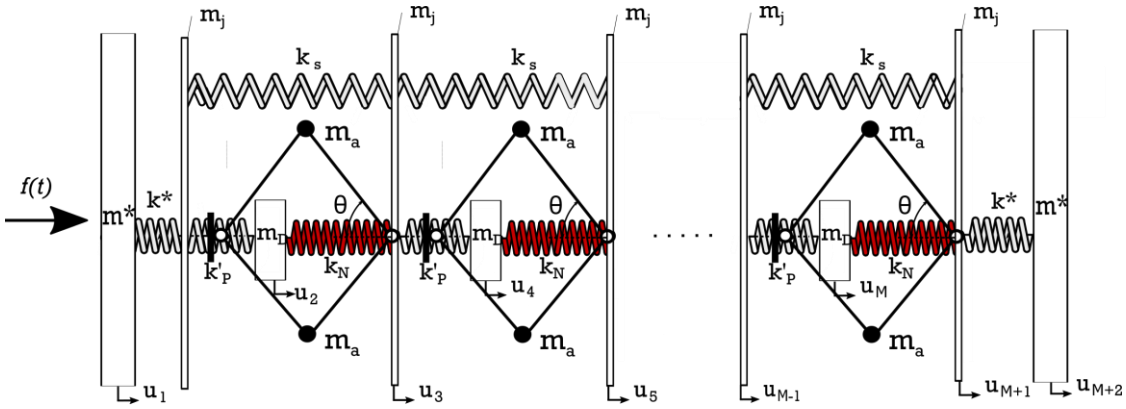

Figure 5-5: KD-IAM acoustic metamaterial finite lattice.

In the case of a single unit-cell, M=1, the mass ($K^{metaKD\text{-}IAM}$), damping ($M^{metaKD\text{-}IAM}$) and stiffness ($M^{metaKD\text{-}IAM}$) matrices are the following:

$$\boldsymbol{M}^{metaKD-IAM}=\begin{bmatrix} m* & 0 & 0 & 0 & 0 \\ 0 & m_B & 0 & 0 & 0 \\ 0 & 0 & m_D & 0 & 0 \\ 0 & 0 & 0 & m_B & 0 \\ 0 & 0 & 0 & 0 & m* \end{bmatrix} \tag{5-56.a}$$

$$\boldsymbol{K}^{metaKD-IAM}=\begin{bmatrix} k* & -k* & 0 & 0 & 0 \\ -k & k_S+k_P+k* & -k_P & -k_S & 0 \\ 0 & -k_P & k_N+k_P & -k_N & 0 \\ 0 & -k_S & -k_N & k_S+k_N+k* & -k* \\ 0 & 0 & 0 & -k* & k* \end{bmatrix} \tag{5-56.b}$$

$$\boldsymbol{F} = \begin{bmatrix} 1 \\ 0 \\ 0 \\ 0 \\ 0 \end{bmatrix} \tag{5-56.c}$$

For $\boldsymbol{M} > 1$, the above matrices of the single unit-cell, are formulated appropriately. Therefore, the transfer functions of each degree of freedom to the excitation may be calculated via the following expression:

$$\boldsymbol{TF}^{metaKD-IAM} = (-\omega^2 \boldsymbol{M}^{metaKD-IAM} + j\boldsymbol{C}^{metaKD-IAM} + \boldsymbol{K}^{metaKD-IAM})^{-1} \boldsymbol{F} \tag{5-57}$$

Figure 5-5 demonstrates the finite lattice of the meta-structure where the KD-IAM unit-cells are enclosed by the masses $m*$ and the spring elements $k*$. This modelling technique is required to simulate the effect of the radiating surface and consequently, to accurately calculate the STL. The acoustic performance is subsequently evaluated for various numbers of unit-cells. In other words, a sandwich panel is simulated instead of a simple chain and the "In-series" approximation (chapter 2) is adopted to calculate the corresponding STL as follows:

$$STL^{metaKD\text{-}IAM} = 20\log_{10}\left(\frac{1}{\tau}\right) \tag{5-58}$$

where,

$$\tau^{metaKD\text{-}IAM} = l_x l_y \left(\frac{4\omega^2 \rho_0}{\pi^3}\right)^2 \frac{1}{\left|\left(-\omega^2 m* + k*\right)\left(1 - TF_{21}\right)\right|^2} I_{\theta\varphi} \tag{5-59}$$

l_x, l_y are the dimensions of the radiating surfaces, ρ_0 the air density, $I_{\theta\varphi}$ the integral over hemispheric surface and $TF_{21} = TF(2)/TF(1)$.

5.4 Numerical example

In this section, an examination of the KD-IAM concept is presented aiming to evaluate the low-frequency acoustic performance of the meta-structure. The values of the KD-IAM parameters are tabulated in Table 5-1 and are obtained after an optimization procedure. The aim is the selection of optimal values for the KDamper and IAM elements in order to obtain the maximum possible STL performance, especially in the resonance region of the system and undertake a comparison with the initial case where the plate is simply supported on its edges. Relevant information about the

optimization procedure can be found in chapter 4. The panels enclosing the periodic KD-IAM structure are assumed as conventional plasterboards, the properties of which are summarized in Table 5-2.

Table 5-1: Values of the optimized KD-IAM parameters.

f_1[Hz]	$f_{KD\text{-}IAM}$ [Hz]	k_0[N/mm]	k_S[N/mm]	k_P[N/mm]	k_N[N/mm]	μ	η	κ_N	m_B[kg]
100	25.1	1.405×10^5	4.121×10^5	1.581×10^5	-1.02×10^5	0.01	0.1	-0.679	3.49

Table 5-2: Plasterboard properties.

ρ_P [kg/m3]	L_x [m]	L_y [m]	h_p [mm]	E_p [MPa]	ν_P	η_p
668	1.2	2.4	6.3	2900	0.31	0.01

Figure 5-5 (a) depicts the bandgap frequencies of the irreducible Brillouin zone for the selected geometry and parameters where $f_H = 163.2Hz$ and $f_l = 56.67Hz$, corresponding to a normalized bandgap width $b_w = 1.89Hz$. Accordingly, Figure 5-5 (b) demonstrates the acoustic performance of the sandwich panel based on the periodic repetition of KD-IAM unit-cells.

It is observed that, the depth and width of the attenuation band are not significantly affected, as far as the STL performance is concerned. However, despite the choice of lower loss factor, the emergence of meta-damping improves the response around the characteristic frequency f_0, which can be very important for certain applications. In the context of the present investigation, it is demonstrated that the physical mechanisms of the KD-IAM concept that provide this extreme attenuation band are present even for a single unit-cell, meaning that, at least in this specific case, the added manufacturing complexity for multiple unit-cells could end up unnecessary.

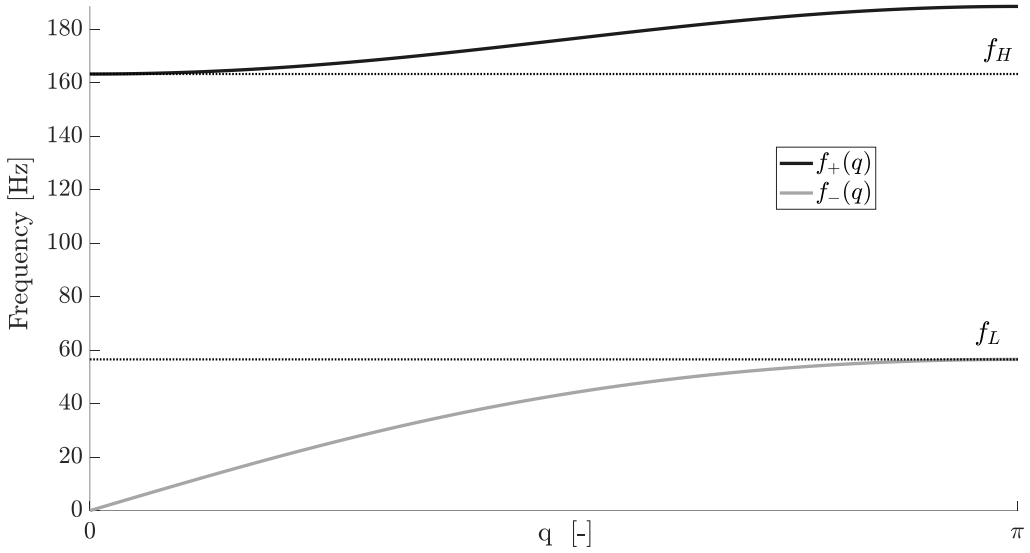

(a)

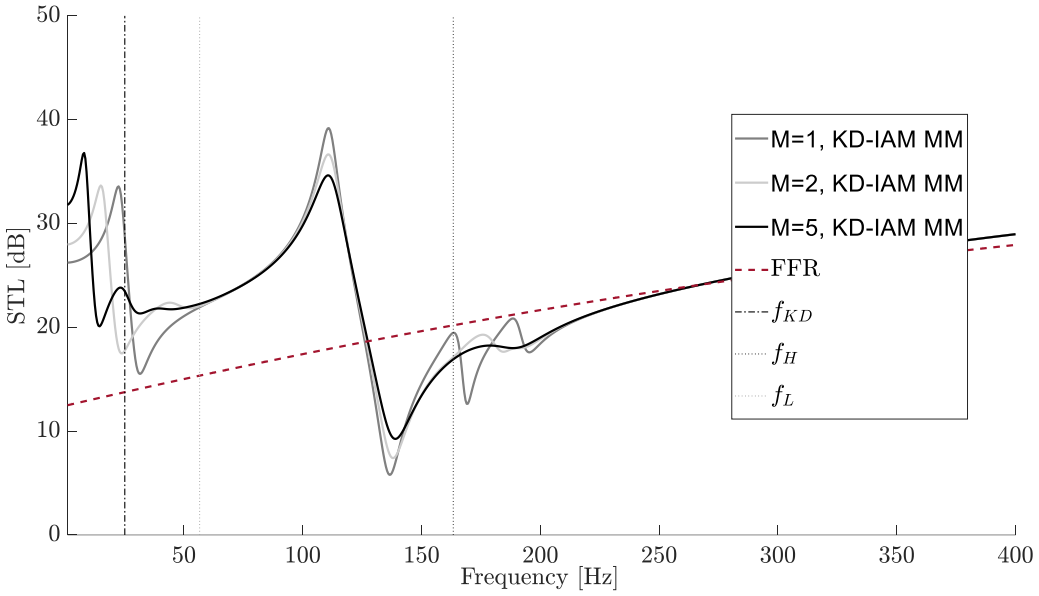

(b)

Figure 5-6: Performance of the KD-IAM periodic structure. (a) Dispersion curves: irreducible Brillouin zone. (b) STL for various numbers M of unit-cells.

5.5 Indicative implementation for Meta-panel designs

5.5.1 KD-IAM Meta-structure design

Figure 5-7 shows a feasible conceptual design of a meta structure panel for M=1 number of unit-cells. Naturally, the various parallel KD-IAM elements can be divided according to the number of positions and are chosen to be positioned on the surfaces of the panels. The rationale behind the quantity of each element lies on the required properties that should be realized, the constraints that apply due to their dimensions, and the requirement of an adequate number of supports in order to achieve a uniform pressure distribution on the surface of each panel. Specifically, sixteen (16) negative stiffness elements are utilized, eight (8) at each panel, and two (2) k_P springs are located on top of each negative spring. Concerning the k_s springs, a total number of thirty-two (32) elements is prescribed, divided accordingly for each of the two panels. Lastly, fifty-four (54) IAMs are employed in order to achieve the required amplification.

The material of the positive springs (k_S and k_P) is envisaged as acrylonitrile butadiene styrene (ABS), a material that can be used in conventional 3D printers. On the other hand, the negative stiffness springs and the amplifiers are made of steel. The ABS material is modelled as linear elastic-perfectly plastic, with Young's modulus equal to $E = 1740MPa$, yield stress $\sigma_{yield} = 27.8MPa$, and mass density

equal to $\rho = 1100 kg/m^3$. Steel is modelled as linear elastic-perfectly plastic with Young's modulus equal to $\mathrm{E} = 210 GPa$, yield stress $\sigma_{yield} = 275 MPa$, and mass density equal to $\rho = 7800 kg/m^3$.

To enable simple fabrication in a single material system without the need for a complex assembly, the positive springs are implemented as arches. The shape of the semi-circular arches implementing the springs are chosen to allow large strains in the linear regime without yielding or buckling. Clearly, this poses a limit on the stiffness of the entire system, as both springs are bending-dominated.

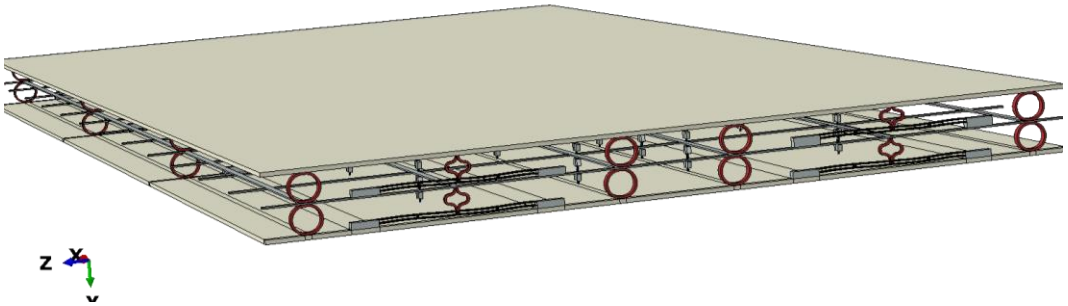

Figure 5-7: KD-IAM meta-structure conceptual design.

The width and thickness of all the elements is properly adjusted to result in the desired stiffness, which was initially calculated based on Eq. (5-60) and (5-61) (Guell Izard et al., 2017).

$$k_p = 1.38 E w_1 \left(\frac{t_1}{l_1} \right)^3 \tag{5-60}$$

$$k_S = 0.46 E w_3 \left(\frac{t_3}{R_3} \right)^3 \tag{5-61}$$

The geometry of the positive springs is depicted in Figure 5-8 (a) and the relevant geometrical parameters are provided in Table 5-3.

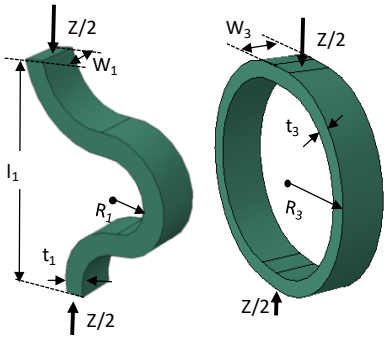

(a)

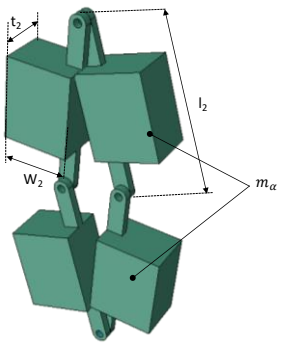

(b)

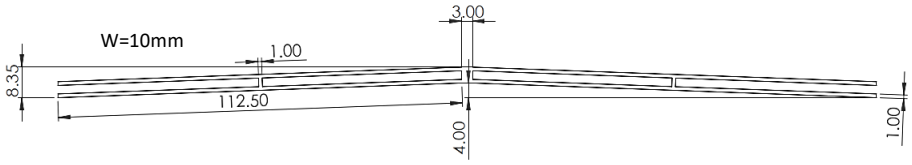

(c)

Figure 5-8: Geometry of the (a) k_S and k_P springs, (b) of the IAM, (c) of the k_N springs.

In order to verify the simple analytical models, Finite Elements (FE) simulation is conducted employing the commercial software ABAQUS®. The springs are modelled with solid elements and a RIKS post-buckling analysis is performed. Snap-through behavior and buckling are two examples of models that may become statically unstable. Riks Analysis is a special method to capture the behavior after the instability The load-displacement curves for these springs are presented in Figure 5-9 (a) and (b), along with the results of the FE predictions. In both cases we may observe that all springs remain in their elastic regime for less than 3mm deformation, which is deemed as adequate.

Table 5-3: Positive springs parameters.

v	t [mm]	R [mm]	w [mm]	l [mm]	Stiffness / spring [N/m]	Number of springs / panel	Stiffness / panel [N/m]
k_s	3	20	9	40	2.4×10^4	16	4.32×10^5
k_p	3	8	5	32	9.9×10^3	16	1.58×10^5

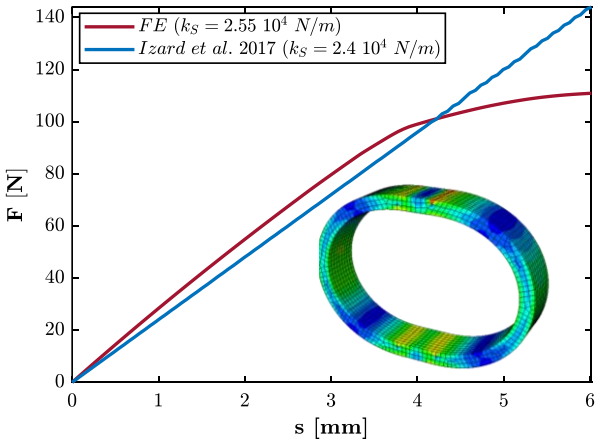

(a)

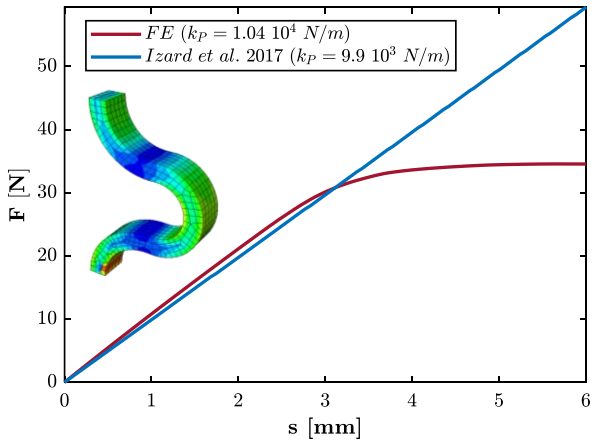

(b)

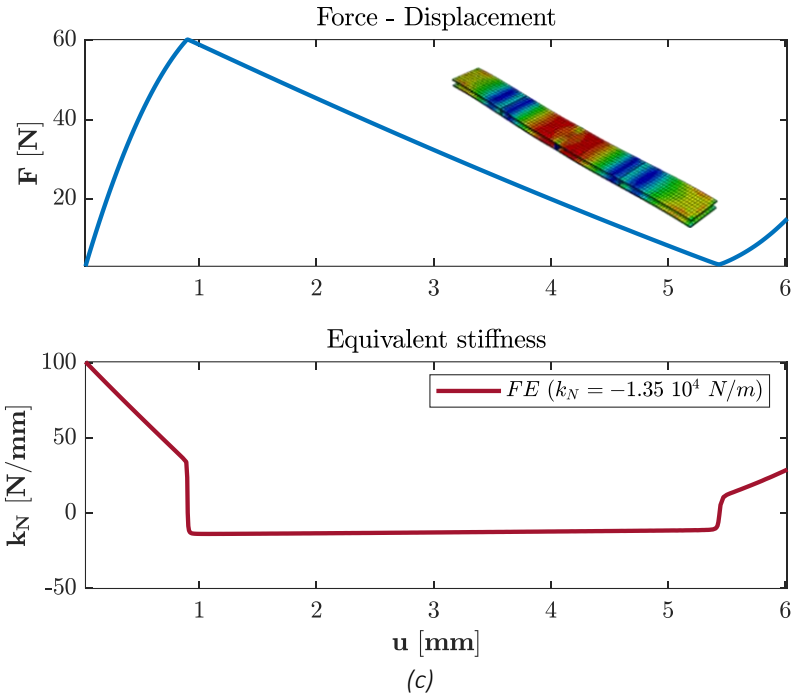

Figure 5-9: Load – displacement curves of the springs (a) k_S (b) k_P (c) k_N.

In this implementation, the negative stiffness element is realized by utilizing inclined pre-stressed beams. The dimensions of the selected beams are depicted in Figure 5-9 (c) where three (3) ABS spacers connect the two (2) steel blades and force the beams to buckle at the required locations. Again, FE RIKS analysis is performed to capture the snap-through behaviour and the load-displacement curves. The range of the vertical displacements where the disk exhibits the desired negative stiffness characteristics is centred around the flat position of the beam where the exerted force and the stiffness attains its maximum negative value. In order to achieve the required negative stiffness value, with the geometrical properties presented herein, eight (8) springs with $k_N / 8 = -1.35 \times 10^4 [Nm^{-1}]$ have to be configured.

The mass m_a of the IAM has an amplification factor $(\cot^2\theta + 1)$. Therefore, for realization of the IAM a combination of (m_a, θ) needs to be selected in order to provide the desired m_B. For this particular design, assuming structural steel for the material of the IAM and hinged connections as shown in Figure 5-9 (b), the relevant parameters for the IAM mechanism are summarized in Table 5-4.

Table 5-4: IAM mechanism parameters.

l_2 [mm]	t_2 [mm]	w_2 [mm]	m_a [kg/IAM]	Number of IAMs / panel	Amplified mass/panel
20	6	10	0.0156	27	0.42

5.5.2 Numerical performance of the KDamper-IAM meta-structure

Finally, the performance of the sandwich meta-panel is assessed through a detailed Finite element vibro-acoustic model. As a simplification, only the transmission side of the air domain is modelled and the panel is excited by directly applying a blocked pressure $(p_b = 2p_i)$ on its surface (see Figure 5-10). The acoustic pressure is extracted from the fluid-structure interface nodes and then the arithmetic average is calculated as follows:

$$\bar{P}_t = \frac{1}{n}\sum_{i=1}^{n}\left|p_{t,i}\right| \tag{5-62}$$

where n denotes the total number of nodes; i denotes the node number; and p_t denotes the transmitted pressure. Then the averaged pressure was used to compute the simulated STL by:

$$STL = 20\log_{10}\left(\frac{P_i}{\bar{P}_t}\right) \tag{5-63}$$

The panel is discretized by 20-node quadratic solid hexahedral elements and the fluid domain is discretized by 20-node quadratic acoustic hexahedral elements. The springs and the amplifiers are modelled based on the design described in the previous section. The deformed mesh of the prestressed beam obtained during the RIKS analysis is inserted to the main model to capture the geometry of the initial deformed state of the negative stiffness element, and the corresponding initial stresses are selected. Tie constraints are used to simulate the coupling of the fluid-structure interface and non-reflecting boundary conditions are specified to generate the infinite fluid domain. Lastly, the discretization of the fluid domain has more than three quadratic elements across the wavelength of interest to increase the accuracy of the computational results (Marburg, 2002).

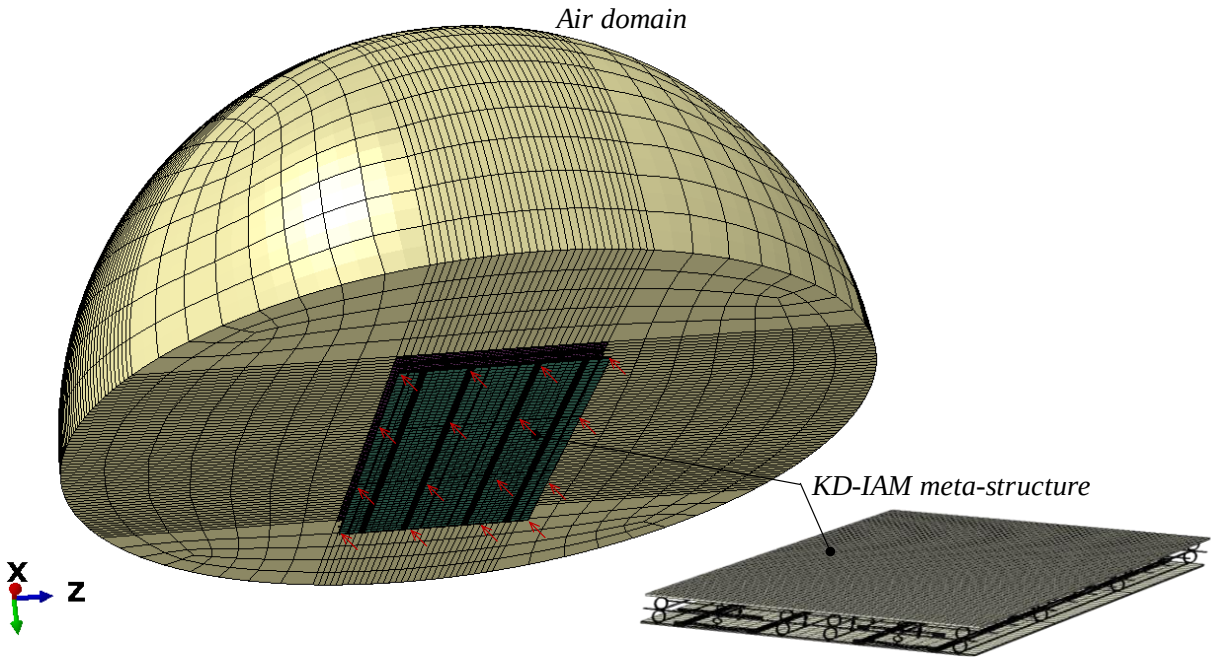

Figure 5-10: KD-IAM meta-structure Finite Element model.

Figure 5-11 presents the results of the FE simulation of the KD-IAM meta-structure with one-unit-cell. Obviously, in reality the acoustic performance of such a meta-structure is much more complex and difficult to be accurately predicted. The main reason is the positioning of the various structural elements between the panels and the panel stiffness. Depending on the selected configuration, the dynamic response may vary significantly. In this particular case, the frequency range of improved STL is slightly higher than what was predicted analytically, specifically between 120 and 220 Hz, compared to the free finite rigid (FFR) panel approximation. In any case, the lumped parameter models of the acoustic meta-structure provide a reasonable approach for the dimensioning of the various elements and an estimation of the expected performance. Additionally, a more refined FE model can provide further insight into the realistic performance of the system, as well as the effect of the configuration and geometry of the stiffness elements.

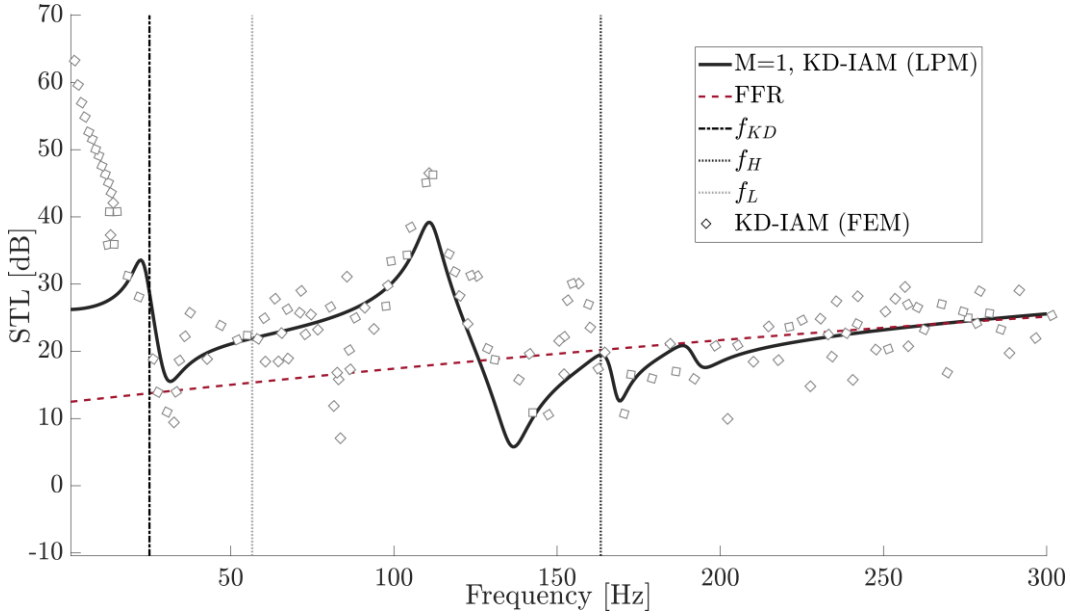

Figure 5-11: STL Performance of the KD-IAM meta structure.

5.6 Concluding Remarks

The vibration and sound properties of a sandwich meta-structure based on the synergetic KDamping and Inertial amplification concepts is studied. First, the theoretical framework of the periodic structure is presented followed by a typical case study of a building acoustics application. It is highlighted that deep and wide bandgaps can be formed in the low-frequency regime. Thus, the KD-IAM is deemed capable for low-frequency acoustic insulation without the requirement of many unit-cells and any added complexity that could be entailed in a practical implementation. Finally, the feasibility of the concept is demonstrated by providing preliminary designs of all the essential parts comprising the KD-IAM meta-structure. Appropriate technological implementations of this concept can lead to significant improvements in all types of low-frequency technological applications, with emphasis on low-frequency noise isolation/absorption.

IV. The Dynamic Directional Amplification Mechanism (DDA)

6 DYNAMIC DIRECTIONAL AMPLIFICATION MECHANISM (DDA) CONCEPT

6.1 Background

As presented in the previous chapters of this thesis, integration of amplification mechanisms to increase the inertia of the oscillating masses of passive vibration absorbers is of key significance to enhance the behavior and improve the dynamic properties of existing technologies. To this end, various inertial and displacement amplification mechanisms have been developed and implemented in numerous engineering fields. From sensors and electromechanical signal amplifiers to Tuned Mass Dampers (TMDs) and other vibration control devices the idea of mass amplification has long been considered by a great number of researchers. A detailed literature review of such amplification mechanisms is provided in chapter 1 of this research work.

In the concept of vibration control, inertial amplification was initially introduced by Smith (2002). The so called inerter, takes advantage of a levered mass mechanism and generates an additional force that is proportional to the acceleration between the two, inerter connected points. Subsequently, the system was used in passive absorbers (e.g., TMDs and NS mechanisms) to increase their damping properties. The concept of mass amplification has been also considered as a method to enhance the vibration attenuation and filtering properties of phononic and locally resonant metamaterial lattices. One of the first studies included lattices with levered amplification mechanisms (Yilmaz and Kikuchi, 2006). Later, experimental tests indicated the existence of large bandgaps that extend to the low-frequency domain (Acar and Yilmaz, 2013), providing insight into a new promising class of inertially amplified metamaterials.

In this Chapter, a novel Dynamic Directional Amplifier, namely the DDA mechanism, is introduced as a means to artificially increase the resonating mass of an oscillator, with no requirement of complex geometries and heavy parasitic masses. The mechanism's rationale lies in the dynamics of a system that is subjected to a holonomic constrain (Udwadia and Kalaba, 1995, 1992); the vibrating mass is fixed to a simple rigid link that increases inertia towards the desired direction of motion by coupling the kinematic DoFs of the resonating mass and forcing the oscillator to move through a prescribed circumferential path. Analysis is undertaken, and results indicate the beneficial effect of the DDA to the dynamic response of the system (transfer functions), when compared to the initial single degree of freedom (SDoF) oscillator. A simple experimental set-up is presented along with parametric shaking-table testing results for various DDA angles; results validate the analytical framework and showcase the efficiency and applicability of the mechanism. It is clearly shown that we can enhance the performance of dynamic structures while retaining mass requirements and complex configurations to a minimum level. The simple geometry and uncomplicated structure of the DDA allows its application to real life structures, as a vibration control mechanism.

6.2 Mechanical design of a DDA mechanism

The DDA mechanism is a simple structure with main features the mass amplification and the diversion of the output motion of the oscillating mass. The physical model of the DDA is shown in Figure 6-1 and comprises the two links AC, A'C', which are welded to the axle along A-A'. In this way, the links are free to rotate and consequently, the panel (mass) attached to the links follows the same rotational movement. The mounting conditions of the bearing shafts are not depicted in this figure; however, it is assumed that they are fixed to a rigid base. A vertical and a horizontal spring provide the necessary stiffness to the system, and the rigid panel (mass) is excited by an applied force (F) towards the y-direction. By all means, other realizations are also feasible; e.g., the entire system could be monolithically manufactured as a compliant structure with flexure hinges (Chen et al., 2012).However, it is deemed at this point that the adopted mechanical design fits better the requirements and purpose of the study.

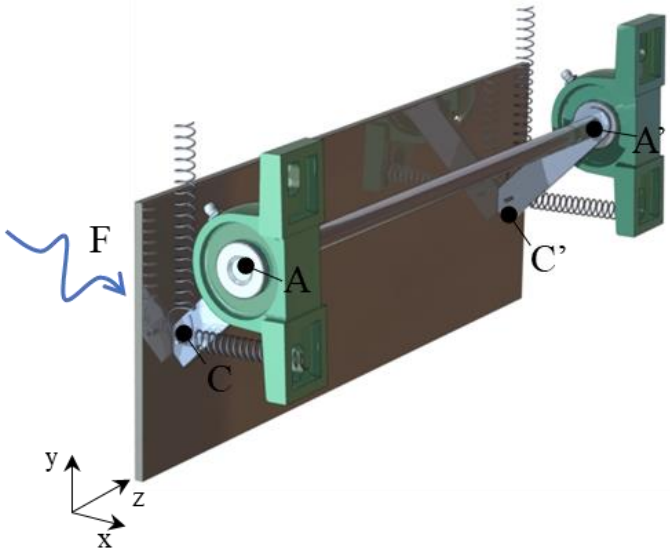

Figure 6-1: 3D realization of the considered Dynamic directional amplification (DDA) mechanism.

6.3 Equations of Motion and Transfer Functions

The Cartesian coordinate system is established as shown in Figure 6-2. Connecting the mass to the origin of the local coordinate system (CSYS) via a hinged, rigid rod of length AB=L which is assumed to be massless for the purpose of this analysis, imposes a kinematic constraint between the DoFs u and v. The lumped parameter model is described by the coordinates of the mass (m) at a generic position $\mathrm{B}(x,\ y)=(x_0+u,\ y_0-v)$, where x_0, y_0 are the initial coordinates of the mass. The initial angle between the horizontal axis and the link is denoted by $\varphi = arctan(x_0 / y_0)$, while θ denotes the rotation of the rod at the generic position B of the moving mass. $k_{x,}\, k_y$ are the springs stiffnesses, $c_x,\ c_y$ the damping coefficient on the horizontal and vertical directions respectively, and F the force exciting the mass in the x direction.

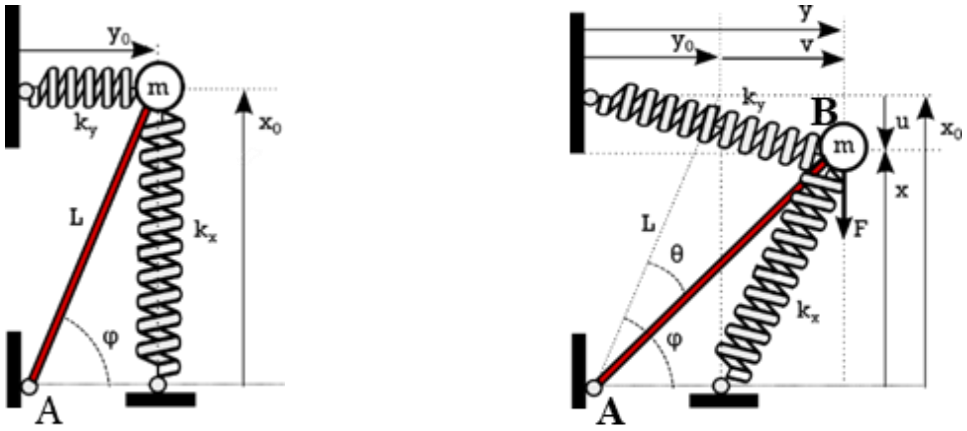

(a) *(b)*

Figure 6-2: Kinematic model of the Dynamic directional amplification (DDA) mechanism, where the motion of v mass m is kinematically constrained to the motion u, (a) initial mass position (b) mass position at deformed state.

Based on the geometric relationship of the DDA mechanism, the following equation is obtained:

$$x_0 = \sqrt{L^2 - y_0^{\,2}} \tag{6-1}$$

When the point B moves along x direction with displacement u, a coupled motion v along the y direction will occur. Hence:

$$x_0^{\,2} + y_o^{\,2} = (x_0 - u)^2 + (y_0 + v)^2 \tag{6-2}$$

To obtain the displacement of point B, Eq. (6-2) can be simplified and rewritten as:

$$u^2 - 2x_0 u + 2y_0 v + v^2 = 0 \tag{6-3}$$

The solution of which is:

$$v = -y_0 \pm \sqrt{-u^2 + 2ux_0 + y_0^{\,2}} \tag{6-4}$$

It is observed from Eq. (6-4) that the relationship between the horizontal and vertical displacement (u, v) is nonlinear. For small displacements of the mass m the relationship between u and v (at $\mathrm{u}=0$) can be expressed after linearization as:

$$\frac{u}{v} \cong \frac{dx_0}{dy_0} = \partial\left(\sqrt{L^2 - y_0^{\,2}}\right) = -\frac{y_0}{\sqrt{L^2 - y_0^{\,2}}} = -\frac{y_0}{x_0} = -\frac{1}{\tan\varphi} \tag{6-5}$$

And for $\rho = \tan\varphi$ Eq. (6-5) becomes:

$$v = u\rho \tag{6-6}$$

The negative sign indicates that a decrease of u results in an increase of v.

6.3.1 Dynamic modelling of the DDA mechanism

Let T be the kinetic energy of m as follows:

$$T = \frac{1}{2} m(\dot{u}^2 + \dot{v}^2) \tag{6-7}$$

Substituting Eq. (6-5) into Eq. (6-7) , the kinetic energy can be rewritten as:

$$T = \frac{1}{2} m\dot{u}^2 \left(1 + \tan\varphi\right)^2 \tag{6-8}$$

Similarly, the potential energy (U) is written as:

$$U = \frac{1}{2} k_x (L_x - L_{x0})^2 + \frac{1}{2} k_y (L_y - L_{y0})^2 \tag{6-9}$$

Where

$$L_x = \sqrt{x^2 + v^2} = \sqrt{(x_0 - u)^2 + v^2} \tag{6-10}$$

$$L_y = \sqrt{u^2 + y^2} = \sqrt{(y_0 + v)^2 + u^2} \tag{6-11}$$

Substituting Eqs. (6-10)-(6-11) into Eq. (6-9), and assuming that $L_{x0}=x_0$ and $L_{yo}=y_0$ the potential energy (U) is the following:

$$U = \frac{1}{2} k_x (\sqrt{(x_0 - u)^2 + (u\tan\varphi)^2} - x_0)^2 + \frac{1}{2} k_y (\sqrt{(y_0 + v)^2 + u^2} - y_0)^2 \tag{6-12}$$

The Rayleigh dissipation function of the mechanism is given as:

$$D = \frac{1}{2} c_x \left(\sqrt{(x_0 - u)^2 + (u\tan\varphi)^2} - x_0\right)^2 + \frac{1}{2} c_y \left(\sqrt{(y_0 + v)^2 + u^2} - y_0\right)^2 \tag{6-13}$$

By employing the Lagrangian equation,

$$\frac{d}{dt}\left[\frac{\partial(T - U)}{\partial \dot{q}_i}\right] - \frac{\partial(T - U)}{\partial q_i} + \frac{\partial D}{\partial \dot{q}_i} = Q_i \tag{6-14}$$

the governing equation of the DDA mechanism in the direction of motion is given as follows:

$$M\ddot{u} + C\dot{u} + Ku = F \tag{6-15}$$

where, $M = (1 + tan^2(\varphi))m$, $C = c_x + c_y tan^2(\varphi)$ and $K = k_x + k_y tan^2(\varphi)$.

and the natural frequency of the mechanism is given as:

$$f_{n,DDA} = \frac{1}{2\pi}\sqrt{\frac{(1+\rho^2)m}{k_x + k_y\rho^2}} \tag{6-16}$$

It is noted that the angle φ will affect the natural frequency of the DDA mechanism, while for k_x=k_y the natural frequency of the mechanism is the same with an equivalent SDoF system.

The damping coefficient (C) of the modified system can be calculated as a function of the damping ratio $\zeta_{n,}$ and can be written as:

$$C = 4\pi m f_{n,DDA}(\zeta_x + \zeta_y\rho^2) \tag{6-17}$$

6.3.2 Transfer functions of the DDA mechanism

The system can be characterized as an oscillator with one apparent DoF, taking into account Eq. (6-15). With the application of a Laplace transform the transfer function of the dynamic magnification factor can be expressed as:

$$\tilde{H}_{Ux} = \frac{\tilde{u}}{\tilde{u}_{ST}} = \frac{k_x + k_y\rho^2}{-m\left(1+\rho^2\right)\omega^2 + \left(c_x + c_y\rho^2\right)j\omega + \left(k_x + k_y\rho^2\right)} \tag{6-18}$$

Another common way to express the amplitude of the response of the system to the amplitude of the excitation is in terms of acceleration to force. Namely, integrating this transfer function twice results in the following:

$$\tilde{T}_{AFx} = \frac{\tilde{\ddot{u}}}{\tilde{F}} = \frac{-\omega^2}{-m\left(1+\rho^2\right)\omega^2 + \left(c_x + c_y\rho^2\right)j\omega + \left(k_x + k_y\rho^2\right)} \tag{6-19}$$

In the case of base excitation of the system $a_B(t) = \tilde{A}_B e^{i\Omega t}$ the transfer functions of the system are:

$$\tilde{T}_{UBx} = \frac{\tilde{u}}{A_B} = \frac{m\left(1+\rho^2\right)}{-m\left(1+\rho^2\right)\omega^2 + \left(c_x + c_y\rho^2\right)j\omega + \left(k_x + k_y\rho^2\right)} \tag{6-20}$$

and

$$\tilde{T}_{ABx} = \frac{\tilde{\ddot{u}}}{A_B} = 1 - \omega^2\tilde{H}_{UBx} = -\frac{\left(c_x + c_y\rho^2\right)j\omega + \left(k_x + k_y\rho^2\right)}{-m\left(1+\rho^2\right)\omega^2 + \left(c_x + c_y\rho^2\right)j\omega + \left(k_x + k_y\rho^2\right)} \tag{6-21}$$

The transfer functions on the y direction can be easily calculated based on Eq. (6-6) as:

$$\begin{bmatrix} \tilde{H}_{Uy} \\ \tilde{T}_{AFy} \\ \tilde{T}_{UBy} \\ \tilde{T}_{ABy} \end{bmatrix} = \rho \begin{bmatrix} \tilde{H}_{Ux} \\ \tilde{T}_{AFx} \\ \tilde{H}_{UBx} \\ \tilde{H}_{ABx} \end{bmatrix} \tag{6-22}$$

6.3.3 Parametric Investigation of the DDA mechanism properties

Prior to the main analysis it is worth examining the mass amplification $1+\tan^2\varphi$ as a function of the amplifier's angle (φ). Figure 6-3 displays that for small angles i.e., less than 45°, the mass is amplified less than two (2) times, while for further increase of the angle, the amplification increases exponentially; for φ=75° the mass is amplified 15 times.

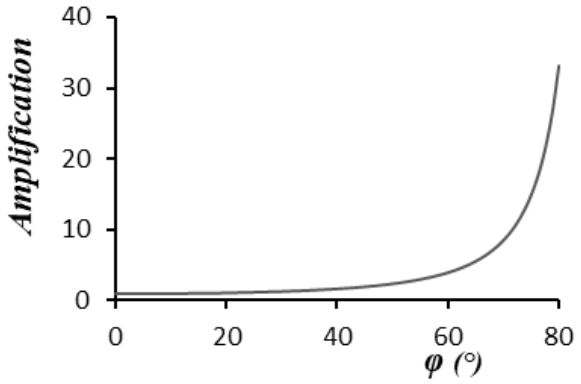

Figure 6-3: Mass amplification as a function of the DDA angle φ(°).

Subsequently, numerical simulations were performed to study the response of the DDA mechanism based on the magnification factor (H_u) and accelerance (T_{AF}). The analysis parameters are the following: mass equal to m=0.89kg, spring stiffness k_x=500N/m and damping ratio ζ_x =0.2. These are selected in accordance with the parameters adopted in the experiment, as described in section 0 of this chapter.

Figure 6-4 (a) and (b) depict the surface plots of accelerance (T_{AF}) and magnification factor (H_u), as a function of the spring ratio (k_y/k_x), assuming that the amplification angle is equal to φ=75°. As expected, when k_y is absent, resonance shifts to lower frequencies while when k_y is utilized, the system becomes stiffer and the resonant frequency increases parabolically, as k_y is a function of $\tan^2\varphi$. In Figure 6-4 (c) and (d) the transfer functions are plotted assuming the case that the vertical and horizontal springs have equal stiffness (k_y/k_x=1). This allows an illustration of the effect of the amplifier's angle (φ) compared to the original SDoF oscillator. It is observed that for both transfer

functions, the resonant frequency is not affected by the amplifier's angle and remains the same with the SDoF system.

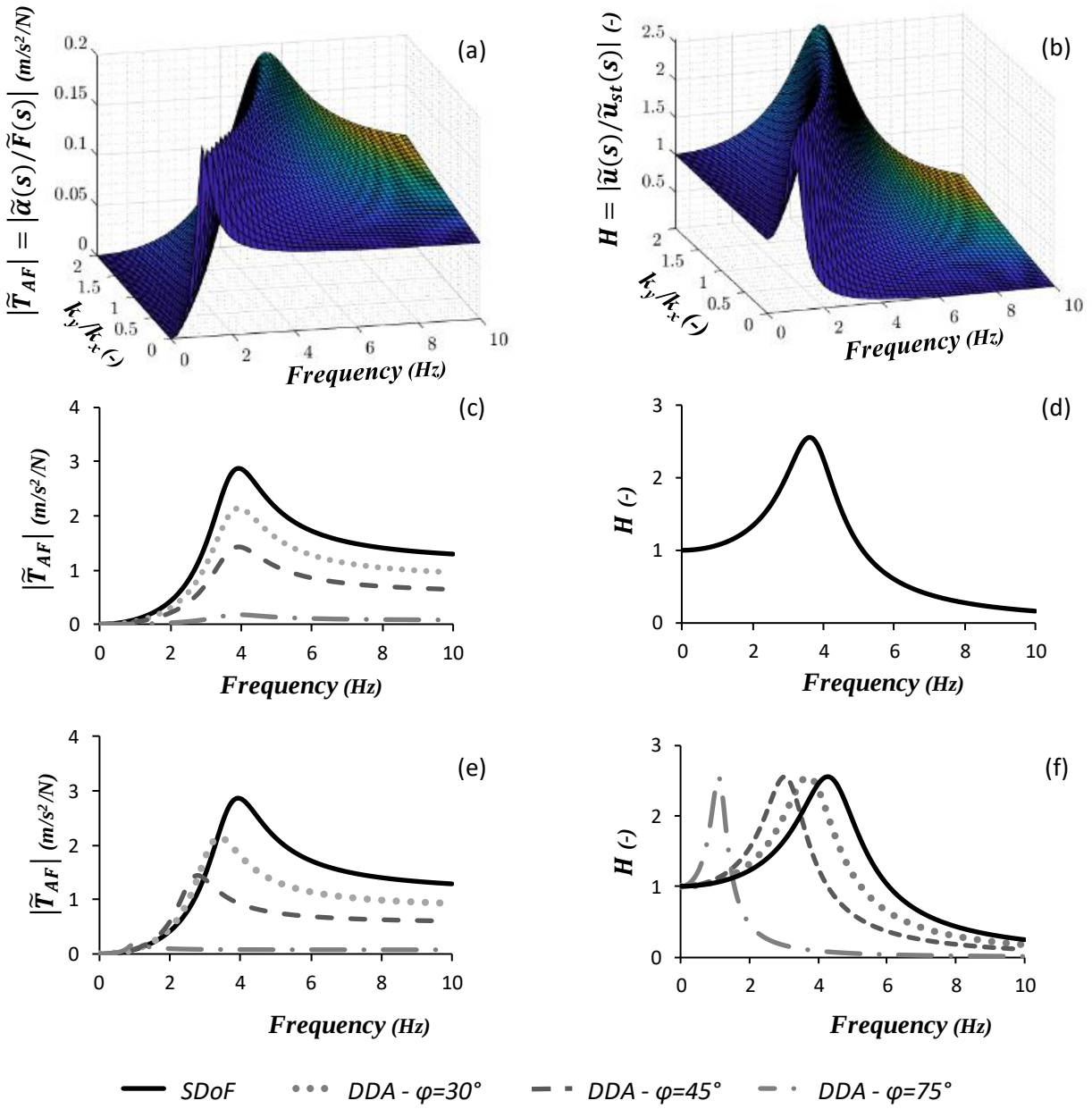

Figure 6-4: Surface plot describing (a) the Frequency response of accelerance (FRF) as a function of the spring's stiffness ratio k_y/k_x=0-2, φ=75° and (b) the magnification factor H as a function of the spring's stiffness ratio k_y/k_x=0-2, φ=75°. (c) Frequency response of accelerance (FRF) and (d) magnification factor H for stiffness ratio k_y/k_x=1 and φ=30, 45, 75° compared to the SDoF oscillator. (e) Frequency response of accelerance (FRF) and (f) magnification factor H for stiffness ratio k_y/k_x=0 and φ=30, 45, 75° compared to the SDoF oscillator.

However, as the angle (φ) increases, accelerations are drastically reduced, while displacements follow the same pattern with the SDoF system regardless of the amplifier's angle (φ). In Figure 6-4 (e) and (d) the spring stiffness k_y is set to zero (k_y=0), and consequently, as described in Eq. (6-16), the resonant frequency of the DDA is determined by the mass amplification ($1+\rho^2$). Ultimately, the mechanism functions as a classic vibration controller; the increase of the amplifier's angle leads to a lower resonant frequency which provides isolation both in terms of acceleration and displacements.

Figure 6-5 illustrates the collateral effect of the out of plane movement of the mechanism. Once again, the transfer functions are presented for two different spring ratios; k_y/k_x=1 in Figure 6-5 (a) and (b), and k_y/k_x=0 in Figure 6-5 (c) and (d). As described in Eq. (6-22), for large amplifier's angle (such as φ=75°) the out of plane accelerations and displacements are larger than those in the direction of interest.

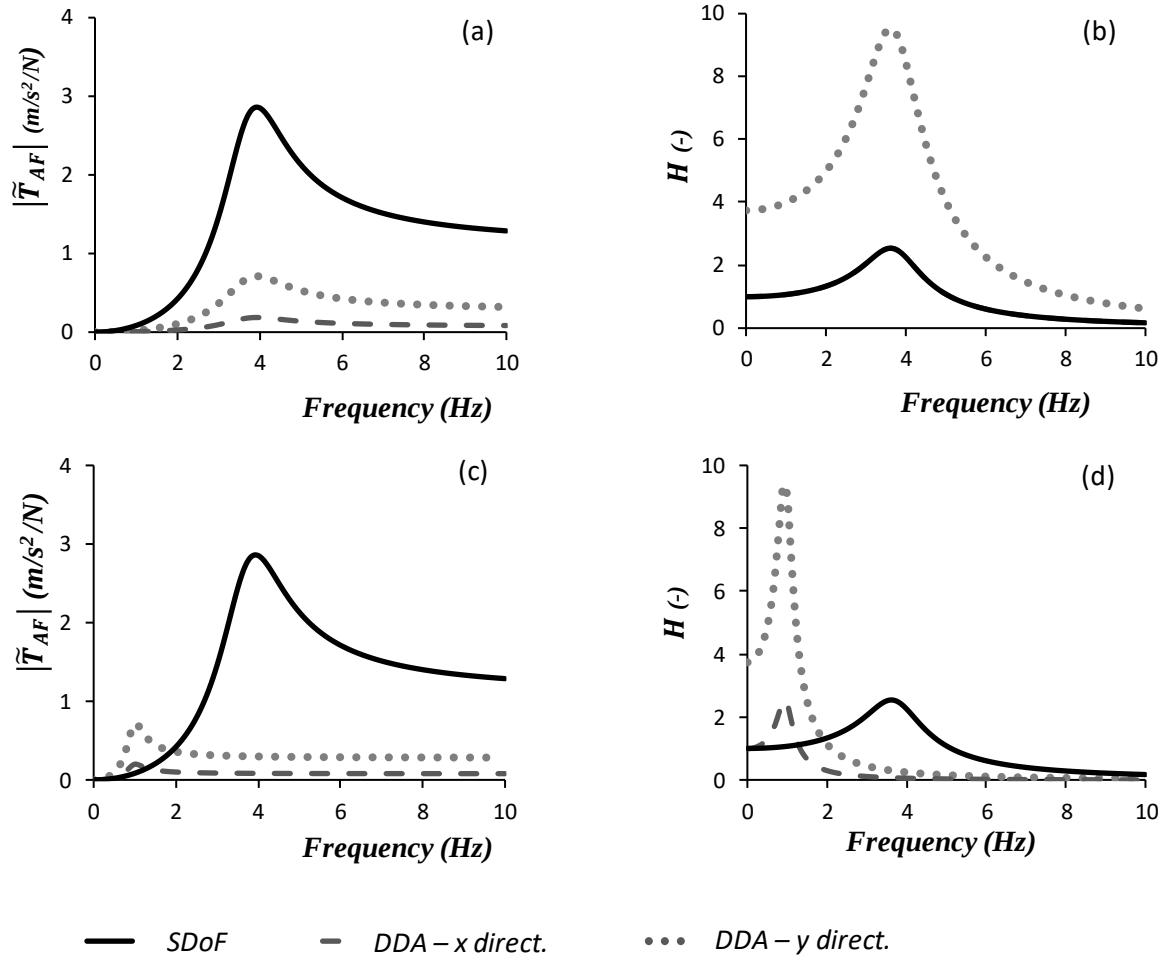

Figure 6-5: (a) Frequency response of accelerance (FRF) and (b) magnification factor H for amplifiers angle φ=75° and k_y/k_x=1. (c) Frequency response of accelerance (FRF) and (d) magnification factor H for amplifiers angle φ=75° and k_y/k_x=0.

Nonetheless, this should not be considered as a discouraging aspect of the DDA, but rather as an essential attribute that should be carefully examined based on the application of interest and other case dependent restrictions. Specifically, regardless of the spring ratio, the out of plane accelerations are always reduced compared to the ones of the SDoF oscillator, while at the same time the maximum displacements may present an increase, especially for the case of large amplifier's angles.

Obviously, the plot of the SDoF transfer functions along with the out of plane DDA transfer functions should not be considered for direct comparison, as the results refer to different movements, yet this graphical representation allows a better understanding of the overall performance of the mechanism.

6.4 Experimental setup & testing

The performance of the developed Dynamic Directional Amplification mechanism is verified, and the developed theoretical models are validated via experimental testing. The configured experimental setup is presented in Figure 6-6. For the experimental measurements, a PCB 356A16 tri-axial accelerometer with 10.2 $mV/m/s^2$ sensitivity is attached to the seismic mass and a PCB 333B30 single-axis accelerometer with 10 $mV/m/s2$ sensitivity is attached on the shaking table to measure the input motion to the oscillator. The accelerometers and load cells are connected to the computer through two PCB 480B21 amplifiers and run through an NI CB-68LP terminal connector block to the NI PCI-6052E PCI card. The recording of the measurements is done via the NI LabView 2013® software, while the post-processing is carried out using in-house developed scripts on the MATLAB R2018a® software.

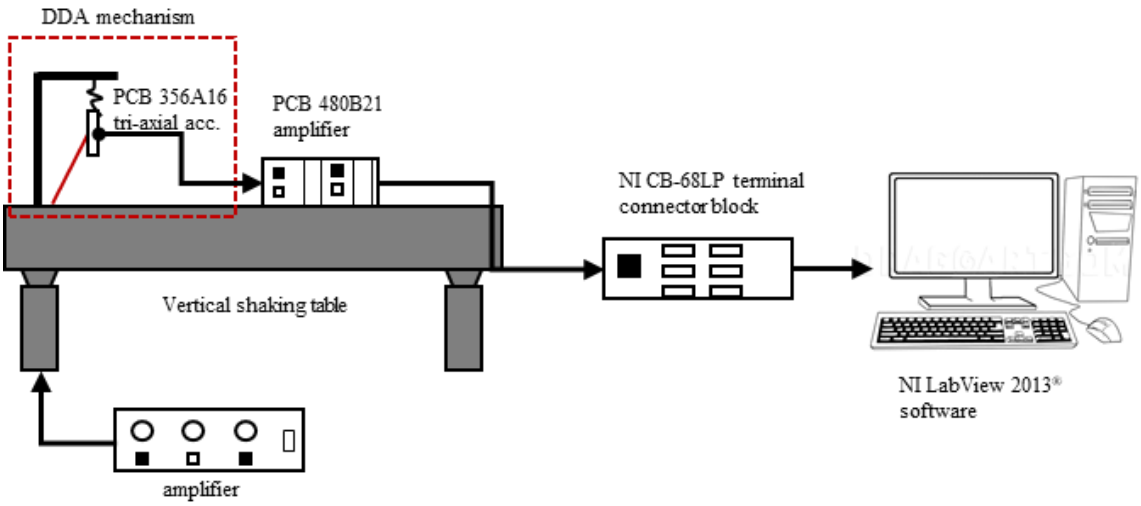

Figure 6-6: Schematic diagram of the experimental setup for the analysis and validation of the dynamic behavior DDA mechanism.

Figure 6-7 shows the device with the oscillating mass at the position of equilibrium. The amplifier's hinges are constructed using bearings and a shaft rod axis. The rigid links are welded to the axis and bolted via an L-shaped section with the mass. Regarding the vertical stiffness elements, two springs are hanged from a stable frame and are attached to the mass through overhangs.

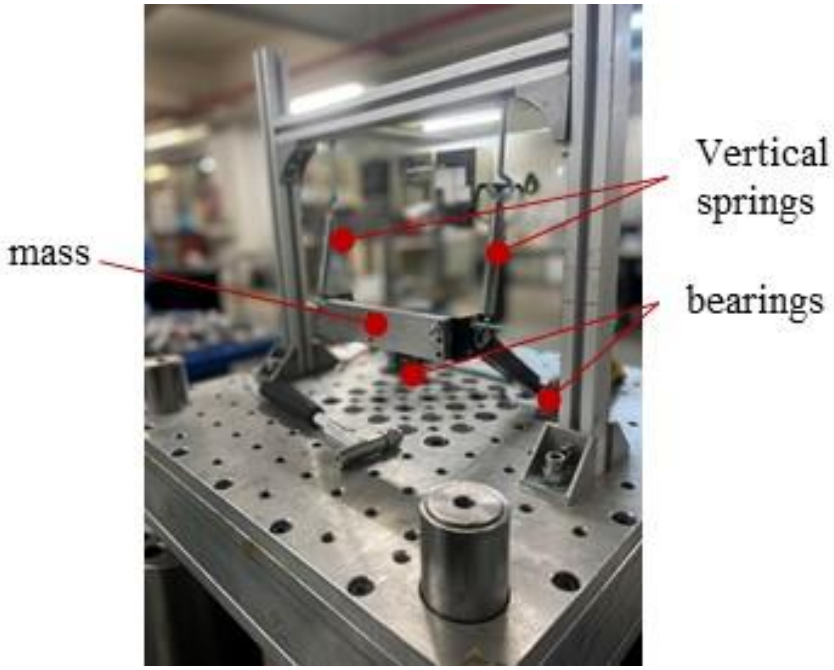

Figure 6-7: Photograph of the DDA mechanism.

6.4.1 Experimental results and discussions

The experimental specimen is fixed on top of a vertical shaking table and a series of sweep tests are conducted by exciting the base of the mechanism. The response of the mass is subsequently evaluated by recording accelerations in both x and y directions via the aforementioned sensors. The adopted oscillating mass is equal to m=0.89 kg and the stiffness of each one of the two springs is equal to k_x=250 N/m. No extra damping elements have been added; however, a small amount of structural damping is expected to take place due to the material properties and the friction developed within the connections of the device as the mechanism oscillates. Three different amplifier's angles are tested, namely φ=30°, 40°, 60° as well as an additional test without the rigid link to model an equivalent SDoF oscillator. The displacement amplitude and the frequency of the excitation are controlled by the built-in control system of the vibration table. For the purposes of the present test, sinusoidal excitations and frequencies of 2–10 Hz are in turn generated by the shaking table. Results are measured in voltage within the time domain and are subsequently converted to acceleration based on the sensitivity of each sensor. Fast Fourier transform (FFT) is deployed to calculate the spectrum at the seismic base (input) and mass (output) of the device.

Figure 6-8 depicts the Frequency response of accelerance $\left|\tilde{T}_{AB}\right| = \left|\tilde{a}_{(s)} / \tilde{a}_{(g)}\right|$, where $a_{(s)}$ is the measured acceleration of the mass and $a_{(g)}$ the acceleration of the shaking table (a) at the x- direction and (b) at the y-direction, according to Figure 6-2. The continuous lines present the root mean square of amplitudes values of the experimental data while the markers indicate the measured values for each one of the three repetitions that were carried out for each amplifiers angle. The experimental results validate the initial theoretical predictions.

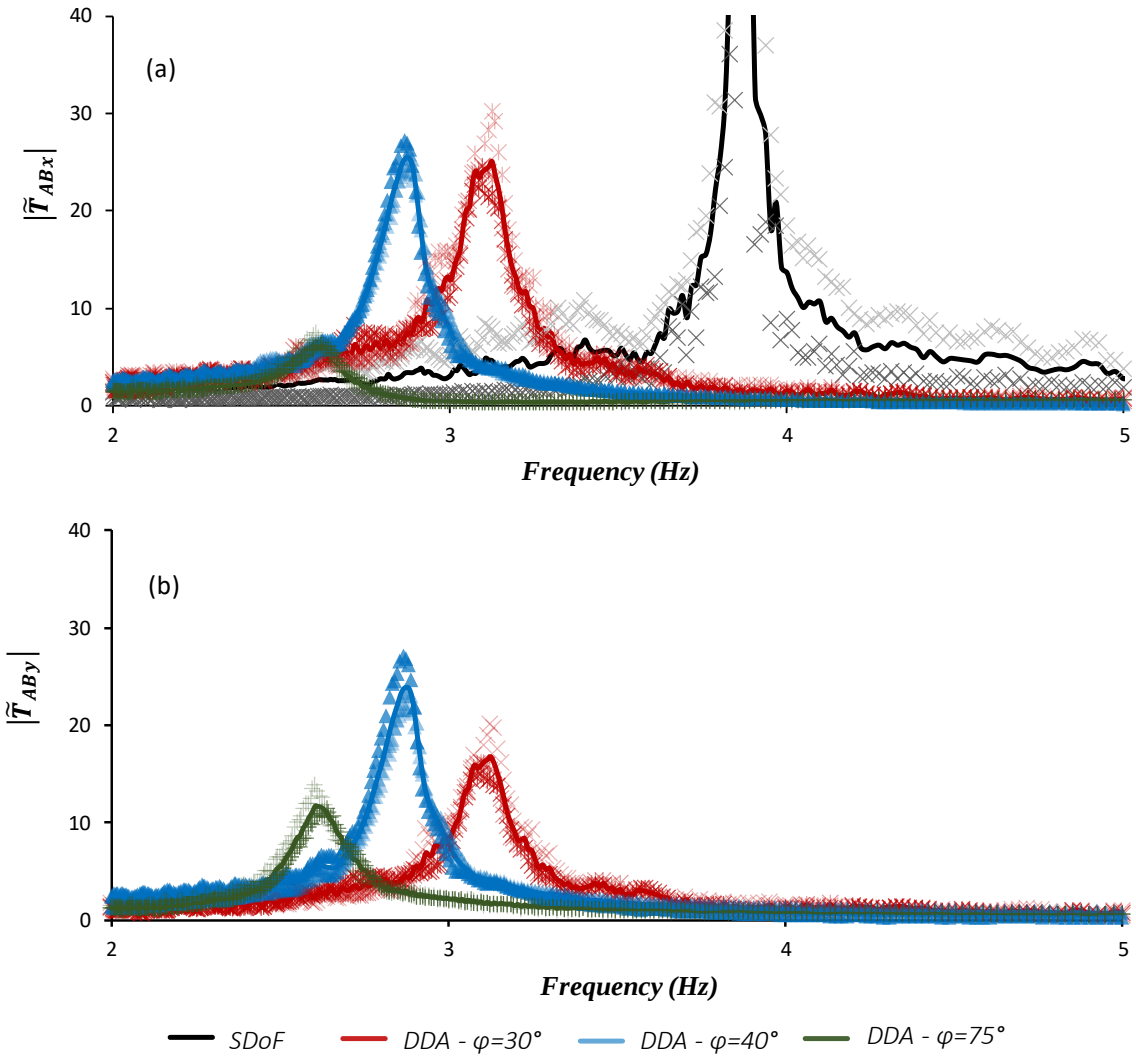

Figure 6-8: Experimentally measured Transfer functions (T_{AB}) of the oscillating mass in (a) x direction (b) y direction acceleration to base acceleration of the DDA. The continuous lines show the averaged experimental results and the markers the measured data of each test.

The comparison in Figure 6-8 (a) with the corresponding Transfer function of the system when the mass is mounted only on the spring elements (SDoF black line) demonstrates the effectiveness of the device. The fundamental resonance peak is reduced, specifically at 3.1 Hz which corresponds to a

19.7% reduction for φ=30° and 25.6 % for φ=40°. By all means, for larger angles the reduction is much greater. Additionally, the extreme peak observed at the SDoF response due to resonance has been diminished and is reduced as the angle (φ°) of the DDA increases.

In Figure 6-9 the experimentally measured Transfer functions for (a) φ=30° and (b) φ=40° are provided and compared with the theoretically evaluated response.

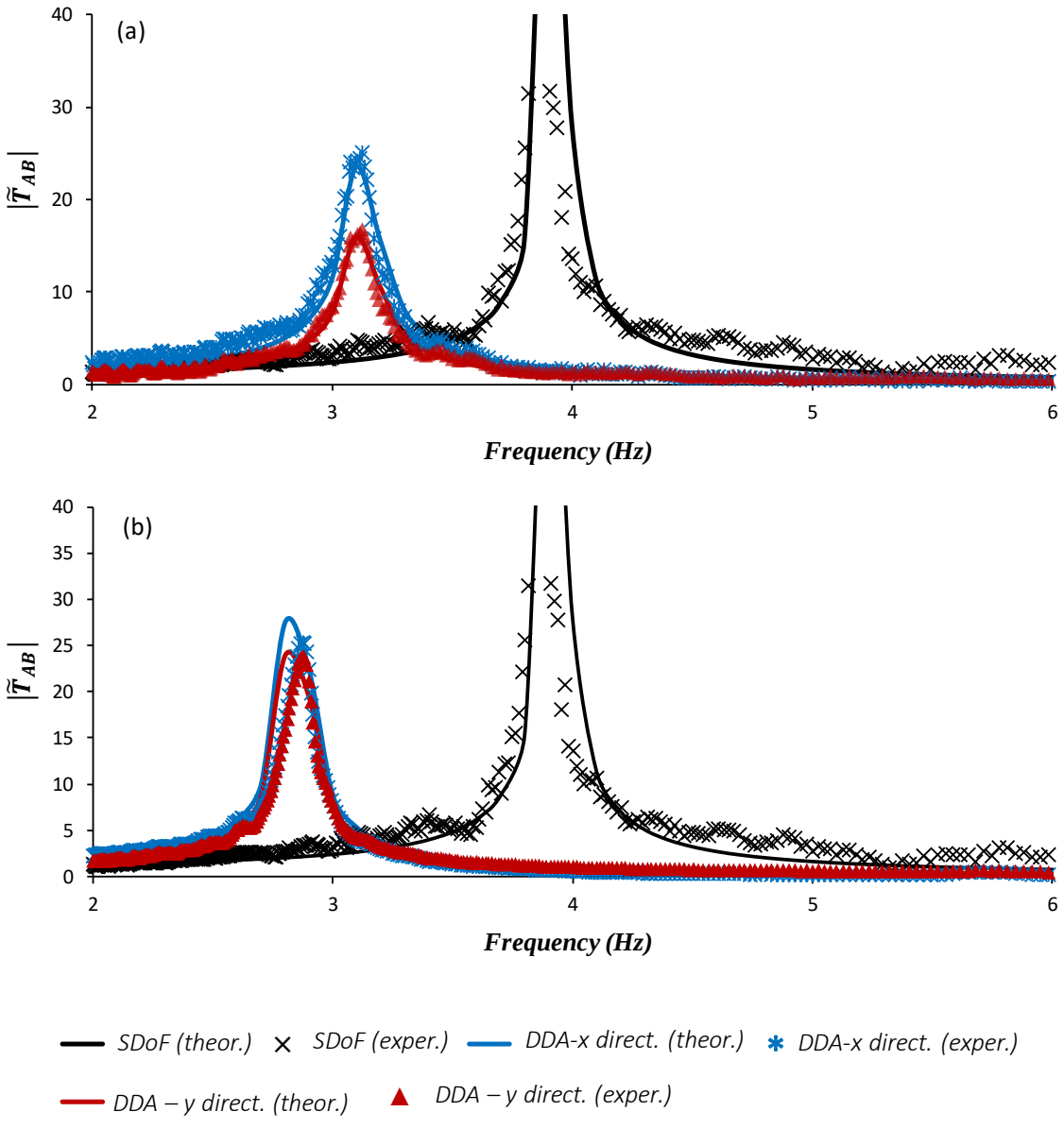

Figure 6-9: Comparison between averaged experimental results (markers) and theoretically calculated (continuous lines) Transfer functions (T_{AB}) for (a) φ=30° (b) φ=40°.

It is clearly shown that the acceleration transmissibility measured from the experimental process and the one calculated from the analytical solution of the DDA are in overall very good agreement for the prescribed (φ) angles. Specifically, for φ=30° the theoretical and experimental response of both the x

and y accelerations are almost identical. Hereafter, it is concluded that the analytical equations can be safely used to describe the performance of such an amplification mechanism.

6.5 Numerical example in acoustic panels

Based on the above observations, we can use the proposed amplification mechanism in many applications. Indicatively, the mechanism can be applied to metamaterials with seismic and acoustic properties (Kalderon et al., 2022, 2021), to machine bases, anti-vibration false floors, acoustic panels, etc. Herein, the applicability of the mechanism to acoustic doors is examined in order to increase their low-frequency acoustic absorption capabilities.

Figure 6-10 (a) shows an ideal implementation of the arrangement. The mechanism is placed inside the door and is attached to one of the two door leaves. The mass of the mechanism comprises a third, rigid partition i.e., a steel sheet, the dimensions and characteristics of which are presented in Table 6-1 while the characteristics of the DDA are presented in Table 6-2. It should be noted that the dimensions of the panel, the stiffnesses of the springs etc., have been chosen in accordance with products that are commercially available. Finally, the elastic supports are assumed to function only in the direction perpendicular to the panel.

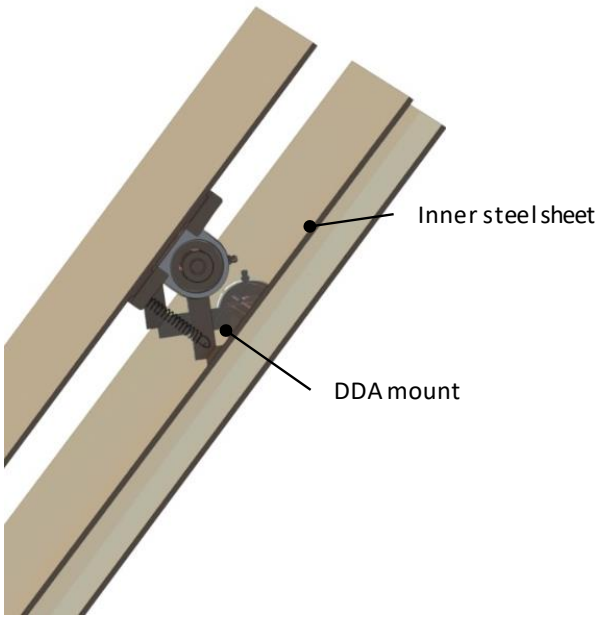

Figure 6-10: Conceptual depiction of the proposed DDA system of an acoustic door .

Table 6-1: Steel sheet properties.

L_x [m]	L_y [m]	t [mm]	ρ_{steel} [kg/m^3]	m [kg]
0.9	2.1	3	7850	44.5

Table 6-2: DDA parameters.

Spring eigenfrequency - f_{0x} [Hz]	φ(°)
50	60

Figure 6-11 shows the STL diagrams for the two cases of panel supports using Eqs. (2-7) - (2-8). For this specific analysis only the soundproofing properties of the additional steel sheet – mechanism system are considered. In addition, the STL modelling method is crude in the sense that the partition rigidity is not taken into account. This also means that the assumed seismic mass is essentially the apparent mass of the fundamental mode of the partition. However, a common practice towards increasing partitions stiffness and enhancing the validity of this approximation is the addition of stiffeners to the panels.

It is observed that the DDA mounting improved the low-frequency sound absorption of the door by shifting the STL curve upwards, while reducing the fundamental frequency of the system. Naturally, further increasing the amplifier angle (φ) would further increase the sound reduction index.

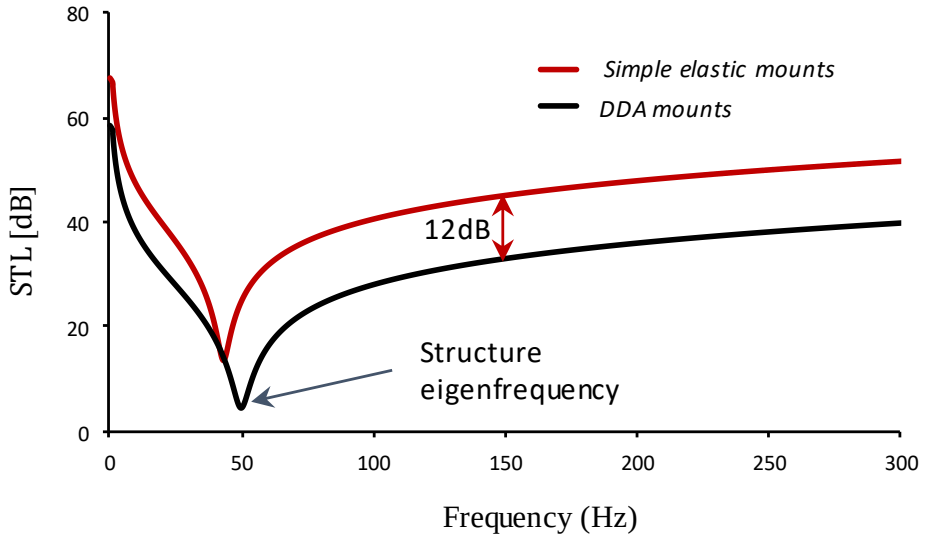

Figure 6-11: STL comparison between the enhanced acoustic door with a DDA mechanism and the one with a simple elastic support system.

6.6 Concluding Remarks

In conclusion, this study demonstrates a novel Dynamic Directional Amplification mechanism, namely the DDA, that aims to increase the inertia and enhance the dynamic properties of vibrating structures. The major innovation of the application lies in the simple geometry of the proposed system; the vibrating mass is fixed to a rigid link that increases inertia towards the desired direction of motion by coupling the kinematic DoFs of the resonating mass and forcing the oscillator to move through a prescribed circumferential path.

An analytical framework is introduced, providing the theory and mathematical formulation of the DDA mechanism. Transfer functions are derived, and a parametric analysis is subsequently undertaken to evaluate the effect of stiffness and amplifier's angle to the dynamic response of the oscillating mass. As a following step, the performance of the developed mechanism is verified, and the developed theoretical models are validated via shaking table experimental testing. Results indicate an overall agreement between the measured and analytically derived calculations, hence placing the concept as a compelling alternative to inertial amplification devices.

The key novelty of the DDA lies in its simple geometry and easy-to-apply structure. To this end, the proposed framework is studied in the following chapters as a means to improve the filtering properties of locally resonant and phononic metamaterials.

7 DYNAMIC DIRECTIONAL AMPLIFICATION (DDA) IN PHONONIC METAMATERIALS

7.1 Background

Phononic structures with unit-cells exhibiting Bragg scattering and local resonance present unique wave propagation properties at wavelengths well below the regime corresponding to bandgap generation based on spatial periodicity. However, both mechanisms show certain constraints in designing systems with wide bandgaps in the low-frequency range.

In this Chapter, a simple dynamic directional amplification (DDA) mechanism is proposed as the base of the phononic lattice to face the main practical challenges encountered in such cases, including heavy oscillating masses. This amplifier is designed to present the same mass and use the same damping element as a reference two-dimensional (2D) phononic metamaterial. Thus, no increase in the structure mass or the viscous damping is needed. The proposed DDA can be realized by imposing kinematic constraints to the structure's degrees of freedom (DoF), improving inertia and damping on the desired direction of motion. Analysis of the 2D lattice via Bloch's theory is performed, and the corresponding dispersion relations are derived. The numerical results of an indicative case study show significant improvements and advantages over a conventional phononic structure, such as broader bandgaps and increased damping ratio. Finally, a conceptual design indicates the usage of the concept in potential applications, such as mechanical filters, sound and vibration isolators, and acoustic waveguides.

7.2 Bloch analysis

The periodic structures considered in this chapter of the dissertation, comprise a finite number of identical unit-cells. These unit-cells are the repetitive units that are used to describe the microstructure. If the unit-cells are inhomogeneous, i.e., made up of different masses and springs, the corresponding structure is periodic, whereas, with a homogeneous unit-cell, the structure is also homogeneous. This structure is named phononic and the general properties of such a structure are described in Appendix D.1.

7.2.1 Bloch's Theorem

Bloch's theorem (1929) allows considering a single unit-cell for studying wave propagation in the entire lattice structure. The displacement of a DoF at a specific position of the lattice may be expressed in a complex notation as:

$$u_{(p,q)} = \hat{U}_{p,q} e^{\lambda t} = \hat{U} e^{j(p\kappa_x a_x + q\kappa_y a_y)} = \tilde{U} e^{j(p\mathrm{q}_x + q\mathrm{q}_y)} \tag{7-1}$$

Where $\tilde{U}$ is the wave amplitude, κ_x, κ_y the wavenumbers along the horizontal and vertical directions. In the time part of the solution, the parameter λ_S is defined as $\lambda_S = \pm j\omega_S(\kappa)$, or in the case where the attenuation between the unit-cells is considered $\lambda_S = -\zeta_S(\kappa)\omega_S(\kappa) \pm j\omega_{d_S}(\kappa)$, where λ represents the branch number, $\zeta_S(\kappa)$ is the wavenumber-dependent damping ratio and $\omega_S(\kappa)$ is the wavenumber-dependent frequency (dispersion relation). As a result, the imaginary part is the frequency of the damped wave propagation, $\omega_{dS}(\kappa) = \mathrm{Im}[\lambda_S(\kappa)]$, and the damping ratio is calculated as:

$$\zeta_S(\kappa) = -\frac{\mathrm{Re}[\lambda_S(\kappa)]}{|\lambda_S(\kappa)|} \tag{7-2}$$

7.2.1.1 Simple 2D Monoatomic Lattice

The establishment of the theoretical framework begins considering the simple damped 2D monoatomic lattice of Figure 7-1, where m is the mass, k_x, k_y the springs stiffness and c_x, c_y the viscous damping elements connecting the masses. In general, if the model's material is linearly elastic and geometric nonlinearity is disregarded, the deformation and interaction between the horizontal and vertical springs are assumed to have a negligible effect on the stiffness of the springs. Therefore, the deformation of one spring does not affect the stiffness of either spring, hence, the stiffness

parameters of springs can be deduced separately and are considered independent of the deformation level.

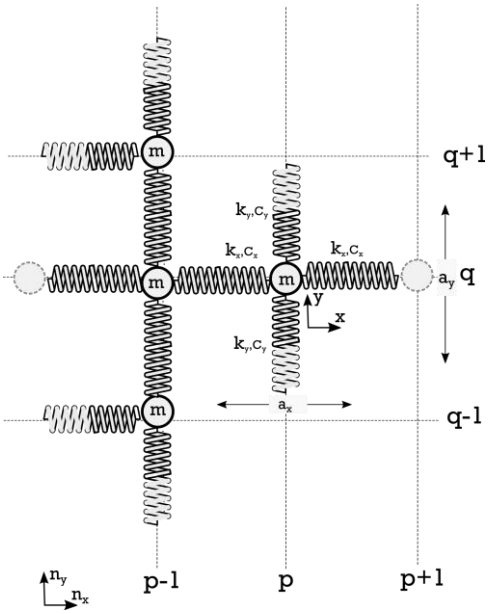

Figure 7-1: 2D monoatomic lattice.

The set of equations that describe the harmonic motion of a typical unit-cell at location $p,\ q$ can be expressed as:

$$m\ddot{u}_{p,q} + k_x(u_{p,q} - u_{p-1,q}) + c_x\left(\dot{u}_{p,q} - \dot{u}_{p+1,q}\right) + k_x(u_{p,q} - u_{p+1,q}) = 0 \tag{7-3.a}$$

$$m\ddot{v}_{p,q} + k_y(v_{p,q} - v_{p,q-1}) + c_y\left(\dot{v}_{p,q} - \dot{v}_{p,q+1}\right) + k_y(v_{p,q} - v_{p,q+1}) = 0 \tag{7-3.b}$$

According to Bloch's theorem, the following wave propagation conditions are imposed to relate the displacement of the mass at location $p,\ q$ with the displacements of the neighbouring masses:

$$u_{p,q} = \tilde{U}_{p,q} e^{jk_x p a_x + jk_y q a_y} e^{\lambda t} = \tilde{U}_{p,q} e^{jp\mathrm{q}_x + jq\mathrm{q}_y} e^{\lambda t} \tag{7-4.a}$$

$$u_{p-1,q} = \tilde{U}_{p,q} e^{jk_x (p-1) a_x + jk_y q a_y} e^{\lambda t} = \tilde{U}_{p,q} e^{j(p-1)\mathrm{q}_x + jq\mathrm{q}_y} e^{\lambda t} = u_{p,q} e^{-j\mathrm{q}_x} \tag{7-4.b}$$

$$u_{p+1,q} = \tilde{U}_{p,q} e^{jk_x (p+1) a_x + jk_y q a_y} e^{\lambda t} = \tilde{U}_{p,q} e^{j(p+1)\mathrm{q}_x + jq\mathrm{q}_y} e^{\lambda t} = u_{p,q} e^{-j\mathrm{q}_x} \tag{7-4.c}$$

$$v_{p,q} = \tilde{V}_{p,q} e^{jk_x p a_x + jk_y q a_y} e^{\lambda t} = \tilde{V}_{p,q} e^{jp\mathrm{q}_x + jq\mathrm{q}_y} e^{\lambda t} \tag{7-4.d}$$

$$v_{p,q-1} = \tilde{V}_{p,q} e^{jk_x p a_x + jk_y (q-1) a_y} e^{\lambda t} = \tilde{V}_{p,q} e^{jp\mathrm{q}_x + j(q-1)\mathrm{q}_y} e^{st} = v_{p,q} e^{-j\mathrm{q}_x} \tag{7-4.e}$$

$$v_{p,q+1} = \tilde{V}_{p,q} e^{jk_x p a_x + jk_y (q+1) a_y} e^{\lambda t} = \tilde{V}_{p,q} e^{jp\mathrm{q}_x + j(q+1)\mathrm{q}_y} e^{\lambda t} = v_{p,q} e^{j\mathrm{q}_x} \tag{7-4.f}$$

where $\tilde{U}_{p,q}$, $\tilde{V}_{p,q}$ are the wave amplitudes at nodes p, q. Then, α_x, α_y are the unit-cell dimensions and q_x, q_y are the normalized wavenumbers in x, y directions.

Substitution of Eqs. (7-4) and their derivatives into Eqs. (7-3) and utilization of the trigonometric transformation $\beta = 2 - e^{jq} + e^{-iq}) = 2(1 - \cos q)$, leads to the following compact matrix notation:

where

$$(-\lambda^2 \boldsymbol{M} + \lambda \boldsymbol{C} + \boldsymbol{K})\boldsymbol{u} = 0 \tag{7-5}$$

$$\boldsymbol{M} = \begin{bmatrix} m & 0 \\ 0 & m \end{bmatrix} \tag{7-6.a}$$

$$\boldsymbol{K} = \begin{bmatrix} 2k_x(1-\cos(q_x)) & 0 \\ 0 & 2k_y(1-\cos(q_y)) \end{bmatrix} \tag{7-6.b}$$

$$\boldsymbol{u} = \begin{bmatrix} u_{p,q} \\ v_{p,q} \end{bmatrix} \tag{7-6.c}$$

Assuming for simplicity that $k_x = k_y = k_0 = m\omega_0^2$ and that the system is undamped ($\zeta_x = \zeta_y = 0$), allows rewriting Eq. (7-5) in the following non-dimensional form (Hussein et al., 2014).

The dispersion relation describes a surface in terms of the components of the propagation vector. Figure 7-2 shows a colour map of the dispersion surface, where the third dimension is frequency ω. The plot clearly illustrates the periodicity of the surface in the wavenumber domain and highlights the "first Brillouin zone" (2013) Γ-M-X-Γ and ΓX-XM. The fundamental period is defined by $q_x, q_y \in [-\pi, +\pi]$:

$$\omega^2 = 2\omega_0^2(2 - \cos q_x - \cos q_y) \tag{7-7}$$

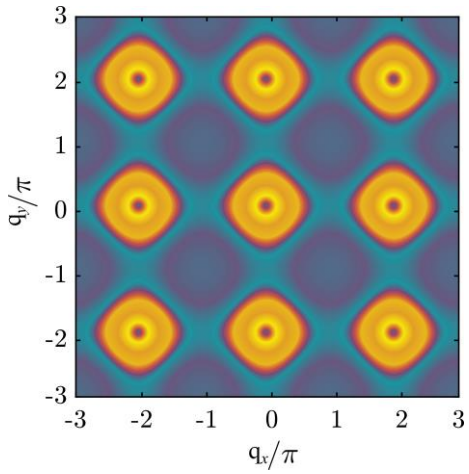

Figure 7-2: Dispersion surface of the 2D spring–mass lattice with spring stiffness, k_x, k_y.

7.2.2 2D monoatomic lattice with Dynamic Directional Amplifiers (DDA)

Once the equation of motion of the DDA is formulated, the properties of directionality in a lattice comprising of masses connected to DDA mechanisms, as in Figure 7-3, can be investigated.

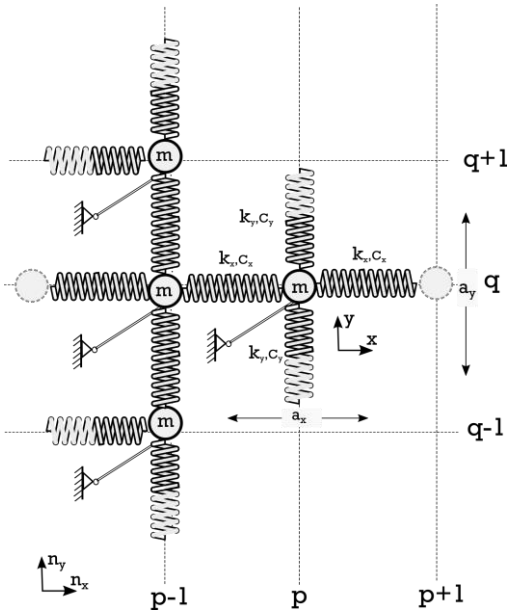

Figure 7-3: Unit lattice of a 2D periodic kinematically constrained system of masses.

By setting $\rho = tan\varphi$, the coupling of u, v DoFs is expressed as:

$$\boldsymbol{u} = \begin{bmatrix} u_{p,q} \\ v_{p,q} \end{bmatrix} = \begin{bmatrix} 1 \\ \rho \end{bmatrix} u_{p,q} \tag{7-8}$$

Then, by the left and right multiplication of the dynamic equation of motion with the eigenvector:

$$\lambda^2 Q^T \boldsymbol{M} Q + \lambda Q^T \boldsymbol{C} Q + Q^T \boldsymbol{K} Q)\boldsymbol{u} = 0 \tag{7-9}$$

the generalized expression is obtained for the calculation of the dispersion relations. Again, for the case of an undamped system, the existence of non-trivial harmonic plane-wave solutions requires that:

$$-\omega^2 m_a + 2k_x(1-\cos \mathrm{q}_x) + 2\omega^2 \sin^2 \varphi(1-\cos \mathrm{q}_y) = 0 \tag{7-10}$$

where $m_a = m(1+\rho^2)$ and $k_{ya} = \rho^2 k_y$.

Defining $\omega_x^2 = k_x / m$, Eq. (7-10) is simplified to:

$$-\omega^2 + 2\omega_x \cos^2 \varphi(1-\cos \mathrm{q}_x) + 2\omega_y{}^2 \sin^2 \varphi(1-\cos \mathrm{q}_y) = 0 \tag{7-11}$$

Figure 7-4 (a)–(e) shows the contour plot of the phase constant for coupling angles $\varphi(^o)$=15 to 75. This representation is particularly convenient as it allows visualizing the direction of the energy flow from evaluating the perpendicular directions to the iso-frequency lines. An example of the unit-cell's iso-frequency lines is provided as a key in Figure 7-4 (a). The dispersion curves are plotted in Figure 7-4 (g) in the ΓX-XM domain against the normalized frequency f / f_{ref}, where $f_{ref} = \omega_x / 2\pi$. As expected, increasing the coupling angle $\varphi(^o)$ between the two springs reduces the maximum frequency on the dispersion curve on the ΓX plane and increases it on the dispersion curve on the XM plane. In this regard, this simple lattice configuration shows interesting characteristics. The energy flow in the case $\varphi(^o)$=15, occurs at both planes. Further increasing this angle, wave propagation occurs mainly in one plane. The phenomenon, where wave propagation at a certain frequency is restricted to only certain directions, denotes the directionality of the periodic structure.

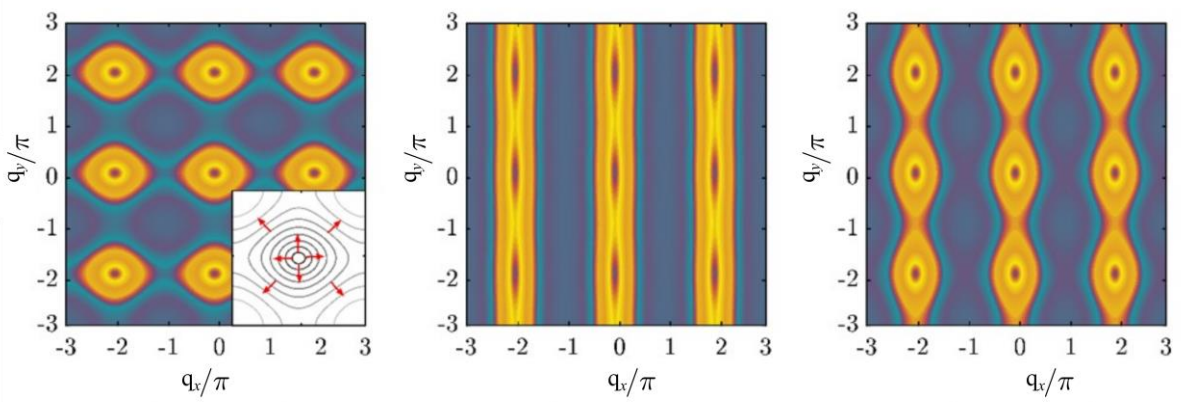

(a) *(b)* *(c)*

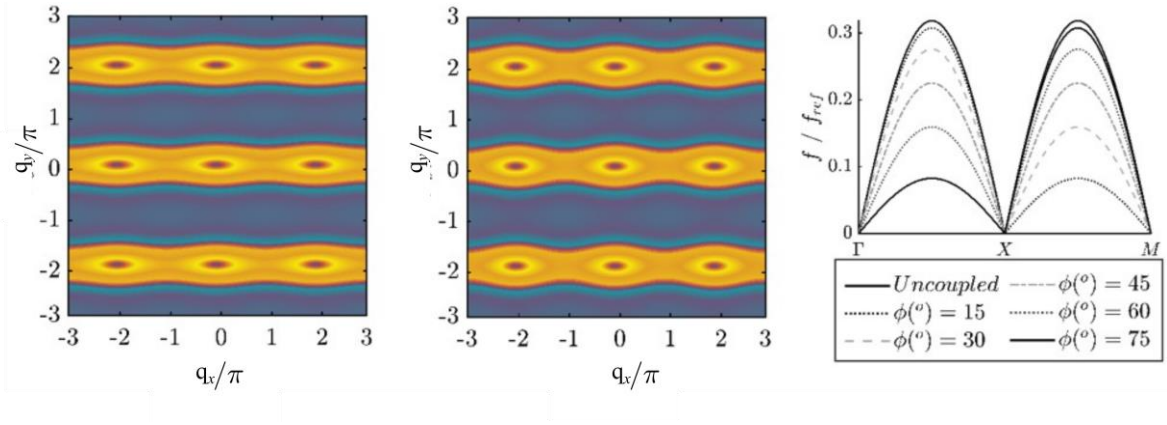

(e) *(f)* *(g)*

Figure 7-4: Dispersion surface of the 2D monoatomic lattice of periodic kinematically constrained DoFs with spring stiffness, $k_x = k_y$. (a) $\varphi(^o) = 15$, (b) $\varphi(^o) = 30$, (c) $\varphi(^o) = 45$, (d) $\varphi(^o) = 60$, (e) $\varphi(^o) = 75$ and (f) dispersion curves.

7.2.3 2D Phononic Lattice with Dynamic Directional Amplifier (DDA)

7.2.3.1 Wave Dispersion Analysis

The infinite mass–spring–dashpot lattice with the DDA of the phononic metamaterial is depicted in Figure 7-5. The lattice is no longer homogeneous due to the presence of two different masses m_L and m_D . k_x, k_y, m_L and m_D form the structural backbone of the lattice, where the angle $\varphi(^o)$ determines the amplification angle generated by the rigid links. The components c_x, c_y of the viscous damping are expressed in terms of the actual to critical damping ratios ζ_i, from the relation $\zeta_i = c_i / (2\sqrt{m_i k_i})$. Considering the case of the lattice under harmonic excitation at a frequency lower than the resonance frequencies of the amplification mechanisms, then the relative motion of the structural nodes will cause amplified motion for the masses m_D generating amplified inertial forces. Then, the wave propagation characteristics of this lattice are determined from the irreducible unit-cell via Bloch's theorem. The equations describing the harmonic motion of a typical unit-cell at a location $p,\ q$ without the directional amplifying mechanism can be expressed as:

$$m_L\ddot{u}_{2p,2q} + c_x\left(\dot{u}_{2p,2q} - \dot{u}_{2p-1,2q}\right) + c_x\left(\dot{u}_{2p,2q} - \dot{u}_{2p+1,2q}\right) + k_x(u_{2p,2q} - u_{2p-1,2q}) + k_x(u_{2p,2q} - u_{2p+1,2q}) = 0 \quad (7\text{-}12.a)$$

$$m_L\ddot{v}_{2p,2q} + c_y\left(\dot{v}_{2p,2q} - \dot{v}_{2p,2q-1}\right) + c_y\left(\dot{v}_{2p,2q} - \dot{v}_{2p,2q+1}\right) + k_y(v_{2p,2q} - v_{2p,2q-1}) + k_y(v_{2p,2q} - v_{2p,2q+1}) = 0 \quad (7\text{-}12.b)$$

$$m_D\ddot{u}_{2p+1,2q}+c_x\left(\dot{u}_{2p+1,2q}-\dot{u}_{2p,2q}\right)+c_x\left(\dot{u}_{2p+1,2q}-\dot{u}_{2p+2,2q}\right)+k_x(u_{2p+1,2q}-u_{2p,2q})+k_x(u_{2p+1,2q}-u_{2p+2,2q})=0 \tag{7-12.c}$$

$$m_D\ddot{v}_{2p+1,2q}+c_y\left(\dot{v}_{2p+1,2q}-\dot{v}_{2p+1,2q-1}\right)+c_y\left(\dot{v}_{2p+1,2q}-\dot{v}_{2p+1,2q+1}\right)+k_y(v_{2p+1,2q}-v_{2p+1,2q-1})+k_y(v_{2p+1,2q}-v_{2p+1,2q+1})=0 \tag{7-12.d}$$

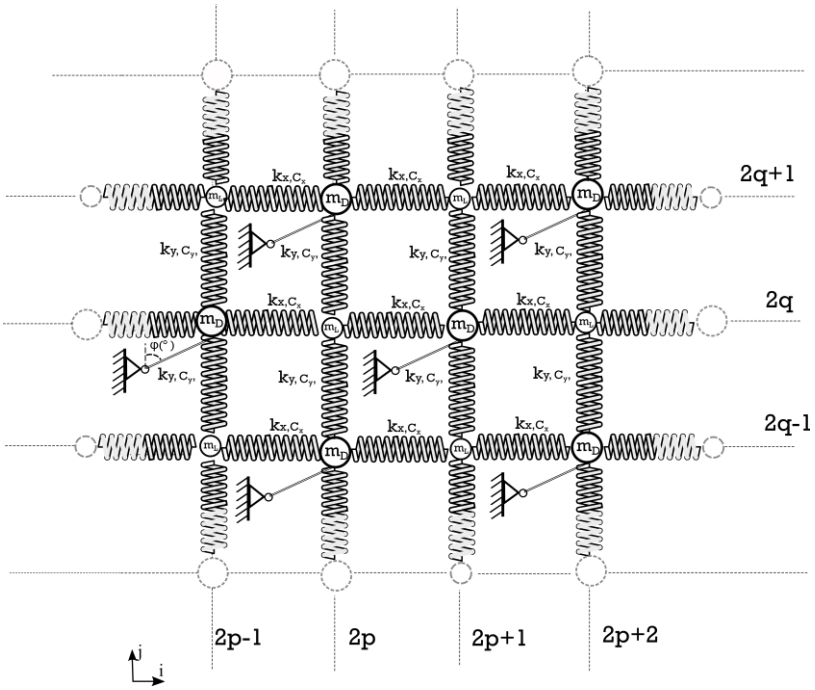

Figure 7-5: 2D phononic lattice with dynamic directional amplifiers (DDA).

For each of the systems of Eq. (7-12), assuming a plane–wave solution leads to the following relations between the DoFs of the lattice:

$$u_{2p-1,2q}=u_{2p+1,2q}e^{-jq_x} \tag{7-13.a}$$

$$u_{2p+2,2q}=u_{2p,2q}e^{jq_x} \tag{7-13.b}$$

$$v_{2p,2q-1}=v_{2p+1,2q}e^{-\frac{jq_x}{2}}e^{-\frac{jq_y}{2}} \tag{7-13.c}$$

$$v_{2p,2q+1}=v_{2p+1,2q}e^{-\frac{jq_x}{2}}e^{\frac{jq_y}{2}} \tag{7-13.d}$$

$$v_{2p+1,2q-1}=v_{2p,2q}e^{\frac{jq_x}{2}}e^{-\frac{jq_y}{2}} \tag{7-13.e}$$

$$v_{2p+1,2q+1}=v_{2p,2q}e^{\frac{jq_x}{2}}e^{\frac{jq_y}{2}} \tag{7-13.f}$$

Substituting these relations into the equations of motion and incorporating the conditions for unit-cell periodicity yields four homogeneous equations, which written in matrix form, are presented as:

$$\boldsymbol{M}_p\ddot{u} + \boldsymbol{C}_p\dot{u} + \boldsymbol{K}_p u = 0 \tag{7-14}$$

Finally, the system with the amplified masses m_D can be calculated by multiplying $\mathbf{M}_p, \mathbf{C}_p$ and $\boldsymbol{K}_p$ by the transformation matrix $\mathbf{Q}_p$.

The dispersion relationship of the phononic structure with directional inertial amplifiers is given by:

$$\det[-\lambda^2 \boldsymbol{M}_{p,a} + \lambda \boldsymbol{C}_{p,a} + \boldsymbol{K}_{p,a}] = 0 \tag{7-15}$$

where

$$\boldsymbol{M}_{p,a} = \boldsymbol{Q}_P^T \boldsymbol{M}_P \boldsymbol{Q}_P \tag{7-16.a}$$

$$\boldsymbol{C}_{p,a} = \boldsymbol{Q}_P^T \boldsymbol{C}_P \boldsymbol{Q}_P \tag{7-16.b}$$

$$\boldsymbol{K}_{p,a} = \boldsymbol{Q}_P^T \boldsymbol{K}_P \boldsymbol{Q}_P \tag{7-16.c}$$

The band structure of the infinite lattice is obtained through solving Eq. (7-14) for the lattice without the amplification mechanism, and Eq. (7-15) for the lattice with the amplification mechanism.

7.3 Transfer functions of the DDA Enhanced Phononic structure

Since the phononic lattice of Figure 7-5 is described by a series of discrete mechanical elements, the profile of the propagating waves is captured by the discretized displacement. Consequently, the equation of motion of the metamaterial, for $M_x \times M_y$ number of units is expressed in matrix formulation as:

$$\boldsymbol{M}\ddot{u}(t) + \boldsymbol{C}\dot{u}(t) + \boldsymbol{K}u(t) = \boldsymbol{F}e^{\lambda t}. \tag{7-17}$$

where $\boldsymbol{M}_{m\times m}, \boldsymbol{C}_{m\times m}, \boldsymbol{K}_{m\times m}, \ddot{\boldsymbol{u}}_{m\times 1}, \dot{\boldsymbol{u}}_{m\times 1}, \boldsymbol{u}_{m\times 1}, \boldsymbol{F}_{m\times 1}$ and m is the number of degrees of freedom (DoFs) of the metamaterial. For the lattice without the amplification mechanism, $m = 2M_xM_y$. Similarly, for the lattice with the DDA, $m = 3/2M_xM_y$ and the global mass $\left[\boldsymbol{M}_{p,\alpha}^G\right]$, damping $\left[\boldsymbol{C}_{p,\alpha}^G\right]$ and stiffness $\left[\boldsymbol{K}_{p,\alpha}^G\right]$ matrices can be calculated as follows:

$$\boldsymbol{M}_{p,a}^G = \boldsymbol{Q}_G^T \boldsymbol{M}_P^G \boldsymbol{Q}_G \tag{7-18.a}$$

$$\boldsymbol{C}_{p,a}^{G} = \boldsymbol{Q}_{G}^{T}\boldsymbol{C}_{P}^{G}\boldsymbol{Q}_{G} \tag{7-18.b}$$

$$\boldsymbol{K}_{p,a}^{G} = \boldsymbol{Q}_{G}^{T}\boldsymbol{K}_{P}^{G}\boldsymbol{Q}_{G} \tag{7-18.c}$$

For $M_x = M_y = 2$ the global mass $\boldsymbol{M}_{p,\alpha}^{G}$, damping $\boldsymbol{C}_{p,\alpha}^{G}$ and stiffness $\boldsymbol{K}_{p,\alpha}^{G}$ matrices are given in Appendix D.2. For $M_x = M_y \geq 2$ the matrices of each unit-cell are assembled as in any finite element analysis to produce the Global matrices of the periodic structure. Assuming that the finite lattice is excited harmonically at certain input nodes with frequency ω, means that the force magnitude vector F is zero everywhere except in the row or column corresponding to the component of the input node for which it has unit amplitude. The transfer matrix is then calculated as:

$$\boldsymbol{TF}_{p,a}^{G} = (-s^2\boldsymbol{M}_{p,a}^{G} + s\boldsymbol{C}_{p,a}^{G} + \boldsymbol{K}_{p,a}^{G})^{-1}\boldsymbol{F} \tag{7-19}$$

and the frequency response function (FRF) of the metamaterial is defined as:

$$\boldsymbol{FRF} = 20\log_{10}(\boldsymbol{TF}_{a,p}^{G}) \tag{7-20}$$

7.4 Numerical example

In this section, the band structure and the frequency response of the metamaterial described in the previous section are computed. In theory, the 2D finite lattice presented in Figure 7-6 works as a passband or stopband filter, where for the infinite case without damping, perfect filtering properties occur. The parameter values are prescribed such that bandgaps can be obtained in the lower to intermediate frequency range, namely between 100 and 200 (Hz). Specifically, the masses (m_L, m_D), springs ($k_x = m_L\left(2\pi f_x\right)^2, k_y = m_L\left(2\pi f_y\right)^2$ and the damping ratios (ζ_x, ζ_y) in the model were chosen as in the case where damping is considered, according to Table 7-1.

Table 7-1: Model parameters.

m_L [kg]	m_D [kg]	f_{ox} [Hz]	f_{oy} [Hz]	ζ_x	ζ_y
1.0	1.1	100	50	0.02	0.05

In the first case, no amplification mechanism is considered. This baseline configuration is then compared with the model that incorporates the DDA connected to the masses m_D. Subsequently, the effect of the number of unit-cells along each direction is investigated, followed by the effect of the amplification angle (φ) in the dynamic damping properties of the lattice. Finally, the location of the

response point on the lattice is briefly examined based on the frequency response functions in characteristic nodes of the structure.

7.4.1 Dynamic Amplification Induced Bandgaps

Figure 7-6 (a) corresponds to the considered lattice without the DDA mechanisms and excluding any damping elements. Figure 7-7 shows the resulting dispersion curves and the corresponding frequency response (FRF) of the 8×8 finite periodic lattices at point A along the x-axis. As expected, there are four branches and a Bragg gap between them. The observed bandgap is generated between 135 and 141 (Hz) and is generally small since the two masses m_L and m_D have been selected in such a way that there is only a 10% difference between them. Naturally, this small band is hardly visible at the FRF_x.

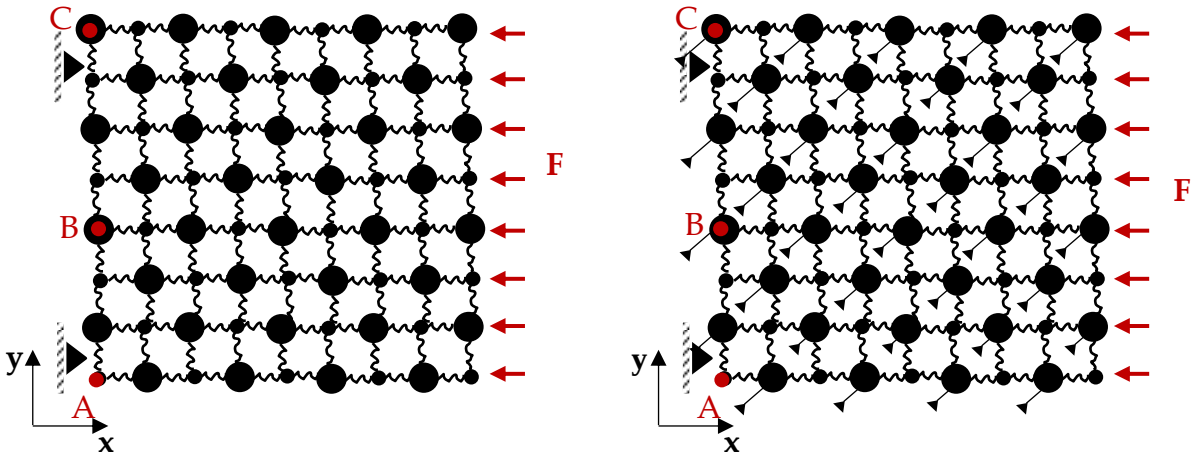

(a) (b)

Figure 7-6: Structure with $M_x \times M_y$ unit cells with a periodic loading acting at the right boundary and simple supports at the left corners (a) without DDA (b) with DDA.

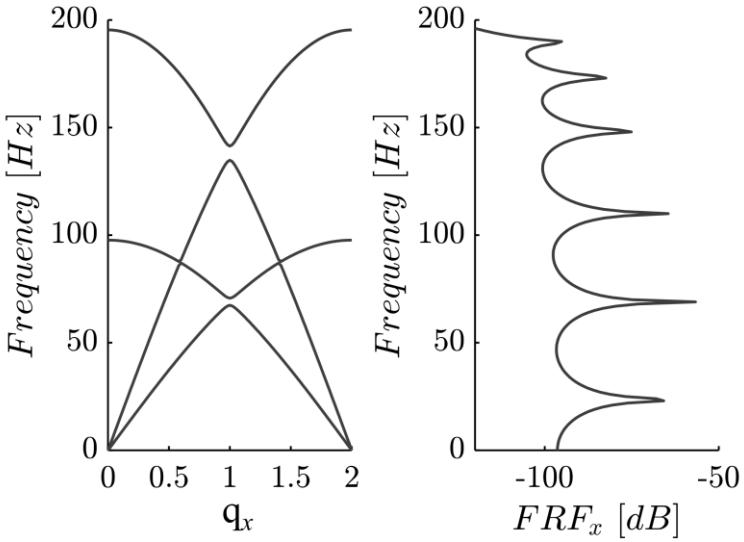

(a) *(b)*

Figure 7-7: (a) Dispersion curves and (b) frequency response of the 2D phononic lattice without the DDA along the Γ-X.

Figure 7-6 (b) corresponds to the considered lattice, including the DDA mechanisms. Aiming to highlight the characteristics of amplification induced phononic gaps in infinite periodic structures, $\varphi(^{o})$ is varied from 15 to 75. The band structure of the infinite lattice is obtained by calculating q_x and q_y from Eq. (7-15). Figure 7-8 (a)–(d) illustrates the "phase constant" surfaces in 3D, where the z-axis shows the frequency corresponding to each pair of normalized wavenumbers (q_x, q_y). Table 7-2 presents the lower and upper limits for the gaps and the normalized bandwidth for the studied cases, which is defined as:

$$b_w = \frac{(f_u - f_l)}{f_{av}}, \quad f_{av} = \frac{(f_u + f_l)}{2} \tag{7-21}$$

where f_l and f_u correspond to the lower and upper bandgap limits, respectively, and f_{av} is the mid-gap frequency. The normalized bandwidths are also plotted against angle $\varphi(^{o})$ in Figure 7-8 (e).

Comparing the dispersion surfaces of the baseline structure with the one, including the DDAs, reveals that the introduction of amplifiers to the lattice plays a critical role in the size of the forming bandgaps. In addition, the number of dispersion surfaces is reduced to three due to coupling between the vertical (v) and horizontal (u) DoFs of the amplified mass, revealing a second small partial bandgap, which is not of interest in the current study. The amplification effect of mass mD is translated to a gradual "flattening" of the intermediate iso-surface, increasing the distance between the two surfaces. For example, increasing the amplifiers angle $\varphi(^{o})$ from 15 to 75 leads to an

approximate 600% increase in the bandgap width, clearly showing the beneficial effect of the DDA on the phononic structure.

Table 7-2: Lower (f_l) , upper (f_u) bandgap limits and normalized gap widths (b_w).

Case	f_u [Hz]	f_l [Hz]	f_{av} [Hz]	b_w
Without DDA	141.4	134.8	138.1	0.05
$\varphi(^o)$=15	141.4	131.9	136.6	0.07
$\varphi(^o)$=45	141.4	113.2	127.3	0.22
$\varphi(^o)$=75	141.4	99.2	120.3	0.35

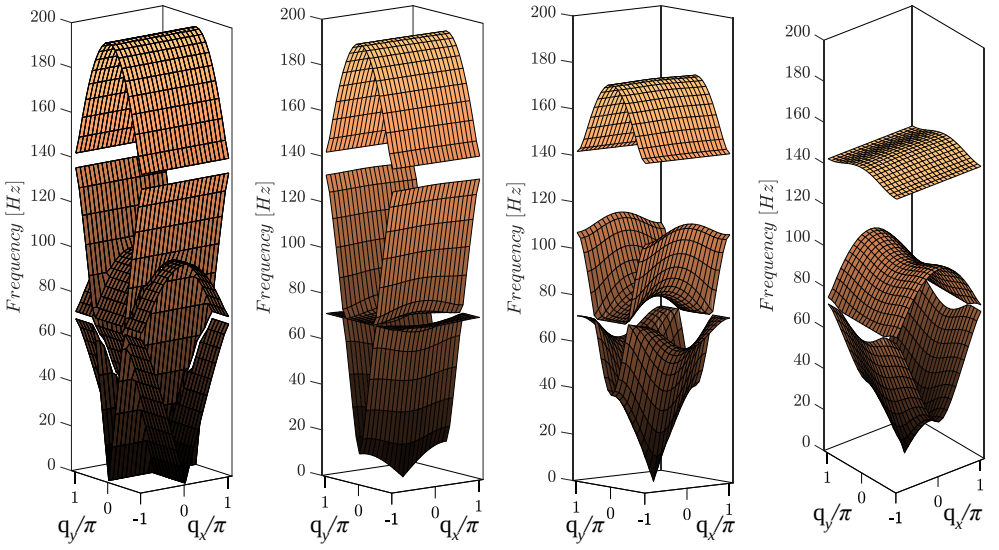

(a) *(b)* *(c)* *(d)*

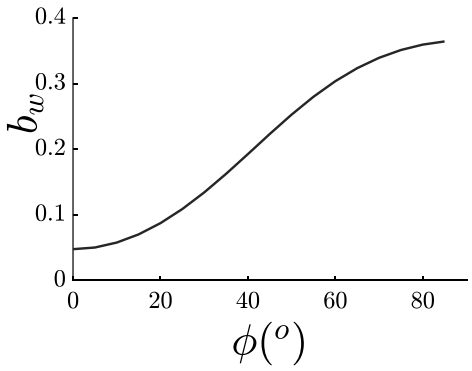

(e)

Figure 7-8: Dispersion contours of 2D phononic lattice for m_L=1.0 kg, m_D=1.1k_g, f_x=100 Hz and f_y=50Hz for the (a) lattice without DDA, (b) the lattice with DDA and $\varphi(^o)$=15, (c) the lattice with DDA and $\varphi(^o)$=45, (d) the lattice with DDA and $\varphi(^o)$=75 (e) Normalized bandgap width as a function of the amplifier's angle.

7.4.2 Effect of Number of Unit-Cells

In general, the attenuation of the signal in the bandgap frequency range is lower only when a few units are utilized. Herein, for the sake of comparison, we retain the total mass and stiffness of the studied undamped lattices while increasing the number of unit-cells. The repetition of unit-cells, as presented in Figure 7-9 for $M_x = M_y$ = 4, 8, 12, 16 unit-cells, increases the depth of the bandgap while bearing a marginal effect on the high-frequency behavior of the system. Figure 7-9 (a) displays the FRF in the x-direction of the last mass in the lattice (point A) when subjected to a periodic loading according to Figure 7-6 (a). Additionally, the corresponding FRF in the y-direction is depicted in Figure 7-6 (b) to display the coupling effect between the two degrees of freedom. In both cases, the response curves are presented for the parameters tabulated in Table 7-11, and for comparison, the bandgap boundaries calculated for the infinite lattice are shown with vertical dashed lines. Naturally, the generated bandgaps are more obvious in FFR_x where the DDA is fully activated. Nonetheless, even in the transverse direction, a significant amount of filtering occurs. For $M_x = M_y = 4$ the bandgap is identifiable from the curve in between 99.2 and 141.4 (Hz), yet the attenuation in response is only marginally larger than the drops being observed among the other resonance frequencies. With more unit-cells, the metamaterial offers an over 50 (dB) bandgap depth. Thus, for further examination regarding the behavior of the structure, the number of unit-cells is selected as $M_x = M_y = 8$.

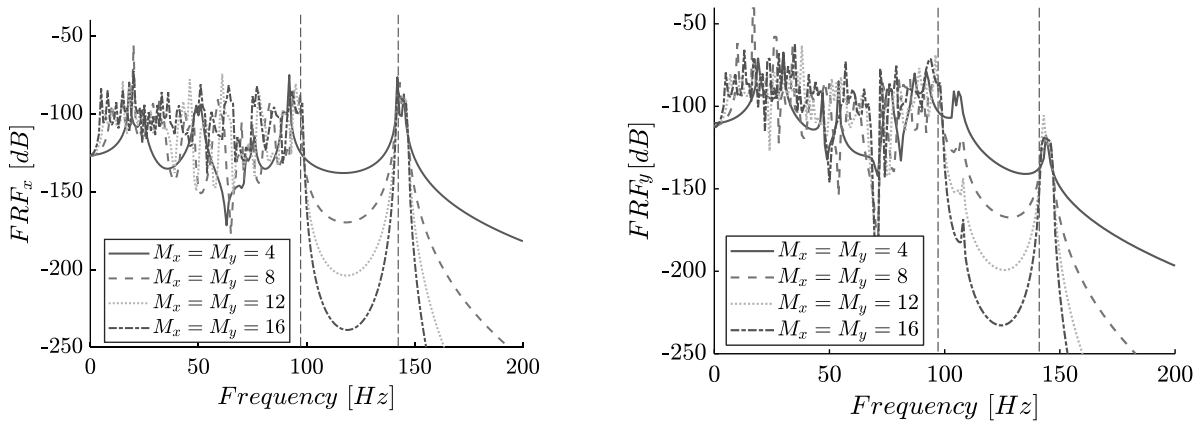

(a) *(b)*

Figure 7-9: Frequency response (FRF) plot in point A (according to Figure 7-6 of the $M_x \times M_y$ finite lattice, without damping and amplifier angle φ(°) = 75 for (a) x-direction (b) y-direction 2D Dynamic Directional Amplification (DDA) in Phononic Metamaterials.

7.4.3 Dynamically Induced Metadamping

Next, as shown in Figure 7-10, the frequency and damping ratio dispersion curves are examined together with the corresponding frequency response functions of the metamaterial for three (3) different values of the amplifier's angle. These describe the usual frequency dispersion curves, which now are affected by the presence of damping, i.e., a complex frequency is assumed, together with curves associated with the attenuation of each Bloch mode. Concerning the damping prescription, we assume dashpots connecting the masses on the horizontal and vertical directions with damping ratios ζ_x = 0.02 and ζ_y=0.05. The aim of this investigation is to show the emergent metadamping phenomenon (Hussein, 2009) accruing from the dynamic directional amplifier. In other words, the prescribed damping ratio remains constant while different angles of the DDA are examined. The low prescribed damping ratio value of the considered viscous dampers in the x-direction is justified by the extraordinary amplification that the following figures are indicating. The results show that there are shifts in the frequency band diagrams along the Γ–X due to the presence of the dynamic damping, which can be observed comparing the two extreme cases that are plotted. This behavior is more obvious in the damping ratio dispersion curves. Despite the same initial viscous damping values, in all three cases, the case with $\varphi(^o)$=75 exhibits higher dissipation for both the acoustic and optical branches. Specifically, an increased damping ratio is observed in the optical branch (almost five times higher than the one initially prescribed), while for the lower angle $\varphi(^o)$= 15, the optical branch drops abruptly. At the same time, the acoustic branch experiences little change, which leads to a reduced bandgap. The two branches meet in the low damping ratio region, and the so-called branch-overtaking phenomenon (Hussein, 2009) occurs. As expected, this phenomenon does not occur for larger amplification angles. This is an indication of the emergence of dissipation, which is present along the whole spectrum and not only for modes close to the bandgap, as seen in Figure 7-10 (c), where the FRF of the damped 8 × 8 finite lattice is plotted. Consequently, the DDA mechanism not only increases the expected bandwidth size but also provides a great example of metadamping emergence.

7.4.4 Effects of Response Point

A distributed source along the edge nodes excites the longitudinal and transverse modes of Figure 7-6 (b) finite lattice. As already mentioned, the DDA mechanism is designed to function in the x-direction; hence a different response is expected along the x and y-axes. To select the input and output nodes on this lattice, we remove the fixed boundary conditions on the output points A–C. Figure 7-11 shows

the FRF plots of the 8 × 8 finite periodic lattice for longitudinal excitation along the x-axis, assuming damping ratios ζ_x= 0.02, ζ_y= 0.05 and amplifier angle $\varphi(^o)$= 75.

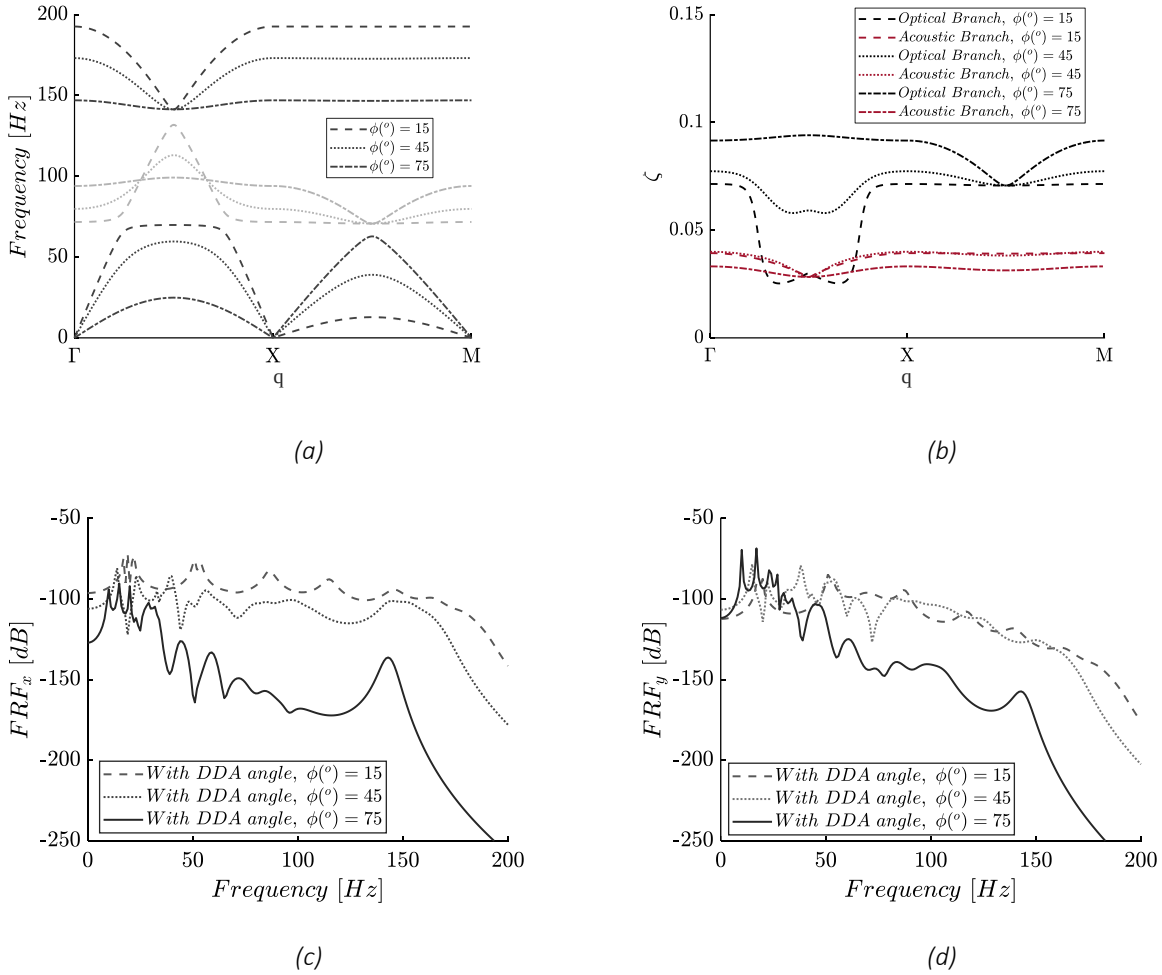

Figure 7-10: (a) Frequency band structure and (b) damping ratio (ζ) band structure. Frequency response function (FRF) plots of the 8 × 8 finite lattice (response in point A) (c) x-direction (d) y-direction.

Notice that in Figure 7-11, there are small resonance peaks in the response of output point A at approximately f = 50 [Hz] close to the antiresonance notches of output points B, C. These peaks are due to the applied boundary conditions. Nevertheless, the peaks do not affect the gap performances, as they are close to the lower limit of the bandgap. Moreover, at low frequencies (below 25 [Hz], the FRF of A is shifted downwards due to the rigid body translation modes, while a larger bandgap depth is observed in A compared to the one of the interim point B. The different response observed between point A and C is justified by the existence of an amplified or not mass in the selected node. Except for these differences, the FRF of the presented output points does not show great deviations, revealing that the proposed metamaterial is effective throughout its length.

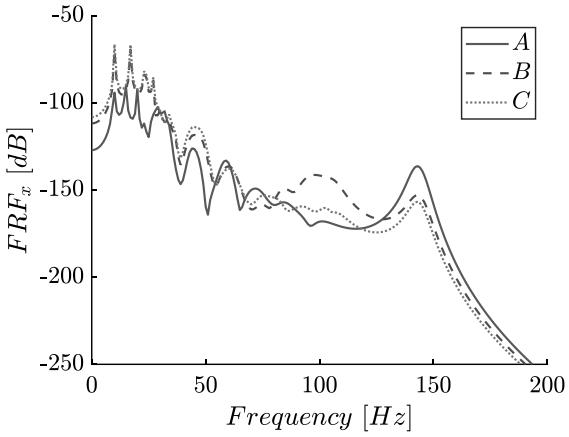

Figure 7-11: Frequency response (FRF_x) of the 8×8 finite lattice, for $\zeta_{0x}= 0.02$, $\zeta_{0y}= 0.05$, and amplifier's angle $\varphi(^o)=75$ at points A–C.

7.5 Conceptual Design

Figure 7-12 presents a conceptual design of the proposed metastructure. Although for the sake of simplicity the system comprises of a single unit-cell, yet larger lattices can be easily constructed by the spatial repetition of this unit-cell. The mass–spring lattice is envisaged as a compliant 3D-printed part, supported by the red-coloured metal frame. The role of this frame is to accommodate the DDA mechanisms at the specified locations providing overhangs for the pinned connections. The proposed realization can be designed either as a microstructure or on a larger scale, allowing the implementation in various applications, including acoustic and vibration control and seismic isolation.

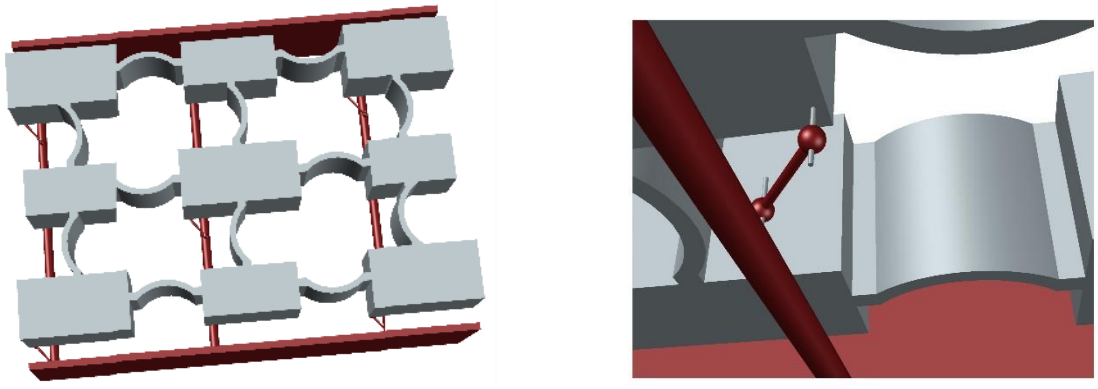

(a) *(b)*

Figure 7-12: Conceptual design of the proposed metastructure, (a) 3D view (b) detail of the dynamic directional amplifier (DDA).

7.6 Concluding Remarks

The present study demonstrated the theoretical framework of a novel 2D phononic metamaterial consisting of dynamically amplified masses. The novelty lies in the simplicity of the proposed system. The dynamic directional amplification (DDA) mechanism is realized without additional masses or complex geometries since the amplification can be achieved by coupling the kinematic DoFs of the mass with a rigid link. Initially, the effect of coupling between the vertical and horizontal motion of the mass–spring system was shown based on a monoatomic configuration. Then, the enhanced phononic structure was formulated based on the proposed amplification mechanism, and a simple indicative example was demonstrated to show its capabilities. The dispersion relationships illustrated that the amplification of the mass could provide large bandgaps in the low-frequency regime without the need for large parasitic mass addition. It was also demonstrated that using dynamic amplification, deep gaps at low-frequencies can be obtained in the direction of wave propagation, using a moderate number of unit-cells, while an emergent metadamping phenomenon occurs even when minuscule damping ratios values are prescribed. To conclude, the provided indicative implementation of this concept shows great promise towards developing acoustic metamaterial designs able to offer low-frequency isolation.

8 LOCALLY RESONANT METAMATERIALS UTILIZING DYNAMIC DIRECTIONAL AMPLIFICATION

8.1 Background

In this chapter, a simple Dynamic Directional Amplifier (DDA) (Kalderon et al., 2021) is introduced as a means to increase the resonating mass of a locally resonant metamaterial (LRM) structure artificially, without the need of complex geometries and additional mass. The amplification is achieved with a rigid link that improves inertia and damping (Mahmoud I Hussein & Frazier, 2013) on the desired direction of motion, by simply coupling the kinematic DoFs of the resonating mass. The main aim of this study is to illustrate, via the use of a formal mathematical framework, that we can enhance the performance of LRM structures while retaining or even improving the practical constraints such as having compact, lightweight, and buildable unit-cells. Towards this goal, a mass-in-mass model is adopted, and a preliminary parametric analysis is performed using both Bloch's theory (1929) on two-dimensional infinite lattices and conventional vibration theory on finite lattices. A numerical example is studied as a seismic mitigation application in order to highlight the advantages of the proposed arrangement over the initial study. To this end, a conceptual design of a seismic metamaterial in the form of a metabarrier is proposed and an investigation of its response under seismic excitation is analyzed. Results indicate the beneficial role of the device and DDA mechanism, hence placing the concept as a compelling alternative to existing seismic protection technologies.

8.2 Bloch analysis

Figure 8-1 illustrates the primary unit-cell of a simple mass-in-mass configuration, which consists of an external mass (m_L) an internal resonator (m_R) and the corresponding massless springs and dashpots. Based on this simple configuration, the enhanced unit-cells are conceptualized. Figure 8-1 (a) depicts the configuration of a conventional locally resonant unit-cell and Figure 8-1 (b) illustrates the configuration with the DDA attached in the resonating mass (m_R).

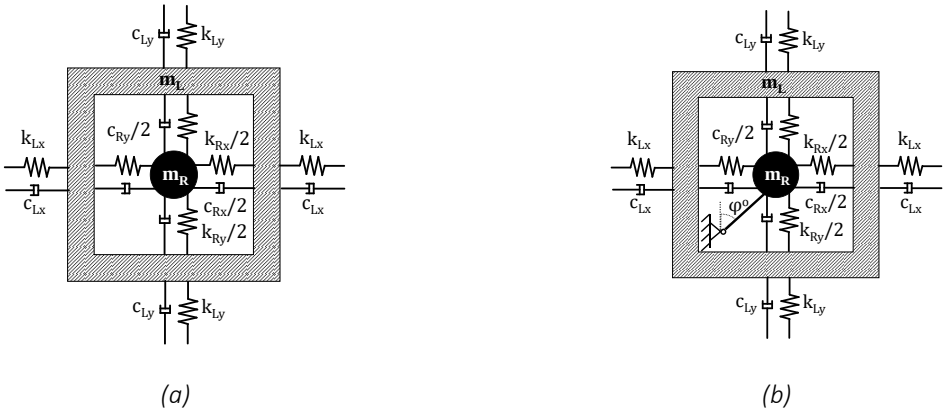

Figure 8-1: The periodic mass-in-mass unit-cell (a) w/o DDA (b) with DDA attached in the resonating mass (m_R)

By placing such units in a lattice, at a distance $L=\alpha_x=\alpha_y$, an infinitely periodic material is composed, as illustrated in Figure 8-2. Harmonic wave propagation in the mass-in-mass lattice system is considered.

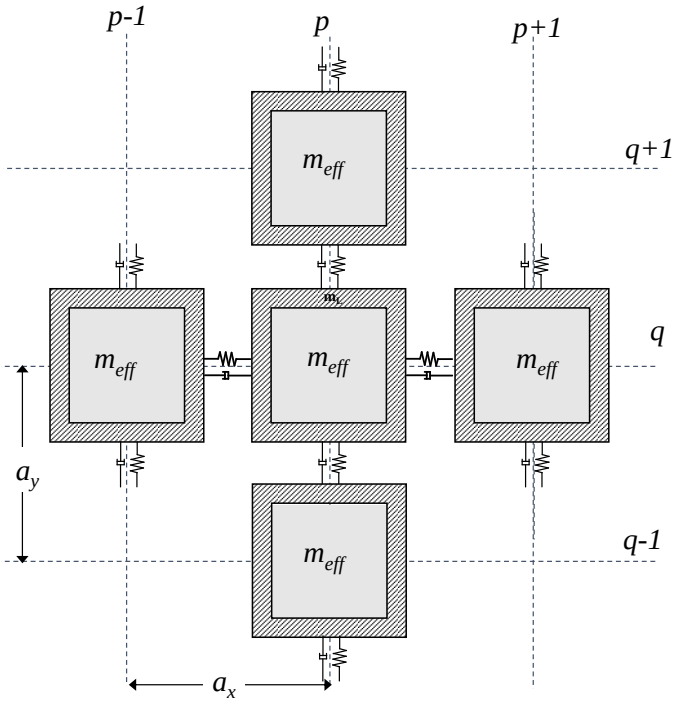

Figure 8-2: 2-D spring-mass effective lattice.

The set of equations that describe the harmonic motion of the simple typical unit-cell of Figure 8-2 (a), at location $p,\ q$, can be expressed as (Mahmoud I Hussein & Frazier, 2013):

$$m_L\ddot{u}_L^{p,q}+k_{L_x}(2u_L{}^{p,q}-u_L^{p-1,q}-u_L^{p+1,q})+k_{Rx}(u_L^{p,q}-u_R^{p,q})+c_{Lx}\left(2\dot{u}_L^{p,q}-\dot{u}_L^{p-1,q}-\dot{u}_L^{p+1,q}\right)$$
$$+c_{Rx}\left(\dot{u}_L^{p,q}-\dot{u}_R^{p,q}\right)=0 \tag{8-1.a}$$

$$m_R\ddot{u}_R^{p,q}+k_{Rx}(u_R^{p,q}-u_L^{p,q})+c_{Rx}\left(\dot{u}_R^{p,q}-\dot{u}_L^{p,q}\right)=0 \tag{8-1.b}$$

$$m_L\ddot{v}_L^{p,q}+k_{L_y}(2v_L{}^{p,q}-v_L^{p,q-1}-v_L^{p,q+1})+k_{Ry}(v_L^{p,q}-v_R^{p,q})+c_{L_y}\left(2\dot{v}_L^{p,q}-\dot{v}_L^{p,q-1}-\dot{v}_L^{p,q+1}\right)$$
$$+c_{R_y}\left(\dot{v}_L^{p,q}-\dot{v}_R^{p,q}\right)=0 \tag{8-1.c}$$

$$m_R\ddot{v}_R^{p,q}+k_{R_y}(v_R^{p,q}-v_L^{p,q})+c_{R_y}\left(\dot{v}_R^{p,q}-\dot{v}_L^{p,q}\right)=0 \tag{8-1.d}$$

The displacement of a DoF at a specific position of the lattice may be expressed in a complex notation as:

$$u_{p,q}=\hat{U}_{p,q}e^{\lambda t}=\hat{U}e^{j(p\kappa_x a_x+q\kappa_y a_y)}=\tilde{U}e^{j(p\mathrm{q}_x+q\mathrm{q}_y)} \tag{8-2.a}$$

Where $\tilde{U}$ is the wave amplitude, κ_x,κ_y the wavenumbers and $\mathrm{q}_x,\mathrm{q}_y$ the propagation constants along the horizontal and vertical directions.

In the time part of the solution, the parameter λ_S is defined as $\lambda_S=\pm j\omega_S(\kappa)$, or in the case where the attenuation between the unit-cells is considered $\lambda_S=-\zeta_S(\kappa)\omega_S(\kappa)\pm j\omega_{d_S}(\kappa)$, where λ represents the branch number, $\zeta_S(\kappa)$ is the wavenumber-dependent damping ratio and $\omega_S(\kappa)$ is the wavenumber-dependent frequency (dispersion relation). As a result, the imaginary part is the frequency of the damped wave propagation, $\omega_{dS}(\kappa)=\mathrm{Im}[\lambda_S(\kappa)]$, and the damping ratio is calculated as:

$$\zeta_S(\kappa)=-\frac{\mathrm{Re}[\lambda_S(\kappa)]}{|\lambda_S(\kappa)|} \tag{8-3}$$

Utilizing Bloch's theorem, the spatial part of the solution is expressed as:

$$u_L^{p,q}=\tilde{U}_L^{p,q}e^{j\kappa_x pa_x+j\kappa_y qa_y}e^{\lambda t}=\tilde{U}_L^{p,q}e^{jp\mathrm{q}_x+jq\mathrm{q}_y}e^{\lambda t} \tag{8-4.a}$$

$$u_L^{p+1,q}=\tilde{U}_L^{p,q}e^{j\kappa_x(p+1)a_x+j\kappa_y qa_y}e^{\lambda t}=\tilde{U}_L^{p,q}e^{j(p+1)\mathrm{q}_x+jq\mathrm{q}_y}e^{\lambda t}=u_L^{p,q}e^{j\mathrm{q}_x} \tag{8-4.b}$$

$$u_L^{p-1,q}=\tilde{U}_L^{p,q}e^{j\kappa_x(p-1)a_x+j\kappa_y qa_y}e^{\lambda t}=\tilde{U}_L^{p,q}e^{j(p-1)\mathrm{q}_x+jq\mathrm{q}_y}e^{\lambda t}=u_L^{p,q}e^{-j\mathrm{q}_x} \tag{8-4.c}$$

$$v_L^{p,q}=\tilde{V}_L^{p,q}e^{j\kappa_x pa_x+j\kappa_y qa_y}e^{\lambda t}=\tilde{V}_L^{p,q}e^{jp\mathrm{q}_x+jq\mathrm{q}_y}e^{\lambda t} \tag{8-4.d}$$

$$v_L^{p,q+1} = \tilde{V}_L^{p,q} e^{j\kappa_x p a_x + j\kappa_y (q+1) a_y} e^{\lambda t} = \tilde{U}_L^{p,q} e^{jp\mathrm{q}_x + j(q+1)\mathrm{q}_y} e^{\lambda t} = v_L^{p,q} e^{j\mathrm{q}_y} \tag{8-4.e}$$

$$v_L^{p,q-1} = \tilde{V}_L^{p,q} e^{j\kappa_x p a_x + j\kappa_y (q-1) a_y} e^{\lambda t} = \tilde{U}_L^{p,q} e^{jp\mathrm{q}_x + j(q-1)\mathrm{q}_y} e^{\lambda t} = v_L^{p,q} e^{-j\mathrm{q}_y} \tag{8-4.f}$$

Substituting these relations into the equations of motion and incorporating the conditions for unit-cell periodicity yields four homogeneous equations, which can be written in a matrix notation as follows:

$$[-\lambda^2 \boldsymbol{M}_{LRM} + \lambda \boldsymbol{C}_{LRM} \boldsymbol{K}_{LRM}] \boldsymbol{u}_{LRM} = 0 \tag{8-5}$$

where

$$\boldsymbol{M}_{LRM} = \begin{bmatrix} m_L & 0 & 0 & 0 \\ 0 & m_L & 0 & 0 \\ 0 & 0 & m_R & 0 \\ 0 & 0 & 0 & m_R \end{bmatrix} \tag{8-6.a}$$

$$\boldsymbol{C}_{LRM} = \begin{bmatrix} c_{Lx}(2-(e^{-j\mathrm{q}_x}+e^{j\mathrm{q}_x})+c_{Rx} & 0 & -c_{Rx} & 0 \\ 0 & c_{Ly}(2-(e^{-j\mathrm{q}_y}+e^{j\mathrm{q}_y})+c_{Ry} & 0 & -c_{Ry} \\ -c_{Ry} & 0 & c_{Rx} & 0 \\ 0 & -c_{Rx} & 0 & c_{Ry} \end{bmatrix} \tag{8-6.b}$$

$$\boldsymbol{K}_{LRM} = \begin{bmatrix} k_{Lx}(2-(e^{-j\mathrm{q}_x}+e^{j\mathrm{q}_x})+k_{Rx} & 0 & -k_{Rx} & 0 \\ 0 & k_{Ly}(2-(e^{-j\mathrm{q}_y}+e^{j\mathrm{q}_y})+k_{Ry} & 0 & -k_{Ry} \\ -k_{Ry} & 0 & k_{Rx} & 0 \\ 0 & -k_{Rx} & 0 & k_{Ry} \end{bmatrix} \tag{8-6.c}$$

$$\boldsymbol{u}_{LRM} = \begin{bmatrix} u_L^{[p,q} \\ v_L^{[p,q} \\ u_R^{[p,q} \\ v_R^{[p,q} \end{bmatrix} \tag{8-6.d}$$

Assuming for simplicity reasons that $k_{Lx} = k_{Ly} = k_L$ and $k_{Rx} = k_{Ry} = k_R$, and that the system has no damping allows the investigation of the problem by adopting the one-dimensional propagation theory. Utilization of the trigonometric transformation $\beta = 2-(e^{j\mathrm{q}}+e^{-j\mathrm{q}}) = 2(1-\cos\mathrm{q})$ leads to the following dispersion equation (M I Hussein et al., 2014):

$$m_L m_R \omega^4 - [(m_L + m_R)k_R + 2m_R k_L(1-\cos\mathrm{q})]\omega^2 + 2k_L k_R(1-\cos\mathrm{q}) = 0 \tag{8-7}$$

Based on Dertimanis (2016), we can deduce a rough estimate of the required quantities to obtain a bandgap within the frequency region of our preference, as follows:

$$m_R = \left[\left(\frac{f_H}{f_L} \right)^2 - 1 \right] m_L \tag{8-8.a}$$

$$k_R = 4\pi^2 f_L^2 m_R = 4\pi^2 (f_H^2 - f_L^2) m_L \tag{8-8.b}$$

with f_L and f_H [Hz] denoting the low and high threshold of the selected bandgap, respectively.

Once the equation of motion of the simple LRM is derived, we can study the band structure of the LRM-DDA metamaterial. The DoFs of the coupled system are the following:

$$\boldsymbol{u}_{LRM-DDA} = \boldsymbol{Q}^T \boldsymbol{u}_{LRM} = \begin{bmatrix} 1 & 0 & 0 \\ 0 & 1 & 0 \\ 0 & 0 & 1 \\ 0 & 0 & \rho \end{bmatrix} \boldsymbol{u}_{LRM} \tag{8-9}$$

The system with the amplified masses m_R can be calculated by multiplying $\boldsymbol{M}_{LRM}$, $\boldsymbol{C}_{LRM}$ and $\boldsymbol{K}_{LRM}$ by the transformation matrix $\boldsymbol{Q}$ .The dispersion relationship of the LR structure with Dynamic Directional Amplifiers is provided by:

$$\det[-\lambda^2 \boldsymbol{M}_{LRM-DDA} + \lambda \boldsymbol{C}_{LRM-DDA} \boldsymbol{K}_{LRM-DDA}] = 0 \tag{8-10}$$

where

$$\boldsymbol{M}_{LRM-DDA} = \boldsymbol{Q}^T \boldsymbol{M}_{LRM} \boldsymbol{Q} = \begin{bmatrix} m_L & 0 & 0 \\ 0 & m_L & 0 \\ 0 & 0 & m_R(1+\rho^2) \end{bmatrix} \tag{8-11.a}$$

$$\boldsymbol{C}_{LRM-DADA} = \boldsymbol{Q}^T \boldsymbol{C}_{LRM} \boldsymbol{Q} = \begin{bmatrix} 2c_{Lx}(1-\cos \mathrm{q}_x) + c_{Rx} & 0 & -c_{Rx} \\ 0 & 2c_{Ly}(1-\cos \mathrm{q}_y) + c_{R_y} & -\rho c_{R_y} \\ -c_{Rx} & -\rho c_{R_y} & c_{R_x} \rho^2 c_{R_y} \end{bmatrix} \tag{8-11.b}$$

$$\boldsymbol{K}_{LRM-DADA} = \boldsymbol{Q}^T \boldsymbol{K}_{LRM} \boldsymbol{Q} = \begin{bmatrix} 2k_{Lx}(1-\cos \mathrm{q}_x) + k_{Rx} & 0 & -k_{Rx} \\ 0 & 2k_{Ly}(1-\cos \mathrm{q}_y) + k_{R_y} & -\rho k_{R_y} \\ -k_{Rx} & -\rho k_{R_y} & k_{R_x} \rho^2 k_{R_y} \end{bmatrix} \tag{8-11.c}$$

8.3 Transfer functions of the DDA Enhanced LRM Structure

Figure 8-3 presents a lattice configuration with finite number of locally resonant unit-cells. Consequently, the equation of motion of the structure, for $M_x \times M_y$ number of unit-cells is presented in matrix formulation as follows:

$$\boldsymbol{M}\ddot{\boldsymbol{u}}(t) + \boldsymbol{C}\dot{\boldsymbol{u}}(t) + \boldsymbol{K}\boldsymbol{u}(t) = \boldsymbol{F}e^{\lambda t} \tag{8-12}$$

Where $\boldsymbol{M}_{m\times m}, \boldsymbol{C}_{m\times m}, \boldsymbol{K}_{m\times m}, \ddot{\boldsymbol{u}}_{m\times 1}, \dot{\boldsymbol{u}}_{m\times 1}, \boldsymbol{u}_{m\times 1}, \boldsymbol{F}_{m\times 1}$ and m is the number of degrees of freedom (DoFs) of the metamaterial.

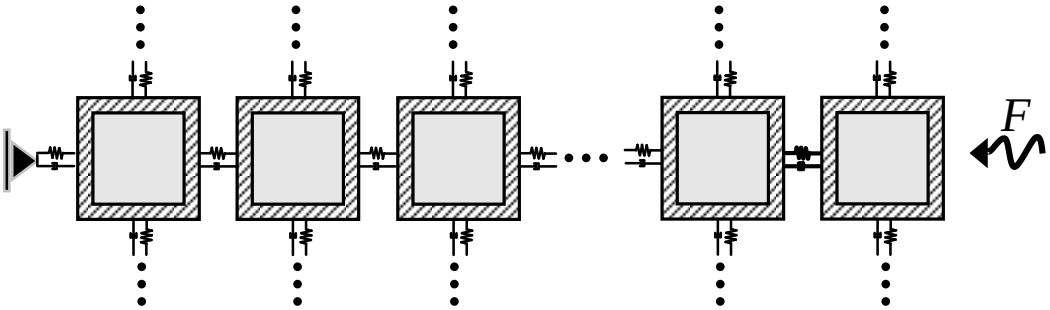

Figure 8-3: Structure with $M_x \times M_y$ unit-cells with a periodic loading acting at the right boundary.

For the case of the lattice without the amplification mechanism, $m = 4M_xM_y$. On the other hand, for the lattice with the *DDA*, $m = 3M_xM_y$ and the global mass $\left[\boldsymbol{M}^G_{LRM-DDA}\right]$, damping $\left[\boldsymbol{C}^G_{LRM-DDA}\right]$ and stiffness $\left[\boldsymbol{K}^G_{LRM-DDA}\right]$ matrices can be calculated as follows:

$$\boldsymbol{M}^G_{LRM-DDA} = \boldsymbol{Q}_G^T \boldsymbol{M}^G_{LRM} \boldsymbol{Q}_G \tag{8-13.a}$$

$$\boldsymbol{C}^G_{LRM-DDA} = \boldsymbol{Q}_G^T \boldsymbol{C}^G_{LRM} \boldsymbol{Q}_G \tag{8-13.b}$$

$$\boldsymbol{K}^G_{LRM-DDA} = \boldsymbol{Q}_G^T \boldsymbol{K}^G_{LRM} \boldsymbol{Q}_G \tag{8 13.c}$$

The transform matrix is expressed as:

$$Q_{G(4M_xM_y)\times(3M_xM_y)}=\begin{bmatrix} 1 & 0 & & \cdots & & & 0 \\ 0 & 1 & 0 & & & & 0 \\ & 0 & 1 & & & & \\ & 0 & \rho & 0 & & & \\ \vdots & 0 & 0 & \ddots & 0 & & \vdots \\ & & 0 & 0 & 1 & 0 & \\ & & & 0 & \rho & 1 & 0 \\ & & & & 0 & 0 & 1 \\ \rho & & & \cdots & & 0 & \rho \end{bmatrix} \tag{8-14}$$

The mass $\left[\boldsymbol{M}^G\right]$ stiffness$\left[\boldsymbol{K}^G\right]$ and damping $\left[\boldsymbol{C}^G\right]$ matrices are assembled to generate the Global matrices of the finite metamaterial lattice. Assuming that the periodic structure is excited harmonically at the input nodes with frequency ω, the force magnitude vector F is equal to zero everywhere except from the row or column corresponding to the component of the input node, for which it has unit amplitude. The transfer function of each degree of freedom may be calculated by the following expression:

$$\boldsymbol{TF}_{LRM-DDA}=[-\lambda^2\boldsymbol{M}^G_{LRM-DDA}+\lambda\boldsymbol{C}^G_{LRM-DDA}+\boldsymbol{K}^G_{LRM-DDA}]^{-1}\boldsymbol{F} \tag{8-15}$$

Thus, the frequency response of the nodal displacements can be obtained. In this case, u_{in} denotes the displacement of the outer masses (m_L), where the input excitation is applied, and u_{fin} denotes the displacement of the rear outer mass of the last unit-cells. The Frequency Response Function (FRF) of the structure is consequently expressed in decibels as follows:

$$FRF=20\log_{10}\left(\frac{u_{fin}}{u_{in}}\right) \tag{8-16}$$

8.4 Numerical results

As previously described, the 2D periodic metamaterial works as a passband or stopband filter, where for the infinite case without damping, perfect filtering properties occur. Naturally, the generated bandgaps are more dominant in the direction of interest, where the DDA is mobilized. Hence, the following analysis concerns only the direction of amplification, assuming for simplicity one row of unit-cells. An indicative case study is presented based on Dertimanis et al. (2016) work on mass-in-mass metamaterials designed to mitigate seismic waves and protect civil engineering structures. According to their publication, three (3) different bands are studied; the first one is between 0.5 – 1.5 Hz, the second one between 1.0 – 2.5 Hz, and the third one between 2.0 – 5.0 Hz. By assuming that the external

mass is m_L =1Mgr, the required resonating mass (m_R) and stiffness (k_R) of the resonator can be estimated from Eq. (8-8) (a), (b). Table 8-1 summarizes the derived values.

Table 8-1: Unit-cell's structural parameters for the three bandgap scenarios of the study.

Scenario	Band thresholds		Parameters		
	$f_L\ [Hz]$	$f_H [Hz]$	$m_L [Mgr]$	$m_R [Mgr]$	$k_R\ [kN/m]$
1	0.5	1.5	1.0	8.0	78.96
2	1.0	2.5	1.0	5.25	207.26
3	2	5	1.0	99.0	829.05

8.4.1 Effect of amplification in bandgap formation and Frequency response

Aiming to study the effect of the DDA amplification mechanism on the band structure and frequency response, the present investigation focuses on scenario 2 (Table 8-1) and $k_L / k_R = 1$. Herein, the band structure and the frequency response (FRF) of the undamped lattice are calculated. The baseline configuration (simple LRM) is subsequently compared with the model that incorporates the DDA. The dispersion curves in Figure 8-4 indicate that the inclusion of the amplification mechanism increases the width of the bandgap, which derives from a drop of the acoustic branch. On the other hand, the optical branch remains unchanged. The frequency response displays that in the very low-frequency region, below 1.0 Hz, the whole curve of the LRM with the DDA is shifted downwards compared to the LRM without the DDA. As expected, the attenuation characteristics are improved as the angle φ of the DDA increases. The resonances of the structural modes before the bandgap for the case of the LRM without the DDA, are replaced with a subband in the very low-frequency region.

The main drawback of the DDA beneficial effect is the reduction of the depth of the bandgap without however, a significant compromise of the overall performance of the metamaterial. The DDA is a mechanism that amplifies the effective oscillating mass of the LRM. This inertia increase of the unit-cell's resonating mass leads to increase of the bandgap width followed, however, by a reduced decay of the frequency response function within the generated bandgap. Similar reduction of the frequency response decay is observed to conventional LRMs as the resonating mass proportionally increases.

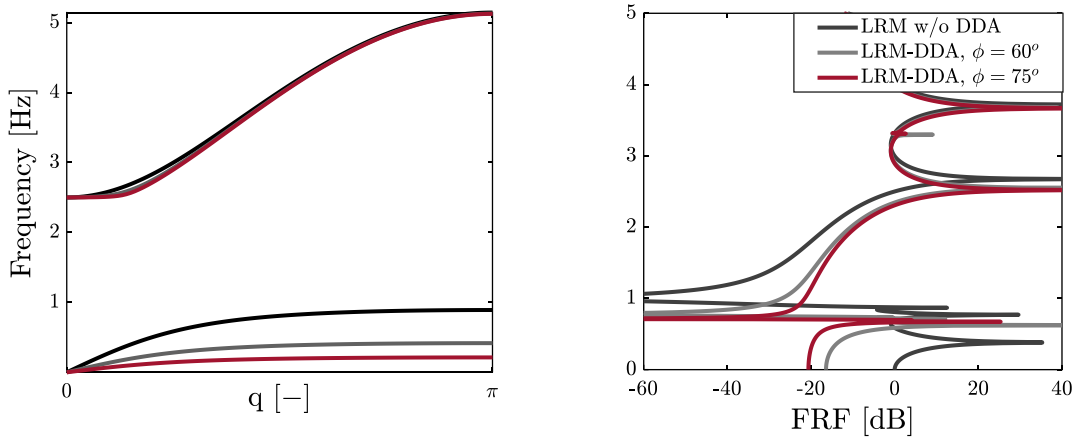

Figure 8-4: (left) Dispersion curves and (right) frequency response of the undamped finite lattice for m_L=1Mgr, m_R=5.25 Mgr, k_L/k_R=1 and N= 4 unit-cells.

8.4.2 Effect of the Number of Unit-Cells

As a following step, the effect of the number of unit-cells on the overall performance of the periodic metamaterial is investigated. Figure 8-5 illustrates the effect of the number of cells on the associated FRFs, for the considered undamped case. It is clear that the attenuation of the signal within the bandgap frequency range increases as the number of employed unit-cells is higher. In this analysis, for the sake of comparison, the total mass and stiffness of the studied undamped lattice is retained stable while the number of unit-cells increases.

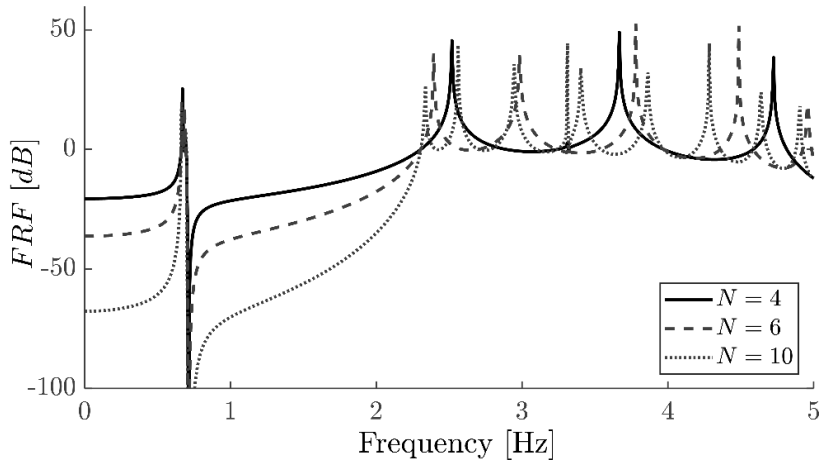

Figure 8-5: Frequency response (FRF) of the undamped finite lattice for the first band and k_L/k_R=1, and amplifier angle φ=75º for different number of unit-cells.

For higher number of unit-cells, the bandgap depth increases while at the same time, a marginal effect on the high-frequency behavior of the system is observed. For N= 4, the maximum bandgap depth

reaches -40dB, yet for more than N=10 units, the metamaterial surpasses -100dB bandgap depth. This increase in bandgap depth is also observed in the very low-frequency subband.

8.4.3 Parametric analysis

A parametric analysis is conducted for three different stiffness ratios k_L / k_R (external to internal spring stiffness), based on the scenarios summarized in Table 8-1.Figure 8-6 presents the dispersion curves for the studied bandgaps and stiffness ratios for the case without DDA and for two amplifier angles, namely 60° and 75° It is shown that the external stiffness k_L does not significantly influence the frequency band, but affects the behavior of the dispersion curves, mainly the optical branch.

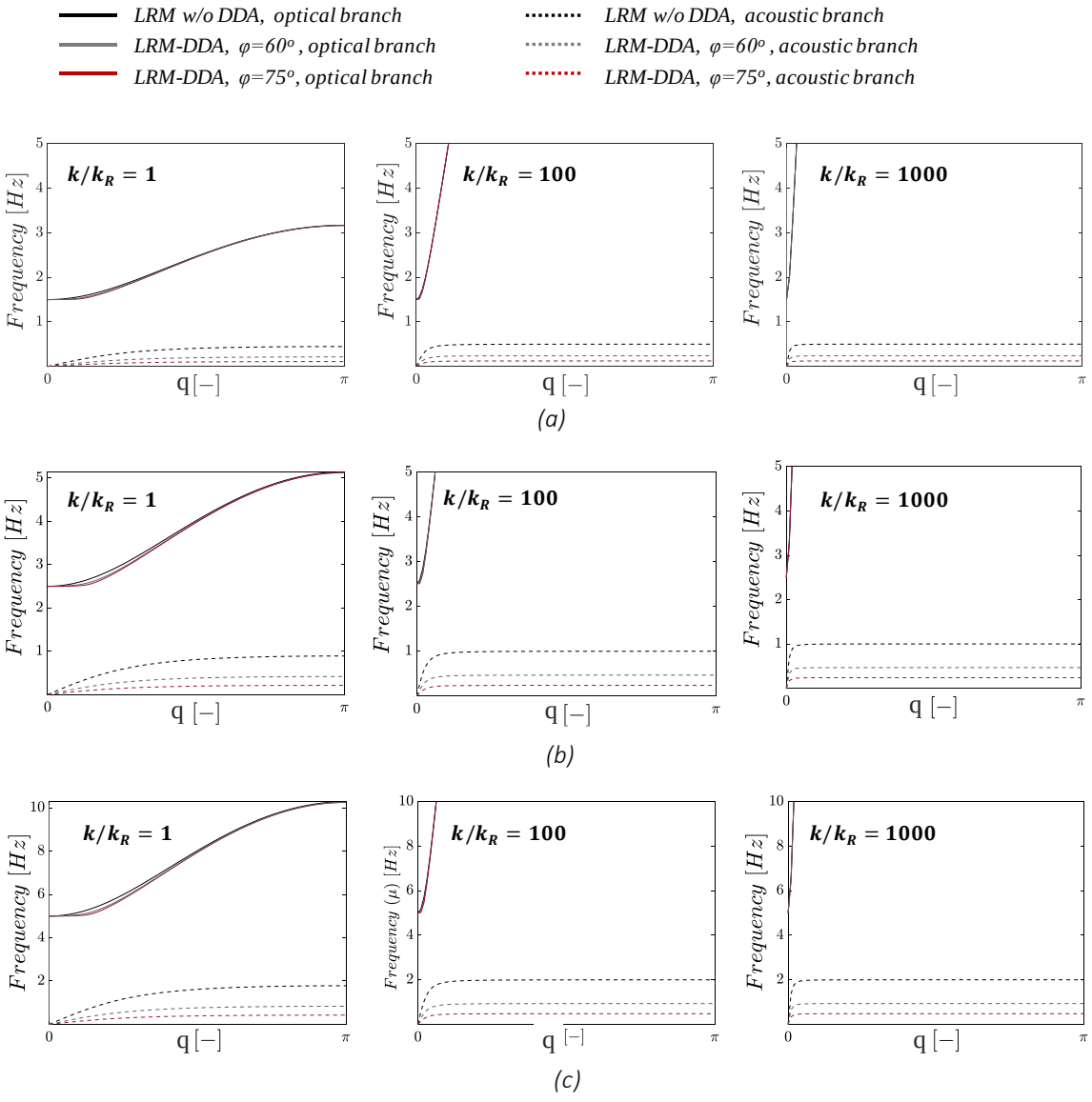

Figure 8-6: Dispersion curves for data of Table 1 and for three stiffness ratios. The simple LRM is compared with the LRM-DDA with φ=60° and 75 (a) first band; (b) second band; (c) third band.

For instance, Figure 8-6 (a) depicts the dispersion curves for case 1. It is observed that for a specific DDA angle the frequency gap remains essentially unaltered, while at the same time, the optical branch reaches higher frequencies as the stiffness ratio increases due to the significant change of the optical mode. This performance is better reflected in the behavior of the finite lattices.

In order to examine in more detail the effect of the amplifier angle compared to the bandgap characteristics of the studied cases, the normalized bandwidth for all the cases and angles is plotted in Figure 8-7. This is defined as:

$$b_w = \left(f_H - f_L \right) / f_{av}, \quad f_{av} = \left(f_H + f_L \right) / 2 \tag{8-17}$$

where f_L and f_H correspond to the lower and upper bandgap limits, respectively, and f_{av} is the mid-gap frequency.

It is illustrated that for large amplifier angles (φ), all cases show a similar normalized bandwidth (b_w) size; however, there are differences in the performance of the metamaterial in the case of smaller angles. For example, the analysis with the parameters of scenario 1 (black line) and $k_L / k_R = 1$ (continuous line) displays the most significant normalized bandwidths when small amplifier angles (φ) are considered; when compared with the case where a larger stiffness ratio is utilized k_L / k_R=100 or 1000 the arrangement with $k_L / k_R = 1$ indicates a better performance. In addition, when a stiffness ratio $k_L / k_R > 100$ is applied, there is no change in the gap size (b_w); in this case, the normalized bandwidth is only a function of the amplifier's angle. In this study, the amplifiers' angle has been indicatively selected as φ=60° and 75°, respectively. The selection of these relatively large angles has been made to showcase the extraordinary capabilities of the mechanism.

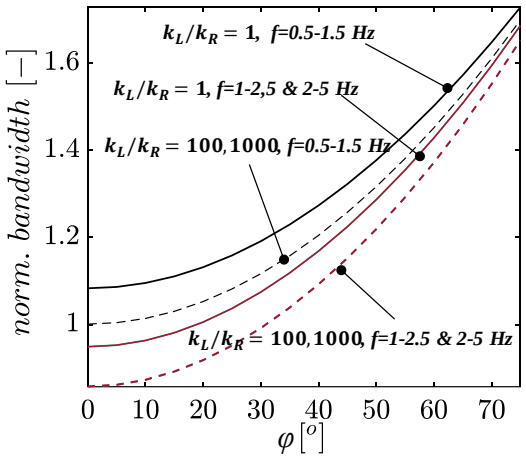

Figure 8-7: Normalized bandgap width as a function of the amplifier's angle.

Figure 8-8 illustrates the frequency response functions (FRF) that correspond to the dispersion curves of Figure 8-6. The specific $FRFs$ refer to a structure with four (4) unit-cells, while again three (3) different cases are compared: without DDA, with DDA of as φ=60°, and with DDA of as φ = 75°. For every case three (3) stiffness ratios $\left(k_L / k_R\right)$ are studied. It is clearly observed that the lower the stiffness ratio is, the more profound the bandgap formation is, and the beneficial effects of the DDA are highlighted. On the contrary, for the stiffness ratio case of $k_L / k_R > 100$, the bandgaps hardly appear and the DDA cannot significantly improve the performance of the lattice, as the natural frequencies of the structure are shifted higher. These results indicate that the normalized bandgap width as a metric, although it may provide a valuable indication of the metamaterial effectiveness, may be deceptive and should be used in conjunction with the frequency response of the structure. In conclusion, the performance of such unit-cells is heavily affected by the stiffness ratio between the inner and the outer springs of the periodic structure and high values should be avoided in the design.

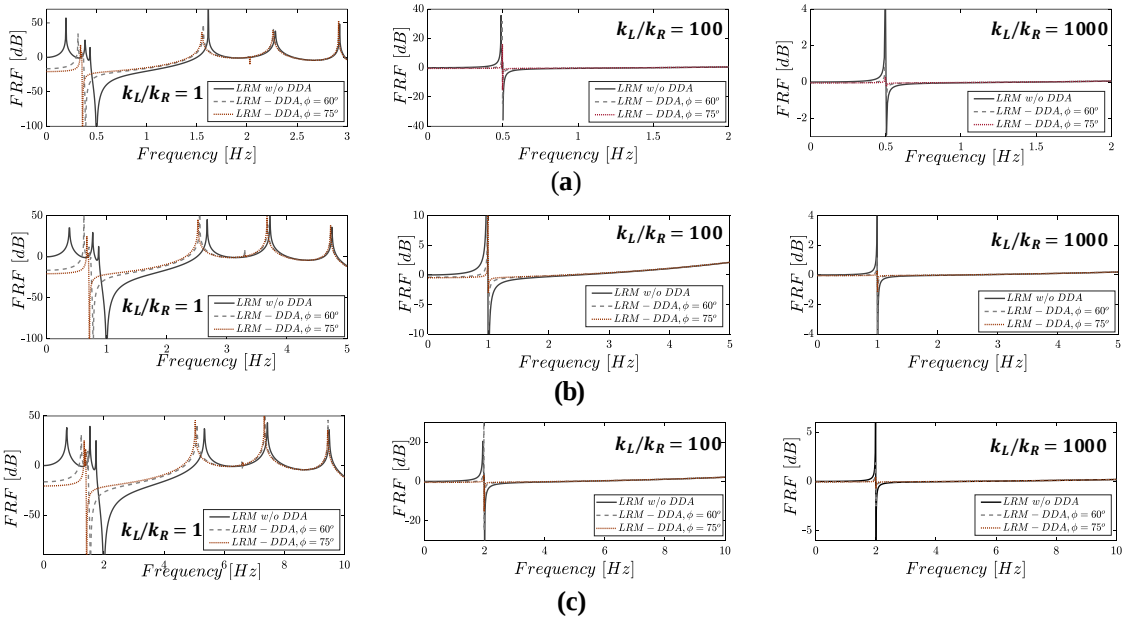

Figure 8-8: FRF of the far-right external mass of the finite lattice for N=4 unit-cells and for three stiffness ratios (a) 1st band (b) 2nd band (c) 3rd band

8.5 Conceptual Design of a metabarrier

Taking into account the initial investigation, a fundamental conceptual design for earthquake mitigation in the form of earthquake-proof seismic metabarriers (Casablanca et al., 2018; Krödel et al., 2015; Miniaci et al., 2016; Palermo et al., 2018; Zaccherini et al., 2020) is proposed. These barriers should be compact, lightweight, and their installation and manufacturing should be feasible in order to comprise

a realistic solution. The external and internal masses m_L and m_R respectively, should be rigid enough to behave similarly to the theoretical mass-in-mass model, and the selected number of unit-cells should be large enough to reveal the properties of the periodic structure.

Figure 8-9 displays a potential arrangement of the proposed system. The locally resonant unit-cells are embedded into the ground in a radial layout, such that the barriers enclose the structures of interest. In the case seismic excitation occurs, the barrier filters out the low-frequency content of the wave by absorbing the seismic energy internally and hence, mitigating the excitation. It is essential to note that due to its geometry, the proposed metabarrier alignment is suitable to protect structures against surface waves (Datta, 2010), which are known for their detrimental effect on man-made structures due to their high amplitude low-frequency components (Anderson, 1990). Mitigation of seismic body waves (S and P waves) is not part of the present study and design concept.

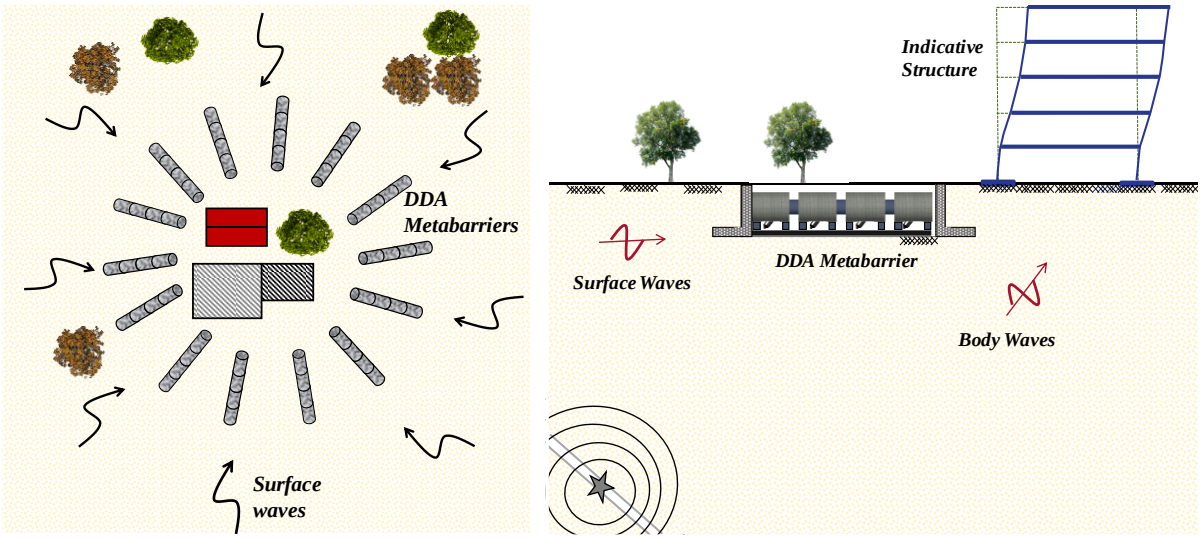

(a) (b)

Figure 8-9: Schematic representation of (a) the DDA metabarrier radial layout in plan-view and (b) the typical cross-section of the installation.

Under this perspective, the device under investigation is presented in Figure 8-10. A reinforced concrete hollow cylindrical section comprises the external mass (m_L) of the unit-cell configuration and a steel cylindrical section the mass of the resonating feature (m_R). The model springs can be realized by some type of elastomeric - rubber material of stiffness equivalent to the theoretical model, which can be reinforced appropriately depending on stiffness and strength requirements. The DDA mechanism can be realized by a simple rigid beam (potentially a robust steel beam) attached to a rigid foundation. The depicted conceptual design comprises only one row of 4 unit-cells and is equivalent to the one-

dimensional chain of the locally resonant units. Nonetheless, the design can be further elaborated by adding more rows and unit-cells to improve the device's performance.

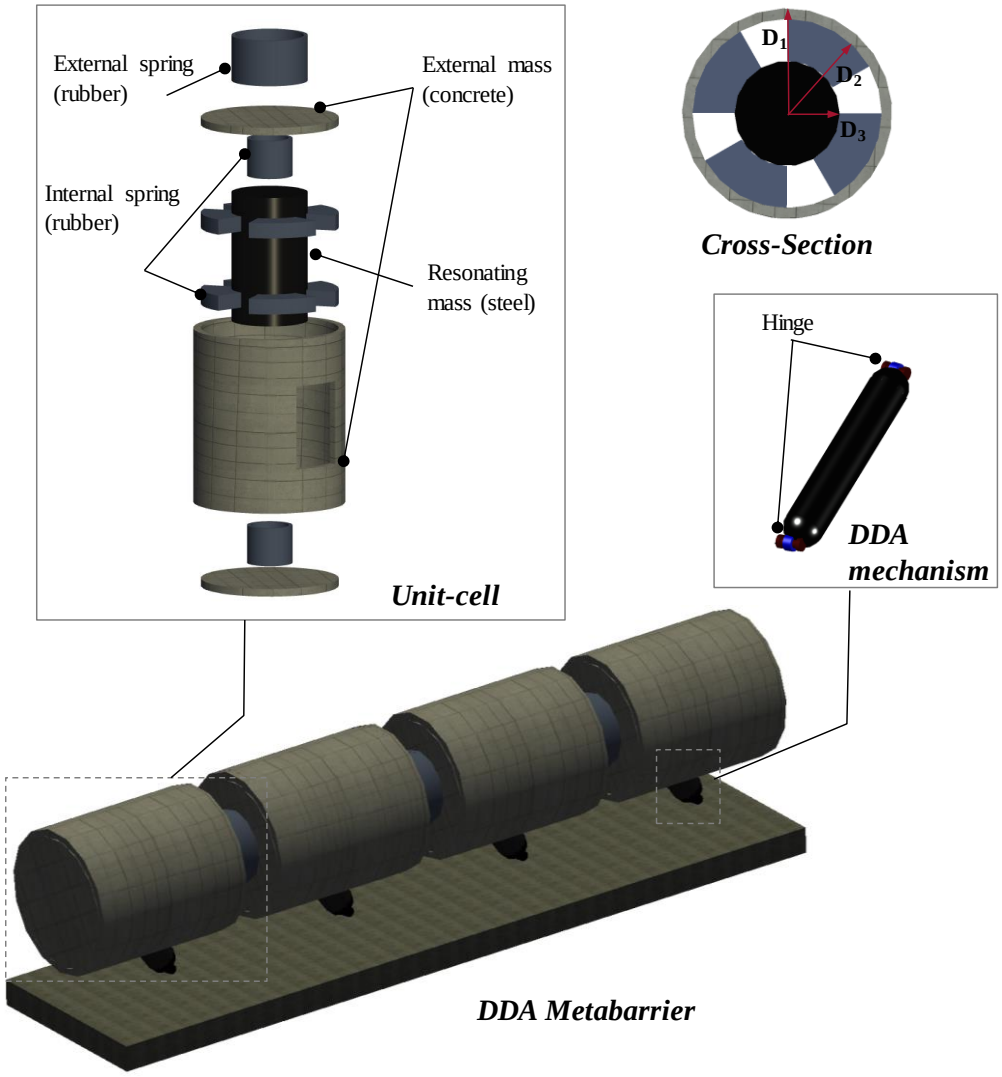

Figure 8-10: Schematic representation of the proposed metabarrier structure with Dynamic Directional Amplifier (DDA) for mitigation of seismic excitation.

8.5.1 Dimensioning

Aiming to quantify the material parameters of the unit-cell, a simple iterative process is followed. Initially, the limits of the frequency bandgap, namely f_L and f_H, are selected, together with the magnitude of the external mass (m_L). As a following step, Eq. (8-8) (a) and (b) are employed to estimate the required design parameters. Based on the material properties of lightweight concrete and steel, an initial geometry (length and radius for each cylindrical section) is specified, such that the required unit-cell masses are attained.

For the case of the internal and external spring properties (k_L and k_R) of the mass-in-mass structure, common rubber materials like chloroprene rubbers with carbon additives may be adopted, as they demonstrate the desired stiffness properties. The stiffness calculation of the material should consider the required (and also allowable due to the geometry limits of the structure) dimensions of the rubber in order to achieve the desired stiffness of the k_L and k_R elements. The compressive stiffness of the rubber pad is calculated as follows:

$$k_{comp} = \frac{E_{rubber}\, A}{h} \tag{8-18}$$

where E_{rubber} is the elastic Young's Modulus of the rubber material, A is the area of the rubber and h its height.

Obviously, the calculation requires the knowledge of the elastic vertical stiffness modulus E_{rubber}, provided by relevant stress-strain tests of the material in question. For the purpose of this indicative design, the hyper-elastic properties of rubber are neglected; consequently, the calculated value from Eq. (8-18) is an approximation that can be used as a starting point of the detailed dimensioning of the rubber pads. We remark that the elastic connections can also be realized with conventional metal springs, leaf springs, truss-like springs, or compliant structures that provide the required stiffness.

Based on the rubber properties and the initially selected dimensions of the unit-cell, the outer and inner diameters of the pad are selected such that the elastomer fits to the unit. In case that the required stiffness and/or masses cannot be achieved, the dimensions of the external and resonating features are readjusted. This procedure is repeated until all the parameters correspond to the desired ones. By all means, a more optimized approach can be programmed that can minimize the required materials and maximize the performance of the metastructure; however, this optimization falls out of the scope of the current contribution.

Table 8-2 displays a feasible set of design data, aiming to obtain the second bandgap, as described in section 8.4. The selected properties are based on the analogies presented in Table 8-1 that correspond to the analysis of the simple LRM configuration without the addition of the DDA mechanism. Therefore, by adopting the above properties, the DDA enhanced lattice should achieve the demanded bandgap and extend its filtering properties to lower frequencies.

Table 8-2: Indicative unit-cell design parameters of the metabarrier.

Theoretical parameters				
Parameters	value	units	Description	
f_L	1	Hz	Low bandgap frequency limit	
f_H	2.5	Hz	Upper bandgap frequency limit	
m_L	250	kg	External mass of each unit-cell	
m_R	1310	kg	Resonating mass of each unit-cell	
k_R	51.82	kN/m	Stiffness of the internal spring	
k_L	51.82	kN/m	Stiffness of the external spring	
Design parameters				
Parameters	value	units	Description	part
ρ_{conc}	1400	kg/m3	Lightweight concrete density	Reinforced concrete – external mass
D_1	1	m	External diameter of the concrete cylinder	
D_2	0.90	m	Internal diameter of the concrete cylinder	
L_{conc}	1.15	m	Length of concrete cylinder	
m_{conc}	241	kg	Mass of concrete part	
ρ_{steel}	7850	kg/m3	Steel density	Steel – resonating mass
D_3	0.5	m	Diameter of the steel cylinder	
L_{steel}	0.85	m	Length of steel cylinder	
m_{steel}	1310	kg	Mass of steel part	
E_{rubber}	1800	kPa	Rubber Young's modulus	Rubber – internal and external springs
t_{rubber}	0.25	m	Height of internal element's rubber	
A_{rubber}	7.85*10-3	m2	Area of internal element's rubber	
k_{rubber}	56.55	kN/m	Stiffness of rubber element	
φ	75	°	Amplifier angle	DDA

8.5.2 FE Numerical Investigation of the DDA Metabarrier

Aiming to validate the performance of the designed metabarrier, the finite element code ABAQUS® is employed for a series of frequency response and seismic time-history analyses. The parameters of the model were formulated by adopting the material values of the conceptual design, as indicated in Table 8-2 of section 8.5.1. For the purposes of this study, a model with N=4 unit-cells is adopted, and its filtering properties are subsequently investigated. The design follows the second scenario bandgap where f_L =1 and f_H =2.5 Hz, respectively.

Three-dimensional FE modeling is used to realistically capture the exact geometry of the design, its kinematic boundaries, as well as the appropriate stiffness properties of the proposed materials of the barrier. Linear elastic spring elements and dashpots model the vertical stiffness (K_{rubber}) and damping (

C_{rubber}) of the rubber elements attached between the masses (internal and external) of the periodic structure. All parts are discretized by 20-node linear-elastic, quadratic solid brick elements, and tie constraints are assigned between the rubber-concrete and the rubber-steel interface.

A frequency response analysis is subsequently undertaken to derive the transmission curve of this finite length metabarrier; analysis is conducted as a frequency sweep by applying a harmonic excitation at a series of different frequencies and recording the response. The excitation is applied on the first unit-cell and the response of the outer mass of the last unit (end of the lattice) is measured. Figure 8-11 depicts the FRF results for the case of a metabarrier with and without the DDA amplifier. As expected from the analytical derivation described in section 8.4.1 of this study, results indicate the superiority of the system with the DDA within the frequency domain, especially within the low-frequency region. It is essential to note that the bandgap, due to the addition of the DDA, is extended below the design expectations of the scenario 2 bandgap (without the DDA) and appears to be promising in the mitigation of lower excitation frequencies, well below 1 Hz.

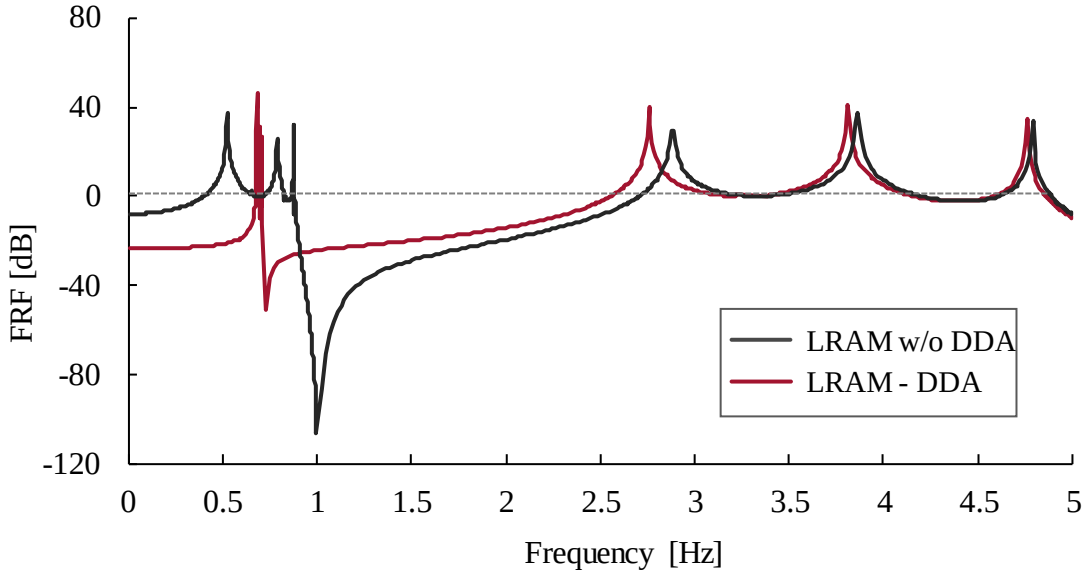

Figure 8-11: Frequency response (FRF) of the metabarrier with and without the DDA amplifier, as calculated from the FE numerical analyses.

As a following step, the performance of the DDA metabarrier concept under earthquake excitation is investigated. Various seismic motions corresponding to different hazard levels and frequencies are employed, and time-history analyses are performed to study the potential seismic mitigation properties of this DDA enhanced metabarrier. An artificial accelerogram with an acceleration response spectrum compatible with the Eurocode 8 design response spectrum is generated using the SeismoArtif Software (2018) and adopted as a baseline for the time-history analyses. For the purposes of this study, the Artificial Accelerogram is designed in accordance with EC8, incorporating the following seismic

properties: ground type C, spectral peak ground acceleration 0.36 g, spectrum type I and importance class II. In addition, the response of the design is investigated to real earthquake input, for the cases of Aegion (1995) and Lixouri (2014) earthquakes. The seismic motions are simplistically applied as horizontal excitation directly on the first unit-cell and the acceleration of the last unit-cell is calculated as an output.

Figure 8-12 presents the response of the DDA enhanced finite lattice, with a relatively low damping ratio equal to ζ =3%, subjected to the aforementioned artificial and real seismic motions. The spectral content and amplitude of the selected excitations are rich, containing frequencies that are outside the bandgaps generated by the designed DDA metabarrier, presented in Figure 8-11. This consequently leads to a diverse filtering behavior of the metabarrier, depending on the frequency components of each accelerogram. Figure 8-12 (a) – (c) present the filtered acceleration time-histories (measured at the end of the lattice) along with the original applied accelerograms. Results indicate a significant reduction of accelerations within the bandgap regime and a corresponding decrease of the maximum acceleration values. Aiming to better visualize the filtering behavior of the metabarrier, the elastic response spectra that emerge from both the original and filtered acceleration time-histories were calculated and presented in Figure 8-12 (d) – (f). As expected from the FRF (Figure 8-11), frequencies that coincide with the resonance of the lattice are amplified. However, results show substantial attenuation of the excitation frequencies below 2.5 Hz, indicating the beneficial role of the barrier for the protection of relatively high period structures.

In order to assess the feasibility of the proposed metabarrier dimensions, an assessment of the maximum deformations of the internal resonating masses has been undertaken. The displacements (u, v) of the resonating masses as well as the corresponding rotation (θ) of the DDA mechanism were measured. The analyses results indicated that for all selected seismic excitations these deformations are relatively small. Specifically, the maximum displacement u,v is less than 2.5cm, while the maximum DDA rotation theta is less than 1 degree. It is clear that these deformation values can be easily accommodated by the proposed conceptual metabarrier design (Table 8-2).

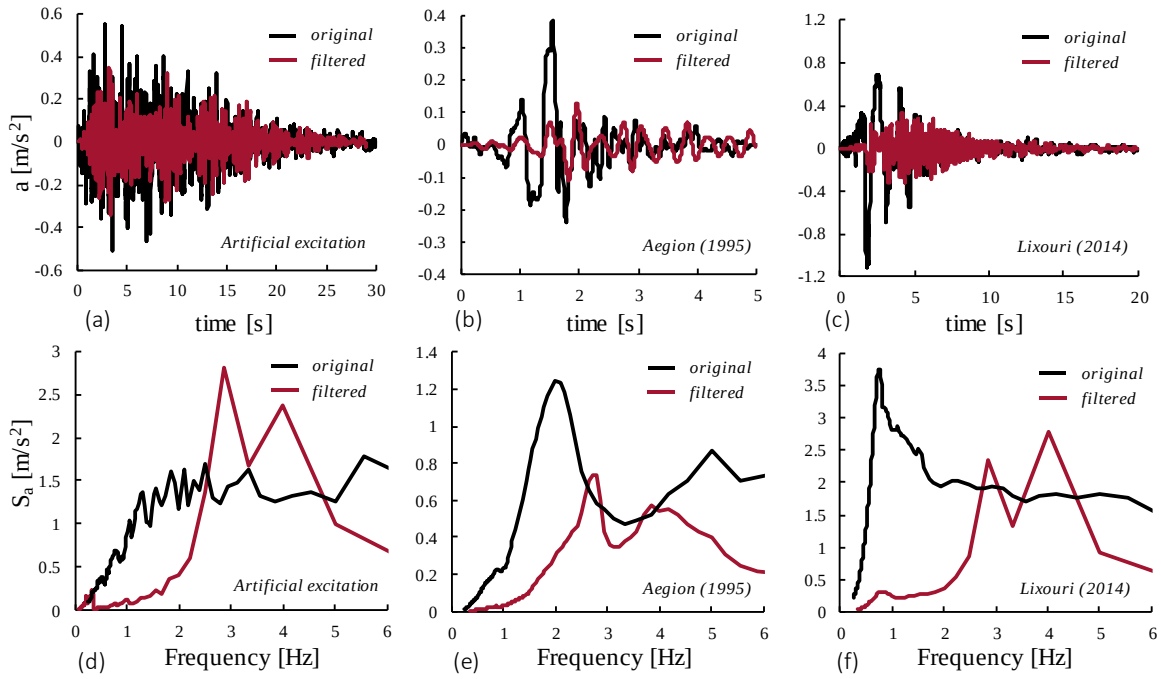

Figure 8-12: Response of the DDA metabarrier to seismic excitation: (a) EC8 compatible artificial excitation, (b) Aegion, 1995 earthquake, (c) Lixouri, 2014 earthquake and (d) – (f) corresponding acceleration frequency response spectra for both the original and filtered motions.

8.6 Concluding Remarks

In conclusion, this study demonstrates the theoretical framework of a novel locally resonant metamaterial consisting of dynamically amplified resonating masses. The major innovation of the application lies in the simple geometry of the proposed system. The dynamic directional amplification (DDA) mechanism is achieved with a rigid link that improves inertia and damping on the desired direction of motion, by simply coupling the kinematic DoFs of the resonating mass of the metamaterial lattice.

It is demonstrated that using dynamic amplification and a moderate number of unit-cells, relatively deep bandgaps at low frequencies can be obtained. By exploiting the dynamic mass of the proposed mass-in-mass periodic structure, it is illustrated that better dispersion properties are obtained compared to the conventional locally resonant metamaterials of equivalent structure. Thus, significant filtering characteristics are achieved while reducing the large parasitic resonating masses. The main drawback of the DDA beneficial effects is the reduction of the maximum depth of the bandgap, without however, a significant compromise of the overall performance of the metamaterial. Another potential disadvantage of the mechanism is the diversion of the resonating mass movement perpendicular to the

direction of the external applied action; this leads to mass movement in both axes (2D movement in the horizontal and vertical axis) that needs to be accommodated depending on the application and design of the lattice structure.

An indicative implementation of the DDA enhanced concept as a seismic protection mechanism in the form of a metabarrier is subsequently proposed. A conceptual design paradigm is numerically analyzed by employing time-history analyses and comprises a priory proof of concept of a simple, feasible design that can be exploited as a baseline for future, more detailed prototypes. Results indicated the beneficial role of the device and DDA mechanism, hence placing the concept as a potential alternative to existing seismic isolation concepts and structural protection devices.

Based on all the above observations, the proposed framework may be incorporated in further applications such as mechanical filters, sound and vibration isolators, or acoustic panels, as it provided promising outcomes and information towards the development of acoustic metamaterial designs, able to offer low-frequency isolation and vibration control.

9 EXPERIMENTAL VALIDATION OF THE VIBRATION-ATTENUATION PROPERTIES OF DDA ENHANCED PHONONIC & LOCALLY RESONANT METAMATERIAL DESIGNS

9.1 Background

In this chapter, for the purpose of validation, the dynamic behavior of the suggested DDA enhanced phononic and locally resonant metamaterial configurations is experimentally investigated. In particular, the metamaterial models are built using LEGO® components and are tested under dynamic loading.

Recently, several architected metamaterial structures with inertial amplification mechanisms (Mazzotti et al., 2023; Muhammad et al., 2020; Zeng et al., 2022) or negative stiffness properties (Lin et al., 2023; Zhou et al., 2021) have been manufactured and experimentally tested. Yilmaz and his research team (Acar & Yilmaz, 2013; Taniker & Yilmaz, 2015, 2017; Yuksel & Yilmaz, 2015, 2020) first introduced designs of periodic structures with embedded inertial amplification mechanisms and conducted a series of experiments in compliant periodic structures, 3D printed specimens, as well as samples manufactured by aluminum beams. Similarly, Bergamini (2019) and Zaccherini (2021) exploited chirality and tested 3D printed elements searching for large low-frequency bandgaps, while Chondrogiannis (2022) examined a geometrically nonlinear metamaterial constructed by LEGO® technic bricks. In general, several attempts have been accomplished by various researchers towards the experimental identification of bandgaps in phononic (D'Alessandro et al., 2016), locally resonant (An et al., 2019; Lin et al., 2021), as well as in auxetic structures (Fischer et al., 2020).

In this chapter, inspired by the benefits induced by the insertion of DDA mechanisms within the structure, one-dimensional inertial amplified lattices are designed for the mitigation of low-frequency mechanical vibrations. To this end, four (4) different arrangements are constructed and tested; a conventional phononic metamaterial chain, a DDA enhanced phononic metamaterial chain, a conventional LR metamaterial chain and a DDA enhanced LR metamaterial chain. Results validate the concept of DDA enhanced structures and prove that the proposed metamaterials can be adequately described by the developed analytical and numerical models. Lastly, the established prototypes indicate that realistic full-scale designs are feasible and suitable for a wide range of applications, i.e., seismic mitigation, vibration isolation, acoustic mitigation etc.

9.2 Design of the Experimental Devices

Within the framework of this research work, two (2) metamaterial concepts are considered using two (2) different configurations; the first one featuring a phononic lattice and the second one a lattice comprised of locally resonant unit-cells. Apart from the extension springs that are custom made, the internal resonating mass m_R of the LR metamaterial that is realized using steel washers and the longitudinal guides that are made of aluminum to increase vertical and lateral rigidity, most of the metamaterial components are assembled using LEGO® parts. The selection of a LEGO® technic assembly is adopted due to the design simplicity, cost and accuracy merits compared to alternatives such as steel structures and 3D printed elements. Both studied devices were initially conceptualized and then drawn in Lego Digital Designer where different arrangements can be easily examined before assembling the actual physical models. Herein, four (4) unit-cells were deemed adequate to capture the bandgap properties of the phononic lattice, while only three (3) were required in case of the LR lattice. Previous studies on various linear and nonlinear metamaterial designs (Chondrogiannis et al., 2022; Colombi et al., 2020; Martakis et al., 2021) suggest that even for a reduced number of unit-cells (two–three) a substantial bandgap can be generated, leading to noticeable motion reduction. This selection is essential for a realistic experimental implementation, where dimensions need to remain limited.

Figure 9-1 (a) shows the schematic representation of the phononic lattice arrangement where the amplifier is located at the base of the mass m_D. A hinged connection is realized using the LEGO® technic parts and allows the link to freely rotate, while a fixed base is built to support independently the DDA mechanisms. The LR structure described in Figure 9-1 (b) is comprised of units with similar to the phononic lattice dimensions and an independent structure that supports the proposed amplifiers. These

illustrations include only the LEGO® parts omitting the extra steel parts such as springs, supports, weights etc.

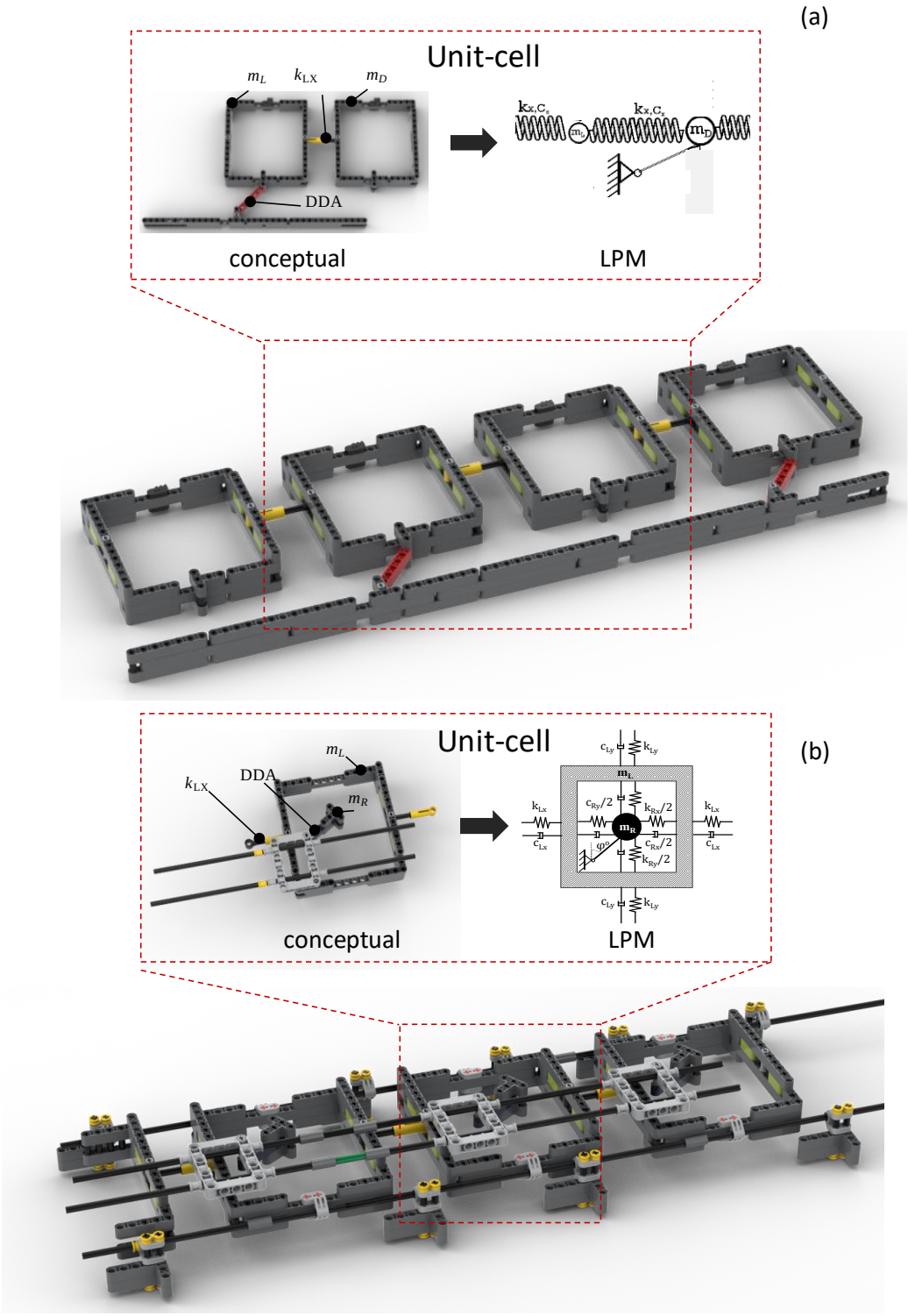

Figure 9-1: Illustration of the rendered LEGO®DDA enhanced (a) phononic (b) locally resonant metamaterial designs.

In both models the unit-cells are connected with an arrangement of springs. To ensure that these springs work properly in both compression and extension, two additional coils of stiffness $k_e/2$ are installed to the LEGO® linear spring of stiffness k_c to keep the latter in a prestressed state (Chondrogiannis et al., 2022), as illustrated in Figure 9-2.

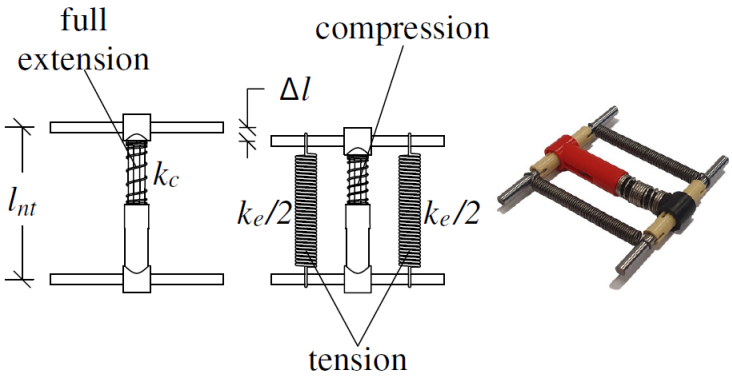

Figure 9-2: Assembly of the linear stiffness elements at rest: (left) original, (center) modified configuration, (right) physical assembly (Chondrogiannis et al., 2022).

The additional components shift the stable equilibrium position backwards by Δl. This allows the system to react equivalently in both the compression and extension states, in contrast to the original configuration, which is at full extension at its equilibrium position. The overall stiffness of the assembly k_n is therefore calculated as:

$$k_n = k_e + k_c \tag{9-1}$$

Table 9-1 summarizes the characteristics of the spring assemblies that are used in the models; these are the stiffness value k_n, as well as the individual stiffness of the extension spring (k_e) and compression spring (k_c).

Table 9-1: Stiffness characteristics of the experimentally tested springs.

category	*Extension spring* k_e [Nm^{-1}]	*Compression spring* k_c [Nm^{-1}]	*Spring Assembly* k_N [Nm^{-1}]
soft	80	320	480

The mass properties of the individual elements of the phononic metamaterial lattice are tabulated in

Table 9-2, while the mass properties of the LR lattice are given in

Table 9-3. Mass m_L is constructed by LEGO ® parts in both assemblies while mass m_D of the phononic lattice is adjusted to reach the required weight by installing supplementary steel weights; i.e., $m_D = m_L + m'$, where m' is the additional weight.

Table 9-2: Mass measurements for the individual parts of the experimental phononic models.

Element	*Mass (g)*
m_L	58
m_D	58
m'	150

Table 9-3: Mass measurements for the individual parts of the experimental LR models.

Element	*Mass (g)*
m_L	58
m_R	58

9.3 Description of the Setup

The configured experimental setup is presented in Figure 9-3 (a). An MB Modal 110 (MB Dynamics) electrodynamic shaker applies a one-dimensional (1D) horizontal input excitation. A timber board is mounted at the shaker's shaft on one side, to function as a shaking table, while longitudinal guides and bearings provide support, maintain the table in a levelled position, and limit parasitic vertical oscillations. A digital signal generator creates the harmonic sweep and a 2050E05 (modal shop INC) amplifier receives the produced signal and activates the shaker. Both sinusoidal inputs as well as sine sweeps can be generated by controlling the voltage signal of the shaker. This signal results to a nearly flat spectrum for a given frequency range, thus exciting uniformly the specified range.

Each metamaterial chain is installed at the shaking table. Longitudinal guides ensure that displacements develop primarily in the desired direction, while lubricant liquid minimizes the effect of friction between the guides and the support. Apart from this minimal inevitable friction, the cells are completely detached from the shaking table. The input is applied to the left end of the chain, where the support of the first cell is mounted to the shacking table, hence creating longitudinal waves to propagate within the lattice.

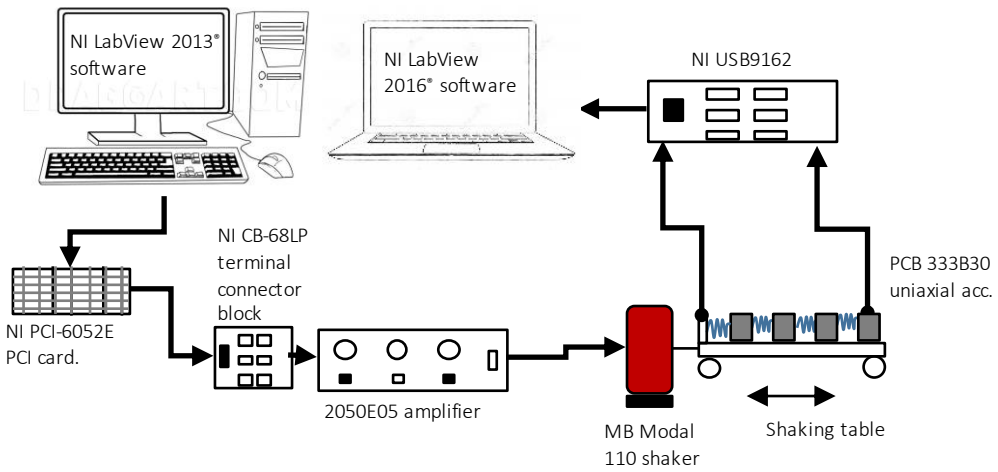

Figure 9-3: Schematic diagram of the experimental setup.

The dynamic response of the system is measured using uniaxial PCB 333B30 accelerometers with 10.2 $mV/m/s^2$ sensitivity and a sampling frequency of 2 kHz. The measuring locations include the last unit-cell, as well as the shaker input signal. The accelerometers are connected to the computer through an NI USB9162 card. The recording of the measurements is done via the NI LabView 2016® software, while the post-processing is carried out using in-house developed scripts on the MATLAB R2020b® software.

9.3.1 Phononic structures

Figure 9-4 illustrates the assembled phononic structure which serves as a baseline configuration to the enhanced phononic assembly. Washers have been added to increase the weight of m_D while four (4) unit-cells where deemed as the minimum number that can reveal bandgaps. The longitudinal guides ensure that the lattice moves only horizontally and any other parasitic movements are suppressed.

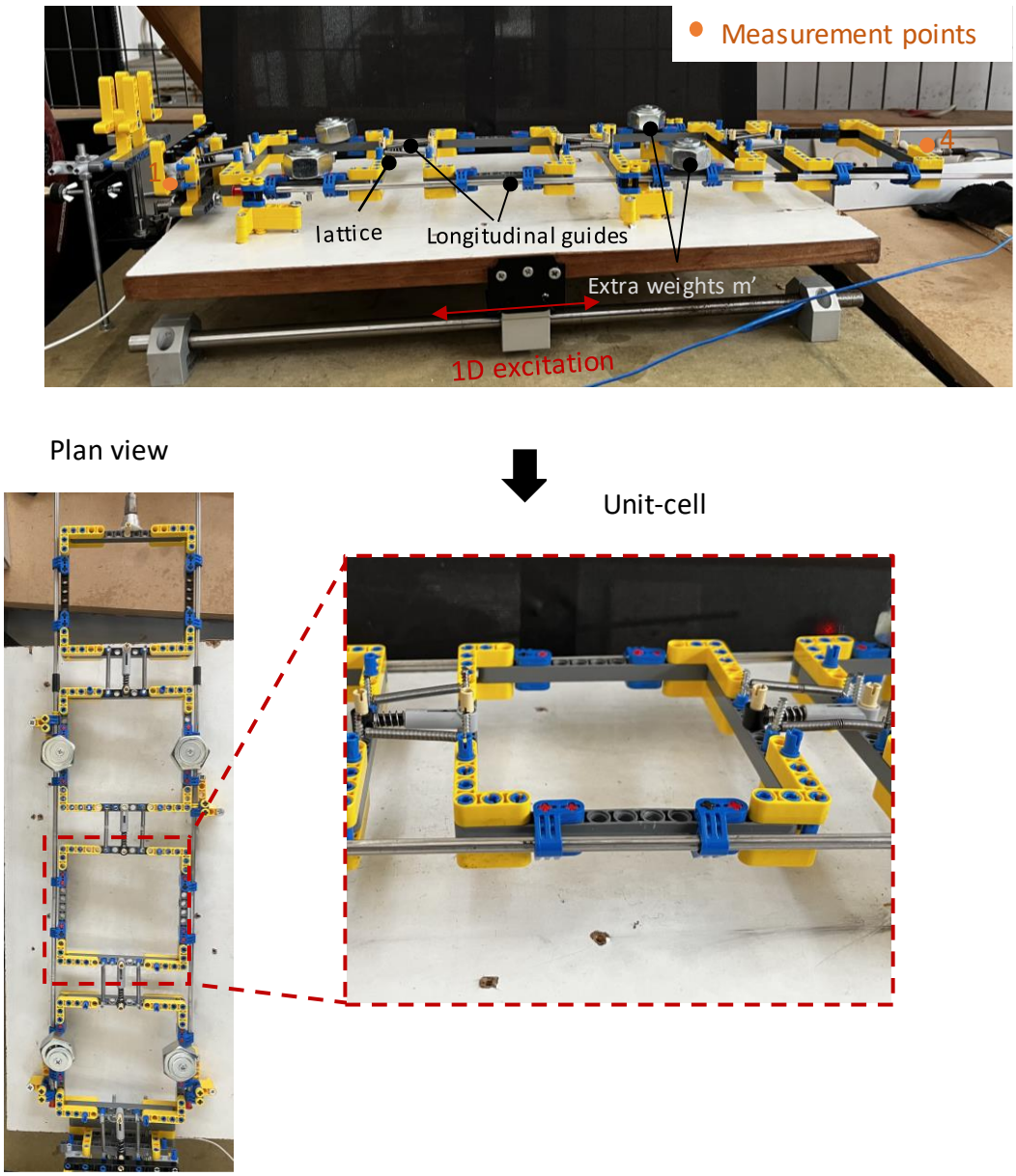

Figure 9-4: Overview of the LEGO® "conventional" phononic structure comprised of four (4) unit-cells.

The DDA enhanced lattice is presented in Figure 9-5. In this case the amplifiers are added to the units with the extra masses m' and an external LEGO® arrangement is erected in front of the shaking table. The links form an angle $\varphi \approx 60°$ with the units and longitudinal guides are added only to those units that are not connected with an amplifier, allowing in this way the others to rotate freely.

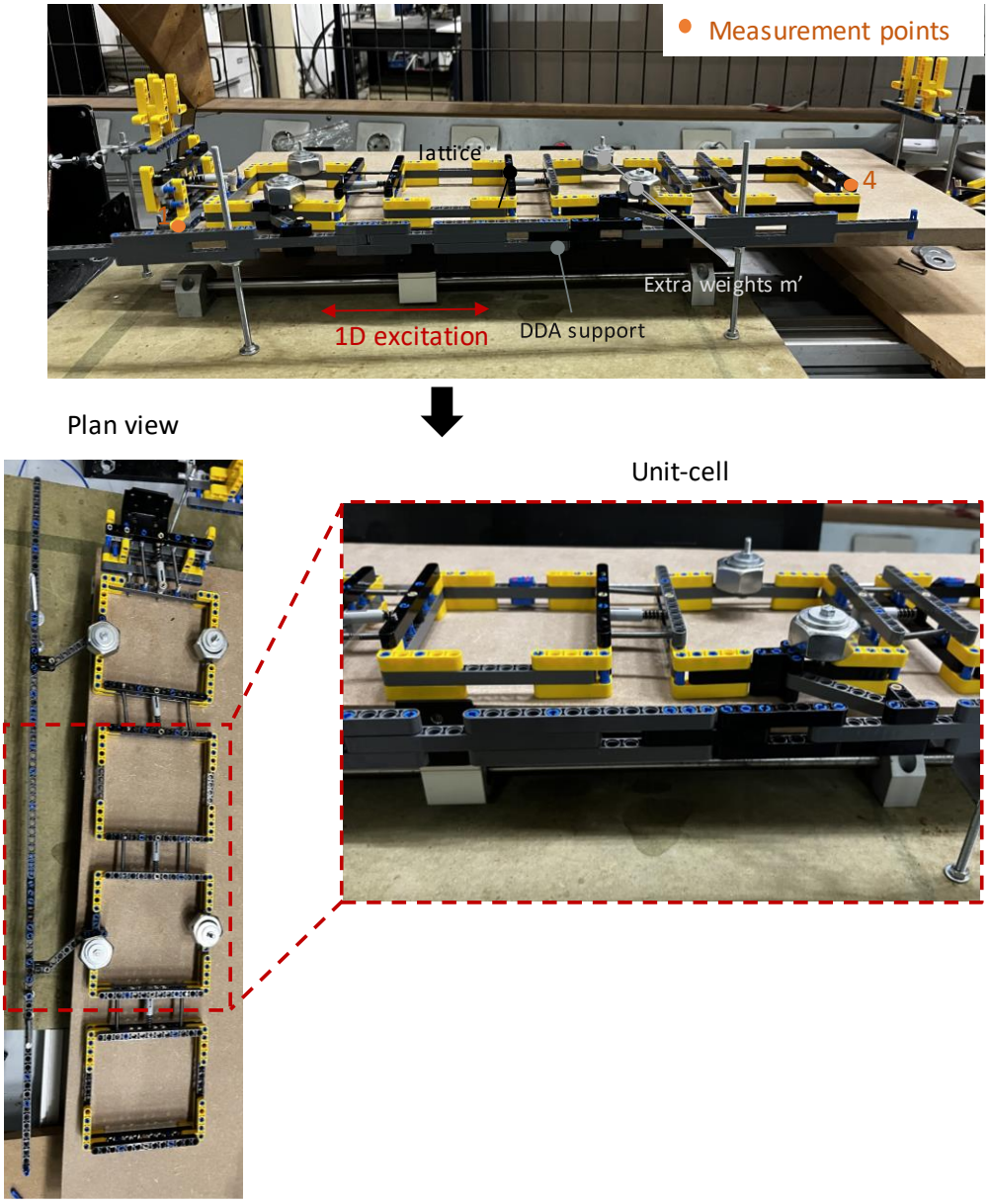

Figure 9-5: Overview of the LEGO® DDA enhanced phononic structure comprised of four (4) unit-cells.

9.3.2 Locally Resonant structures

Following the description of the phononic assemblies, the locally resonant metamaterial lattice is depicted in Figure 9-6. The proposed design is based on a mass-in-mass arrangement where the resonating mass m_R is connected with the external mass m_L through two extension springs. Once again, guides ensure the one-dimensional movement of the structure; however, herein a supplementary guide is added above the lattice to facilitate the longitudinal movement of the resonating masses and prohibit any transverse or rotational modes. Moreover, as already mentioned, in this case three (3) unit-cells can capture the anticipated attenuation zone, hence the fourth unit-cell is removed from the lattice.

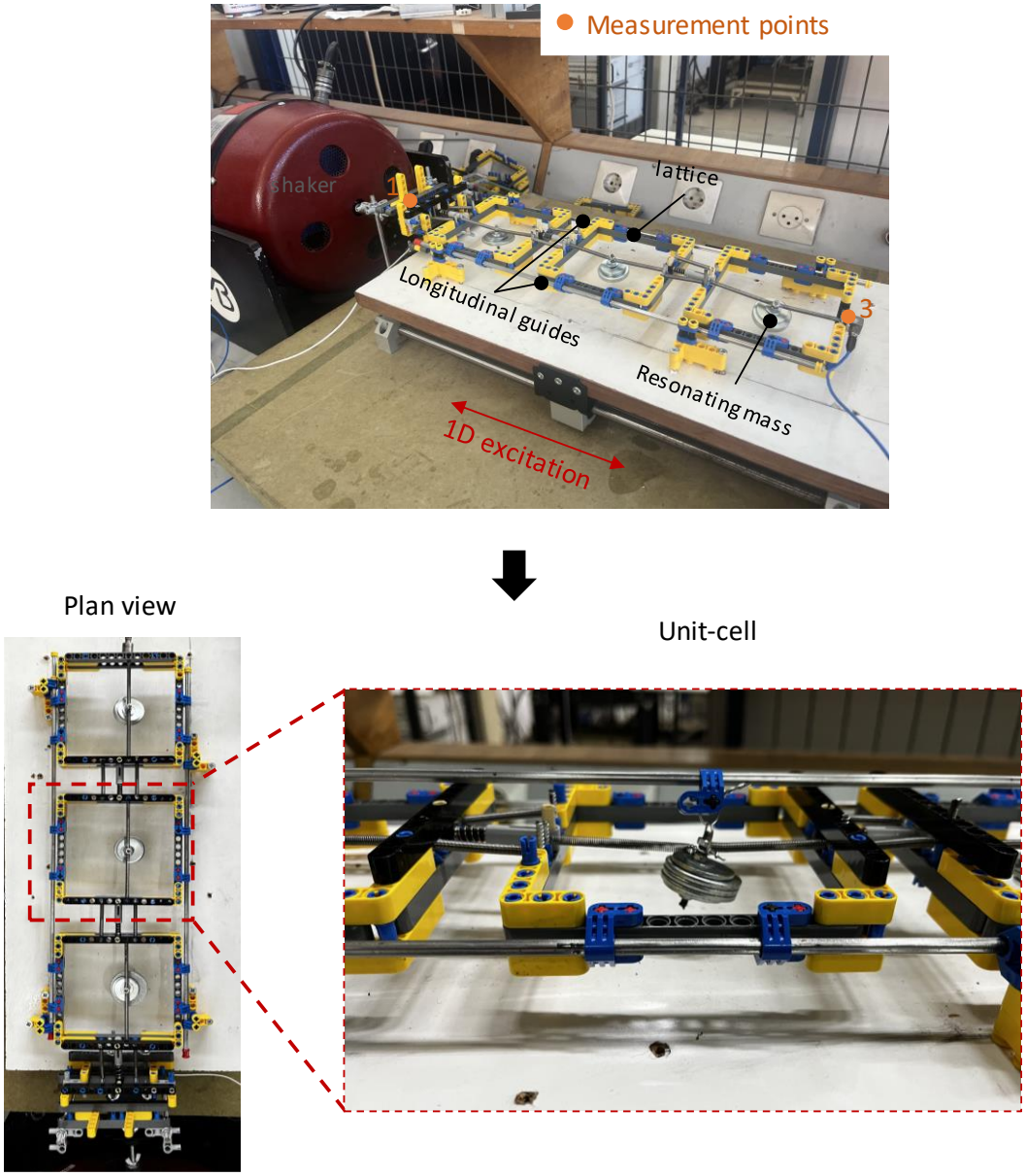

Figure 9-6: Overview of the LEGO® "conventional" locally resonant (LR) structure comprised of three (3) unit-cells.

Figure 9-7 depicts the DDA enhanced LR structure. A LEGO® assembly supports the amplifiers above the shaking table providing a steady ground to the hinged connections. The Amplifier's angle is selected as $\varphi \approx 55°$.

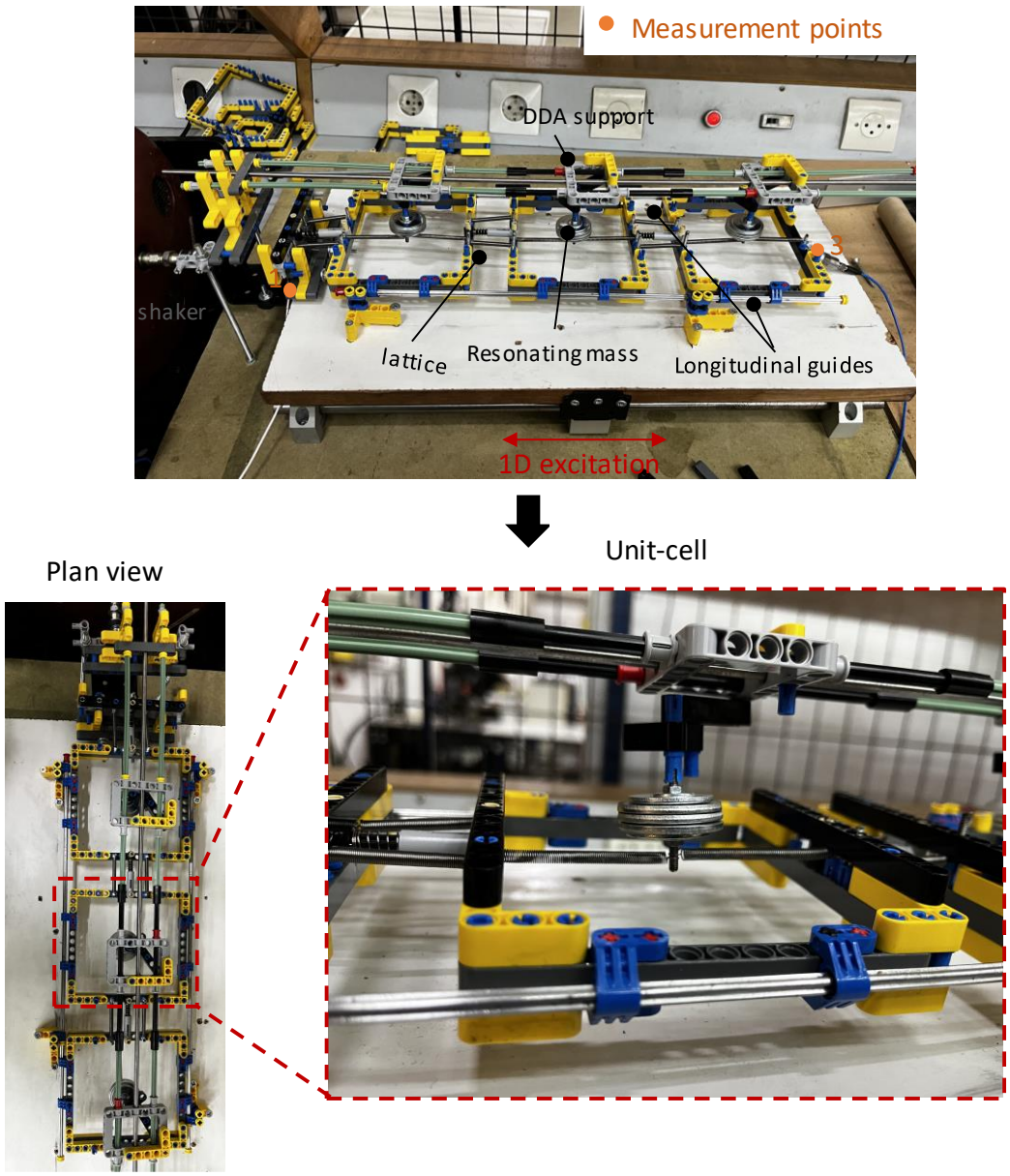

Figure 9-7: Overview of the LEGO® DDA enhanced Locally resonant (LR) structure comprised of three (3) unit-cells.

9.4 Experimental Results

This section discusses the obtained experimental results. The tests include inputs of sine-sweep excitation and validation through single-harmonic inputs. The acceleration measurements are carried out with small amplitude excitations to ensure that the metamaterial features a linear elastic behaviour. The experimental wave transmission spectrum is obtained as the ratio between the output and input spectral accelerations $\left\{\ddot{u}_{fin}^{out} / \ddot{u}_{1}^{in}\right\}$ using the FFT function and the efficiency of each metamaterial device is evaluated upon their attenuation capabilities. The attenuation zone of the tested metamaterial device

corresponds to the regions where the ratio of the frequency content between output and input falls below unity and is compared to the analytically predicted bandgaps.

9.4.1 Phononic structures

The analysis of the experimental results of the Phononic structures begins with the theoretical estimation of the dispersion curves. Figure 9-8 indicates the frequency range that an attenuation zone is expected from the experimental measurements before and after the addition of the amplifiers. The amplifiers improve the expected bandgap by 60%; the acoustic branch of the dispersion curves are expected to shift from 8.5 to 4.5 Hz. Then, a comparison is carried out in Figure 9-9 between the theoretically estimated dynamic response and the experimentally measured frequency response of the phononic lattice to identify the degree that the analytical model matches the experimental data.

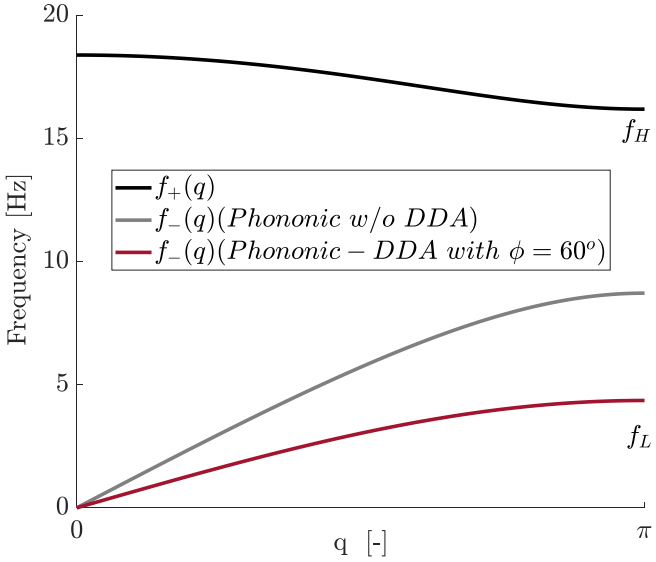

Figure 9-8: Expected theoretical dispersion curves of the phononic LEGO® technics assemblies.

It is obvious that only the acoustic part of the dispersion relation is explored, as the optical branch corresponds to much higher frequencies which are not studied herein. Therefore, in this low-frequency regime, only the opening frequency of the bandgap is spotted, where for lower values wave propagation is not prohibited and for higher ones attenuation is present. Furthermore, it is observed that the two curves show some differences in terms of the opening frequency of the attenuation zone and the resonance peak before, yet, the general dynamic performance of the metamaterial is captured and the experimental bandgap due to Bragg scattering is realised. At this point it should be mentioned that a minimal amount of damping ($\zeta = 5\%$) is prescribed arising from the developed friction between the guides and the units.

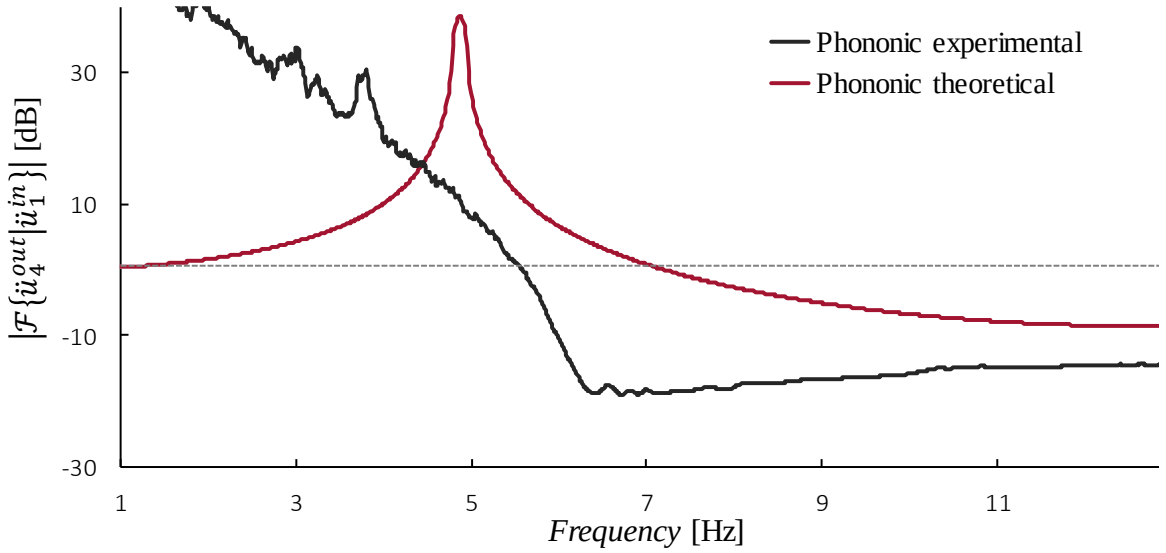

Figure 9-9: Comparison between the experimental and analytically estimated frequency response $\mathcal{F}\{\ddot{u}_4^{out}|\ddot{u}_1^{in}\}$ *for the four (4) unit-cell lattice of the phononic structure.*

It is interesting to compare the attenuation zone formed with the two types of cells; the simple phononic and the DDA enhanced. Figure 9-10 illustrates the experimental dynamic response of the two structures, where the enlargement of the attenuation zone is apparent after the inclusion of the DDA. As discussed, the upper limit of the bandgap has not been measured, nonetheless, the opening theoretical estimated frequencies are demonstrated by the shaded areas.

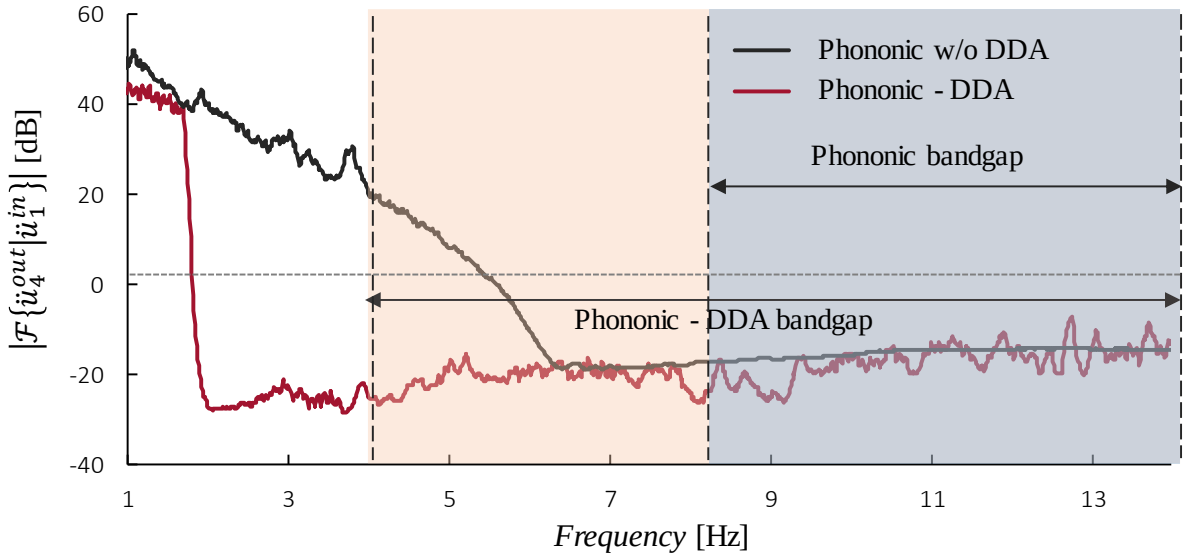

Figure 9-10: Frequency content of the response of the phononic lattice with and w/o the DDA $\left(\varphi = 60^{\circ}\right)$ *for a four (4) unit-cell lattice. The maximum acceleration of each unit* p *is denoted as max* $\ddot{u}_p^L$.

Comparing the expected attenuation zones with the measured ones it is deduced that the size is similar, while a shift is noted (~1.5Hz) in lower frequencies for both lattices. Overall, the dynamic response of the proposed prototypes verifies the analytically predicted response of the two arrangements, exhibiting the capabilities of the DDA enhanced phononic lattices.

9.4.2 Locally Resonant structures

Figure 9-11 shows the theoretically predicted dispersion curves assuming the properties of the locally resonant metamaterial devices. The baseline structure is expected to present an attenuation zone between 7.1 and 10.1 Hz and this zone is expected to be increased by 113% after the inclusion of the DDA.

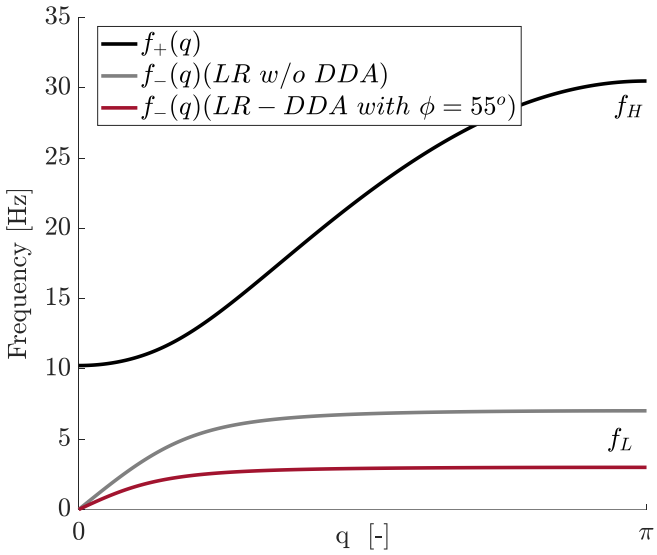

Figure 9-11: Expected theoretical dispersion curves of the LR LEGO® technics assemblies

Thus, in order to validate the design of the locally resonant structure before progressing with the enhanced lattice, the experimentally measured dynamic response of the metamaterial is compared with the analytically estimated frequency response, provided in Figure 9-12. Indeed, the two curves are in agreement, bearing in mind all the potential discrepancies and especially the role of friction among the units and the guides. A certain amount of damping, in the form of damping ratio ($\zeta = 7\%$) is assumed in the theoretical model, originating from the guides-units friction, aiming to fit the experimental curve.

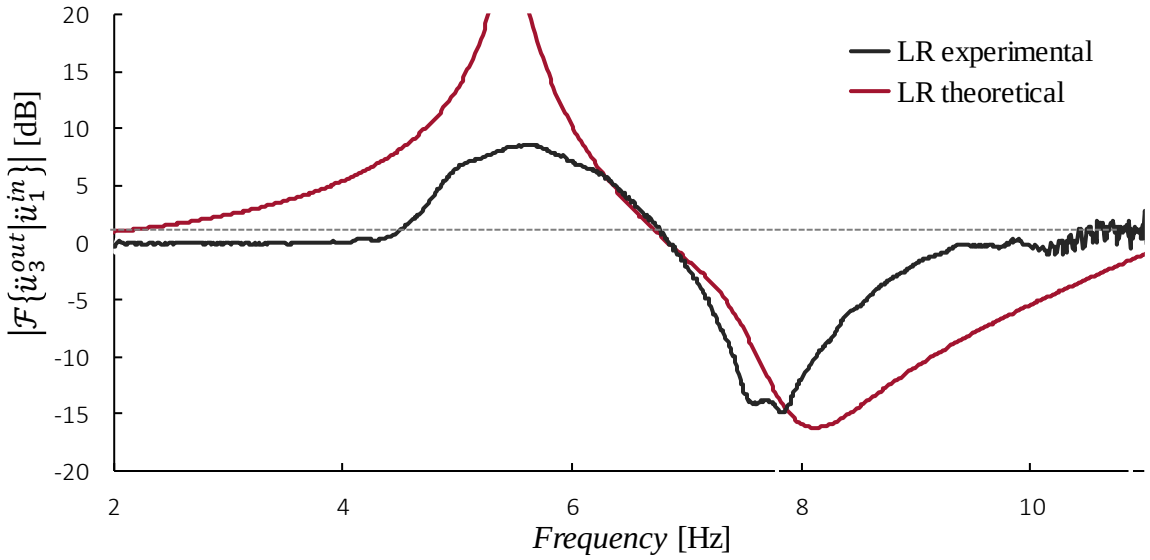

Figure 9-12: Comparison between the experimental and analytically estimated frequency response $\mathcal{F}\{\ddot{u}_3^{out}|\ddot{u}_1^{in}\}$ *for the three (3) unit-cell lattice of the LR structure.*

Figure 9-13 depicts the acceleration response of the setups presented in Figure 9-6 and Figure 9-7. Again, the acceleration response of the two metamaterials is assessed based on the size of the attenuation zones. The "conventional" locally resonant structure reveals a bandgap between 7.5 and 10.1 Hz, which is in accordance with the theoretical estimation, and the DDA enhanced structure displays a bandgap in between 4.5 and 9.5 Hz which is slightly smaller compared to the theoretical estimations (shaded areas in Figure 9-13).

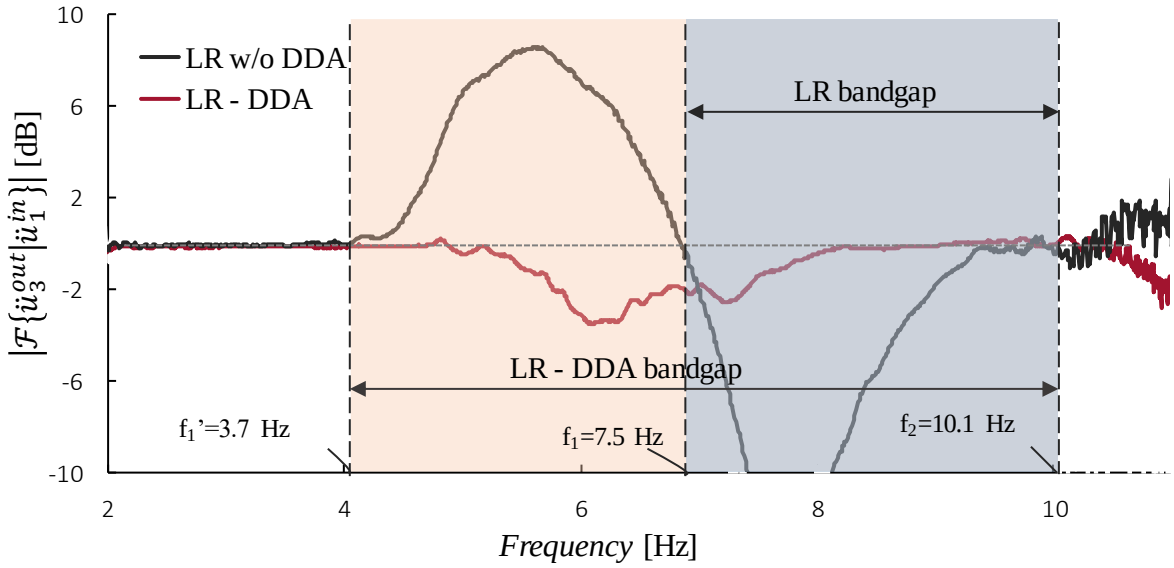

Figure 9-13: Frequency content of the response of the LR lattice with and w/o the DDA $(\varphi = 55^{\circ})$ *for a three (3) unit-cell lattice. The maximum acceleration of each unit* p *is denoted as max* $\ddot{u}_p^L$.

The enhanced structure verifies the merits of the proposed framework described in Chapter 8, as larger bandgaps are attained compared to the conventional LR structure and at the same time the abrupt resonance peaks before and after the attenuation zone are strongly mitigated.

9.5 Concluding Remarks

In this chapter, the dynamics and the filtering properties of the DDA enhanced phononic and LR structures, described in the previous chapters, are experimentally investigated. The lattices' unit blocks consist of LEGO® assemblies connected to each other through spring assemblies comprised of compression and extension springs.

The phononic LEGO® lattice Bragg bandgaps are sought in the very low-frequency regime based on the theoretical predictions of the dispersion analysis. The tests showcase the existence of an attenuation zone and reveal the opening bandgap frequency, however more tests should be contacted to provide an accurate identification of the lattice dynamic response. The DDA enhanced lattice, on the other hand, showed clearly a better response shifting the lower bound of the bandgap, to lower frequencies.

The experimental transmission spectrum of the finite sized locally resonant structure exhibits a wide signal reduction within the bandgap region, identified initially by the dispersion analysis, when only three (3) unit cells are considered. The addition of the DDA mechanism improves the behaviour of the metamaterial extending the attenuation zone to lower frequencies while the reduction of the bandgap depth comes with a mitigation of the resonant peaks outside the attenuation zone.

It is concluded that the DDA inertial amplification mechanism can be used for enhancing the design of vibration mitigation structures and shock-absorbing materials at various length scales. While this is an initial investigation, validated by a scaled proof-of-concept system, the feasibility of the proposed designs as well as the potential practical limitations should be further studied prior to proceeding to realistic full-scale applications. The practical implementation aspects of the proposed designs for seismic protection of structures, energy harvesting, or acoustic absorption are topics of interest for future examination.

III. Conclusions & Future Research

10 CONCLUSIONS & FUTURE RESEARCH

10.1 Research Overview & Concluding Remarks

In this doctoral dissertation, novel low-frequency noise mitigation and vibration control strategies are studied employing metamaterial concepts, advanced negative stiffness absorbers and amplification mechanisms. The main subjects investigated are the following:

- The background of acoustic theory and the introduction of a more accurate methodology to be used as a basis for the investigation of the subsequent proposed noise mitigation concepts;
- The adoption of negative stiffness elements in combination with inertial amplifiers as a means to enhance the sound attenuation properties of conventional panels;
- The introduction of a proposed KDamper – IAM system in metamaterials to increase the efficiency of the structure, specifically in the low-frequency regime.
- A novel amplification mechanism, namely the DDA, that is analytically, numerically and experimentally tested and implemented to both phononic and acoustic metamaterials.

For the purposes of this study, various analytical, numerical and experimental frameworks are developed, and realistic configurations are formulated aiming to explore the potentials of the proposed mechanisms. Analysis is carried out and comparison is undertaken with other conventional vibration control and noise mitigation systems. The main conclusions that can be drawn from this study are provided separately for each of the presented concepts and are summarized in the following:

Acoustic Mounts Based on the Enhanced KDamper-IAM Concept:

i. The implementation of the proposed KD-IAM advanced absorber as a panel's mounting system presents a wide and deep frequency band of improved vibration and noise attenuation in terms of STL, specifically in the resonance regime at frequencies within the range of 20 to 150 Hz;

ii. By employing stiffeners to increase the rigidity and, consequently, the fundamental frequency of a panel, the resulting effect of the optimized KD-IAM mounts is significantly improved;

iii. It is highlighted that the addition of the inertial amplification mechanism (IAM) to the KD mounting system is beneficial for the dynamic response of the structure in the low-frequency domain, where the mass-law prevails;

iv. Realistic designs can be derived using Belleville (disc) springs, rubber pads (KDamper) and simple steel hinged structures (IAM).

Metamaterial Designs Based on the Enhanced KDamper-IAM Concept:

i. The virtues of the KD-IAM metamaterial are investigated showcasing the extraordinary capabilities of the structure to generate deep and wide bandgaps in the low-frequency range without the need of a large number of unit-cells;

ii. Simple, feasible designs of all the essential parts comprising the KD-IAM meta-structure demonstrate that the panel can be produced without high precision requirements and complex geometries;

iii. Appropriate technological implementations of this concept can lead to significant improvements in all types of low-frequency technological applications, with emphasis in low-frequency noise isolation-absorption.

The Dynamic Directional Amplification Mechanism (DDA):

i. A simple mass amplification mechanism is introduced that increases inertia towards the desired direction of motion. The major innovation of the application lies in the simple geometry of the proposed system; the vibrating mass is fixed to a rigid link that increases inertia by coupling the kinematic DoFs of the resonating mass and forcing the oscillator to move through a prescribed circumferential path.

ii. The derived analytical framework and transfer functions indicate a shift in the frequency of the DDA enhanced oscillator, compared to the original m-c-k, showing that the inertia of the system is artificially increased. An experimental set-up serves as a proof-of-concept that validates the numerical results.

iii. The proposed system increases significantly the sound absorption performance of a panel compared to an equivalent panel - simple elastic mount.

Dynamic Directional Amplification (DDA) in Phononic Metamaterials:

i. The DDA mechanism is applied in phononic metamaterial structures, and its theoretical framework is developed;

ii. The dispersion relationships illustrated that the mass amplification provides large bandgaps in the low-frequency regime, without the need for large parasitic mass addition.

iii. Using dynamic amplification, deep gaps at low-frequencies manifest in the direction of wave propagation, using a moderate number of unit-cells.

iv. Indicative implementation of this concept shows great promise towards developing metamaterial designs able to offer low-frequency noise isolation.

Dynamic Directional Amplification (DDA) in Locally Resonant Metamaterials:

i. By harnessing the potency of the DDA to the proposed mass-in-mass periodic structure, better dispersion properties are obtained compared to the conventional locally resonant metamaterials of equivalent structure. Thus, significant filtering characteristics are achieved while reducing the large parasitic resonating masses.

ii. The main drawback of the DDA beneficial effects is the reduction of the maximum depth of the bandgap, without however, a significant compromise of the overall performance of the metamaterial.

iii. Another potential disadvantage of the mechanism is the diversion of the resonating mass movement perpendicular to the direction of the external applied action; this leads to mass movement in both axes (2D movement in the horizontal and vertical axis) that needs to be accommodated depending on the application and design of the lattice structure.

iv. An indicative implementation of the DDA enhanced concept as a seismic protection mechanism in the form of a metabarrier is subsequently proposed. Results indicated the beneficial role of the device and DDA mechanism, hence placing the concept as a potential alternative to existing seismic isolation concepts and structural protection devices.

Experimental validation of Dynamic Directional Amplification (DDA) enhanced Metamaterials:

i. The dynamics and the filtering properties of the DDA enhanced phononic and LR structures, described in the previous chapters, are experimentally investigated. The lattices' unit blocks consist of LEGO® technic assemblies connected to each other through spring assemblies comprised of compression and extension springs.

ii. As expected from the analytical and numerical investigations, the addition of the DDA mechanism improves the behaviour of both phononic and LR metamaterial structures by extending the attenuation zone (bandgap) to lower frequencies.

iii. Through the experimental process, the potential and beneficial effect of the DDA concept is validated. It is concluded that the mechanism can be used for enhancing the design of vibration mitigation structures and shock-absorbing materials at various length scales. The practical implementation aspects of the proposed designs for seismic protection of structures, energy harvesting, or acoustic absorption are topics of interest for future examination.

10.2 Future Research

Based on the research that was carried out during this doctoral dissertation, the following recommendations are suggested for possible future study. These are research directions that will further improve the present investigation, and will provide even more realistic configurations and devices suitable to address low-frequency excitations. Hence, the following work is recommended:

i. Construction of the KD-IAM mount designs and metapanels and execution of acoustic real scale experiments in order to measure the sound transmission loss of the proposed configurations.

ii. Detailed numerical modelling and simulation of the LEGO® DDA enhanced phononic and locally resonant small scale prototypes in FEM commercial software packages using realistic constitutive models. These models will provide valuable insights towards the calibration of such devices and will give a better understanding on any uncertainties (ex. Additional weight of the Lego® parts, friction, effect of damping, etc.).

iii. In depth investigation of the Damping effect and especially the metadamping effect of the proposed DDA enhanced phononic and locally resonant metamaterials, using numerical and analytical tools.

iv. Investigation of the potential implementation of the DDA enhanced metamaterials in energy harvesting systems, in combination with vibration control.

v. Produce an acoustic metabarrier, namely the “Dy.Ba” suitable to address a wide spectrum of urban noise sources exploiting two novel metamaterial concepts; amplification and sonic scattering. Specifically, the proposed “Dy.Ba” will consist of a hybrid system; an arrangement of sonic scatterers combined with the DDA enhanced periodic structure. The Sonic scatterers will function as a filter for the mid frequencies, while the low-frequency noise components will be addressed by the DDA wall behind.

vi. Execution of shaking table experiments in small scale specimens of the DDA seismic metabarrier buried in a sand tank in order to assess the efficiency of the concept in the protection of structures against surface waves.

APPENDIX

Appendix - A. SOUND TRANSMISSION

A.1 Far-field approximation

The distance R can be written as

$$R = \sqrt{r^2 - 2x\xi' - 2y\eta' + \xi\eta'^2 + \eta'^2} \tag{A-1}$$

where $r = |r| = \sqrt{x^2 + y^2 + z^2}$. In spherical coordinates R becomes

$$R = \rho\sqrt{1 - 2\frac{\sin\theta}{r}\left(\xi\cos\varphi + \eta'\sin\varphi\right) + \frac{\xi'^2 + \eta'^2}{r}} \tag{A-2}$$

The solution of Eq. (2-12) is not trivial and has been calculated analytically only for a few cases of boundary conditions. A way around this obstacle comes by utilizing the far field approximation. In the far field we can ignore the weak dependence of the amplitude of the integrand on the position but not the dependence of the phase, namely it holds that

$$\frac{1}{R} \approx \frac{1}{r} \tag{A-3}$$

$$e^{-j\kappa R} \simeq e^{-j\kappa r\left[1 - \frac{\sin\theta}{r}(\xi'\cos\varphi + \eta'\sin\varphi)\right]} \tag{A-4}$$

Since r is independent of ξ' and η', the corresponding terms in Eq. (2-12) can be moved outside the double integral, leading to

$$p_t(r,\ t)\ = \frac{j\omega\rho_0}{2\pi r} e^{j(\omega t-\kappa r)} \int_{-l_x/2}^{l_x/2} \int_{-l_y/2}^{l_y/2} \frac{\partial w(\xi',\eta')}{\partial t} e^{j\kappa(\xi' \sin\theta\cos\varphi+\eta' \sin\theta\sin\varphi)} d\eta' d\xi' \tag{A-5}$$

A.2 Free Finite Rigid (FFR) Panel Approximation

Then, the transmitted pressure by considering the far-field approximation, is calculated from the expression

$$p_t(r,\ t)\ = \frac{-\omega^2\rho_0 W}{2\pi} \frac{e^{-j\kappa r}}{r} e^{j\omega t} \int_{-l_x/2}^{l_x/2} \int_{-l_y/2}^{l_y/2} e^{j\kappa(\xi' \sin\theta\cos\varphi+\eta' \sin\theta\sin\varphi)} d\eta' d\xi' \tag{A-6}$$

where the surface integral is calculated

$$I_{\xi'\eta'} = \frac{8\sin(\sigma_x)\sin(\sigma_y)}{k^2 \sin^2\theta \sin 2\varphi} \tag{A-7}$$

And

$$\sigma_x(\theta,\varphi) = k\frac{l_x}{2}\sin\theta\cos\varphi \tag{A-8}$$

$$\sigma_y(\theta,\varphi) = k\frac{l_y}{2}\sin\theta\sin\varphi \tag{A-9}$$

The transmitted intensity It and consequently the transmitted power, are calculated from Eqs. (2-14)-(2-15) where $I_{\theta\varphi}$ is defined as

$$I_{\theta\varphi} = \int_0^{2\pi} \int_0^{\pi/2} \left|\mathrm{I}_{\xi'\eta'}\right|^2 \sin\theta d\theta d\varphi \tag{A-10}$$

A.3 Analytic solution for Simply Supported plate – Roussos (1985)

Assuming that the transverse displacement of the panel is expressed as

$$w(\xi,\eta) = W(\xi,\eta)e^{-j\omega t} \tag{A-11}$$

and the boundary conditions for a panel with simply supported edges should satisfy

$$w\big|_{x=0}, \left.\frac{\partial^2 w}{\partial x^2}\right|_{x=0} \tag{A-12}$$

the shape functions $W\left(\xi,\ \eta\right)$ for a simply supported panel are of the form

$$W(\xi,\eta)=\sum_{m=1}^{\infty}\sum_{n=1}^{\infty}\sin\frac{m\pi x}{l_x}\sin\frac{n\pi y}{l_y} \tag{A-13}$$

The natural frequencies of a simply supported panel ω_{mn} are given by

$$\omega_{mn}=\sqrt{\frac{D}{\rho h}}\left(\frac{m\pi}{l_x^2}+\frac{n\pi}{l_y^2}\right) \tag{A-14}$$

The coefficient p_{mn} of a simply supported plate subjected to obliquely incident pressure wave can be calculated as

$$p_{mn}=8p_i\bar{I}_m\bar{I}_n \tag{A-15}$$

Where

$$\bar{I}_m=\begin{cases}\dfrac{-j}{2}sign(\sin\theta\cos\varphi), if\ (m\pi)^2=(\kappa_x l_x)^2\\ (m\pi)\dfrac{1-(-1)^m e^{-j\alpha}}{(m\pi)^2-a^2}, if\ (m\pi)^2\neq(\kappa_x l_x)^2\end{cases} \tag{A-16}$$

$$\bar{I}_n=\begin{cases}\dfrac{-j}{2}sign(\sin\theta\cos\varphi), if\ (n\pi)^2=(\kappa_y l_y)^2\\ (n\pi)\dfrac{1-(-1)^n e^{-j\beta}}{(n\pi)^2-\beta^2}, if\ (n\pi)^2\neq(\kappa_y l_y)^2\end{cases} \tag{A-17}$$

The power Π_t that is transmitted (radiated) by the panel is calculated as the integral of the sound intensity over an imaginary far-field hemisphere as

$$\Pi_t=\int_{\varphi=0}^{2\pi}\int_{\theta=0}^{\pi/2}\left|\sum_{m=1}^{\infty}\sum_{n=1}^{\infty}p_{mn}\right|^2\frac{r^2}{2\rho_0 c_0}\sin\theta d\theta d\varphi \tag{A-18}$$

and the power that is incident on the panel is given by Eq. (2-16).

A.4 Simply Supported Plate - 1st Mode Approximation

Considering only the 1st mode for interpolation of the transverse displacement the derivatives to be substituted in the equation of motion are calculated as

$$\frac{\partial^2 w(\xi,\eta)}{\partial t^2}=-\omega^2 W_1(\xi,\eta)e^{-j\omega t} \tag{A-19}$$

$$\frac{\partial^4 w(\xi,\eta)}{\partial \xi^4} = C_1 \left(\frac{\pi}{l_x}\right)^4 \sin\left(\frac{\pi\xi}{l_x}\right)\sin\left(\frac{\pi\eta}{l_y}\right) = \left(\frac{\pi}{l_x}\right)^4 W_1(\xi,\eta) \tag{A-20}$$

$$\frac{\partial^4 W_1(\xi,\eta)}{\partial \eta^4} = C_1 \left(\frac{\pi}{l_y}\right)^4 \sin\left(\frac{\pi\xi}{l_x}\right)\sin\left(\frac{\pi\eta}{l_y}\right) = \left(\frac{\pi}{l_y}\right)^4 W_1(\xi,\eta) \tag{A-21}$$

$$\frac{\partial^4 W_1(\xi,\eta)}{\partial \xi^2 \partial \eta^2} = C_1 \left(\frac{\pi^2}{l_x l_y}\right)^2 \sin\left(\frac{\pi\xi}{l_x}\right)\sin\left(\frac{\pi\eta}{l_y}\right) = \left(\frac{\pi^2}{l_x l_y}\right)^4 W_1(\xi,\eta) \tag{A-22}$$

Considering the far field approximation for the transmitted pressure and normal incident waves $(\theta_i = 0)$, the equation of motion becomes

$$\left[D\pi^4 \left(\frac{1}{l_x^2} + 2\frac{1}{l_x^2 + l_y^2}\right) - \omega^2 \rho h \right] W_1(\xi,\eta) = 2P_i + \frac{\omega^2 \rho_0}{\pi r} e^{-j\kappa r} I_{\xi',\eta'} \tag{A-23}$$

where $I_{\xi'\eta'}$ is the double integral on the surface of the plate

$$I_{\xi',\eta'} = \int_{-l_x/2}^{l_x/2} \int_{-l_y/2}^{l_y/2} W_1(\xi',\eta) e^{j\kappa(\xi' \sin\theta\cos\varphi + \eta' \sin\theta\sin\varphi)} d\eta' d\xi' \tag{A-24}$$

and the local coordinates $\xi' = \xi - l_x$, $\eta' = \eta - l_y$. For ξ', η' the shape function from Eq. (2-24) becomes

$$W_1(\xi',\eta') = C_1 \cos\left(\frac{\pi\xi'}{l_x}\right)\cos\left(\frac{\pi\eta'}{l_y}\right) \tag{A-25}$$

The surface integral is then calculated as

$$I_{\xi',\eta'} = C_1 I_{\xi,\eta} \tag{A-26}$$

Where

$$I_{\xi,\eta} = 4\pi^2 l_x l_y \frac{\cos(\sigma_x)}{\left(l_x \kappa \sin\theta\cos\varphi\right)^2 - \pi^2} \frac{\cos(\sigma_y)}{\left(l_y \kappa \sin\theta\sin\varphi\right)^2 - \pi^2} \tag{A-27}$$

and σ_x, σ_y are the same as in Eq.(A-8)-(A-9). Solving Eq. (2-24) for C_1, the surface integral can be written as

$$I_{\xi',\eta'} = \frac{W_1(\xi,\eta)}{\sin\left(\frac{\pi\xi}{l_x}\right)\sin\left(\frac{\pi\eta}{l_y}\right)} I_{\xi,\eta} \tag{A-28}$$

Substituting to equation (A-20), multiplying with W_1 and integrating over the panel surface gives

$$\int_0^{l_x}\int_0^{l_y}\left[D\pi^4\left(\frac{1}{l_x^2}+\frac{1}{l_y^2}\right)^2 - \frac{\omega^2\rho_0 e^{-j\kappa r}}{\pi r}\frac{I_{\xi\eta}(\theta,\varphi)}{\sin\left(\frac{\pi\xi}{l_x}\right)\sin\left(\frac{\pi\eta}{l_y}\right)} - \omega^2\rho h \right]... \tag{A-29}$$

$$...W_1^2(\xi,\eta)d\eta d\xi = \int_0^{l_x}\int_0^{l_y} 2P_i W_1(\xi,\eta)d\eta d\xi$$

and inserting ω_1 from Eq. (2-27) leads to

$$\rho h\left(\omega_1^2-\omega^2\right)\int_0^{l_x}\int_0^{l_y} W_1^2(\xi,\eta)d\eta d\xi = \\ = \left[2P_i + \frac{\omega^2\rho_0}{\pi}\frac{e^{-j\kappa r}}{r}C_1 I_{\xi\eta}(\theta,\varphi)\right]\int_0^{l_x}\int_0^{l_y} W_1(\xi,\eta)d\eta d\xi \tag{A-30}$$

The two integrals are calculated as

$$\int_0^{l_x}\int_0^{l_y} W_1^2(\xi,\eta)d\eta d\xi = \frac{l_x l_y}{4}C_1^2 \tag{A-31}$$

$$\int_0^{l_x}\int_0^{l_y} W_1(\xi,\eta)d\eta d\xi = \frac{4 l_x l_y}{\pi^2}C_1 \tag{A-32}$$

Substituting in Eq. (A-30) and solving the quadratic equation for C_1 leads to:

$$C_1 = \frac{8P_i}{\pi^2\left[\rho_0 h\frac{\omega_1^2-\omega^2}{4} - \frac{4\omega^2\rho_0}{\pi^3}\frac{e^{-j\kappa r}}{r}I_{\xi,\eta}(\theta,\varphi)\right]} = \frac{32P_i + p_t}{\pi^2\rho h(\omega_1^2-\omega^2)} \tag{A-33}$$

Therefore, substituting in Eq. (A-5) for the transmitted pressure, comes:

$$p_t(r,t) = \frac{\omega^2\rho_0 e^{-j\kappa r}}{2\pi r}C_1 I_{\xi\eta}(\theta,\varphi)e^{j\omega t}$$

$$\Rightarrow p_t(r,t) = \frac{16\omega^2\rho_0 \mathrm{I}_{\xi\eta}(\theta,\varphi)P_i}{r[\pi^3\rho h(\omega_1^2-\omega^2) - 16\omega^2\rho_0 e^{\frac{-j\kappa r}{r}}]}e^{\frac{-j\kappa r}{r}}e^{j\omega t} \tag{A-34}$$

The transmitted intensity I_t is calculated from Eq. (2-14) as

$$I_t(r,\theta,\varphi)=\frac{1}{2\rho_0 c_0 r^2}\left(\frac{16\omega^2\rho_0\left|\mathrm{I}_{\xi\eta}\right|P_i}{\left|\pi^3\rho h(\omega_1^2-\omega^2)-16\omega^2\rho_0 e^{\frac{-j\kappa r}{r}}\right|}\right)^2 \tag{A-35}$$

and the transmitted power comes from Eq. (2-15) as

$$\Pi_t=\frac{P_i^2}{2\rho_0 c_0}\frac{16\omega^2\rho_0\left|\mathrm{I}_{\xi\eta}\right|P_i}{\left|\pi^3\rho h(\omega_1^2-\omega^2)-16\omega^2\rho_0 e^{\frac{-j\kappa r}{r}}\right|^2}I_{\theta\varphi} \tag{A-36}$$

where $I_{\theta\varphi}$ is the double integral over a hemispheric surface in the receiver domain

$$I_{\theta\varphi}=\int_0^{2\pi}\int_0^{\pi/2}\left|\mathrm{I}_{\xi\eta}\right|^2\sin\theta d\theta d\varphi \tag{A-37}$$

and $I_{\xi\eta}$ is defined in Eq. (A-27).

A.5 Lumped Parameter Model (LPM)

Let us rewrite the transverse displacement as

$$w(\xi,\eta,t)=\sin\left(\frac{\pi\xi}{l_x}\right)\sin\left(\frac{\pi\eta}{l_y}\right)q(t) \tag{A-38}$$

Where

$$q(t)=C_1 e^{j\omega t} \tag{A-39}$$

The kinetic energy of the system is defined as

$$\mathrm{T}=\frac{1}{2}\rho h\int_0^{l_x}\int_0^{l_y}\left(\frac{\partial w}{\partial t}\right)^2 d\xi d\xi=\frac{1}{2}\frac{\rho h l_x l_y}{4}\dot{q}^2(t)=\frac{1}{2}\frac{m_1^*}{4}\dot{q}^2(t) \tag{A-40}$$

and the potential energy as

$$\mathrm{U}=\frac{1}{2}D\int_0^{l_x}\int_0^{l_y}\left[\nabla^2 w(\xi,\eta,t)\right]^2 d\xi d\eta=\frac{1}{2}\frac{D\pi^4 l_x l_y}{4}\left(\frac{1}{l_x^2}+\frac{1}{l_y^2}\right)^2 q^2(t)=\frac{1}{2}k_1^* q^2(t) \tag{A-41}$$

where m_1^* and k_1^* are the generalized mass and stiffness of the fundamental, 1st mode. The equation of motion of the equivalent SDOF model is

$$m_1^* \ddot{q} + k_1^* q = f^*(t) \tag{A-42}$$

where the generalized excitation, considering only the blocked pressure, comes as

$$f^*(t) = 2p_i \int_0^{l_x} \int_0^{l_y} W_1(\xi,\eta) d\xi d\eta = \frac{8P_i l_x l_y}{\pi^2} e^{j\omega t} \tag{A-43}$$

Consequently, by substituting in Eq. (A-42), and since $k_1^* = m_1^* \omega_1^2$, the factor C_1 is calculated as:

$$C_1 = \frac{8P_i l_x l_y}{\pi^2} \frac{1}{m_1^*(\omega_i^2 - \omega^2)} \tag{A-44}$$

A.6 KDamper Mounts

The equations of motion resulting from the model of the panel mounted in KDamper mounts as illustrated in Figure 4-1, come as

$$m^* \ddot{q}_1 + k^*(q_1 - q_2) = \frac{8P_i l_x l_y}{\pi^2} e^{j\omega t} \tag{A-45}$$

$$m_j \ddot{q}_2 - k^* q_1 + (k^* + k_P^{'} + k_S^{'}) q_2 - k_P^{'} q_3 = 0 \tag{A-46}$$

$$m_D \ddot{q}_3 + (k_P^{'} + k_S^{'}) q_3 - k_P^{'} q_2 = 0 \tag{A-47}$$

Where

$$q_i(t) = C_i e^{j\omega t} \tag{A-48}$$

The relevant transfer functions come as

$$TF_{21} = \frac{C_2}{C_1} = \frac{k^*}{k^* + k_S^{'} + k_P^{'}(1 - TF_{32})} \tag{A-49}$$

$$TF_{32} = \frac{C_3}{C_2} = \frac{k_P^{'}}{-\omega^2 m_D + k_P^{'} + k_N} \tag{A-50}$$

Appendix - B. INERTIA AMPLIFICATION MECHANISM (IAM)

A schematic of the proposed in Cheng et al. (2020) IAM is shown in Figure B-1 (a). The mechanism consists of four rigid bars, connected by hinges, and two lateral masses (m_a). The IAM undeformed configuration is defined by the angle θ, between the x–axis and the rigid bars. The top and bottom hinges can be connected to others mechanical elements in a dynamic system which operates in x–direction.

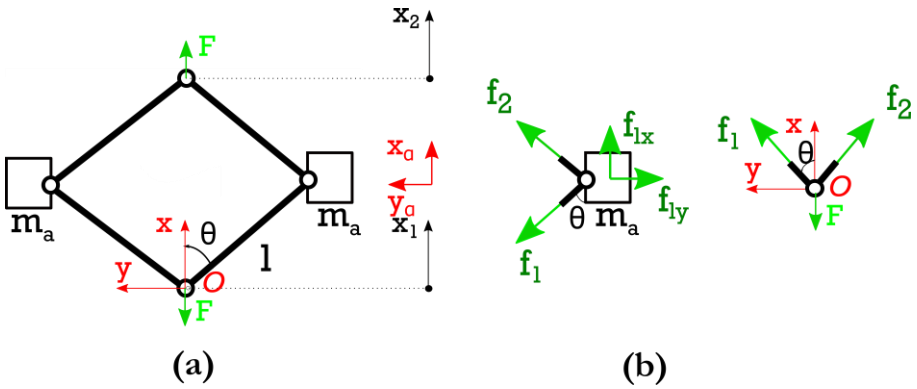

Figure B-1: IAM schematic diagram, (b) equilibrium configuration of the proposed IAM system.

Under the assumptions of small displacements along the x–axis, the displacements of the lateral masses are:

$$x_a = \frac{x_1 + x_2}{2}, \quad y_a = \pm \frac{y_2 - y_1}{2\tan\theta} \tag{B-1}$$

To balance the inertial forces $f_{Ix} = m_a \ddot{x}_a$ and $f_{Iy} = m_a \ddot{y}_a$, the internal forces f_1 and f_2, as well as the overall reaction force F in Figure B-1 (b) are derived:

$$f_1 = \frac{1}{2}\left(\frac{f_{Iy}}{\sin\theta} - \frac{f_{Ix}}{\cos\theta} \right) \tag{B-2}$$

$$f_2 = \frac{1}{2}\left(\frac{f_{Iy}}{\sin\theta} + \frac{f_{Ix}}{\cos\theta} \right) \tag{B-3}$$

$$F = 2 f_1 \cos\theta = b(\ddot{x}_2 - \ddot{x}_1) + b^*(\ddot{x}_2 + \ddot{x}_1) \tag{B-4}$$

In which $b = \frac{1}{2} m_a \tan^{-2}\theta$ and $b^* = 0.5 m_a$ are the inertial constants.

As a result, the IAM can be seen as a one-dimensional mechanical system, which couples a classical inerter with a dead mass. For the classical inerter part, the inertial reaction force is proportional to the relative acceleration between the two terminals ($\ddot{x}_2 - \ddot{x}_1$), where the inertial constant b is governed by the geometrical configuration and lateral mass of the IAM. For the dead mass part, the inertial reaction force is proportional to the average acceleration between the two terminals ($(\ddot{x}_2 + \ddot{x}_1)/2$), where the inertial constant is only governed by the lateral mass.

Appendix - C. SDOF "M-C-K" OSCILLATOR

The monogramic diagram of such a system is presented in Figure C-1. The equation of motion of an "m-c-k" system subjected to an excitation $f(t)$ is

$$m\ddot{u}(t) + c\dot{u} + ku(t) = f(t) \tag{C-1}$$

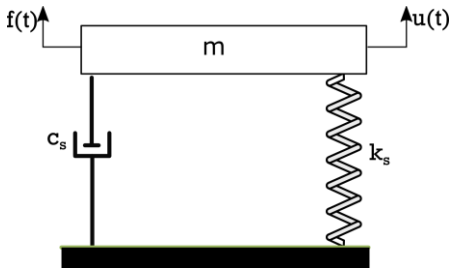

Figure C-1: Mass-spring single DoF system.

Assuming an external harmonic excitation of the form $f(t) = \tilde{F}e^{j\omega t} = \hat{F}e^{j\omega t}$, the steady-state response of the seismic mass, which comes from the partial solution of the differential equation, follows the frequency of excitation with a phase difference φ as

$$u(t) = \tilde{U}e^{j\omega t} = \hat{U}e^{j(\omega t - \varphi)} \tag{C-2}$$

The steady-state (SS) frequency response to a harmonic excitation can be examined via the transfer function of the amplitude $\tilde{U}$ of the response $u(t)$ to the amplitude $\tilde{F}$ of an excitation $f(t)$ in the frequency domain, which comes as

$$\tilde{T}_{UF}(s) = \frac{\tilde{U}}{\tilde{F}} = \frac{1}{ms^2 + cs + k} \tag{C-3}$$

where $s = j\omega$ is the complex variable. Defining the equivalent static amplitude as $U_{ST} = \frac{\tilde{F}}{k}$, the transfer function of the dynamic magnification factor can be expressed as

$$\tilde{H}(s) = \frac{\tilde{U}}{\tilde{U}_{ST}} = \frac{k}{ms^2 + cs + k} \tag{C-4}$$

Furthermore, by also defining the ratio of excitation frequency to natural frequency as $q = \frac{\omega}{\omega_n}$ and $\zeta = \frac{c}{2\omega_n m}$ as the damping ratio or fraction of critical damping, the dynamic magnification factor can be expressed as

$$\left|\tilde{H}(s)\right| = \tilde{H}(q,\zeta) = \frac{1}{\sqrt{(1-q^2)^2 + (2\zeta q)^2}} \tag{C-5}$$

The factor H is maximized when the amplitude of the displacement is maximized, namely for a certain damping ratio ζ

$$\frac{\partial \mathrm{H}}{\partial q} = 0 \tag{C-6}$$

leads to

$$q = \sqrt{1-2\zeta^2} \tag{C-7}$$

This means that the amplitude $\hat{U}$ and consequently the factor H assume their maximum values at a frequency

$$\omega = \omega_n\sqrt{1-2\zeta^2} = \omega_R \tag{C-8}$$

which is the resonant frequency of the system. Lastly, the phase difference comes as

$$\varphi = \arctan\left(\frac{-2q\zeta}{1-q^2}\right) \tag{C-9}$$

In the case of base excitation of the system $u_b(t) = \tilde{U}e^{j\omega t} = \hat{U}e^{j\omega t}$, the equation of motion becomes

$$m\ddot{u} + c(\dot{u} - \dot{u}_B) + k(u - u_B) = 0 \tag{C-10}$$

which leads to

$$m\ddot{u} + c\dot{u} + ku = c\dot{u}_B + ku_B = f_B(t) = \tilde{F}e^{(j\omega t - \theta)} \tag{C-11}$$

where now the phase difference between excitation and response is

$$\theta = \arctan(-2\zeta q) \tag{C-12}$$

and $F = k\tilde{U}_B\sqrt{1+(2\zeta q)^2}$. Thus, the transmissibility factor (TR) is defined as

$$TR(q,\zeta) = \frac{\hat{U}}{\hat{U}_B} = \left|\frac{\tilde{U}}{\tilde{U}_B}\right| = H(q,\zeta)\sqrt{1+(2\zeta q)^2} \tag{C-13}$$

In view of Eq. (C-13), another common way to express the amplitude of response of the system to the amplitude of the excitation is in terms of acceleration to force. Namely, by integrating this transfer function twice gives

$$\tilde{T}_{AF}(s) = \frac{\tilde{a}}{\tilde{F}} = \frac{s^2}{ms^2+cs+k} \tag{C-14}$$

and the magnitude comes as

$$FRF = \left|\tilde{T}_{AF}(s)\right| = \frac{1}{m}\frac{q^2}{\sqrt{(1-q^2)^2+(2\zeta q)^2}} \tag{C-15}$$

which is often called the "accelerance" of the system, or just FRF (frequency response function). Of course all of the above transfer functions are frequency response functions, however usually FRF refers to the accelerance.

Figure C-2 shows the resulting frequency response of the dynamic magnification factor H . This is a fundamental graph in vibration isolation. The curve can be divided into three regions:

- Static Region: The excitation frequency is significantly smaller than the natural frequency of the system, thus the mass following the excitation moves at slow speed and with low acceleration. In this region the elastic forces due to the spring, dominate the response of the system.
- Resonance Region: The excitation frequency is close to the natural frequency of the system. When they become equal the system is in resonance and the response is dominated the damping forces due to the energy dissipation element. The amplitude of the response is inversely proportional to the damping ratio ζ .
- High Frequency (Inertial) Region: The excitation frequency is significantly larger than the natural frequency of the system. The amplitude of oscillation is getting smaller while the acceleration of the mass increases. Thus, the response is dominated by the inertial forces due to the seismic mass.

Inside the High Frequency Region, there is a certain value of the frequency ratio q where H becomes unity, and as the frequency of excitation increases, the value of H tends to zero. This value may be calculated as

$$q_{is} = \sqrt{2}\sqrt{1-2\zeta^2} \tag{C-16}$$

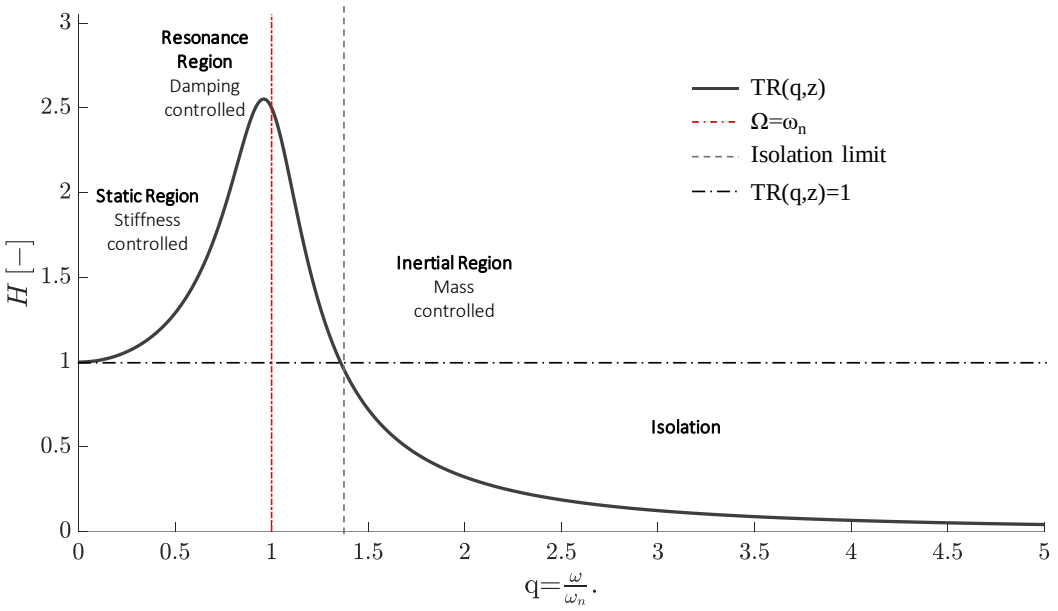

Figure C-2: Frequency response of 1 DoF mass-spring system to harmonic and base excitation - Dynamic magnification factor H.

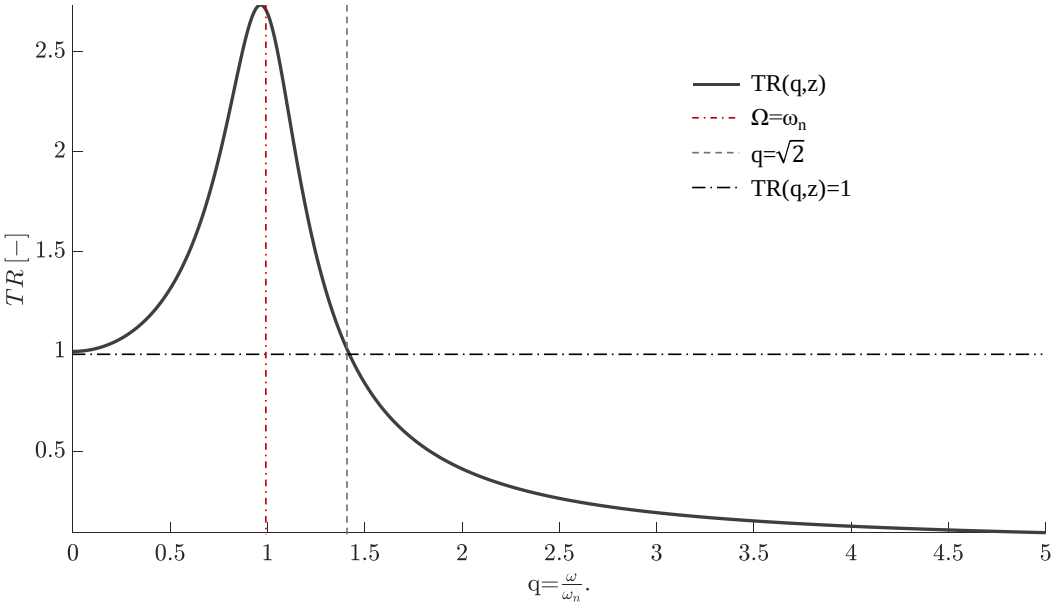

Figure C-3: Frequency response of 1 DoF mass-spring system to harmonic and base excitation - Transmissibility factor TR.

This means that above this frequency the amplitude of the response becomes smaller than the equivalent static amplitude, therefore the seismic mass enters an isolation region. Thus, for the design of an engine mount for example, subjected to periodic excitation due to the rotation of the engine, the stiffness and damping elements of the mount have to be selected appropriately so that

$$q_{is} = \sqrt{2}\sqrt{1-2\zeta^2} \tag{C-17}$$

if ω is the frequency of the rotating engine at the operational point for example.

Finally, Figure C-4 shows the corresponding phase angles φ and θ of the transfer functions H and TR respectively. An important conclusion from the curve of angle is the value of $\varphi = -\pi/2$ when the system is at resonance ($q=1$). In view of Eq. (C-2), this means that the response of the system is maximized when the force is instantly zeroed. Additionally, for all the above figures, a value of ζ= 0:2 was considered for the damping ratio. By increasing the damping ratio, the response of angle - is flattened around the resonant frequency, which means that the excitation and the response of the system have a significant phase difference over a wider frequency range. In the opposite case, as the damping ratio decreases, angle - presents a sharper variation around resonance and the response of the system has the same phase with the excitation over a wider frequency range.

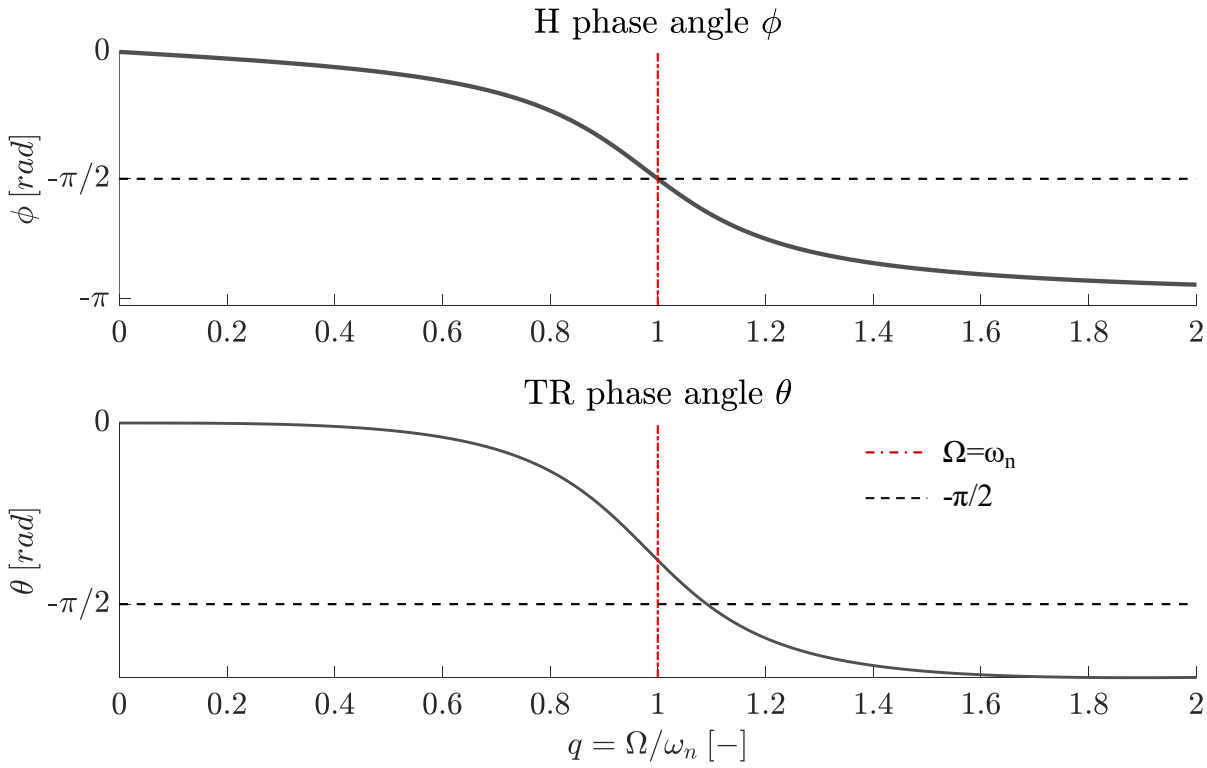

Figure C-4: Corresponding phase angles of H and TR.

As for the accelerance of the oscillator, the resulting frequency response is presented in Figure C-5. A way to study this response is by considering the extreme values of an underdamped system, meaning ζ = 0 for an undamped system and ζ = 1 for a critically damped system. Then by examining the limits of accelerance

$$\lim_{q\to\infty} FRF(q,\zeta=0) = \left|-1/m\right| = 1/m \tag{C-18}$$

$$\lim_{q\to 1} FRF(q,\zeta=0) = \infty \tag{C-19}$$

$$\lim_{q\to\infty} FRF(q,\zeta=1) = 1/m \tag{C-20}$$

$$\lim_{q\to 1} FRF(q,\zeta=1) = 1/(2m) \tag{C-21}$$

This shows that regardless of the damping ratio, at frequencies significantly higher than the natural frequency, the accelerance converges to a defined value $1/m$. On the other hand, as the damping decreases the resulting acceleration in the resonance region is increasing. The units of accelerance are either in $\frac{m/s^2}{N}$ or g/N, where g is the acceleration of gravity.

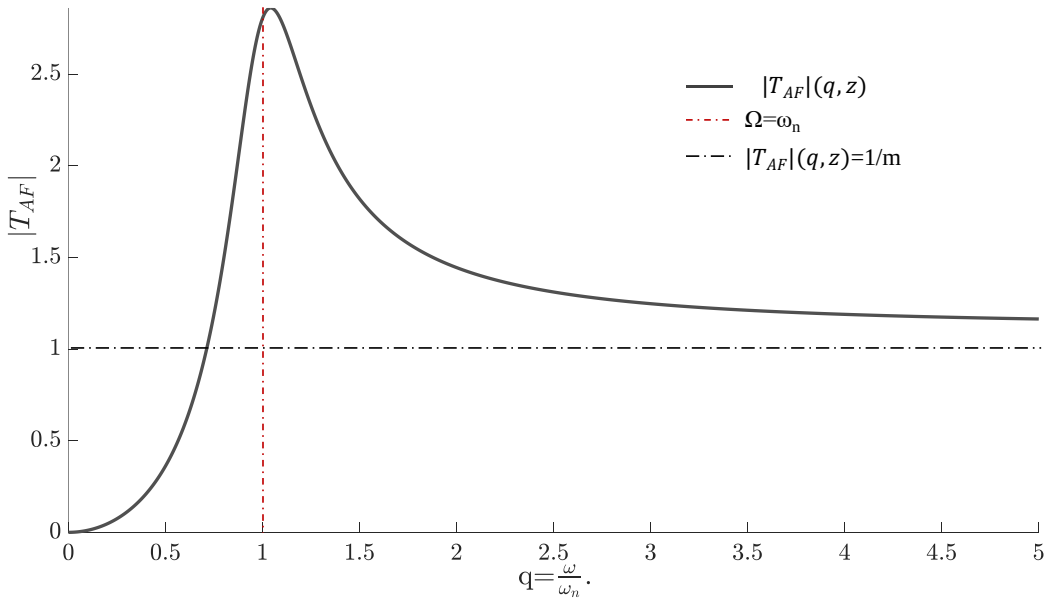

Figure C-5: Frequency response of Accelerance (FRF).

Appendix - D. METAMATERIAL DESIGNS

D.1 Structural Configurations For Low-Frequency Band Gaps (Wang et al., 2022)

One of the key issues of the metamaterials is how to devise suitable configurations to obtain low-frequency band gaps. This section aims to summarize the fundamental configurations that are capable of obtaining band gaps in the frequency range below 100Hz. The structural configurations of metamaterials can be classified into 5 categories according to their structural complexity and supporting capacity.

Spring-mass configuration

The spring-mass configuration is the simplest constitution of the metamaterials but is the most useful model to analyze the formation mechanism of the band gap. Consider the first scenario that all mass elements and spring elements utilized to constitute the spring-mass chain are identical, the spring-mass chain is homogeneous, and its vibration frequency spectrum is composed of only an acoustical branch. For the second case, a unit cell contains two types of mass elements, as illustrated in Figure D-1, and the vibration frequency spectrum of the inhomogeneous metamaterials consists of an acoustical branch and an optical branch. As depicted in the right panel of Figure D-1, a band gap capable of forbidding the wave propagation appears between the acoustical branch and the optical branch (Patterson & Bailey, 2018). The beginning frequency and ending frequency of the band gap opened by the diatomic spring-mass chain can be given by Jensen (2003).

$$\omega_B = \sqrt{\frac{2k}{m_L}}, \quad \omega_E = \sqrt{\frac{2k}{m_D}}, \tag{D-1}$$

where m_D and m_L denote the masses of two types of mass elements. k is the stiffness of the connecting spring. Apparently, the band gap is related to the properties of the spring-mass unit cell, which provides an approach to lower the beginning frequency of the band gap by decreasing the stiffness or increasing the mass

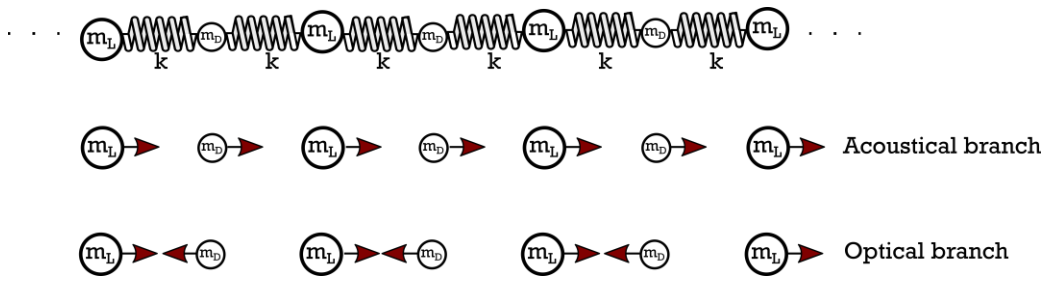

(a)

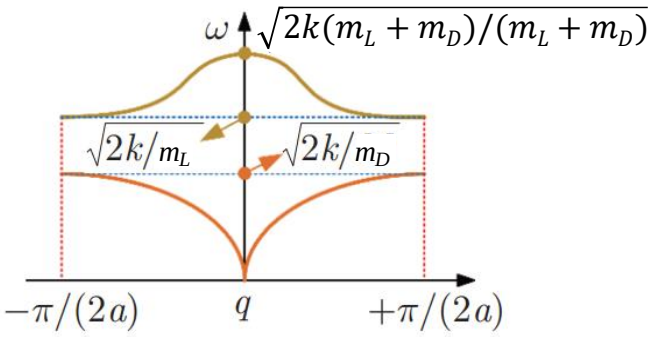

(b)

Figure D-1: (a) Schematic diagram of a one-dimensional spring-mass chain and (b) its corresponding vibration frequency spectrum.

Mounting spring-mass local resonators onto the primary structure, for instance, the spring- mass chain (Lazarov & Jensen, 2007), the beam (Yu et al., 2006), and the plate (Xiao et al., 2012), is the second way to open low-frequency band gaps. The operational principle of opening such low-frequency band gaps is the local resonance. That is, much of the energy transfers from the primary structure to the resonators when the excitation frequency is near the resonant frequency of the spring-mass resonator. Such a phenomenon is referred to as the local resonance, resulting in large-amplitude oscillations of the resonator and a restrained wave propagation along the primary structure (Xiao et al., 2012). The band features of the metamaterials, including the frequency and width, are dependent on the mass and stiffness of the spring-mass mechanism. That is, it is possible to obtain a band gap in the frequency range below 100Hz without taking into account the support capacity (Jensen, 2003). Generally, the gravity of the resonator is completely supported by the linear spring.

However, the limited supporting capacity of the linear spring with a low stiffness may result in the structure destabilization. Therefore, it is just a theoretical possibility for obtaining low-frequency band gaps using spring-mass resonators, leading to difficulty in the engineering applications of the metamaterials. Additionally, the space-consuming configuration of the metamaterials composed by the spring-mass mechanism is the second obstacle for its applications.

D.2 Dispersion analysis (DDA Enhanced Phononic Lattice)

In this appendix, we provide the explicit form of the $\boldsymbol{M, C, K}$ matrices used in the dispersion equation of the lattice without the DDA–Eq. (7-14) and, including the DDA—Eq. (7-15). Starting with the lattice without the amplification mechanism, the dispersion relationship can be calculated from:

$$\det\left[\boldsymbol{M}_p\ddot{\boldsymbol{u}}+\boldsymbol{C}_P\dot{\boldsymbol{u}}+\boldsymbol{K}_P\boldsymbol{u}\right]=0 \tag{D-2}$$

with the $\boldsymbol{M}_p$, $\boldsymbol{C}_p$ and $\boldsymbol{K}_p$ matrices defined as follows:

$$\boldsymbol{K}_P=\begin{bmatrix} 2k_x & 0 & -k_x(1+e^{-j\mu_x}) & 0 \\ 0 & 2k_y & 0 & -k_y e^{-\frac{j\mu_x}{2}}\left(e^{-\frac{j\mu_y}{2}}+e^{\frac{j\mu_y}{2}}\right) \\ -k_x\left(1+e^{j\mu_x}\right) & 0 & 2k_x & 0 \\ 0 & -k_y e^{\frac{j\mu_x}{2}}\left(e^{-\frac{j\mu_y}{2}}+e^{\frac{j\mu_y}{2}}\right) & 0 & 2k_y \end{bmatrix} \tag{D-3}$$

$$\boldsymbol{C}_P=\begin{bmatrix} 2c_x & 0 & -c_x(1+e^{-j\mu_x}) & 0 \\ 0 & 2c_y & 0 & -c_y e^{-\frac{j\mu_x}{2}}\left(e^{-\frac{j\mu_y}{2}}+e^{\frac{j\mu_y}{2}}\right) \\ -c_x\left(1+e^{j\mu_x}\right) & 0 & 2c_x & 0 \\ 0 & -c_y e^{\frac{j\mu_x}{2}}\left(e^{-\frac{j\mu_y}{2}}+e^{\frac{j\mu_y}{2}}\right) & 0 & 2c_y \end{bmatrix} \tag{D-4}$$

Finally, the system with the amplified masses mD can be calculated by multiplying $\boldsymbol{M}_p$, $\boldsymbol{C}_p$ and $\boldsymbol{K}_p$ by the transformation matrix:

$$\boldsymbol{Q}_P=\begin{bmatrix} 1 & 0 & 0 \\ 0 & 1 & 0 \\ 0 & 0 & 1 \\ 0 & 0 & \rho \end{bmatrix} \tag{D-5}$$

The dispersion relationship of the phononic structure with directional inertial amplifiers is given by:

$$\det\left[-\lambda^2 \boldsymbol{M}_p \ddot{\boldsymbol{u}} + \lambda \boldsymbol{C}_P \dot{\boldsymbol{u}} + \boldsymbol{K}_P \boldsymbol{u}\right] = 0 \tag{D-6}$$

Where

$$\boldsymbol{M}_{p,\alpha} = \begin{bmatrix} m_L & 0 & 0 \\ 0 & m_L & 0 \\ 0 & 0 & m_D(1+\rho^2) \end{bmatrix} \tag{D-7}$$

$$\boldsymbol{K}_{p,a} = \begin{bmatrix} 2k_x & 0 & -k_x(1+e^{-j\mu_x}) \\ 0 & 2k_y & 2\rho k_y e^{\frac{-j\mu_x}{2}} \cos\left(\frac{\mu_y}{2}\right) \\ -k_x\left(1+e^{j\mu_x}\right) & 2\rho k_y e^{\frac{j\mu_x}{2}} \cos\left(\frac{\mu_y}{2}\right) & 2k_x + 2\rho^2 k_y \end{bmatrix} \tag{D-8}$$

$$\boldsymbol{C}_{p,a} = \begin{bmatrix} 2c_x & 0 & -c_x(1+e^{-j\mu_x}) \\ 0 & 2c_y & 2\rho c_y e^{\frac{-j\mu_x}{2}} \cos\left(\frac{\mu_y}{2}\right) \\ -c_x\left(1+e^{j\mu_x}\right) & 2\rho c_y e^{\frac{j\mu_x}{2}} \cos\left(\frac{\mu_y}{2}\right) & 2c_x + 2\rho^2 c_y \end{bmatrix} \tag{D-9}$$

D.3 Dynamics of the DDA Enhanced Phononic Latticed

In this appendix is given the explicit form of Eq. (20) of the lattice with and without the DDA for $M_x = M_y = 2$. The equation of motion of the finite phononic lattice without the DDA, for 2×2 number of units is expressed in matrix formulation as:

$$\boldsymbol{M}\ddot{\boldsymbol{u}}(t) + \boldsymbol{C}\dot{\boldsymbol{u}}(t) + \boldsymbol{K}_P \boldsymbol{u}(t) = \boldsymbol{F}e^{st} \tag{D-10}$$

where $\boldsymbol{M}_{8\times8}$, $\boldsymbol{C}_{8\times8}, \boldsymbol{K}_{8\times8}$, $\ddot{\boldsymbol{u}}_{8\times1}$, $\dot{\boldsymbol{u}}_{8\times1}, \boldsymbol{u}_{8\times1}$, $\boldsymbol{F}_{8\times1}$. The Global mass $\left[\boldsymbol{M}_p^G\right]$, damping $\left[\boldsymbol{C}_p^G\right]$ and stiffness $\left[K_p^G\right]$ matrices are defined as follows:

$$\boldsymbol{M}_p^G = \begin{bmatrix} m_L & 0 & 0 & 0 & 0 & 0 & 0 & 0 \\ 0 & m_L & 0 & 0 & 0 & 0 & 0 & 0 \\ 0 & 0 & m_D & 0 & 0 & 0 & 0 & 0 \\ 0 & 0 & 0 & m_D & 0 & 0 & 0 & 0 \\ 0 & 0 & 0 & 0 & m_D & 0 & 0 & 0 \\ 0 & 0 & 0 & 0 & 0 & m_D & 0 & 0 \\ 0 & 0 & 0 & 0 & 0 & 0 & m_L & 0 \\ 0 & 0 & 0 & 0 & 0 & 0 & 0 & m_L \end{bmatrix} \tag{D-11}$$

$$\boldsymbol{C}_p^G = \begin{bmatrix} 2c_x & 0 & -c_x & 0 & 0 & 0 & 0 & 0 \\ 0 & 2c_y & 0 & 0 & 0 & -c_y & 0 & 0 \\ -c_x & 0 & c_x & 0 & 0 & 0 & 0 & 0 \\ 0 & 0 & 0 & 2c_y & 0 & 0 & 0 & -c_y \\ 0 & 0 & 0 & 0 & 2c_x & 0 & -c_x & 0 \\ 0 & -c_y & 0 & 0 & 0 & c_y & 0 & 0 \\ 0 & 0 & 0 & 0 & -c_x & 0 & c_x & 0 \\ 0 & 0 & 0 & -c_y & 0 & 0 & 0 & c_y \end{bmatrix} \tag{D-12}$$

$$\boldsymbol{K}_p^G = \begin{bmatrix} 2k_x & 0 & -k_x & 0 & 0 & 0 & 0 & 0 \\ 0 & 2k_y & 0 & 0 & 0 & -k_y & 0 & 0 \\ -k_x & 0 & k_x & 0 & 0 & 0 & 0 & 0 \\ 0 & 0 & 0 & 2k_y & 0 & 0 & 0 & -k_y \\ 0 & 0 & 0 & 0 & 2k_x & 0 & -k_x & 0 \\ 0 & -k_y & 0 & 0 & 0 & k_y & 0 & 0 \\ 0 & 0 & 0 & 0 & -k_x & 0 & k_x & 0 \\ 0 & 0 & 0 & -k_y & 0 & 0 & 0 & k_y \end{bmatrix} \tag{D-13}$$

Similarly, for the lattice with the DDA, for M_x=M_y=2 the global mass $\left[\boldsymbol{M}_{p,\alpha}^G\right]$, damping $\left[\boldsymbol{C}_{p,\alpha}^G\right]$ and stiffness $\left[\boldsymbol{K}_{p,\alpha}^G\right]$ matrices can be calculated from:

$$\boldsymbol{M}_{p,\alpha}^G = \boldsymbol{Q}_G^T \boldsymbol{M}_p^G \boldsymbol{Q}_G \tag{D-14}$$

$$\boldsymbol{C}_{p,\alpha}^G = \boldsymbol{Q}_G^T \boldsymbol{C}_p^G \boldsymbol{Q}_G \tag{D-15}$$

$$\boldsymbol{K}_{p,\alpha}^G = \boldsymbol{Q}_G^T \boldsymbol{K}_p^G \boldsymbol{Q}_G \tag{D-16}$$

where the transform matrix in this case is:

$$\boldsymbol{Q}^{G} = \begin{bmatrix} 1 & 0 & 0 & 0 & 0 & 0 \\ 0 & 1 & 0 & 0 & 0 & 0 \\ 0 & 0 & 1 & 0 & 0 & 0 \\ 0 & 0 & \rho & 0 & 0 & 0 \\ 0 & 0 & 0 & 1 & 0 & 0 \\ 0 & 0 & 0 & \rho & 0 & 0 \\ 0 & 0 & 0 & 0 & 1 & 0 \\ 0 & 0 & 0 & 0 & 0 & 1 \end{bmatrix} \tag{D-17}$$

REFERENCES

Acar, G., & Yilmaz, C. (2013). Experimental and numerical evidence for the existence of wide and deep phononic gaps induced by inertial amplification in two-dimensional solid structures. *Journal of Sound and Vibration*, 332(24), 6389–6404. DOI: 10.1016/j.jsv.2013.06.022.

Adhikari, S., & Banerjee, A. (2022). Enhanced low-frequency vibration energy harvesting with inertial amplifiers. *Journal of Intelligent Material Systems and Structures*, 33(6), 822–838. DOI: 10.1177/1045389X211032281.

Aghamohammadi, M., Sorokin, V., & Mace, B. (2020). Response of linear parametric amplifiers with arbitrary direct and parametric excitations. *Mechanics Research Communications*, 109, 2–5. DOI: 10.1016/j.mechrescom.2020.103585.

Al-Shudeifat, M. A. (2014). Highly efficient nonlinear energy sink. *Nonlinear Dynamics*, 76(4), 1905–1920. DOI: 10.1007/s11071-014-1256-x.

An, X., Lai, C., He, W., & Fan, H. (2019). Three-dimensional meta-truss lattice composite structures with vibration isolation performance. *Extreme Mechanics Letters*, 33, 100577. DOI: 10.1016/j.eml.2019.100577

Anderson, J.G. (1989). Strong motion seismology. In: *Geophysics. Encyclopedia of Earth Science*. Springer, Boston, MA. DOI: 10.1007/0-387-30752-4_148.

Ang, L. Y. L., Koh, Y. K., & Lee, H. P. (2017). Broadband sound transmission loss of a large-scale membrane-type acoustic metamaterial for low-frequency noise control. *Applied Physics Letters*, 111(4), 41903. DOI: 10.1063/1.4995405.

Antoniadis, I. A., Kanarachos, S. A., Gryllias, K., & Sapountzakis, I. E. (2016). KDamping: A stiffness based vibration absorption concept. *Journal of Vibration and Control*, 24(3), 588–606. DOI: 10.1177/1077546316646514.

Antoniadis, I., & Paradeisiotis, A. (2018a). Acoustic Meta-materials Incorporating the KDamper Concept for Low Frequency Acoustic Isolation. *Acta Acustica United with Acustica*, 104(4), 636–646. DOI: 10.3813/AAA.919203.

Antoniadis, I., & Paradeisiotis, A. (2018b). A periodic acoustic meta-material concept incorporating negative stiffness elements for low-frequency acoustic insulation/absorption. In: *Proceedings of International Conference on Noise and Vibration Engineering and USD 2018 - International Conference on Uncertainty in Structural Dynamics (ISMA 2018)*, 1179–1193.

Antoniadis, I., Chronopoulos, D., Spitas, V., & Koulocheris, D. (2015). Hyper-damping properties of a stiff and stable linear oscillator with a negative stiffness element. *Journal of Sound and Vibration*, 346, 37–52. DOI: 10.1016/j.jsv.2015.02.028.

Aretz, M., & Vorländer, M. (2010). Efficient Modelling of Absorbing Boundaries in Room Acoustic FE Simulations. *Acta Acustica United with Acustica*, 96(6), 1042–1050. DOI: 10.3813/AAA.918366.

Ayr, U., Martellotta, F., & Rospi, G. (2017). A method for the low frequency qualification of reverberation test rooms using a validated finite element model. *Applied Acoustics*, 116, 33–42. DOI: 10.1016/j.apacoust.2016.09.001.

Bauer, C. (2008). Disc springs-theory and practice. Available at: https://www.christianbauer.com/en/img-cust/3_Theory_and_practice.pdf.

Beranek, L. L., & Vér, I. L. (1992). Noise and Vibration Control Engineering: Principles and Applications. *John Wiley & Sons*, Inc. DOI: 10.1002/9780470172568.

Bergamini, A., Miniaci, M., Delpero, T., Tallarico, D., Van Damme, B., Hannema, G., Leibacher, I., & Zemp, A. (2019). Tacticity in chiral phononic crystals. *Nature Communications*, 10(1), 4525. DOI: 10.1038/s41467-019-12587-7.

Bilal, O. R., & Hussein, M. I. (2013). Trampoline metamaterial: Local resonance enhancement by springboards. *Applied Physics Letters*, 103(11), 111901. DOI: 10.1063/1.4820796.

Bloch, F. (1929). Über die Quantenmechanik der Elektronen in Kristallgittern. *Zeitschrift Für Physik*, 52(7), 555–600. DOI: 10.1007/BF01339455.

Brillouin, L. (1946). Wave Propagation in Periodic Structures: Electric Filters and Crystal Lattices (1st ed.). *Dover Publications, Inc*.

Brûlé, S., Javelaud, E. H., Enoch, S., & Guenneau, S. (2013). Experiments on seismic metamaterials: Molding surface waves. *Physical Review Letters*, 112(13), 1–5. DOI: 10.1103/PhysRevLett.112.133901.

Callister, J. R., George, A. R., & Freeman, G. E. (1999). An empyrical scheme to predict the sound transmission loss of single-thickness panels. *Journal of Sound and Vibration*, 222(1), 145–151.

Carfagni, M., Lenzi, E., & Pierini, M. (1998). The Loss Factor as a Measure of Mechanical Damping. In: *Proc. SPIE Vol. 3243, Proceedings of the 16th International Modal Analysis Conference*., p.580.

Carrella, A., Brennan, M. J., & Waters, T. P. (2007). Static analysis of a passive vibration isolator with quasi-zero-stiffness characteristics. *Journal of Sound and Vibration*, 301 (3-5), 678–689. DOI: 10.1016/j.jsv.2006.10.-11.

Casablanca, O., Ventura, G., Garescì, F., Azzerboni, B., Chiaia, B., Chiappini, M., & Finocchio, G. (2018). Seismic isolation of buildings using composite foundations based on metamaterials. *Journal of Applied Physics*, 123(17), 174903. DOI: 10.1063/1.5018005.

Chen, C.-M., Hsu, Y.-C., & Fung, R.-F. (2012). System identification of a Scott–Russell amplifying mechanism with offset driven by a piezoelectric actuator. *Applied Mathematical Modelling*, 36(6), 2788–2802. DOI: 10.1016/j.apm.2011.09.064.

Chen, F., Zhang, Q., Gao, Y., & Dong, W. (2020). A review on the flexure-based displacement amplification mechanisms. *IEEE Access*, 8, 205919–205937. DOI: 10.1109/ACCESS.2020.3037827.

Chen, H., & Chan, C. T. (2007). Acoustic cloaking in three dimensions using acoustic metamaterials. *Applied Physics Letters*, 91(18), 183518. DOI: 10.1063/1.2803315.

Chen, M. Z. Q., Papageorgiou, C., Scheibe, F., Wang, F. C., & Smith, M. (2009). The missing mechanical circuit element. *IEEE Circuits and Systems Magazine*, 9(1), 10–26. DOI: 10.1109/MCAS.2008.931738

Chen, S., Wang, B., Zhu, S., Tan, X., Hu, J., Lian, X., Wang, L., & Wu, L. (2020). A novel composite negative stiffness structure for recoverable trapping energy. *Composites Part A: Applied Science and Manufacturing*, 129, 105697. DOI: 10.1016/j.compositesa.2019.105697

Chen, Y., Huang, G., Zhou, X., Hu, G., & Sun, C.-T. (2014). Analytical coupled vibroacoustic modeling of membrane-type acoustic metamaterials: Plate model. *The Journal of the Acoustical Society of America*, 136(6), 2926–2934. DOI: 10.1121/1.4901706.

Cheng, Z., Palermo, A., Shi, Z., & Marzani, A. (2020). Enhanced tuned mass damper using an inertial amplification mechanism. *Journal of Sound and Vibration*, 475, 115267. DOI: 10.1016/j.jsv.2020.115267.

Chondrogiannis, K. A., Colombi, A., Dertimanis, V., & Chatzi, E. (2022). Computational Verification and Experimental Validation of the Vibration-Attenuation Properties of a Geometrically Nonlinear Metamaterial Design. *Physical Review Applied*, 17(5), 54023. DOI: 10.1103/PhysRevApplied.17.054023.

Chowdhury, S., Banerjee, A., & Adhikari, S. (2021). Enhanced seismic base isolation using inertial amplifiers. *Structures*, 33, 1340–1353. DOI: 10.1016/j.istruc.2021.04.089.

Chronopoulos, D, Antoniadis, I., & Ampatzidis, T. (2017). Enhanced acoustic insulation properties of composite metamaterials having embedded negative stiffness inclusions. *Extreme Mechanics Letters*, 12, 48–54. DOI: 10.1016/j.eml.2016.10.012.

Chronopoulos, Dimitrios, Antoniadis, I., Collet, M., & Ichchou, M. (2015). Enhancement of wave damping within metamaterials having embedded negative stiffness inclusions. *Wave Motion*, 58, 165–179. DOI: 10.1016/j.wavemoti.2015.05.005.

Colombi, A., Roux, P., Guenneau, S., Gueguen, P., & Craster, R. V. (2016). Forests as a natural seismic metamaterial: Rayleigh wave bandgaps induced by local resonances. *Scientific Reports*, 1–7. DOI: 10.1038/srep19238.

Colombi, A., Zaccherini, R., Aguzzi, G., Palermo, A., & Chatzi, E. (2020). Mitigation of seismic waves: Metabarriers and metafoundations bench tested. *Journal of Sound and Vibration*, 485, 115537. DOI: 10.1016/j.jsv.2020.115537

Conlon, S. C., & Feurtado, P. A. (2018). Progressive phase trends in plates with embedded acoustic black holes. *The Journal of the Acoustical Society of America*, 143(2), 921. DOI: 10.1121/1.5024235.

Cowan, A. J. (2013). Sound Transmission Loss of Composite Sandwich Panels. *Department of Mechanical Engineering, University of Canterbury*, DOI: 10.26021/2698

Cremer, L., Heckl, M., & Petersson, B. A. T. (2005). Structure-borne sound: structural vibrations and sound radiation at audio frequencies. *Springer Berlin, Heidelberg*. DOI: 10.1007/b137728

Crocker, M. J. (2008). Handbook of Noise and Vibration Control. *John Wiley & Sons*, 1–1569. DOI: 10.1002/9780470209707.

Cummer, S. A., & Schurig, D. (2007). One path to acoustic cloaking. *New Journal of Physics*, 9(3), 45. DOI: 10.1088/1367-2630/9/3/045.

D'Alessandro, L., Belloni, E., Ardito, R., Corigliano, A., & Braghin, F. (2016). Modeling and experimental verification of an ultra-wide bandgap in 3D phononic crystal. *Applied Physics Letters*, 109(22), 221907. DOI: 10.1063/1.4971290.

Dai, W., & Yang, J. (2021). Vibration transmission and energy flow of impact oscillators with nonlinear motion constraints created by diamond-shaped linkage mechanism. *International Journal of Mechanical Sciences*, 194, 106212. DOI: 10.1016/j.ijmecsci.2020.106212.

Datta, T. K. (2010). Seismic Analysis of Structures. *John Wiley & Sons (Asia) Pte Ltd.* DOI:10.1002/9780470824634.

De Domenico, D., & Ricciardi, G. (2018a). Optimal design and seismic performance of tuned mass damper inerter (TMDI) for structures with nonlinear base isolation systems. *Earthquake Engineering & Structural Dynamics*, 47(12), 2539–2560. DOI; 10.1002/eqe.3098.

De Domenico, D., & Ricciardi, G. (2018b). Earthquake-resilient design of base isolated buildings with TMD at basement: Application to a case study. *Soil Dynamics and Earthquake Engineering*, 113, 503–521. DOI: 10.1016/j.soildyn.2018.06.022.

de Melo Filho, N. G. R., Van Belle, L., Claeys, C., Deckers, E., & Desmet, W. (2019). Dynamic mass based sound transmission loss prediction of vibro-acoustic metamaterial double panels applied to the mass-air-mass resonance. *Journal of Sound and Vibration*, 442, 28–44. DOI: 10.1016/j.jsv.2018.10.047.

Den Hartog JP (1956) Mechanical Vibrations. *McGraw-Hill, New York. 4th ed. New York*. DOI: 10.1038/161503c0.

den Wyngaert, J. C. E. Van, Schevenels, M., & Reynders, E. P. B. (2018). Predicting the sound insulation of finite double-leaf walls with a flexible frame. *Applied Acoustics*, 141, 93–105. DOI: 10.1016/j.apacoust.2018.06.020.

Dertimanis, V., Antoniadis, I., & Chatzi, E. (2016). Feasibility Analysis on the Attenuation of Strong Ground Motions Using Finite Periodic Lattices of Mass-in-Mass Barriers. *Journal of Engineering Mechanics*, 142(9), 4016060. DOI: 10.1061/(ASCE)EM.1943-7889.0001120.

Ding, C. L., & Zhao, X. P. (2011). Multi-band and broadband acoustic metamaterial with resonant structures. *Journal of Physics D: Applied Physics*, 44(21), 215402. DOI: 10.1088/0022-3727/44/21/215402.

Ding, H., Ji, J., & Chen, L. Q. (2019). Nonlinear vibration isolation for fluid-conveying pipes using quasi-zero stiffness characteristics. *Mechanical Systems and Signal Processing*, 121, 675–688. DOI: 10.1016/j.ymssp.2018.11.057.

Dolev, A., & Bucher, I. (2016). Experimental and Numerical Validation of Digital, Electromechanical, Parametrically Excited Amplifiers. Journal of Vibration and Acoustics, *Transactions of the ASME*, 138(6). DOI: 10.1115/1.4033897.

Du, J. T., Li, W. L., Xu, H. A., & Liu, Z. G. (2012). Vibro-acoustic analysis of a rectangular cavity bounded by a flexible panel with elastically restrained edges. *The Journal of the Acoustical Society of America*, 131(4), 2799–2810. DOI: 10.1121/1.3693652.

Fang, N., Xi, D., Xu, J., Ambati, M., Srituravanich, W., Sun, C., & Zhang, X. (2006). Ultrasonic metamaterials with negative modulus. *Nature Materials*, 5(6), 452–456. DOI: 10.1038/NMAT1644.

Feifei, S., & Lei, X. (2019). Bandgap Characteristics and Seismic Applications of Inerter-in-Lattice Metamaterials. *Journal of Engineering Mechanics*, 145(9), 4019067. DOI: 10.1061/(ASCE)EM.1943-7889.0001642.

Feng, X., & Jing, X. (2019). Human body inspired vibration isolation: Beneficial nonlinear stiffness, nonlinear damping & nonlinear inertia. *Mechanical Systems and Signal Processing*, 117, 786–812. DOI: 10.1016/j.ymssp.2018.08.040.

Feng, X., Jing, X., Xu, Z., & Guo, Y. (2019). Bio-inspired anti-vibration with nonlinear inertia coupling. *Mechanical Systems and Signal Processing*, 124, 562–595. DOI: 10.1016/j.ymssp.2019.02.001.

Firdaus, G., & Ahmad, A. (2010). Noise Pollution and Human Health: A Case Study of Municipal Corporation of Delhi. *Indoor and Built Environment*, 19(6), 648–656. DOI: 10.1177/1420326X10370532.

Fischer, S. C. L., Hillen, L., & Eberl, C. (2020). Mechanical Metamaterials on the Way from Laboratory Scale to Industrial Applications: Challenges for Characterization and Scalability. *Materials*, 13(16), 3605. DOI: 10.3390/ma13163605

Frahm, H. (1911). Device for damping of bodies (Patent No. US patent #989958). In: *U.S. Patent (US patent #989958)*.

Frandsen, N. M. M., Bilal, O. R., Jensen, J. S., & Hussein, M. I. (2016b). Inertial amplification of continuous structures: Large band gaps from small masses. *Journal of Applied Physics*, 119(12), 124902. DOI: 10.1063/1.4944429.

Gao, N., Hou, H., & Wu, J. H. (2018). A composite and deformable honeycomb acoustic metamaterial. *International Journal of Modern Physics B*, 32(20), 1850204. DOI: 10.1142/S0217979218502041.

Gao, N., Zhang, Z., Deng, J., Guo, X., Cheng, B., & Hou, H. (2022). Acoustic Metamaterials for Noise Reduction: A Review. *Advanced Materials Technologies*, 7(6), 2100698. DOI: 10.1002/admt.202100698

Giaralis, A., & Taflanidis, A. A. (2018). Optimal tuned mass-damper-inerter (TMDI) design for seismically excited MDOF structures with model uncertainties based on reliability criteria. *Structural Control and Health Monitoring*, 25(2), 1–22. DOI: 10.1002/stc.2082.

Goines, L., & Hagler, L. (2007). Noise pollution: a modern plague. *Southern Medical Journal*, 100(3), 287–294. DOI: 10.1097/smj.0b013e3180318be5.

Groby, J.-P., Lagarrigue, C., Brouard, B., Dazel, O., Tournat, V., & Nennig, B. (2014). Using simple shape three-dimensional rigid inclusions to enhance porous layer absorption. *The Journal of the Acoustical Society of America*, 136(3), 1139–1148. DOI: 10.1121/1.4892760.

Guell Izard, A., Fabian Alfonso, R., McKnight, G., & Valdevit, L. (2017). Optimal design of a cellular material encompassing negative stiffness elements for unique combinations of stiffness and elastic hysteresis. *Materials & Design*, 135, 37–50. DOI: 10.1016/j.matdes.2017.09.001.

Guo, F., Sun, Z., Zhang, S., Cao, R., & Li, H. (2022). Optimal design and reliability analysis of a compliant stroke amplification mechanism. *Mechanism and Machine Theory*, 171, 104748. DOI: 10.1016/J.MECHMACHTHEORY.2022.104748.

Ha, L., & Fang, L. J. (2014). Error analysis of a non-contact parallel plane sensor based on Monte Carlo method. *Advanced Materials Research*, 1022(4), 96–99. DOI: 10.4028/www.scientific.net/AMR.1022.96

Hao, J., Wang, J., Liu, X., Padilla, W. J., Zhou, L., & Qiu, M. (2010). High performance optical absorber based on a plasmonic metamaterial. *Applied Physics Letters*, 96(25), 251104. DOI: 10.1063/1.3442904.

Ho, K. M., Cheng, C. K., Yang, Z., Zhang, X. X., & Sheng, P. (2003). Broadband locally resonant sonic shields. *Applied Physics Letters*, 83(26), 5566. DOI: 10.1063/1.1637152.

Hong, Y., Wu, Y., Jin, S., Liu, D., & Chi, B. (2022). Design and Analysis of a Microgripper with Three-Stage Amplification Mechanism for Micromanipulation. *Micromachines*, 13(3), 336. DOI: 10.3390/mi13030366.

Huang, H. H., & Sun, C. T. (2009). Wave attenuation mechanism in an acoustic metamaterial with negative effective mass density. *New Journal of Physics*, 11(1), 13003. DOI: 10.1088/1367-2630/11/1/013003.

Huang, H. H., & Sun, C. T. (2012). Anomalous wave propagation in a one-dimensional acoustic metamaterial having simultaneously negative mass density and Young's modulus. *The Journal of the Acoustical Society of America*, 132(4), 2887–2895. DOI: 10.1121/1.4744977.

Huang, H. H., Sun, C. T., & Huang, G. L. (2009). On the negative effective mass density in acoustic metamaterials. *International Journal of Engineering Science*, 47(4), 610–617. DOI: 10.1016/j.ijengsci.2008.12.007.

Hussein, M I, Leamy, M. J., & Ruzzene, M. (2014). Dynamics of phononic materials and structures: Historical origins, recent progress, and future outlook. *Applied Mechanics Reviews*, 66(4), 040802. DOI: 10.1115/1.4026911.

Hussein, Mahmoud I, & Frazier, M. J. (2013). Metadamping: An emergent phenomenon in dissipative metamaterials. *Journal of Sound and Vibration*, 332(20), 4767–4774. DOI: 10.1016/j.jsv.2013.04.041.

Hussein, Mahmoud I. (2009). Theory of damped Bloch waves in elastic media. *Physical Review B*, 80(21), 212301. DOI: 10.1103/PhysRevB.80.212301.

Ibrahim, R. (2008). Recent advances in nonlinear passive vibration isolators. *Journal of Sound and Vibration*, 314 (3-5), 371–452. DOI: 10.1016/j.jsv.2008.01.014.

Iqbal, S., Lai, Y. J., Shakoor, R. I., Raffi, M., & Bazaz, S. A. (2021). Design, analysis, and experimental investigation of micro-displacement amplification compliant mechanism for micro-transducers. *Review of Scientific Instruments*, 92(10). DOI: 10.1063/5.0061820

ISO 10140 Acoustics — Laboratory measurement of sound insulation of building elements.

ISO 15186, Acoustics —Measurement of sound insulation in buildings and of building elements using sound intensity.

ISO 717, Acoustics — Rating of sound insulation in buildings and of building elements.

Jung, J., Kook, J., Goo, S., & Wang, S. (2017). Sound transmission analysis of plate structures using the finite element method and elementary radiator approach with radiator error index. *Advances in Engineering Software*, 112, 1–15. DOI: 10.1016/j.advengsoft.2017.06.001.

Kalderon, M., Mantakas, A., Paradeisiotis, A., Antoniadis, I., & Sapountzakis, E. J. (2022). Locally resonant metamaterials utilizing dynamic directional amplification: An application for seismic mitigation. *Applied Mathematical Modelling*, 110, 1–16. DOI: 10.1016/J.APM.2022.05.037.

Kalderon, M., Paradeisiotis, A., & Antoniadis, I. (2021). 2D Dynamic Directional Amplification (DDA) in Phononic Metamaterials. *Materials*, 14(9). DOI: 10.3390/ma14092302.

Kalderon, M., Paradeisiotis, A., & Antoniadis, I. (2021). A Meta-structure for Low-frequency Acoustic Treatment Based on a KDamper-Inertial Amplification Concept. In: *Proceedings of Euronoise 2021*, 1333–1343.

Kampitsis, A., Kapasakalis, K., & Via-Estrem, L. (2022). An integrated FEA-CFD simulation of offshore wind turbines with vibration control systems. *Engineering Structures*, 254, 113859. DOI: 10.1016/J.ENGSTRUCT.2022.113859.

Kapasakalis, K. (2020). Dynamic Vibration Absorbers in Civil Engineering Structures, *PHD Thesis, National Technical University of Athens*. DOI: 10.12681/eadd/48215.

Kapasakalis, K. A., Alvertos, A. E., Mantakas, A. G., Antoniadis, I. A., & Sapountzakis, E. J. (2020). Advanced negative stiffness vibration absorber coupled with soil-structure interaction for seismic protection of buildings. *In: Proceedings of the International Conference on Structural Dynamic, (EURODYN 2020),* 4160–4176. DOI: 10.47964/1120.9340.19963.

Kapasakalis, K. A., Antoniadis, I. A., & Sapountzakis, E. J. (2020). Performance assessment of the KDamper as a seismic Absorption Base. *Structural Control and Health Monitoring*, 27(4), e2482. DOI: 10.1002/stc.2482.

Kapasakalis, K. A., Antoniadis, I. A., & Sapountzakis, E. J. (2021). STIFF vertical seismic absorbers. *Journal of Vibration and Control*, 28(15-16). DOI: 10.1177/10775463211001624.

Kapasakalis, K.A., Antoniadis, I. A., & Sapountzakis, E. J. (2021). Constrained optimal design of seismic base absorbers based on an extended KDamper concept. *Engineering Structures*, 226, 111312. DOI: 10.1016/j.engstruct.2020.111312.

Kapasakalis, Konstantinos A., Antoniadis, I. A., Sapountzakis, E. J., & Kampitsis, A. E. (2021). Vibration Mitigation of Wind Turbine Towers Using Negative Stiffness Absorbers. *Journal of Civil Engineering and Construction*, 10(3), 123–139. DOI: 10.32732/JCEC.2021.10.3.123.

Kim, Y. H. (2010). Sound propagation: an impedance based approach. *John Wiley & Sons*.

Kishore, S. E., Sujithra, R., & Dhatreyi, B. (2021). A review on latest acoustic noise mitigation materials. *Materials Today: Proceedings*, 47(14), 4700–4707. DOI: 10.1016/j.matpr.2021.05.600.

Koblar, D., & Boltežar, M. (2013). Evaluation of the Frequency-Dependent Young's Modulus and Damping Factor of Rubber from Experiment and Their Implementation in a Finite-Element Analysis. *Experimental Techniques*, 40(235-244). DOI: 10.1111/ext.12066.

Krödel, S., Thomé, N., & Daraio, C. (2015). Wide band-gap seismic metastructures. *Extreme Mechanics Letters*, 4, 111–117. DOI: 10.1016/j.eml.2015.05.004

Kulkarni, P. P., & Manimala, J. M. (2016). Longitudinal elastic wave propagation characteristics of inertant acoustic metamaterials. *Journal of Applied Physics*, 119(24), 245101. DOI: 10.1063/1.4954074.

Kushwaha, M. S., Halevi, P., Dobrzynski, L., & Djafari-Rouhani, B. (1993). Acoustic band structure of periodic elastic composites. *Physical Review Letters*, 71(13), 2022–2025. DOI: 10.1103/PhysRevLett.71.2022.

Kushwaha, M. S., Halevi, P., Martínez, G., Dobrzynski, L., & Djafari-Rouhani, B. (1994). Theory of acoustic band structure of periodic elastic composites. *Physical Review B*, 49(4), 2313. DOI: 10.1103/PhysRevB.49.2313.

Lakes, R. (1993). Advances in negative Poisson's ratio materials. *Advanced Materials*, 5(4), 293–296. DOI: 10.1002/adma.19930050416.

Langfeldt, F., & Gleine, W. (2019). Membrane- and plate-type acoustic metamaterials with elastic unit cell edges. *Journal of Sound and Vibration*, 453, 65–86. DOI: 10.1016/J.JSV.2019.04.018.

Langfeldt, F., Gleine, W., & Von Estorff, O. (2015). Analytical model for low-frequency transmission loss calculation of membranes loaded with arbitrarily shaped masses. *Journal of Sound and Vibration*, 349, 315–329. DOI: 10.1016/J.JSV.2015.03.037.

Lazar, I. F., Neild, S. A., & Wagg, D. J. (2014). Using an inerter-based device for structural vibration suppression. *Earthquake Engineering and Structural Dynamics,* 43(8), 1129–1147. DOI: 10.1002/eqe.2390.

Le, T. D., & Ahn, K. K. (2013). Experimental investigation of a vibration isolation system using negative stiffness structure. *International Journal of Mechanical Sciences*, 70, 99–112. DOI: 10.1016/j.ijmecsci.2013.02.009.

Lee, C. M., & Goverdovskiy, V. N. (2012). A multi-stage high-speed railroad vibration isolation system with "negative" stiffness. *Journal of Sound and Vibration*, 331(4), 914–921. DOI: 10.1016/j.jsv.2011.09.014.

Lee, J.-H., & Ih, J.-G. (2004). Significance of resonant sound transmission in finite single partitions. *Journal of Sound and Vibration*, 277(4), 881–893. DOI: 10.1016/j.jsv.2003.09.023.

Leppington, F. G., Heron, K. H., Broadbent, E. G., & Mead, S. M. (1987). Resonant and Non-Resonant Acoustic Properties of Elastic Panels. II. The Transmission Problem. *Proceedings of the Royal Society of London Series A*, 412(1843), 309–337. DOI: 10.1098/rspa.1987.0091.

Li, Jensen, & Chan, C. T. (2004). Double-negative acoustic metamaterial. *Phys. Rev. E*, 70(5), 55602. DOI: 10.1103/PhysRevE.70.055602.

Li, Jingru, & Li, S. (2018). Generating ultra wide low-frequency gap for transverse wave isolation via inertial amplification effects. *Physics Letters A*, 382(5), 241–247. DOI: 10.1016/j.physleta.2017.11.023.

Li, W. L., Zhang, X., Du, J., & Liu, Z. (2009). An exact series solution for the transverse vibration of rectangular plates with general elastic boundary supports. *Journal of Sound and Vibration*, 321(1), 254–269. DOI: 10.1016/j.jsv.2008.09.035.

Liao, G., Luan, C., Wang, Z., Liu, J., Yao, X., & Fu, J. (2021). Acoustic Metamaterials: A Review of Theories, Structures, Fabrication Approaches, and Applications. *Advanced Materials Technologies*, 6(5), 1–29. DOI: 10.1002/admt.202000787.

Lin, Q., Zhou, J., Pan, H., Xu, D., & Wen, G. (2021). Numerical and Experimental Investigations on Tunable Low-frequency Locally Resonant Metamaterials. *Acta Mechanica Solida Sinica*, 34(5), 612–623. DOI: 10.1007/s10338-021-00220-4.

Lin, Q., Zhou, J., Wang, K., Xu, D., Wen, G., & Wang, Q. (2023). Three-dimensional quasi-zero-stiffness metamaterial for low-frequency and wide complete band gap. *Composite Structures*, 307, 116656. DOI: 10.1016/j.compstruct.2022.116656.

Liu, J., Guo, H., & Wang, T. (2020). A Review of Acoustic Metamaterials and Phononic Crystals. *Crystals*, 10(4). DOI: 10.3390/cryst10040305.

Liu, X., Tyler, T., Starr, T., Starr, A. F., Jokerst, N. M., & Padilla, W. J. (2011). Taming the blackbody with infrared metamaterials as selective thermal emitters. *Physical Review Letters*, 107(4), 045901. DOI: 10.1103/PHYSREVLETT.107.045901.

Liu, Z., Zhang, X., Mao, Y., Zhu, Y. Y., Yang, Z., Chan, C. T., & Sheng, P. (2000). Locally resonant sonic materials. *Science*, 289(5485), 1734–1736. DOI: 10.1126/science.289.5485.1734.

London, A. (1950). Transmission of Reverberant Sound through Double Walls. *The Journal of the Acoustical Society of America*, 22(2), 270–279. DOI: 10.1121/1.1906601.

Løvholt, F., Madshus, C., & Norén-Cosgriff, K. (2011). Analysis of low frequency sound and sound induced vibration in a Norwegian wooden building. *Noise Control Engineering Journal*, 59(4), 383–396. DOI: 10.3397/1.3596618.

Løvholt, F., Norèn-Cosgriff, K., Madshus, C., & Ellingsen, S. E. (2017). Simulating low frequency sound transmission through walls and windows by a two-way coupled fluid structure interaction model. *Journal of Sound and Vibration*, 396, 203–216. DOI: 10.1016/j.jsv.2017.02.026.

Lu, M.-H., Feng, L., & Chen, Y.-F. (2009). Phononic crystals and acoustic metamaterials. *Materials Today*, 12(12), 34–42. DOI: 10.1016/S1369-7021(09)70315-3.

Ma, R., Bi, K., & Hao, H. (2021). Inerter-based structural vibration control: A state-of-the-art review. *Engineering Structures*, 243, 112655. DOI: 10.1016/j.engstruct.2021.112655.

Maidanik, G. (1966). The influence of fluid loading on the radiation from orthotropic plates. Journal of Sound and Vibration, 3(3), 288–299. DOI: 10.1016/0022-460X(66)90097-6.

Makris, S. E., Dym, C. L., & Smith, J. M. (1986). Transmission loss optimization in acoustic sandwich panels. *The Journal of the Acoustical Society of America*, 79(6), 1833–1843. DOI: 10.1121/1.393746.

Mantakas, A. G., Kapasakalis, K. A., Alvertos, A. E., Antoniadis, I. A., & Sapountzakis, E. J. (2022). A negative stiffness dynamic base absorber for seismic retrofitting of residential buildings. *Structural Control and Health Monitoring*, 29(12), e3127. DOI: 10.1002/STC.3127.

Mantakas, A., Chondrogiannis, K. A., Kalderon, M., Kapasakalis, K., Chatzi, E., Sapountzakis, E., & Antoniadis, I. (2023).. Design and Experimental Verification of an Extended KDamper - Based Vibration Absorber. In: *Proceedings of EURODYN 2023*.

Marburg, S. (2002). Six boundary elements per wavelength: Is that enough? *Journal of Computational Acoustics*, 10(01), 25–51. DOI: 10.1142/S0218396X02001401.

Marian, L., & Giaralis, A. (2014). Optimal design of a novel tuned mass-damper-inerter (TMDI) passive vibration control configuration for stochastically support-excited structural systems. *Probabilistic Engineering Mechanics*, 38, 156–164. DOI: 10.1016/j.probengmech.2014.03.007.

Martakis, P., Aguzzi, G., Dertimanis, V. K., Chatzi, E. N., & Colombi, A. (2021). Nonlinear periodic foundations for seismic protection: Practical design, realistic evaluation and stability considerations. *Soil Dynamics and Earthquake Engineering*, 150, 106934. DOI: 10.1016/j.soildyn.2021.106934.

Martínez-Sala, R., Sancho, J., Sánchez, J. V., Gómez, V., Llinares, J., & Meseguer, F. (1995). Sound attenuation by sculpture. *Nature*, 378(6554), 241. DOI: 10.1038/378241a0.

Mazzotti, M., Foehr, A., Bilal, O. R., Bergamini, A., Bosia, F., Daraio, C., Pugno, N. M., & Miniaci, M. (2023). Bio-inspired non self-similar hierarchical elastic metamaterials. *International Journal of Mechanical Sciences*, 241, 107915. DOI: 10.1016/j.ijmecsci.2022.107915.

McNamara, R. J. (1977). Tuned Mass Dampers for Buildings. *Journal of the Structural Division*, 103(9), 1785–1798. DOI:10.1061/JSDEAG.0004721.

Mead, D. M. (1996). Wave Propagation in Continuous Periodic Structures: Research Contribution from Southampton, 1964–1995. *Journal of Sound and Vibration*, 190(3), 495–524. DOI: 10.1006/jsvi.1996.0076.

Mei, J, Liu, Z., Wen, W., & Sheng, P. (2006). Effective mass density of fluid-solid composites. *Physical Review Letters*, 96(2), 24301. DOI: 10.1103/PhysRevLett.96.024301.

Mei, J., Ma, G., Yang, M., Yang, J., Sheng, P. (2013). Dynamic Mass Density and Acoustic Metamaterials. In: *Deymier, P. (eds) Acoustic Metamaterials and Phononic Crystals. Springer Series in Solid-State Sciences*, vol 173. Springer, Berlin, Heidelberg. DOI: 10.1007/978-3-642-31232-8_5.

Mei, Jun, Ma, G., Yang, M., Yang, Z., Wen, W., & Sheng, P. (2012). Dark acoustic metamaterials as super absorbers for low-frequency sound. *Nature Communications*, 3(1), 1–7. DOI: 10.1038/ncomms1758.

Mi, Y., & Yu, X. (2021). Sound transmission of acoustic metamaterial beams with periodic inertial amplification mechanisms. *Journal of Sound and Vibration*, 499, 116009. DOI: 10.1016/j.jsv.2021.116009.

Michelis, P., & Spitas, V. (2010). Numerical and experimental analysis of a triangular auxetic core made of CFR-PEEK using the Directionally Reinforced Integrated Single-yarn (DIRIS) architecture. *Composites Science and Technology*, 70(7), 1064–1071. DOI: 10.1016/J.COMPSCITECH.2010.01.013.

Milton, G. W., & Nicorovici, N. A. P. (2006). On the cloaking effects associated with anomalous localized resonance. *Proceedings of the Royal Society A: Mathematical, Physical and Engineering Sciences*, 462(2074), 3027–3059. DOI: 10.1098/RSPA.2006.1715.

Milton, G. W., Briane, M., & Willis, J. R. (2006). On cloaking for elasticity and physical equations with a transformation invariant form. *New Journal of Physics*, 8(10), 248. DOI: 10.1088/1367-2630/8/10/248.

Miniaci, M., Krushynska, A., Bosia, F., & Pugno, N. M. (2016). Large scale mechanical metamaterials as seismic shields. *New Journal of Physics*, 18(8), 83041. DOI: 10.1088/1367-2630/18/8/083041.

Miranda, R., Babilio, E., Singh, N., Santos, F., & Fraternali, F. (2020). Mechanics of smart origami sunscreens with energy harvesting ability. *Mechanics Research Communications*, 105, 103503. DOI: 10.1016/j.mechrescom.2020.103503.

Molyneaux W (1957) *Supports for Vibration Isolation*. G. Britain: ARC/CP-322, Aer Res Council.

Montero de Espinosa, F. R., Jiménez, E., & Torres, M. (1998). Ultrasonic Band Gap in a Periodic Two-Dimensional Composite. *Physical Review Letters*, 80(6), 1208. DOI: 10.1103/PhysRevLett.80.1208.

Moore, J. A., & Lyon, R. H. (1991). Sound transmission loss characteristics of sandwich panel constructions. *The Journal of the Acoustical Society of America*, 89(2), 777–791. DOI: 10.1121/1.1894638.

Moraes, F. H., Silveira, M., & Gonçalves, P. J. P. (2018). On the dynamics of a vibration isolator with geometrically nonlinear inerter. *Nonlinear Dynamics*, 93(3), 1325–1340. DOI: 10.1007/s11071-018-4262-6.

Morris, C., Bekker, L., Spadaccini, C., Haberman, M., & Seepersad, C. (2019). Tunable Mechanical Metamaterial with Constrained Negative Stiffness for Improved Quasi-Static and Dynamic Energy Dissipation. *Advanced Engineering Materials*, 21(7), 1900163. DOI: 10.1002/adem.201900163.

Muhammad, S., Wang, S., Li, F., & Zhang, C. (2020). Bandgap enhancement of periodic nonuniform metamaterial beams with inertial amplification mechanisms. *Journal of Vibration and Control*, 26(15–16), 1309–1318. DOI: 1077546319895630.

Nagarajaiah, S., & Sonmez, E. (2007). Structures with Semiactive Variable Stiffness Single/Multiple Tuned Mass Dampers. *Journal of Structural Engineering*, 133(1), 67–77. DOI: 10.1061/(asce)0733-9445(2007)133:1(67).

Nakamura, Y., Fukukita, A., Tamura, K., Yamazaki, I., Matsuoka, T., Hiramoto, K., & Sunakoda, K. (2014). Seismic response control using electromagnetic inertial mass dampers. *Earthquake Engineering & Structural Dynamics*, 43(4), 507–527. DOI: 10.1002/eqe.2355.

Narayanamurti, V., Störmer, H. L., Chin, M. A., Gossard, A. C., & Wiegmann, W. (1979). Selective Transmission of High-Frequency Phonons by a Superlattice: The "Dielectric" Phonon Filter. *Physical Review Letters*, 43(27), 2012. DOI: 10.1103/PhysRevLett.43.2012.

Norén-Cosgriff, K., Løvholt, F., Brekke, A., Madshus, C., & Høilund-Kaupang, H. (2016). Countermeasures against noise and vibrations in lightweight wooden buildings caused by outdoor sources with strong low frequency components. *Noise Control Engineering Journal*, 64, 737–752. DOI: 10.3397/1/376416.

Norris, A. N. (2009). Acoustic metafluids. *The Journal of the Acoustical Society of America*, 125(2), 839–849. DOI: 10.1121/1.3050288

Ordubadi, A., & Lyon, R. H. (1979). Effect of orthotropy on the sound transmission through plywood panels. *The Journal of the Acoustical Society of America*, 65(1), 133–139. DOI: 10.1121/1.382255.

Ou, D. Y. (2015). Low frequency sound insulation analysis and evaluation of stiffened building structures. *Building and Environment*, 94, 802–809. DOI: 10.1016/j.buildenv.2015.05.016.

Palazzo, B., Petti, L., & de Ligio, M. (1997). Response of base isolated systems equipped with tuned mass dampers to random excitations. *Journal of Structural Control*, 4(1), 9–22. DOI: 10.1002/stc.4300040105.

Palermo, A., Krödel, S., Marzani, A., & Daraio, C. (2016). Engineered metabarrier as shield from seismic surface waves. *Scientific Reports*, 6, 1–10. DOI: 10.1038/srep39356.

Palermo, A., Vitali, M., & Marzani, A. (2018). Metabarriers with multi-mass locally resonating units for broad band Rayleigh waves attenuation. *Soil Dynamics and Earthquake Engineering*, 113, 265–277. DOI: 10.1016/j.soildyn.2018.05.035.

Paradeisiotis, A. (2019). Applications of oscillators in energy conversion. *PHD thesis, National Technical University of Athens*. DOI: 10.26240/heal.ntua.18666.

Paradeisiotis, A., Antoniadis, I. (2021). Implementation of a Low-Frequency Acoustic Isolation Panel Incorporating KDamper-Based Mounts. In: *Proceedings of the 14th International Conference on Vibration Problems. Lecture Notes in Mechanical Engineering. Springer, Singapore*. DOI: 10.1007/978-981-15-8049-9_14.

Paradeisiotis, A., Kalderon, M., & Antoniadis, I. (2021). Advanced negative stiffness absorber for low-frequency noise insulation of panels. *AIP Advances*, 11(6), 65003. DOI: 10.1063/5.0045937.

Paradeisiotis, A., Kalderon, M., Antoniadis, I., & Fouriki, L. (2020). Acoustic Performance Evaluation of a panel utilizing negative stiffness mounting for low frequency noise control. In: *Proceedings of EURODYN 2020*, 4093–4110. DOI: 10.47964/1120.9335.19276.

Paradeisiotis, A., Tsioumanis, K., Antoniadis, I., & Fouriki, K. (2020). A machine based mount based on the KDamper for vibration absorption at low frequencies. In: *Proceedings of EURODYN 2020*, 4111–4124. DOI: 10.47964/1120.9336.19278.

Pasala, D. T., Sarlis, A., Nagarajaiah, S., Reinhorn, A., Constantinou, M., & Taylor, D. (2013). Adaptive Negative Stiffness: New Structural Modification Approach for Seismic Protection. *Advanced Materials Research*, 639–640. DOI: 10.4028/www.scientific.net/AMR.639-640.54.

Passchier-Vermeer, W., & Passchier, W. F. (2000). Noise exposure and public health. *Environmental Health Perspectives*, 108, 123–131. DOI: 10.1289/ehp.00108s1123.

Pellicier, A., & Trompette, N. (2007). A review of analytical methods, based on the wave approach, to compute partitions transmission loss. *Applied Acoustics*, 68(10), 1192–1212. DOI: 10.1016/j.apacoust.2006.06.010.

Pennec, Y., Djafari-Rouhani, B., Larabi, H., Vasseur, J. O., & Hladky-Hennion, A. C. (2008). Low-frequency gaps in a phononic crystal constituted of cylindrical dots deposited on a thin homogeneous plate. *Physical Review B*, 78(10), 104105. DOI: 10.1103/PhysRevB.78.104105.

Platus D. L., (1992). Negative-stiffness-mechanism vibration isolation systems. In: *Proc. of SPIE, 1992, Vibration Control in Microelectronics, Optics, and Metrology*, 44–54. DOI: 10.1117/12.56823.

Putra, A., & Thompson, D. J. (2010). Sound radiation from rectangular baffled and unbaffled plates. *Applied Acoustics*, 71(12), 1113–1125. DOI: 10.1016/j.apacoust.2010.06.009.

Qin, L., Yan, W., & Li, Y. (2009). Design of frictional pendulum TMD and its wind control effectiveness. *Journal of Earthquake Engineering and Engineering Vibration*, 29(5), 153–157.

Rayleigh, J. W. S. B., & Strutt, J. W. (1896). The Theory of Sound (Vol. 1). *Macmillan, 1894*. DOI: 10.1017/CBO9781139058087.

Romero-Garca, V., Snchez-Pérez, J. V., & Garcia-Raffi, L. M. (2011). Tunable wideband bandstop acoustic filter based on two-dimensional multiphysical phenomena periodic systems. *Journal of Applied Physics*, 110(1). DOI: 10.1063/1.3599886.

Roussos, L. (1985). Noise transmission loss of a rectangular plate in an infinite baffle. *The Journal of the Acoustical Society of America*, 75. DOI: 10.1121/1.2021367.

Saitoh, M. (2012). On the performance of gyro-mass devices for displacement mitigation in base isolation systems. *Structural Control and Health Monitoring*, 19(2), 246–259. DOI: 10.1002/stc.419.

Salari-Sharif, L., Haghpanah, B., Guell Izard, A., Tootkaboni, M., & Valdevit, L. (2019). Negative-Stiffness Inclusions as a Platform for Real-Time Tunable Phononic Metamaterials. *Physical Review Applied*, 11(2), 1. DOI: 10.1103/PhysRevApplied.11.024062.

Sánchez-Pérez, J. V., Caballero, D., Mártinez-Sala, R., Rubio, C., Sánchez-Dehesa, J., Meseguer, F., Llinares, J., & Gálvez, F. (1998). Sound Attenuation by a Two-Dimensional Array of Rigid Cylinders. *Physical Review Letters*, 80(24), 5325. DOI: 10.1103/PhysRevLett.80.5325.

Sapountzakis, E. J., Syrimi, P. G., & Antoniadis, I. A. (2016). KDamper Concept in Seismic Isolation of Bridges. In Proceedings of the 1st International Conference on Natural Hazards & Infrastructure (ICONHIC 2016), 28–30.

Sapountzakis, E. J., Syrimi, P. G., Pantazis, I. A., & Antoniadis, I. A. (2017). KDamper concept in seismic isolation of bridges with flexible piers. *Engineering Structures*, 153, 525–539. DOI: 10.1016/j.engstruct.2017.10.044.

Sarlis, A. A., Pasala, D. T. R., Constantinou, M. C., Reinhorn, A. M., Nagarajaiah, S., & Taylor, D. P. (2016). Negative Stiffness Device for Seismic Protection of Structures: Shake Table Testing of a Seismically Isolated Structure. *Journal of Structural Engineering*, 142(5), 04016005. DOI: 10.1061/(asce)st.1943-541x.0001455.

Seismosoft. *SeismoArtif*—A Computer Program for Generating Artificial Earthquake Accelerograms Matched to a Specific Target Response Spectrum; 2018:2018.

Shahosseini, I., & Najafi, K. (2014). Mechanical amplifier for translational kinetic energy harvesters. *Journal of Physics: Conference Series*, 557(1), 012135. DOI: 10.1088/1742-6596/557/1/012135.

Shen, Y., Peng, H., Li, X., & Yang, S. (2017). Analytically optimal parameters of dynamic vibration absorber with negative stiffness. *Mechanical Systems and Signal Processing*. DOI: 10.1016/j.ymssp.2016.08.018

Shi, B., Dai, W., & Yang, J. (2022). Performance analysis of a nonlinear inerter-based vibration isolator with inerter embedded in a linkage mechanism. *Nonlinear Dynamics*, 109, 419-442. DOI: 10.1007/s11071-022-07564-7.

Sigalas, M. M., & Economou, E. N. (1992). Elastic and acoustic wave band structure. *Journal of Sound and Vibration*, 158(2), 377–382. DOI: 10.1016/0022-460X(92)90059-7.

Sigalas, M., & Economou, E. N. (1993). Band structure of elastic waves in two dimensional systems. *Solid State Communications*, 86(3), 141–143. DOI: 10.1016/0038-1098(93)90888-T.

Smith, D. R., Padilla, W. J., Vier, D. C., Nemat-Nasser, S. C., & Schultz, S. (2000). Composite Medium with Simultaneously Negative Permeability and Permittivity. *Physical Review Letters*, 84(18), 4184. DOI: 10.1103/PhysRevLett.84.4184.

Smith, M. (2009). ABAQUS/Standard User's Manual, Version 6.9.

Smith, M. C. (2002). Synthesis of mechanical networks: The inerter. *IEEE Transactions on Automatic Control*, 47(10), 1648–1662. DOI: 10.1109/TAC.2002.803532.

Spiousas, I., Torrent, D., & Sánchez-Dehesa, J. (2011). Experimental realization of broadband tunable resonators based on anisotropic metafluids. *Applied Physics Letters*, 98(24), 244102. DOI: 10.1063/1.3599849.

Sprik, R., & Wegdam, G. H. (1998). Acoustic band gaps in composites of solids and viscous liquids. *Solid State Communications*, 106(2), 77–81. DOI: 10.1016/S0038-1098(98)00029-5.

Sun, T., Lai, Z., Nagarajaiah, S., & Li, H. N. (2017). Negative stiffness device for seismic protection of smart base isolated benchmark building. *Structural Control and Health Monitoring*, 24(11), e1968. DOI: 10.1002/stc.1968.

Sun, X., Wang, J., Yi, S., & Hu, W. (2022). Design and analysis of a novel piezoelectric inertial actuator with large stepping displacement amplified by compliant mechanism. *Microsystem Technologies*, 28(4), 1025–1035. DOI: 10.1007/s00542-022-05257-0.

Suzuki, T., & Yu, P. K. L. (1998). Complex elastic wave band structures in three-dimensional periodic elastic media. *Journal of the Mechanics and Physics of Solids*, 46(1), 115–138. DOI: 10.1016/S0022-5096(97)00023-9.

Takahashi, D. (1995). Effects of panel boundedness on sound transmission problems. *The Journal of the Acoustical Society of America*, 98(5), 2598–2606. DOI: 10.1121/1.413226.

Takewaki, I., Murakami, S., Yoshitomi, S., & Tsuji, M. (2012). Fundamental mechanism of earthquake response reduction in building structures with inertial dampers. *Structural Control and Health Monitoring*, 19(6), 590–608. DOI: 10.1002/STC.457.

Taniker, S., & Yilmaz, C. (2015). Design, analysis and experimental investigation of three-dimensional structures with inertial amplification induced vibration stop bands. *International Journal of Solids and Structures*, 72, 88–97. DOI: 10.1016/j.ijsolstr.2015.07.013.

Taniker, S., & Yilmaz, C. (2017). Generating ultra wide vibration stop bands by a novel inertial amplification mechanism topology with flexure hinges. *International Journal of Solids and Structures*, 106–107, 129–138. DOI: 10.1016/j.ijsolstr.2016.11.026.

Tsai, H. C. (1995). The effect of tuned-mass dampers on the seismic response of base-isolated structures. *International Journal of Solids and Structures*, 32(8–9), 1195–1210. DOI: 10.1016/0020-7683(94)00150-U.

Udwadia, F. E., & Kalaba, R. E. (1992). A new perspective on constrained motion. *Proceedings of the Royal Society of London. Series A: Mathematical and Physical Sciences*, 439(1906), 407–410. DOI: 10.1098/rspa.1992.0158.

Udwadia, F. E., & Kalaba, R. E. (1995). An alternate proof for the equation of motion for constrained mechanical systems. *Applied Mathematics and Computation*, 70(2–3), 339–342. DOI: 10.1016/0096-3003(94)00113-I.

Varanasi, S., Bolton, J. S., Siegmund, T. H., & Cipra, R. J. (2013). The low frequency performance of metamaterial barriers based on cellular structures. *Applied Acoustics*, 74(4), 485–495. DOI: 10.1016/J.APACOUST.2012.09.008.

Veselago, V. G. (1968). The Electrodynamics of Substances with Simultaneously Negative Values of E and μ. *Soviet Physics Uspekhi*, 10(4), 509–514. DOI: 10.1070/pu1968v010n04abeh003699.

Virgin, L. N., Santillan, S. T., & Plaut, R. H. (2008). Vibration isolation using extreme geometric nonlinearity. *Journal of Sound and Vibration*, 315(3), 721–731. DOI: 10.1016/j.jsv.2007.12.025.

Wallace, C. E. (1972). Radiation Resistance of a Rectangular Panel. *The Journal of the Acoustical Society of America*, 51(3B), 946–952. DOI: 10.1121/1.1912943.

Wang, C. (2015). Modal sound transmission loss of a single leaf panel: Asymptotic solutions. *The Journal of the Acoustical Society of America*, 138(6), 3964–3975. DOI: 10.1121/1.4938222.

Wang, F. C., Hsieh, M. R., & Chen, H. J. (2012). Stability and performance analysis of a full-train system with inerters. *Vehicle System Dynamics*, 50(4), 545–571. DOI: 10.1080/00423114.2011.606368.

Wang, K., Zhou, J., Tan, D., Li, Z., Lin, Q., & Xu, D. (2022). A brief review of metamaterials for opening low-frequency band gaps. *Applied Mathematics and Mechanics*, 43(7), 1125–1144. DOI: 10.1007/s10483-022-2870-9.

Wang, M., Sun, F. fei, Yang, J. qi, & Nagarajaiah, S. (2019). Seismic protection of SDOF systems with a negative stiffness amplifying damper. *Engineering Structures*, 190, 128–141. DOI: 10.1016/J.ENGSTRUCT.2019.03.110.

Wang, T. (2020). Tunable band gaps in an inertant metamaterial plate with two-degree-of-freedom local resonance. *Physics Letters A*, 384(21), 126420. DOI: 10.1016/j.physleta.2020.126420.

Wang, Xianfeng, Shi, Z., Wang, J., & Xiang, H. (2016). A stack-based flex-compressive piezoelectric energy harvesting cell for large quasi-static loads. *Smart Materials and Structures*, 25, 055005. DOI: 10.1088/0964-1726/25/5/055005.

Wang, Xiaopeng, Chen, Y., Zhou, G., Chen, T., & Ma, F. (2019). Synergetic coupling large-scale plate-type acoustic metamaterial panel for broadband sound insulation. *Journal of Sound and Vibration*, 459, 114867. DOI: 10.1016/J.JSV.2019.114867.

Wang, Y., & Jing, X. (2019). Nonlinear stiffness and dynamical response characteristics of an asymmetric X-shaped structure. *Mechanical Systems and Signal Processing*, 125, 142–169. DOI: 10.1016/j.ymssp.2018.03.045.

Wanjura, C. C., Brunelli, M., & Nunnenkamp, A. (2020). Topological framework for directional amplification in driven-dissipative cavity arrays. *Nature Communications*, 11(1), 3149. DOI: 10.1038/s41467-020-16863-9.

Weber, B., & Feltrin, G. (2010). Assessment of long-term behavior of tuned mass dampers by system identification. *Engineering Structures*, 32(11), 3670–3682. DOI: 10.1016/j.engstruct.2010.08.011.

Weisser, T., Schwan, L., Groby, J.-P., Lagarrigue, C., Deckers, E., & Dazel, O. (2016). Poroelastic subwavelength absorber with both elastic and acoustic embedded resonator. In: *Proceedings of the 27th International Conference on Noise and Vibration Engineering*, 2127–2136.

Winterflood, J., Blair, D. ., & Slagmolen, B. (2002). High performance vibration isolation using springs in Euler column buckling mode. *Physics Letters A*, 300(2–3), 122–130. DOI: 10.1016/S0375-9601(02)00258-X.

Wu, T.-T., Huang, Z.-G., Tsai, T.-C., & Wu, T.-C. (2008). Evidence of complete band gap and resonances in a plate with periodic stubbed surface. *Applied Physics Letters*, 93(11), 111902. DOI: 10.1063/1.2970992.

Yablonovitch, E. (1987). Inhibited spontaneous emission in solid-state physics and electronics. *Physical Review Letters*, 58(20), 2059–2062. DOI: 10.1103/PhysRevLett.58.2059.

Yang, T., Zhou, S., Fang, S., Qin, W., & Inman, D. J. (2021). Nonlinear vibration energy harvesting and vibration suppression technologies: Designs, analysis, and applications. *Applied Physics Reviews*, 8(3), 031317. DOI: 10.1063/5.0051432.

Yang, Y., lam, N. T. K., & Zhang, l. (2012). Estimation of response of plate structure subject to low veloctiy impact by a solid object. *International Journal of Structural Stability and Dynamics*, 12(06), 1250053. DOI: 10.1142/S0219455412500538.

Yang, Z., Mei, J., Yang, M., Chan, N. H., & Sheng, P. (2008). Membrane-type acoustic metamaterial with negative dynamic mass. *Physical Review Letters*, 101(20), 204301. DOI: 10.1103/PhysRevLett.101.204301.

Yao, S., Zhou, X., & Hu, G. (2008). Experimental study on negative effective mass in a 1D mass-spring system. *New Journal of Physics*, 10(4), 43020. DOI: 10.1088/1367-2630/10/4/043020.

Yilmaz, C. (2018). Inertial Amplification Induced Phononic Band Gaps in a Chiral Elastic Metamaterial. In: *12th International Congress on Artificial Materials for Novel Wave Phenomena, METAMATERIALS 2018*, 451–453. DOI: 10.1109/MetaMaterials.2018.8534125.

Yilmaz, C., & Hulbert, G. M. (2010). Theory of phononic gaps induced by inertial amplification in finite structures. *Physics Letters A*, 374(34), 3576–3584. DOI: 10.1016/j.physleta.2010.07.001.

Yilmaz, C., & Kikuchi, N. (2006). Analysis and design of passive low-pass filter-type vibration isolators considering stiffness and mass limitations. *Journal of Sound and Vibration*, 293(1–2), 171–195. DOI: 10.1016/j.jsv.2005.09.016.

Yuksel, O., & Yilmaz, C. (2015). Shape optimization of phononic band gap structures incorporating inertial amplification mechanisms. *Journal of Sound and Vibration*, 355, 232–245. DOI: 10.1016/j.jsv.2015.06.016.

Yuksel, O., & Yilmaz, C. (2020). Realization of an ultrawide stop band in a 2-D elastic metamaterial with topologically optimized inertial amplification mechanisms. *International Journal of Solids and Structures*, 203, 138–150. DOI: 10.1016/j.ijsolstr.2020.07.018.

Zaccherini, R., Colombi, A., Palermo, A., Thomsen, H. R., & Chatzi, E. N. (2021). Stress-optimized inertial amplified metastructure with opposite chirality for vibration attenuation. *ArXiv*. DOI: 10.48550/arXiv.2111.08594

Zaccherini, R., Palermo, A., Marzani, A., Colombi, A., Dertimanis, V., & Chatzi, E. (2020). Mitigation of Rayleigh-like waves in granular media via multi-layer resonant metabarriers. *Applied Physics Letters*, 117(25), 254103. DOI: 10.1063/5.0031113.

Zeng, Y., Cao, L., Wan, S., Guo, T., Wang, Y.-F., Du, Q.-J., Assouar, B., & Wang, Y.-S. (2022). Seismic metamaterials: Generating low-frequency bandgaps induced by inertial amplification. *International Journal of Mechanical Sciences*, 221, 107224. DOI: 10.1016/j.ijmecsci.2022.107224.

Zhang, S., & Sheng, X. (2018). Analysis of sound transmission loss of a rectangular plate with acoustic treatments. In: *Proceedings of ISMA 2018 and USD 2018*, 2167–2181.

Zhang, X., & Li, W. L. (2010). A unified approach for predicting sound radiation from baffled rectangular plates with arbitrary boundary conditions. *Journal of Sound and Vibration*, 329(25), 5307–5320. DOI: 10.1016/j.jsv.2010.07.014.

Zhang, Y., Wen, J., Xiao, Y., Wen, X., & Wang, J. (2012). Theoretical investigation of the sound attenuation of membrane-type acoustic metamaterials. *Physics Letters A*, 376(17), 1489–1494. DOI: 10.1016/j.physleta.2012.03.010.

Zheng, X., Lee, H., Weisgraber, T. H., Shusteff, M., DeOtte, J., Duoss, E. B., Kuntz, J. D., Biener, M. M., Ge, Q., Jackson, J. A., Kucheyev, S. O., Fang, N. X., & Spadaccini, C. M. (2014). Ultralight, ultrastiff mechanical metamaterials. *Science*, 344(6190), 1373–1377. DOI: 10.1126/science.1252291.

Zhou, G., Wu, J. H., Lu, K., Tian, X., Huang, W., & Zhu, K. (2020). Broadband low-frequency membrane-type acoustic metamaterials with multi-state anti-resonances. *Applied Acoustics*, 159, 107078. DOI: 10.1016/J.APACOUST.2019.107078.

Zhou, J., Pan, H., Cai, C., & Xu, D. (2021). Tunable ultralow frequency wave attenuations in one-dimensional quasi-zero-stiffness metamaterial. *International Journal of Mechanics and Materials in Design*, 17(2), 285–300. DOI: 10.1007/s10999-020-09525-7.

Zhou, J., Wang, K., Xu, D., & Ouyang, H. (2017). Local resonator with high-static-low-dynamic stiffness for lowering band gaps of flexural wave in beams. *Journal of Applied Physics*, 121(4), 44902. DOI: 10.1063/1.4974299.

Zhou, J., Xu, D., & Bishop, S. (2015). A torsion quasi-zero stiffness vibration isolator. *Journal of Sound and Vibration*, 338, 121–133. DOI: 10.1016/j.jsv.2014.10.027.

Zhu, W.-L., Zhu, Z., Shi, Y., Wang, X., Guan, K., & Ju, B.-F. (2016). Design, modeling, analysis and testing of a novel piezo-actuated XY compliant mechanism for large workspace nano-positioning, *Smart Materials and Structures*, 25(11), 115033. DOI: 10.1088/0964-1726/25/11/115033.

Καπασακάλης, Κ., Μάντακας, Α., Καλδερών, Μ., Σαπουντζάκης, Ε., & Αντωνιάδης, Ι. (2022). Σεισμική Προστασία Υφιστάμενων Κτιρίων με Σεισμική Βάση Απορρόφησης Κραδασμών Αρνητικής Στιβαρότητας. Στα: *Πρακτικά - 5ο Πανελλήνιο Συνέδριο Αντισεισμικής Μηχανικής Και Τεχνικής Σεισμολογίας, 5ΠΣΑΜΤΣ*.

Εκτενης Περιληψη

ΚΑΙΝΟΤΟΜΕΣ ΔΙΑΤΑΞΕΙΣ ΑΠΟΡΡΟΦΗΣΗΣ ΚΡΑΔΑΣΜΩΝ ΚΑΙ ΜΕΤΑΫΛΙΚΩΝ ΓΙΑ ΕΛΕΓΧΟ ΧΑΜΗΛΟΣΥΧΝΩΝ ΚΥΜΑΤΩΝ

1. ΕΙΣΑΓΩΓΗ

Το αντικείμενο της παρούσας διδακτορικής διατριβής επικεντρώνεται σε συστήματα ελέγχου ταλαντώσεων και απορρόφησης κυμάτων καθώς και μεθόδους βελτίωσης της δυναμικής συμπεριφοράς κατασκευών. Συγκεκριμένα, η έρευνα εστιάζει στη μελέτη μηχανισμών και διατάξεων ακουστικής μόνωσης, με σκοπό τη μείωση χαμηλόσυχνων ακουστικών κυμάτων. Οι προτεινόμενες υπό εξέταση διατάξεις βασίζονται στη θεωρία των μεταϋλικών και της δυναμικής ενίσχυσης καθώς και στην εφαρμογή συστημάτων αρνητικής στιβαρότητας, τα οποία σχεδιάζονται λαμβάνοντας υπόψιν τους εν γένει περιορισμούς.

Σήμερα, η περιβαλλοντική ηχορύπανση θεωρείται η δεύτερη μεγαλύτερη αιτία ρύπανσης στον κόσμο, μετά την ατμοσφαιρική ρύπανση. Η έκθεση σε έντονο περιβαλλοντικό θόρυβο συμβάλλει σε διάφορες επιπτώσεις στην υγεία και αποτελεί μία αυξανόμενη ανησυχία τόσο του κοινού όσο και της παγκόσμιας πολιτικής. Πρόκειται αναμφίβολα για ένα σοβαρό ζήτημα στις σύγχρονες αστικές περιοχές που μπορεί να υποβαθμίσει σημαντικά την ποιότητα ζωής των ανθρώπων που ζουν σε αυτές. Σύμφωνα με τον ΠΟΥ, η υπερβολική έκθεση στα υψηλά επίπεδα θορύβου προερχόμενα από την οδική κυκλοφορία μπορεί να αυξήσει τους κινδύνους εμφάνισης ισχαιμικής καρδιοπάθειας (IHD), εγκεφαλικού επεισοδίου και διαβήτη. Επιπλέον, σημαντικές διαταραχές του ύπνου μπορούν να προκληθούν σε άτομα που εκτίθενται σε υψηλά επίπεδα περιβαλλοντικού θορύβου για μεγάλα χρονικά διαστήματα.

Τα τρέχοντα μέτρα προστασίας από τον θόρυβο στην περιοχή χαμηλών συχνοτήτων, κάτω από 500Hz, και ιδιαίτερα στην περιοχή μεταξύ 20Hz και 100Hz, δεν είναι ούτε αποτελεσματικά ούτε εφαρμόσιμα. Ταυτοχρόνως, πολλές πηγές περιβαλλοντικού θορύβου διαθέτουν σημαντικό συχνοτικό περιεχόμενο σε αυτή την περιοχή. Χαρακτηριστικό παράδειγμα αποτελούν τα οχήματα όλων των τύπων (αυτοκίνητα, φορτηγά, τρένα, αεροπλάνα κ.λπ.) και οι κατασκευαστικές δραστηριότητες (π.χ. δυναμική συμπίεση, συμπίεση οδοστρώματος, πασσαλόμπηξη, ανατινάξεις). Συνεπώς, ο σχεδιασμός ελαφρών κατασκευών με αντικραδασμικές και ηχοαπορροφητικές ιδιότητες ήταν πάντα τεχνικά απαιτητικός και πρακτικά κρίσιμος.

Τις τελευταίες δύο δεκαετίες, υπάρχει τεράστια ανάπτυξη στον τομέα της ακουστικής με σκοπό την απορρόφηση της διάδοσης των ηχητικών κυμάτων. Ωστόσο, τα παραδοσιακά ακουστικά υλικά έχουν ορισμένους περιορισμούς όσον αφορά την ηχομόνωση και την απορρόφηση σε χαμηλές συχνότητες. Η έρευνα για την διερεύνηση της ακουστικής απόδοσης των κοινών μέσων ακουστικής μόνωσης, όπως τα πετάσματα γυψοσανίδας, εστιάζει τις περισσότερες φορές στις περιοχές μεσαίων και υψηλών συχνοτήτων. Απεναντίας, η μετάδοση του ήχου στην κρίσιμη περιοχή των συχνοτήτων 0-200 Hz έχει αρχίσει να εξετάζεται μόλις πρόσφατα.

Συνοπτικά, η σύγχρονη έρευνα περιλαμβάνει διάφορα ακουστικά υλικά, όπως φυσικές ίνες και ανακυκλωμένα υλικά, ακουστικές μαύρες τρύπες, διάτρητα πάνελ και προηγμένα αφρώδη υλικά με στόχο την επίτευξη ηχητικής μόνωσης σε μεγάλο εύρος συχνοτήτων. Η ικανότητα των νέων τεχνολογιών και της έρευνας επιτρέπει την κατασκευή πολύπλοκων συστημάτων όπως περιοδικές δομές με βάση τα μεταϋλικά, που αναζητούν λύση προς την κατεύθυνση του μετριασμού του θορύβου χαμηλών συχνοτήτων. Τα μεταϋλικά είναι τεχνητές, συνήθως περιοδικές ή τυχαίες δομές, των οποίων η περιοδικότητα μπορεί να αφορά τις φάσεις του υλικού, την εσωτερική γεωμετρία ή τις συνοριακές συνθήκες, και επιτρέπουν με αυτόν τον τρόπο τον χειρισμό της μετάδοσης των ακουστικών κυμάτων.

Αν και τα συμβατικά μεταϋλικά με τοπικό συντονισμό φαίνονται πολλά υποσχόμενα στον τομέα του ελέγχου των ταλαντώσεων και της ηχητικής εξασθένησης, εξακολουθούν να υπάρχουν ορισμένοι κρίσιμοι περιορισμοί που απαιτούν επιστημονική προσοχή και περαιτέρω μελέτη. Ένα από τα σημαντικότερα ζητήματα είναι η απαίτηση ογκωδών, εσωτερικών μαζών και μεγάλων μετακινήσεων των εσωτερικά ταλαντευόμενων δομών, οι οποίες μπορεί να περιπλέξουν την εφαρμογή τους. Για το σκοπό αυτό, η σύγχρονη έρευνα επικεντρώνεται σε διάφορους μηχανισμούς με σκοπό την τεχνητή αύξηση της αδράνειας της συντονιζόμενης μάζας, και την ανάπτυξη ρεαλιστικών μηχανισμών που μπορούν να επιτύχουν ευρυζωνική εξασθένηση των ακουστικών κυμάτων. Μια σύντομη

βιβλιογραφική ανασκόπηση της τεχνολογίας των μεταϋλικών καθώς και μεθοδολογιών ενίσχυσης παρέχεται στο ολοκληρωμένο τεύχος της διατριβής.

Έχοντας ως στόχο την μείωση των απαιτήσεων μάζας των υφιστάμενων συστημάτων, έχουν γίνει προσπάθειες προς την κατεύθυνση της τεχνητής αύξησης της αδράνειας της συντονιζόμενης μάζας μέσω μηχανισμών ενίσχυσης. Η εισαγωγή στοιχείων αρνητικής στιβαρότητας (NS) έχει προταθεί ως τεχνητός τρόπος αύξησης της αδράνειας των ταλαντωτών και βελτίωσης της δυναμικής απόκρισης διαφόρων κατασκευών. Ένα παράδειγμα ενός τέτοιου απορροφητή με βάση το NS είναι ο KDamper (KD) που έχει εξεταστεί σε διάφορες μηχανολογικές εφαρμογές, όπως η σεισμική μόνωση, η προστασία κατασκευών (Konstantinos A Kapasakalis et al., 2020; Konstantinos A. Kapasakalis et al., 2020) και η ηχομείωση χαμηλών συχνοτήτων (Kalderon et al., 2021; Paradeisiotis et al., 2020). Στο πλαίσιο των μεταϋλικών, η ενσωμάτωση στοιχείων αρνητικής στιβαρότητας στο ταλαντευόμενο σύστημα παρουσιάζει ελπιδοφόρα αποτελέσματα, αποκαλύπτοντας τις δυνατότητες χρήσης της αρνητικής στιβαρότητας (Antoniadis et al., 2015, 2016; Paradeisiotis et al., 2020) προς την κατεύθυνση του σχεδιασμού ακουστικών μεταϋλικών (I. Antoniadis and Paradeisiotis, 2018; I. A. Antoniadis and Paradeisiotis, 2018; Chronopoulos et al., 2017, 2015).

Οι εφαρμογές που παρουσιάζονται και μελετώνται στην παρούσα διατριβή περιλαμβάνουν την εισαγωγή στοιχείων αρνητικής στιβαρότητας (μηχανισμός KDamper) σε συνδυασμό με δυναμικούς ενισχυτές με τη μορφή βάσεων που ενισχύουν τις ιδιότητες ηχομείωσης ακουστικών πετασμάτων. Επιπλέον, παρουσιάζονται εφαρμογές μεταϋλικών με την ενσωμάτωση αποσβεστήρων KDamper προς την κατεύθυνση της μόνωσης του ήχου χαμηλών συχνοτήτων. Με στόχο την περαιτέρω διερεύνηση των δυνατοτήτων των μεταϋλικών στις χαμηλές συχνότητες, παρουσιάζεται ένας απλός, καινοτόμος μηχανισμός δυναμικής ενίσχυσης, ονόματι DDA (Dynamic Directional Amplifier), και εισάγεται για πρώτη φορά σε διάφορες εφαρμογές. Αυτές περιλαμβάνουν φωνονικούς κρυστάλλους και τοπικά συντονιζόμενα μεταϋλικά, καθώς και πετάσματα ακουστικής μόνωσης. Η ανάλυση περιλαμβάνει αναλυτική, αριθμητική και πειραματική αξιολόγηση και αναδεικνύει την ευεργετική επίδραση του μηχανισμού DDA προς τον έλεγχο ταλαντώσεων χαμηλής συχνότητας. Ο γενικός στόχος της διατριβής είναι να εμβαθύνει στην αιχμή της έρευνας στον έλεγχο ακουστικών κυμάτων και ταλαντώσεων, διερευνώντας τις εξαιρετικές ιδιότητες των μεταϋλικών ενισχύοντάς τα με στοιχεία αρνητικής στιβαρότητας, καθώς και άλλους μηχανισμούς ενίσχυσης.

Συγκεκριμένα, στο κεφάλαιο 2 παρουσιάζεται μία απλή αναλυτική μέθοδος για την προσομοίωση της απώλειας διάδοσης ήχου μέσω πετασμάτων εδραζόμενων σε εύκαμπτες στηρίξεις. Η μέθοδος χρησιμοποιείται στη συνέχεια ως κύριο εργαλείο για τον υπολογισμό των ιδιοτήτων ηχομείωσης των προτεινόμενων ακουστικών συστημάτων και μεταϋλικών. Στο κεφάλαιο 3, παρουσιάζονται τα

προτεινόμενα συστήματα αρνητικής στιβαρότητας (KDamper) καθώς και εφαρμογές τους σε ακουστικά πετάσματα και μεταϋλικά απορρόφησης ταλαντώσεων χαμηλής συχνότητας. Στο κεφάλαιο 4, παρουσιάζεται το καινοτόμο σύστημα δυναμικής ενίσχυσης DDA (Dynamic Directional Amplifier) καθώς και εφαρμογές του σε φωνονικούς κρυστάλλους και τοπικά συντονιζόμενα μεταϋλικά. Έπειτα, οι δυναμικές ιδιότητες των μεταϋλικών (με και χωρίς ενισχυτές DDA) επαληθεύονται πειραματικά με τη χρήση πρωτότυπων LEGO® κατασκευών οι οποίες εξετάζονται έναντι διεγέρσεων χαμηλής συχνότητας.

2. ΠΡΟΣΟΜΟΙΩΣΗ ΤΗΣ ΑΠΩΛΕΙΑΣ ΔΙΑΔΟΣΗΣ ΗΧΟΥ ΜΕΣΩ ΠΕΤΑΣΜΑΤΩΝ ΕΔΡΑΖΟΜΕΝΩΝ ΣΕ ΕΥΚΑΜΠΤΕΣ ΣΤΗΡΙΞΕΙΣ

2.1 Εισαγωγή

Σκοπός του κεφαλαίου είναι η παρουσίαση μιας απλής, αναλυτικής μεθόδου για τον υπολογισμό του δείκτη ηχομείωσης (STL) εύκαμπτων πετασμάτων. Η μέθοδος αυτή από εδώ και στο εξής θα προσδιορίζεται ως “In series LPM” και βασίζεται σε ένα απλό προσομοίωμα συγκεντρωμένων παραμέτρων. Το πλεονέκτημα της προτεινόμενης μεθόδου, σε σύγκριση με την Rayleigh-Ritz ή οποιαδήποτε άλλη αναλυτική λύση, είναι η δυνατότητα προσομοίωσης οποιονδήποτε συνοριακών συνθήκων χωρίς τη χρήση πολύπλοκων μαθηματικών μοντέλων ή αριθμητικών προσομοιώσεων. Φυσικά, το αντιστάθμισμα είναι η μειωμένη ακρίβεια, καθώς λαμβάνεται υπόψη μόνο η πρώτη ιδιόμορφή των πετασμάτων. Στην αρχή παρουσιάζεται ο υπολογισμός του STL για την βασική περίπτωση απλά εδραζόμενων πετασμάτων και στη συνέχεια η θεώρηση επεκτείνεται για να καλύψει περιπτώσεις ελαστικών εδράσεων ή πιο πολύπλοκών στηρίξεων (κεφάλαιο 3).

2.2 Απλά εδραζόμενο πέτασμα – προσέγγιση 1ης ιδιομορφής

Αναλυτικές λύσεις για την επίλυση του προβλήματος διάδοσης ήχου διαμέσου ενός απλά εδραζόμενου πετάσματος μπορούν να προκύψουν μέσω μεθόδων υπέρθεσης ιδιομορφών όπως η διατύπωση του Roussos (1985) - Παράρτημα Α.3. Ωστόσο, προκειμένου να μειωθεί η πολυπλοκότητα, σε αυτές τις αναλυτικές προσεγγίσεις συνήθως αποφεύγεται στους υπολογισμούς ο όρος της επανεκπεμπόμενης πίεσης $2p_t(\xi,\eta,t)$ (που συχνά αναφέρεται ως "φόρτιση ρευστού"). Σύμφωνα με τον Roussos (1985), η παράλειψη της επίδρασης της επανεκπεμπόμενης πίεσης επιτρέπει ακριβή λύση σε μεγάλο εύρος συχνοτήτων, ενώ η ακρίβεια μειώνεται όταν λύσεις αναζητούνται κοντά στη θεμελιώδη συχνότητα συντονισμού του πετάσματος. Στο Σχήμα 1 απεικονίζεται το υποεξέταση

πεπερασμένων διαστάσεων (l_x, l_y, h) ομογενές πέτασμα, και τα διανύσματα προσπίπτουσας (p_i), ανακλώμενης (p_r), και μεταδιδόμενης (p_{rad}^-) ηχητικής πίεσης

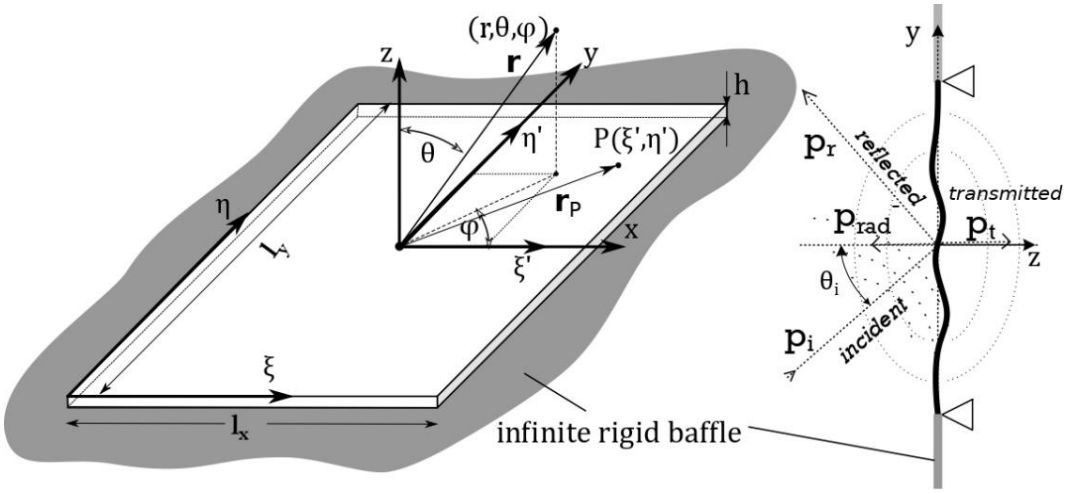

Σχήμα 1: (Αριστερά) Διάδοση ήχου σε πεπερασμένη πλάκα. (Δεξιά) τομή πλάκας με απεικόνιση διανυσμάτων ηχητικής πίεσης .

Δεδομένου ότι στην παρούσα έρευνα η ηχητική πίεση αφορά συχνότητές κοντά στον συντονισμό του πετάσματος, η προτεινόμενη προσέγγιση περιλαμβάνει την επίδραση της φόρτισης ρευστού. Λαμβάνοντας υπόψιν μόνο τον θεμελιώδη ιδιομορφή μιας απλά στηριζόμενης πλάκας, το χωρικά εξαρτώμενο πλάτος της εγκάρσιας μετατόπισης $w(\xi,\eta) = W_1(\xi,\eta,t)e^{-j\omega t}$ υπολογίζεται από τη συνάρτηση σχήματος:

$$W_1 = C_1 \sin\left(\frac{\pi\xi}{l_x}\right)\sin\left(\frac{\pi\eta}{l_y}\right) \tag{1}$$

Η προκύπτουσα έκφραση για την εκπεμπόμενη (ακτινοβολούμενη) ισχύ Π_t δίνεται από την Εξ. (Α-37) παράρτημα Α.4. Υποθέτοντας κανονικά προσπίπτοντα κύματα $(\theta_i = 0)$, η προσπίπτουσα ισχύς υπολογίζεται ως:

$$\Pi_i = \frac{P_i^2 l_x l_y}{2\rho_0 c_0} \tag{2}$$

Και ο συντελεστής μεταδοτικότητας τ ως:

$$\tau_1 = \frac{1}{l_x l_y} \frac{\left(16\omega^2 \rho_0\right)^2}{\left| \pi^3 rh(\omega_1^2 - \omega^2) - 16\omega^2 \rho_0 \frac{e^{-jkr}}{r} \right|^2} I_{\theta\varphi} \tag{3}$$

όπου η απόσταση r πρέπει να είναι αρκετά μεγάλη ώστε να ικανοποιείται η προσέγγιση του μακρινού πεδίου και $\omega_1^2 = \frac{D\pi^4}{\rho h}\left(\frac{1}{l_x^2} + \frac{1}{l_y^2}\right)^2$ η ιδιοσυχνότητα του απλά εδραζόμενου πετάσματος. Ως $I_{\theta\varphi}$ συμβολίζεται το διπλό ολοκλήρωμα που περιγράφει την ημισφαιρική διάδοση (Appendix A.2).

Αντίστοιχα, ο συντελεστής μεταδοτικότητας στην περίπτωση που δεν λαμβάνεται υπόψιν η "φόρτιση ρευστού" υπολογίζεται ως:

$$\tau_{LPM} = l_x l_y \left(\frac{4\omega^2 \rho_0}{\pi^3}\right)^2 \frac{1}{\left[m_1^* \left| \omega_1^2 - \omega^2 \right| \right]^2} \mathrm{I}_{\theta\varphi} \tag{4}$$

όπου η γενικευμένη μάζα m_1^* και στιβαρότητα k_1^* του ισοδύναμου μονοβάθμιου προσομοιώματος θεωρώντας μόνο την πρώτη ιδιομορφή του πετάσματος (YANG et al., 2012), μπορούν να υπολογιστούν από τις παρακάτω εκφράσεις:

$$m_1^* = \frac{\rho h l_x l_y}{4} = \frac{\bar{m} l_x l_y}{4} = \frac{m}{4} \tag{5}$$

$$k_1^* = \frac{D\pi^4 l_x l_y}{4} = \left(\frac{1}{l_x^2} + \frac{1}{l_y^2}\right)^2 \tag{6}$$

Στο Σχήμα 2, παρουσιάζεται η σύγκριση του δείκτη ηχομείωσης (STL) ενός απλά εδραζόμενου πετάσματος, υπολογισμένο με τη μέθοδο μιας ιδιομορφής με "φόρτιση ρευστού" (κίτρινη καμπύλη), χωρίς τη φόρτιση ρευστού (μπλε καμπύλη), και με την μέθοδο του Roussos (1985). Η κόκκινη διακεκομμένη γραμμή αντιπροσωπεύει την συμπεριφορά ενός άκαμπτου πετάσματος πεπερασμένων διαστάσεων, η οποία μπορεί να λειτουργήσει ως καμπύλη αναφοράς για διάφορες συγκρίσεις. Συγκρίνοντας της μεθόδους με και χωρίς την επιρροή του όρου "φόρτιση ρευστού", παρατηρείται ότι η φόρτιση με ρευστό έχει πολύ μικρή επίδραση στην απόσβεση της πρώτης ιδιομορφής.

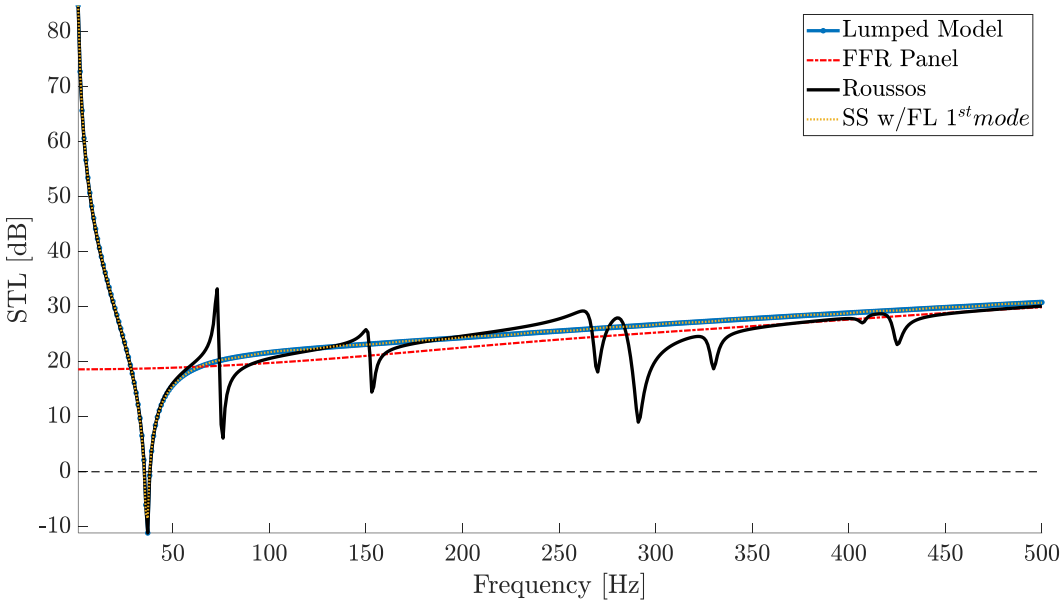

Σχήμα 2: Σύγκριση μεταξύ μεθόδων Roussos, 1st mode και LPM για τον υπολογισμό του STL απλά εδραζόμενων εύκαμπτων πλακών.

2.3 Μέθοδος υπολογισμού του δείκτη ηχομείωσης – "In series LPM"

Ο ακριβής θεωρητικός υπολογισμός του τρόπου με τον οποίο η καμπτική στιβαρότητα ενός πετάσματος συνδυάζεται με τη στιβαρότητα των ελαστικών βάσεων στήριξης είναι μια δύσκολη και περίπλοκη διαδικασία (Du et al., 2012; Zhang and Li, 2010). Συνεπώς, στόχος είναι η διατύπωση μιας εξορθολογισμένης διαδικασίας και ο υπολογισμός του δείκτη ηχομείωσης (STL). Η βασική παραδοχή της θεώρησης αυτής, είναι ότι η καμπτική στιβαρότητα της παραμορφώσιμης πλάκας είναι κατά κάποιο τρόπο σε σειρά με τη στιβαρότητα της στήριξης. Η συνολική στιβαρότητα του συστήματος δηλαδή μπορεί να υπολογιστεί ως:

$$\mathrm{k_{tot}} = \frac{k_1^* k'_0}{k_1^* + k'_0} \tag{7}$$

Όταν η στήριξη είναι πολύ δύσκαμπτη ($k_0' \gg k_1^*$) οδηγεί σε $k_{tot} = k_1^*$, δηλαδή προσεγγίζεται η περίπτωση της απλά στηριζόμενης πλάκας. Όταν η στιβαρότητα της στήριξης τείνει στο μηδέν, το πέτασμα ουσιαστικά κινείται ελευθέρα. Στην περίπτωση που η στιβαρότητα στήριξης k_0 είναι συγκριτικής τάξης μεγέθους με τη στιβαρότητα του πετάσματος k^*_1 , υπάρχει κάποια απόκλιση μεταξύ της υπολογιζόμενης ιδιοσυχνότητας του συστήματος και της πραγματικής. Ωστόσο, στις περιπτώσεις όπου $k_0' \gg k_1^*$ ή $k_0' \ll k_1^*$, η απόκλιση μειώνεται.

Στο Σχήμα 3, παρουσιάζεται το ισοδύναμο δυναμικό προσομοίωμα ενός λεπτού, παραμορφώσιμου πετάσματος επί ελαστικών στηρίξεων. Αυτό επιτυγχάνεται με τη χρήση των γενικευμένων τιμών της κατασκευής, δηλαδή της γενικευμένης μάζας και της αντίστοιχης γενικευμένης στιβαρότητας λαμβάνοντας υπόψιν μόνο τη πρώτη ιδιομορφή, σύμφωνα με τις Εξ. (5)-(6) που χρησιμοποιούνται στις περίπτωση του απλά εδραζόμενου πετάσματος.

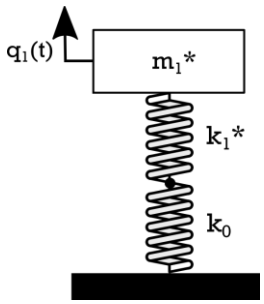

Σχήμα 3: Μονογραμμικό διάγραμμα παραμορφώσιμης πλάκας επί ελαστικής έδρασης στιβαρότητας k_0.

το STL υπολογίζεται στη συνέχεια ως ,

$$STL = 10\log_{10}\left(\frac{1}{\tau}\right) \tag{8}$$

όπου ο συντελεστής μεταδοτικότητας δίνεται από την έκφραση:

$$\tau = l_x l_y \left(\frac{4\omega^2\rho_0}{\pi^3}\right)^2 \frac{1}{\left|-\omega^2 m_1^* + k_1^*(1-TF_{21})\right|^2} I_{\theta\varphi} \tag{9}$$

Η συνάρτηση μεταφοράς TF αφορά τον τύπο της στήριξης, ενώ στη περίπτωση απλών ελαστικών εδράσεων $TF = 0$. Συνεπώς:

$$\tau_{el} = l_x l_y \left(\frac{4\omega^2\rho_0}{\pi^3}\right)^2 \frac{1}{\left|-\omega^2 m_1^* + k_{tot}\right|^2} I_{\theta\varphi} \tag{10}$$

2.4 Σύνοψη

Σε αυτό το κεφάλαιο, παρουσιάστηκε το θεωρητικό υπόβαθρο της ακουστικής θεωρίας “In series LPM”, η οποία στη συνέχεια εφαρμόζεται στις διατάξεις απορρόφησης ταλαντώσεων και μεταϋλικών. Το πλεονέκτημα της προτεινόμενης μεθόδου σε σχέση με τις πιο σύνθετες αναλυτικές, είναι η δυνατότητα μοντελοποίησης οποιονδήποτε συνοριακών συνθήκων χωρίς τη χρήση πολύπλοκων μαθηματικών μοντέλων ή αριθμητικών προσομοιώσεων. Φυσικά, το αντιστάθμισμα είναι η μειωμένη ακρίβεια, καθώς λαμβάνεται υπόψιν μόνο η πρώτη ιδιόμορφή των πετασμάτων.

3. ΣΥΣΤΗΜΑΤΑ ΑΠΟΡΡΟΦΗΣΗΣ ΤΑΛΑΝΤΩΣΕΩΝ ΑΡΝΗΤΙΚΗΣ ΣΤΙΒΑΡΟΤΗΤΑΣ

3.1 Εισαγωγή

Στο κεφάλαιο αυτό παρουσιάζεται η εξέταση συστημάτων απορρόφησης ταλαντώσεων με στοιχεία αρνητικής στιβαρότητας. Οι προτεινόμενες διατάξεις βασίζονται στον μηχανισμό KDamper, μία νέα πρωτοποριακή ιδέα μόνωσης ταλαντώσεων και απόσβεσης που διαμορφώνεται μέσω του βέλτιστου συνδυασμού στοιχείων θετικής και αρνητικής στιβαρότητας (Antoniadis et al., 2018). Συγκεκριμένα, η ιδέα αυτή συνδυάζεται με έναν δυναμικό ενισχυτή (IAM), με σκοπό την περεταίρω αύξηση των δυνατοτήτων του KDamper και προσαρμόζεται για την ανάπτυξη στηρίξεων ακουστικών πετασμάτων και πετασμάτων τύπου σάντουιτς, με ιδιότητες χαμηλόσυχνης ακουστικής μόνωσης. Τα ακουστικά στηρίγματα βασίζονται στο θεωρητικό προσομοίωμα KD-IAM (ενότητα 3.3), ενώ το πέτασμα τύπου σάντουιτς στην περιοδική επανάληψη μοναδιαίων κελιών KD-IAM, δηλαδή στη θεωρία των ακουστικών μεταϋλικών (ενότητα 3.4). Αρχικά, στην ενότητα 3.1 παρατίθεται η θεωρία του KDamper μαζί με την πειραματική επαλήθευση των δυνατοτήτων του μηχανισμού και στη συνέχεια το θεωρητικό υπόβαθρο, η επαλήθευση με τη χρήση πεπερασμένων στοιχείων (Π.Σ), και ο σχεδιασμός των προτεινόμενων διατάξεων.

3.2 Δυναμικό Σύστημα Απορρόφησης Ταλαντώσεων KDamper

Το KDamper παρουσιάστηκε για πρώτη φορά το 2018 από τους Antoniadis et al. (2018) ως ένα καινοτόμο παθητικό σύστημα ελέγχου ταλαντώσεων. Η ιδέα βασίζεται στον βέλτιστο συνδυασμό στοιχείων στιβαρότητας, μάζας και απόσβεσης, συμπεριλαμβανομένου ενός στοιχείου αρνητικής στιβαρότητας. Η εισαγωγή του στοιχείο αρνητικής στιβαρότητας στον μηχανισμό βοηθάει στην κίνηση σε αντίθεση με τα συμβατικά ελατήρια που την δυσχεραίνουν (Molyneaux, 1957). Το σύστημα συνδυάζει τα ευεργετικά χαρακτηριστικά της αρνητικής στιβαρότητας και του παραδοσιακού αποσβεστήρα συντονιζόμενης μάζας (TMD), οδηγώντας σε μια διάταξη που εισάγει εξαιρετικές δυνατότητες απόσβεσης. Για δομικά συστήματα, η απαιτούμενη αρνητική στιβαρότητα μπορεί να επιτευχθεί με τη χρήση συμβατικών προ-συμπιεσμένων ελατηρίων τοποθετημένων σε κατάλληλη γεωμετρία, δοκών υπό λυγισμό, πλακών και άλλων προενταμένων μηχανικών στοιχείων (Virgin et al., 2008; Winterflood et al., 2002), ενώ σε περιπτώσεις ακουστικών εφαρμογών, ακόμα και με τη χρήση προεντεταμένων δισκοειδών ελατηρίων (Belleville) (Antoniadis et al., 2018). Η ενσωμάτωση του στοιχείου αρνητικής στιβαρότητας αυξάνει τις αδρανειακές δυνάμεις του αποσβεστήρα και μειώνει σημαντικά την ανάγκη για μεγάλη μάζα (Kapasakalis et al., 2020; Paradeisiotis et al., 2021, 2020). Επιπλέον, η σωστή κατανομή των στοιχείων στιβαρότητας και μάζας στη διάταξη, οδηγεί σε ένα

σύστημα που είναι τόσο στατικά όσο και δυναμικά ευσταθές όπου με την κατάλληλη σχεδίαση διατηρείται η αρχική/στατική στιβαρότητα της κατασκευής. Το Σχήμα 4 παρουσιάζει σχηματικά τους μηχανισμούς του συμβατικού TMD, του TMDI καθώς, και της καινοτόμου ιδέας του KDamper.

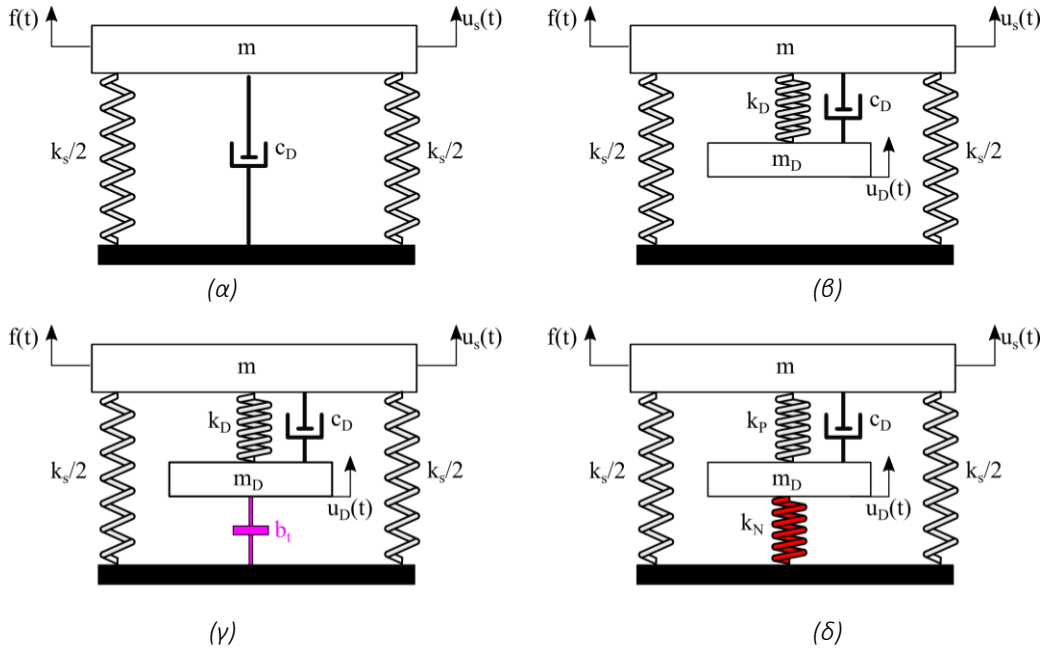

Σχήμα 4: Σχηματική αναπαράσταση δυναμικών συστημάτων απορρόφησης ταλαντώσεων: (α) μονοβάθμιος ταλαντωτής (m-c-k), (β) αποσβεστήρας συντονισμένης μάζας (TMD), (γ) βελτιωμένος αποσβεστήρας συντονισμένης μάζας με στοιχείο inerter (TMDI), (δ) ταλαντωτής KDamper.

Έχουν προταθεί διάφορες παραλλαγές του ταλαντωτή KDamper όπου η διέγερση ασκείτε στη βάση του ή στην κορυφή του, οι σημαντικότερες από τις οποίες είναι: (i) το "κλασικό" KDamper, (ii) η διευρυμένη έκδοση του KDamper (EKD), (iii) η διευρυμένη έκδοση του KDamper με inerter (EKDI) (Kapasakalis, 2020). Στην παρούσα εργασία παρουσιάζεται μια νέα βελτιωμένη έκδοση του μηχανισμού όπου το KDamper συνδυάζεται με έναν μηχανισμό αδρανειακής ενίσχυσης (IAM).

3.2.1 Κλασική έκδοση του KDamper

Στο Σχήμα 4 (δ) παρουσιάζεται η βασική ιδέα του «κλασικού» KDamper. Η πρώτη βασική απαίτηση του KDamper είναι να διατηρείται η συνολική στατική στιβαρότητα του συστήματος:

$$k_0 = k_S + \frac{k_p k_N}{k_p + k_N} = (2\pi f_0)^2 (m + m_D) \tag{11}$$

Οι εξισώσεις κίνησης του KDamper στην περίπτωση που εφαρμόζεται μια αρμονική διέγερση στην θέση της μάζας m είναι:

$$m\ddot{u}_S + c_D(\dot{u}_S - \dot{u}_D) + k_S u_S + k_P(u_S - u_D) = f(t) \tag{12}$$

$$m_D\ddot{u}_D - c_D(\dot{u}_S - \dot{u}_D) + k_N u_D - k_P(u_S - u_D) = 0 \tag{13}$$

Υποθέτοντας ότι η αρμονική διέγερση έχει τη μορφή

$$f(t) = \tilde{F}e^{j\omega t} = k_0 U_{ST} e^{j\omega t} \tag{14}$$

και οι αποκρίσεις σταθερής κατάστασης είναι της μορφής:

$$u_S(t) = \tilde{U}_S e^{j\omega t} \tag{15}$$

$$u_D(t) = \tilde{U}_D e^{j\omega t} \tag{16}$$

όπου $\tilde{U}_S, \tilde{U}_D$ τα μιγαδικά πλάτη της απόκρισης.

Οι εξισώσεις κίνησης του KDamper διατυπώνονται ως:

$$-\omega^2 m\tilde{U}_S + j\omega c_D(\tilde{U}_S - \tilde{U}_D) + k_P(\tilde{U}_S - \tilde{U}_D) + k_S\tilde{U}_S = f(t) \tag{17.α}$$

$$-\omega^2 m\tilde{U}_D + j\omega c_D(\tilde{U}_S - \tilde{U}_D) - k_P\ (\tilde{U}_S - \tilde{U}_D) + k_N\tilde{U}_D = 0 \tag{17.β}$$

Ένας προσεκτικός έλεγχος των Εξισώσεων (17.α, β), αποκαλύπτει ότι το πλάτος της δύναμης αδράνειας F_{MD} της πρόσθετης μάζας και το πλάτος F_N της αρνητικής δύναμης στιβαρότητας είναι ακριβώς σε φάση, λόγω της αρνητικής τιμής της k_N. Οι δυνάμεις αυτές υπολογίζονται ως εξής:

$$F_{MD} = -\omega^2 m_D \left|\tilde{U}_D\right| \tag{18.α}$$

$$F_N = k_N \left|\tilde{U}_D\right| \le 0 \tag{18.β}$$

Έτσι, παρόμοια με το inerter (Smith, 2002), ο KDamper αυξάνει έμμεσα την αδράνεια της πρόσθετης μάζας m_D. Επίσης θα πρέπει να σημειωθεί ότι η τιμή της δύναμης F_{MD} εξαρτάται από την συχνότητα διέγερσης, ενώ η τιμή της F_N είναι σταθερή.

Οι συναρτήσεις μεταφοράς του KDamper για αρμονική διέγερση $f(t)$ στην κορυφή του διατυπώνονται ως εξής:

$$\tilde{T}_{UF} = \frac{\tilde{U}_S}{F} = \frac{-m_D\omega^2 + j\omega c_D + k_P + k_N}{mm_D\omega^4 - (m+m_D)c_D\omega^3 - (m(k_P+k_N) + m_Dk_S + m_Dk_P)\omega^2 + c_D(k_S+k_N)s + k_S(k_P+k_N) + k_Pk_N} \tag{19}$$

$$\tilde{H}_{US} = \frac{\tilde{U}_S}{U_{ST}} = k_0\tilde{T}_{UF} \tag{20}$$

$$\tilde{H}_{UD} = \frac{\tilde{U}_D}{U_{ST}} = \frac{\tilde{U}_D}{\tilde{U}_S}\tilde{H}_{US} = \frac{(j\omega c_D + k_P)k_0}{-\omega^2 m_D + j\omega c_D + k_D}\tilde{H}_{US} \quad (21)$$

Συνεπώς εισάγονται οι ακόλουθες παράμετροι:

$$\mu = m_D / m \quad (22.\alpha)$$

$$k_D = k_N + k_P \quad (22.\beta)$$

$$\omega_D = \sqrt{k_D / m_D} = \sqrt{(k_N + k_P)/m_D} \quad (22.\gamma)$$

$$\zeta_D = c_D / 2\omega_D m_D = c_D / 2\sqrt{(k_N + k_P)m_D} \quad (22.\delta)$$

$$m_{tot} = m + m_D \quad (17.\varepsilon)$$

$$f_0 = \sqrt{k / m_{tot}} / 2\pi = \sqrt{(k_S + k_P k_N / k_P + k_N)/(m + m_D)} / 2\pi \quad (22.\sigma\tau)$$

3.2.2 Διευρυμένη έκδοση του KDamper (EKD)

Η ιδέα της διευρυμένης έκδοσης του KDamper (EKD) συνίσταται στην εναλλαγή θέσεων του θετικού και αρνητικού στοιχείου στιβαρότητας k_P, k_N, και στην προσθήκη ενός αποσβεστήρα παράλληλα σε κάθε ένα από αυτά τα στοιχεία. Αρχικά, η εναλλαγή αυτή γίνεται για τεχνικούς λόγους. Πρώτον, με αυτή τη διάταξη, στο στοιχείο αρνητικής στιβαρότητας δεν ασκείται καμία εξωτερική δύναμη, όπως στην περίπτωση του KDamper όπου ασκείται το ίδιο βάρος της m_D. Δεύτερον, με την προσθήκη αποσβεστήρων παράλληλα σε κάθε στοιχείο στιβαρότητας, επιτυγχάνεται περεταίρω βελτίωση της δυναμικής συμπεριφοράς του αρχικού συστήματος, καθώς επίσης και μείωση στη σχετική μετατόπιση μεταξύ των δύο τερματικών του στοιχείου αρνητικής στιβαρότητας, κάτι που είναι εξαιρετικής σημασίας για τον ρεαλιστικό σχεδιασμό του.

Οι εξισώσεις κινήσεις του EKD σε περίπτωση που η διέγερση είναι στη βάση του ταλαντωτή διαμορφώνονται ως εξής:

$$-\omega^2 m\tilde{U}_S + j\omega c_{NS}(\tilde{U}_S - \tilde{U}_D) + k_{NS}(\tilde{U}_S - \tilde{U}_D) + k_S\tilde{U}_S = -m\ddot{U}_G \quad (23.\alpha)$$

$$-\omega^2 m_D\tilde{U}_D - j\omega c_{NS}(\tilde{U}_S - \tilde{U}_D) - k_{NS}(\tilde{U}_S - \tilde{U}_D) + k_{PS}\tilde{U}_D + j\omega c_{pS}U_D = -m_D\ddot{U}_G \quad (23.\beta)$$

και οι συναρτήσεις μεταφοράς:

$$\begin{bmatrix}\tilde{H}_{US}\\ \tilde{H}_{UD}\end{bmatrix} = \begin{bmatrix}\tilde{U}_S / \ddot{U}_G\\ \tilde{U}_D / \ddot{U}_G\end{bmatrix} = -\tilde{H}^{-1}\begin{bmatrix}m\\ m_D\end{bmatrix} \quad (24)$$

$$\tilde{H}_{AS} = \ddot{U}_S / \ddot{U}_G = 1 - \omega^2\tilde{H}_{US} \quad (25)$$

$$\tilde{H}_{AD} = \ddot{U}_D / \ddot{U}_G = 1 - \omega^2 \tilde{H}_{UD} \tag{26}$$

$$\tilde{H} = \begin{bmatrix} -\omega^2 m + j\omega c_{NS} + k_{NS} + k_S & -j\omega c_{NS} - k_{NS} \\ -j\omega c_{NS} - k_{NS} & -\omega^2 m_D + j\omega(c_{NS} + c_{PS}) + k_{PS} + k_{NS} \end{bmatrix} \tag{27}$$

3.2.3 Πειραματική επαλήθευση της διάταξης EKD

Η αξιοπιστία της διάταξης EKD διερευνάται πειραματικά (Mantakas et al., 2023; Καπασακάλης et al., 2022), ώστε να επιβεβαιωθούν οι δυνατότητες των μηχανισμών KDamper. Η πειραματική διάταξη απεικονίζεται στο Σχήμα 5 (α). Στην συγκεκριμένη υλοποίηση υιοθετείται ο μηχανισμός που προτάθηκε από τους Kapasakalis et al. (2021) όπως παρουσιάζεται στο Σχήμα 5 (β). Εδώ, το στοιχείο αρνητικής στιβαρότητας υλοποιείται από ένα προεντεταμένο ελατήριο και έναν άκαμπτο χαλύβδινο σύνδεσμο που συνδέει την εσωτερική μάζα (m_D) με την μάζα (m) του EKD μέσω αρθρωτών συνδέσεων (ρουλεμάν). Οι ακόλουθες εκφράσεις προκύπτουν για την Δυναμική ενέργεια U, την μη γραμμική δύναμή N, και την ισοδύναμη μη γραμμική στιβαρότητα k_N του μηχανισμού:

$$U(u_{NS}) = \frac{1}{2} k_c \left(l_H - l_{Hi} \right)^2 \tag{28}$$

$$N(u_{NS}) = \frac{\partial U}{\partial u_{NS}} = -k_c \left(1 + \frac{l_{Hi} - d}{\sqrt{a^2 - u_{NS}^2}} \right) u_{NS} \tag{29}$$

$$K_N(u_{NS}) = \frac{\partial N}{\partial u_{NS}} = -k_c \left(1 + \frac{\left(l_{Hi} - d \right) / a}{\sqrt[3]{\left(1 - u_{NS}^2 / a^2 \right)}} \right) \tag{30}$$

Όπου a είναι το μη παραμορφωμένο ύψος της συσκευής, d το μήκος του μοχλοβραχίονα, l_{HI} το μήκος του μη παραμορφωμένου ελατηρίου και k_c η στιβαρότητα του ελατηρίου. Η διάταξη αρνητικής στιβαρότητας παρουσιάζεται στο Σχήμα 5 (α) και οι παράμετροι του μηχανισμού NS παρουσιάζονται αναλυτικά στον Πίνακας 1.

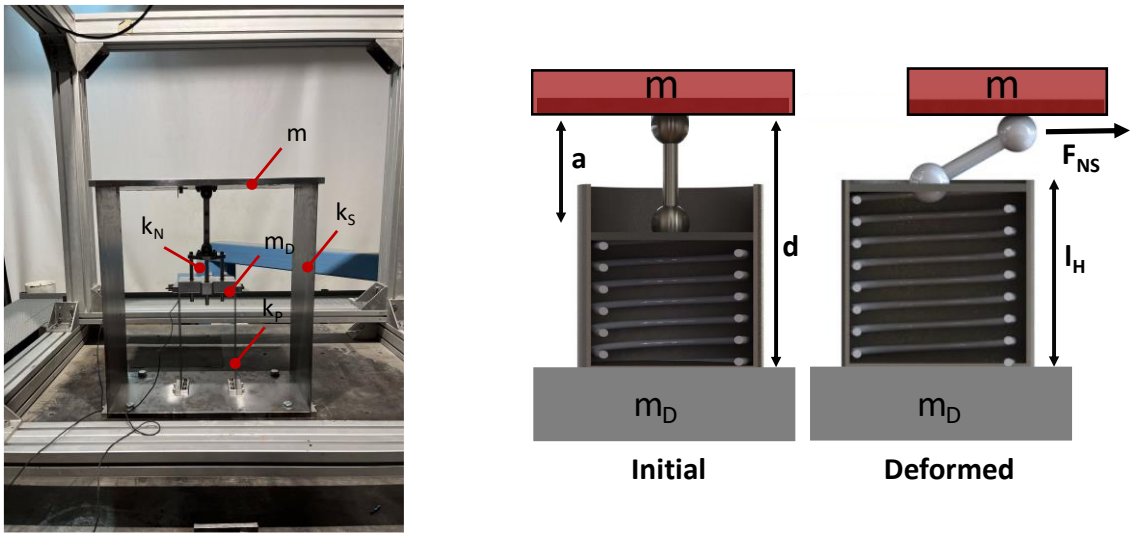

(α) *(β)*

Σχήμα 5: (α) Φωτογραφία του πρωτοτύπου ΕΚD στο ΕΜΠ . (β) Απεικόνιση της υλοποίησης του στοιχείου αρνητικής στιβαρότητας .

Πίνακας 1: Παράμετροι υλοποίησης του στοιχείου αρνητικής στιβαρότητας.

k_c [kN/m]	a [m]	l_{HI} [m]	d [m]	F_{NS}
4100	0.146	0.1	0.203	73.8

Η μάζα (m) κατασκευάζεται από χαλύβδινη πλάκα διαστάσεων 0.25x0.15x0.01, η εσωτερική μάζα του αποσβεστήρα (m_D) από χαλύβδινη πλάκα διαστάσεων 0.1x0.5x0.015, και τα στοιχεία θετικής στιβαρότητας από χαλύβδινα φύλλα διαστάσεων 0.27x0.0.07x0.001 και 0.585x0.0,25x0.0015, αντίστοιχα. Οι τιμές των βελτιστοποιημένων στοιχείων του ΕΚD παρουσιάζονται στον Πίνακας 2.

Πίνακας 2: Βέλτιστες τιμές των παραμέτρων του ΕΚD.

m [kg]	m_D [kg]	k_S [kN/m]	k_P [kN/m]	k_N (u_{NS}=0) [kN/m]
16.3	0.815	1770	1440	-500

Η συσκευή τοποθετήθηκε στη σεισμική τράπεζα οριζόντιας διέγερσης του Εργαστηρίου Εδαφομηχανικής του Εθνικού Μετσόβιου Πολυτεχνείου, όπου και διεξήχθησαν σειρά μετρήσεων για αρμονικές διεγέρσεις στο εύρος 1 έως 5 Hz. Για τις πειραματικές μετρήσεις, τοποθετήθηκαν επιταχυνσιόμετρα στη βάση της συσκευής, στην μάζα (m) και στην εσωτερική μάζα (m_D), ενώ εφαρμόστηκαν διεγέρσεις μικρού πλάτους για να εξασφαλιστεί η γραμμική συμπεριφορά του συστήματος. Δοκιμάστηκαν δύο διαφορετικές διατάξεις: (α) η διευρυμένη έκδοση του KDamper (EKD) και (β) ένας μονοβάθμιος μηχανισμός (SDoF) με ίδιες σταθερές μάζας και στιβαρότητας ελατηρίου με αυτές του ΕΚD. Σε καμία από τις δύο διαμορφώσεις δεν προστέθηκαν επιπλέον στοιχεία απόσβεσης.

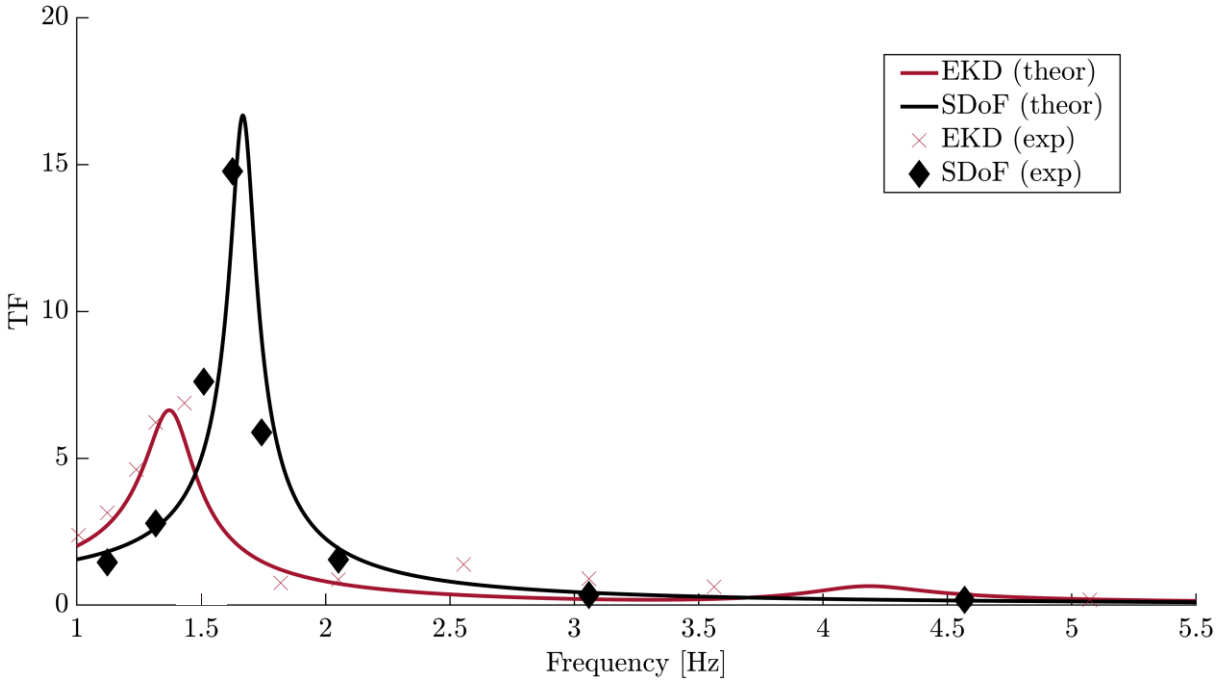

Σχήμα 6: Θεωρητική και πειραματική δυναμική απόκριση της διάταξης EKD έναντι του ταλαντωτή SDoF.

Στο Σχήμα 6 απεικονίζεται η πειραματικά και η θεωρητικά εκτιμώμενη απόκριση συχνότητας της διευρυμένη έκδοσης του KDamper (EKD). Τα πειραματικά αποτελέσματα επιβεβαιώνουν την προβλεπόμενη συμπεριφορά του ταλαντωτή καθώς και την ύπαρξη ρεαλιστικών τρόπων υλοποίησης των απαιτούμενων τιμών αρνητικής στιβαρότητας. Συγκριτικά με τον απλό μονοβάθμιο ταλαντωτή η θεμελιώδης κορυφή συντονισμού μειώνεται κατά περίπου 60% και κατ' επέκταση αυτό οδηγεί σε συχνότητα μόνωσης ≈ 1,4 Hz, η οποία είναι σύμφωνη με τον επιδιωκόμενο στόχο της διάταξης.

3.3 Εδράσεις ακουστικών πετασμάτων βασισμένες στο βελτιωμένο σύστημα KDamper με μηχανισμό αδρανειακής ενίσχυσης (KD-IAM)

Η ιδέα πετασμάτων εδραζόμενων σε στηρίξεις τύπου KDamper παρουσιάστηκε για πρώτη φορά από τον Paradeisiotis et al. (2019; 2019) όπου ο υπολογισμός του δείκτη ηχομείωσης (STL) πραγματοποιήθηκε μέσω της προσέγγισης ακουστικής αντίστασης (Kim, 2010): κανονικά, επίπεδα, κύματα προσπίπτουν σε απαραμόρφωτη επίπεδη επιφάνεια. Προφανώς, λόγω της προσεγγιστικής φύσης της μεθόδου δεν είναι δυνατός ο ακριβής προσδιορισμός των τιμών του δείκτη ηχητικής μείωσης. Παρ ’όλα αυτά, η σύγκριση με άλλους ταλαντωτές υπέδειξε τα πλεονεκτήματα του KDamper ως προς την ακουστική μόνωση πετασμάτων.

Σε συνέχεια της αρχικής αυτής έρευνας, προτείνεται η βελτίωση των στηρίξεων τύπου KDamper ενσωματώνοντας έναν μηχανισμό αδρανειακής ενίσχυσης (IAM), με στόχο την αύξηση του πλάτους και του βάθους της παραγόμενης ζώνης εξασθένησης διάδοσής ήχου χαμηλών συχνοτήτων. Ο προτεινόμενος μηχανισμός αυτός θα ονομάζεται εν συντομία από εδώ και στο εξής KD-IAM. Η

μέθοδος υπολογισμού του δείκτη ηχομείωσης (STL) που χρησιμοποιείται είναι αυτή του In series approximation, όπως περιγράφεται στο κεφάλαιο ΙΙ, όπου σε σχέση με την προσέγγιση ακουστικής αντίστασης λαμβάνεται υπόψιν, έστω και προσεγγιστικά, η παραμορφωσιμότητα του πετάσματος.

Η διερεύνηση δείχνει ότι η αύξηση της στιβαρότητας του πάνελ βελτιώνει τη ζώνη εξασθένησης. Με βάση την παρατήρηση αυτή, παρουσιάζεται μια ενδεικτική εφαρμογή, ο σχεδιασμός των βάσεων KD-IAM, καθώς και ο τρόπος υλοποίησης του συστήματος βάσεων – δύσκαμπτου πετάσματος. Η μελέτη αυτή έχει ως στόχο να καταδείξει τις δυνατότητες αυτού του προηγμένου συστήματος αρνητικής στιβαρότητας, μέσω αναλυτικών και αριθμητικών μεθόδων, σε εφαρμογές μόνωσης χαμηλόσυχνου θορύβου.

3.3.1 Σχεδιασμός του ταλαντωτή KD-IAM

Στο Σχήμα 7 παρουσιάζεται το μαθηματικό προσομοίωμα του ευκάμπτου πετάσματος το οποίο εδράζεται στον μηχανισμό KD-IAM. Για την καλύτερη περιγραφή των ιδιοτήτων του μηχανισμού, χρησιμοποιείται υστερητική απόσβεση (Carfagni et al., 1998; Koblar and Boltežar, 2013) σύμφωνα με τις εξισώσεις (31)-(32).

$$k'_S = k_S(1+jn) \tag{31}$$

$$k'_P = k_P(1+jn) \tag{32}$$

Όπου n ο συντελεστής απώλειας.

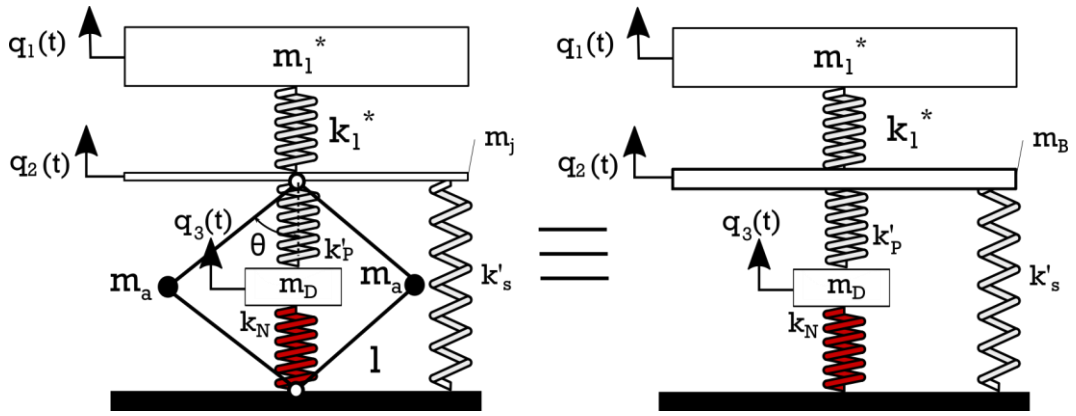

Σχήμα 7: (Αριστερά) Μονογραμμικό διάγραμμα ενός εύκαμπτου πετάσματος εδραζόμενο στον ταλαντωτή KD-IAM και (δεξιά) το ισοδύναμο προσομοίωμα KD-IAM που λαμβάνει υπόψιν την ενεργή μάζα του ενισχυτή.

Οι εξισώσεις κίνησης του ταλαντωτή είναι οι παρακάτω:

$$m_1^*\ddot{q}_1 + k_1^*(q_1 - q_2) = \frac{8P_i l_x l_y}{\pi^2} e^{j\omega t} \tag{33}$$

$$m_a\left(cot^2\theta + 1\right)\ddot{q}_2 - k_1 q_1 + (k_1 + k'_P + k'_S)q_2 - k'_P q_3 = 0 \tag{34}$$

$$m_D\ddot{q}_3 + (k'_P + k'_S)q_3 - k'_P q_2 = 0 \tag{35}$$

όπου οι γενικευμένοι βαθμοί ελευθερίας ορίζονται ως:

$$q_i(t) = C_i e^{j\omega t} \tag{36}$$

όπου C_i το πλάτος κίνησης. Οι εξισώσεις μεταφοράς του συστήματος είναι:

$$TF_{21} = \frac{C_2}{C_1} = \frac{k^*}{-\omega^2 m_B + k_1 + k'_S + k'_P(1 - TF_{32})} \tag{37}$$

$$TF_{32} = \frac{C_3}{C_2} = \frac{k'_P}{-\omega^2 m_D + k'_P + k_N} \tag{38}$$

ενώ ο συντελεστής διάδοσης του ήχου (STL) υπολογίζεται από την εξ. (8).

Το Σχήμα 8 παρουσιάζει την απόδοση ακουστικών πετασμάτων με εδράσεις τύπου (α) KDamper (β) KDamper με προσθήκη αδρανειακού ενισχυτή (KD-IAM), για διάφορες τιμές στιβαρότητας. Η στιβαρότητα αυτή υλοποιείται με τοποθέτηση συνδέσμων στιβαρότητας στο πρόσωπο του πετάσματος.

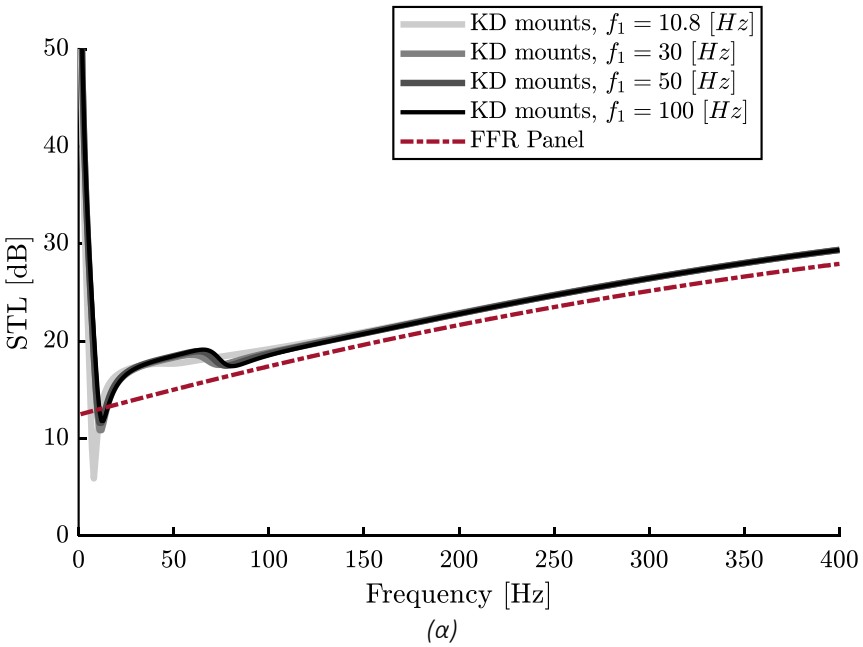

(α)

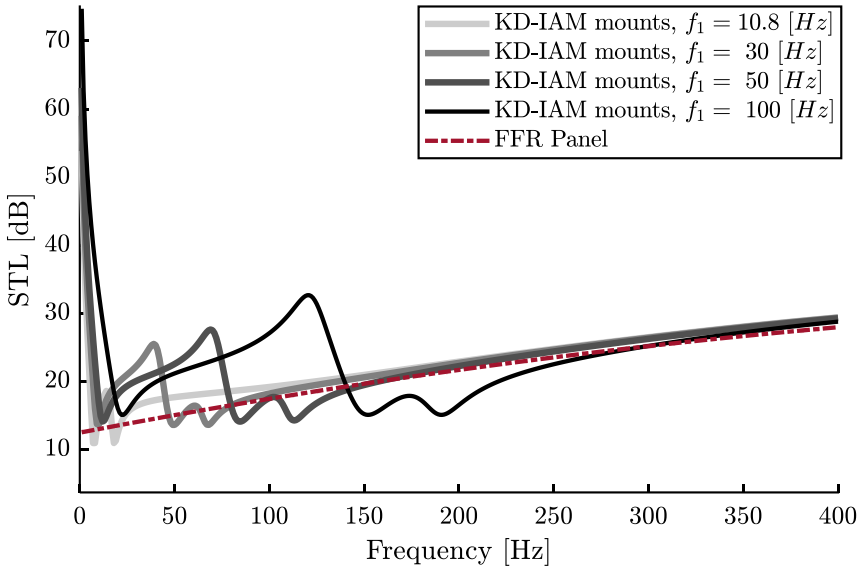

(β)

Σχήμα 8: Επιρροή της στιβαρότητας στις ηχομονωτικές δυνατότητες ενός πετάσματος εδραζόμενου (α) σε στηρίγματα τύπου KDamper (β) σε στηρίγματα τύπου KD-IAM.

Ως φαινόμενη μάζα, στην διερεύνηση αυτή, θεωρείται γύψινο πλαίσιο γεωμετρίας και ιδιοτήτων που παρουσιάζονται στον Πίνακας 3.

Πίνακας 3: Plasterboard properties.

ρ_p [kg/m^3]	l_x [m]	l_y [m]	h_p [mm]	E_p [MPa]	ν_p [-]	η_p [-]
668	1.2	2.4	12.5	2900	0.31	0.01

Οι παράμετροι σχεδιασμού των στηρίξεων προκύπτουν μέσω ενός προβλήματος βελτιστοποίησης βασισμένο στον αλγόριθμο του Kapasakalis et al. (2020), όπου εισάγονται όρια ανοχών για τις τιμές των ελατηρίων k_s, k_P, k_N, το συχνοτικό εύρος της ζώνης ηχομείωσης, καθώς και η στιβαρότητα του πετάσματος. Στόχος του αλγορίθμου είναι ο προσδιορισμός των παραμέτρων k_s, k_P, k_N, m_B για τον οποίο προκύπτει ο βέλτιστος δείκτης ηχομείωσης (STL) για την επιλεγμένη ζώνη.

Συγκρίνοντας την απόδοση του συστήματος με και χωρίς τον ενισχυτή (IAM) προκύπτει ότι το βελτιωμένο σύστημα αυξάνει την ηχητική απόδοση του πετάσματος τόσο σε όρους εύρους ζώνης εξασθένησης αλλά και μέγιστης μείωσης. Η βέλτιστη απόκριση του βελτιωμένου συστήματος παρατηρείται όταν η ιδιοσυχνότητα του πετάσματος είναι f_0=100Hz, όπου για συχνότητες μικρότερες των 150Hz οι τιμές του STL είναι μεγαλύτερες αυτών του νόμου μάζας. Στην περίπτωση χωρίς τον ενισχυτή ($m_B = 0$) (Σχήμα 8.α) παρατηρείται ότι το εύρος της ζώνης παραμένει σταθερό με την αύξηση της στιβαρότητας του πετάσματος, ενώ βελτιώνεται η απόκριση του στην περιοχή συντονισμού.

3.3.2 Πρακτική Υλοποίηση των στηρίξεων τύπου KD-IAM

Στην ενότητα αυτή παρουσιάζεται η πρακτική υλοποίηση ενός ακουστικού πετάσματος ιδιοσυχνότητας f_0=90.2Hz και εδράσεις βασισμένες στο KD-IAM. Το υπό εξέταση πλαίσιο απεικονίζεται στο Σχήμα 9 και οι ιδιότητες/διαστάσεις των συνδέσμων δυσκαμψίας δίνονται στον Πίνακας 4.

Πίνακας 4: Ιδιότητες συνδέσμων δυσκαμψίας.

ρ_S [kg/m^3]	a_s [mm]	b_S [mm]	h_S [mm]	w_x [m]	w_y [m]	E_S [GPa]	v_p [-]
7800	50	50	7	0.375	0.575	210	0.3

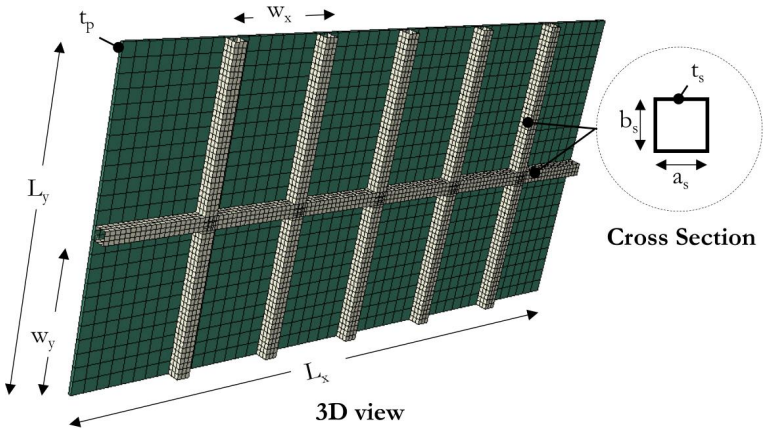

Σχήμα 9: Γεωμετρία ενός ενισχυμένου πετάσματος με τη χρήση συνδέσμων δυσκαμψίας.

Συνοπτικά, η επιλογή συγκεκριμένων παραμέτρων καταλήγει στην ευκολία υλοποίησης τους από πρακτική άποψη, ειδικά όσον αφορά το στοιχείο αρνητικής στιβαρότητας. Λαμβάνοντας υπόψιν τα προαναφερθέντα, οι βέλτιστες επιλεγμένες τιμές των στοιχείων των στηριγμάτων και άλλες σχετικές παράμετροι της κατασκευής συνοψίζονται στον Πίνακας 5. Με βάση τις τιμές αυτές υλοποιείται και ο ενδεικτικός σχεδιασμός του συστήματος.

Πίνακας 5: Βέλτιστες τιμές παραμέτρων του συστήματος KD-IAM.

f_1 [Hz]	f_0 [Hz]	k_0 [Nm^{-1}]	k_S [Nm^{-1}]	k_P [Nm^{-1}]	k_N [Nm^{-1}]	μ [-]	η [-]	κ_N [-]	m_B [kg]
90.1	25.1	1.405×10^5	3.613×10^5	1.386×10^5	-8.654×10^4	0.01	0.1	-0.660	3.35

Όπως και οι στηρίξεις δυναμικής ενίσχυσης (IAM), έτσι και οι στηρίξεις τύπου KDamper είναι τέσσερις (4) στην συγκεκριμένη υλοποίηση και τοποθετούνται περιμετρικά του πετάσματος, μια σε κάθε γωνία. Ο σχεδιασμός των στηρίξεων KDamper βασίζεται στην υλοποίηση του Paradeisiotis (2019).

3.3.2.1 Στοιχείο αδρανειακής ενίσχυσης (IAM)

Στο Σχήμα 10 απεικονίζεται η υλοποίηση του IAM. Για το συγκεκριμένο πλαίσιο χρησιμοποιούνται τέσσερις χαλύβδινοι μηχανισμοί διαστάσεων 10×30×35 [mm^3], όπου η αδρανειακή μάζα είναι $m_a = 0.051kg$, η γωνία $\theta = 10^\circ$ και το μήκος του συνδέσμου $l = 0.02m$.

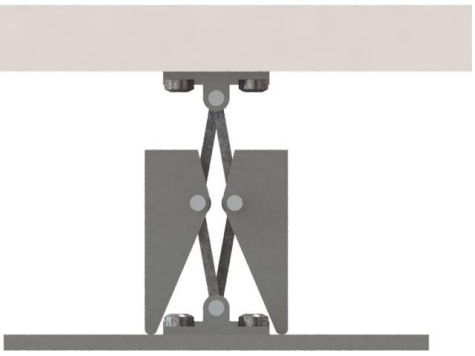

Σχήμα 10: Ιδεατή απεικόνιση συστήματος αδρανειακής ενίσχυσης (IAM).

3.3.2.2 Στοιχεία αρνητικής στιβαρότητας

Το στοιχείο αρνητικής στιβαρότητας του μηχανισμού υλοποιείται μέσω δισκοειδών ελατηρίων τύπου "Belleville". Η ασκούμενη δύναμη $F_N(s)$ των δισκοειδών ελατηρίων είναι μη-γραμμική συνάρτηση της κάθετης παραμόρφωσης s της εσωτερικής διαμέτρου D_i του δίσκου. Το ύψος του δίσκου συμβολίζεται με l_0, D_e είναι η εξωτερική διάμετρος, και $h_0 = l_0 - t$, όπου t είναι το πάχος (Bauer, 2008). Η ασκούμενη δύναμη $F_c = F(s = h_0)$ συμβολίζει τη δύναμή στην κατάσταση που ο δίσκος βρίσκεται στην επίπεδη του μορφή και ταλαντώνεται κάθετα κατά *s* γύρω από την θέση ισορροπίας $s = h_0$. Συνεπώς, η επιθυμητή αρνητική στιβαρότητα εμφανίζεται στην περιοχή αυτή. Λόγω των υψηλών τιμών αρνητικής στιβαρότητας που απαιτούνται στο σύστημα, η υλοποίηση με ένα δισκοειδές ελατήριο δεν προτείνεται (ανάπτυξη υψηλών τάσεων στη διατομή του, αδυναμία εύρεσης ελατηρίων στο εμπόριο κλπ.). Επομένως, στη συγκεκριμένη εφαρμογή για την επίτευξη της απαιτούμενης αρνητικής στιβαρότητας k_N / 4 =-2.193×10^4 [Nm^{-1}], θεωρούνται σε παράλληλη διάταξη στοιβαγμένα έξι (6) δισκοειδή ελατήρια κατασκευασμένα από πλαστικό ABS ($\rho = 1020kg/m^3, \sigma_{yield} = 48MPa, E = 2206.3MPa, v = 0.3$) τα χαρακτηριστικά των οποίων συνοψίζονται στον Πίνακας 6.

Πίνακας 6: Γεωμετρικά χαρακτηριστικά δισκοειδών ελατηρίων τύπου Belleville .

T [mm]	δ [-]	D_e/t [-]	h_0/t [-]	F_c [N]	$k_{N,max}$ [Nm^{-1}]
1.3	2.5	32	1.64	31.797	-3.570×10^3

Η προκύπτουσα στιβαρότητα αυτής της διάταξης σε σύγκριση με την καμπύλη του ενός ελατηρίου παρουσιάζεται στο Σχήμα 11 (α). Η έντονη διακεκομμένη γραμμή δείχνει τη μέγιστη αρνητική τιμή στιβαρότητας k_N, η οποία αντιστοιχεί στην τιμή $k_N / 4$, κάθε διάταξης.

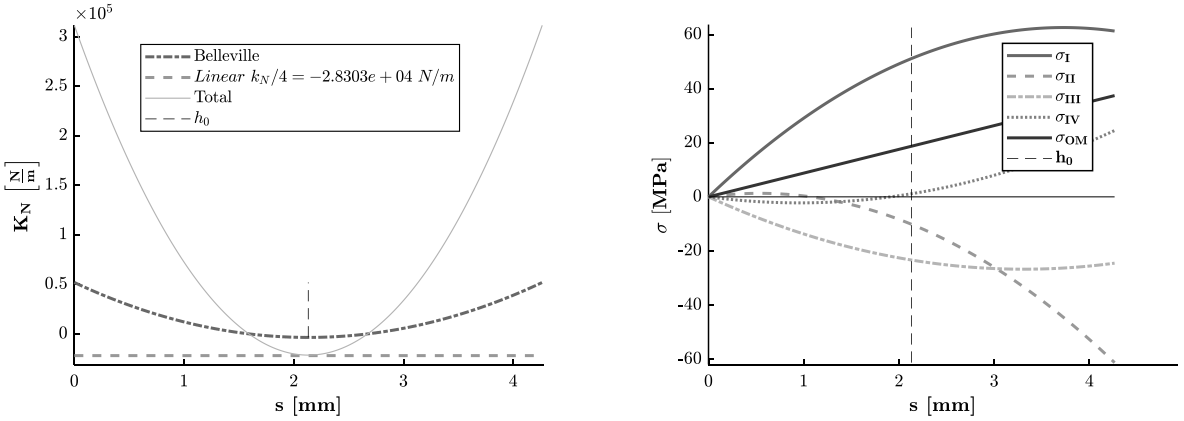

(α) *(β)*

Σχήμα 11: Προκύπτουσα στιβαρότητα και αναπτυσσόμενες τάσεις των δισκοειδών ελατηρίων κατά την παραμόρφωση τους. (α) Ισοδύναμη τιμή στιβαρότητας του δισκοειδούς ελατηρίου και των έξι (6) παραλλήλων ελατηρίων (β) Αναπτυσσόμενες τάσεις κατά την παραμόρφωση του δισκοειδούς ελατηρίου.

Στο Σχήμα 11 (β) παρουσιάζονται οι αναπτυσσόμενες τάσεις σε πέντε χαρακτηριστικά σημεία του δίσκου, σε συνάρτηση με την παραμόρφωση του. Οι τάσεις σ_I , σ_{II}, σ_{III} ,σ_{IV} αντιστοιχούν στις τέσσερις γωνίες της διατομής του δίσκου, ενώ είναι η ισοδύναμη τάση Von Mises στο κέντρο της διατομής. Η τιμή της προκύπτουσας τάσης σ_{OM} πρέπει να βρίσκεται εντός ορισμένων ορίων που καθορίζονται από τον αριθμό μέγιστων κύκλων λειτουργίας του ελατηρίου. Οι τιμές αυτές προκύπτουν με τη χρήση διαγραμμάτων αντοχής και κόπωσης.

Τέλος, η υλοποίηση του στοιχείου αρνητικής στιβαρότητας μέσω έξι (6) παράλληλων δίσκων, αναδιαμορφώνεται σε δύο στοίβες των τριών, τοποθετημένες σε σταθερή βάση, όπως φαίνεται στο Σχήμα 12. Οι δίσκοι συγκρατούνται σε επίπεδη θέση μεταξύ τους με έναν κοχλία και δύο ροδέλες. Με αυτόν τον τρόπο, οι δύο στοίβες εξακολουθούν να λειτουργούν ως δύο παράλληλα ελατήρια, με αποτέλεσμα την επιθυμητή τιμή. Ωστόσο, οι ασκούμενες δυνάμεις κάθε στοίβας έχουν το ίδιο μέγεθος αλλά αντίθετες κατευθύνσεις, πράγμα που σημαίνει ότι αλληλοεξουδετερώνονται και η θέση ισορροπίας είναι ουδέτερα σταθερή.

3.3.2.3 Στοιχεία θετικής στιβαρότητας

Το υλικό που επιλέχθηκε για την υλοποίηση των θετικών στοιχείων στιβαρότητας των στηριγμάτων ($k_S / 4$ και $k_P / 4$) είναι ελαστομερή ποιότητας CR07 (καουτσούκ χλωροπρενίου με 7% αιθάλη). Η

στιβαρότητα των ελαστικών εξαρτάται από τις διαστάσεις τους ενώ παρουσιάζουν υψηλές τιμές συντελεστή απώλειας ($\eta = 0,05-0,7$).

Ένας δείκτης της θλιπτικής στιβαρότητας ενός ελαστομερούς είναι ο συντελεστής σχήματος S, ο οποίος ορίζεται ως ο λόγος της επιφάνειας A που φορτίζεται προς την επιφάνεια που είναι ελεύθερη να διογκωθεί. Ειδικότερα, για κοίλα κυλινδρικά ελαστομερή, ο συντελεστής σχήματος υπολογίζεται ως εξής:

$$S = \frac{\left(D^2 - d^2\right)}{4\left(D-d\right)h} \tag{39}$$

όπου D και d είναι η εξωτερική και η εσωτερική διάμετρος, αντίστοιχα, και t είναι το πάχος του ελαστομερούς, ενώ η θλιπτική στιβαρότητα υπολογίζεται ως:

$$k_{comp} = \frac{E_{corr} A}{h} \tag{40}$$

όπου

$$E_{corr} = E_0(1+S^2) \tag{41}$$

είναι το διορθωμένο μέτρο ελαστικότητας του υλικού που προκύπτει με τη χρήση του συντελεστή σχήματος. Προφανώς, αυτό απαιτεί τη γνώση του αρχικού E_0 το οποίο μπορεί να προσδιοριστεί από δοκιμές τάσης - παραμόρφωσης. Στην παρούσα σχεδίαση, οι υπερελαστικές ιδιότητες του ελαστομερούς αγνοούντα και η υπολογιζόμενη τιμή από την εξ. (40) είναι προσεγγιστική. Οι απαιτούμενες διαστάσεις των ελαστομερών παρουσιάζονται στον Πίνακας 7.

Πίνακας 7: Διαστάσεις ελαστομερών θετικών στοιχείων στιβαρότητας (CR07).

	D [mm]	d [mm]	h [mm]
$k_P/4$	34	10	38.9
$k_S/4$	75	52	47

Το Σχήμα 12 (β) παρουσιάζει μια ενδεικτική διάταξη για την ενσωμάτωση των οκτώ στηρίξεων στο πλαίσιο από γυψοσανίδα. Στην πραγματικότητα, η σταθερή βάση κάθε στήριξης εγκαθίσταται στους ορθοστάτες ή στου συνδέσμους στιβαρότητας στα οποία στερεώνεται η γυψοσανίδα.

3.3.3 Αριθμητική προσομοίωση του πετάσματος σε στηρίγματα τύπου KD-IAM

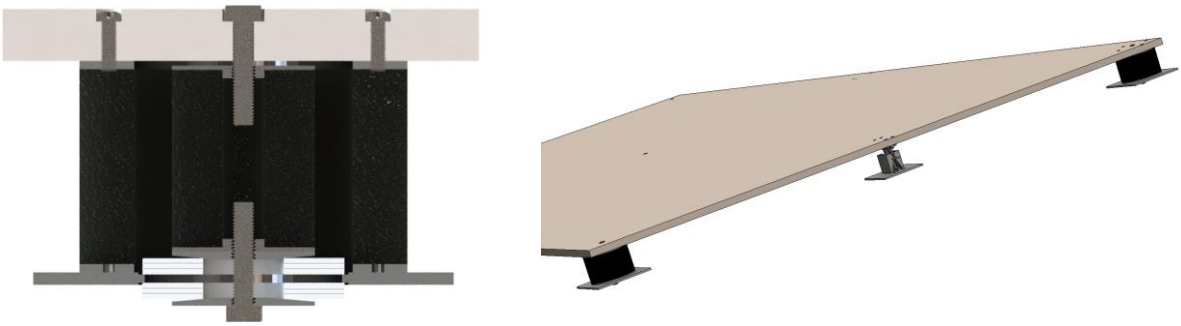

(α) *(β)*

Σχήμα 12: Ενδεικτική υλοποίηση των ακουστικών στηρίξεων τύπου KD-IAM. (α) τομή της έδρασης τύπου KDamper, (β) διάταξη των εδράσεων στο πλαίσιο.

Με σκοπό την επικύρωση της αναλυτικής μεθόδου LPM, αναπτύχθηκε ένα τρισδιάστατο προσομοίωμα πεπερασμένων στοιχείων (vibro-acoustic model) στο εμπορικό λογισμικό ABAQUS®. Η απεικόνιση του προσομοιώματος παρουσιάζεται στο Σχήμα 13 (α).

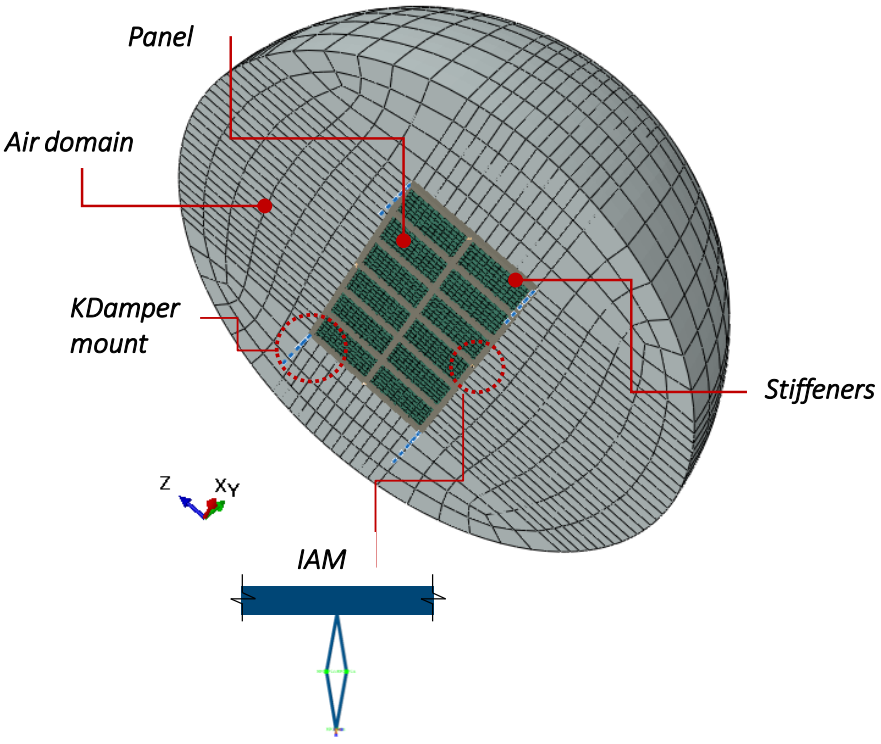

(α)

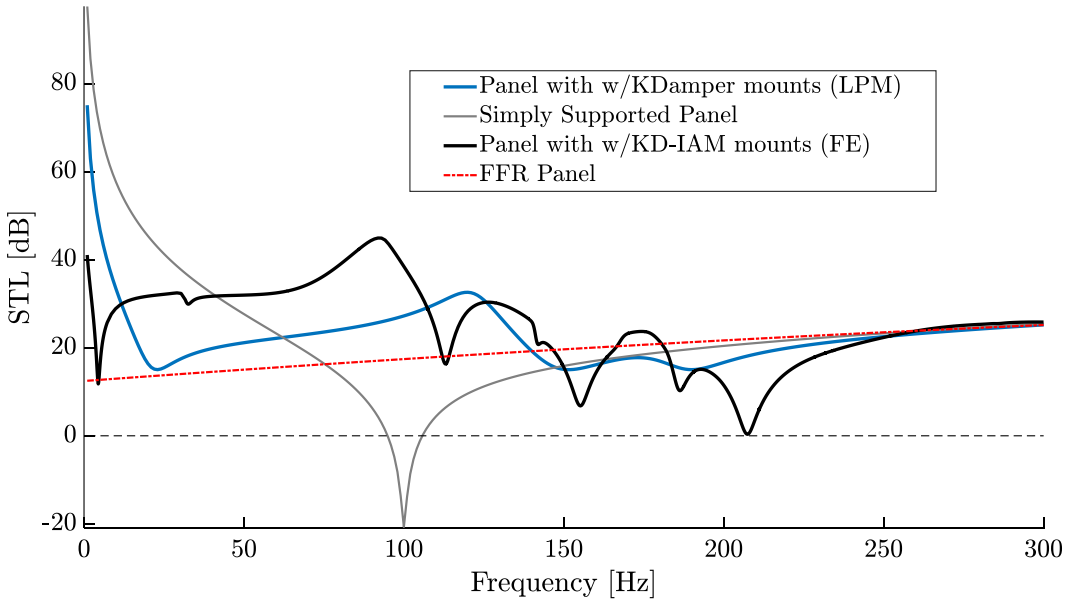

(β)

Σχήμα 13: (α) Απεικόνιση του 3-Δ προσομοιώματος πεπερασμένων στοιχείων (ΠΣ) του πετάσματος σε στηρίγματα τύπου KD-IAM. (β) αποτελέσματα δείκτη ηχομείωσης (STL) για το υποεξέταση πλαίσιο; Σύγκριση μεταξύ μεθόδου ΠΣ και της αναλυτικής μεθόδου LPM.

Η άμεση σύγκριση μεταξύ των καμπυλών STL που προκύπτουν από την προσέγγιση LMP και της ανάλυσης πεπερασμένων στοιχείων δείχνει ότι το αναλυτικό προσομοίωμα προβλέπει με ακρίβεια τις ακουστικές ιδιότητες του συστήματος, λαμβάνοντας υπόψιν τις παραδοχές της μεθόδου. Συγκεκριμένα, η ζώνη ηχομείωσης υπολογισμένη με τη μέθοδο LMP είναι μετατοπισμένη κατά περίπου 20Hz σε σύγκριση με το προσομοίωμα Π.Σ, ενώ το εύρος της ζώνης ηχομείωσης παραμένει το ίδιο.

3.4 Ακουστικά μεταϋλικά βασισμένα στο βελτιωμένο σύστημα KDamper με μηχανισμό αδρανειακής ενίσχυσης (KD-IAM)

Με την περιοδική επανάληψη μονάδων του βελτιωμένου συστήματος “KD-IAM” προκύπτει ένα καινοτόμο μεταϋλικό. Η βελτιωμένη δομή υλοποιείται με την υιοθέτηση της μονάδας KDamper και την προσθήκη ενός αδρανειακού ενισχυτή (IAM). Ο μηχανισμός KDamper μπορεί να βρει πολλαπλές εφαρμογές σε συστήματα απόσβεσης και απορρόφησης χαμηλών συχνοτήτων. Στο παρόν, εξετάζεται η υιοθέτηση μεταϋλικών με βάση τον μηχανισμό KD-IAM για τη σχεδίαση ακουστικών πετασμάτων τύπου "σάντουιτς" με ιδιότητες χαμηλόσυχνης ακουστικής μόνωσης.

3.4.1 Ανάλυση Bloch

Το μεταϋλικό συνίσταται στην περιοδική επανάληψη μοναδιαίων κελιών “KD-IAM” όπως παρουσιάζεται στο Σχήμα 14.

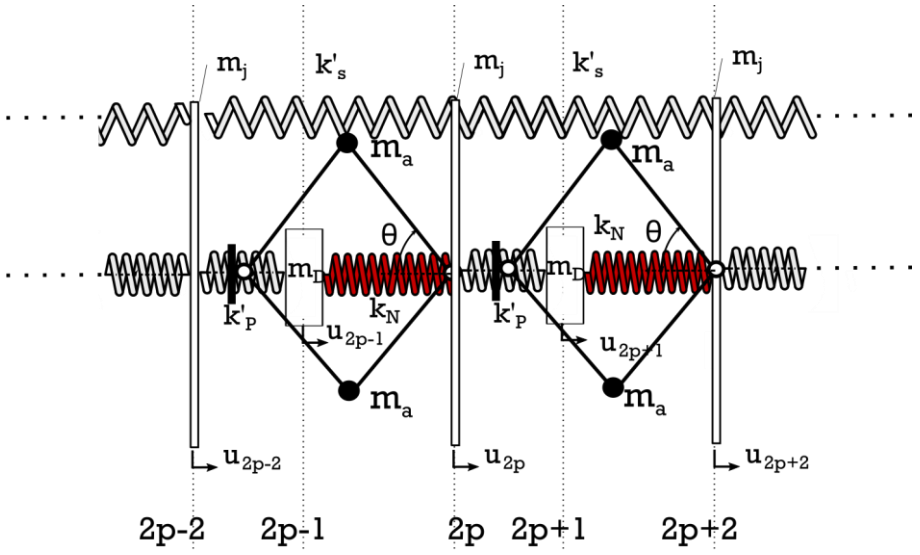

Σχήμα 14: Μοναδιαίο κελί τύπου KD-IAM.

Παρατηρώντας το Σχήμα 14, η κίνηση του βαθμού ελευθερίας (β.ε.) στη θέση $2p$ του πλέγματος μπορεί να εκφραστεί ως:

$$u_{2p} = \tilde{u}_{2p} e^{\lambda t} = U(2p\kappa l) e^{j2p\kappa l} \tag{42}$$

Όπου κ είναι ο αριθμός κύματος και l το μήκος του μοναδιαίου κελιού.

Χρησιμοποιώντας τη θεωρία του Bloch, η διάδοση των ελαστικών κυμάτων μεταξύ των μοναδιαίων κελιών μπορεί να προσδιοριστεί εξετάζοντας την αλληλεπίδραση των μετατοπίσεων και των δυνάμεων. Λαμβάνοντας υπόψιν το χωρικό μέρος της λύσης, προκύπτει:

$$u_{2p} = U e^{j2p\kappa l} \tag{43.α}$$

$$u_{2p-2} = u_{2p} e^{-j2\kappa l} \tag{43.β}$$

$$u_{2p+2} = u_{2p} e^{j2\kappa l} \tag{43.γ}$$

$$u_{2p-1} = U_D e^{j2p\kappa l} e^{-j2\kappa l} \tag{43.δ}$$

$$u_{2p+1} = u_{2p-1} e^{j2\kappa l} \tag{43.ε}$$

και υιοθετώντας την περίπτωση χωρίς απόσβεση, η αντικατάσταση στις εξισώσεις κίνησης του μοναδιαίου κελιού οδηγεί:

$$m_B m_D \omega^4 - [m_B k_D + (\gamma k_s + k_D) m_D] \omega^2 + \gamma (k_s k_D + k_P k_N) = 0 \tag{44}$$

Όπου για $\gamma = 2(1 - \cos q)$, $q = 2\kappa L$ και $k_D = k_P + k_N$. Αντικαθιστώντας όπου $\lambda = \omega^2$, η Εξ. (44) μπορεί να γραφεί στη μορφή:

$$A\lambda^2 + B\lambda + C = 0 \tag{45}$$

όπου οι παράμετροι A, B, C ορίζονται ως:

$$A = 1 \tag{46.α}$$

$$B = -[(1+\mu_B)\omega_D^2 + \gamma\omega_{S,B}^2] \tag{46.β}$$

$$C = \gamma\omega_B^2\omega_D^2 \tag{46.γ}$$

και

$$\omega_B = \sqrt{\frac{k_0}{m_B}},\ \omega_{S,B} = \sqrt{\frac{k_S}{m_B}},\ \mu_B = \frac{m_D}{m_B} \tag{47}$$

τελικά οι καμπύλες διασποράς υπολογίζονται από τις ρίζες της Εξ. (45) ως $\omega_+(\mathrm{q}) = \sqrt{\lambda_1}$ και $\omega_-(\mathrm{q}) = \sqrt{\lambda_2}$.

Η προκύπτουσα σχέση διασποράς του μεταϋλικού είναι 2π-περιοδική, δηλαδή $\omega(\mathrm{q}) = \omega(\mathrm{q}+2\pi)$. Επίσης, η παραγόμενη ζώνη εξασθένησης (ή διακοπής - bandgap) σημειώνεται μεταξύ των συχνοτήτων ω_H και ω_L (ζώνη Brillouin), οι οποίες υπολογίζονται από τις Εξ. (48)-(49) ως:

$$\omega_H = \omega_+(\mathrm{q}=0) = \omega_D\sqrt{1+\mu_B} = \omega_{\mathbf{B}}\rho_B\sqrt{1+\mu_B} \tag{48}$$

$$\omega_L = \omega_-(\mathrm{q}=\pi) = \frac{1}{\sqrt{2}}\sqrt{(4\omega_{S,B}^2 + \omega_H^2)^2 - (4\omega_B\omega_D)^2} \tag{49}$$

όπου $\rho_B = \omega_D\omega_B$. Το κανονικοποιημένο εύρος της ζώνης διακοπής ορίζεται ως:

$$b_w = \frac{\omega_H - \omega_L}{\omega_L} \tag{50}$$

3.4.2 Εφαρμογή ακουστικής μόνωσης

Στο Σχήμα 15 (α), υπολογίζονται και παρουσιάζονται οι συχνότητες της ζώνης διακοπής χρησιμοποιώντας τις ίδιες τιμές παραμέτρων που υπολογίστηκαν για τον σχεδιασμό των στηριγμάτων KD-IAM. Η παραγομένη ζώνη σημειώνεται μεταξύ των συχνοτήτων $f_H = 163\ Hz$ και $f_L = 57\ Hz$, που αντιστοιχούν σε κανονικοποιημένο εύρος ζώνης διακοπής $b_w = 1.9$.

Στο Σχήμα 15 (β), συγκρίνεται η ακουστική συμπεριφορά σε όρους STL, ενός ακουστικού πετάσματος με βάση την περιοδική επανάληψη των KD-IAM μοναδιαίων κελιών σε σύγκριση με την ενδεικτική υλοποίηση του πετάσματος στηριζόμενο σε KD-IAM βάσεις.

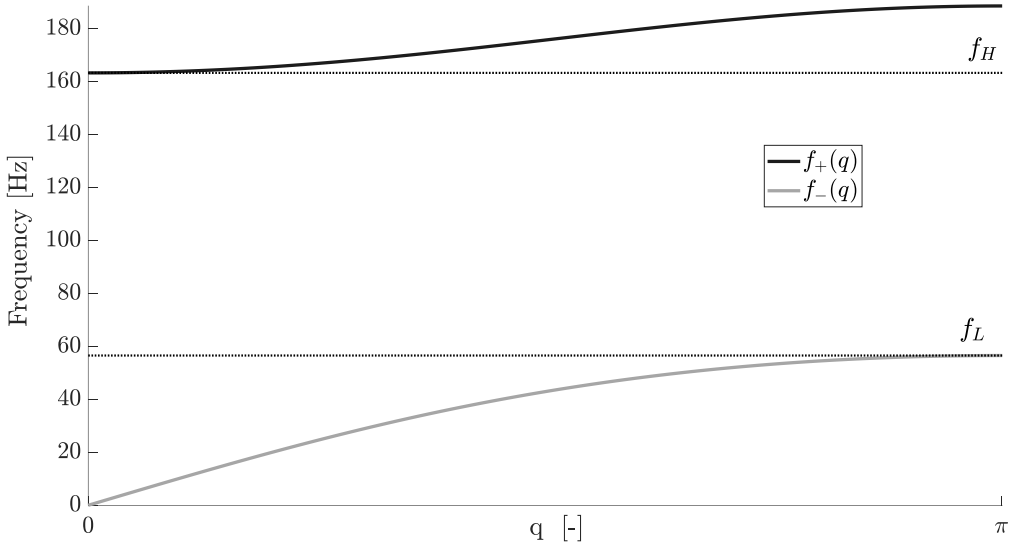

(α)

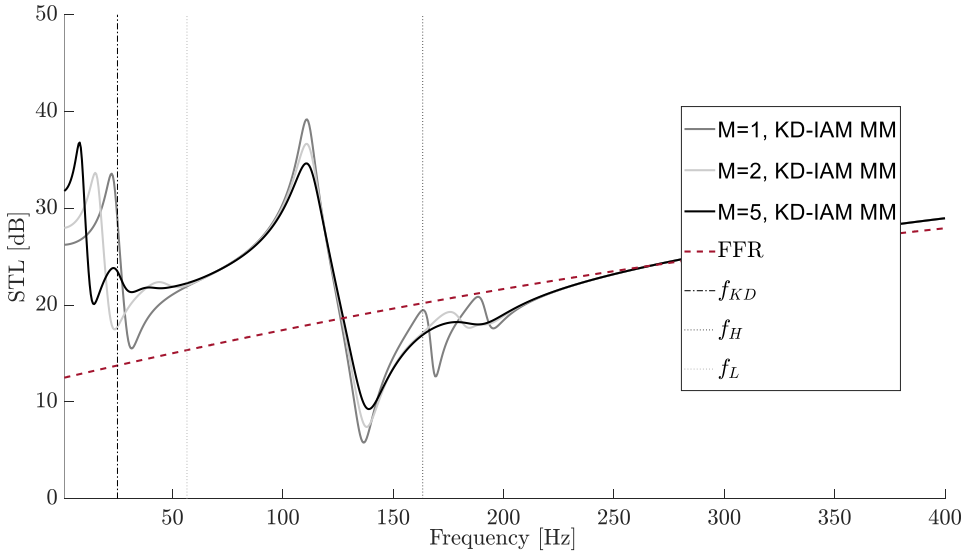

(β)

Σχήμα 15: (α) Αμείωτη ζώνη Brillouin και η παραγόμενη ζώνη εξασθένησης. (β) Απόκριση συχνότητας του STL του μεταϋλικού για αυξανόμενο αριθμό μοναδιαίων κελιών.

Για τους σκοπούς αυτής της σύγκρισης, θεωρείται ότι η περιοδική αλυσίδα περικλείεται από δύο ακτινοβολούσες επιφάνειες στα δύο άκρα της, μάζας $m_1^*/2$ η κάθε μία. Με τον τρόπο αυτό η προσομοίωση γίνεται σύμφωνα με την θεωρία της ενότητας 2. Η ακουστική απόδοση αξιολογείται στη συνέχεια για διάφορους αριθμούς μοναδιαίων κελιών. Η σύγκριση δείχνει ότι αυξάνοντας τον αριθμό των μονάδων, με ταυτόχρονη διατήρηση της μάζας των επιφανειών ακτινοβολίας, η δομή παρέχει βελτιωμένη απόσβεση, ιδίως στην περιοχή συντονισμών. Θα πρέπει να σημειωθεί ότι ο συντελεστής απωλειών των στοιχείων στιβαρότητας $\left(k_S^{'}, k_P^{'}\right)$ έχει επιλεγεί ως $\eta = 0.02$, ο οποίος είναι πέντε φορές μικρότερος από αυτόν που θεωρήθηκε στην περίπτωση των στηριγμάτων KD-IAM. Μια ακόμη ενδιαφέρουσα παρατήρηση που προκύπτει από το διάγραμμα STL, είναι ότι το βάθος και

το πλάτος της ζώνης εξασθένησης δεν επηρεάζεται σημαντικά από την αύξηση των μοναδιαίων κελιών. Στο πλαίσιο της παρούσας έρευνας, αποδεικνύεται ότι οι φυσικοί μηχανισμοί του KD-IAM δημιουργούν τη ζώνη εξασθένησης, με την χρήση ελάχιστου αριθμού κελιών. Συνεπώς, η κατασκευαστική πολυπλοκότητα που συνοδεύει την χρήση πολλαπλών μονάδων θα μπορούσε να θεωρηθεί περιττή.

3.4.3 Σχεδιασμός ακουστικού πετάσματος τύπου «σάντουιτς» βασισμένο στο μεταϋλικό KD-IAM

Στο Σχήμα 16, παρουσιάζεται ένας εφικτός σχεδιασμός ενός πετάσματος τύπου «σάντουιτς» βασισμένο στο μεταϋλικό KD-IAM για ένα μοναδιαίο κελί. Συγκεκριμένα, χρησιμοποιούνται δεκαέξι (16) στοιχεία αρνητικής στιβαρότητας, οκτώ (8) στην επιφάνεια του κάθε πετάσματος ενώ δύο (2) θετικά ελατήρια τοποθετούνται πάνω σε κάθε αρνητικό ελατήριο συνολικής στιβαρότητας k_p. Όσον αφορά τα ελατήρια k_s, προβλέπεται ο συνολικός αριθμός τριάντα δύο (32) στοιχείων, τα οποία κατανέμονται ανάλογα για κάθε ένα από τα δύο πάνελ. Τέλος, χρησιμοποιούνται πενήντα τέσσερα (54) ενισχυτές IAM προκειμένου να επιτευχθεί η απαιτούμενη ενίσχυση.

Τα θετικά ελατήρια (k_S και k_p) έχουν ιδιότητες του υλικού ABS (συμπολυμερές ακρυλονιτριλίου – βουταδιενίου - στυρενίου), το οποίο χρησιμοποιείται σε συμβατικούς τρισδιάστατους εκτυπωτές. Αντίθετα, τα ελατήρια αρνητικής στιβαρότητας και οι ενισχυτές κατασκευάζονται από χάλυβα. Το υλικό ABS μοντελοποιείται ως γραμμικά ελαστικό-απολύτως πλαστικό, με μέτρο ελαστικότητας $E = 1740MPa$, τάση διαρροής $\sigma_{yield} = 27.8MPa$, και πυκνότητα $\rho = 1100kg/m^3$. Για να είναι δυνατή η απλή κατασκευή σε ένα ενιαίο σύστημα υλικών χωρίς την ανάγκη σύνθετης συναρμολόγησης, τα θετικά ελατήρια υλοποιούνται ως τόξα. Το σχήμα των ημικυκλικών τόξων που υλοποιούν τα ελατήρια επιλέγεται έτσι ώστε να επιτρέπει μεγάλες ελαστικές παραμορφώσεις, προς αποφυγή φαινομένων διαρροής και λυγισμού.

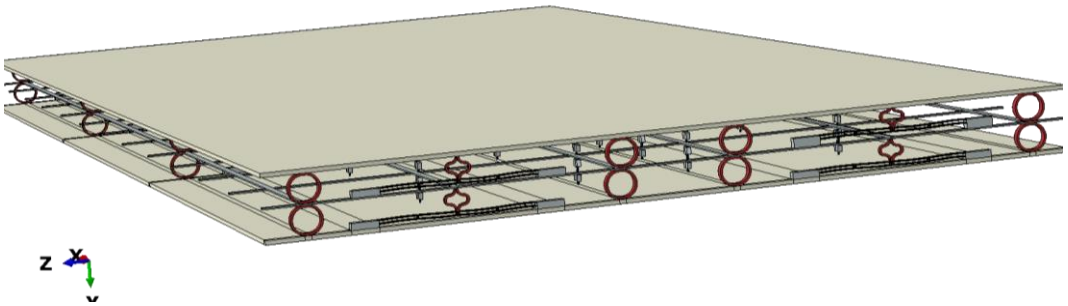

Σχήμα 16: Απεικόνιση του πετάσματος τύπου σάντουιτς.

Η διαστασιολόγηση και ο υπολογισμός της στιβαρότητας των στοιχείων έγινε μέσω αναλυτικών τύπων κατά Guell Izard et al. (2017) και επαληθεύθηκε με προσομοιώσεις ΠΣ στο λογισμικό ABAQUS®.

Οι καμπύλες δύναμης-μετατόπισης των θετικών ελατηρίων παρουσιάζονται στο Σχήμα 17 (α) και (β). Και στις δύο περιπτώσεις μπορούμε να παρατηρήσουμε ότι όλα τα ελατήρια παραμένουν στον ελαστικό κλάδο για παραμόρφωση μικρότερη των 3mm, η οποία θεωρείται επαρκής σε ακουστικές εφαρμογές.

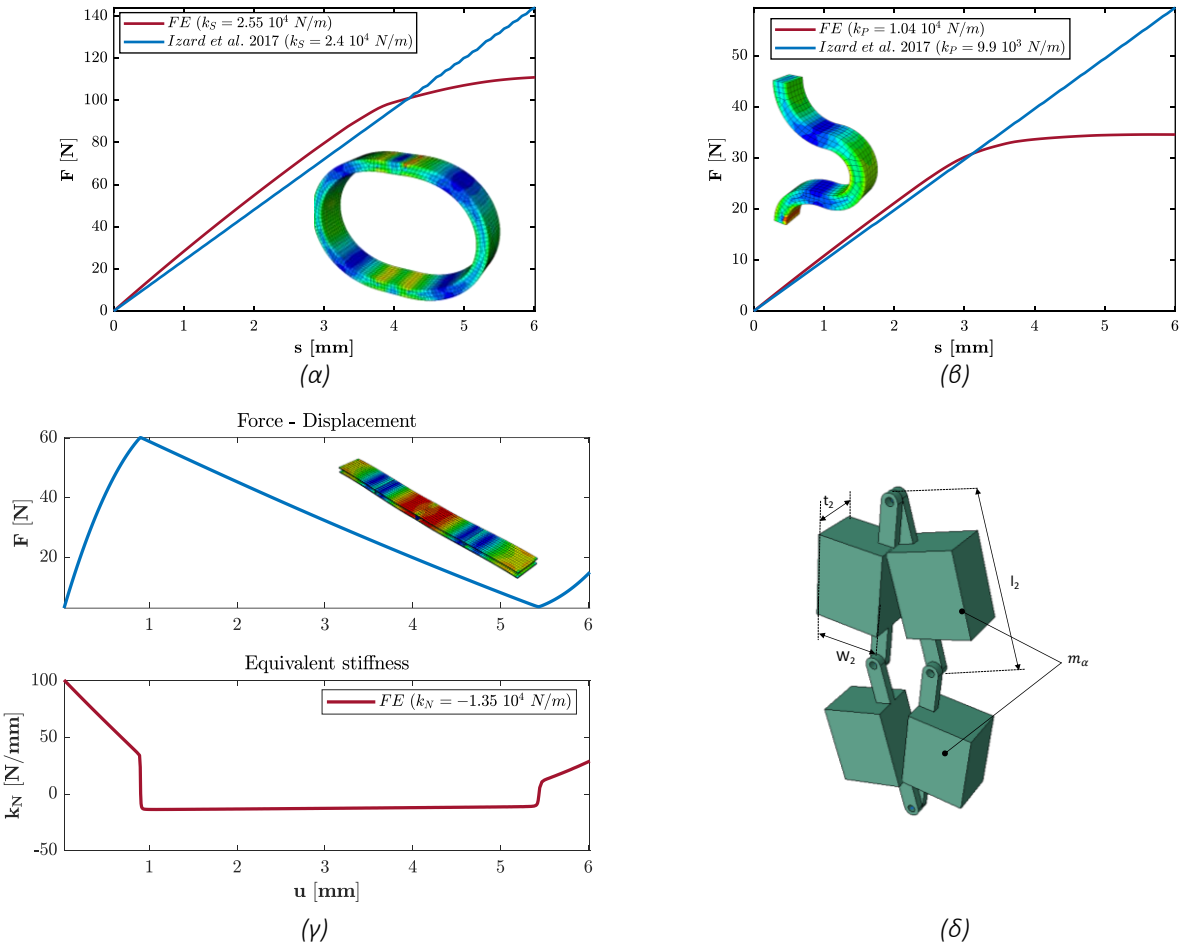

Σχήμα 17: (α) Καμπύλες δύναμης–μετατόπισης των ελατήριων (α) k_S, (β) k_P, (γ) k_N. (δ) Γεωμετρία ενισχυτή (IAM).

Το στοιχείο αρνητικής στιβαρότητας υλοποιείται με τη χρήση κεκλιμένων προεντεταμένων δοκών. Στην περίπτωση αυτή, αρνητική στιβαρότητα δημιουργείται λόγω λυγισμού της δοκού για το εύρος των κατακόρυφων μετατοπίσεων γύρω από την επίπεδη κατάσταση, που φαίνεται στο Σχήμα 17 (γ). Για την υλοποίηση του IAM πρέπει να επιλεγεί ένας συνδυασμός (m_a, θ) προκειμένου να παρέχεται η επιθυμητή ενεργή μάζα m_B. Για τον συγκεκριμένο σχεδιασμό, Σχήμα 17 (δ), θεωρώντας δομικό χάλυβα για το υλικό του IAM και αρθρωτές, συνδέσεις απαιτούνται είκοσι επτά (27) ενισχυτές ανά πέτασμα μάζας $m_a = 0.0156 kg$ σε κάθε ενισχυτή.

3.5 Σύνοψη

Στην ενότητα αυτή παρουσιάστηκε μια νέα διάταξη αρνητικής στιβαρότητας που βασίζεται στον συνδυασμό του ταλαντωτή KDamper και ενός συστήματος αδρανειακής ενίσχυσης (IAM). Αρχικά, παρουσιάστηκε εν συντομία η θεωρία του KDamper καθώς και τα πειραματικά αποτελέσματα επαλήθευσης των δυνατοτήτων του. Στη συνέχεια, περιγράφηκε το θεωρητικό υπόβαθρό του ταλαντωτή KD-IAM καθώς και η δυνατότητα σχεδιασμού στηρίξεων ακουστικών πετασμάτων με δυνατότητες χαμηλόσυχνης ακουστικής μόνωσης. Υιοθετώντας την θεωρία διάδοσης ακουστικών κυμάτων του κεφαλαίου 2, καθώς και τη χρήση Π.Σ, η ανάλυση υποδεικνύει ότι με τις κατάλληλες προσαρμογές είναι δυνατή η αύξηση του δείκτη ηχομείωσης, στην περίπτωση χαμηλόσυχνων διεγέρσεων ιδιαίτερά στην περιοχή συντονισμού του πετάσματος, δημιουργώντας μια ευρεία ζώνη εξασθένησης. Στη συνέχεια, αναγνωρίζοντας τις δυνατότητες του μηχανισμού, εξετάστηκε η περιοδική χρήση του, δηλαδή μια διάταξη ακουστικού μεταϋλικού όπου το μοναδιαίο κελί αποτελεί ο KD-IAM. Τα αποτελέσματα έδειξαν την δημιουργία μεγάλων και βαθιών ζωνών εξασθένησης χωρίς την απαίτηση μεγάλου αριθμού μοναδιαίων κελιών. Τέλος, με βάση την διάταξη αυτή, παρουσιάζεται ο ενδεικτικός σχεδιασμός ενός πετάσματος τύπου σάντουιτς.

4. ΚΑΙΝΟΤΟΜΟ ΣΥΣΤΗΜΑ ΔΥΝΑΜΙΚΗΣ ΕΝΙΣΧΥΣΗΣ (DDA)

4.1 Εισαγωγή

Η ενσωμάτωση μηχανισμών δυναμικής ενίσχυσης με σκοπό την αύξηση της αδράνειας των ταλαντευόμενων μαζών παθητικών συστημάτων απορρόφησης κραδασμών, είναι υψίστης σημασίας για τη βελτίωση των δυναμικών ιδιοτήτων των υφιστάμενων αυτών τεχνολογιών. Για το σκοπό αυτό, έχουν αναπτυχθεί και εφαρμοστεί πληθώρα μηχανισμών ενίσχυσης σε πολυάριθμους τομείς της μηχανικής. Ξεκινώντας από αισθητήρες και ηλεκτρομηχανικούς ενισχυτές σήματος, έως αποσβεστήρες συντονισμένης μάζας (TMD), η ιδέα της ενίσχυσης της μάζας εξετάζεται εδώ και πολύ καιρό από μεγάλο αριθμό ερευνητών.

Στο παρόν κεφάλαιο, παρουσιάζεται ένα νέο σύστημα δυναμικής ενίσχυσης, ο μηχανισμός DDA, ως μέσο τεχνητής αύξησης της αδράνειας ενός ταλαντωτή, ο οποίος δύναται να κατασκευαστεί χωρίς την απαίτηση πολύπλοκων γεωμετριών και επιπλέον παρασιτικών μαζών. Η λογική του μηχανισμού έγκειται στη δυναμική ενός συστήματος που υπόκειται σε έναν ολονομικό περιορισμό (Udwadia and Kalaba, 1995, 1992): η ταλαντευόμενη μάζα είναι πακτωμένη σε μία άκαμπτη ράβδο, η οποία επιτυγχάνει την αύξηση της αδράνειας προς την κατεύθυνση της κίνησης, συνδέοντας τους βαθμούς ελευθερίας της μάζας και αναγκάζοντας έτσι τον ταλαντωτή να κινηθεί μέσω μιας

προδιαγεγραμμένης περιμετρικής διαδρομής. Τα αναλυτικά αποτελέσματα υποδεικνύουν την ευεργετική επίδραση του DDA στη δυναμική απόκριση του συστήματος (συναρτήσεις μεταφοράς), σε σύγκριση με τον αρχικό μονοβάθμιο ταλαντωτή (SDoF). Στη συνέχεια, παρουσιάζεται μια απλή πειραματική διάταξη καθώς και αποτελέσματα δοκιμών σε σεισμική τράπεζα κατακόρυφης διέγερσης για διάφορες γωνίες του DDA. Τα αποτελέσματα επαληθεύουν το αναλυτικό πλαίσιο και αναδεικνύουν την αποτελεσματικότητα του μηχανισμού. Αποδεικνύεται σαφώς ότι μπορούμε να βελτιώσουμε την απόδοση των δυναμικών συστημάτων διατηρώντας παράλληλα τις απαιτήσεις σε μάζα και τις πολύπλοκες διαμορφώσεις σε χαμηλό επίπεδο. Συνεπώς, φαίνεται ότι η απλή γεωμετρία και δομή του DDA επιτρέπει την εφαρμογή του σε πραγματικές κατασκευές, ως μηχανισμό απομείωσης ταλαντώσεων.

Στη συνέχεια, ο δυναμικός ενισχυτής (DDA) εφαρμόζεται ως μέσο για την τεχνητή αύξηση της μάζας φωνονικών κρυστάλλων καθώς και μεταϋλικών συντονιζόμενης μάζας (LRM). Ο κύριος στόχος είναι να αποδειχθεί, μέσω της χρήσης ενός μαθηματικού πλαισίου, ότι μπορούμε να βελτιώσουμε την απόδοση των φωνονικών κρυστάλλων και LRM μεταϋλικών βελτιώνοντας τους πρακτικούς περιορισμούς και εισάγοντας ελαφριά και κατασκευάσιμα μοναδιαία κελιά. Για την επίτευξη αυτού του στόχου, υιοθετείται ένα προσομοίωμα μάζας σε μάζα (mass-in-mass) και πραγματοποιείται ανάλυση με τη χρήση τόσο της θεωρίας του Bloch (1929) για δισδιάστατα πλέγματα άπειρων κελιών, όσο και της συμβατικής θεωρίας ταλαντώσεων σε πεπερασμένα πλέγματα. Στην περίπτωση του LRM μεταϋλικού, μελετάται μία αριθμητική εφαρμογή ως μέσο σεισμικής προστασίας. Σκοπός είναι να αναδειχθούν τα πλεονεκτήματα της προτεινόμενης διάταξης σε σχέση με τον αρχικό συμβατικό σχεδιασμό. Τέλος, οι δυναμικές ιδιότητες των φωνονικών κρυστάλλων καθώς και των LRM μεταϋλικών με DDA επαληθεύονται πειραματικά με τη χρήση πρωτότυπων LEGO® κατασκευών οι οποίες εξετάζονται σε αρμονικές διεγέρσεις χαμηλής συχνότητας.

4.2 Μηχανισμός και εξισώσεις κίνησης του DDA Ενισχυτή

Ο μηχανισμός DDA είναι ένα απλό σύστημα με κύρια χαρακτηριστικά την ενίσχυση της αδράνειας και την εκτροπή της κίνησης της ταλαντευόμενης μάζας, η οποία αναγκάζεται να κινηθεί σε δύο διευθύνσεις. Το μαθηματικό προσομοίωμα του DDA παρουσιάζεται στο Σχήμα 18 και περιλαμβάνει τον σύνδεσμο AB, ο οποίος είναι πακτωμένος στην μάζα m και συνδέεται αρθρωτά στο σημείο A. Με τον τρόπο αυτό, η μάζα που είναι προσαρτημένη στον σύνδεσμο εξαναγκάζεται σε μία περιστροφική κίνηση. Συνεπώς, η σύνδεση αυτή δημιουργεί εξάρτηση των βαθμών ελευθερίας u, v. Το απλοποιημένο προσομοίωμα περιγράφεται από τις συντεταγμένες της μάζας m στην τυχαία θέση $\mathrm{B}(x,\ y)=(x_0+u,\ y_0-v)$, όπου x_0, y_0 οι αρχικές συντεταγμένες της μάζας, την αρχική γωνία

φ=arctan(x_0/y_0), που σχηματίζεται μεταξύ του κατακόρυφου άξονα και του άκαμπτου μέλους και την γωνία θ που δηλώνει την περιστροφή της μάζας στην τυχαία θέση B. Τέλος, k_x, k_y είναι οι στιβαρότητες των ελατηρίων, και F η δύναμη που διεγείρει τον μηχανισμό.

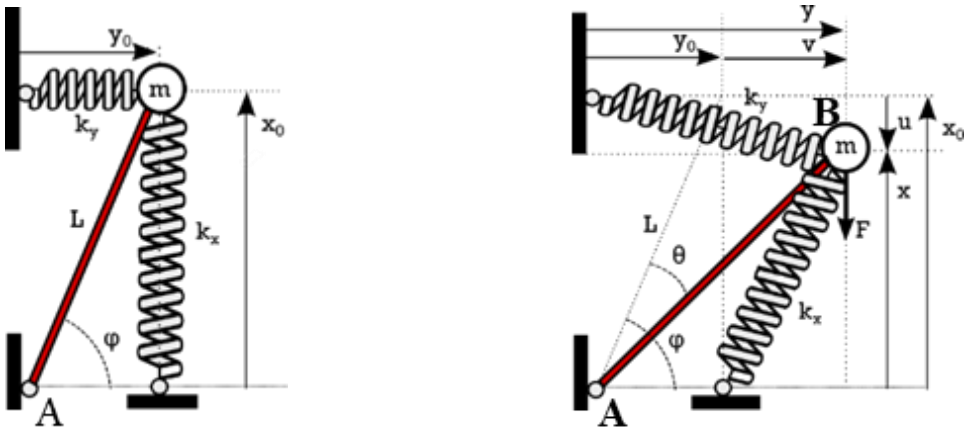

(α) *(β)*

Σχήμα 18: Σχηματική απεικόνιση του συστήματος δυναμικής ενίσχυσης (DDA) όπου η κίνηση v (y κατεύθυνση) είναι εξαρτώμενη από την κίνηση u (x κατεύθυνση) (α) αρχική θέση μάζας, (β) θέση μάζας σε παραμορφωμένη κατάσταση.

Η εξίσωση κίνησης του DDA προκύπτει μέσω της γεωμετρίας του μηχανισμού και της ενεργειακής αρχής Lagrange ως εξής:

$$M\ddot{u} + C\dot{u} + Ku = F \tag{51}$$

όπου, $M = (1 + tan^2(\varphi))m$, $C = c_x + c_y tan^2(\varphi)$ and $K = k_x + k_y tan^2(\varphi)$.

Εκμεταλλευόμενοι την εξίσωση κίνησης και θεωρώντας ότι ο μηχανισμός έχει απόσβεση ίση με c_x, c_y, η συνάρτηση μεταφοράς του μηχανισμού ενίσχυσης στη διεύθυνση της διέγερσης περιγράφεται ως:

$$\tilde{T}_x = -\frac{\left(c_x + c_y\rho^2\right) j\omega + \left(k_x + k_y\rho^2\right)}{-m\left(1+\rho^2\right)\omega^2 + \left(c_x + c_y\rho^2\right) j\omega + \left(k_x + k_y\rho^2\right)} \tag{52}$$

όπου, ρ=tanφ.

4.3 Πειραματική Διάταξη του DDA και Επαλήθευση Αριθμητικών Αποτελεσμάτων

Η δυναμική απόκριση του προτεινόμενου μηχανισμού DDA επαληθεύθηκε πειραματικά διεγείροντας τη βάση του στη σεισμική τράπεζα του εργαστηρίου Δυναμικής & Ακουστικής της σχολής Μηχανολόγων Μηχανικών του ΕΜΠ. Το υπό εξέταση πειραματικό πρωτότυπο παρουσιάζεται στο, Σχήμα 19, όπου τα κατακόρυφα ελατήρια έλξεως είναι συνολικής στιβαρότητας ίση με k_x=500 N/m, η μάζα της κατασκευής απαρτίζεται κυρίως από μεταλλικά ελάσματα και ισούται με m=0.89 kg, ενώ η άρθρωση στη βάση του μηχανισμού υλοποιείται με τη χρήση ρουλεμάν. Για την επίτευξη των σκοπών

του πειράματος εφαρμοστήκαν διαδοχικά αρμονικές διεγέρσεις συχνοτήτων 2-10 Hz, ενώ οι μετρήσεις έγιναν με την χρήση επιταχυνσιομέτρων τριών διευθύνσεων.

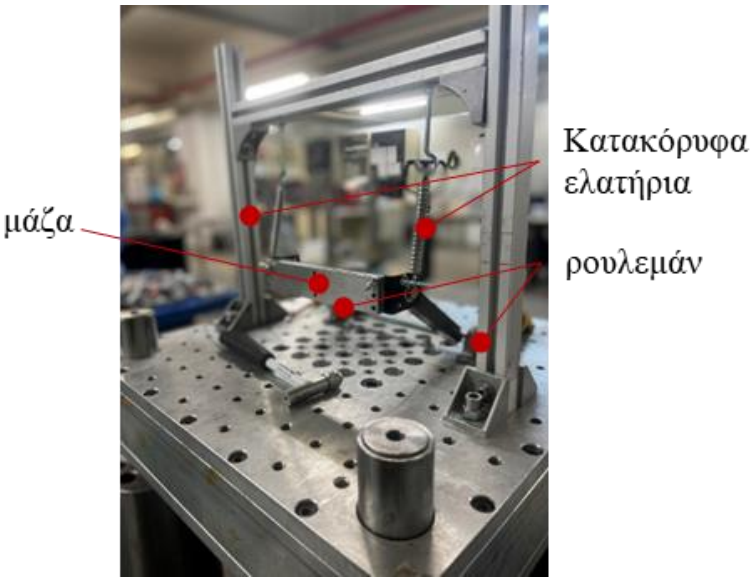

Σχήμα 19: Απεικόνιση πειραματικής διάταξης.

Στο Σχήμα 19 συγκρίνεται η πειραματική με τη θεωρητική απόκριση του μηχανισμού DDA με γωνία φ=30° και φ=40° σε αντιστοιχία με έναν ισοδύναμο μονοβάθμιο ταλαντωτή (ίδια μάζα και στιβαρότητα ελατηρίων). Το θεωρητικώς υπολογιζόμενο φάσμα συμπίπτει με το πειραματικό επαληθεύοντας το προτεινόμενο μαθηματικό προσομοίωμα. Από τη σύγκριση μεταξύ του απλού μονοβάθμιου ταλαντωτή και του προσομοιώματος με τον μηχανισμό ενίσχυσης, παρατηρείται η μείωση της ιδιοσυχνότητας του συστήματος από τα 3.9 στα 3.1Hz, για φ=30°, ενώ για φ=40° από τα 3.9 στα 2.8Hz. Παράλληλα, παρατηρείται μείωση του μέγιστου πλάτους της ταλάντωσης. Η μείωση της ιδιοσυχνότητας που επιτυγχάνεται αντιστοιχεί σε μείωση κατά 19.7% για φ=30° και 25.6 % για φ=40°, αντίστοιχα. Για μεγαλύτερες γωνίες του μηχανισμού DDA η μείωση που μετρήθηκε είναι ακόμα μεγαλύτερη (δεν παρουσιάζεται στο παρόν).

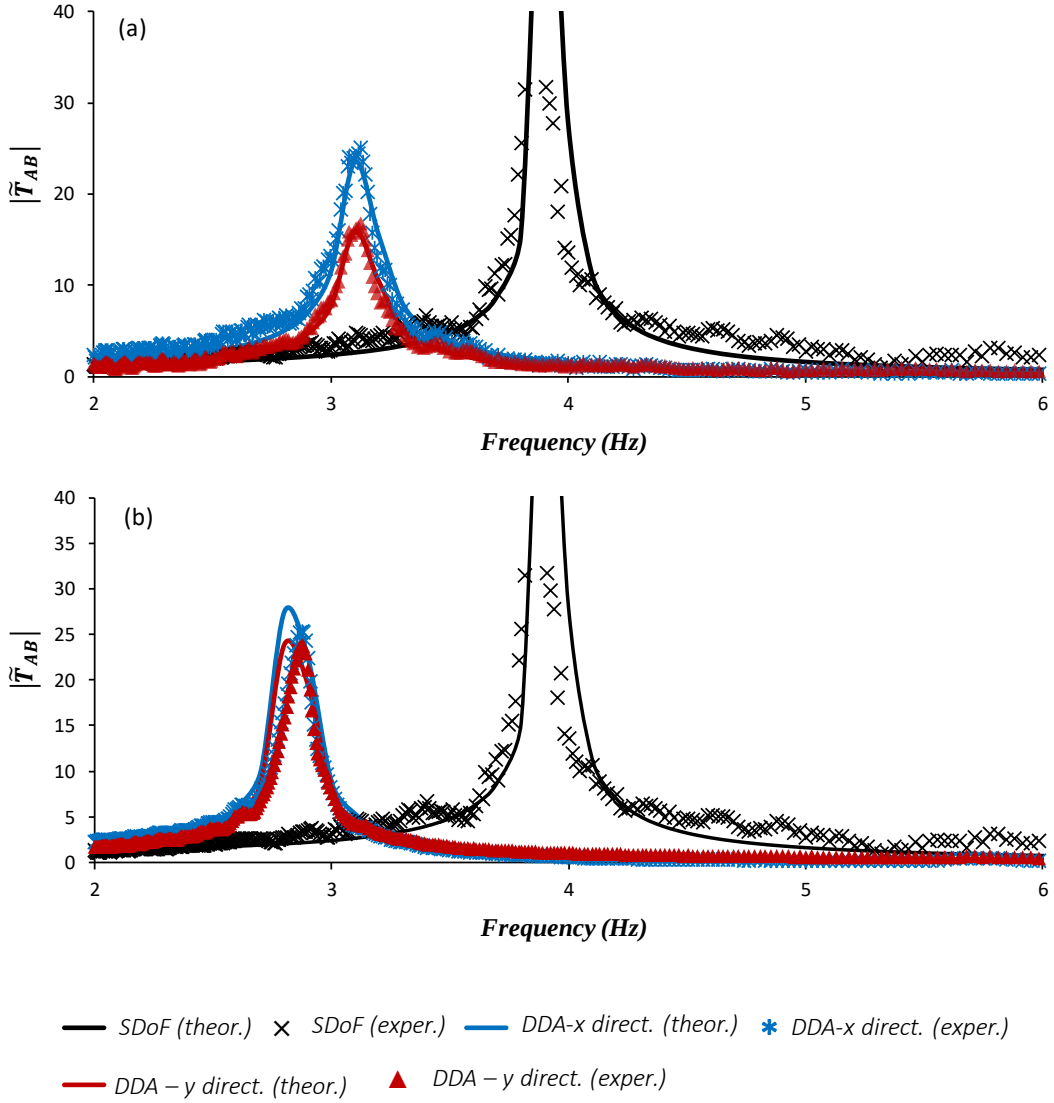

Σχήμα 20: Σύγκριση πειραματικών συναρτήσεων (σημεία) μεταφοράς με αναλυτικά αποτελέσματα (συνεχείς γραμμές) για γωνία συστήματος δυναμικής ενίσχυσης (DDA) (α) φ=30° (β) φ=40°.

4.4 Εφαρμογή του Δυναμικού ενισχυτή DDA σε φωνονικούς κρυστάλλους

Οι φωνονικοί κρύσταλλοι είναι τεχνητά κατασκευασμένες περιοδικές δομές που σχεδιάζονται με σκοπό τον έλεγχο της διασποράς κυμάτων μέσω της σκέδασης Bragg, οδηγώντας σε ζώνες εξασθένησης, υπό την προϋπόθεση ότι οι διαστάσεις και οι περίοδοι της δομής είναι συγκρίσιμες με το μήκος κύματος της διέγερσης.

Στην ενότητα αυτή προτείνεται η εφαρμογή του ενισχυτή DDA, στη δομή του φωνονικού πλέγματος με σκοπό την βελτίωση των ιδιοτήτων του, μειώνοντας τις απαιτήσεις για μεγάλες ταλαντευόμενες μάζες. Πραγματοποιείται ανάλυση του δισδιάστατου πλέγματος με τη χρήση της θεωρίας του Bloch και υπολογίζονται οι καμπύλες διασποράς. Τα προκαταρκτικά αριθμητικά αποτελέσματα της

διερεύνησης υποδεικνύουν σημαντικές βελτιώσεις και πλεονεκτήματα σε σχέση με τους συμβατικούς φωνονικούς κρυστάλλους, όπως ευρύτερες ζώνες εξασθένησης και αυξημένο λόγο απόσβεσης.

4.4.1 Ανάλυση Bloch

Το δισδιάστατο φωνονικό, ενισχυμένο με DDA, πλέγμα, θεωρώντας άπειρη περιοδική επανάληψη μοναδιαίων κελιών, παρουσιάζεται στο Σχήμα 21. Το πλέγμα δεν είναι ομοιογενές λόγω της παρουσίας δύο διαφορετικών μαζών m_L και m_D. k_x, k_y, m_L και m_D αποτελούν την κύρια δομή του πλέγματος, όπου η γωνία $\varphi(^o)$ των άκαμπτων συνδέσμων καθορίζει το μέγεθος της ενίσχυσης. Οι συντελεστές ιξώδους απόσβεσης c_x, c_y εκφράζονται από τους λόγους απόσβεσης, από τη σχέση $\zeta_i = c_i / (2\sqrt{m_i k_i})$.

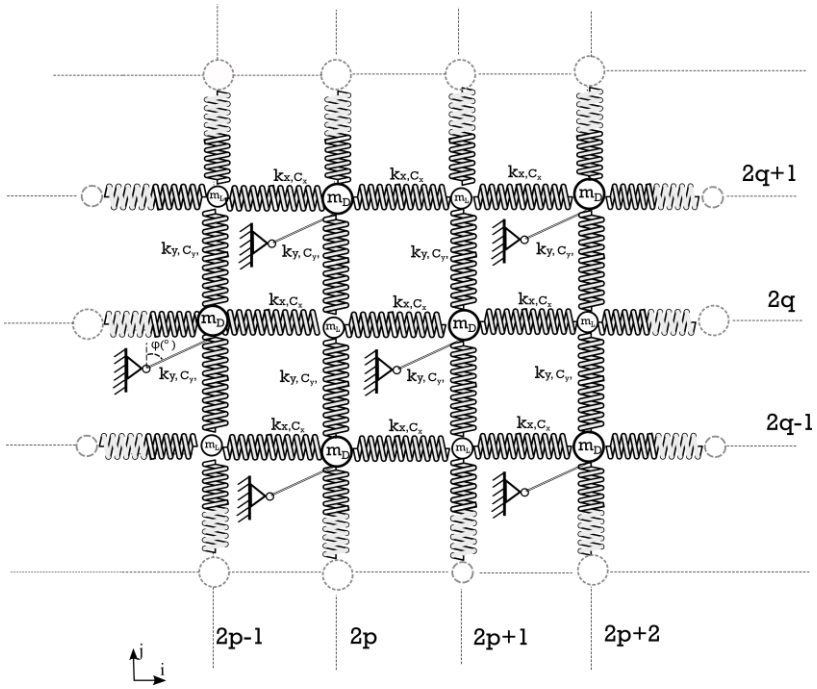

Σχήμα 21: Δισδιάστατο φωνονικό πλέγμα με δυναμικούς ενισχυτές (DDA).

Οι εξισώσεις που περιγράφουν την αρμονική κίνηση ενός τυπικού μοναδιαίου κελιού στη θέση p, q μπορούν να εκφραστούν ως εξής:

$$m_L \ddot{u}_{2p,2q} + c_x\left(\dot{u}_{2p,2q} - \dot{u}_{2p-1,2q}\right) + c_x\left(\dot{u}_{2p,2q} - \dot{u}_{2p+1,2q}\right) + k_x(u_{2p,2q} - u_{2p-1,2q}) + k_x(u_{2p,2q} - u_{2p+1,2q}) = 0 \quad (53.\alpha)$$

$$m_L \ddot{v}_{2p,2q} + c_y\left(\dot{v}_{2p,2q} - \dot{v}_{2p,2q-1}\right) + c_y\left(\dot{v}_{2p,2q} - \dot{v}_{2p,2q+1}\right) + k_y(v_{2p,2q} - v_{2p,2q-1}) + k_y(v_{2p,2q} - v_{2p,2q+1}) = 0 \quad (53.\beta)$$

$$m_D\ddot{u}_{2p+1,2q} + c_x\left(\dot{u}_{2p+1,2q} - \dot{u}_{2p,2q}\right) + c_x\left(\dot{u}_{2p+1,2q} - \dot{u}_{2p+2,2q}\right) + k_x(u_{2p+1,2q} - u_{2p,2q}) + k_x(u_{2p+1,2q} - u_{2p+2,2q}) = 0 \quad (53.\gamma)$$

$$m_D\ddot{v}_{2p+1,2q} + c_y\left(\dot{v}_{2p+1,2q} - \dot{v}_{2p+1,2q-1}\right) + c_y\left(\dot{v}_{2p+1,2q} - \dot{v}_{2p+1,2q+1}\right) + k_y(v_{2p+1,2q} - v_{2p+1,2q-1}) + k_y(v_{2p+1,2q} - v_{2p+1,2q+1}) = 0 \quad (53.\delta)$$

Υποθέτοντας λύσεις επιπέδου κύματος, καταλήγουμε στις παρακάτω σχέσεις μεταξύ των β.ε. του πλέγματος:

$$u_{2p-1,2q} = u_{2p+1,2q}e^{-j\mathrm{q}_x} \quad (54.\alpha)$$

$$u_{2p+2,2q} = u_{2p,2q}e^{j\mathrm{q}_x} \quad (54.\beta)$$

$$v_{2p,2q-1} = v_{2p+1,2q}e^{-\frac{j\mathrm{q}_x}{2}}e^{-\frac{j\mathrm{q}_y}{2}} \quad (54.\gamma)$$

$$v_{2p,2q+1} = v_{2p+1,2q}e^{-\frac{j\mathrm{q}_x}{2}}e^{\frac{j\mathrm{q}_y}{2}} \quad (54.\delta)$$

$$v_{2p+1,2q-1} = v_{2p,2q}e^{\frac{j\mathrm{q}_x}{2}}e^{-\frac{j\mathrm{q}_y}{2}} \quad (54.\varepsilon)$$

$$v_{2p+1,2q+1} = v_{2p,2q}e^{\frac{j\mathrm{q}_x}{2}}e^{\frac{j\mathrm{q}_y}{2}} \quad (54.\sigma\tau)$$

Αντικαθιστώντας τις Εξ. (53) στις εξισώσεις κίνησης (52), προκύπτει ένα σύστημα τεσσάρων (4) εξισώσεων που μπορούν να εκφραστούν σε μορφή πίνακα. Οι σχέσεις διασποράς υπολογίζονται από την ορίζουσα του συστήματος ως:

$$\det[-\lambda^2\boldsymbol{M}_{p,a} + \lambda\boldsymbol{C}_{p,a} + \boldsymbol{K}_{p,a}] = 0 \quad (55)$$

όπου

$$\boldsymbol{M}_{p,a} = \boldsymbol{Q}_P^T\boldsymbol{M}_P\boldsymbol{Q}_P \quad (56.\alpha)$$

$$\boldsymbol{C}_{p,a} = \boldsymbol{Q}_P^T\boldsymbol{C}_P\boldsymbol{Q}_P \quad (56.\beta)$$

$$\boldsymbol{K}_{p,a} = \boldsymbol{Q}_P^T\boldsymbol{K}_P\boldsymbol{Q}_P \quad (56.\gamma)$$

$$\mathbf{Q}_p = \begin{bmatrix} 1 & 0 & 0 \\ 0 & 1 & 0 \\ 0 & 0 & 1 \\ 0 & 0 & \rho \end{bmatrix} \quad (56.\gamma)$$

είναι το μητρώο μετασχηματισμού λόγω της προσθήκης του DDA.

Η συχνοτική απόκριση της συνάρτησης μεταφοράς του βελτιωμένου με DDA φωνονικού πλέγματος που αποτελείται από πεπερασμένο αριθμό μοναδιαίων κελιών $M_x \times M_y$, μπορεί να εκφραστεί υπό μορφή πίνακα ως:

$$\boldsymbol{M}_{p,a}^{G}\ddot{u}(t)+\boldsymbol{C}_{p,a}^{G}\dot{u}(t)+\boldsymbol{K}_{p,a}^{G}u(t)=\boldsymbol{F}e^{\lambda t} \tag{57}$$

όπου $\boldsymbol{M}_{m\times m}, \boldsymbol{C}_{m\times m}, \boldsymbol{K}_{m\times m}, \ddot{\boldsymbol{u}}_{m\times 1}, \dot{\boldsymbol{u}}_{m\times 1}, \boldsymbol{u}_{m\times 1}$ $\boldsymbol{F}_{m\times 1}$ και $m = 3/2M_xM_y$ ο αριθμός των βαθμών ελευθερίας της δομής. Ο πίνακας μεταφοράς υπολογίζεται ως:

$$\boldsymbol{TF}_{p,a}^{G}=(-s^2\boldsymbol{M}_{p,a}^{G}+s\boldsymbol{C}_{p,a}^{G}+\boldsymbol{K}_{p,a}^{G})^{-1}\boldsymbol{F} \tag{58}$$

Και η συχνοτική απόκριση ως:

$$\boldsymbol{FRF}=20\log_{10}(\boldsymbol{TF}_{a,p}^{G}) \tag{59}$$

4.4.2 Αριθμητικό παράδειγμα

Χρησιμοποιώντας την θεωρία της προηγούμενης ενότητας και στοχεύοντας σε ζώνες εξασθένησης χαμηλών συχνοτήτων, δηλαδή μεταξύ 100-200, διερευνάται ο φωνονικός κρύσταλλος με τα χαρακτηριστικά του Πίνακας 8.

Πίνακας 8: Παράμετροι προσομοιώματος.

m_L [kg]	m_D [kg]	f_{ox} [Hz]	f_{oy} [Hz]	ζ_x	ζ_y
1.0	1.1	100	50	0.02	0.05

Όπου, $k_x = m_L\left(2\pi f_x\right)^2, k_y = m_L\left(2\pi f_y\right)^2$.

Το Σχήμα 22 απεικονίζει (α) τις καμπύλες διασποράς και (β) τη συχνοτική απόκριση του δισδιάστατου φωνονικού 8×8 πλέγματος χωρίς ενισχυτή DDA. Στην περίπτωση αυτή παρατηρείται η δημιουργία μιας μικρής ζώνης διακοπής μεταξύ 135 -141 Hz, λόγω της μικρής διαφοράς των μαζών m_L και m_D (10% διαφορά).

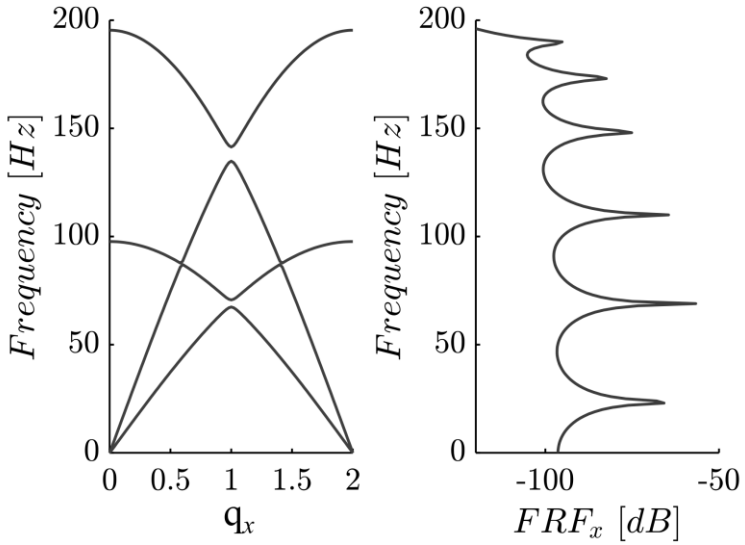

(α) *(β)*

Σχήμα 22: (α) Καμπύλες διασποράς και (β) συχνοτική απόκριση του δισδιάστατου φωνονικού πλέγματος χωρίς τον ενισχυτή DDA.

Τα πλεονεκτήματα της προσθήκης του ενισχυτή DDA μπορούν να περιγράφουν μέσω της κανονικοποιημένης ζώνης εξασθένησης όπως παρουσιάστηκε στην Εξ. (50).

Οι ευεργετικές δυνατότητες του ενισχυτή DDA φαίνονται στον Πίνακας 9 για γωνίες ενισχυτή $\varphi(^{o})$ από 15 έως 75, (Εξ. (53.α)-(56.α)). Παρατηρείται ότι η αύξηση της γωνίας $\varphi(^{o})$ από τις 15 στις 75 οδηγεί σε 600% αύξηση της κανονικοποιημένης ζώνης διακοπής (b_w).

Πίνακας 9: Συχνότητα ανοίγματος (f_l), συχνότητα κλεισίματος (f_u) και πλάτος κανονικοποιημένης ζώνης διακοπής (b_w).

Case	f_u [Hz]	f_l [Hz]	f_{av} [Hz]	b_w
Without DDA	141.4	134.8	138.1	0.05
$\varphi(^{o})$=15	141.4	131.9	136.6	0.07
$\varphi(^{o})$=45	141.4	113.2	127.3	0.22
$\varphi(^{o})$=75	141.4	99.2	120.3	0.35

Στο Σχήμα 23, απεικονίζεται η απόκριση συχνότητας του φωνονικού πλέγματος με ενισχυτή DDA ($\varphi = 75^{\circ}$) για αυξανόμενο αριθμό μοναδιαίων κελίων $M_x = M_y = 4,8,12,16$. Φυσικά, η αύξηση αυτή οδηγεί σε βελτίωση της ζώνης εξασθένησης αυξάνοντας την απομείωση του διερχόμενου κύματος εντός ζώνης, με άλλα λόγια, αυξάνοντας το βάθος της ζώνης.

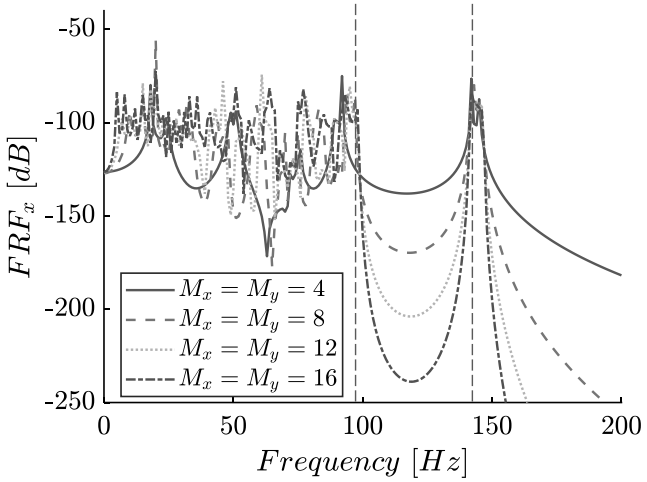

Σχήμα 23: Απόκριση συχνότητας φωνονικού πλέγματος με ενισχυτή DDA (φ=75°) για $M_x = M_y = 4,8,12,16$ *μοναδιαία κελιά.*

Στο Σχήμα 24, παρουσιάζεται μια ιδεατή υλοποίηση της διάταξης ως μια προκαταρκτική, ρεαλιστική δομή που μπορεί να χρησιμοποιηθεί είτε ως μικροδομή ή σε μεγαλύτερης κλίμακας εφαρμογές όπως μόνωσης κραδασμών/ σεισμικής μόνωσης, ηχομόνωσης κλπ.

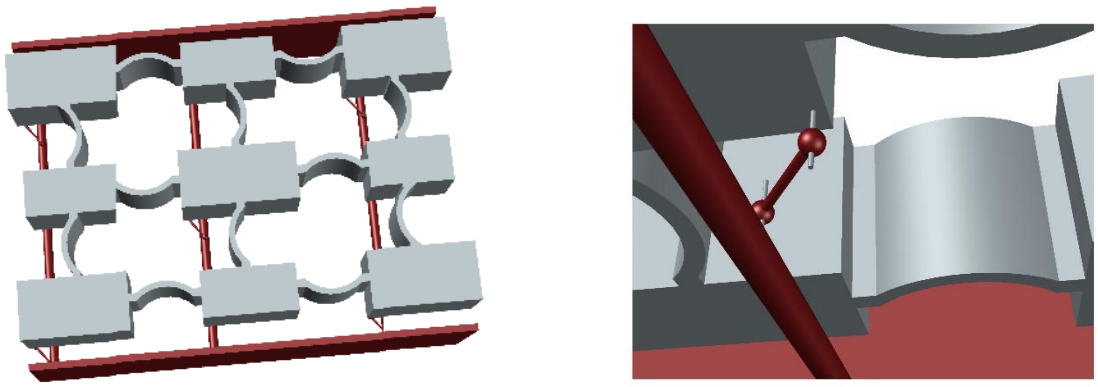

(α) *(β)*

Σχήμα 24: Απεικόνιση της προτεινόμενης ιδεατής υλοποίησης της δομής βασισμένη στη θεωρία φωνονικών κρυστάλλων με ενισχυτή DDA (α) τρισδιάστατη απεικόνιση (β) λεπτομέρεια ενισχυτή DDA.

4.5 Εφαρμογή του δυναμικού ενισχυτή DDA σε τοπικά συντονιζόμενα (LRM) μεταϋλικά

Σε αυτήν την ενότητα, ο δυναμικός ενισχυτής (DDA) εφαρμόζεται ως μέσο για την τεχνητή αύξηση της μάζας συντονισμού ενός μεταϋλικού με τοπικό συντονισμό (LRM). Ο κύριος στόχος είναι να υποδειχθεί, μέσω της χρήσης ενός μαθηματικού πλαισίου, ότι μπορούμε να βελτιώσουμε την απόδοση των LRM μεταϋλικών βελτιώνοντας τους πρακτικούς περιορισμούς, εισάγοντας ελαφριά και κατασκευάσιμα μοναδιαία κελιά. Για την επίτευξη αυτού του στόχου, υιοθετείται ένα προσομοίωμα μάζας σε μάζα (mass-in-mass) και πραγματοποιείται μια προκαταρκτική παραμετρική ανάλυση με τη

χρήση τόσο της θεωρίας του Bloch (1929) για δισδιάστατα πλέγματα άπειρων κελιών, όσο και της συμβατικής θεωρίας ταλαντώσεων σε πεπερασμένα πλέγματα. Στη συνέχεα, μελετάται μία αριθμητική εφαρμογή του μεταϋλικού ως μέσο σεισμικής προστασίας. Σκοπός είναι να αναδειχθούν τα πλεονεκτήματα της προτεινόμενης διάταξης σε σχέση με τον αρχικό συμβατικό σχεδιασμό. Τα αποτελέσματα υποδεικνύουν τον ευεργετικό ρόλο της διάταξης και του μηχανισμού DDA, τοποθετώντας έτσι την ιδέα ως μια πιθανή εναλλακτική λύση στις υπάρχουσες τεχνολογίες σεισμικής προστασίας.

Το Σχήμα 25 απεικονίζει το μοναδιαίο κελί μιας απλής διάταξης μάζας σε μάζα, η οποία αποτελείται από μια εξωτερική μάζα (m_L), έναν εσωτερικό ταλαντωτή μάζας (m_R) και τα αντίστοιχα ελατήρια και αποσβεστήρες. Με βάση αυτή την απλή διάταξη, διαμορφώνονται τα ενισχυμένα (με DDA) μοναδιαία κελιά. Στο Σχήμα 25 (α) απεικονίζεται η διαμόρφωση ενός συμβατικού μοναδιαίου κελιού με τοπικά συντονιζόμενη μάζα ενώ στο Σχήμα 25 (β) απεικονίζεται η διαμόρφωση με το DDA προσαρτημένο στην εσωτερική μάζα (m_R).

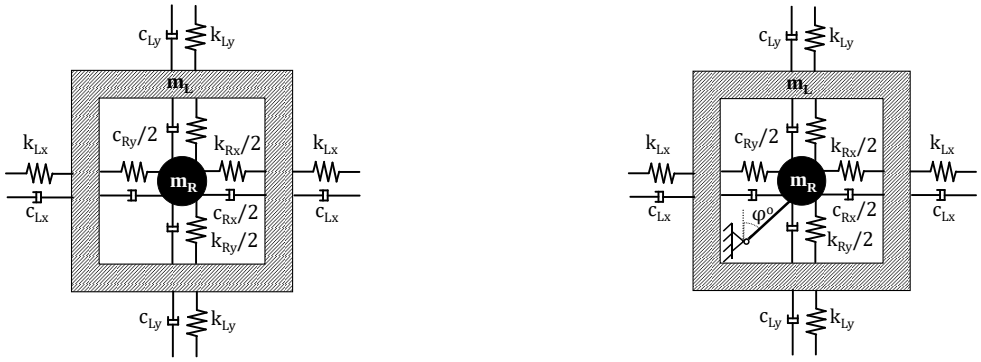

Σχήμα 25: Σχηματική αναπαράσταση του μοναδιαίου κελιού (α) χωρίς DDA, (β) με DDA προσαρτημένο στη μάζα συντονισμού (m_R)

Με την τοποθέτηση τέτοιων μονάδων σε ένα πλέγμα μπορούμε να δημιουργήσουμε ένα απείρως περιοδικό μεταϋλικό. Οι σχέσεις διασποράς του τοπικά συντονιζόμενου πλέγματος με ενισχυτές DDA υπολογίζονται από την ορίζουσα της Εξ. (60) ως:

$$\det[-\lambda^2 \boldsymbol{M}_{LRM-DDA} + \lambda \boldsymbol{C}_{LRM-DDA} \boldsymbol{K}_{LRM-DDA}] = 0 \tag{60}$$

όπου

$$\boldsymbol{M}_{LRM-DDA} = \boldsymbol{Q}^T \boldsymbol{M}_{LRM} \boldsymbol{Q} = \begin{bmatrix} m_L & 0 & 0 \\ 0 & m_L & 0 \\ 0 & 0 & m_R(1+\rho^2) \end{bmatrix} \tag{61.α}$$

$$\boldsymbol{C}_{LRM-DADA}=\boldsymbol{Q}^T\boldsymbol{C}_{LRM}\boldsymbol{Q}=\begin{bmatrix}2c_{Lx}(1-\cos q_x)+c_{Rx} & 0 & -c_{Rx}\\ 0 & 2c_{Ly}(1-\cos q_y)+c_{R_y} & -\rho c_{R_y}\\ -c_{Rx} & -\rho c_{R_y} & c_{R_x}\rho^2 c_{R_y}\end{bmatrix} \tag{61.β}$$

$$\boldsymbol{K}_{LRM-DADA}=\boldsymbol{Q}^T\boldsymbol{K}_{LRM}\boldsymbol{Q}=\begin{bmatrix}2k_{Lx}(1-\cos q_x)+k_{Rx} & 0 & -k_{Rx}\\ 0 & 2k_{Ly}(1-\cos q_y)+k_{R_y} & -\rho k_{R_y}\\ -k_{Rx} & -\rho k_{R_y} & k_{R_x}\rho^2 k_{R_y}\end{bmatrix} \tag{61.γ}$$

Στο Σχήμα 26 παρουσιάζεται μια δισδιάστατη (2D) διάταξη πλέγματος με πεπερασμένο αριθμό τοπικά συντονιζόμενων μοναδιαίων κελιών. Η εξίσωση κίνησης της δομής, για $M_x \times M_y$ αριθμό κελιών παρουσιάζεται υπό την μορφή πίνακα ως εξής:

$$\boldsymbol{M}\ddot{\boldsymbol{u}}(t)+\boldsymbol{C}\dot{\boldsymbol{u}}(t)+\boldsymbol{K}\boldsymbol{u}(t)=\boldsymbol{F}e^{\lambda t} \tag{62}$$

Οπου $\boldsymbol{M}_{m\times m}, \boldsymbol{C}_{m\times m}, \boldsymbol{K}_{m\times m}, \ddot{\boldsymbol{u}}_{m\times 1}, \dot{\boldsymbol{u}}_{m\times 1}, \boldsymbol{u}_{m\times 1}, \boldsymbol{F}_{m\times 1}$ και m είναι ο αριθμός των βαθμών ελευθερίας (DoF) του μεταϋλικού.

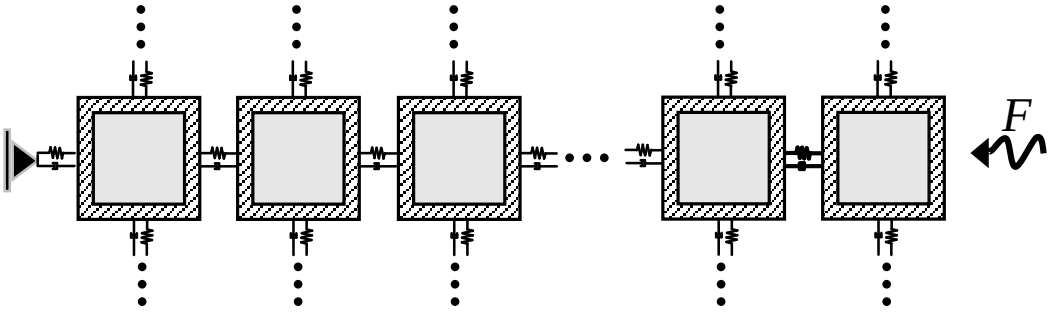

Σχήμα 26: Δομή με $M_x \times M_y$ μοναδιαία κελιά με αρμονική διέγερση (F) στο δεξιό της όριο.

Για την περίπτωση της διάταξης χωρίς τον μηχανισμό ενίσχυσης, $m=4M_xM_y$. Για την διάταξη με το DDA, $m=3M_xM_y$ και οι πίνακες μάζας $\left[\boldsymbol{M}^G_{LRM-DDA}\right]$, απόσβεσης $\left[\boldsymbol{C}^G_{LRM-DDA}\right]$ και στιβαρότητας $\left[\boldsymbol{K}^G_{LRM-DDA}\right]$ μπορούν να υπολογιστούν ως εξής:

$$\boldsymbol{M}^G_{LRM-DDA}=\boldsymbol{Q}_G^T\boldsymbol{M}^G_{LRM}\boldsymbol{Q}_G \tag{63}$$

$$\boldsymbol{C}^G_{LRM-DDA}=\boldsymbol{Q}_G^T\boldsymbol{C}^G_{LRM}\boldsymbol{Q}_G \tag{64}$$

$$\boldsymbol{K}^G_{LRM-DDA}=\boldsymbol{Q}_G^T\boldsymbol{K}^G_{LRM}\boldsymbol{Q}_G \tag{65}$$

Ο πίνακας μετασχηματισμού μπορεί να εκφραστεί ως εξής:

$$Q_{G(4M_xM_y)\times(3M_xM_y)}=\begin{bmatrix} 1 & 0 & & \cdots & & & 0 \\ 0 & 1 & 0 & & & & 0 \\ & 0 & 1 & & & & \\ & 0 & \rho & 0 & & & \\ \vdots & 0 & 0 & \ddots & 0 & & \vdots \\ & & 0 & 0 & 1 & 0 & \\ & & & 0 & \rho & 1 & 0 \\ & & & & 0 & 0 & 1 \\ \rho & & & \cdots & & 0 & \rho \end{bmatrix} \tag{66}$$

Οι πίνακες μάζας $\left[\boldsymbol{M}^G\right]$ στιβαρότητας $\left[\boldsymbol{K}^G\right]$ και απόσβεσης $\left[\boldsymbol{C}^G\right]$ κατασκευάζονται για τη δημιουργία του πεπερασμένου μεταϋλικού. Υποθέτοντας ότι η περιοδική δομή διεγείρεται αρμονικά στους κόμβους εισόδου με συχνότητα ω, η συνάρτηση μεταφοράς κάθε βαθμού ελευθερίας μπορεί να υπολογιστεί από την ακόλουθη έκφραση:

$$\boldsymbol{TF}_{LRM-DDA}=[-\lambda^2\boldsymbol{M}^G_{LRM-DDA}+\lambda\boldsymbol{C}^G_{LRM-DDA}+\boldsymbol{K}^G_{LRM-DDA}]^{-1}\boldsymbol{F} \tag{67}$$

Συνεπώς, μπορούμε να υπολογίσουμε την συχνοτική απόκριση σε κάθε κόμβο. Συγκεκριμένα, η συνάρτηση συχνοτικής απόκρισης (Frequency Response Function - FRF) της κατασκευής εκφράζεται σε ντεσιμπέλ ως εξής:

$$FRF=20\log_{10}\left(\frac{u_{fin}}{u_{in}}\right) \tag{68}$$

Στην παραπάνω περίπτωση, u_{in} είναι η μετατόπιση των εξωτερικών μαζών (m_L), όπου εφαρμόζεται η διέγερση εισόδου, και u_{fin} η μετατόπιση της εξωτερικής μάζας των τελευταίων μοναδιαίων κελιών.

4.5.1 Αριθμητικά Αποτελέσματα

Όπως περιεγράφηκε προηγουμένως, το περιοδικό μεταϋλικό λειτουργεί ως φίλτρο ζώνης διέλευσης ή ζώνης διακοπής, όπου για την περίπτωση άπειρων μοναδιαίων κελιών χωρίς απόσβεση εμφανίζονται τέλειες ιδιότητες φιλτραρίσματος. Στο παρόν κεφάλαιο, παρουσιάζεται μια ενδεικτική μελέτη βασιζόμενη στην εργασία των Dertimanis et al. (2016) για LRM μεταϋλικά που έχουν σχεδιαστεί για τον μετριασμό σεισμικών κυμάτων και την προστασία κατασκευών πολιτικού μηχανικού. Σύμφωνα με την παραπάνω δημοσίευση, μελετώνται τρεις (3) διαφορετικές ζώνες διακοπής (bandgaps) - η πρώτη είναι μεταξύ 0.5 – 1.5 Hz, η δεύτερη μεταξύ 1.0 – 2.5 Hz και η τρίτη μεταξύ 2.0 – 5.0 Hz. Θεωρώντας εξωτερική μάζα ίση με m_L =1Mgr, η απαιτούμενη εσωτερική συντονιζόμενη μάζα (m_R) και στιβαρότητα (k_R) του ταλαντωτή υπολογίζονται κατά Dertimanis et al. (2016) σύμφωνα με τα εξής:

$$m_R = \left[\left(\frac{f_H}{f_L} \right)^2 - 1 \right] m_L \tag{69}$$

$$k_R = 4\pi^2 f_L^2 m_R = 4\pi^2 (f_H^2 - f_L^2) m_L \tag{70}$$

όπου f_L και f_H [Hz] αντιστοιχούν στο χαμηλό και υψηλό κατώφλι της επιλεγμένης ζώνης διακοπής (bandgap).

Με στόχο τη μελέτη της επίδρασης του μηχανισμού ενίσχυσης DDA στην συχνοτική απόκριση του μεταϋλικού, η παρούσα έρευνα επικεντρώνεται στο σενάριο 2 (ζώνη διακοπής μεταξύ 1.0 – 2.5 Hz) και $k_L / k_R = 1$. Στο πλαίσιο αυτό, υπολογίζονται η ζώνη διακοπής και η συχνοτική απόκριση (FRF) της περιοδικής κατασκευής, θεωρώντας μηδενική απόσβεση. Στη συνέχεια συγκρίνεται η βασική διαμόρφωση (αρχικό LRM μεταϋλικό κατά Dertimanis et al.) με το αντίστοιχο μεταϋλικό που περιλαμβάνει το DDA (LRM-DDA). Οι καμπύλες διασποράς στο Σχήμα 27 δείχνουν ότι η εφαρμογή του μηχανισμού ενίσχυσης αυξάνει το πλάτος της ζώνης διακοπής, λόγω της πτώσης του ακουστικού κλάδου. Από την άλλη πλευρά, ο οπτικός κλάδος παραμένει αμετάβλητος. Η συχνοτική απόκριση δείχνει ότι στην περιοχή πολύ χαμηλών συχνοτήτων, κάτω από 1.0 Hz, η καμπύλη του LRM με το DDA μετατοπίζεται προς τα κάτω σε σύγκριση με το LRM χωρίς το DDA. Όπως αναμενόταν, τα χαρακτηριστικά εξασθένησης βελτιώνονται όσο αυξάνεται η γωνία του DDA.

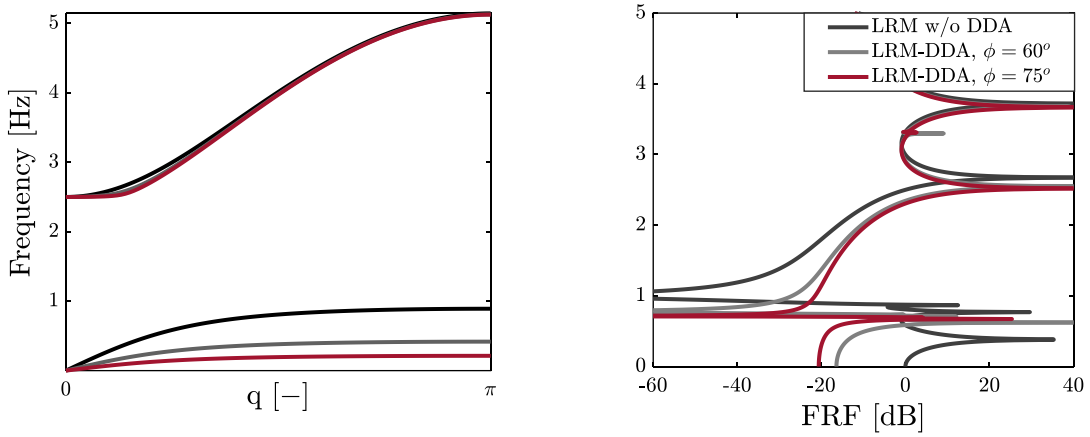

Σχήμα 27: (αριστερά) Καμπύλες διασποράς και (δεξιά) συχνοτική απόκριση του μεταϋλικού για m_L=1Mgr, m_R=5.25 Mgr, k_L/k_R=1, N= 4 μοναδιαία κελιά (unit-cells) και θεώρηση μηδενικής απόσβεσης..

Αποτελέσματα παραμετρικών αναλύσεων για διαφορετικές γωνίες του DDA ενισχυτή και μεγαλύτερο αριθμό μοναδιαίων κελιών παρουσιάζονται στο ολοκληρωμένο τεύχος της διδακτορικής διατριβής.

4.5.2 Εφαρμογή του DDA σε ένα μεταϋλικό για σεισμική προστασία κατασκευών

Στο Σχήμα 28 παρουσιάζεται μια πιθανή διάταξη ενός προτεινόμενου μεταϋλικού συστήματος για την σεισμική προστασία κατασκευών πολιτικού μηχανικού. Τα τοπικά συντονιζόμενα μοναδιαία κελιά τοποθετούνται στο έδαφος σε ακτινική διάταξη, έτσι ώστε να περικλείουν τις κατασκευές ενδιαφέροντος. Σε περίπτωση σεισμικής διέγερσης, το μεταϋλικό φιλτράρει το χαμηλής συχνότητας περιεχόμενο του κύματος απορροφώντας εσωτερικά τη σεισμική ενέργεια και, ως εκ τούτου, μετριάζοντας τη διέγερση. Είναι σημαντικό να σημειωθεί ότι λόγω της γεωμετρίας της κατασκευής, η προτεινόμενη διαρρύθμιση των σεισμικών μεταϋλικών είναι κατάλληλη για προστασία κατασκευών από επιφανειακά κύματα (Datta, 2010), τα οποία, λόγω της χαμηλής τους συχνότητας και το υψηλό σχετικά πλάτος, οδηγούν σε σημαντικές επιπτώσεις και προκαλούν βλάβες στις ανθρώπινες κατασκευές (Anderson, 1990). Ο μετριασμός των σεισμικών διατμητικών και διαμηκών κυμάτων (κύματα S και P) δεν αποτελεί μέρος της παρούσας μελέτης και της ιδέας σχεδιασμού.

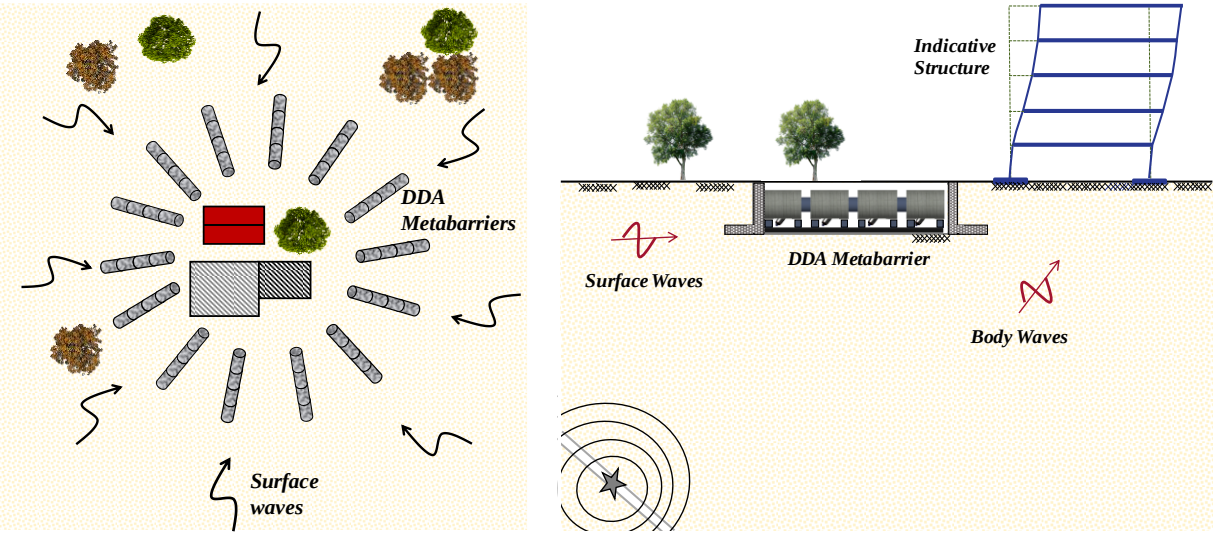

(α) *(β)*

Σχήμα 28: Σχηματική αναπαράσταση (α) της ακτινικής διάταξης του DDA μεταϋλικού σε κάτοψη και (β) της τυπικής διατομής της εγκατάστασης.

Η υπό εξέταση διάταξη παρουσιάζεται στο Σχήμα 29. Ένα κοίλο κυλινδρικό τμήμα από οπλισμένο σκυρόδεμα (ΟΣ) αποτελεί την εξωτερική μάζα του μοναδιαίου κελιού (m_L) ενώ ένα χαλύβδινο κυλινδρικό τμήμα αποτελεί την εσωτερική συντονιζόμενη μάζα (m_R). Τα ελατήρια του προσομοιώματος μπορούν να υλοποιηθούν από ένα ελαστομερές - ελαστικό υλικό με στιβαρότητα ισοδύναμη με το θεωρητικό προσομοίωμα, το οποίο μπορεί να ενισχυθεί κατάλληλα ανάλογα με τις απαιτήσεις στιβαρότητας και αντοχής. Ο μηχανισμός DDA μπορεί να υλοποιηθεί με μια απλή άκαμπτη δοκό (ενδεχομένως μια στιβαρή χαλύβδινη δοκό) συνδεδεμένη σε ένα άκαμπτο θεμέλιο.

Με στόχο την επικύρωση της απόδοσης του σχεδιασμένου μεταϋλικού, ο κώδικας πεπερασμένων στοιχείων ABAQUS® χρησιμοποιείται για μια σειρά αναλύσεων συχνοτικής απόκρισης και σεισμικής χρονοϊστορίας. Οι παράμετροι του προσομοιώματος διαμορφώθηκαν υιοθετώντας τις τιμές των υλικών του ιδεατού σχεδιασμού, όπως αναφέρεται στις προηγούμενες παραγράφους. Για τους σκοπούς της παρούσας μελέτης, υιοθετείται ένα προσομοίωμα με N=4 μοναδιαία κελιά. Ο σχεδιασμός ακολουθεί το δεύτερο σενάριο ζώνης διακοπής, όπου f_L =1 και f_H =2.5 Hz, αντίστοιχα. Η ανάλυση πραγματοποιείται σε προσομοίωμα τρισδιάστατων (3D) πεπερασμένων στοιχείων για το μεταϋλικό με και χωρίς το DDA. Αρχικά, πραγματοποιείται μία ανάλυση αρμονικών διεγέρσεων (sweep tests) που εφαρμόζεται στο πρώτο μοναδιαίο κελί της διάταξης.

Ως επόμενο βήμα, διερευνάται η απόδοση του DDA μεταϋλικού υπό σεισμική διέγερση. Χρησιμοποιούνται διάφορες σεισμικές διεγέρσεις που αντιστοιχούν σε διαφορετικά επίπεδα επικινδυνότητας και συχνοτήτων και εκτελούνται αναλύσεις χρονοϊστορίας για τη μελέτη των δυναμικών ιδιοτήτων του προτεινόμενου συστήματος. Ένα τεχνητό επιταχυνσιογράφημα με φάσμα απόκρισης επιτάχυνσης συμβατό με το φάσμα απόκρισης σχεδιασμού του Ευρωκώδικα 8 παράγεται με τη χρήση του λογισμικού SeismoArtif (2018) και υιοθετείται ως βάση για τις αναλύσεις χρονοϊστορίας. Επιπλέον, διερευνάται η απόκριση του σχεδιασμού σε πραγματικές σεισμικές διεγέρσεις, για τις περιπτώσεις των σεισμών του Αιγίου (1995) και του Ληξουρίου (2014). Οι σεισμικές επιταχύνσεις εφαρμόζονται απλουστευτικά ως οριζόντια διέγερση στο πρώτο μοναδιαίο κελί και στη συνέχεια υπολογίζεται η απόκριση του τελικού κελιού.

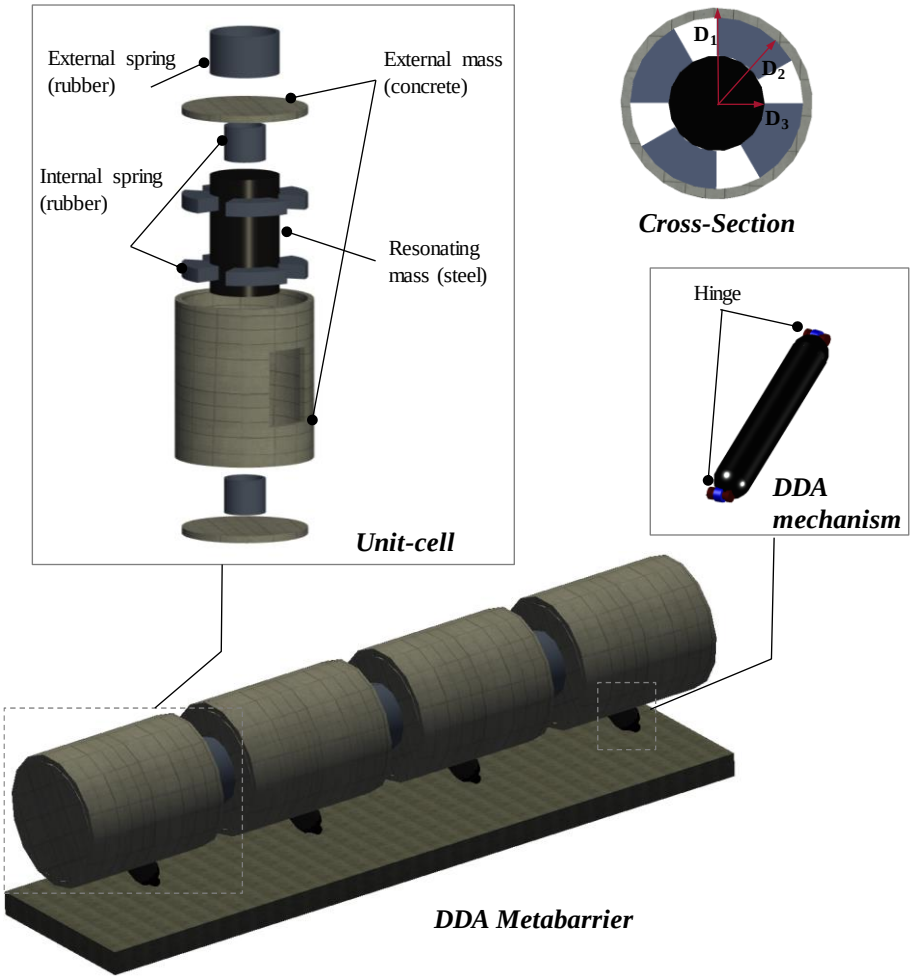

Σχήμα 29: Σχηματική αναπαράσταση του προτεινόμενου μεταϋλικού με το δυναμικό σύστημα ενίσχυσης DDA, με σκοπό την προστασία κατασκευών από σεισμικά κύματα.

Στο Σχήμα 30 παρουσιάζεται η συχνοτική απόκριση του προτεινόμενου συστήματος με και χωρίς τον μηχανισμό DDA ενώ στο Σχήμα 31 η απόκριση του μεταϋλικού σε πραγματικές σεισμικές διεγέρσεις.

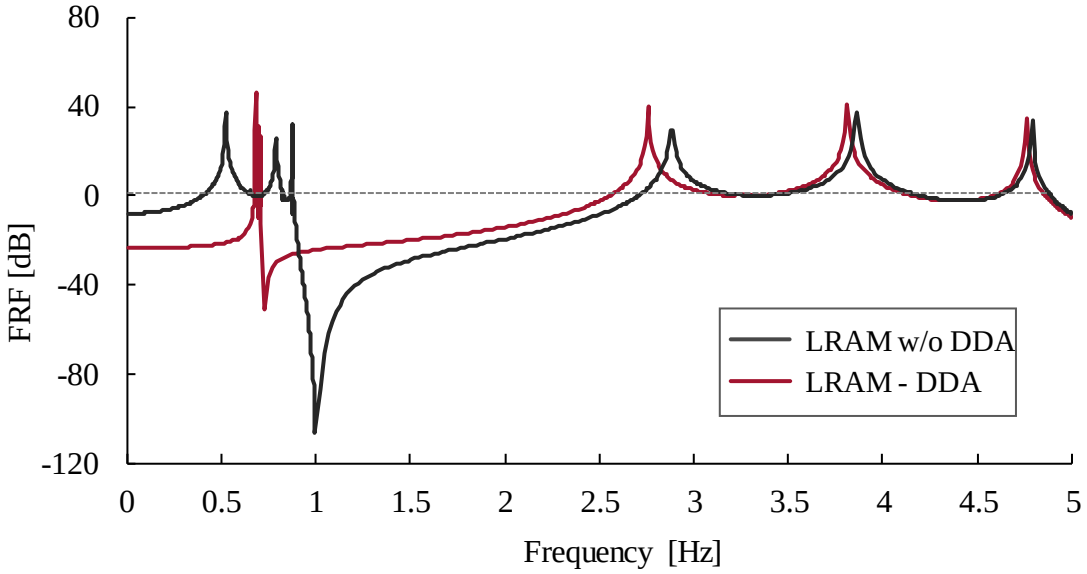

Σχήμα 30: Συχνοτική απόκριση (FRF) του σεισμικού μεταϋλικού με και χωρίς τον μηχανισμό DDA, όπως υπολογίστηκε από την ανάλυση πεπερασμένων στοιχείων.

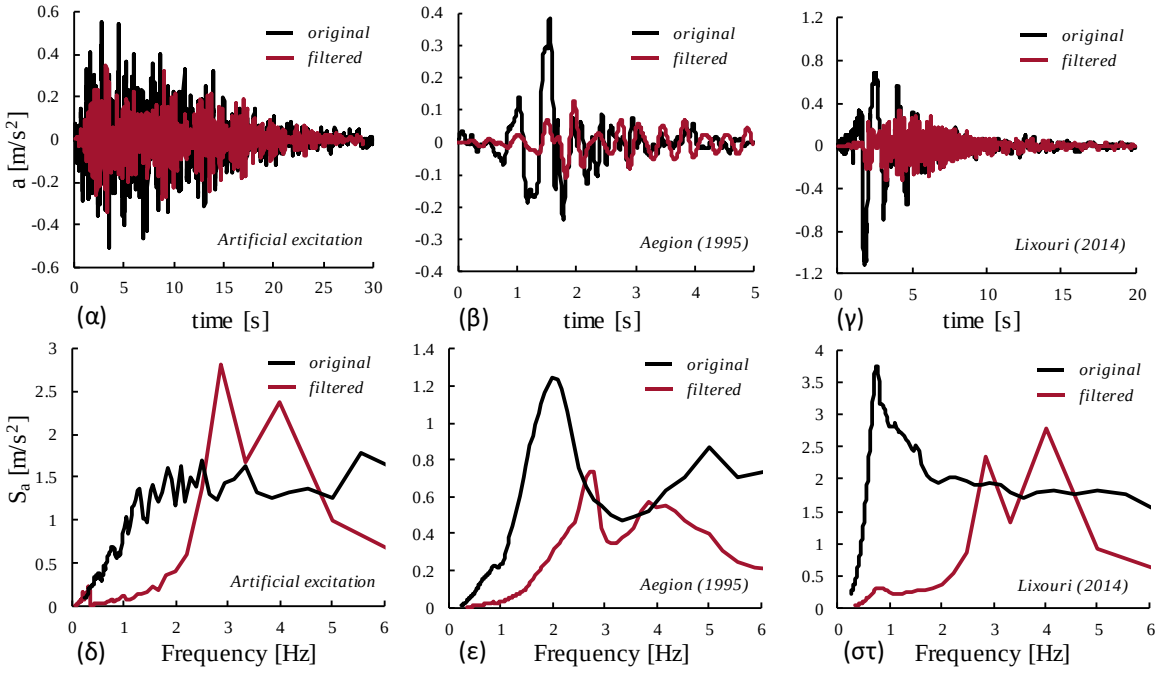

Σχήμα 31: Απόκριση του DDA μεταϋλικού σε πραγματικές σεισμικές διεγέρσεις: (α) τεχνητό επιταχυνσιογράφημα συμβατό με EC8, (β) Αίγιο, 1995 επιταχυνσιογράφημα, (γ) Ληξούρι, 2014 επιταχυνσιογράφημα και (δ) – (στ) αντίστοιχα φάσματα επιτάχυνσης για τις αρχικές και φιλτραρισμένες διεγέρσεις.

4.6 Πειραματική διερεύνηση των ιδιοτήτων απορρόφησης ταλαντώσεων των φωνονικών και τοπικά συντονιζόμενων μεταϋλικών με DDA Ενισχυτή

Στην ενότητα αυτή διερευνάται πειραματικά η δυναμική συμπεριφορά των προτεινόμενων διαμορφώσεων φωνονικών και τοπικά συντονιζόμενων (LRM) μεταϋλικών με DDA ενισχυτή. Συγκεκριμένα, τα πειραματικά πρωτότυπα μεταϋλικών κατασκευάζονται από στοιχεία LEGO® και δοκιμάζονται υπό δυναμική φόρτιση με σκοπό την επαλήθευση των αναλυτικών και αριθμητικών αποτελεσμάτων. Για το σκοπό αυτό, κατασκευάζονται και δοκιμάζονται τέσσερις (4) διαφορετικές διατάξεις: μια συμβατική φωνονική αλυσίδα, μια ενισχυμένη με DDA φωνονική αλυσίδα, μια συμβατική τοπικά συντονιζόμενη (LR) αλυσίδα και μια ενισχυμένη με DDA τοπικά συντονιζόμενη (LR) αλυσίδα. Τα αποτελέσματα επιβεβαιώνουν τις δυνατότητες των ενισχυμένων με DDA δομών και αποδεικνύουν ότι τα προτεινόμενα μεταϋλικά μπορούν να περιγραφούν επαρκώς από τα αναλυτικά και αριθμητικά μοντέλα που αναπτύχθηκαν. Τέλος, τα LEGO® πρωτότυπα υποδεικνύουν ότι ρεαλιστικές κατασκευές πλήρους κλίμακας είναι εφικτές και κατάλληλες για ένα ευρύ φάσμα εφαρμογών, π.χ. μετριασμό σεισμών, απομόνωση κραδασμών, ακουστική μόνωση κ.λπ.

Πέρα από τα ελατήρια έλξεως που κατασκευάζονται κατά παραγγελία, την εσωτερική συντονιζόμενη μάζα του μεταϋλικού LR που υλοποιείται με τη χρήση χαλύβδινων ροδελών και τους διαμήκεις οδηγούς που είναι κατασκευασμένοι από αλουμίνιο για την αύξηση της κάθετης και πλευρικής στιβαρότητας, τα περισσότερα εξαρτήματα του μεταϋλικού συναρμολογούνται με τη χρήση εξαρτημάτων LEGO®. Η επιλογή των στοιχείων LEGO® υιοθετείται λόγω της σχεδιαστικής απλότητας, του χαμηλού κόστους και της ακρίβειας σε γεωμετρία που μπορούν να προσφέρουν σε σύγκριση με εναλλακτικές λύσεις όπως οι χαλύβδινες κατασκευές και τα τρισδιάστατα εκτυπωμένα στοιχεία.

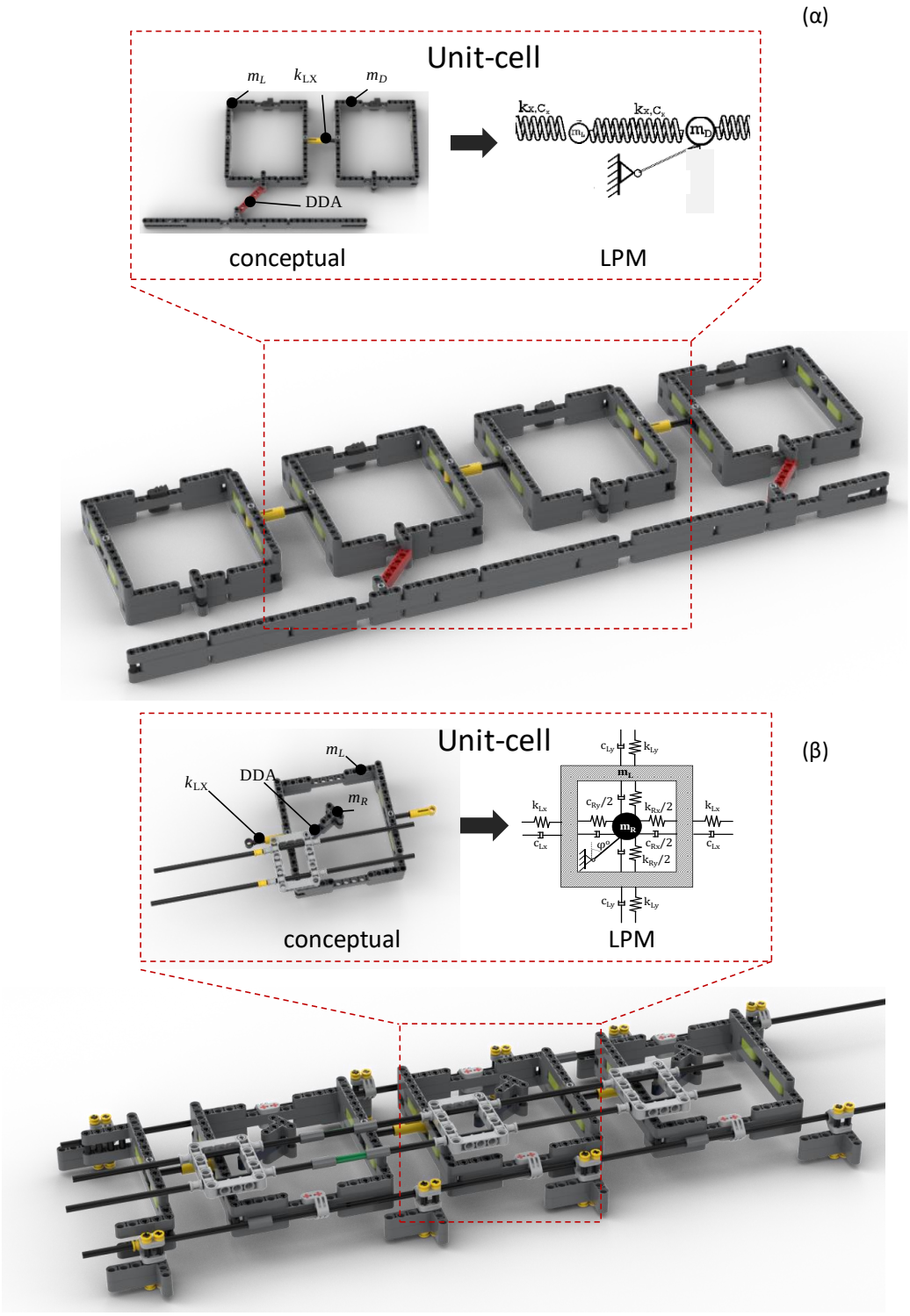

Σχήμα 32: Απεικόνιση των ενισχυμένων με DDA (α) φωνονικών κρυστάλλων, και (β) τοπικά συντονιζόμενων (LR) LEGO® μεταϋλικών.

Στο Σχήμα 32 (α) παρουσιάζεται η σχηματική αναπαράσταση της διάταξης της φωνονικής αλυσίδας, όπου ο ενισχυτής DDA βρίσκεται στη βάση της ταλαντευόμενης μάζας. Μια αρθρωτή σύνδεση υλοποιείται με τη χρήση στοιχείων LEGO® και επιτρέπει στον σύνδεσμο DDA να περιστρέφεται

ελεύθερα, ενώ μια σταθερή βάση κατασκευάζεται προκειμένου να στηρίξει τους εν λόγω μηχανισμούς. Η δομή LR που απεικονίζεται στο Σχήμα 32 (β), αποτελείται από μοναδιαία κελιά (unit-cells) με παρόμοιες διαστάσεις με τις διαστάσεις του φωνονικού πλέγματος και μια ανεξάρτητη κατασκευή που υποστηρίζει τους ενισχυτές DDA.

4.6.1 Πειραματική Διάταξη

Η πειραματική διάταξη παρουσιάζεται στο Σχήμα 33. Ο ηλεκτροδυναμικός διεγέρτης (shaker) MB Modal 110 (MB Dynamics) εφαρμόζει μονοδιάστατη οριζόντια διέγερση στην αρχή του συστήματος. Στον άξονα του διεγέρτη τοποθετείται στη μία πλευρά του μία ξύλινη βάση, η οποία λειτουργεί ως σεισμική τράπεζα, ενώ διαμήκεις οδηγοί και έδρανα παρέχουν στήριξη, διατηρούν το τραπέζι σε οριζόντια θέση και περιορίζουν τις παρασιτικές κατακόρυφες ταλαντώσεις. Η ψηφιακή γεννήτρια σήματος παράγει αρμονικές ταλαντώσεις σε προκαθορισμένο εύρος συχνοτήτων και ο ενισχυτής (2050E05 - modal shop INC) λαμβάνει το παραγόμενο σήμα και ενεργοποιεί τον διεγέρτη. Η διέγερση εφαρμόζεται στο αριστερό άκρο της αλυσίδας, όπου το στήριγμα του πρώτου κελιού είναι τοποθετημένο στην σεισμική τράπεζα, δημιουργώντας έτσι διαμήκη κύματα που διαδίδονται στην αλυσίδα από LEGO®.

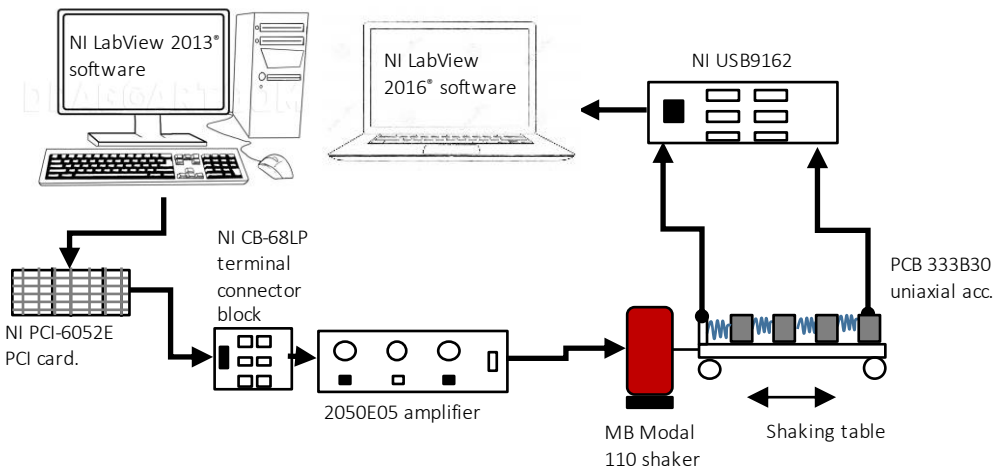

Σχήμα 33: Σχηματική αναπαράσταση της πειραματικής διάταξης.

Επιταχυνσιόμετρα εγκαθίστανται στο τελευταίο κελί καθώς και στο σημείο εφαρμογής της διέγερσης προκειμένου να μετρηθούν με ακρίβεια οι επιταχύνσεις στην είσοδο και έξοδο των μεταϋλικών. Η καταγραφή των μετρήσεων γίνεται μέσω του λογισμικού NI LabView 2016®, ενώ η επεξεργασία πραγματοποιείται με τη χρήση απλών αλγορίθμων που αναπτύσσονται στο λογισμικό MATLAB R2020b®.

Για τις ανάγκες της πειραματικής διαδικασίας, επιλέγεται να χρησιμοποιηθούν N=4 μοναδιαία κελιά (unit-cells) για τα φωνονικά και N=3 για τα τοπικά συντονιζόμενα μεταϋλικά (με και χωρίς DDA). Και στις δύο περιπτώσεις μεταλλικές ροδέλες χρησιμοποιούνται για να αυξήσουν την μάζα των κελιών (όπου χρειάζεται). Ο ενισχυτής DDA τοποθετείται εναλλάξ στην περίπτωση του φωνονικού κρυστάλλου (δηλαδή στο κελί 2 και 4) ενώ στην περίπτωση της τοπικά συντονιζόμενης αλυσίδας, το DDA τοποθετείται σε όλες τις εσωτερικές μάζες. Η γωνία του DDA επιλέγεται ίση με $\varphi \approx 60°$ και $\varphi \approx 55°$ για το φωνονικό και το LR μεταϋλικό αντίστοιχα. Περισσότερες πληροφορίες σχετικά με τον σχεδιασμό, τις τιμές των μαζών, στιβαρότητες των ελατηρίων κλπ. παρέχονται στο ολοκληρωμένο τεύχος της διδακτορικής διατριβής.

4.6.2 Πειραματικά Αποτελέσματα

Το πειραματικό φάσμα μετάδοσης λαμβάνεται ως ο λόγος μεταξύ των φασματικών επιταχύνσεων εξόδου και εισόδου $\left\{\ddot{u}_{fin}^{out} / \ddot{u}_{1}^{in}\right\}$ με τη χρήση της συνάρτησης μετασχηματισμού Fourier (FFT). Η ζώνη διακοπής του εξεταζόμενου μεταϋλικού αντιστοιχεί στις περιοχές όπου ο λόγος του φάσματος μεταξύ εξόδου και εισόδου πέφτει κάτω από τη μονάδα. Επιπλέον, σύγκριση πραγματοποιείται με τις αντίστοιχες τιμές των αναλυτικών υπολογισμών.

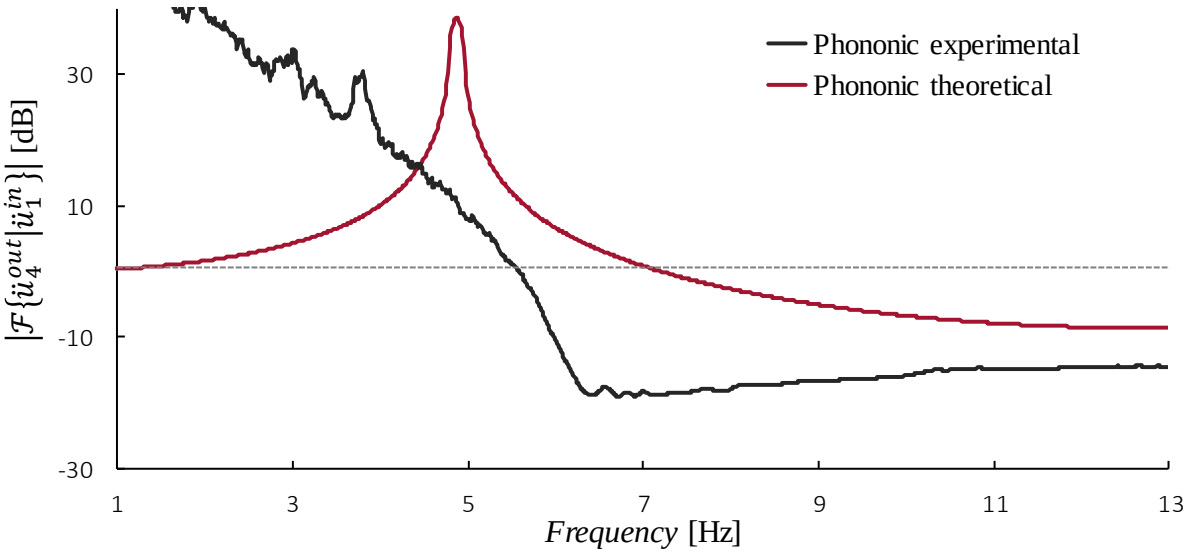

Σχήμα 34: Σύγκριση μεταξύ της πειραματικής και της αναλυτικά εκτιμώμενης συχνοτικής απόκρισης $\mathcal{F}\left\{\ddot{u}_4^{out} / \ddot{u}_1^{in}\right\}$ για το μεταϋλικό τεσσάρων (4) μοναδιαίων κελιών της φωνονικής δομής.

Στο Σχήμα 34 παρουσιάζονται τα αποτελέσματα της θεωρητικά εκτιμώμενης δυναμικής απόκρισης καθώς και της πειραματικά μετρούμενης απόκρισης του φωνονικού μεταϋλικού προκειμένου να προσδιοριστεί ο βαθμός στον οποίο το αναλυτικό προσομοίωμα ταιριάζει με τα πειραματικά δεδομένα. Παρατηρείται ότι οι δύο καμπύλες παρουσιάζουν κάποιες διαφορές όσον αφορά τη συχνότητα ανοίγματος της ζώνης διακοπής και το σημείου συντονισμού, ωστόσο, αποτυπώνεται η αναμενόμενη δυναμική απόδοση του μεταϋλικού και φαίνεται καθαρά η δημιουργία ζώνης εξασθένησης στις υπολογισμένες συχνότητες.

Στο Σχήμα 35, απεικονίζεται η πειραματική δυναμική απόκριση των δύο κατασκευών (με και χωρίς DDA), όπου είναι εμφανής η διεύρυνση της ζώνης εξασθένησης μετά την προσθήκη του DDA. Συγκρίνοντας τις αναμενόμενες ζώνες διακοπής με τις αντίστοιχες πειραματικές συμπεραίνεται ότι το μέγεθος είναι παρόμοιο, ενώ παρατηρείται μια μετατόπιση (~1.5Hz) στις χαμηλότερες συχνότητες και για τις δύο αλυσίδες. Συνολικά, η δυναμική απόκριση των προτεινόμενων πειραματικών διατάξεων επαληθεύει τους αναλυτικούς υπολογισμούς, επιδεικνύοντας κατά αυτόν τον τρόπο τις δυνατότητες των ενισχυμένων με DDA φωνονικών μεταϋλικών.

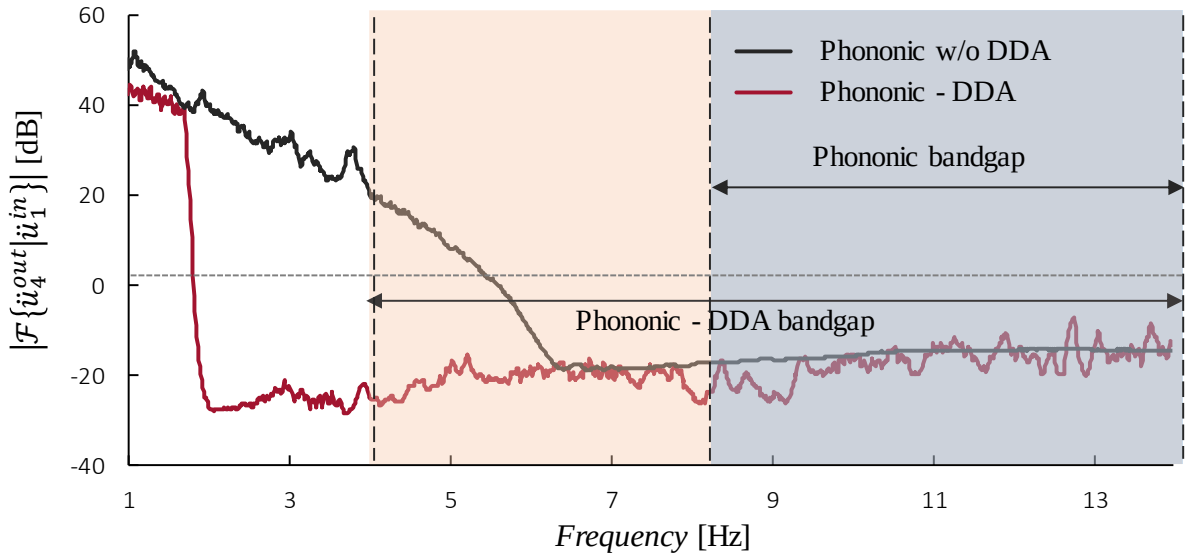

Σχήμα 35: Συχνοτικό περιεχόμενο της απόκρισης του φωνονικού μεταϋλικού με και χωρίς DDA $\left(\varphi = 60^{\circ}\right)$ *για ένα πλέγμα τεσσάρων (4) μοναδιαίων κελιών. Η μέγιστη επιτάχυνση κάθε μονάδας* p *συμβολίζεται ως max* $\ddot{u}_p^L$.

Στην περίπτωση του τοπικά συντονιζόμενου μεταϋλικού, σε αντιστοιχία με την περίπτωση του φωνονικού κρυστάλλου, η σύγκριση μεταξύ της πειραματικής και της αναλυτικά εκτιμώμενης συχνοτικής απόκρισης παρουσιάζεται στο Σχήμα 36, ενώ τα αποτελέσματα της πειραματικής διερεύνησης με και χωρίς DDA στο Σχήμα 37. Πράγματι, η πειραματική με την αναλυτική καμπύλη είναι σε σχετική συμφωνία, λαμβάνοντας υπόψιν ότι η απόσβεση λόγω των τριβών στην πειραματική διάταξη δεν μπορεί να μετρηθεί με ακρίβεια και είναι μεταβαλλόμενη ανάλογα με την διέγερση.

Η αρχική τοπικά συντονιζόμενη αλυσίδα (χωρίς DDA) παρουσιάζει ζώνη εξασθένησης μεταξύ 7.5 και 10.1 Hz, η οποία είναι σύμφωνη με τη θεωρητική εκτίμηση, ενώ η ενισχυμένη με DDA αλυσίδα, εμφανίζει ζώνη εξασθένησης μεταξύ 4.5 και 9.5 Hz, η οποία είναι ελαφρώς μικρότερη σε σύγκριση με τις θεωρητικές εκτιμήσεις (σκιασμένες περιοχές στο Σχήμα 37).

Η ενισχυμένη με DDA διάταξη επαληθεύει τα πλεονεκτήματα της εφαρμογής του ενισχυτή DDA, όπως περιεγράφηκε σε προηγούμενες παραγράφους, καθώς επιτυγχάνονται μεγαλύτερες ζώνες διακοπής σε σύγκριση με τις συμβατικές διατάξεις LR. Ταυτόχρονα, μετριάζονται σημαντικά τα πλάτη των κορυφών συντονισμού, πριν και μετά τη ζώνη εξασθένησης.

Συμπεραίνεται ότι ο μηχανισμός αδρανειακής ενίσχυσης DDA μπορεί να χρησιμοποιηθεί για τη βελτίωση των δυναμικών ιδιοτήτων μεταϋλικών καθώς και άλλων συστημάτων απορρόφησης κραδασμών. Άλλες πτυχές εφαρμογής του προτεινόμενου μηχανισμού για σεισμική προστασία κατασκευών, συλλογή ενέργειας ή ακουστική απορρόφηση, αποτελούν θέματα με ιδιαίτερο ερευνητικό ενδιαφέρον για το μέλλον.

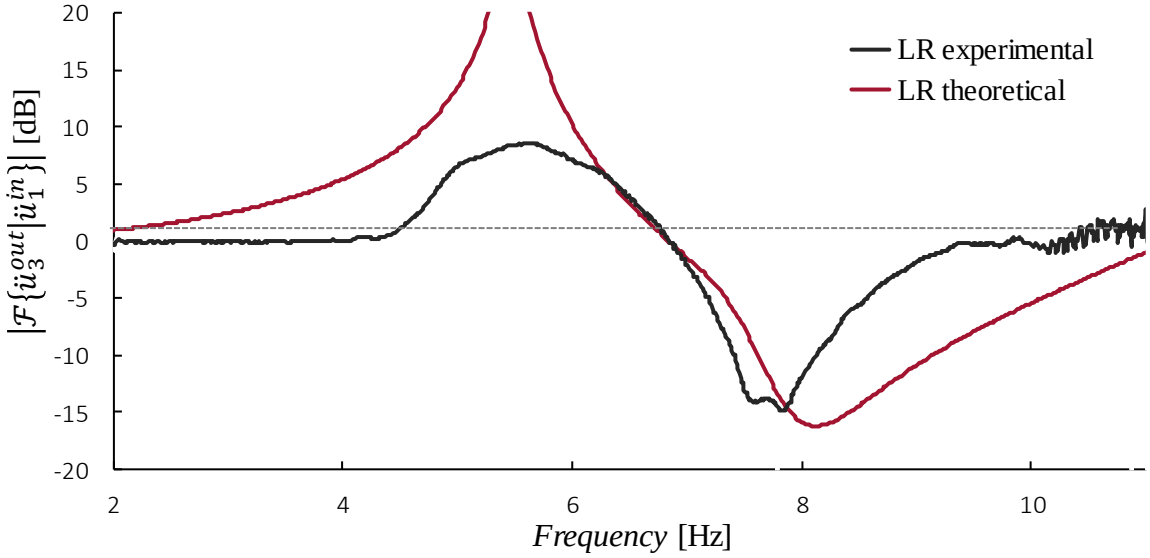

Σχήμα 36: Σύγκριση μεταξύ της πειραματικής και της αναλυτικά εκτιμώμενης συχνοτικής απόκρισης $\mathcal{F}\left\{\ddot{u}_3^{out} / \ddot{u}_1^{in}\right\}$ για το μεταϋλικό τριών (3) μοναδιαίων κελιών της τοπικά συντονιζόμενης δομής.

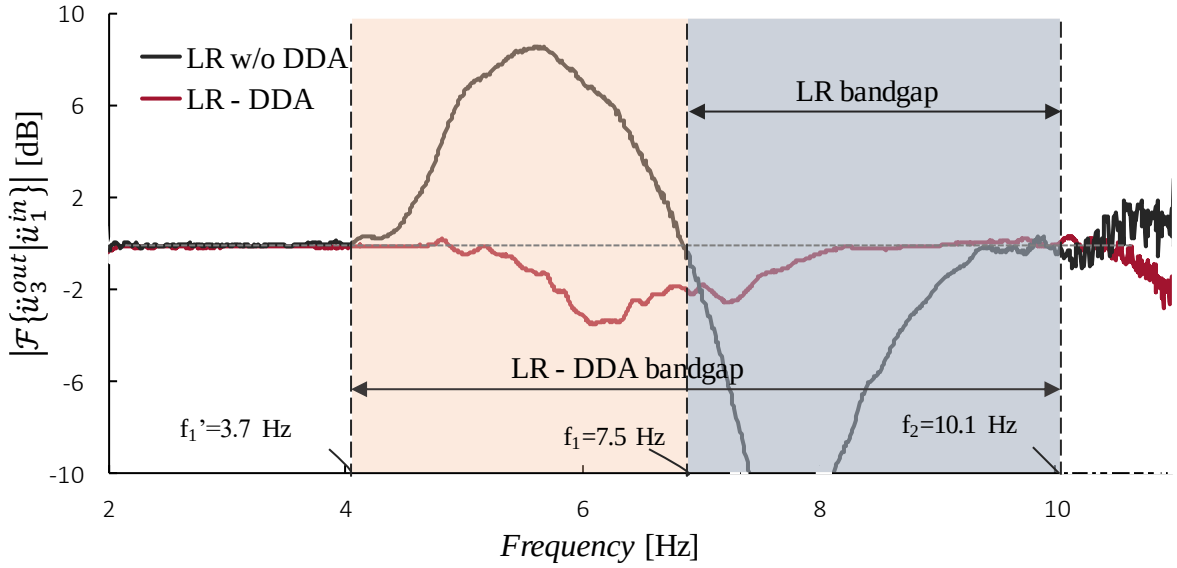

Σχήμα 37: Συχνοτικό περιεχόμενο της απόκρισης του τοπικά συντονιζόμενου μεταϋλικού με και χωρίς DDA $\left(\varphi = 55^{\circ}\right)$ για ένα πλέγμα τριών (3) μοναδιαίων κελιών. Η μέγιστη επιτάχυνση κάθε μονάδας p συμβολίζεται ως max $\ddot{u}_p^L$.

4.7 Σύνοψη

Εν κατακλείδι, η παρούσα μελέτη παρουσιάζει έναν νέο μηχανισμό δυναμικής ενίσχυσης, το DDA, ο οποίος αποσκοπεί στην αύξηση της αδράνειας και την ενίσχυση των δυναμικών ιδιοτήτων των ταλαντευόμενων κατασκευών. Η κύρια καινοτομία της εφαρμογής έγκειται στην απλή γεωμετρία του προτεινόμενου συστήματος - η ταλαντευόμενη μάζα είναι στερεωμένη σε έναν άκαμπτο σύνδεσμο που αυξάνει την αδράνεια προς την κατεύθυνση της κίνησης, αναγκάζοντας τον ταλαντωτή να κινηθεί μέσω μιας προκαθορισμένης περιμετρικής διαδρομής.

Παρουσιάζεται ένα αναλυτικό πλαίσιο, το οποίο παρέχει τη θεωρία και τη μαθηματική διατύπωση του μηχανισμού DDA. Ως επόμενο βήμα, επαληθεύεται η απόδοση του μηχανισμού που αναπτύχθηκε και επικυρώνονται τα θεωρητικά προσομοιώματα μέσω πειραματικών δοκιμών σε κατακόρυφη σεισμική τράπεζα. Τα αποτελέσματα δείχνουν μια συνολική συμφωνία μεταξύ των μετρήσεων και των αναλυτικών υπολογισμών, τοποθετώντας έτσι την ιδέα ως μια ρεαλιστική λύση αδρανειακής ενίσχυσης.

Στη συνέχεια, ο ενισχυτής DDA εφαρμόζεται σε φωνονικούς κρυστάλλους και τοπικά συντονιζόμενα μεταϋλικά με σκοπό την βελτίωση των δυναμικών τους ιδιοτήτων. Πραγματοποιούνται αναλυτικές, αριθμητικές αλλά και πειραματικές αναλύσεις σε υπό κλίμακα πρωτότυπα και αποδεικνύεται η δυνατότητα του μηχανισμού να αυξάνει το εύρος της ζώνης εξασθένησης. Κατά συνέπεια, φαίνεται

ότι τα μεταϋλικά με DDA μπορούν να αποτελέσουν μία καινοτόμα λύση για τον μετριασμό ταλαντώσεων χαμηλής συχνότητας.

5. Συμπεράσματα

Στην παρούσα διδακτορική διατριβή, μελετήθηκαν νέες στρατηγικές μείωσης του χαμηλόσυχνου θορύβου και ελέγχου ταλαντώσεων, προτείνοντας καινοτόμες διατάξεις βασισμένες σε συστήματα μεταϋλικών, προηγμένους αποσβεστήρες αρνητικής στιβαρότητας και μηχανισμούς ενίσχυσης. Τα κύρια θέματα που διερευνήθηκαν είναι τα εξής:

- Ο σχεδιασμός ακουστικών στηρίξεων για την βελτίωση των ηχομονωτικών δυνατοτήτων πετασμάτων με διατάξεις αρνητικής στιβαρότητας και αδρανειακούς ενισχυτές.
- Ο σχεδιασμός πετασμάτων τύπου σάντουιτς με χαμηλόσυχνες ηχομονωτικές δυνατότητες με βάση τη θεώρηση του μεταϋλικού KDamper – IAM.
- Οι δυνατότητες του καινοτόμου μηχανισμού ενίσχυσης, DDA, και η ενσωμάτωση του σε φωνονικούς κρυστάλλους και ακουστικά μεταϋλικά, με σκοπό την χρήση του σε ακουστικές, αντισεισμικές και αντικραδασμικές εφαρμογές.

Τα κύρια συμπεράσματα που εξάγονται από την παρούσα διδακτορική διατριβή συνοψίζονται στα ακόλουθα:

i. Η εφαρμογή του μηχανισμού KD-IAM ως σύστημα στήριξης ακουστικών πετασμάτων, δημιουργεί μια ευρεία και βαθιά ζώνη σίγασης.

ii. Το μεταϋλικό μορφής KD-IAM έχε εξαιρετική συμπεριφορά στις χαμηλές συχνότητες δημιουργώντας βαθιές και ευρείες ζώνες εξασθένησης δίχως να απαιτείται μεγάλος αριθμός μοναδιαίων κελιών.

iii. Η παραγωγή πετασμάτων τύπου σάντουιτς, βασισμένα στη θεωρία του μεταϋλικού KD-IAM, είναι εφικτή, χωρίς την απαίτηση περίπλοκών και κοστοβόρων γεωμετριών με την χρήση τρισδιάστατων εκτυπωτών .

iv. Η προσθήκη του μηχανισμού ενίσχυσης αδράνειας (IAM) στο σύστημα στήριξης KDamper έχει ευεργετικά αποτελέσματα στη δυναμική απόκριση των κατασκευών στο πεδίο των χαμηλών συχνοτήτων.

v. Ο προτεινόμενος μηχανισμός ενίσχυσης αδράνειας, DDA αυξάνει την αδράνεια ενός συστήματος προς την επιθυμητή κατεύθυνση κίνησης. Η κύρια καινοτομία της διάταξης έγκειται στην απλότητα του συστήματος.

vi. Η εφαρμογή του DDA σε δομές φωνονικών κρυστάλλων έδειξε τόσο θεωρητικά όσο και πειραματικά αυξημένες ζώνες εξασθένησης, δίνοντας τη δυνατότητα μείωσης των απαιτήσεων για μεγάλες μάζες.

vii. Η ενσωμάτωση του ενισχυτή DDA στη συντονιζόμενη μάζα ακουστικών μεταϋλικών βελτιώνει το εύρος της ζώνης εξασθένησης. Αριθμητικά και πειραματικά αποτελέσματα έδειξαν ότι το κύριο μειονέκτημα της ενσωμάτωσης στου ενισχυτή σε τοπικά συντονιζόμενες δομές είναι η μείωση του βάθους της ζώνης εξασθένησης.

viii. Ο προκαταρκτικός σχεδιασμός περιοδικών διατάξεων για την αντιμετώπιση επιφανειακών σεισμικών κυμάτων βασισμένων στο βελτιωμένο μεταϋλικό με DDA έδειξε ότι ρεαλιστικές διατάξεις μπορούν να κατασκευασθούν και να χρησιμοποιηθούν για την προστασία διαφόρων κατασκευών.

ix. Η ανάπτυξη διατάξεων (π.χ. πετασμάτων, πλωτών δαπέδων, ψευδοροφών κλπ.) με σκοπό την χαμηλόσυχνη ακουστική μόνωση βασισμένα σε δομές ενισχυμένων με DDA φωνονικών κρυστάλλων και ακουστικών μεταϋλικών είναι εφικτή, συνεπώς περεταίρω διερεύνηση απαιτείται προς την κατεύθυνση αυτή.